Automatic Design of Concrete Structures Using a Strut & Tie Approach

Lee Scott Cunningham

A thesis submitted for the degree of

Doctor of Philosophy

Department of Civil Engineering

University of Glasgow

June 2000

This thesis is dedicated to my grandfather, James McKeirnan.

Στο ονομα του Θεου,
που ειναι, που ηταν και που
θα ειναι, αλφα και ωμεγα

In the name of God,
who is, and was and
is to come, A and Ω

Contents

Chapter 8
Strut & Tie Design

Chapter 9
Conclusions

Acknowledgements

Firstly I wish to express sincere thanks to my supervisor, Dr P.Bhatt, for his valuable supervision and guidance throughout the course of this work.

I would like to thank Prof. N.Bicanic, the Head of the Department, for making the facilities available. I am grateful to Dr A.Agar, Dr C.Pearce and Dr D.Phillips for their useful discussions and advice.

I am most grateful to the staff of the structural laboratory, especially: Mr R.Boyd, Mr A.Burnett, Mr I.Gardner, Mr R.McCaskie, Miss J.McCulloch, Mr S.McLean, Mr W.Thomson, and Mr A.Yuill, for all their assistance in preparing and testing the models.

For all his assistance with computing facilities, I wish to thank Mr K.McColl. Thanks are also due to Dr A.Bensalem, for his early and useful advice on programming issues.

To my friends and colleagues, Dr Xiaowei Gao, Dr Hashim Musavi, Dr Mohamed Rouainia and Dr Ben Zhang, I wish to express thanks for our discussions and friendship.

I would like to express thanks to all my friends and colleagues in the department, especially the following: Ali Al-Nuaimi, Francesco Basile, Igor Bojanic, Alan Cuthbertson, Graeme Forbes, Domenico Gallipoli, Vassiliki Kochila, Boon-Tiong Lim, Andy Macauley, Andrey Shvidchenko, Xiao-ya Tao. Their friendship will be forever maintained.

Special thanks are due to my parents for their vital encouragement and support throughout all the years of my studies. Finally, I wish to thank God for giving me strength and lighting my path.

Summary

The major part of the work presented in this thesis is an investigation of the strut and tie method for designing 2-D in-plane, reinforced concrete structures. Two important issues relating to this method are addressed. Firstly, the issue of visualising an appropriate strut and tie model is dealt with. In many situations it may be difficult to visualise an appropriate model for a given structural system. Here, a convenient method of visualising strut and tie models is presented. Using elastic finite element analysis, low stressed parts of a structure are removed in a step by step process until the main stress paths, which represent the ties and struts, are defined.

The second important issue to be addressed is that of serviceability of the designed structure because the strut and tie model naturally represents a great departure from the elastic stress distribution. Since the strut-tie model is used to design for the ultimate load situation, it is necessary to assess the suitability of the same model in relation to serviceability characteristics of the resulting design. It is important that ductility of the structure should be maintained at ultimate loads while avoiding excessive deflections and cracking at service loads. A wide variety of structures were designed, and to assess the performance of each design, non-linear finite element analysis was used. Verification of some of the numerical results was carried out through physical testing in the laboratory which also allowed the serviceability behaviour of the structures to be assessed.. The test program comprised of three corbel joints and two frame corner joints.

It was concluded that design from the strut and tie method can produce adequate performance both at service and ultimate loads. In terms of ultimate load prediction, the strut-tie method can produce results of comparable accuracy to non-linear finite element analysis

As an interesting extension to the work here, the same visualisation process is also applied to the direct design of reinforced concrete slabs and the resulting designs are tested numerically using non-linear finite element analysis.

It was found that application of the visualisation process to the direct design of slabs can result in increases of steel provision, over that which results from the initial elastic pattern. However, in areas where the steel can be orientated along the direction of the principal moment paths, a reduction in steel provision can occur. Where a pre-determined steel layout is envisaged, the visualisation process can prove useful by directing the load paths accordingly.

Notation

A_s	Area of steel
A_{sx}	Area of steel in x-direction
A_{sy}	Area of steel in y-direction
B	Shear retention factor at cracking strain of concrete
[B]	Strain matrix
C_1, C_2	Tension stiffening coefficients
C	Strut
[D]	Elasticity matrix
[D']	Instantaneous elasticity matrix
$[D_{cr}]$	Rigidity inplane matrix for cracked concrete
E	Young's Modulus
E_c	Young's Modulus of concrete
E_i	Instantaneous Young's Modulus of concrete
E_s	Young's Modulus of steel
f_c	Effective compressive strength of concrete
f_c'	Cylinder compressive strength of concrete
f_{cc}	Intermediate yield surface strength of concrete
f_{cd}	Design compressive strength of concrete
f_{cu}	Cube compressive strength of concrete
f_t	Tensile strength of concrete
f_y	Tensile strength of steel
{F}	Nodal forces vector in Cartesian coords
{F'}	Nodal forces vector in local coord system, (n,t)
G	Shear modulus
H	Strain hardening parameter for steel
[K]	Stiffness matrix
M	Bending Moment
M_1, M_2	Principal Moments
M_d	Design Moment
M_p	Plastic Moment
M_x, M_y, M_{xy}	Applied Moments at in point in Cartesian coords
M_n, M_t, M_{nt}	Applied Moments at a point in local coord system (n,t)
M_x*, M_y*	Design Moments in x and y directions
M_u	Ultimate Moment
n_x, n_y, n_z	Applied inplane forces in Cartesian coords
N	Total number of nodal points
N_i	Shape function associated with node I.
P	Applied load
P_{cr}	First cracking load
P_d	Design load
P_u	Ultimate load
q	Intensity of uniformly distributed load
rr	Rejection Ratio

$1/R$	Curvature
$1/R_y$	Curvature at yield
$\{R\}$	Residual force vector
T	Tie
T_c	Concrete Tie
T_s	Steel Tie
[T]	Transformation matrix
u,v,w	Displacements at a point in x, y, z coords
u_0,v_0,w_0	Displacements at a point in the reference plane of a plate
x,y,z	Cartesian coord system
z_i	Distance from the reference plane to the centre of the ith layer
α	Design compressive strength factor
β	Shear retention factor
γ	Material factor
γ_{xz}, γ_{yz}	Shear strain components in Cartesian coords
$\{\delta\}$	Nodal displacement vector in Cartesian coords
ε_{cr}	Cracking strain of concrete
ε_o	Strain at peak stress of concrete
ε_x, ε_y, γ_{xy}	Strain components in Cartesian coords.
ε_x	Yield strain of steel
ζ	Variation of σ_e^{VM} from σ_{max}^{VM} in a structure
θ	Angle of the principal plane
θ_{cr}	Angle of crack with respect to x-axis
θ_x, θ_y	Rotations about x and y axes respectively
θ_n, θ_t	Rotations about n and t axes respectively
ν	Poisson's ratio
ξ, η	Local, (natural) coord system
ρ_x, ρ_y	Steel ratios in x and y directions
σ	Stress at a point
$\{\sigma\}$	Stress vector
σ_1, σ_2	Principal stresses
σ_p	Peak stress
σ_n	Normal Stress
σ_{oct}	Octahedral stress
σ_x, σ_y, σ_{xy}	Stress components in Cartesian coords.
σ_e^{VM}	Average von Mises stress in an element
σ_{max}^{VM}	Maximum von Mises stress in structure
τ_{oct}	Octahedral shear stress
τ_{xy}, τ_{xz}, τ_{xz}	The shear stresses in xy, xz, yz planes respectively
ϕ	Reinforcement bar diameter
ϕ_x, ϕ_y	Transverse shear rotations about xz and yz planes respectively
ϑ	Convergence Tolerance
ω	Degree of transverse reinforcement

Chapter 1

Introduction

The strut and tie method presents a rational and consistent approach to the design of all parts in a reinforced concrete structure. With this approach, the load carrying mechanism of the structure is represented by approximating the compressive stress fields as struts, and tensile stress fields as ties. The stress in the struts and ties should not exceed the allowable compressive strength of the concrete or yield strength of the steel respectively.

In the design of structures by this method there are two important issues to be addressed. The first issue is that of the visualisation of an appropriate strut-tie model for a given structural system. In many structures there may be various load paths available and hence no unique strut-tie model exists. The second issue is that of validity of chosen models in relation to the serviceability and ultimate load characteristics of the resulting structure. It is important that the ductility of the structure should be maintained by ensuring that crushing of concrete prior to yielding of steel is avoided at design loads. Since the strut and tie method involves a re-distribution of the stresses from the elastic pattern, it is necessary to determine the extent to which that re-distribution can be allowed for, while preserving the required performance from the structure. Details of strut-tie model theory are given in the next chapter.

The purpose of the work carried out here, is to address the two issues described above. In this work, visualisation of strut-tie models was carried out using elastic finite element analysis in combination with a procedure adapted from optimisation

techniques. The visualisation process is the subject of chapter 4. This process was also applied to the direct design of reinforced concrete slabs. Direct design theory is also discussed in chapter 4. The effect of using the redistributed stress fields which result from visualisation, on the slab performance at service and ultimate loads was assessed using an in-house non-linear finite element program. A full description of the finite element method and the material model used for analysis is given in chapters 3 and 5 respectively. The applicability of the visualisation process to direct design of slabs and the performance achieved is discussed in chapter 6

Using the visualisation process, strut-tie models were developed for a number of structures. The test series presented here consisted of deep beams, corbel joints and corner joints. Analysis of these structures was carried out using the same finite element program as described above. In addition, three corbel joints and two frame corner joints from the series were physically tested in the laboratory. Details of the test-series and results are given in chapters 7 and 8.

In this thesis, all references are listed in alphabetic order at the end. All figures are numbered according to the section in which they were first referenced.

Chapter 2

The Strut & Tie Method

2.1 Introduction

In the design of structural concrete, considerable effort has been spent on developing safe and efficient design procedures. There exists, however a difference in the level of accuracy employed in the design of each part of the structure, i.e. certain parts are designed from sound theoretical principles while other parts are designed from rules of thumb and past experience. Examples of this occur in the design of a column with a corbel joint. In this case, the column would be designed from bending theory, while the corbel may be designed from empirical formulae. Similarly, in the design of frame corner joints, the adjoining members of the frame are designed using bending theory, and the corner itself is treated empirically. All parts of the structure are of equal importance since their integrated behaviour will control the overall performance of the whole structure. It is therefore necessary to develop a consistent and unified approach to the design of members. The strut and tie method provides such a consistent method.

Strut and tie models are discrete representations of the actual stress fields which result from a given applied load and support conditions in a structure. The models represent the load carrying mechanism of a member by representing the flow of internal forces within a structure through struts (representing compressive stresses) and ties (representing tensile stresses).

2.2 Background

The precedent for the strut and tie model can be found in the early investigations of Ritter (1899) and Morsch (1909). In their work a truss analogy was applied to a cracked reinforced concrete beam (fig 2.2). The truss analogy assumes that the concrete is incapable of carrying tensile forces and hence the beam is made up of a number of concrete struts which are separated by diagonal cracks. The struts on interaction with the stirrups and longitudinal reinforcement form a plane truss with the following components:

- top and bottom reinforcement together with the concrete acting as top and bottom chords.
- stirrups acting as vertical tensile web members.
- concrete struts acting as diagonal compression web members.

Although aware of the possibility of varying angle inclination for the diagonals, Morsch proposed the use of a 45-degree truss in order to simplify design. Many national codes have incorporated design methods based on this model e.g. BS 8110, Eurocode 2, however, only certain parts of the structure are dealt with. The truss analogy was later modified by Leonhardt (1965) by taking into account the thickness of the web on the internal distribution of forces. In this work, it was found that the diagonal shear cracks could be inclined over a range of 30^{o}-45^{o} depending on the web thickness. The application of ultimate strength considerations to the truss model and the formulation of a scientific basis through plasticity theory of reinforced concrete was carried out by Thurliman et al. (1975), Muller (1976) and Marti (1985). This work furnished a logical design procedure but was limited to certain specific cases such as a deep beam. The strut and tie method has since been used for the analysis and design of deep beams and is adopted by national codes such as the Canadian Code, see Kong et al. (1977,1978,1990), Rogowsky & MacGregor (1986,1988), Cook and Mitchell (1988), Tan et al. (1997,1998). Similarly the strut-tie method has been used for the design and analysis of pile caps, see Adebar et. al (1990,1996), Siao (1993), Huang et al. (1998). The use of generalised strut tie models, able to be applied to all parts of the structure was proposed by Schlaich et al. (1987,1991). In this work the

elastic stress paths of the structure which have been realised through finite element analysis, are used to create the strut-tie model.

The visualisation of an appropriate strut and tie model is a significant problem. Development of the model is an iterative procedure and there is often no unique model associated with a given structure. Alshegir and Ramirez (1992a) developed a means of constructing the strut and tie models by means of elastic finite elements and an interactive computer graphics package. With this method the user is able to superimpose the strut or tie member over the elastic principal stress plot in order to develop the model. The model when completed, is automatically discretised and analysed as a truss in order to obtain the member forces for design. Examples of the application of this procedure were presented by Alshegir and Remirez (1992b) for the case of a pre-tensioned deep beam, and by Yun et al. (1994) with a corbel joint. This method is similar to that of Schlaich et al. in that the model is derived from the elastic principal stress pattern. The advantage of this method is that it makes for ease of computation since the model is automatically discretised and analysed and allows the model to be adjusted easily if members are found to be inadequate. However, one disadvantage of the system is that in many cases the main stress paths are not clear and hence any number of strut-tie models may result. In the system used in this thesis, the main stress paths are identified automatically, which then helps to identify a unique strut-tie model solution.

The procedure developed by Alshegir and Ramirez (1992a), was further extended by Yun (1997, 2000), by carrying out non-linear analysis of the plain concrete structure, and using the resulting principle stress flows to generate the strut and tie model. Hence, in this case, the strut-tie model is derived from a redistributed stress field. This may in some cases allow for ease of identification of main stress paths. However, by deviating from the elastic pattern, it must be ensured that the resulting strut-tie model does not exceed the ductility capacity of the structure.

2.3 Strut-Tie Terminology

2.3.1 Structure's B and D regions

Due to the presence of concentrated loads and changes in geometry, the stress and strain distributions within a structure are not always uniform. Schlaich et al (1988) proposed that the structure be categorised into one of two regions B or D depending on the strain distribution present. The respective B and D regions of a typical cantilever beam are shown in figure 2.3.1(a)

A 'B-region' is an area of the structure where the strain distribution is linear and stress distribution is smooth or undisturbed as can be seen from figure 2.3.1(a). The term 'B' stands for Bernoulli since in these regions Bernoulli hypothesis of plane sections remaining plane is assumed valid. In an uncracked section, the internal forces and stresses can be calculated from moment, shear and axial forces using well defined formulae from bending theory. In a cracked section, the truss model can be applied to derive the internal stresses.

Where the strain distribution in a structure becomes non-linear, the region is described as a 'D-region'. The term 'D' stands for discontinuity or disturbance in this case. Such a disturbance of stress distribution can occur at concentrated loads, corners, bends and openings. Some typical D-regions of a structure are shown in figure 2.3.1(b). Because the strain distribution is significantly non-linear in these regions, Bernoulli hypothesis is no longer valid. The design of D-regions has in the past been based upon rules of thumb and past experience. It is proposed to implement the strut and tie method in these regions as a means of rational design. Using the strut and tie model approach, the first stage of design would be to divide the structure up into its corresponding B and D regions. The truss model for the B-regions can be readily applied and only the strut and tie models for the D-regions need to be developed

2.3.2 Identification of D-regions

The identification of D-regions within the structure is relatively straightforward when examining the stress plot of a structure. At the D-region, the flow of the stresses becomes disturbed, the direction of stress flow will change rapidly and the stresses become non-uniform. The extent of a D-region boundary can be defined through application of the Saint Venant principle (see ref. 102). This states that the stress distribution at a point far removed from the point of load application will depend purely on the resultant force and not upon the actual distribution of forces. As a means of illustrating this procedure the column shown in figure 2.3.2(a) was analysed using elastic finite elements. The figure details the elastic principal stress plot. It can be clearly seen that the stresses around the concentrated load are high and have a steep gradient. The stresses gradually spread out moving away from the load point until a uniform state of stress is reached i.e. a B-region. The boundary between the B and D region can be assumed to lie at a distance h from the applied load, where h is equal to the width b of the column. The stress plots at sections 1-4 in the column illustrate the stress variation in each region. At sections 2 and 4, the stress is non-uniform, reaching a peak close to the point of load application. At sections 1 and 3, which are removed from the point of load application, the stress is uniform.

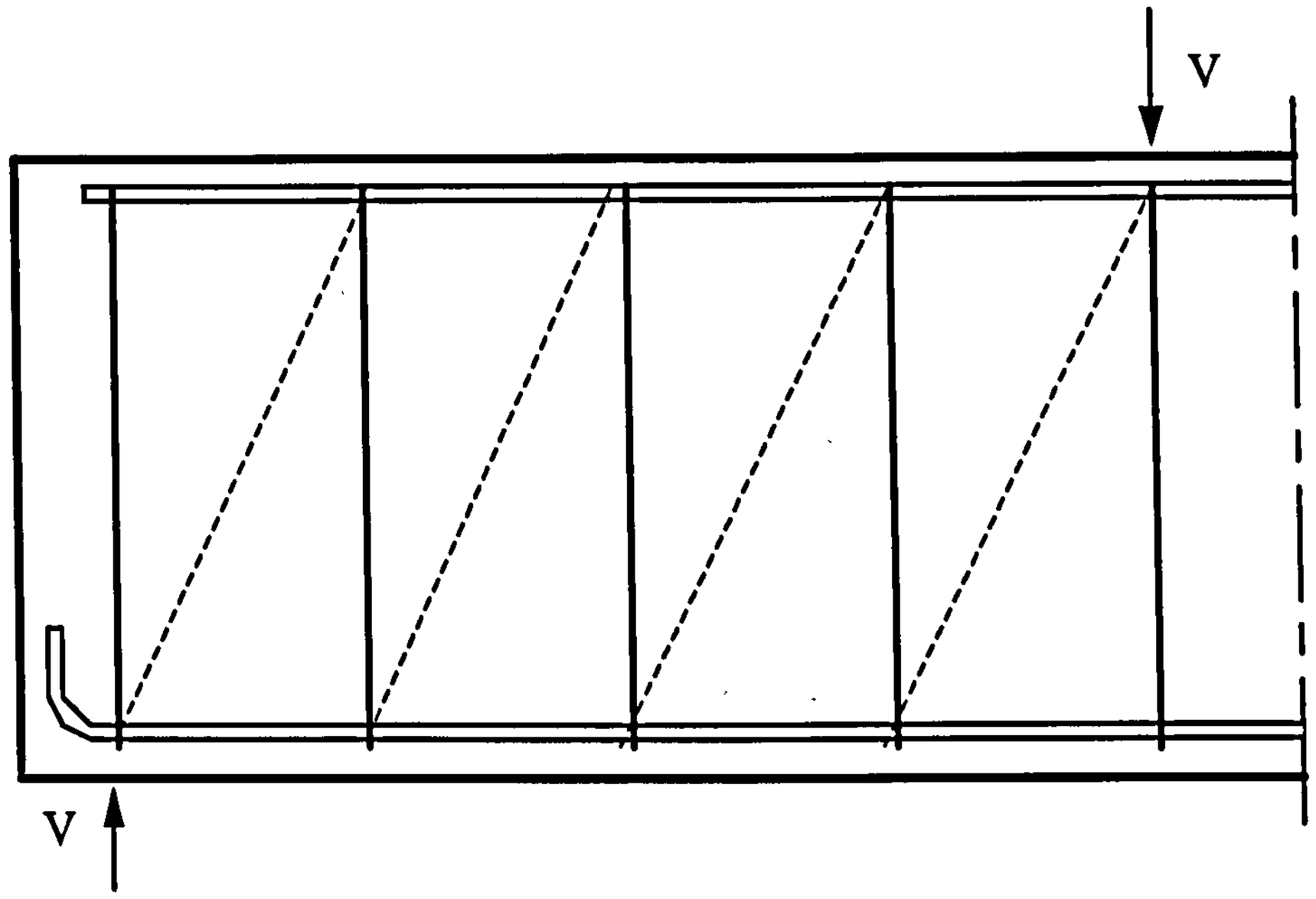

fig.2.2 Truss Analogy in Cracked Beam

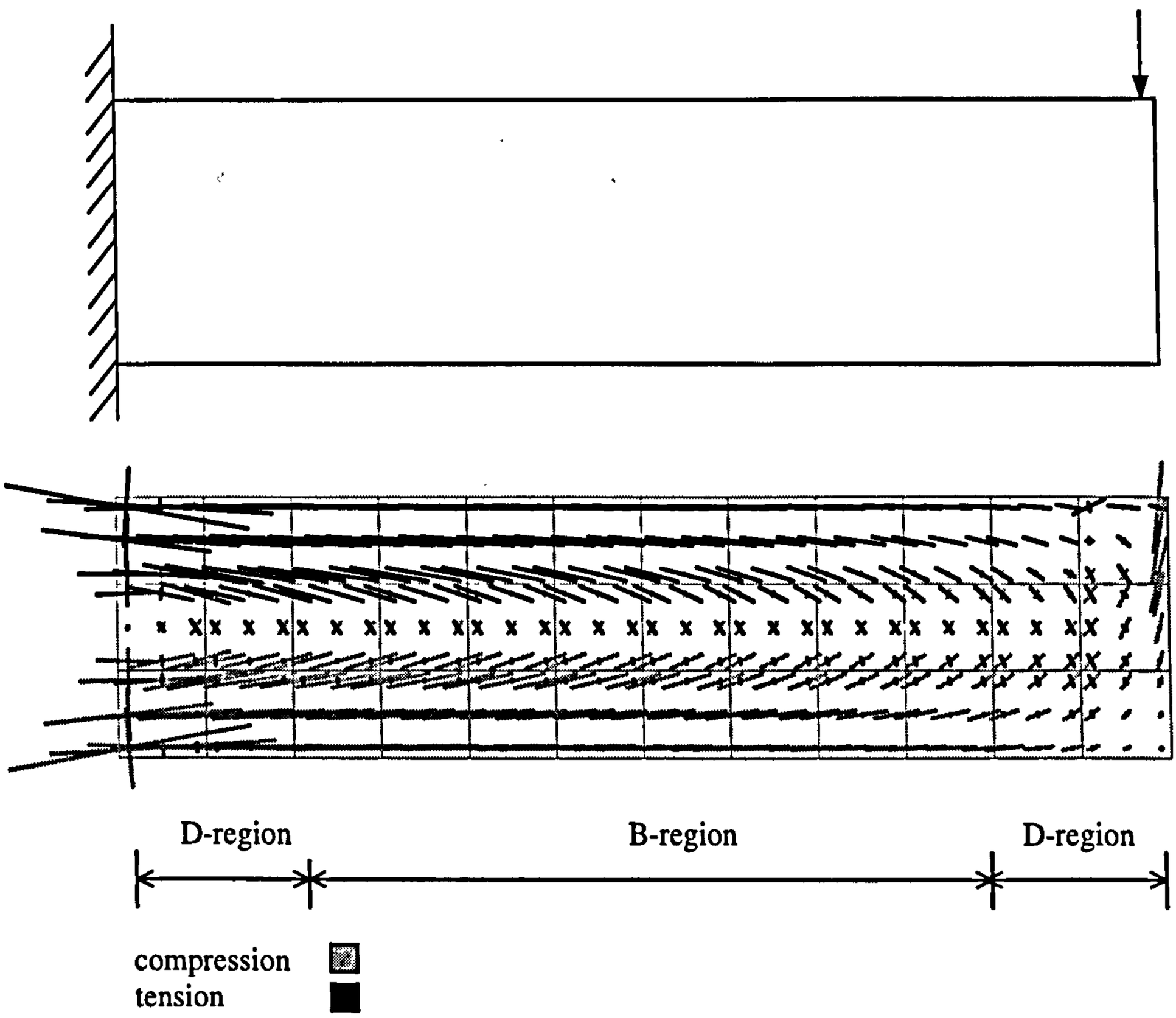

fig.2.3.1(a) Elastic Principal Stresses in a Cantilever Beam

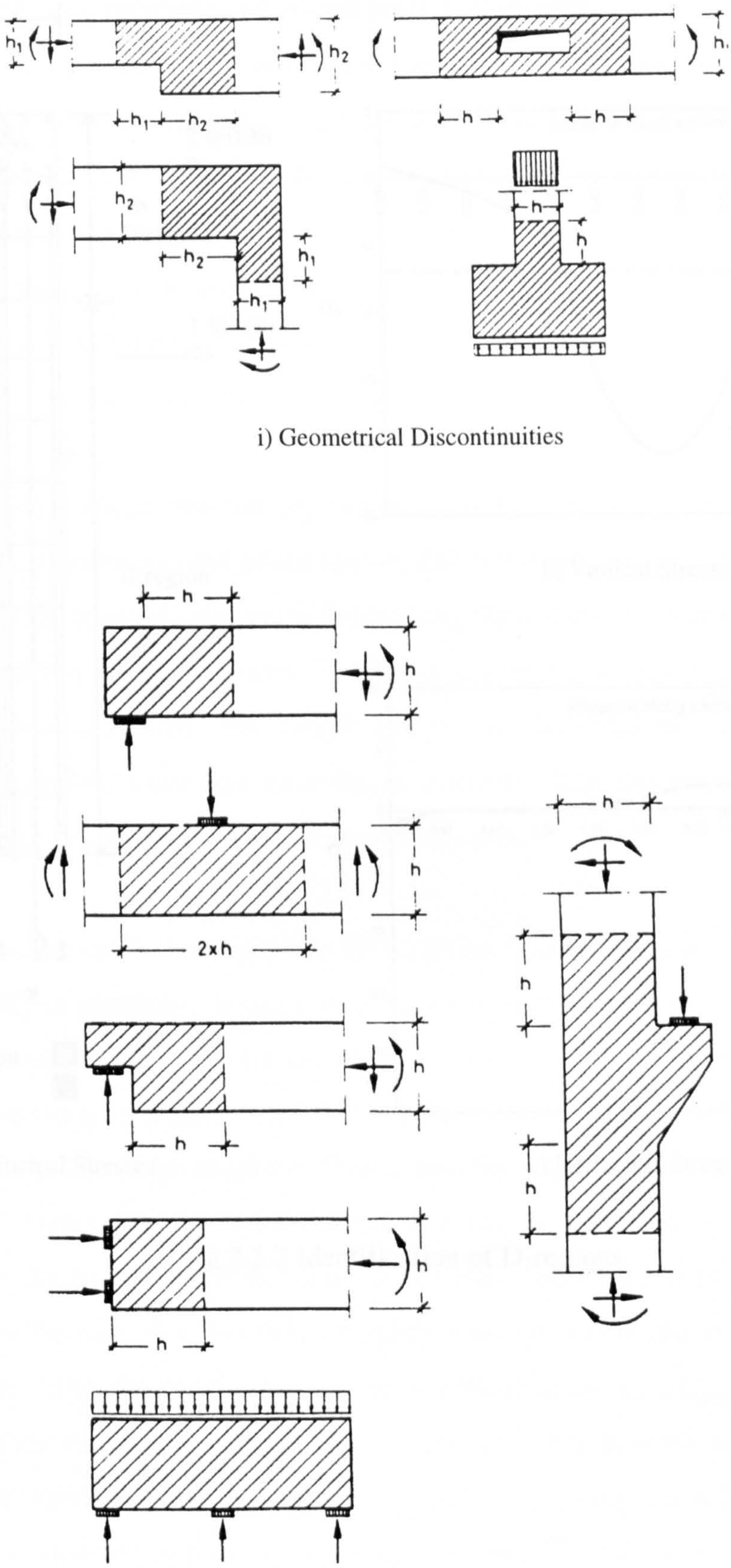

i) Geometrical Discontinuities

ii) Statical and/or Geometrical Discontinuities

fig.2.3.1(b) Typical D-regions

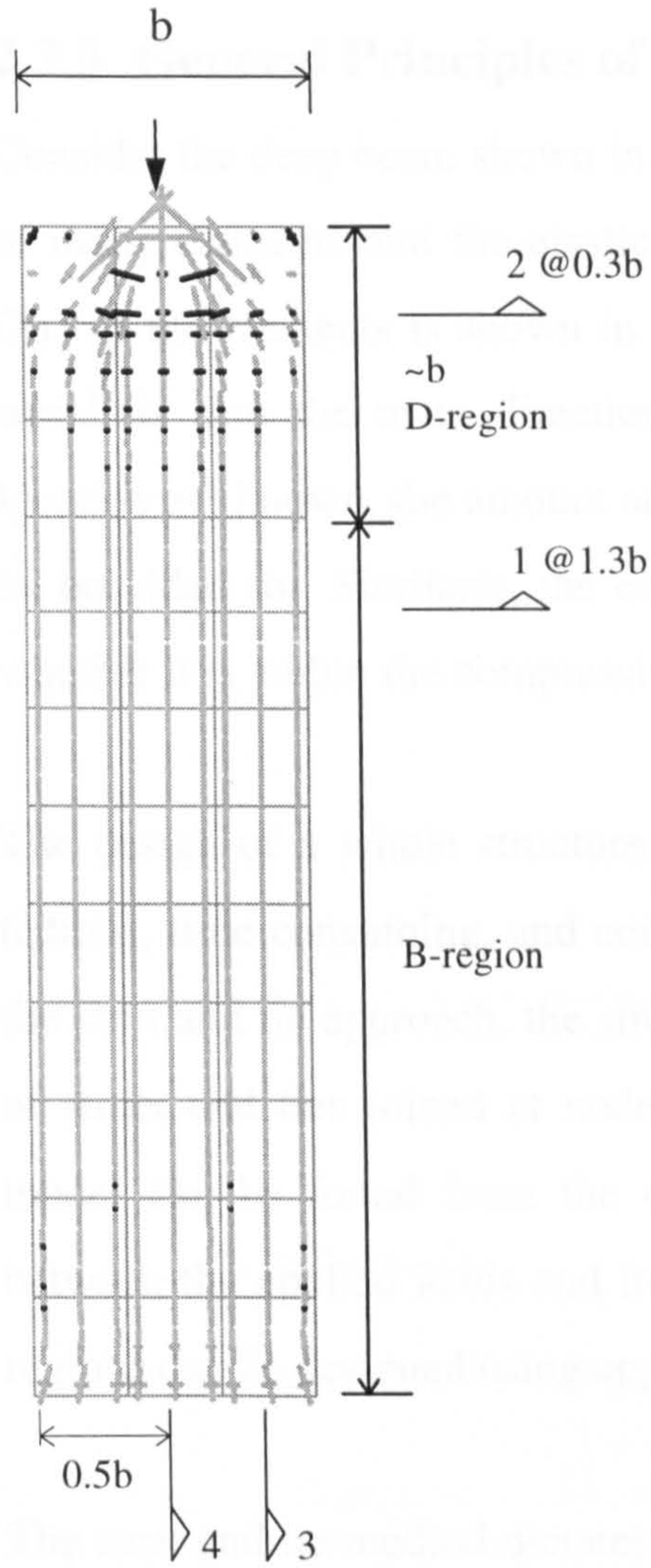

a) Elastic Principal Stresses

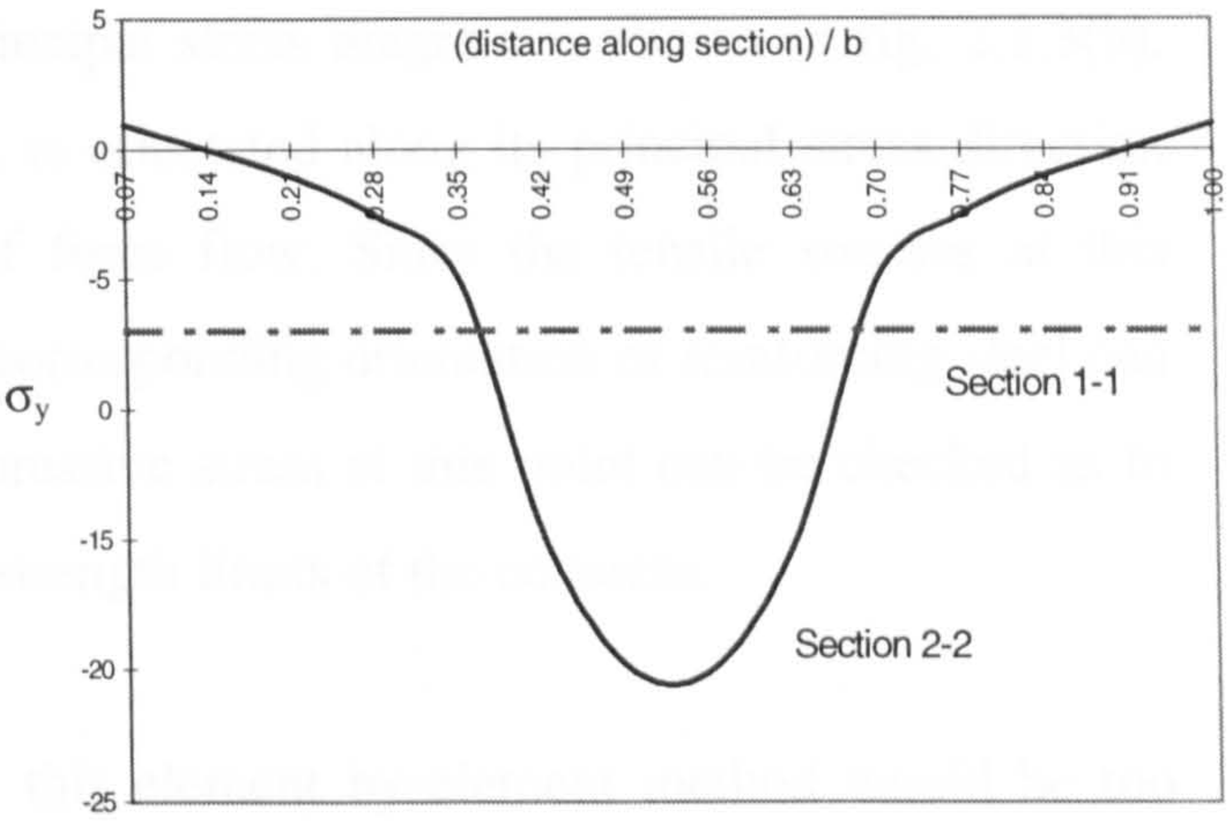

b) Vertical Stresses at 1&2

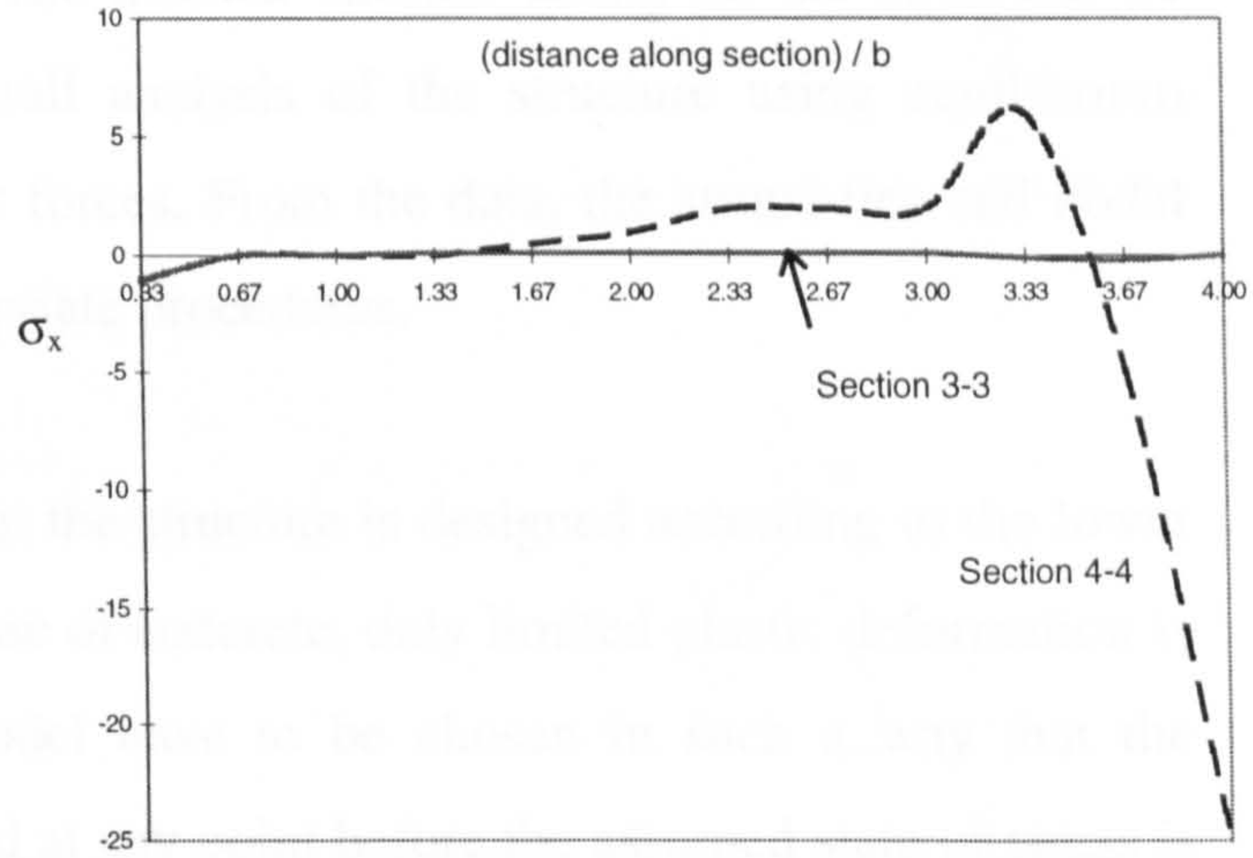

c) Horizontal Stresses at 3&4

fig.2.3.2 Identification of D-regions

2.3.3 General Principles of Strut and Tie model

Consider the deep beam shown in figure 2.3.3(a). The beam is discretised into a mesh of many elements and the elastic principal stress diagram is shown in fig. 2.3.3(b). One of the elements is shown in (a), is orientated along its principal stress direction which is also the main direction of force flow. Since the tensile stresses at this location are known, the amount and corresponding orientation of reinforcing steel can be provided for. Similarly, the compressive stress at this point can be checked as to whether it is within the compressive strength limits of the concrete.

The design of a whole structure by this element by element method would be too tedious, time consuming, and could lead to difficulties in reinforcement detailing. In the strut and tie approach, the stress fields along these paths are replaced by a system of struts and ties joined at nodes. The internal stresses acting on the strut and tie model can be found from the overall analysis of the structure using equilibrium between the applied loads and inner forces. From the data, the struts, ties and nodal regions can be designed using appropriate procedures.

The strut and tie method dictates that the structure is designed according to the lower bound theory of plasticity. In the case of concrete, only limited plastic deformation is permitted and the strut and tie model have to be chosen in such a way that the deformation capacity is not exceeded at any point before the assumed state of stress is reached in the rest of the structure. Thus a ductility requirement is imposed, which in the case of highly stressed regions of the structure, is fulfilled by adapting the struts and ties of the model to the direction of the main force flow resulting from elastic analysis. In the case of a normally or lightly stressed region, the strut/tie directions can deviate from the elastic pattern, by a limited amount, without exceeding the structure's ductility. As a result of this adaptability, it is possible to arrange the ties and hence reinforcement according to practical detailing considerations. In this process it is assumed that the designed structure can adapt itself to the assumed state of internal structural system, without excess demand on the ductility of the cross section.

Typical element subjected to normal and shear stresses

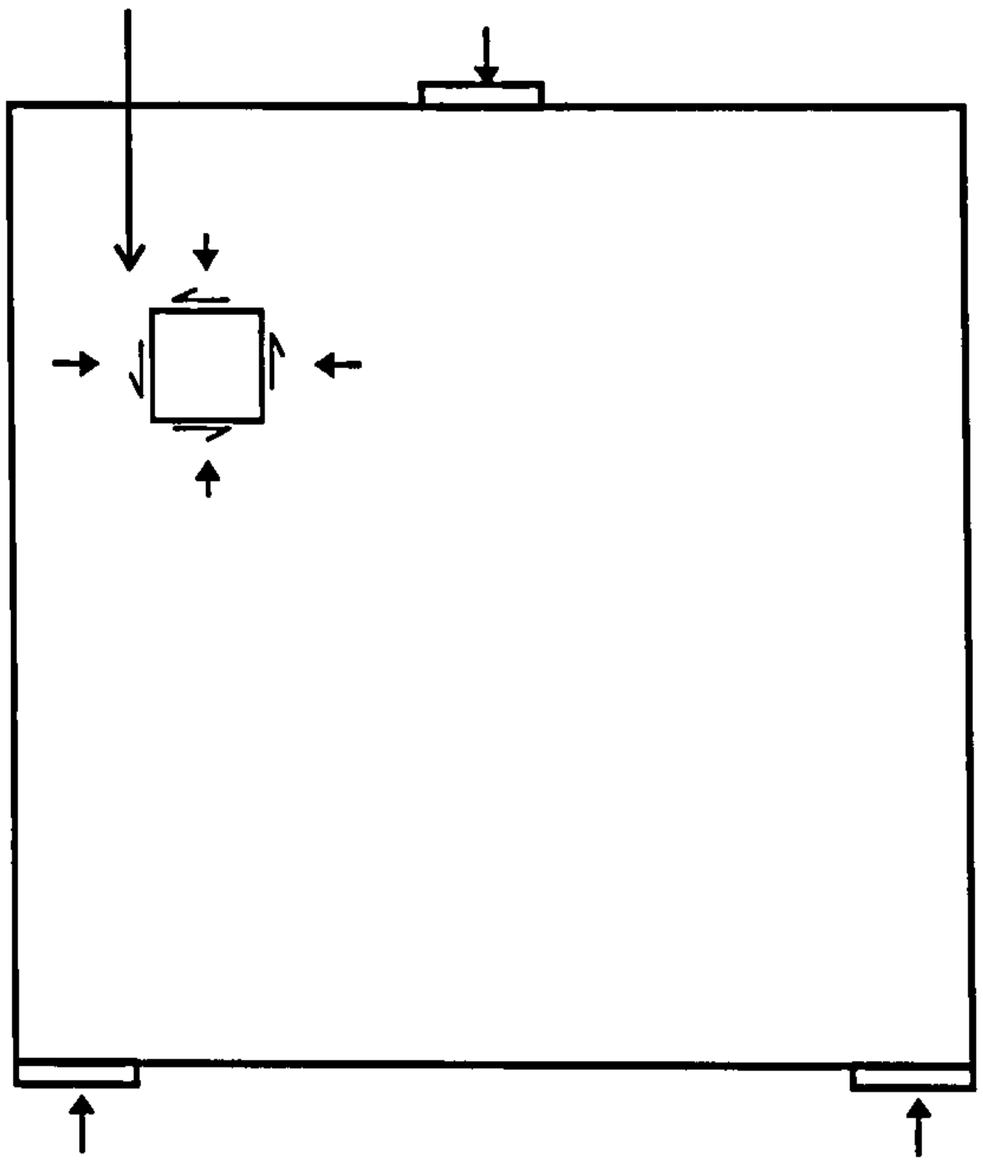

a) Deep beam

Element orientated along direction of main force flow

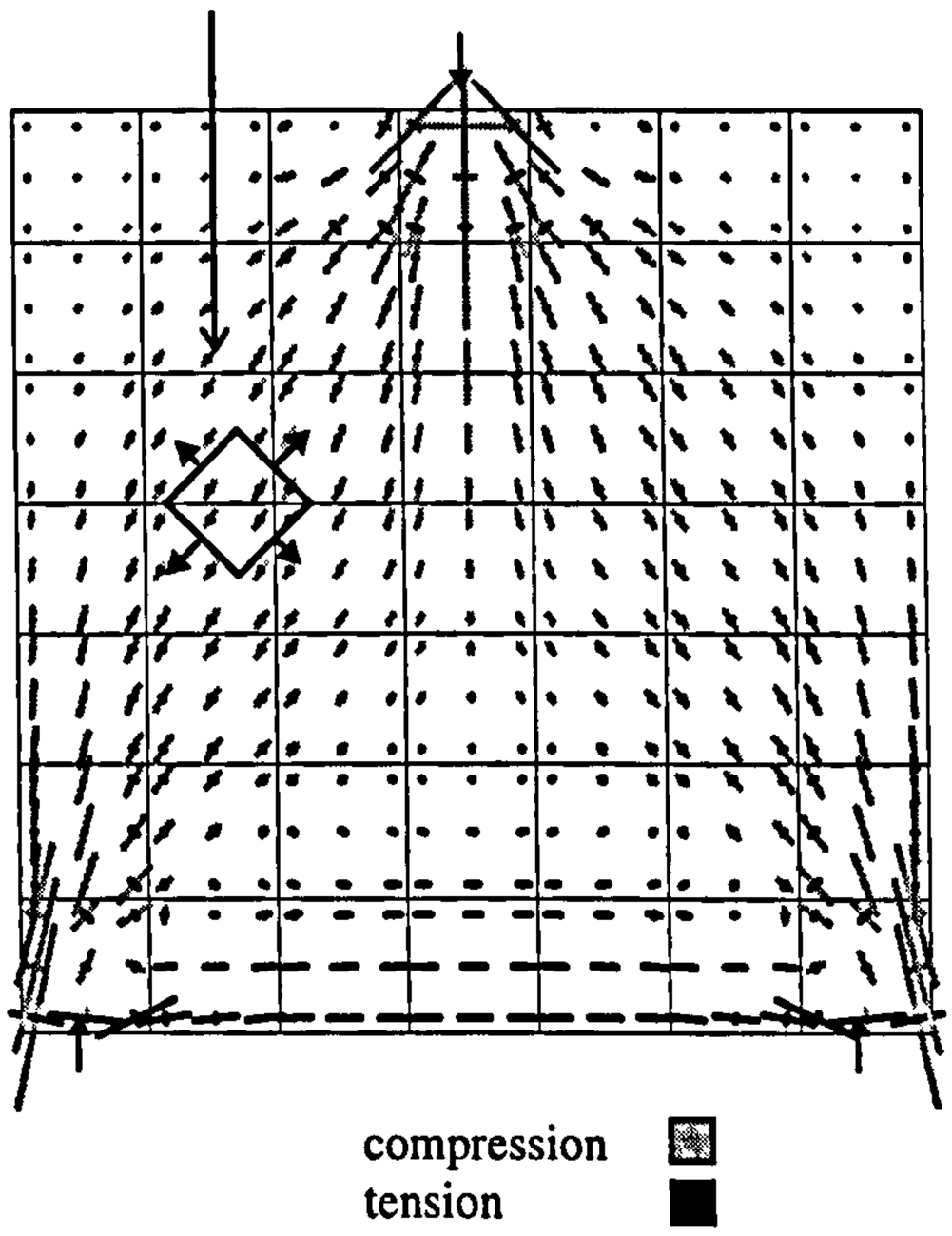

b) Elastic Principal Stresses

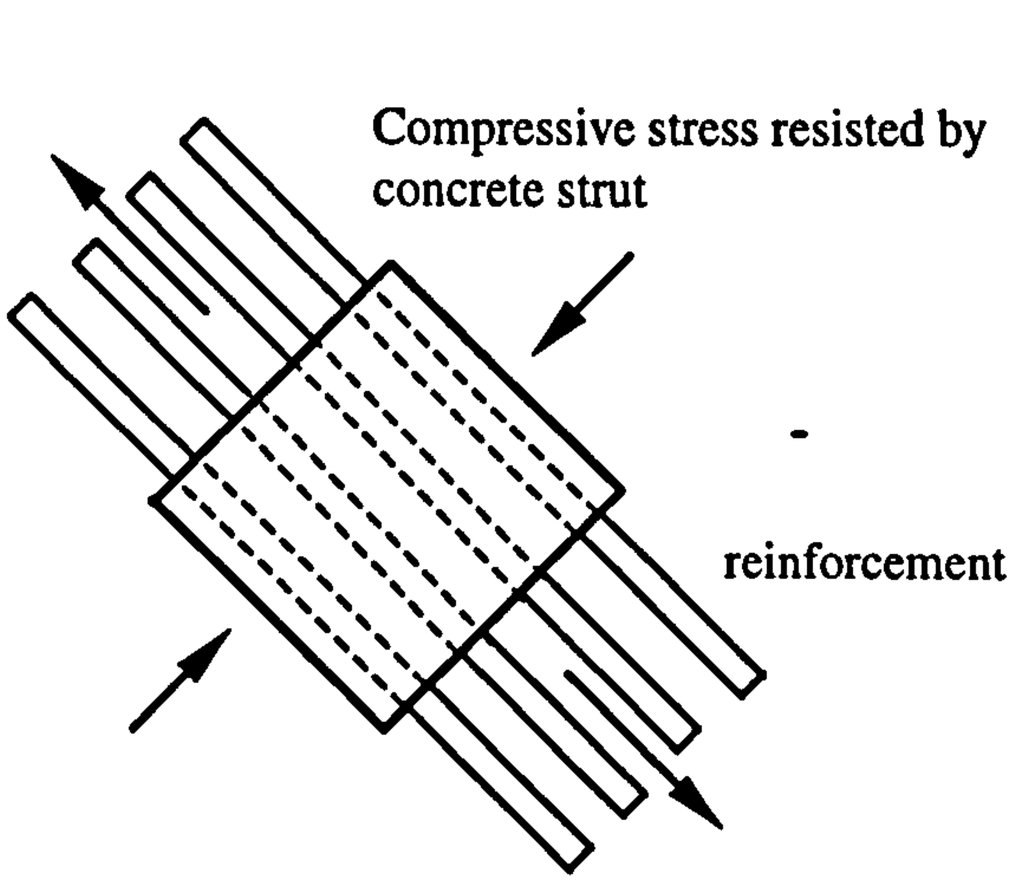

c) Typical Element Principal Stresses

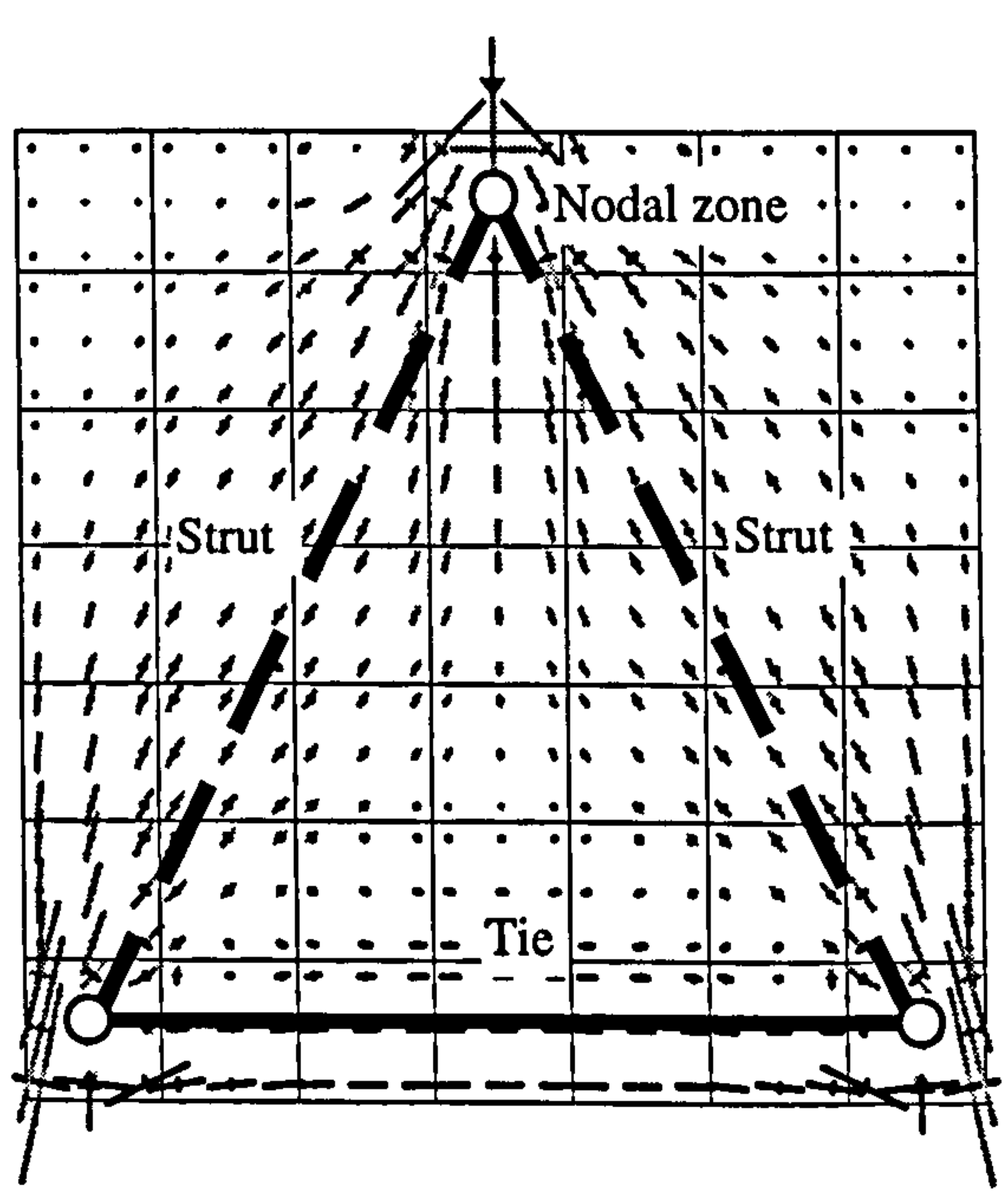

d) Strut and Tie Model

fig.2.3.3 General Principles of Strut-tie model

2.4 Dimensioning Struts, Ties and Nodes

2.4.1 General Procedure

Figures 2.4.1 a-c show some common stress fields occurring in structures and the resulting strut and tie model. The resulting stress fields were derived from elastic finite element analysis. Each of these strut-tie models can be analysed from statics and the resulting struts, ties and nodes can be dimensioned. The process of dimensioning involves sizing the individual struts and ties for the forces they carry but also ensuring the load transfer between these members by checking the nodal zones. Because nodal zones concentrate the flow of forces, choice of node detail will affect the strength of the struts bearing on to them and the ties anchored in them. For this reason it may be necessary to check whether a chosen strut-tie model is still valid after detailing.

2.4.2 Strut and Tie Types

The types of strut and ties to be dimensioned can be generally categorised as one of the following:

1. C_c: concrete struts in compression
2. T_c: concrete ties in tension without reinforcement
3. T_s: ties in tension with reinforcement

T_s can be considered as one dimensional elements between two nodes. The C_c and T_c are two-, or three- dimensional stress fields which tend to spread in between adjacent nodes. The spreading as illustrated by the bulging of the struts in fig. 2.4.1(b) can result in transverse tensile and compressive stresses. The effect of these transverse tensile stresses must be accounted for by adapting the failure criterion of the strut (i.e. reduction of design compressive strength) , or by adapting the strut-tie model (i.e. introduction of additional ties)

Some of the commonly occurring compression stress fields can be defined as one of three configurations:

1. *The fan shaped stress field*: this is an idealised stress field with negligible curvature and where transverse stresses are not developed (fig 2.4.2(a))
2. *The bottle shaped stress field*: in this type the bulging stress trajectories develop considerable transverse stresses. Such transverse stresses will initiate cracking and substantially reduce the compressive strength of the strut. Therefore, such areas need to be reinforced to take account of this.(fig 2.4.2(b))
3. *The prismatic or parallel stress field*: is the limit case of both a=0 and b/a=1, (fig 2.4.2(c)).

2.4.3 Node Types

Nodes are the regions of the model where the strut and ties meet. They are a simplified idealisation of reality. The introduction of a node implies an abrupt change in the direction of forces. In the actual reinforced concrete structure this deviation will take place over a specific length and width. The nodal types which occur in strut-tie models can be categorised as either *smeared* or *singular*. Examples of each of these node categories are shown in figures 2.4.1 (a-c).

At a nodal region where one of the struts or ties represents a concentrated stress field, the deviation of forces will tend to be locally concentrated. In this case, the resulting node is referred to as a *singular* node. Conversely, where wide compressive stress fields meet with other compressive stress fields or tensile ties, the deviation of forces will be spread or be smeared over a particular area. These type of nodes are referred to as *smeared* nodes. Within these two types of categories, there are in practice, four types of nodes which can be formed depending on the combination of adjoining struts (C) and ties (T):

1. *CCC-node*: nodes where the intersection of three compressive stress fields or struts occurs. Examples of this type of node are illustrated in figure 2.4.1(b). A schematic view of the stress fields in these nodes is given in figure 2.4.3(a).

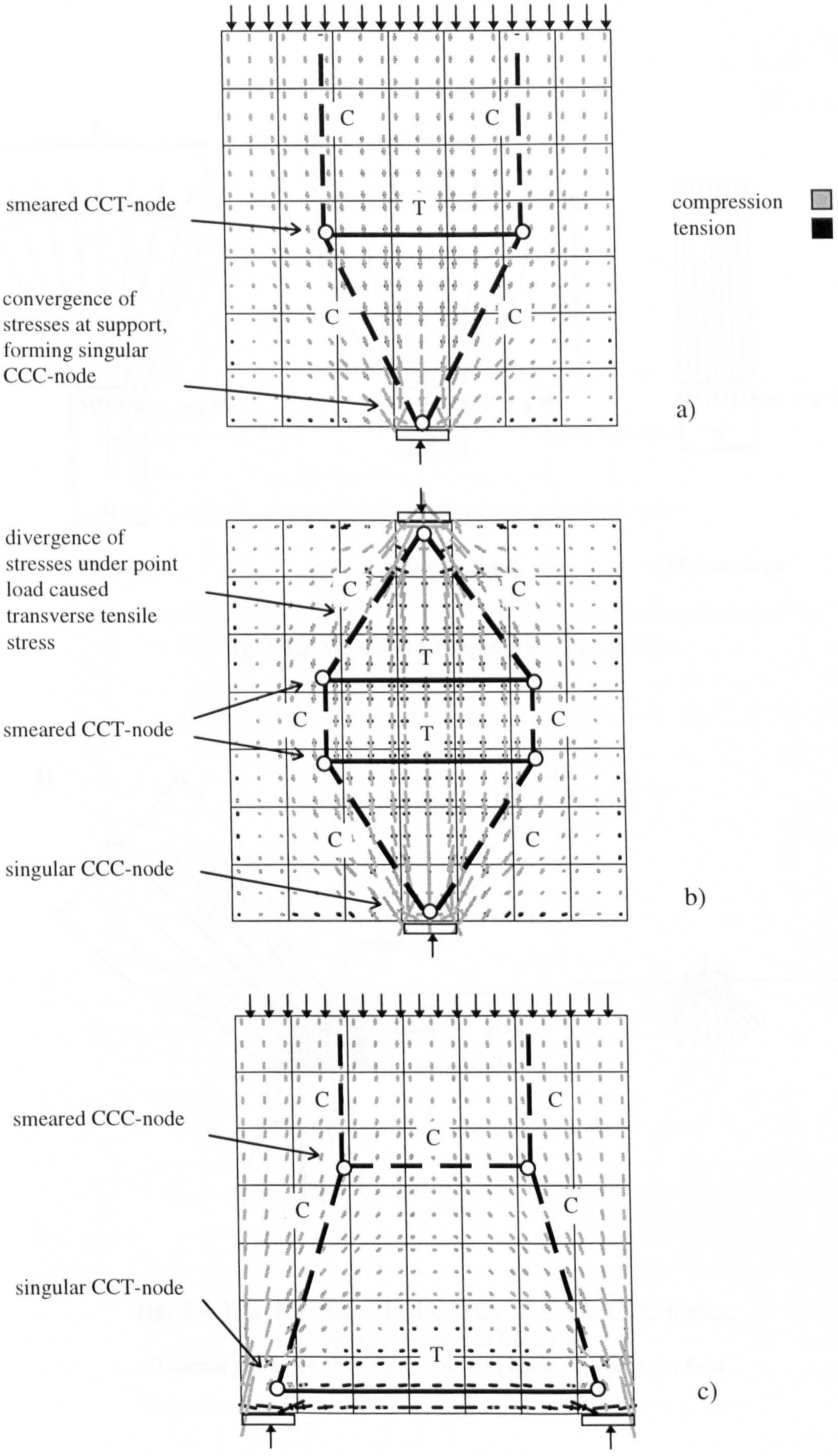

fig.2.4.1 Typical Stress Fields and Corresponding Strut-Tie Model

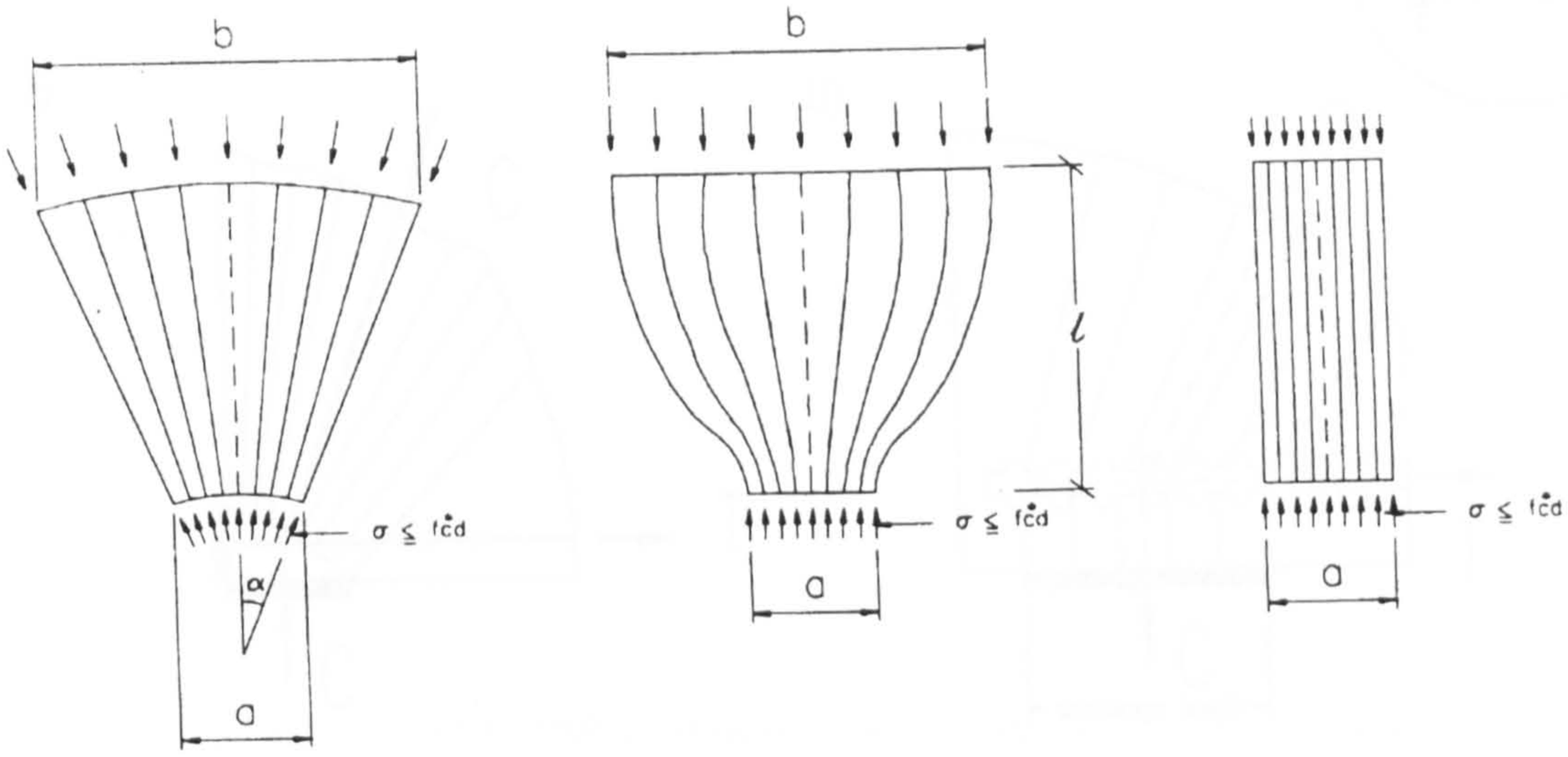

a) Fan shape b) Bottle shape c) Prism shape

fig.2.4.2 Standard Compression Fields

i)

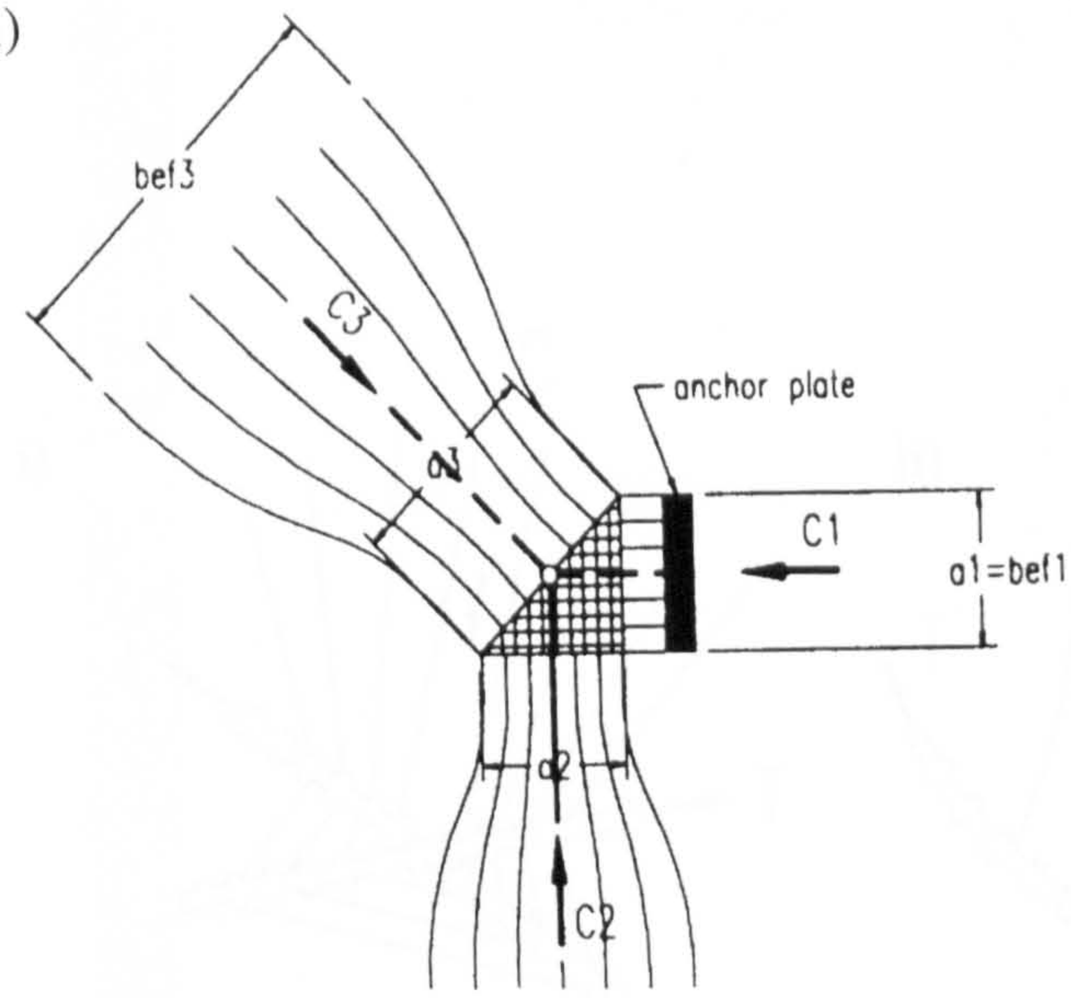

ii)

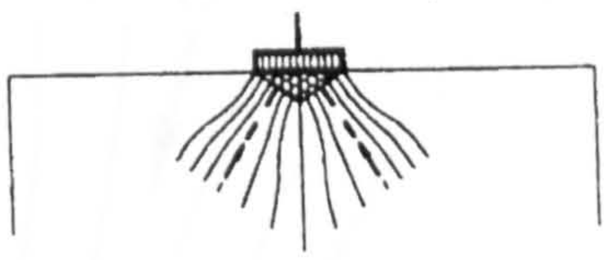

fig. 2.4.3(a) Idealised 'hydrostatic' stress in CCC nodes,
transferring concentrated loads from:
i) anchor plates, ii) or bearing plate, into bottle shaped stress field

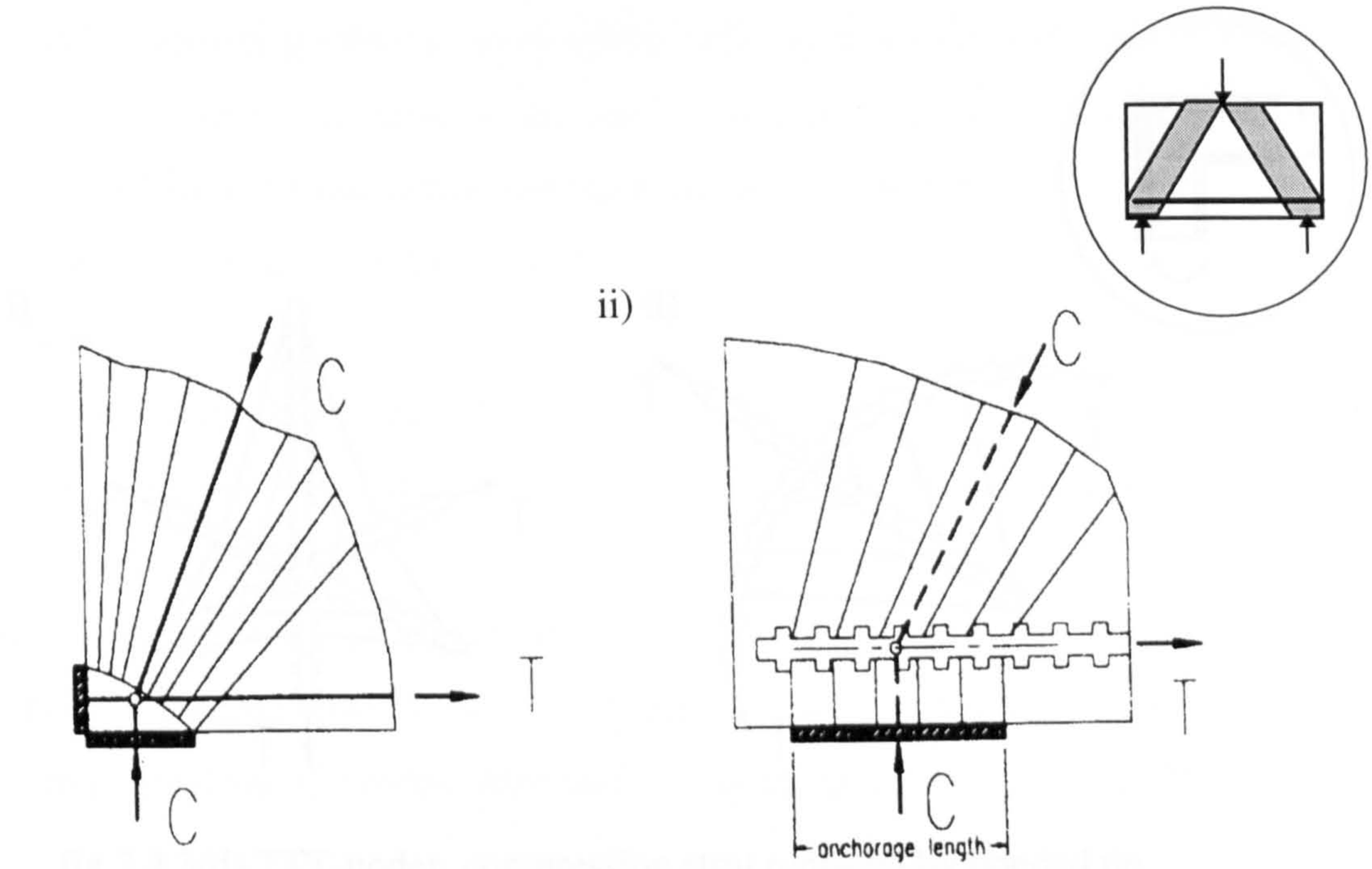

fig.2.4.3(b) CCT nodes:
diagonal strut and support reaction balance with reinforcing tie anchored by:
i) anchor plate behind the node, ii) bond within the node,

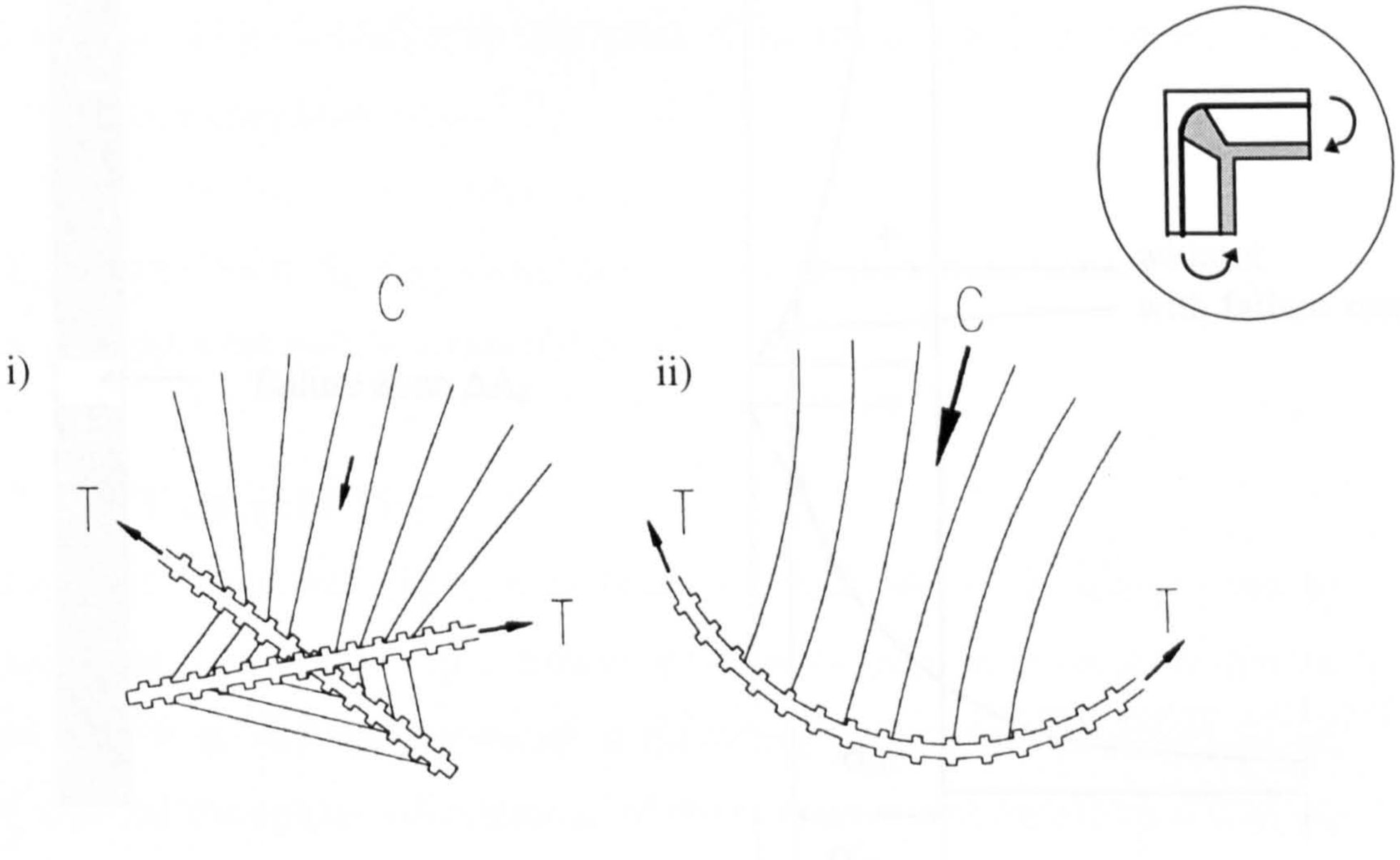

fig.2.4.3(c) CTT nodes:
compression strut is supported by
i) two bonded reinforcing bars, ii) radial pressure form bent up bar

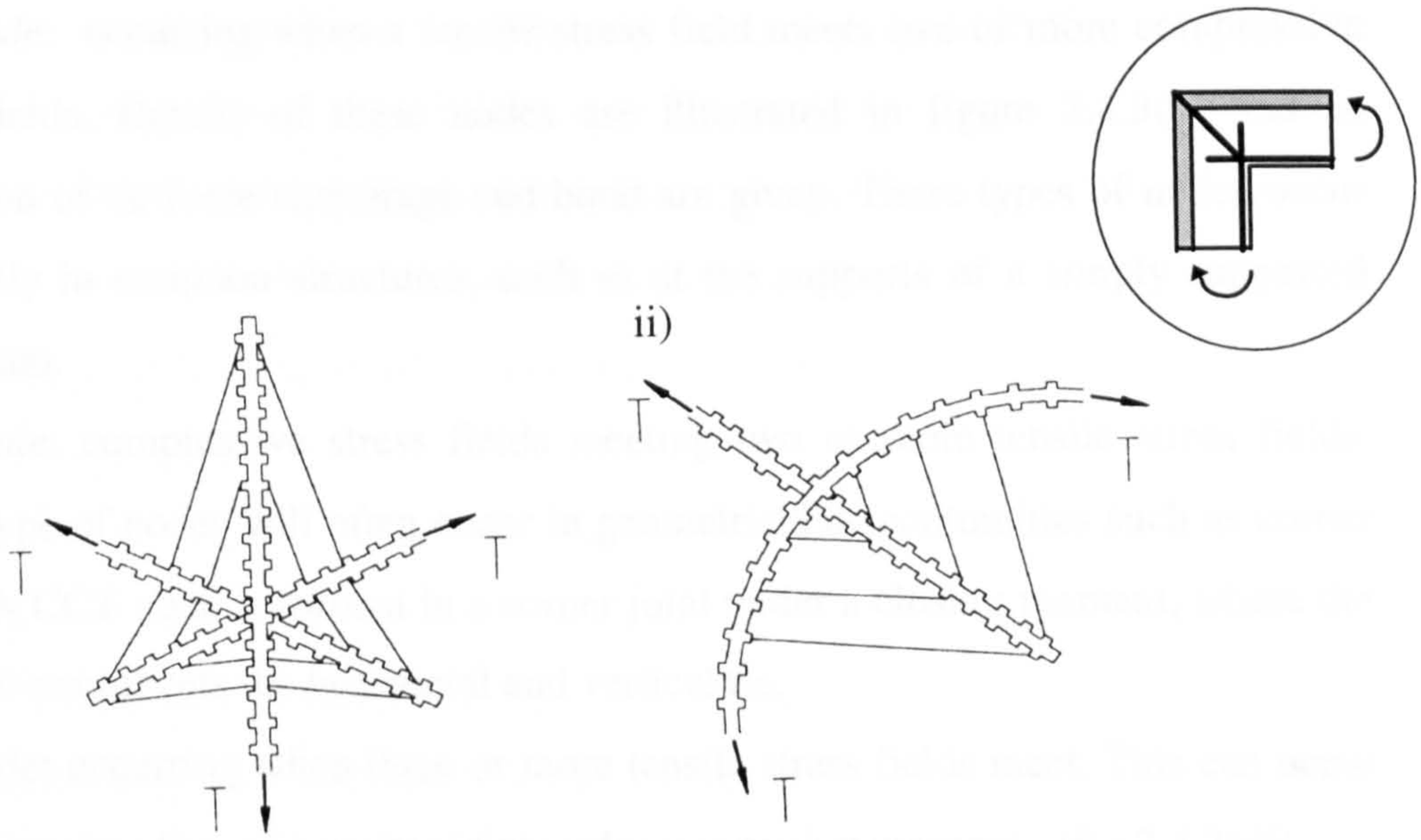

fig.2.4.3(d) TTT-nodes, compression strut replaced by bonded tie

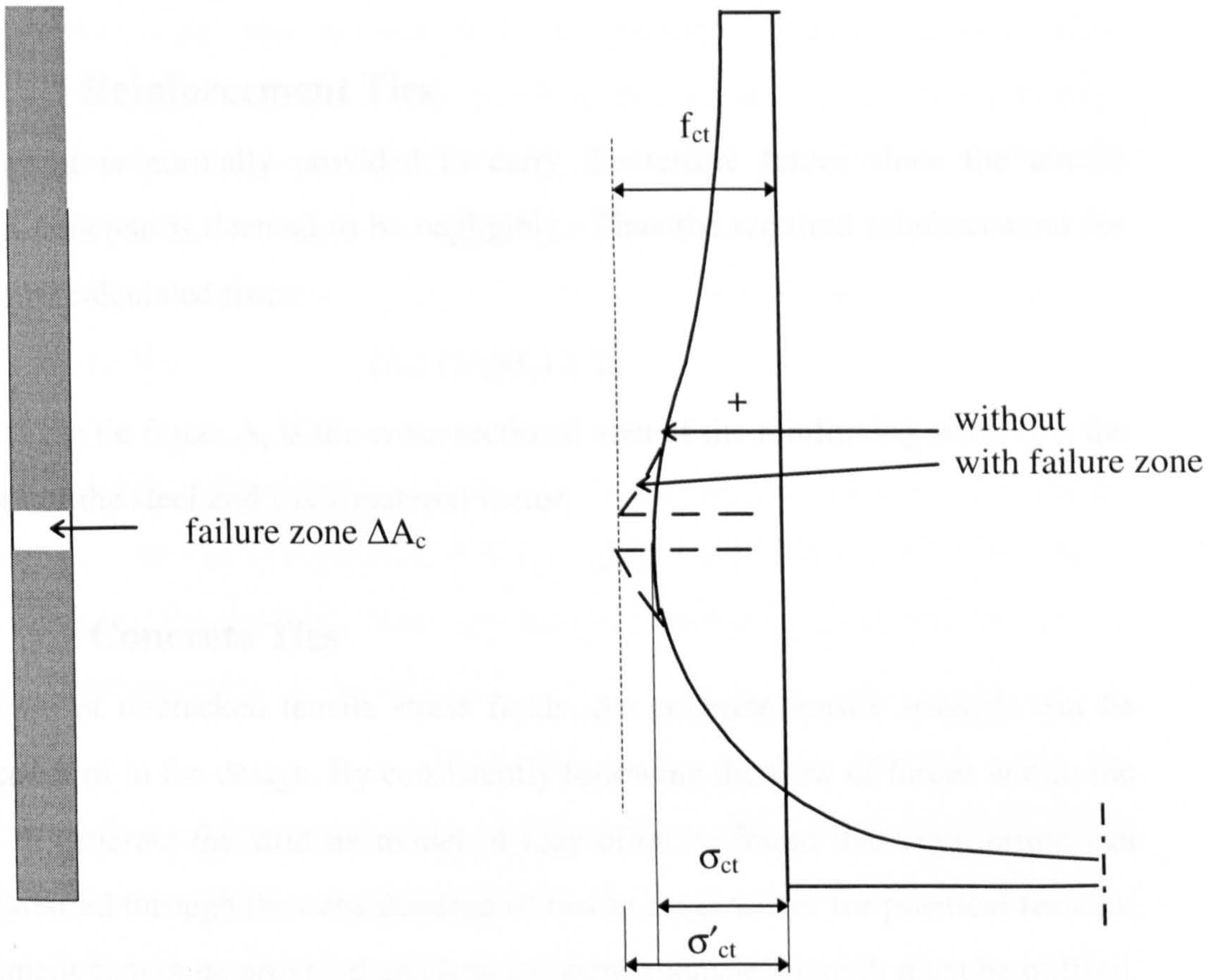

fig. 2.4.4.2 (a) Assumption of failure zone for check on the tensile strength of a concrete tension tie T_c.

2. *CCT-node*: occurring when a tensile stress field meets two or more compressive stress fields. Details of these nodes are illustrated in figure 2.4.3(b) and an indication of tie force anchorage and bond are given. These types of nodes occur frequently in common structures, such as at the supports of a simply supported deep beam.
3. *CTT node*: compressive stress fields meeting two or more tensile stress fields. These type of nodes will often occur in geometrical discontinuities such as corner joints. A CCT node is formed in a corner joint under a closing moment, where the diagonal strut meets the horizontal and vertical tie.
4. *TTT* node: occurring when three or more tensile stress fields meet. This can occur at the inner junction of a corner joint under an opening moment. (fig 2.4.3(d))

2.4.4 Dimensioning of Ties

2.4.4.1 Reinforcement Ties

Reinforcement is normally provided to carry the tensile forces since the tensile strength of concrete is deemed to be negligible. Thus the required reinforcement for the tie can be calculated from:

$$(A_s)\,(1/\gamma)(f_y) \geq T_s$$

where T_s is the tie force, A_s is the cross sectional area of the reinforcing steel, f_y is the yield stress of the steel and γ is a material factor.

2.4.4.2 Concrete Ties

For the case of uncracked tensile stress fields, the concrete tensile strength can be taken account of in the design. By consistently following the flow of forces within the structure to generate the strut-tie model, it may often be found that equilibrium can only be satisfied through the consideration of ties in areas where for practical reasons, reinforcement cannot be provided and hence concrete tensile strength must be utilised. Schlaich et al (1987) proposed some guidelines and an empirical formula based on the experimental work of Reinke (1986), for the use of concrete tensile strength. The tensile strength of concrete should only be used to achieve equilibrium in areas where no progressive failure is anticipated. Thus, restraint forces and micro-cracks have to

be taken into account whether the concrete is loaded or unloaded, cracked or uncracked. Redistribution of stresses in a structure which avoids progressive cracking is assumed to take place under the condition that at any point in a cracked failure zone of area ΔA_c , the remaining increased tensile stresses do not exceed the tensile strength f_{ct} (fig 2.4.4.2a). As an initial proposal, the following formula was suggested by Schlaich et al. (1987):

$$\Delta A_c = 4d_g^2 \text{ and } \geq A_{ct}/10$$

where A_{ct} is the area of the tension zone and d_g is the diameter of the largest aggregate. In practice, it is desirable not to rely on the tensile strength of concrete in the design as the only means of carrying tensile force.

2.4.5 Dimensioning of Struts

The dimensioning of the struts is more complicated than for ties since the state of stress present within the strut member can be multi-axial. Depending on the existing state of stress within the strut, the attainable compressive strength or effective stress f_c within the concrete will vary. For the case of bi-axial compression-tension, the compressive strength of the concrete will decrease as the tensile stresses increase. For the case of bi-axial compression-compression, the compressive strength will increase as the stresses increase.

Investigations on the effective strength of concrete struts have been carried out by many researchers such as Nielsen et al. (1978), Vecchio and Collins (1982). At a basic level, the effective strength of a concrete strut is defined as some fraction of the concrete cylinder compressive strength f_c' i.e.

$$f_c = (\alpha)(f_c')$$

where α is a factor taking into account the effect of the given stress state. Based on test results, empirical equations for the effective stress levels of concrete struts have been derived. The following empirical equation was proposed by Nielsen et. al (1978) for the effective stress of concrete struts in beam webs:

$$f_c = \left(0.7 - \frac{f_c'}{200}\right) f_c'$$

This formula was limited to cases where $f_c' < 60$ MPa. Ramirez and Breen (1983), proposed a value of $2.82(f_c')/\sqrt{(f_c')}$ as an estimate of the maximum diagonal compression stress for beams and beam type regions. Marti (1985) proposed an average effective stress level of 0.6 (f_c') for all types of struts and nodes. Bergmeister et al. (1991) proposed an equation for effective stress levels of concrete struts which is applicable for $20 < f_c < 80$ MPa:

$$f_c = (0.5 + 1.25/\sqrt{f_c'})f_c'$$

For comparison, the equations described above are shown for a range of cylinder strengths in figure 2.4.5(a). It can be seen, that a large difference in values is obtained. All the equations described so far, do not take into account the individual stress-state characteristics of a given strut. They simply serve as an empirical upper limit for design strength. Depending on the choice of equation, a wide range of concrete strengths would be required in design. In the work by Schlaich et al. (1987) and MacGregor (1988), strut types were categorised according to geometry and stress state. Applicable effective stress levels were suggested for each strut category. A summary of these categories is given in table 2.4.5. These values were based on experimental work. Further work by Alshegir (1992), determined the effective stress levels of concrete struts from the analysis of experimental results from four continuous deep beams, subjected to two point loads, three pre-stressed deep beams subjected to high shear stresses and four simply supported beams with varying stirrup reinforcement. The resulting formulae are also shown in table 2.4.5.

As a means of quantifying the qualitative descriptions of the strut condition, the tensile stress ratio (σ_1 / f_c') corresponding to the compressive strength reduction is also given in table 2.4.5. The ratio was derived from the bi-axial failure envelop of Kupfer et al (1969). In general, the proposals are consistent with one another and are conservative. It can be seen from the table that the smallest reduction in compressive strength is 5%. Using the description of the strut condition corresponding to this reduction, it would be assumed that the strut is in a state of uni-axial or bi-axial stress. i.e $\sigma_1 \leq .0.0$. From the bi-axial envelop of Kupfer et al. a corresponding tensile stress ratio of 2% is associated with this reduction in strength. For the most seriously

cracked strut, a 75% reduction in compressive strength is proposed and this corresponds with a tensile stress ratio of 9.5%.

Effective stress level	Concrete Strut Condition	Proposed by	σ_1 / f_c' Kupfer et.al. (1969)
0.85 f_c'	Undisturbed and uniaxial state of compressive stress such as in a prismatic strut.	Schlaich et al. (1987)	5%
0.68 f_c'	Tensile strains and or reinforcement perpendicular to the axis of the strut that may cause cracking parallel to the strut with normal crack width.	Schlaich et al. (1987)	7.5%
0.51 f_c'	Tensile strains causing skew cracks and/or reinforcement at skew angles to the strut's axis.	Schlaich et al. (1987)	8.5%
0.34 f_c'	For skew cracks with extraordinary crack width. Skew cracks would be expected if modelling of the struts departs significantly from the elastic flow of internal stresses.	Schlaich et al. (1987)	9%
0.50 f_c'	Isolated compression struts in deep beams or D-regions	MacGregor (1988)	8.5%
0.25 f_c'	Severely cracked webs of slender beams with strut angle of 30°	MacGregor (1988)	9.5%
0.45 f_c'	Severely cracked webs of slender beams with strut angle of 45°	MacGregor (1988)	8.7%
0.85 f_c'	Moderately confined diagonal struts going directly from point load to support with shear span-depth ratio less than 2.0.	Alshegir (1992)	5%
0.75 f_c'	Struts forming arch mechanism	Alshegir (1992)	6.5%
0.50 f_c'	Arch members in pre-stressed beams and fan compression members.	Alshegir (1992)	8.5%
0.95 f_c'	Undisturbed and highly stressed compression struts	Alshegir (1992)	2%

Table 2.4.5 Effective Stress Levels in Concrete Struts

Yun and Ramirez (1996) proposed a method of determining the effective stress of concrete struts from the principal stress ratios. These ratios are determined from finite element analysis by averaging the principal stress ratios present within each element of a finite element mesh. Experimental work on two-dimensional concrete under bi-axial states of stress was carried out by Kupfer et al. (1969), and the relationship between effective stress and principal stress ratio derived from this work is detailed in figure 2.4.5(b). Once the principal stress ratios have been found, the effective stress is derived from interpolation of figure 2.4.5(b). The use of figure 2.4.5(b) is limited to struts inclined up to ±10° from the principal compressive stress flows, after which

account must be made of the inclination. In cases where the strut angle deviates outside this limit, then the value obtained from figure 2.4.5(a) is multiplied by cos ϕ, where ϕ is the deviation angle between the strut and the compressive stress flow. Depending on the level of confinement provided by reinforcement, anchorage or bearing plates, the effective stress level is increased from 5-20%. This method is advantageous since the use of finite element analysis, makes it is easy to determine the stress-state characteristics of an individual strut. Using the bi-axial yield criterion described, it is then straightforward to assign the appropriate effective stress for design.

For the particular case of dimensioning the bottle shaped compression stress field, Schlaich et al. (1987) proposed the diagram shown in figure 2.4.5(b), based on the experimental work of Reinke (1986). This case occurs when compressive forces are introduced to concrete which is unreinforced in the transverse direction. The spreading of the forces in the transverse direction causes biaxial or triaxial compression under the point of load application and transverse tensions further away from the load. The stress field is characterised by the width of the anchor plate *a*, the maximum width *b* available for the stress field in the structure, and the distance *l* of the anchor plate to where the stresses become more uniform, i.e. the D-region ends. The chart shows the permissible ratio of applied pressure (p_a) to the concrete design compressive strength (f_{cd}) (for an undisturbed uni-axial compression field). The plot for compression fields without transverse reinforcement (shown as the bold line) is based on elastic analysis with a concrete tensile strength $f_{ct} = f_c'/15$. The chart also takes into account the effect of transverse reinforcement. The amount of transverse reinforcement ω, is measured as

$$\omega = a_s f_{sy} / t\, f_{cd}$$

where a_s is the area of steel and f_{sy} is the yield stress of the steel.

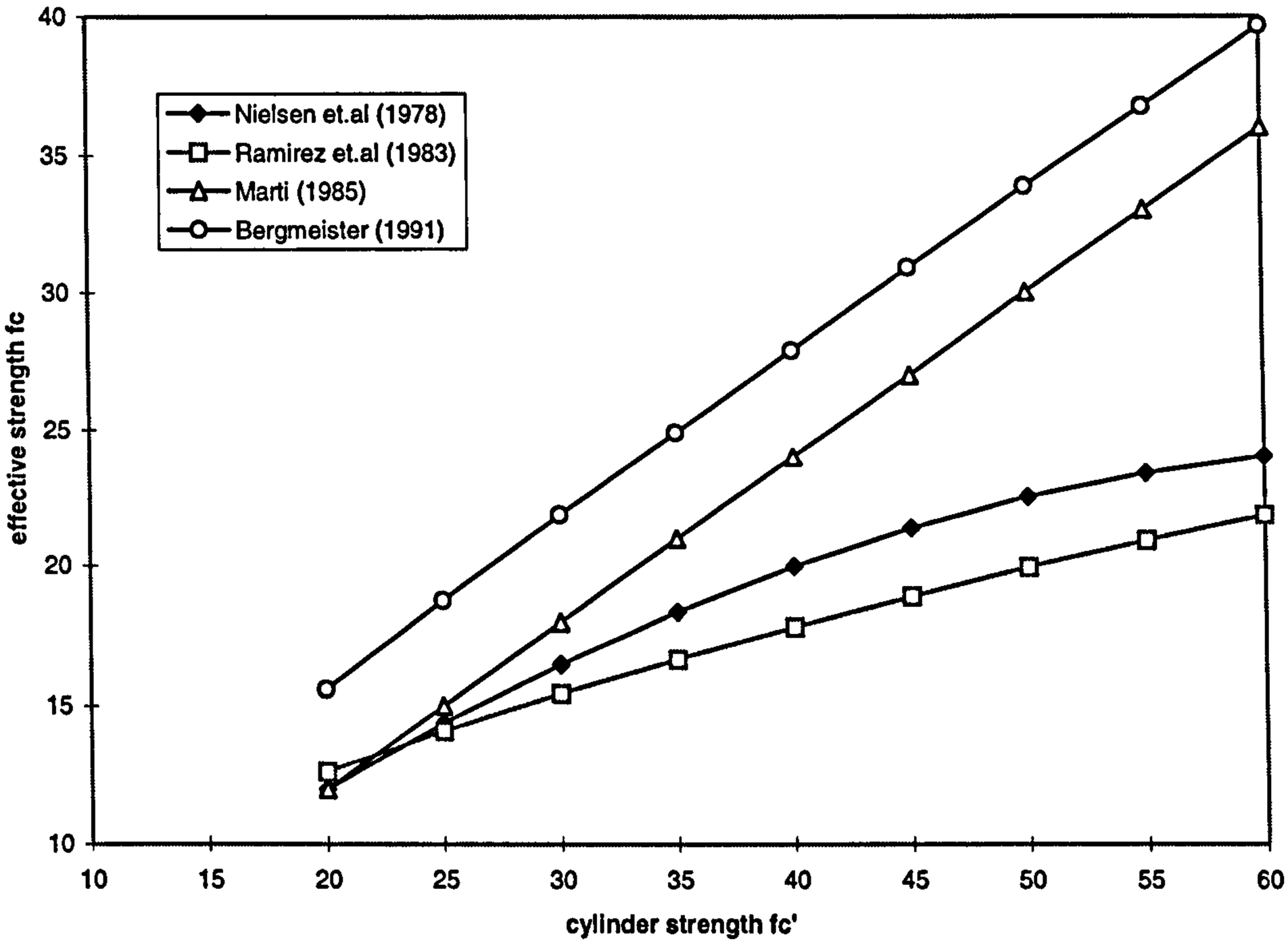

fig.2.4.5(a) Empirical Formulae for Effective Stress f_c in Concrete Struts

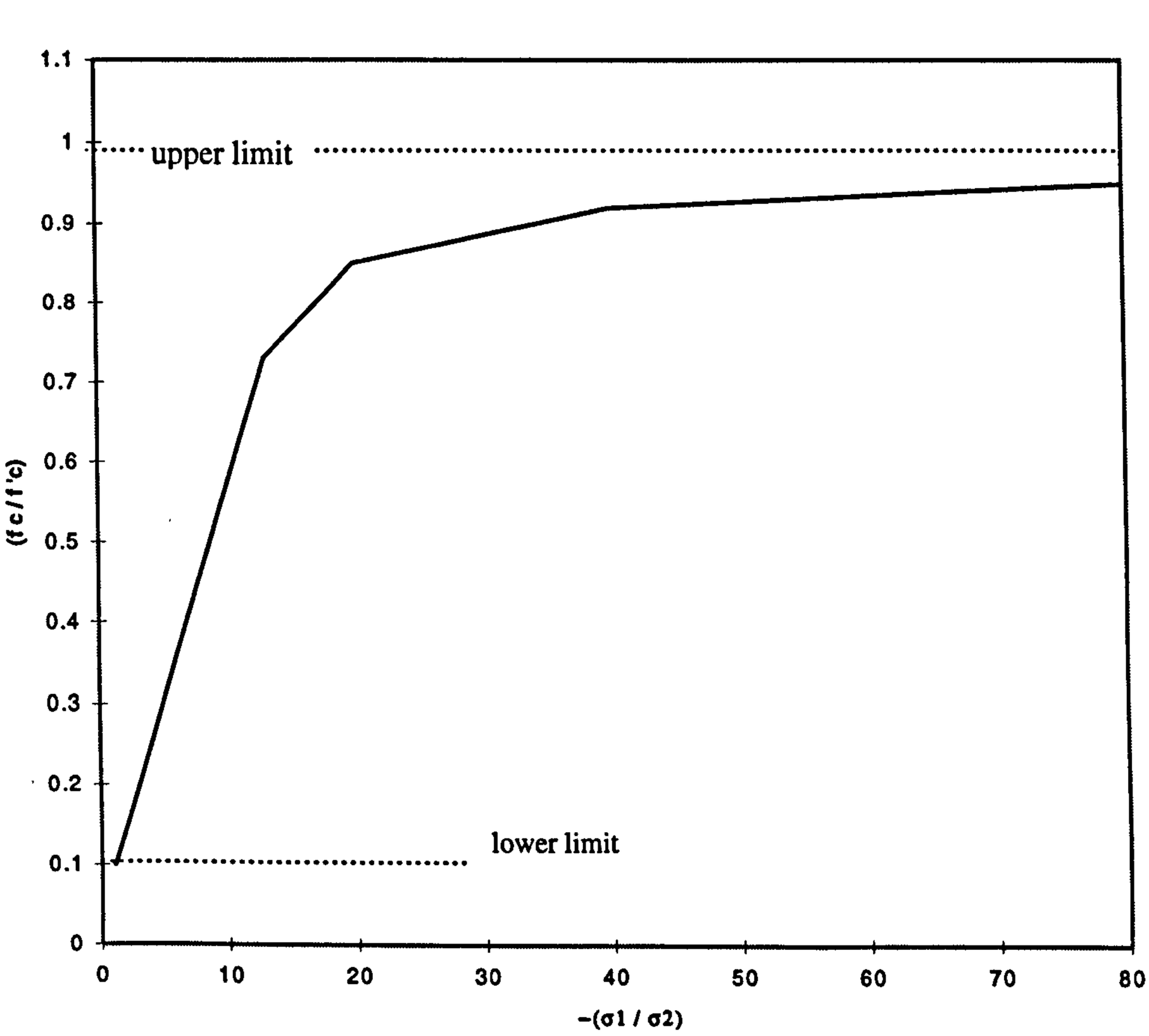

fig.2.4.5(b) Effective Stress f_c in the Strut, Yun & Ramirez (1996)

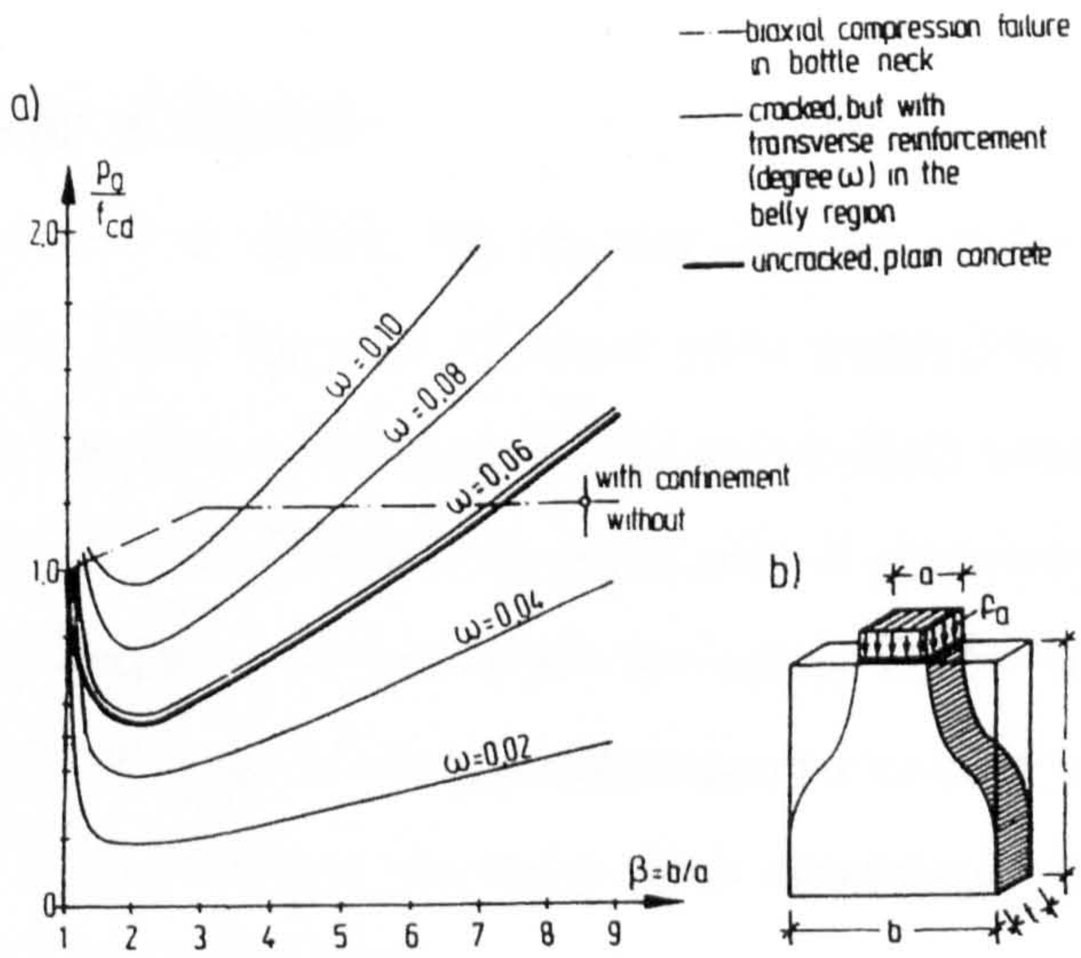

fig.2.4.5(c) Dimensioning of Bottle-shaped Compression Fields, Schlaich et al (1987)
a) Chart showing safe bearing pressure P_a, with regard to cracking and crushing of plain unreinforced concrete stress fields, yielding of transverse reinforcement and biaxial compression failure in the bottle neck region, b) geometry of stress field, c) model and reinforcement layout of stress field with transverse reinforcement ω.

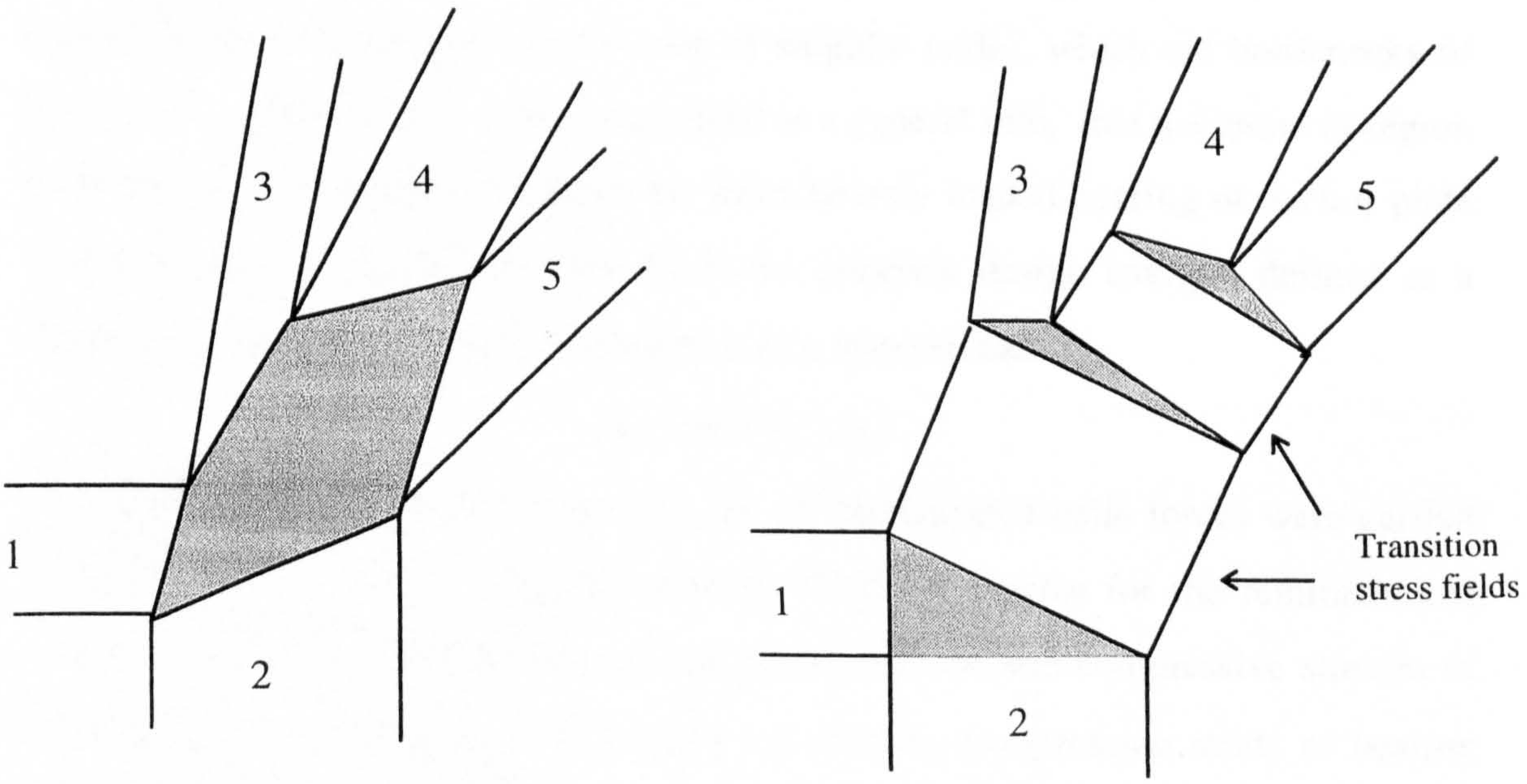

a) Original nodal region intersected by 5 one-dimensional stress fields

b)New nodal stress field

fig.2.4.6 Determination of nodal zone shape, Schlaich et .al (1990)

2.4.6 Dimensioning of Nodes

In the strut and tie method of design, the bearing capacity of the nodal zones are of paramount importance. Since the size of nodal zone formed by the intersection of incoming stress fields can be smaller than that of the existing boundaries of the struts and ties, there is a greater potential for crushing and or cracking in the nodal zone. Thus safe nodal zone design is necessary for the safety of the whole structure. The strength of concrete in nodal regions is dependent upon a number of factors relating to the stress conditions present. There are three main conditions occurring which will affect concrete stress in the nodal zone:

- level of confinement provided by reactions, compression struts, anchorage plates for pre-stressing, bearing plates, reinforcement from adjoining members and hoop reinforcement
- strain discontinuities present within the nodal zone such as when ties are anchored in or across a compressed nodal zone
- splitting stresses occurring from anchorage of reinforcing bars in or directly behind a nodal zone.

As for the concrete struts, various formulae defining the design stress limits for nodal regions have been proposed. In the case of singular nodes, which are bottlenecks of the stresses, Schlaich et al. (1987) suggested as a general rule, that the entire D-region would be safe if the pressure under the most heavily loaded bearing or anchor plate was less than 0.6 f_{cd}. In this case, f_{cd} is the concrete design strength defined as a fraction of the concrete cylinder strength, γ_c is a material factor:

$$f_{cd} = (0.85\, f_c')/(\gamma_c)$$

This assumption was based on the fact that all significant tensile forces were carried by the reinforcement and that sufficient development lengths for the reinforcement were achieved. The 1984 Canadian Code limits the concrete compressive stresses in nodal zones to $0.85\phi(f_c')$ in nodal zones bounded by compression struts or bearing areas, $0.75\phi(f_c')$ in nodal zones anchoring only one tension tie and $0.6\phi(f_c')$ in nodal zones anchoring tension ties in more than one direction, where ϕ is a safety factor.

These formulae are based on experimental work and are similar to those described in the previous section.

A procedure for evaluating the stresses in CCC nodes with equal or unequal stress fields using Mohr's circle technique was developed by Marti (1985). In this technique, the tie forces are converted to compressive forces acting behind the nodal zone by anchoring the tie using end plates. Marti proposed that the nodal zones could be stressed up to $0.6f_c'$ along with the concrete struts. This idealisation is close to reality since the anchorage of the tensile reinforcement will tend to generate compressive force behind the nodal zone as shown previously in figure 2.4.3(b).

Schlaich et al (1987) and MacGregor (1988) proposed values of effective stress levels in nodal zones, taking into account the state of stress; a summary of these is presented in table 2.4.6. A general procedure for checking the nodal stresses based on geometry was proposed by Schlaich and Anagnostou (1990). In this work, the geometry of the nodes is only limited by the existing boundary of the incoming members and not by the area formed by the intersection of the stress fields reaching the node. In contrast to a real truss, the nodal geometry of an idealised strut-tie model is not limited. The node is surrounded by concrete whose compressive strength may be exploited. The stress fields consists of several triangular and rectangular areas which are separated by lines of stress discontinuity. The stress state in each of the fields is either uniform or hydrostatic, as in figure 2.4.3(a). The introduction of transition stress fields allows nodal zones for stress fields of different intensities to be formed (see fig 2.4.6a).

The effect of confinement upon the nodal zone effective stresses was studied by Bergmeister et al. (1991). He proposed effective stress equations for nodes confined by spiral reinforcement, square confined nodes with or without longitudinal reinforcement, unconfined nodes with bearing plates and triaxially confined nodes. A summary of these formulae is presented in table 2.4.6. More recently, Adebar and Zhou (1993), carried out experimental work on the compressive strength of struts confined by plain concrete. Concrete cylinders of varying diameters and heights were loaded over a constant bearing area. The travel time of an ultrasonic pulse was used to

indicate the level of cracking. It was found that the level of cracking depended on the amount of confinement provided by the plain concrete and the height/width ratio of the concrete strut. From this work and analytical studies, they proposed some equations for bearing strength. The maximum bearing stress when designing D-regions without sufficient reinforcement is limited to

$$f_c \leq 0.6f_c'(1+2\alpha\beta)$$

where

$$\alpha = 0.33\{(A_2/A_1)^{1/2}-1\} \leq 1.0$$

$$\beta = 0.33(h/b-1) \leq 1.0$$

The ratio h/b is the height/width or aspect ratio of the strut and should not be taken as less than one. The parameter α accounts for the level of confinement and the parameter β accounts for the geometry of the compression stress field. A_1 and A_2 represent the load area and the supporting surface area respectively. A lower limit of $0.6f_c'$ for the bearing stress was suggested for areas where there is no confinement and an upper limit of $1.8f_c'$ was suggested. Again, these proposals are similar to those described earlier in the section and given in table 2.4.6. Similarly, the corresponding tensile stress ratios from Kupfer et al. (1969) are presented. The proposed values are consistent and conservative. The following section provides a generalised procedure for the design of singular and smeared nodes.

2.4.6.1 Singular nodes

In singular nodes the deviation of forces is often made more abruptly than in smeared nodes. These nodes mainly originate from single loads or support reactions, from concentrated forces introduced by the reinforcement through anchor plates, bond, or radial pressure inside bent bars such as loops. In addition to these, geometrical discontinuities such as re-entrant corners will cause stress concentrations which are represented by a singular node.

Effective stress level	Node Type	Proposed by	σ_1 / f_c' Kupfer et.al. (1969)
0.85 f_c'	Compression-compression-compression	Schlaich et al. (1987)	5%
0.68 f_c'	Nodes where reinforcement is anchored in or crossing the node	Schlaich et al. (1987)	7.5%
0.85 f_c'	Nodes bounded by compressive struts and bearing areas	MacGregor (1988)	5%
0.65 f_c'	Nodes anchoring one tension tie	MacGregor (1988)	7.5%
0.5 f_c'	Nodes anchoring tension ties in more than one direction	MacGregor (1988)	8.5%
0.8 f_c' $f_c' \leq 27.6$ MPa	Unconfined nodes without bearing plates	Bergmeister et al. (1991)	6%
(0.9-0.25 f_c' /69) f_c' $27.6 \leq f_c' \leq 69$ MPa	Unconfined nodes without bearing plates	Bergmeister et al. (1991)	-
0.65 f_c' $f_c' \geq 69$ MPa	Unconfined nodes without bearing plates	Bergmeister et al. (1991)	7.5%
$k f_c'(A/A_b)^{0.5} + \alpha(A_{core}/A_b)f_{lat}(1-s/d)^2$	Confined nodes	Bergmeister et al. (1991)	-
$k f_c'(A/A_b)^{0.5}$	Unconfined nodes with bearing plates	Bergmeister et al. (1991)	-
2.5 f_c'	Triaxially confined nodes	Bergmeister et al. (1991)	-

Note:

A = area of confined concrete, A_b = area of bearing plate, A_{core} = area of confined strut,
f_{lat} = lateral pressure = $2f_yA_s/(ds)$ for $f_c' < 48.3$ MPa ; $2f_yA_s/(ds)$ for $f_c' > 48.3$,
s = pitch or spacing of confinement reinforcement, d = diameter of confined core,
α = parameter (4.0 for spiral confinement, 2.0 for square closed hoop confinement anchored with longitudinal reinforcement, 1.0 for square closed hoop confinement without longitudinal reinforcement anchorage)
$k = 0.5 + 1.25/\sqrt{f_c}$

Table 2.4.6 Effective stress levels in nodal zones

In general, equilibrium in singular nodes is achieved by the balance of forces in the interior of the node through direct concrete compressive stresses. In the ideal situation, tie anchorage is provided by an anchorage plate which transfers the load from behind the node thus causing compression in the node (fig. 2.4.3.b(i)). Bond is essentially load transfer via concrete compressive stresses which are supported by the

ribs of the steel bar (fig 2.4.3.b(ii)/(iii)) and by radial pressure in bent bars (fig. 2.4.3.b(iv)). The dimensioning of a singular node involves three main steps:

- Adapting the geometry of the node with the applied forces: In the case of CCC-nodes the borderline of the node can be assumed to be perpendicular to the resultant of the stress field and the state of stress within the interior of the node to be plane hydrostatic. (fig 2.4.3.a(i)). In this case the resulting geometrical relation $a_1:a_2:a_3 = C_1:C_2:C_3$ can be used to dimension the length of the support or the width of an anchor plate.
- Checking the concrete stresses are within the associated limit: This condition is automatically satisfied for the entire nodal region if the stresses along the borderlines of the node do not exceed those limits and if the reinforcement anchorage if sufficient. In the case of CCT nodes (fig 2.4.6.1) with bonded reinforcement, it is sufficient to check the concrete stresses σ_1 and σ_2 in the adjacent compression struts. In most cases it is clear from the geometry of the node which of the pressures out the two struts is the controlling pressure and hence it is necessary to analyse only one. Figure 2.4.6.1 shows a number of multi-layered and singly reinforced CCT nodes and the dimensioning limits proposed by Schlaich et al (1987).
- Provision of adequate anchorage for ties in the nodal zone: For anchor plates, this involves a check on the bending strength of the anchor plate and the welded connection with the tie. In this case, a tie having a smooth surface where it crosses the node is better than good bond quality because strain compatibility within the bar will tend to crack the concrete within the node. In the case of directly anchored reinforcing bars, hoop or loop anchorages are preferable. For straight bar anchorages, the design engineer must ensure that anchorage is located within and behind the node as shown in fig 2.4.3.b(i-ii). Anchorage begins where the transverse compression stress trajectories of the struts meet the bar and are deviated; in order to catch the outermost fibres of the deviated compression field , the bar must extend through to the opposite end of the nodal region.

2.4.6.2 Smeared nodes

It is normal for D-regions to contain both singular and smeared nodes. In most cases the singular nodal region is most critical and a check on concrete stresses within the smeared node is unnecessary since the applied stress levels are less than in the singular node. In addition, the geometry of the smeared node may be of a similar magnitude to that of the singular node. This gives rise to the rule of thumb proposed by Schlaich et al; that the structure is safe, if the stress under the most heavily loaded bearing plate is less than $0.6f_{cd}$.

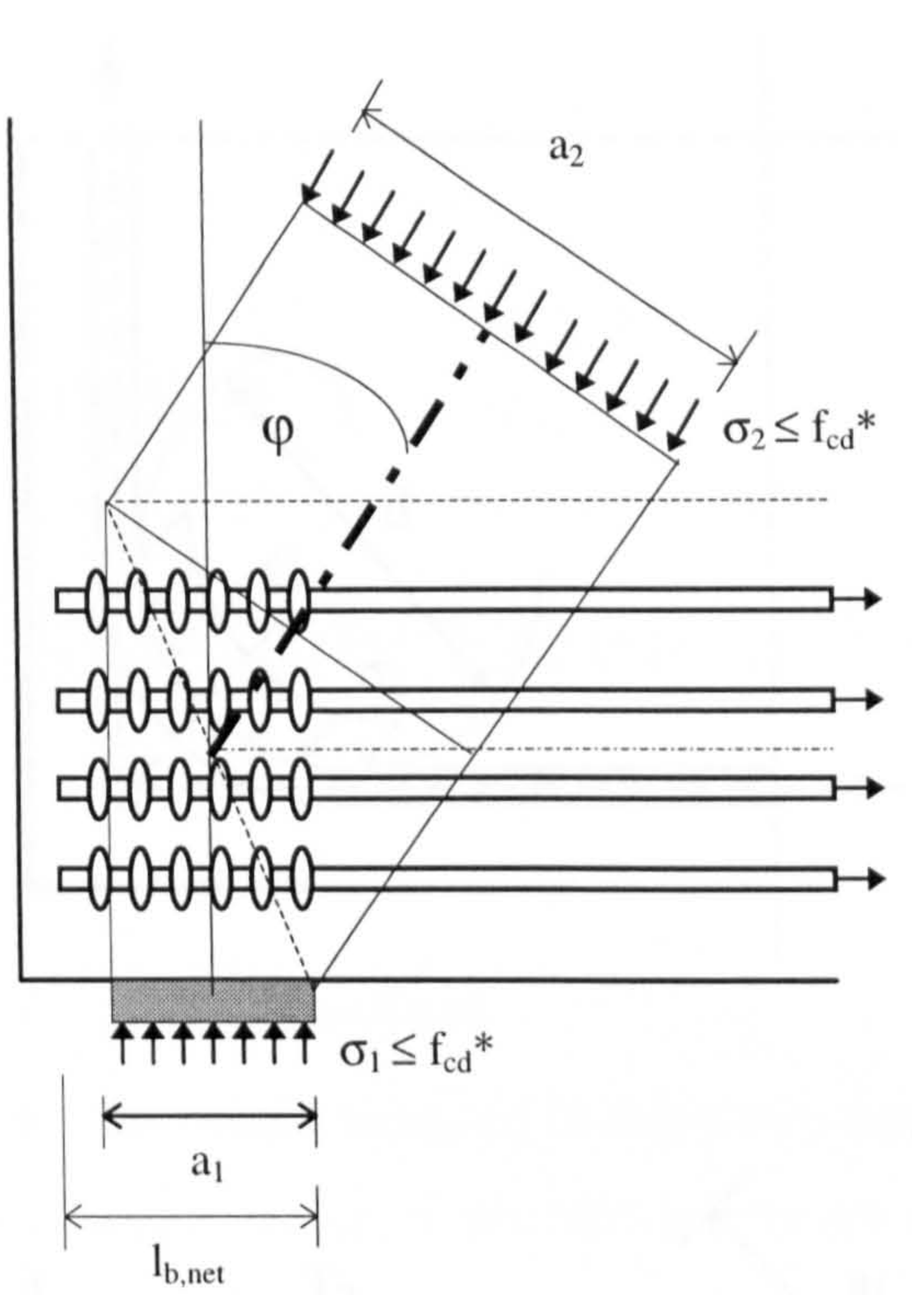

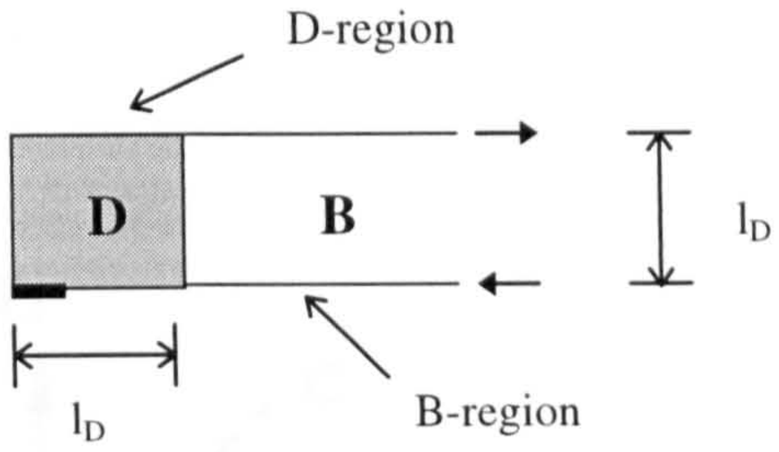

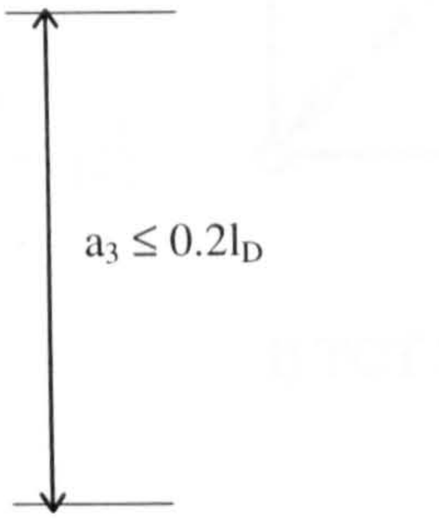

$\sigma_1 = \sigma_2 \, [1+(a_3/a_1)\tan\varphi] \cos^2\varphi$

$l_{b,net} \geq a_1$

i) multi-layered tie

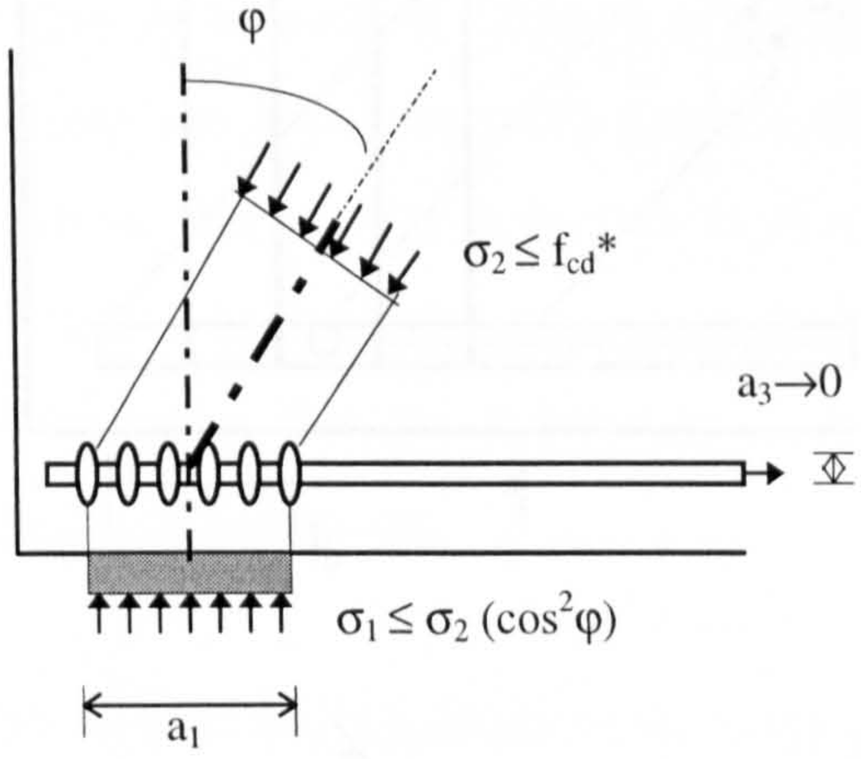

ii) single-layered tie

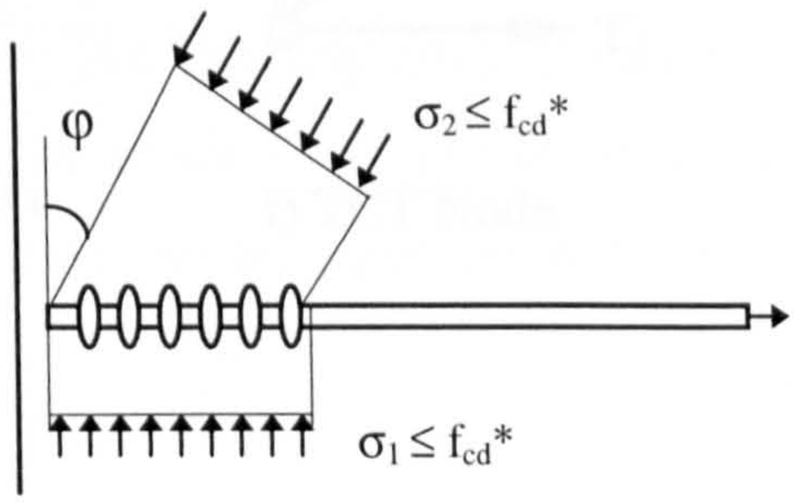

iii) as ii), with incoming compression field

fig.2.4.6.1(a) Stresses in Typical CCT Nodes, Schlaich et al. (1987)

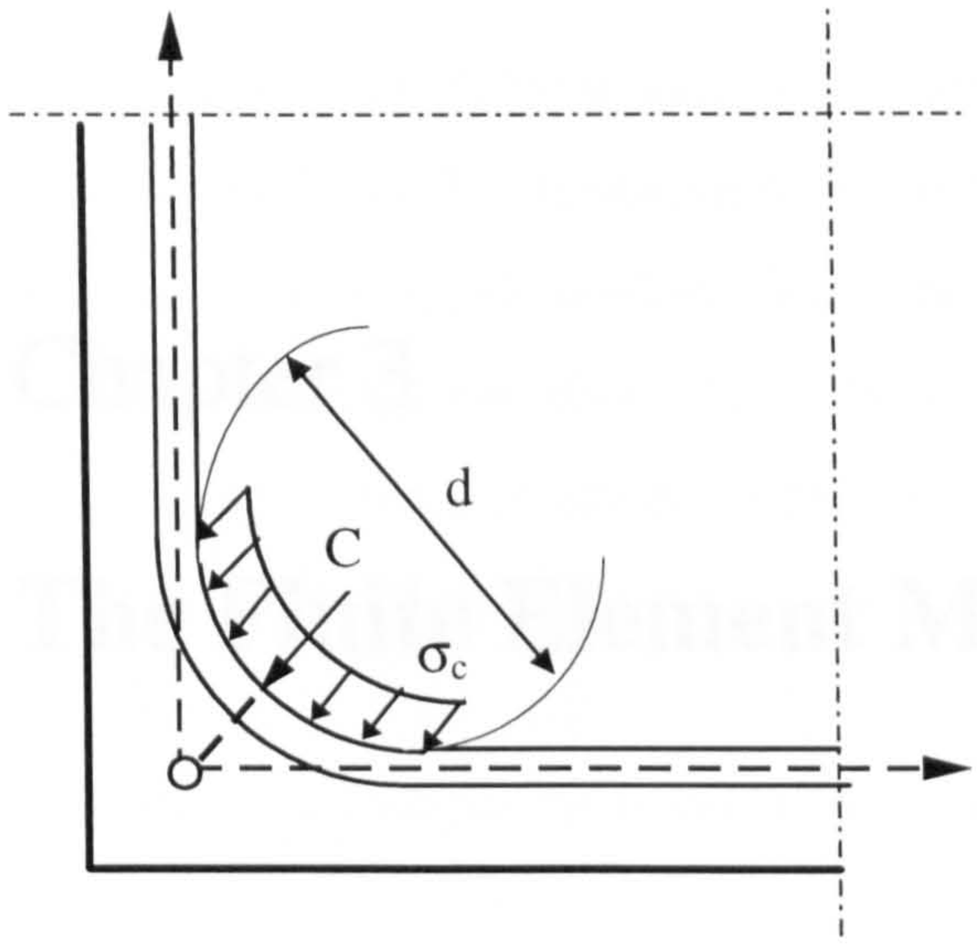

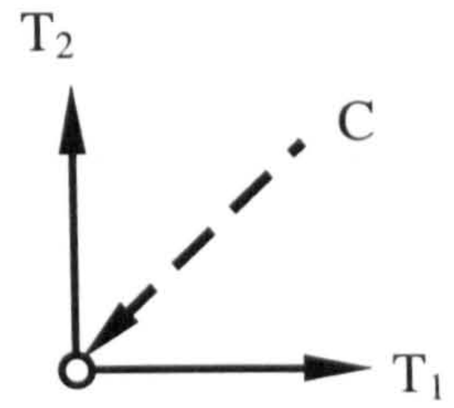

i) TCT Node

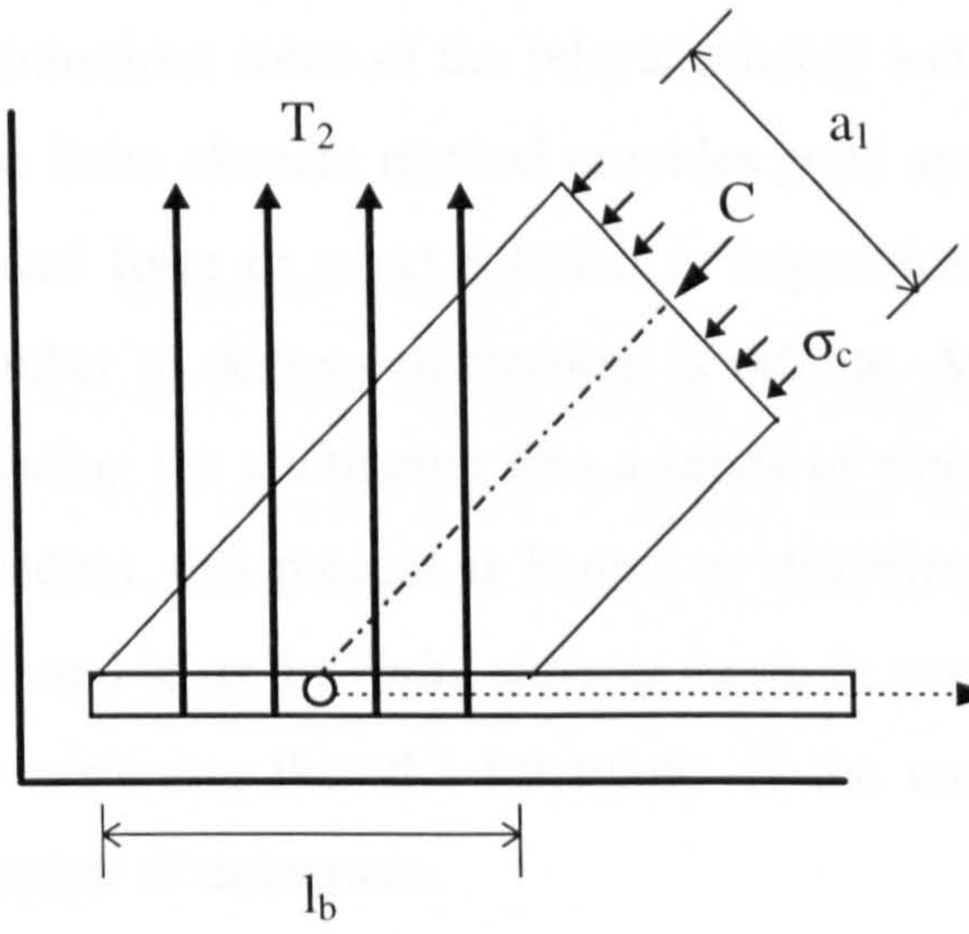

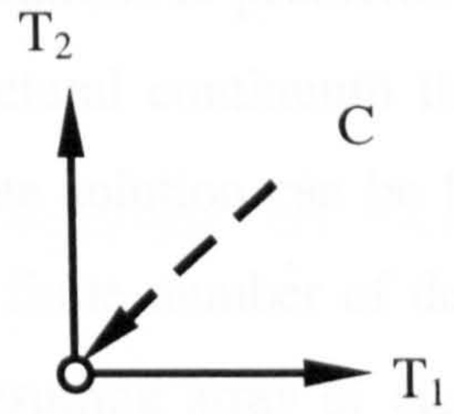

i) TCT Node

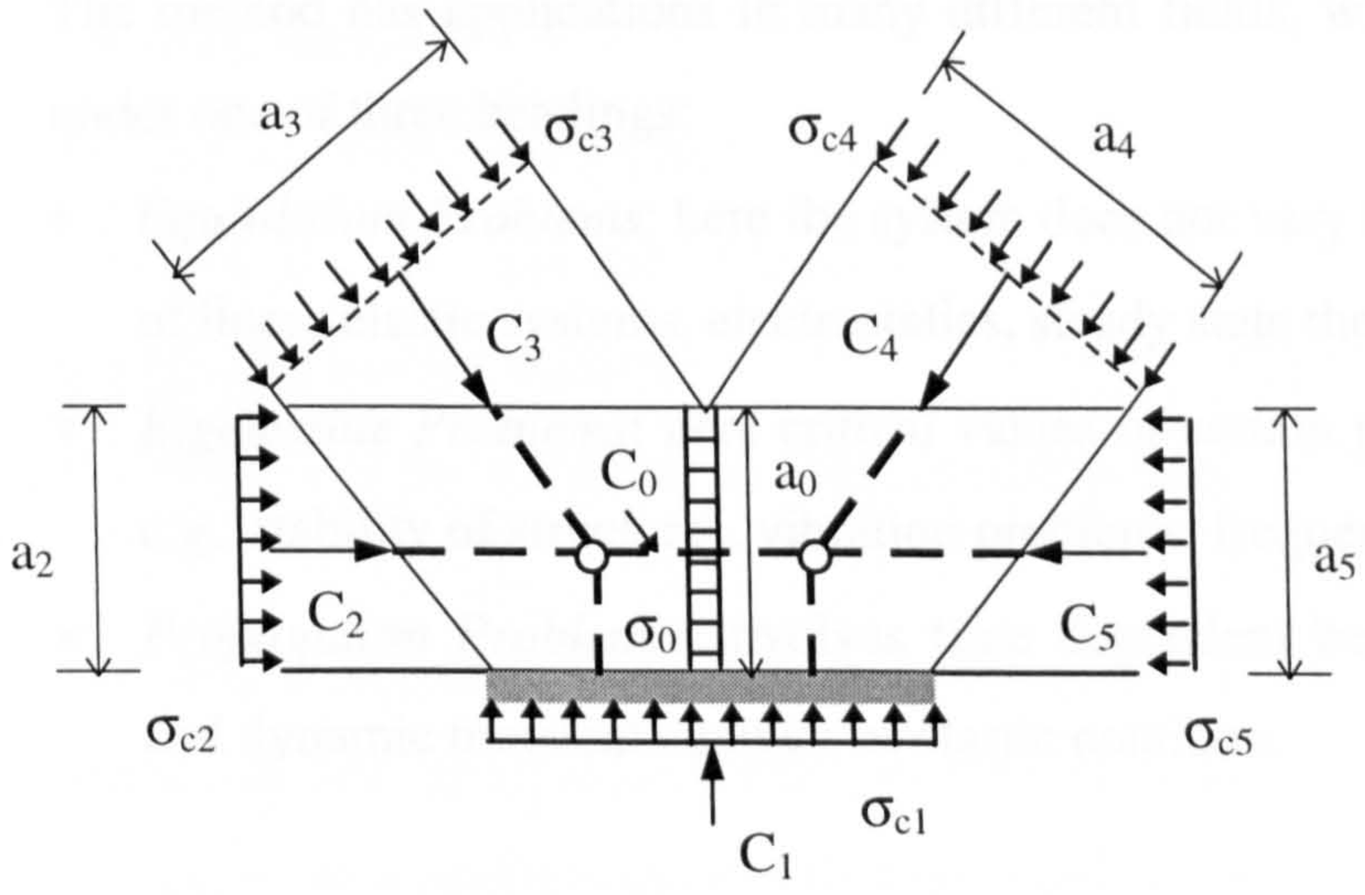

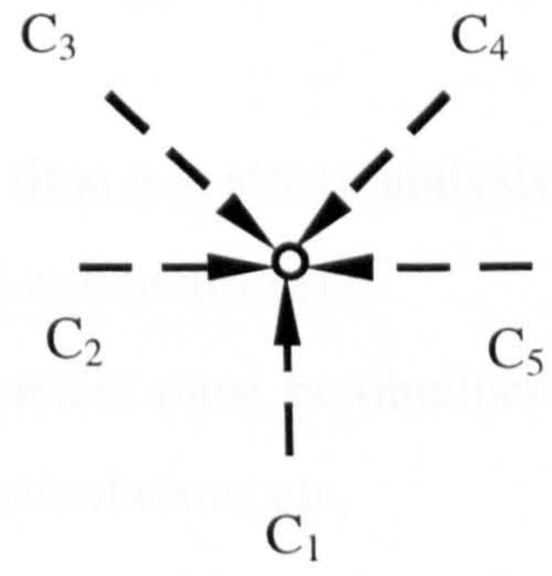

iii) CCCCC Node

2.4.6.1(b) Stresses in Typical Nodal Zones

Chapter 3

The Finite Element Method

3.1 Introduction

Since the work presented in this thesis involves finite element analysis, it is necessary to introduce some of the relevant theory and a description of the program used here. The finite element method provides good approximate solutions to problems where a closed form or exact solution is impractical. In a structural continuum the actual number of degrees of freedom is infinite. An approximate solution can be found by dividing the continuum into a series of elements with a finite number of degrees of freedom, this process is known as *discretisation*. The resulting array of elements is referred to as the *finite element mesh*. In essence an approximate solution is achieved by assuming that the behaviour of the continuum can be represented by a finite number of unknowns.

The method has applications in many different fields, with each application coming under one of three headings:

- *Equilibrium Problems*: here the system does not vary with time e.g. stress analysis of linear elastic systems, electrostatics, steady state thermal conduction etc.
- *Eigenvalue Problems*: here critical values of certain parameters must be obtained e.g. stability of structures, vibration problems, frequency calculations etc.
- *Propagation Problems*: involves time dependent behaviour e.g. hydrodynamics and dynamic transient analysis of elastic continua.

The finite element method will accommodate the inclusion of non-linear characteristics which invariably adds to the complexity of the problem. Finite element stress analysis can be carried out using three basic approaches:

- The *displacement method*: here the displacements are chosen as the initial unknowns and the stresses are determined from the calculated displacement field
- The *equilibrium method*: here the stresses are the initial unknowns and the displacements are calculated from the resulting stresses.
- The third is the *hybrid* or *mixed* method in which the displacements and the stresses are employed simultaneously as variables.

The displacement method is the most commonly used due to its ease of implementation in programs. This method was implemented in the program used in this work.

3.2 General Theory

In structural applications, the governing equilibrium equations are obtained by minimising the total potential energy π of the system.

$$\pi = \frac{1}{2}\int_v [\sigma]^T \varepsilon.dV - \int_v [\delta]^T \mathbf{p}.dV - \int_s [\delta]^T \mathbf{q}.dS \qquad (3.1)$$

where:

σ = stress vector

ε = strain vector

δ = displacements at any point

$\mathbf{p}$ = body of forces per unit volume

$\mathbf{q}$ = applied surface tractions

V = volume of the structure, S = loaded surface area

The above equation is known as the *functional*. On the right hand side of the functional the first, second and third terms represent respectively; internal strain energy, work contributions of body forces and work contributions from surface loads

In the finite element displacement method, the displacement is assumed to have unknown values only at nodal points, so that the variation within any element is described in terms of nodal values by means of interpolation functions or shape functions i.e.

$$\delta = \mathbf{N}\,\delta^e \tag{3.2}$$

where **N** is the set of shape functions and δ^e is the vector of nodal displacements of the element. The strains within the element are expressed in terms of the nodal displacements via the strain-displacement relationship:

$$\varepsilon = \mathbf{B}\delta^e \tag{3.3}$$

where **B** is the strain matrix which is composed of derivatives of the shape functions. Likewise the stresses are related to the strains via the elasticity matrix **D** :

$$\sigma = \mathbf{D}\varepsilon \tag{3.4}$$

The total potential energy of the continuum is the sum of the energy contributions from each individual element (provided that the chosen shape functions are so as to cause no singularities in the integrands of the functional). i.e.

$$\pi = \sum_e \pi_e \tag{3.5}$$

where π_e represents the total potential energy of element *e* which on use of the functional can be written

$$\pi_e = \left(\frac{1}{2}\int_{V_e} [\delta_e]^T [\mathbf{B}]^T \mathbf{D}\mathbf{B}\delta^e .dV - \int_{V_e} [\delta^e]^T [\mathbf{N}]^T \mathbf{p}.dV - \int_{S_e} [\delta^e]^T [\mathbf{N}]^T \mathbf{q}.dS\right) \tag{3.6}$$

where V_e is the element volume and S_e the loaded element surface area. Differentiation of the above equation with respect to the nodal displacements δ^e for the element results in :

$$\frac{\partial \pi_e}{\partial \delta^e} = \left(\int_{V_e} ([\mathbf{B}]^T \mathbf{D}\mathbf{B})\delta^e .dV - \int_{V_e} [\mathbf{N}]^T \mathbf{p}.dV - \int_{S_e} [\mathbf{N}]^T \mathbf{q}.dS\right) = \mathbf{K}^e\delta^e - \mathbf{F}^e \tag{3.7}$$

where

$$\mathbf{F}^e = \int_{V_e} [\mathbf{N}]^T \mathbf{p}.dV + \int_{S_e} [\mathbf{N}]^T \mathbf{q}.dS \tag{3.8}$$

are the equivalent nodal forces for the element, and

$$\mathbf{K}^e = \int_{V_e} [\mathbf{B}]^T \mathbf{D}\mathbf{B}.dV \qquad (3.9)$$

is termed the *element stiffness* matrix. The summation of the terms in equations 3.8 and 3.9 over all the elements when equated to zero results in a system of equilibrium equations for the complete continuum. These equations can be solved by a standard technique such as Gaussian elimination in order to obtain the nodal displacements. From this the element stresses can be obtained using the aforementioned relationships.

The following is a summary of the basic steps involved in the solution of equilibrium problems by the finite element method:

- Creation of a finite element mesh i.e. discretisation.
- Evaluation of the element stiffness and load vector.
- Assembly of the element stiffness and load vector in to an overall *stiffness matrix* and *load vector.*
- Solution of the resulting linear simultaneous equations for the unknown nodal variables.
- Evaluation of the element stresses.

3.2.1 Isoparametric Elements

For the purpose of this study, eight node isoparametric elements were used in all the finite element analysis. An isoparametric element may be defined as an element whereby the same interpolation function is used to describe the displacement variation within the element as well as the element geometry.

The element coordinates and the displacements are defined by functions expressed in terms of the natural coordinates of the element. The natural coordinate system is a local system which is defined by the element geometry and is independent of the element orientation in the global system. This system is normally arranged such that

the natural coords have a unit magnitude at the element corners .i.e. ±1 (see fig 3.2a). The main advantages of isoparametric elements are as follows:

- Improved accuracy over simple elements
- Improved computational efficiency by simultaneous definition of element geometry and displacement definition
- Can facilitate the use of curved elements when modelling curved boundaries.

3.2.2 Shape functions

The interpolation or shape function N_i has the fundamental property of having a value equal to unity at node i and zero at all other nodes. Shape functions define the variation of a given variable e.g. length, displacement etc., through the element in terms of the values of that variable at the nodes of the element. As a result of this, shape functions are related to the number of nodes in an element and hence the element type. Shape functions in the form of polynomials are usually chosen due to their relative ease of mathematical manipulation, in particular when it comes to integration and differentiation.

The degree of polynomial chosen is dependent upon the number of nodes in the element and the degrees of freedom associated with the element. The following formulae represent the shape functions for eight node isoparametric elements expressed in terms of the natural coords (ξ, η):

corner nodes:

$$N_i = \frac{1}{4}(1+\xi\xi_i)(1+\eta\eta_i)(\xi\xi_i+\eta\eta_i-1) \qquad (3.10)$$

midside nodes:

$$N_i = \frac{1}{2}\xi_i(1+\xi\xi_i)(1-\eta^2)+\frac{1}{2}\eta_i(1+\eta\eta_i)(1-\xi^2) \qquad (3.11)$$

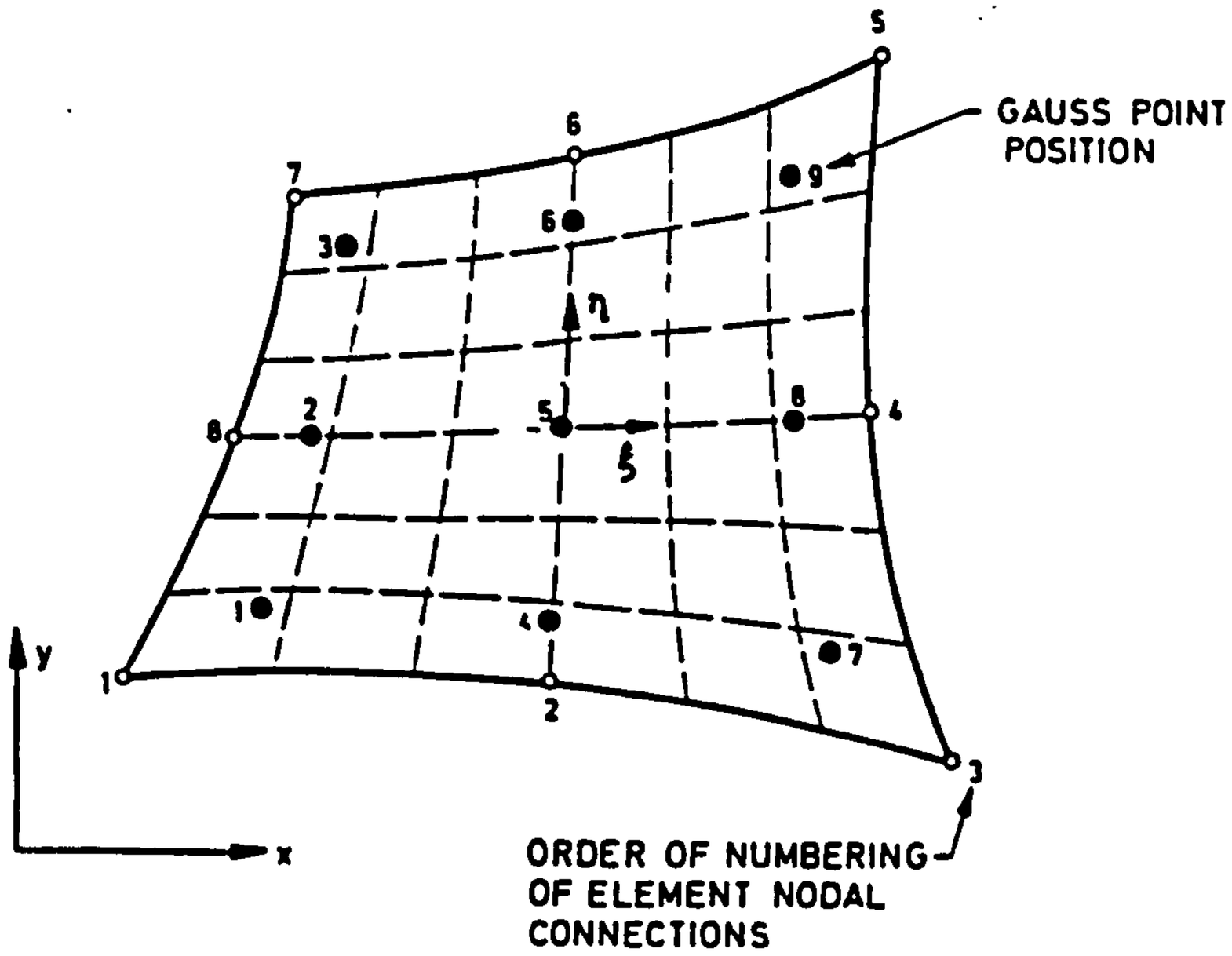

fig.3.2(a) 8-node Isoparametric Element

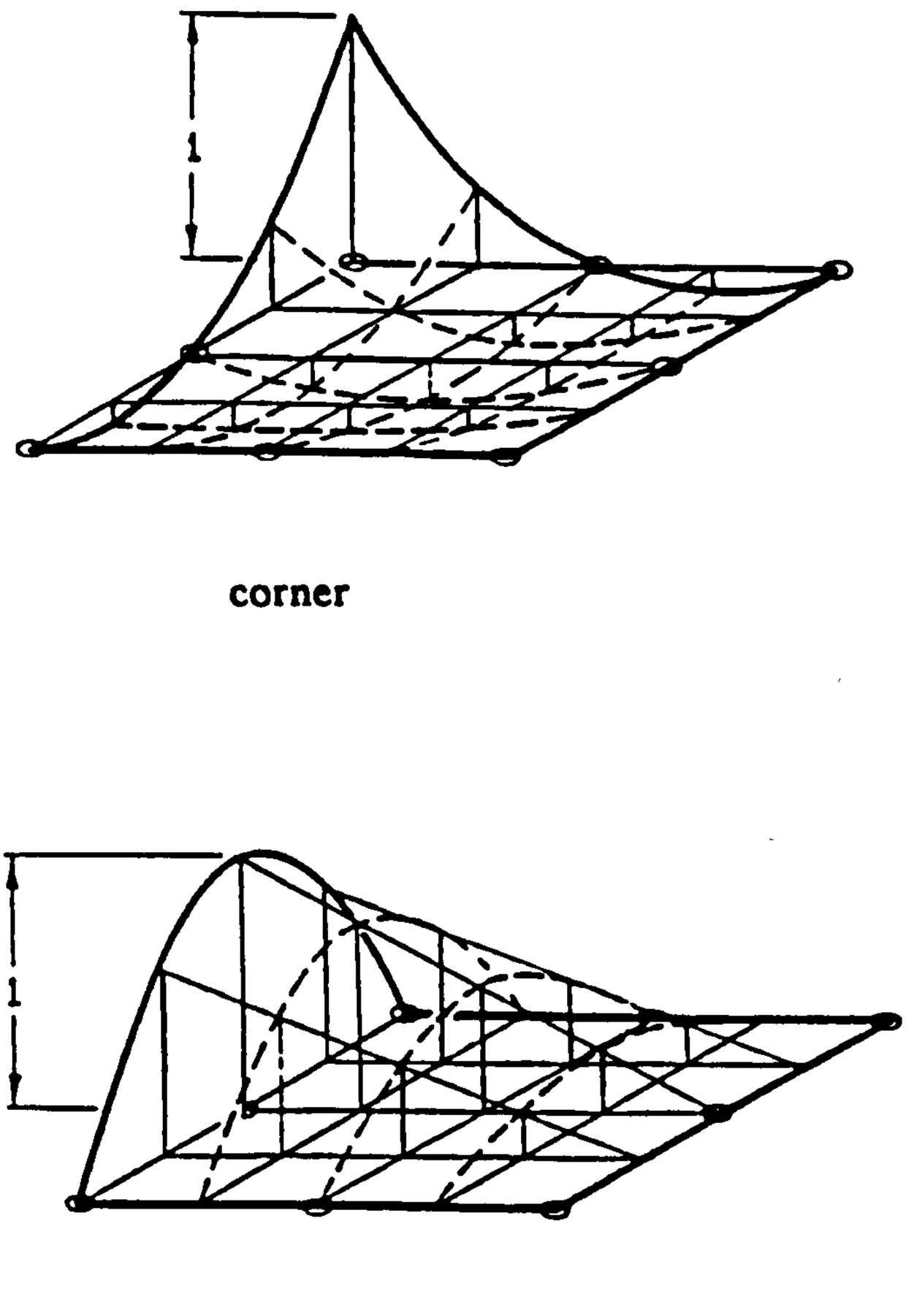

fig.3.2(b) Shape function for 8-node isoparametric element

These shape functions are part of the serendipity family (Zienkiewicz 1977) and are shown graphically in fig 3.2(b). By definition, the displacements at any point inside the element δ can be expressed in terms of these shape functions:

$$\delta(\xi,\eta) = \sum_{i=1}^{8} N_i(\xi,\eta)\delta_i \qquad (3.12)$$

where N_i is the shape function of node i and δ_i is the vector of nodal displacements at node i.

$$u = \sum_{i=1}^{8} N_i(\xi,\eta)u_i$$

$$v = \sum_{i=1}^{8} N_i(\xi,\eta)v_i \qquad (3.13)$$

Where u and v are the displacements parallel to the global x and y axes respectively. Likewise, the position of a point within the element in global coordinates can be defined as:

$$x = \sum_{i=1}^{8} N_i(\xi,\eta)x_i$$

$$y = \sum_{i=1}^{8} N_i(\xi,\eta)y_i \qquad (3.14)$$

3.3 The Layer approach

In the case of flexural deformation, a layered approach is used to take account of the variation of material property through the thickness of an element. In this system the plate thickness is either divided up into a finite number of layers parallel to the middle plane of the plate (see fig 3.3(a)) or numerical integration points are applied through the thickness.

This scheme has been used successfully in the past by many research workers. Johnarry (1979), Hago and Bhatt (1986), employed the system using rectangular elements with five degrees of freedom (u,v,w,θ_x,θ_y). Later, El-Hafez (1986) and

Bensalem (1993) used an eight node isotropic element with five degrees of freedom and this formed the basis for the current model adopted in this work.

3.3.1 Assumptions

In the model, each layer is assumed to be in a state of plane stress with a linear strain variation through the depth based on small deflection theory. The layers are allowed to resist transverse shear stresses (fig 3.3(b)). Variation of stress through the thickness of the layer is ignored. Since each layer can be of a different material, in reinforced concrete each constituent material can be assigned a different layer. Perfect bond between all the layers is normally assumed. The main assumptions for the case of plate bending are as follows:

- Displacements are small compared with the dimensions of the plate
- The stress normal to the plate is negligible
- The normal to the reference surface deformation remains straight but not necessarily normal to the reference surface after deformation (see fig 3.3(c))

3.3.2 Displacement Representation

From the above assumptions, the displacements (u, v, w) at any point within the structure coords (x,y,z) can be expressed as:

$$\begin{Bmatrix} u \\ v \\ w \end{Bmatrix} = \begin{pmatrix} u_0(x,y) - z\theta_x(x,y) \\ v_0(x,y) - z\theta_y(x,y) \\ w_0(x,y) \end{pmatrix} \tag{3.15}$$

where u_0, v_0, w_0 are the displacements at the plate reference surface in the x, y, z directions respectively. θx and θy are the rotations of the normal in the xz and xy planes respectively. In this case z is the distance from the reference surface to the mid-plane of the layer under consideration. Determination of the rotations is as follows:

$$\begin{Bmatrix}\theta_x\\ \theta_y\end{Bmatrix}=\begin{Bmatrix}\dfrac{\partial w(x,y)}{\partial x}+\phi_x(x,y)\\ \dfrac{\partial w(x,y)}{\partial y}+\phi_y(x,y)\end{Bmatrix} \tag{3.16}$$

where ϕ_x and ϕ_y are the shear deformations (see fig 3.3(c))

3.3.3 Strain Displacement Relationship

Since the nodal displacements are now defined in terms of the shape functions, the strain within the element can be expressed in terms of the displacement derivatives. In two dimensional analysis based on Mindlin plate bending and plane stress assumptions, the strain displacement relationship may be written as:

$$\begin{Bmatrix}\varepsilon_x\\ \varepsilon_y\\ \gamma_{xy}\\ \cdots\\ \gamma_{xz}\\ \gamma_{yz}\end{Bmatrix}=\left[\begin{array}{cc:ccc}\dfrac{\partial N_i}{\partial x} & 0 & 0 & -Z\dfrac{\partial N_i}{\partial x} & 0\\ 0 & \dfrac{\partial N_i}{\partial y} & 0 & 0 & -Z\dfrac{\partial N_i}{\partial y}\\ \dfrac{\partial N_i}{\partial x} & \dfrac{\partial N_i}{\partial x} & & \dfrac{\partial N_i}{\partial y} & \dfrac{\partial N_i}{\partial x}\\ \hdashline 0 & 0 & C\dfrac{\partial N_i}{\partial x} & -CN_i & 0\\ 0 & 0 & C\dfrac{\partial N_i}{\partial y} & 0 & -CN_i\end{array}\right]\begin{Bmatrix}u_i\\ v_i\\ \cdots\\ \theta_{xi}\\ \theta_{yi}\end{Bmatrix} \tag{3.17}$$

where ε_x, ε_y and γ_{xy} are the in-plane strain components, γ_{xz} and γ_{yz} are the transverse shear components. The distance from the reference plane to the layer centre is denoted by Z (see fig.3.3(b)). C is the strain coefficient which is dependent upon the shape of the cross section and is assumed to be equal to 1.0. The strain displacement relationship can be expressed in the simple form previously shown

$$\{\varepsilon\}=\sum_{i=1}^{n}[B_i]\{\delta_i\}$$

where $[B_I]$ is a 5x5 matrix which contains Cartesian derivatives of the shape functions the formation of which are described next.

3.3.4 Cartesian Shape Function Derivatives

As mentioned previously, the shape functions N_i are expressed in terms of the local natural coordinate system (ξ, η) of the element, it is therefore necessary to transform in to global coordinates to obtain the strain matrix [B]. Using the chain rule the derivatives of the shape functions are expressed as:

$$\frac{\partial N_i}{\partial \xi} = \frac{\partial N_i}{\partial x}\frac{\partial x}{\partial \xi} + \frac{\partial N_i}{\partial y}\frac{\partial y}{\partial \xi}$$
$$\frac{\partial N_i}{\partial \eta} = \frac{\partial N_i}{\partial x}\frac{\partial x}{\partial \eta} + \frac{\partial N_i}{\partial y}\frac{\partial y}{\partial \eta} \qquad (3.18)$$

and in matrix from:

$$\begin{Bmatrix} \frac{\partial N_i}{\partial \xi} \\ \\ \frac{\partial N_i}{\partial \eta} \end{Bmatrix} = \begin{bmatrix} \frac{\partial x}{\partial \xi} & \frac{\partial y}{\partial \xi} \\ \\ \frac{\partial x}{\partial \eta} & \frac{\partial y}{\partial \eta} \end{bmatrix} \begin{Bmatrix} \frac{\partial N_i}{\partial x} \\ \\ \frac{\partial N_i}{\partial y} \end{Bmatrix} = [J] \begin{Bmatrix} \frac{\partial N_i}{\partial x} \\ \\ \frac{\partial N_i}{\partial y} \end{Bmatrix} \qquad (3.19)$$

$$\begin{Bmatrix} \frac{\partial N_i}{\partial x} \\ \\ \frac{\partial N_i}{\partial y} \end{Bmatrix} = [J]^{-1} \begin{Bmatrix} \frac{\partial N_i}{\partial \xi} \\ \\ \frac{\partial N_i}{\partial \eta} \end{Bmatrix} \qquad (3.20)$$

where [J] is the Jacobian matrix defined as:

$$[J] = \begin{bmatrix} \frac{\partial x}{\partial \xi} & \frac{\partial y}{\partial \xi} \\ \frac{\partial x}{\partial \eta} & \frac{\partial y}{\partial \eta} \end{bmatrix} \qquad (3.21)$$

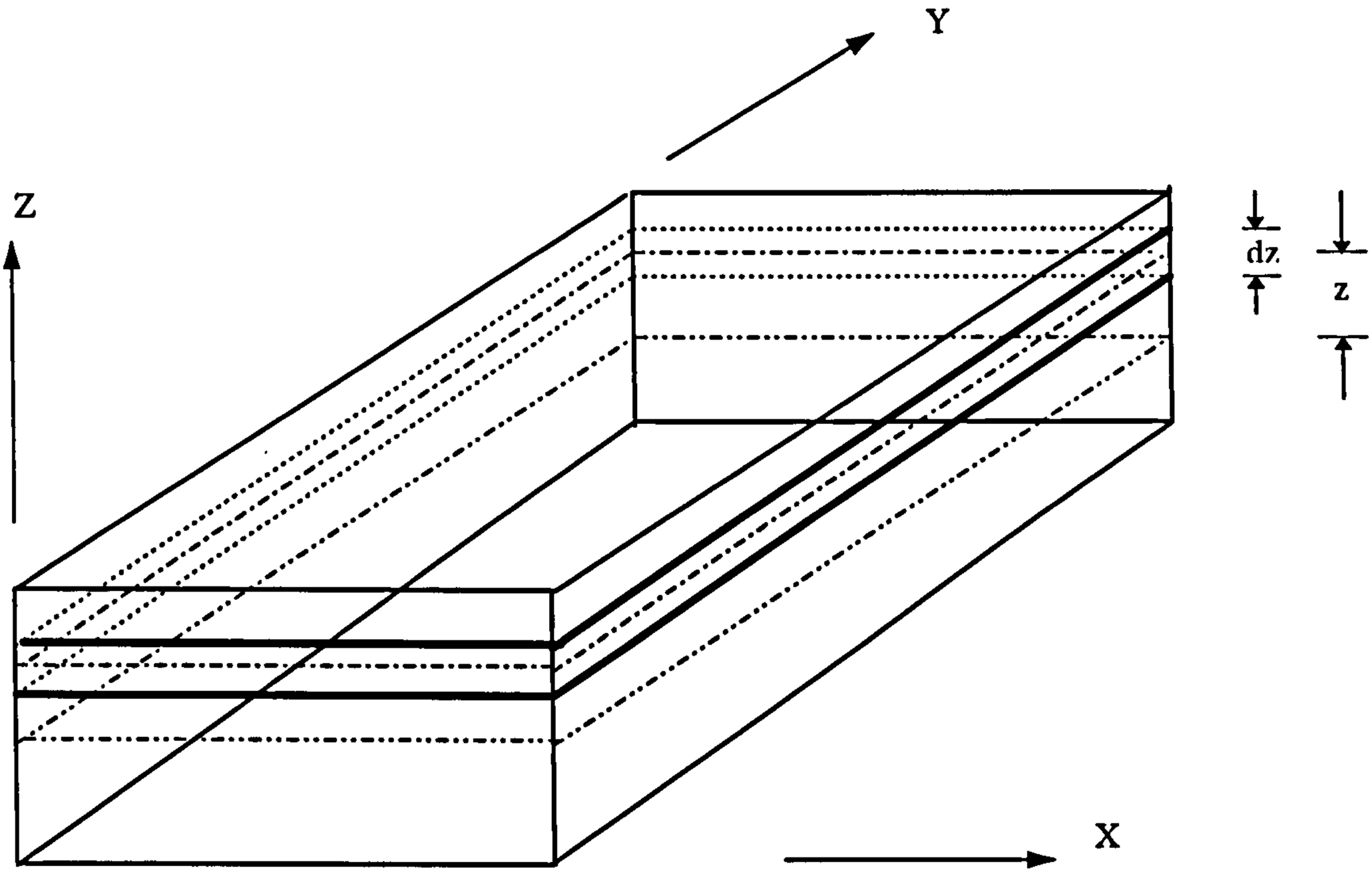

fig.3.3(a) Layer Idealisation

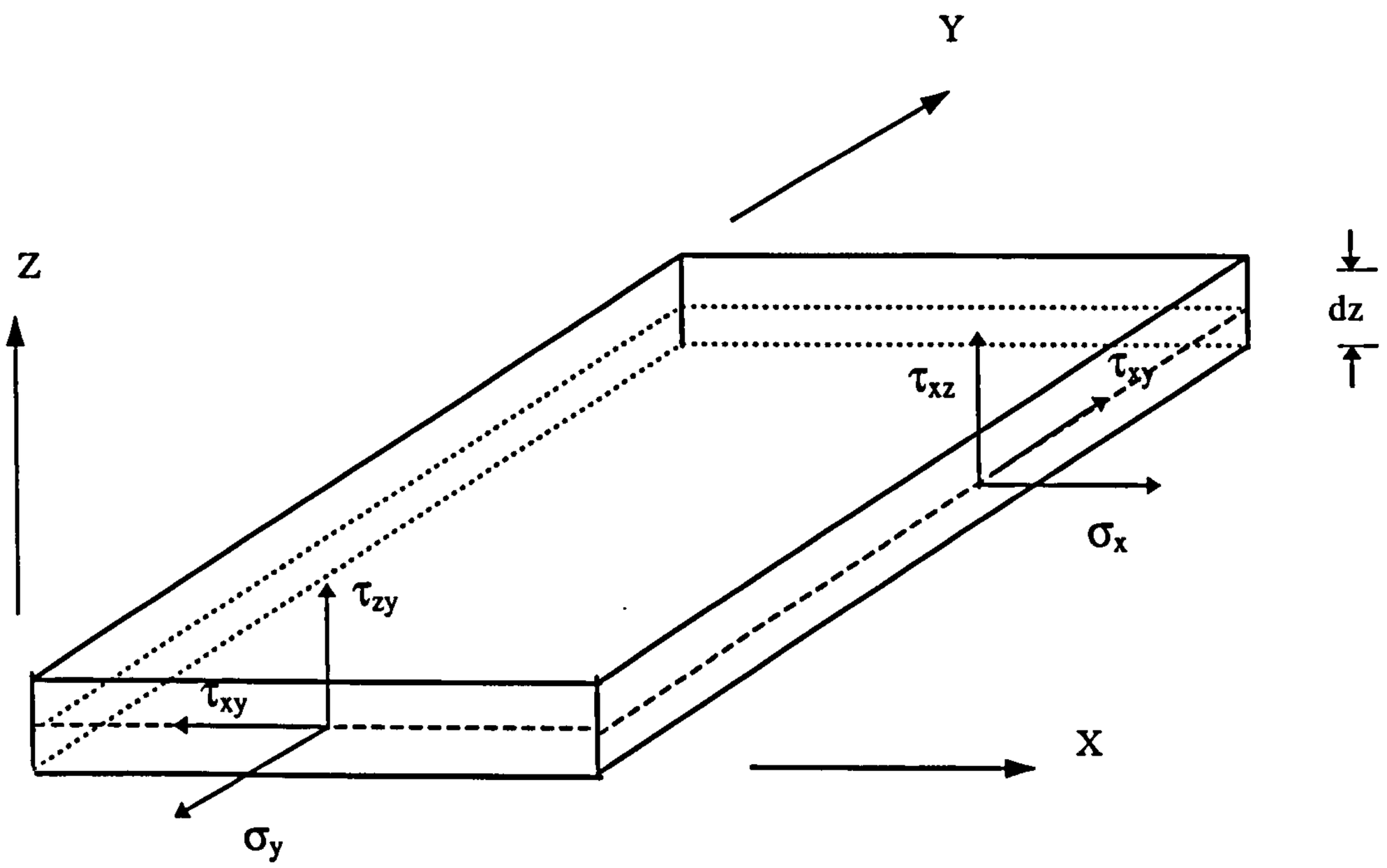

fig 3.3(b) Layer Plate Model, Stress Sign Convention

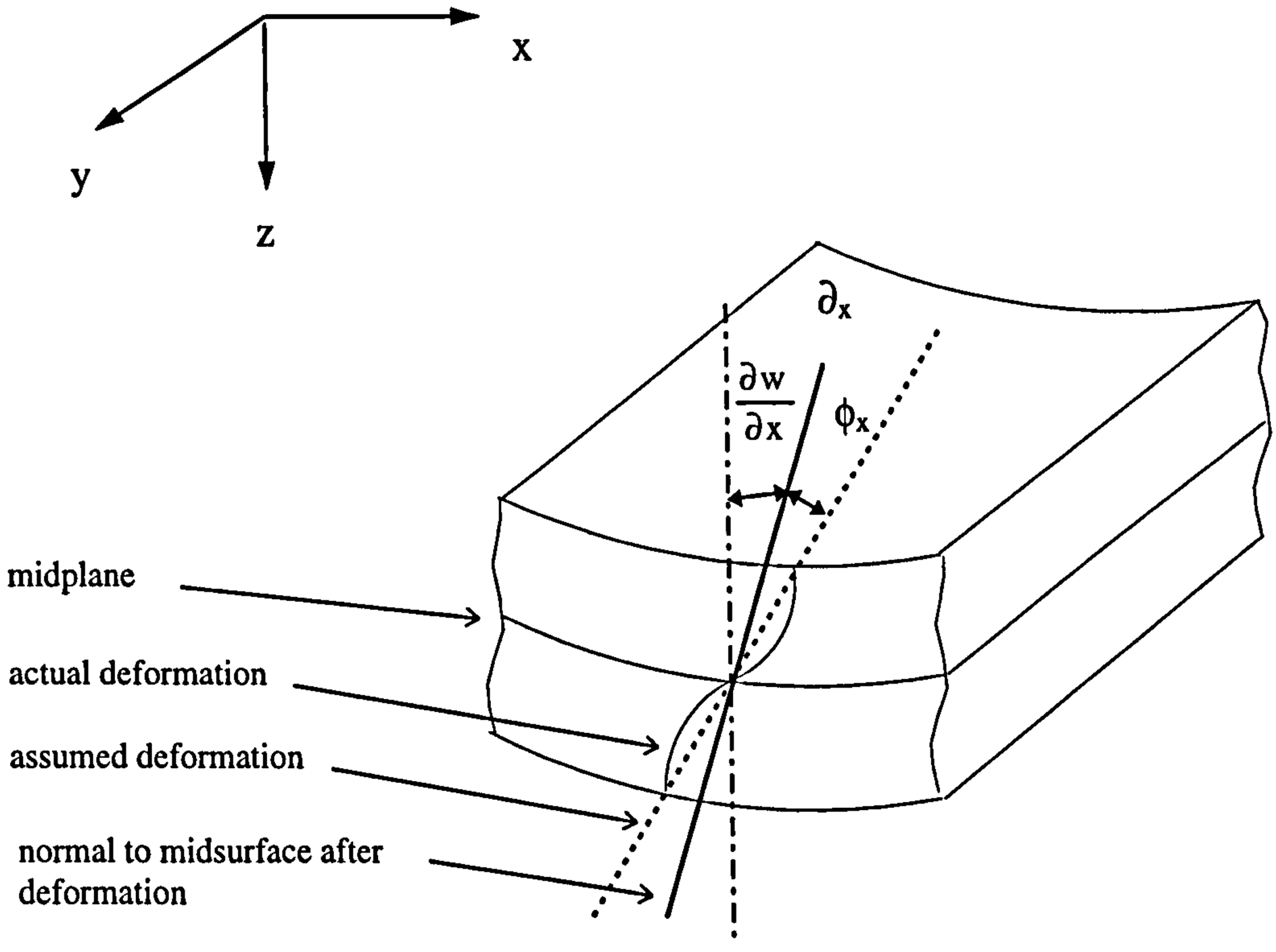

Fig 3.3(c) Cross Section Deformation of Mindlin Plate

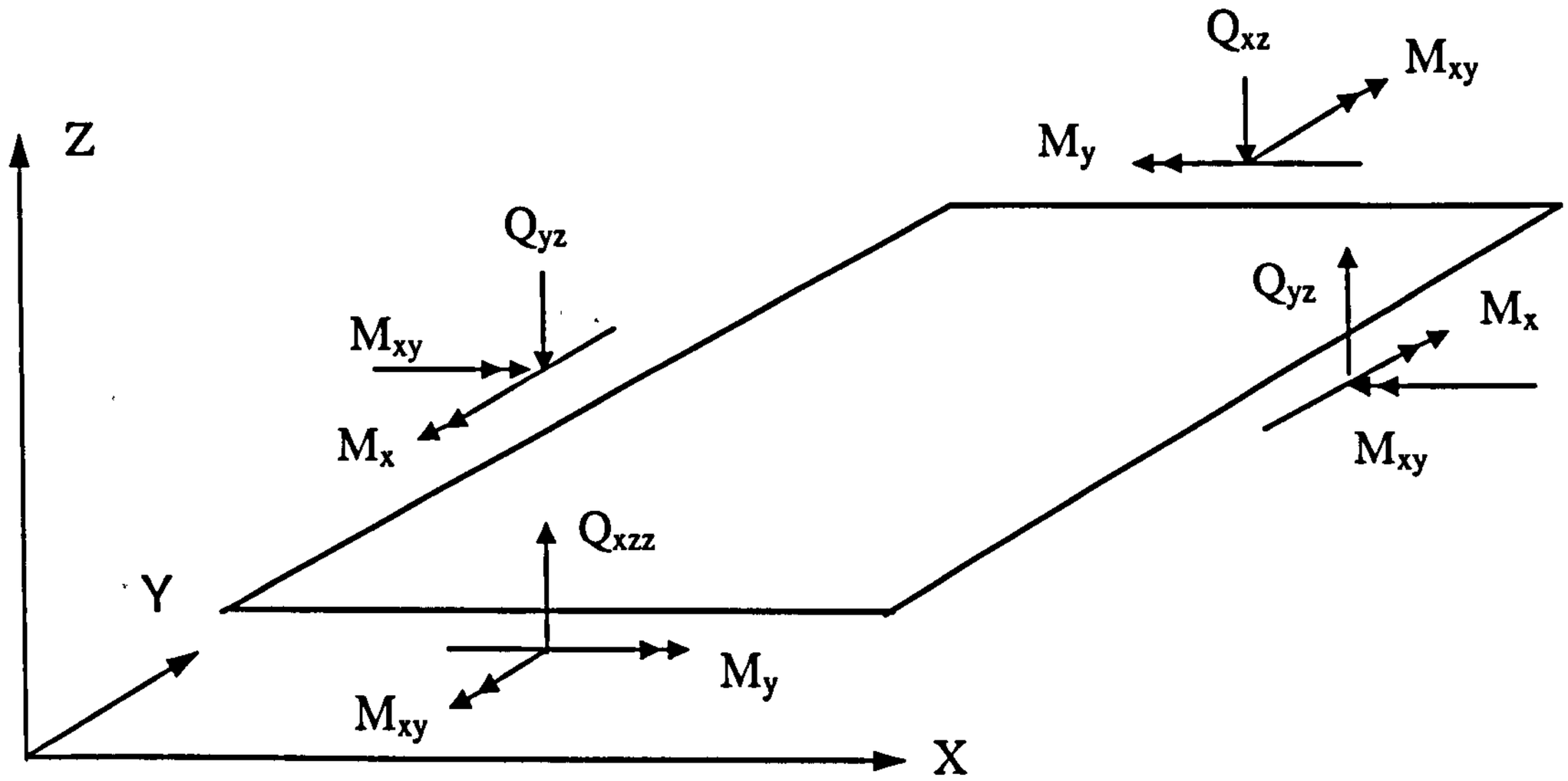

Fig 3.3(d) A Typical Mindlin Plate (positive as shown)

Since an isoparametric formulation is being implemented, i.e. where $x = \Sigma N_i x_i$ and $y = \Sigma N_i y_i$, then:

$$\frac{\partial x}{\partial \xi} = \sum_{i=1}^{8} \frac{\partial N_i}{\partial \xi} x_i , \qquad \frac{\partial x}{\partial \eta} = \sum_{i=1}^{8} \frac{\partial N_i}{\partial \eta} x_i$$

$$\frac{\partial y}{\partial \xi} = \sum_{i=1}^{8} \frac{\partial N_i}{\partial \xi} y_i , \qquad \frac{\partial y}{\partial \eta} = \sum_{i=1}^{8} \frac{\partial N_i}{\partial \eta} y_i \tag{3.22}$$

Thus [J] can be expressed in terms of the nodal coords x_i and y_i by the following

$$[J] = \sum_{i=1}^{8} \begin{bmatrix} \frac{\partial N_i}{\partial \xi} x_i & \frac{\partial N_i}{\partial \xi} y_i \\ \frac{\partial N_i}{\partial \eta} x_i & \frac{\partial N_i}{\partial \eta} y_i \end{bmatrix} \tag{3.23}$$

The inverse of the Jacobian matrix is defined as:

$$[J]^{-1} = \begin{bmatrix} \frac{\partial \xi}{\partial x} & \frac{\partial \eta}{\partial x} \\ \frac{\partial \xi}{\partial y} & \frac{\partial \eta}{\partial y} \end{bmatrix} = \frac{1}{\det J} \begin{bmatrix} \frac{\partial y}{\partial \eta} & \frac{\partial y}{\partial \xi} \\ \frac{\partial x}{\partial \eta} & \frac{\partial x}{\partial \xi} \end{bmatrix} \tag{3.24}$$

3.3.5 Stress-Strain Relationship

From the theory of elasticity the stress strain relationship for each layer can be written as:

$$\{\sigma\} = \begin{Bmatrix} \sigma_x \\ \sigma_y \\ \tau_{xy} \\ \tau_{xz} \\ \tau_{yz} \end{Bmatrix} = [D]\ \{\varepsilon\}$$

where D is the elasticity matrix given by:

$$[D]=\frac{E}{1-\nu^2}\left[\begin{array}{ccc:cc} 1 & \nu & 0 & 0 & 0 \\ \nu & 1 & 0 & 0 & 0 \\ 0 & 0 & \frac{1-\nu}{2} & 0 & 0 \\ \hdashline 0 & 0 & 0 & \frac{1-\nu}{2(1.2)} & 0 \\ 0 & 0 & 0 & 0 & \frac{1-\nu}{2(1.2)} \end{array}\right] \qquad (3.25)$$

In the above, E and ν represent Young's modulus and Poisson's ratio's respectively. The values in the top left portion refer to plane stresses. In the bottom right portion, the values refer to transverse shear stresses, the 1.2 factor is the shear deformation shape factor.

A reinforcing steel layer is assumed to be smeared into a thin layer of steel equivalent to its total area. This smeared layer of steel is assumed to have unidirectional stiffness corresponding to direction in which the actual bars lie. In this case the [D] matrix is given by

$$[D]=E_s\begin{bmatrix} 1 & 0 & 0 \\ 0 & 0 & 0 \\ 0 & 0 & 0 \end{bmatrix} \qquad (3.26)$$

In cases where the steel is positioned at an angle counter clockwise from the x-axis, the local modulus matrix is transformed to the global Cartesian axis.

3.3.6 Element Stiffness Matrix & Force Vector

The information to evaluate the element stiffness matrix for elastic material behaviour has been given. As defined previously, evaluation of [K] is carried out from the following equation:

$$[K]=\sum_{i=1}^{n}\iint [B]^T[D][B]\,dx\,dy\,t_i$$

Where t_i is the thickness of the ith layer, n is the total number of layers, [B] is the strain matrix and [D] is the material constitutive matrix depending on the material type (steel/concrete etc.) and the state of stress (elastic, cracked, plastic etc..). The constitutive material matrix will be discussed in the next chapter. Evaluation of the above equation is carried out using numerical integration and Gaussian integration rules are used to integrate over the element area as follows.

$$[K] = \sum_{i=1}^{n} \int_{-1}^{1} \int_{-1}^{1} [B]^T [D][B] \det [J] \, d\xi \, d\eta \, t_i \qquad (3.27)$$

and numerically written as:

$$[K] = \sum_{i=1}^{n} \sum_{j=1}^{m} \sum_{k=1}^{m} w_j w_k [B]^T [D][B] \det [J] \, t_i \qquad (3.28)$$

where m is the number of Gauss points in each direction, n is the number of layers, w_j and w_k are the weight coefficients corresponding to the specified Gauss point with local coords (ξ, η).

The equivalent load vector at the nodes due to the effect of uniformly distributed element surface loads is defined as:

$$[F] = \int_s [N]^T \{q\} \, ds \qquad (3.29)$$

or in numerical form:

$$\{F\} = \sum_{j=1}^{m} \sum_{i=1}^{m} w_j w_k [N]^T \{q\} \det [J] \qquad (3.30)$$

3.3.7 Numerical Integration

In numerical integration, the exact integral is replaced by evaluating the integrand at various sampling points and then taking a weighted summation of these values. For this work, Gauss Legendre quadrature values was employed due to its relative ease of implementation and high accuracy. In this method an *n*-point rule integrates any polynomial of degree x^{2n-1}, or less, exactly.

In general, the one-dimensional Gaussian Quadrature formula takes the form:

$$\int_{-1}^{+1} f(\xi)d\xi = \sum_{i=1}^{m} w_i f(\xi_i) \qquad (3.31)$$

where ξ_i is the coordinate of the ith integration point, w_i is the weighting factor and *m* is the total number of integration points. For the case of double integration i.e. over 2 dimensions the following form is taken:

$$\begin{aligned}\int_{-1-1}^{+1+1} f(\xi,\eta)d\xi d\eta &= \int_{-1}^{+1}\left[\sum_{i=1}^{m} w_i f(\xi_i,\eta)\right]d\eta \\ &= \int_{-1}^{+1}\left[\sum_{i=1}^{m} w_i g_i(\eta)\right]d\eta \\ &= \sum_{i=1}^{m}\sum_{j=1}^{m} w_i w_j g(\eta_j) \\ &= \sum_{i=1}^{m}\sum_{j=1}^{m} w_i w_j f(\xi_i,\eta_j)\end{aligned}$$

where w_i, w_j are the ith and jth weighting factors and $\xi_i\,\eta_j$ are the coordinates of the ith integration point. The fact that limits of integration (-1 / +1) coincide with the local natural coordinate system on the element boundaries makes them particularly applicable to isoparametric elements. The symmetrical positions of Gauss points ξ_i and the corresponding weighting factors wi for m=1-4 are given in table 3.3.7

3.4 Non-linear Solution Techniques

In a non-linear problem the relationship between the force vector and the displacement vector is no longer linear. As in the case of plastic material behaviour the current displacements may depend on the displacements at earlier stages.

In finite element analysis, the displacement vector is calculated such that a state of equilibrium is achieved between the external and internal forces. Unlike linear analysis, the solution vector in a non-linear analysis cannot be found right away. In non-linear analysis, the loading of the structure is divided into a series of increments.

In order to achieve equilibrium at the end of each increment, an iterative solution algorithm is employed. A purely incremental method could lead to inaccuracies unless very small increments are used. In an iterative method the occurring errors within the increment are successively reduced. Hence, most solutions in non-linear analysis are based upon the incremental-iterative method. The general procedure in this method involves adapting the total displacement increment $\Delta\mathbf{u}$ by iterative increments $\delta\mathbf{u}$ until equilibrium is reached within a pre-defined tolerance. The incremental displacements at iteration i+1 are calculated from

$$\Delta\mathbf{u}_{i+1} = \Delta\mathbf{u}_i + \delta\mathbf{u}_{i+1} \tag{3.32}$$

There a number of iteration procedures which calculate $\delta\mathbf{u}$ in different ways. The iterative increments are calculated via the stiffness matrix $\mathbf{K}$ which represents a linearized form of the relation between the force vector and the displacement vector. The stiffness matrix can change for every ith iteration. Hence the iterative increments can be found by the following :

$$\delta\mathbf{u}_i = \mathbf{K}_i^{-1}\,\mathbf{R}_i \tag{3.33}$$

where $\mathbf{R}_i$ is the residual force vector at the beginning of the ith iteration. One of the most common iterative methods is the Newton-Raphson method. Within the method

itself there are two variations, the second of which is known is the Modified Newton Raphson method.

3.4.1 Standard Newton-Raphson

In general the stiffness matrix $\mathbf{K}_i$ represents the tangential stiffness of the structure:

$$\mathbf{K}_i = \frac{\partial \mathbf{R}}{\partial \Delta \mathbf{u}} \tag{3.34}$$

In the normal Newton-Raphson iteration, the stiffness relation shown above is evaluated every iteration. Therefore the prediction of the iterative increments (eq.3.33) is based on the last-known or predicted situation, regardless of whether a state of equilibrium is achieved. Since the normal Newton-Raphson method yields a quadratic convergence characteristic, only a few iterations are needed for convergence. The main disadvantage of this method is that the stiffness matrix has to be set up at every iteration. Second to this, if the linear equations are solved through a direct solver, the matrix will have to be decomposed at every iteration as well, see fig.3.4.1. If the initial prediction is far from the final solution, the method will fail due to divergence.

3.4.2 Modified Newton-Raphson

In this method the stiffness matrix is only evaluated at the start of each increment which means the prediction is always based upon converged equilibrium state. In general the modified Newton-Raphson technique converges to equilibrium slower than the standard method. The advantage of this method is that for every iteration only the prediction of the incremental displacements and the internal force vector has to be calculated , it is not necessary to set up a new stiffness matrix, see fig.3.4.2.

In comparison with the standard method the Modified Newton-Raphson iteration sometimes provide convergence in problems where the standard method has failed to converge.

3.4.3 Incremental procedures

In the previous section the iteration techniques used in non-linear analysis were discussed. This section deals with the incremental techniques employed in the incremental-iterative method. The two most common techniques are load and displacement control:

- *Load control*: as described in the previous section, the external load is increased at the start of each increment by increasing the external force vector $\mathbf{f}_{ext}$.
- *Displacement control*: the external load is applied in the form of prescribed displacements $\mathbf{u}^c$.

As can be seen from figure 3.4.3 the unloading branch of the load-displacement curve can be obtained when using displacement control. In real cases however it may be necessary to obtain the unloading branch of the load/displacement curve which results from a given design load. The *Arc-length* or *Riks* method can be used to obtain the required results in this case, (Crisfield 1991).

3.4.4 Convergence criteria

In the numerical process the equilibrium conditions are unlikely to be satisfied exactly and hence criteria to determine convergence have to be defined. The convergence criterion will monitor the out-of balance residual forces until a desired level of accuracy has been achieved. Convergence criterion can be based on the out-of balance force norms, the displacements or the internal strain energy. The method adopted for the present work is based upon the out-of balance force norms. It is difficult and expensive to check the decay of each residual force for each degree of freedom and hence force norms are used to achieve an overall evaluation of convergence.

The criterion assumes convergence when the following condition is met:

$$\frac{\Delta R_i^*}{F_i^*} \leq \vartheta \qquad (3.35)$$

where:

$\Delta R_i^* = \sqrt{\{R_i\}^T \{R_i\}}$ = norm of the residuals

$\{R_i\}$ = residual force vector at ith iteration

$F_i^* = \sqrt{\{F_i\}^T \{F_i\}}$ = norm of the total applied loads

$\{F_i\}$ = total applied load vector

ϑ = specified convergence tolerance

In the interest of accuracy it is desirable to set as fine a tolerance as possible, however this has to be balanced with the need to reduce computation time i.e. a finer the tolerance usually requires a higher number of iterations. The required number of iterations will often increase as more non-linear phenomena (e.g. concrete cracking, concrete crushing, steel yielding etc.) are encountered . These discontinuities in the material laws result in high residuals having to be distributed which may result in further discontinuities in other parts of the structure.

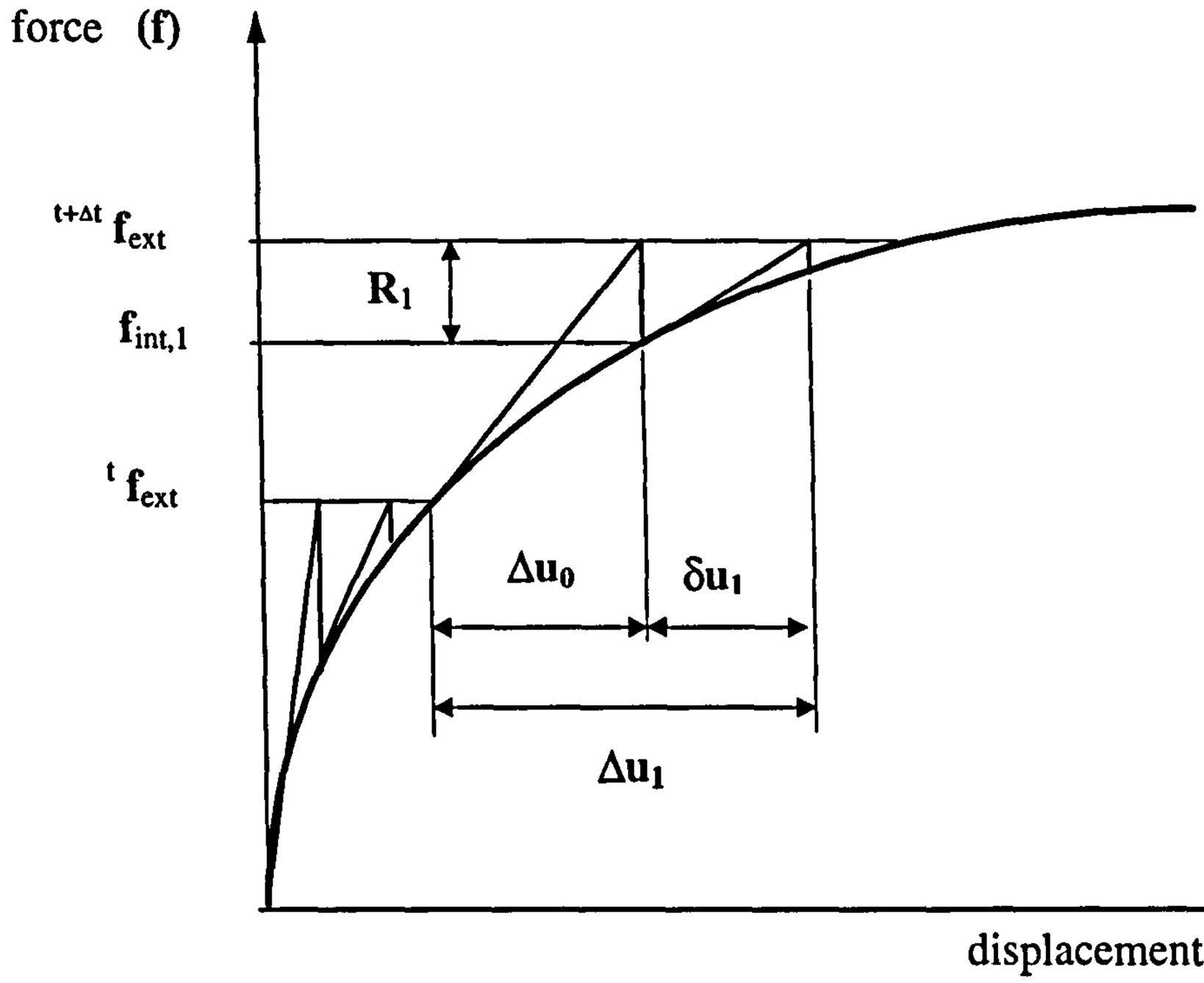

fig.3.4.1 Standard Newton-Raphson iteration

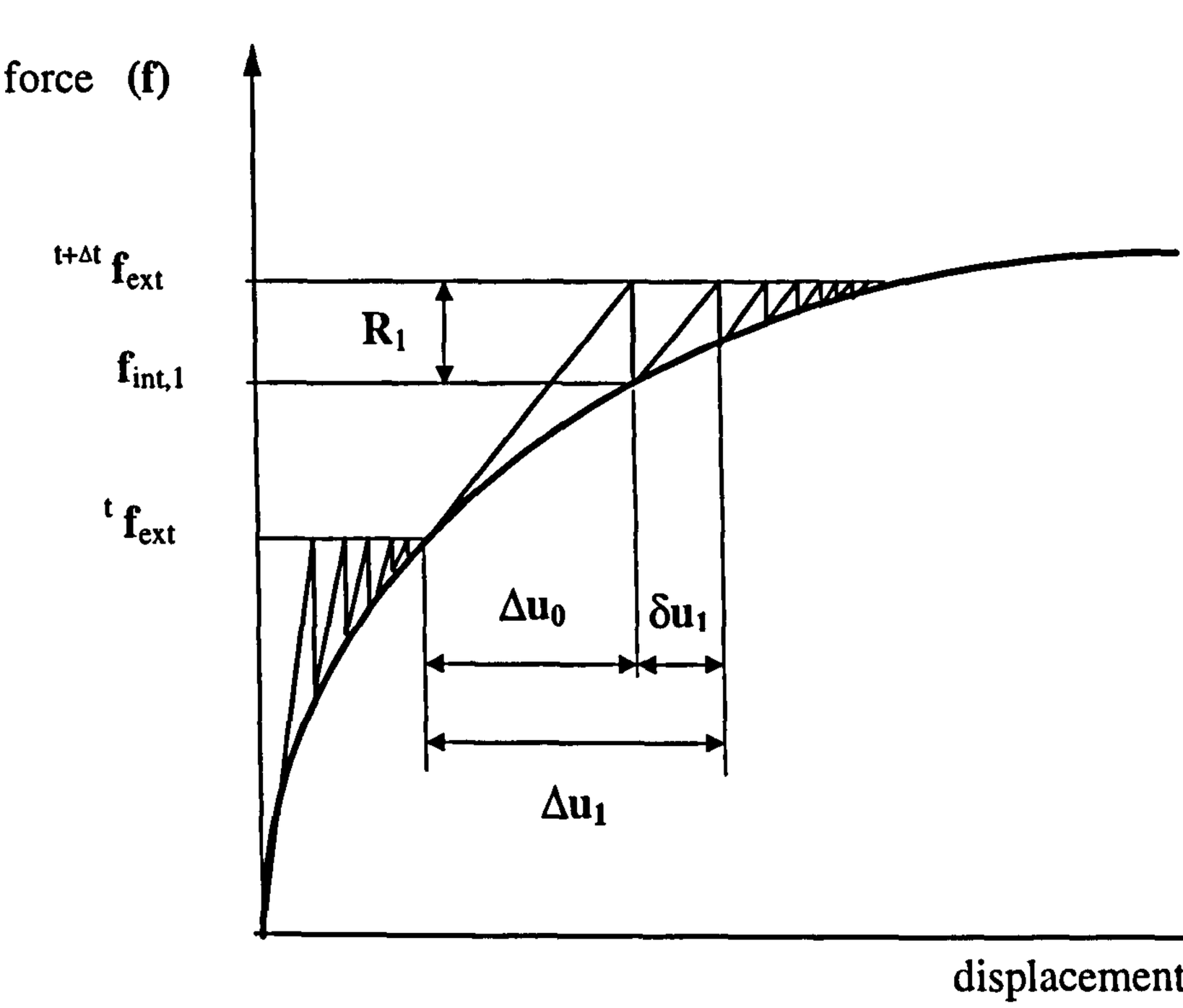

fig.3.4.2 Modified Newton-Raphson iteration

m	i	ξ_i	a_i
1	I	0	2
2	I	$+1/\sqrt{3}$	+1
	II	$-1/\sqrt{3}$	+1
3	I	0	8/9
	II	$+\sqrt{0.6}$	5/9
	III	$-\sqrt{0.6}$	5/9
4	I	$\sqrt{\frac{3+\sqrt{4.8}}{7}}$	$\frac{1}{2}-\frac{\sqrt{30}}{36}$
	II	$-\sqrt{\frac{3+\sqrt{4.8}}{7}}$	$\frac{1}{2}-\frac{\sqrt{30}}{36}$
	III	$\sqrt{\frac{3-\sqrt{4.8}}{7}}$	$\frac{1}{2}+\frac{\sqrt{30}}{36}$
	IV	$-\sqrt{\frac{3-\sqrt{4.8}}{7}}$	$\frac{1}{2}+\frac{\sqrt{30}}{36}$

Table 3.3.7 Gauss Point Positions and Corresponding Weighting Factors

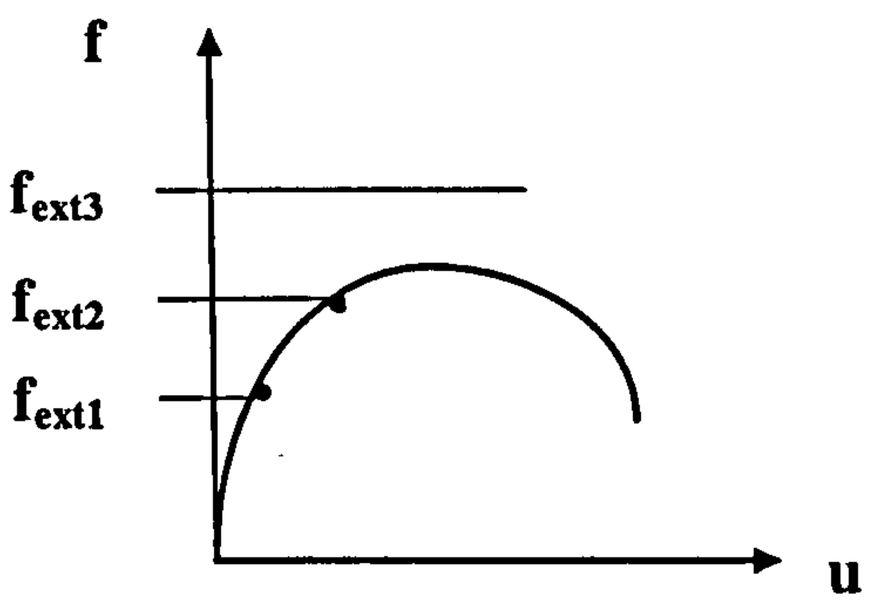

a) load control

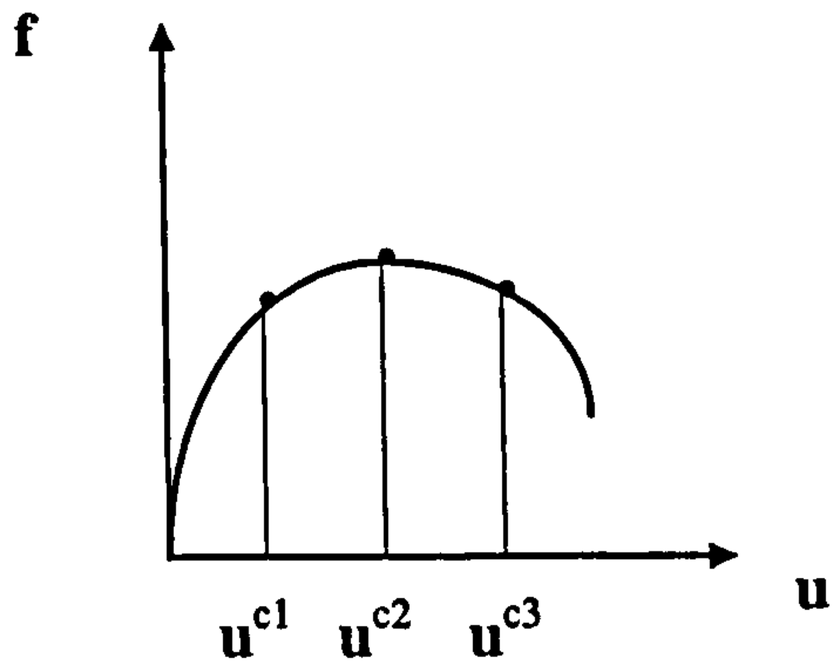

b) displacement control

fig.3.4.3 load & displacement control

Chapter 4

Model Visualisation & Direct Design

4.1 Introduction

This chapter details the visualisation process used in the formation of strut-tie models in this work. The method is also applied to slabs and is used in conjunction with direct design procedure to derive reinforcement layouts. The results of this work are given in subsequent chapters. Details of the direct design method are presented here.

4.2 The Visualisation Process

As a means of automatically defining the major stress paths and hence strut-tie model, an evolutionary procedure is proposed. This method, is adapted from the structural optimisation work first presented by Xie & Steven (1993), (1994). The general process leads to isolation of the main stress paths within the structure and hence aid in the identification of suitable strut-tie models for a given load case.

4.2.1 Theory

The process begins with an elastic analysis of the original structure. It is often found that parts of the structure are lowly stressed and can be removed without affecting the overall strength. In the finite element mesh, a low stressed element can be removed by assigning a negligible stiffness, hence it is not necessary to redefine the mesh. As a criterion for element removal, the average vonMises stress present within the element, σ_e^{VM}, is compared to the maximum vonMises Stress present in the structure, σ_{max}^{VM}. If σ_e^{VM} is less than a certain percentage of σ_{max}^{VM} , known as the rejection ratio (*rr*), i.e. if $\sigma_e^{VM} < rr\ (\sigma_{max}^{VM})$, it is removed

The von Mises stress was chosen as for this purpose because it is a measure of all the stresses present, and was calculated from the following:

$\sigma_e{}^{VM} = \sqrt{(\sigma_x{}^2 + \sigma_y{}^2 - \sigma_x\sigma_y + 3\tau_{xy}{}^2)}$, where $(\sigma_x,\sigma_y,\tau_{xy})$ are the Cartesian stresses.

Each time an element is removed, the finite element analysis is carried out using the same value of *rr* until a steady state is reached, i.e no more elements are removed. When this stage is reached, *rr* can be increased. This process is repeated until one of the following criteria is met:

- the main stress paths become clear
- *rr* becomes too great, typically a maximum value of 35% is used for *rr*. Any elements remaining after this point are not considered to be lowly stressed
- the structure becomes unstable

Once the main stress paths have been isolated, the strut-tie models are generated by placing strut or tie members along the centre lines of the main stress fields. It is necessary to exercise some degree of design experience when generating the model in terms of the stability of the resulting truss, and in terms of the practical constraints on reinforcement layouts. The object of the visualisation process is to obtain a set of stress distributions along clearly defined paths which are in equilibrium with the external loads.

4.2.2 Examples

Three examples of the visualisation process are shown. The first, shown in figure 4.2(a) is a simply supported deep beam having a span/depth ratio, (l/d), of 1.67, with a vertical load at the centre. The second, shown in figure 4.2(b), is the same beam cantilevered with a vertical load at the free end. The third, is similar to the second example but with a smaller span/depth ratio of 1.0. In each case, a clearly defined stress path is formed at a *rr* value of between 20-25%. The second and third case illustrate the effect of span-depth ratio on the load path behaviour. Strut-tie models resulting from the visualisation process are illustrated in figure 4.2.3(d). In the case of the deep beam, the resulting strut-tie model is statically determinate since the diagonal part ABCD is acting as a rigid block and hence a mechanism is not formed. The reason for the incorporation of the ties in the diagonal truss is to take account of the transverse tensile stresses which can be clearly seen from the stress plot 4.2(a).

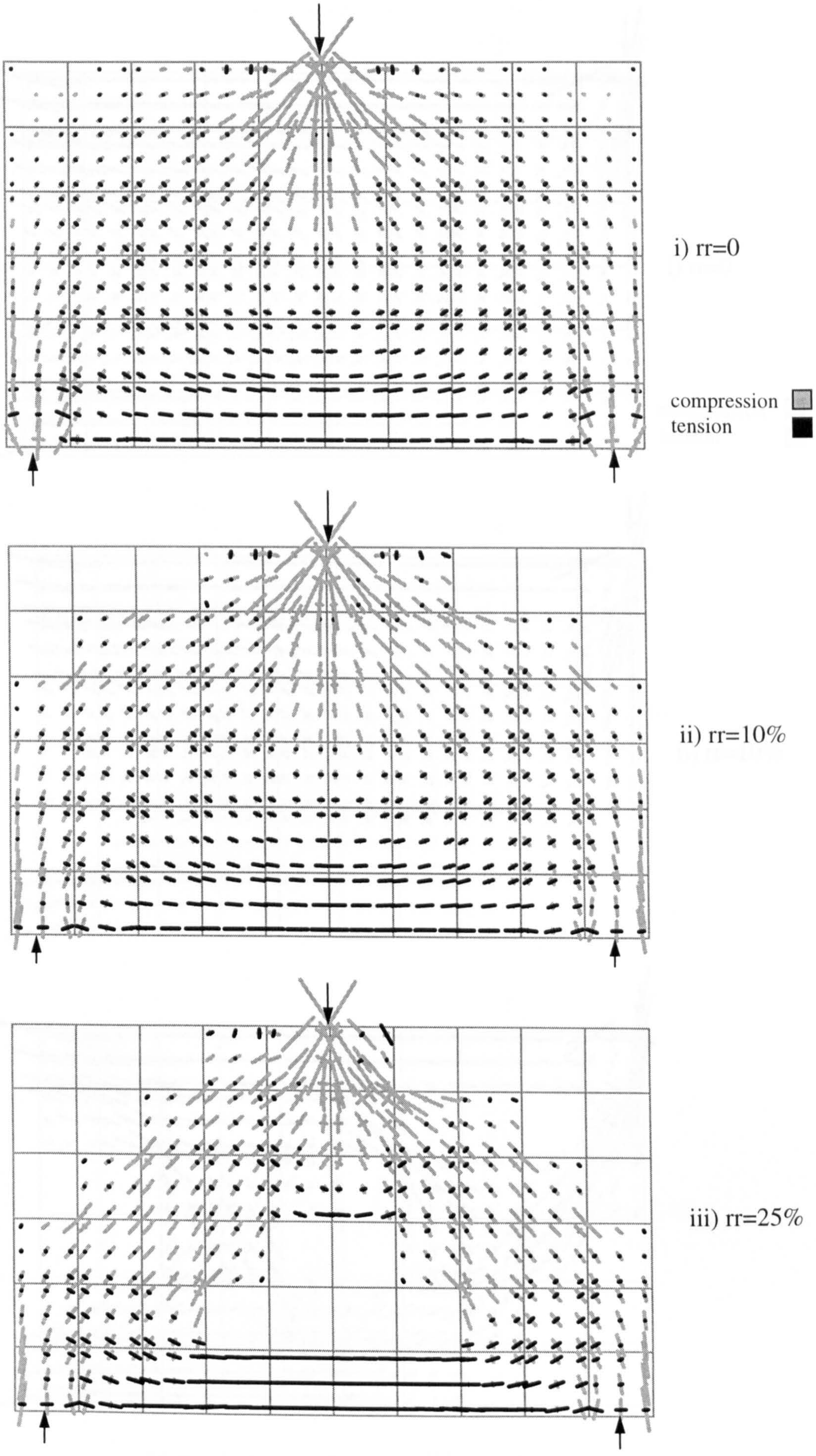

fig.4.2(a) Deep Beam (l/d=1.67): Principal Stresses During Stages of Visualisation

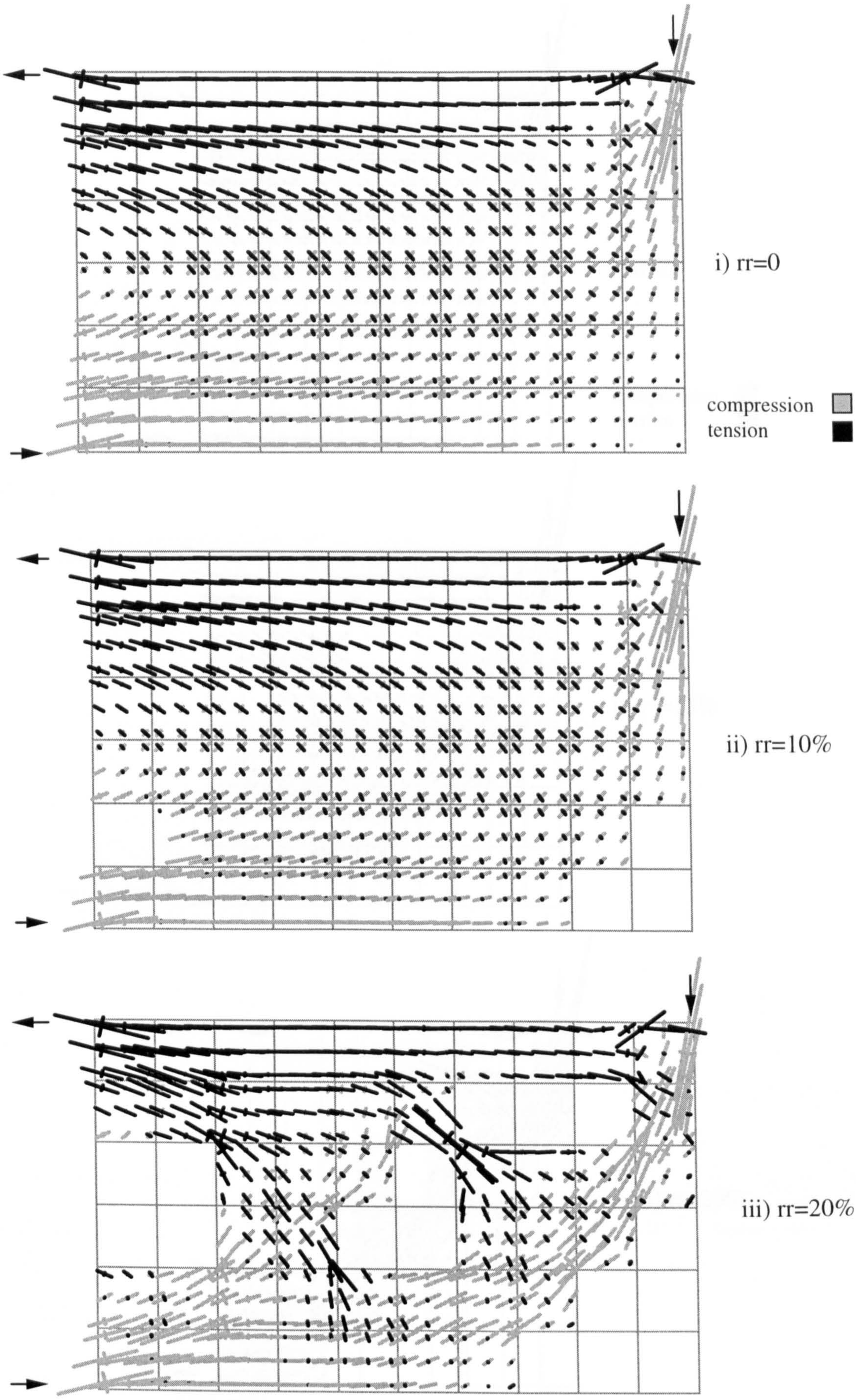

fig.4.2(b) Cantilever, (l/d=1.67): Principal Stresses During Stages of Visualisation

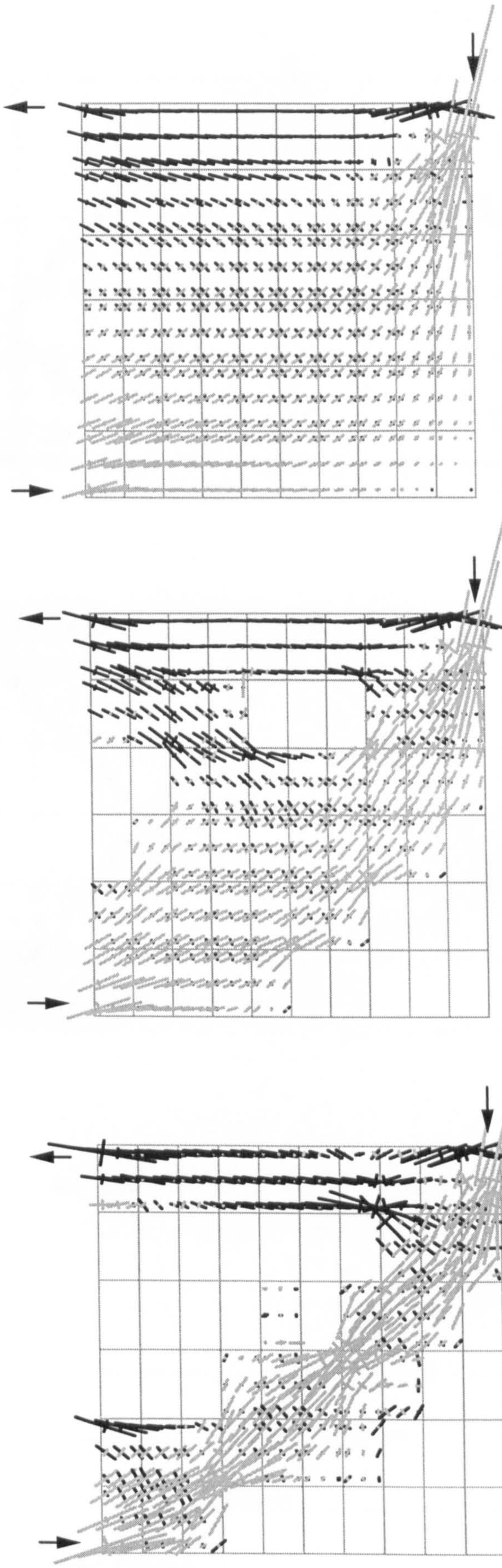

i) rr=0

compression
tension

ii) rr=15%

iii) rr=20%

fig.4.2(c) Deep Cantilever, (l/d=1.0):
Principal Stresses During Stages of Visualisation

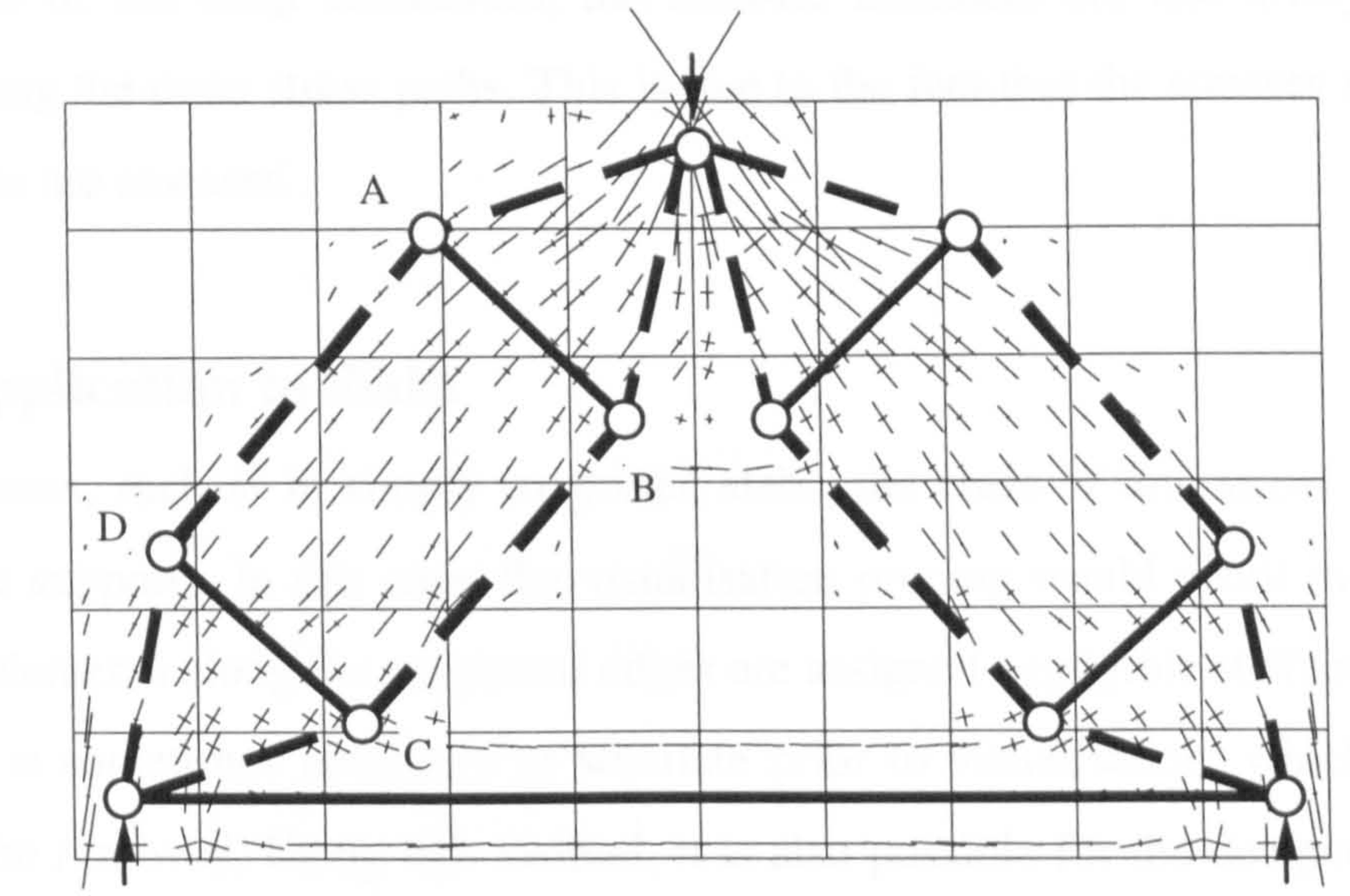

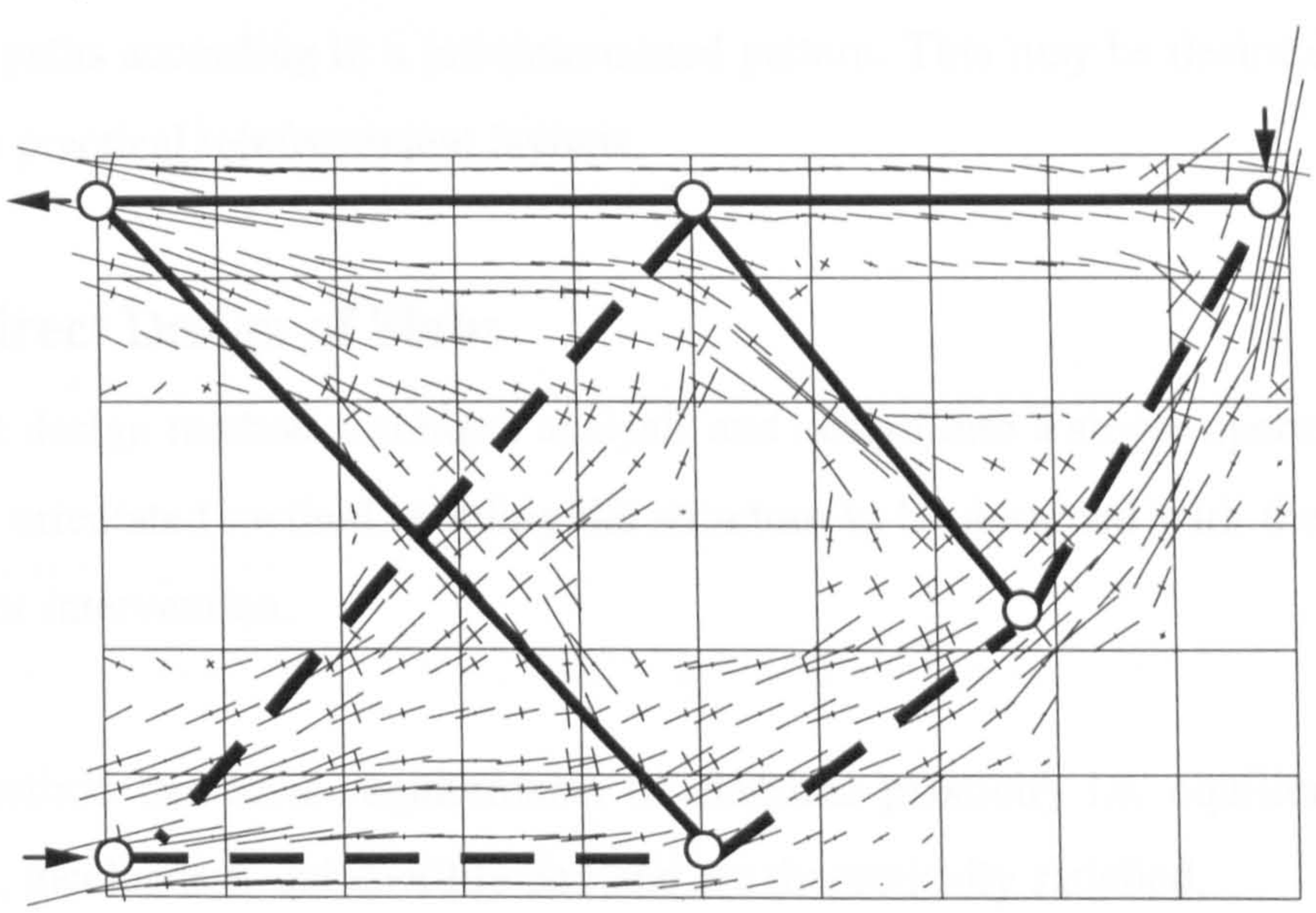

fig.4.2(d) Strut-Tie Models Resulting from Visualisation

In the case of the deep cantilevers, the strut-tie members are not always aligned exactly along the main stress paths. This is due to the fact that the stresses around the nodal zones are smeared .

4.2.3 Application to Slabs

In some cases, such as in simply supported slabs, the areas of low stress may occur around the supports. In this case, the visualisation process would result in instability since the elements along the supported edges are assigned negligible stiffness. For this reason, it is sometimes necessary to stipulate prior to visualisation, which elements must not be removed. Using this method, it is also possible for the designer to direct the stress paths according to a pre-determined pattern. This may be desirable in order to achieve practical reinforcement layouts.

4.3 Direct Design of Slabs

The direct design method combines analysis and design into a single operation. It is a computer orientated method enabling the structure to be designed with the minimum of designer intervention.

In this method the basic requirements of classical plasticity i.e. equilibrium, yield condition, mechanism and ductility demand are theoretically satisfied.

- *Equilibrium condition*: Any stress distribution in equilibrium with the applied loads can be used for design. In the proposed method the stress fields are obtained using FE analysis of the unreinforced concrete structure with the uncracked properties of the concrete so that the equilibrium condition is satisfied.
- *Yield condition*: The required steel for the structure is determined directly from the yield criteria. Therefore, the resistance provided by concrete and steel is equal to or greater than the applied stresses.
- *Mechanism condition*: The resistance at each point in the structure is matched as closely as possible to the applied stresses. This means that at ultimate load, all points in the structure attain their ultimate strength with a minimum redistribution of the stresses, thus converting the structure into a mechanism

- *Ductility demand*: In classical plastic theory the material is assumed to possess unlimited ductility. This means that any part of the structure that yields early in the loading history, will continue to deform without any reduction in strength. This requirement is avoided when the difference between the yield load and ultimate load are made as small as possible. As a result of this, the early yielded points can deform at constant stress before reaching the descending branch of the material stress-stain curve. In the direct design method this condition is satisfied automatically since theoretically all parts of the structure yield simultaneously.

The first method for the provision of reinforcement for slabs according to elastic theory was proposed by Hillerborg (1953). This method was re-examined by Wood (1968) who established simple rules and equations for the optimum steel in slab elements subject to a moment field (M_x, M_y , M_{xy}) without membrane forces. Woods' equations for orthogonal steel in the top and bottom face of the slab were extended by Armer (1968) to cover skew reinforcement.

4.3.1 Assumptions

The main assumptions in the direct design approach are summarised as follows;

- The reinforcing bars are only able to carry uni-axial stresses in their original directions, i.e. dowel action and bending of the bars is ignored
- The bars are elastic-perfectly plastic with yield stress f_s in tension and f_s' in compression, see figure 4.3.1(a)
- The bars are taken as an area per unit width rather than individual bars , because the bar spacing is small compared with the overall dimensions of the slab.
- The tensile strength of the concrete is ignored.
- The concrete is perfectly plastic, satisfying the square yield criterion shown in figure 4.3.1(b)
- Instability or bond failure of the bars is assumed not to occur and is avoided by proper choice of section and reinforcement.

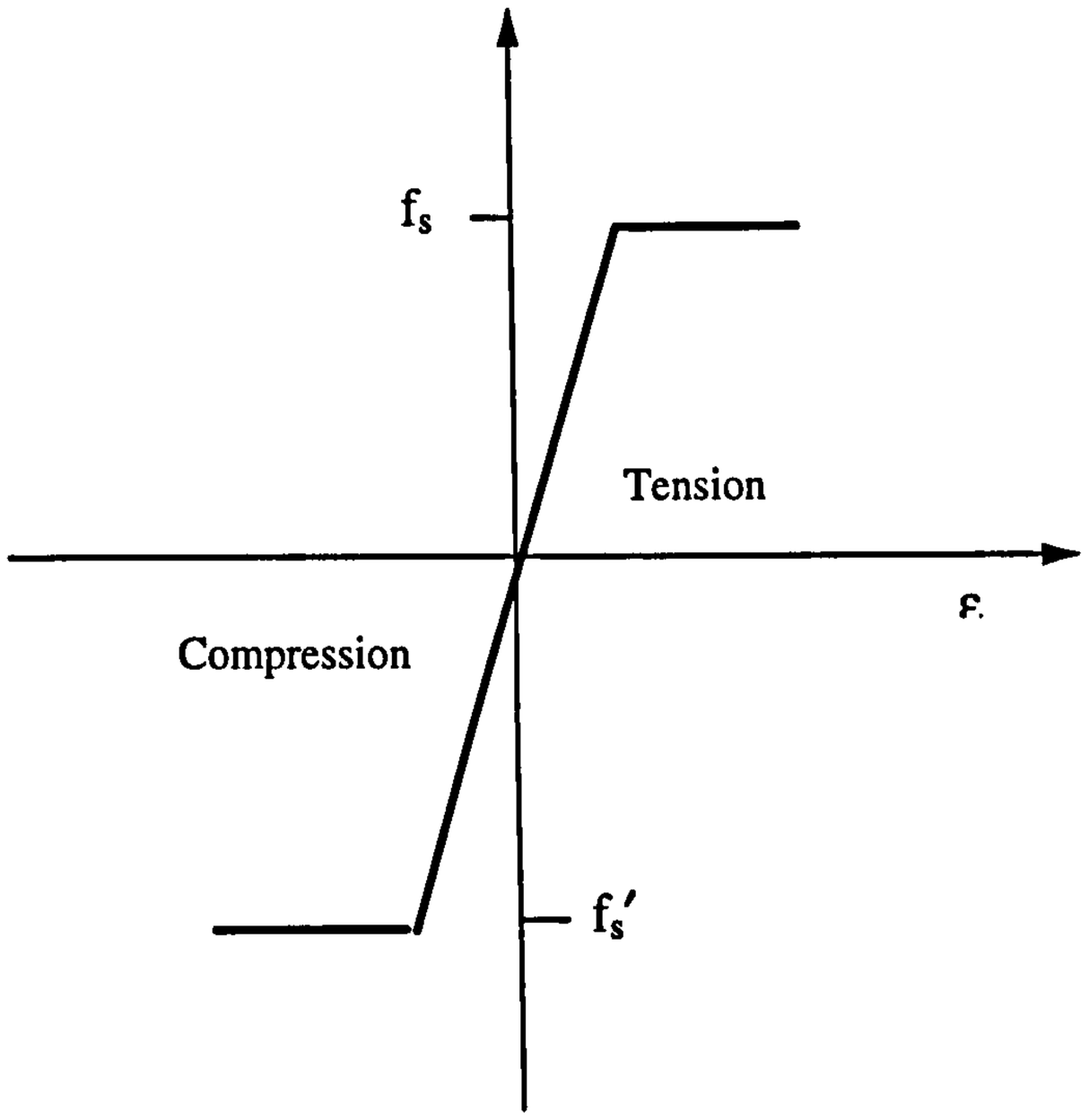

fig4.3.1(a) Assumed Reinforcement Steel Stress-strain Response

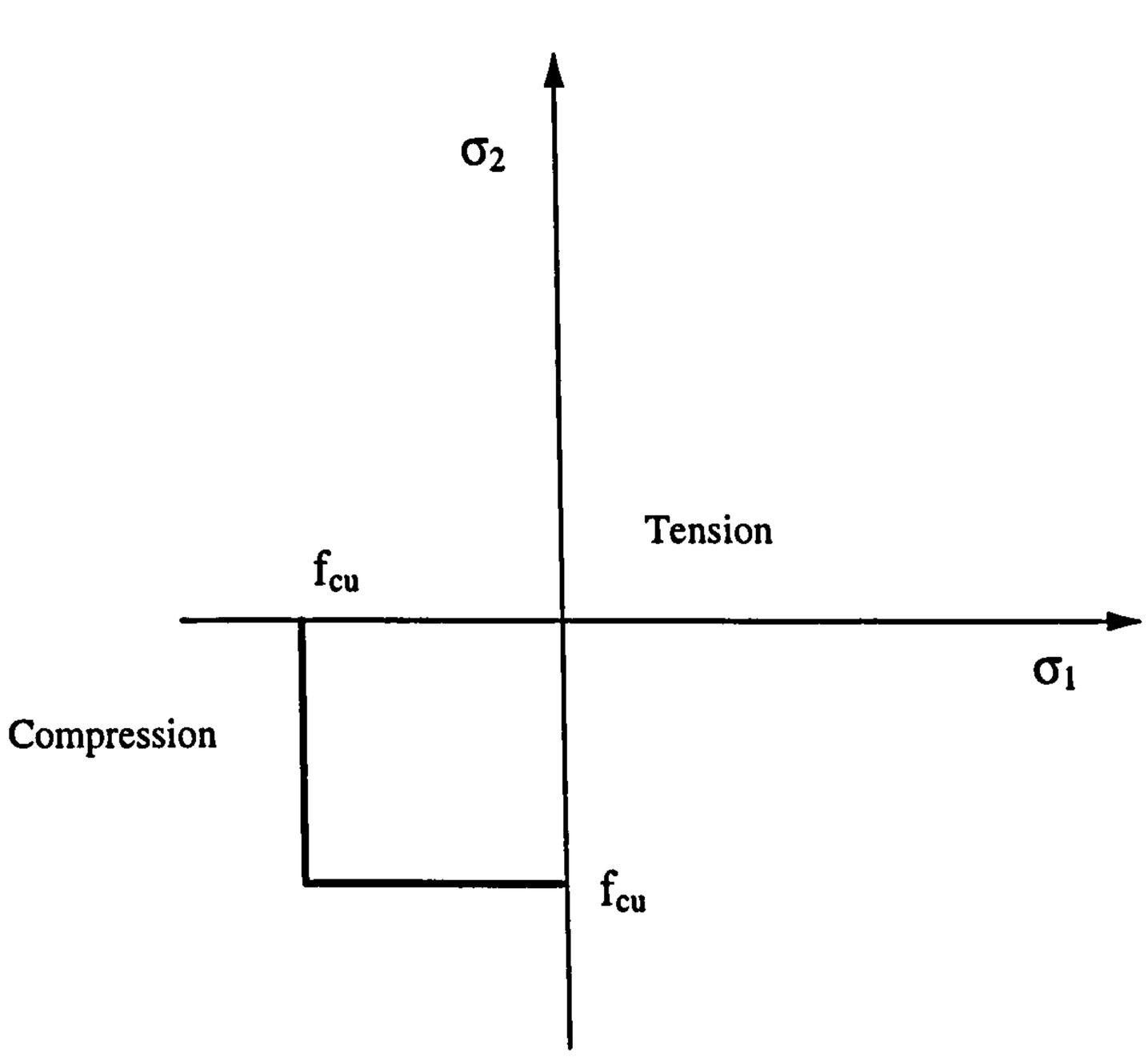

fig.4.3.1(b) Square Yield Criterion For Concrete

4.3.2 Yield criteria for reinforced concrete slabs

Consider an element of a slab subjected to bending and torsion moments as shown in figure 4.3.2(a). The flexural strength provided by the slab is M_x^* and M_y^* in the x and y directions respectively (fig 4.3.2(b)). The yield criterion is a mathematical relationship between the applied set of stresses and the strength of the material. Hence the yield criteria for the slab element can be written as:

$$F(M_x , M_y , M_{xy} , M_x^*, M_y^*) = 0.0 \qquad (4.1)$$

Now consider as shown in figure 4.3.2(c), at any point in the slab element a line with a normal n and a tangent t. The normal applied moment M_n must not exceed the value of the moment of resistance generated by the slab in that direction.

Taking the normal to the yield line at an angle θ to the x-axis, the equilibrium of the element in figure 4.3.2(c), results in the following:

$$M_n = M_x\cos^2\theta + M_y\sin^2\theta - 2M_{xy}\sin\theta\cos\theta \qquad (4.2)$$

$$M_t = M_x\sin^2\theta + M_y\cos^2\theta + 2M_{xy}\sin\theta\cos\theta \qquad (4.3)$$

$$M_{nt} = (M_x - M_y)\sin\theta\cos\theta + M_{xy}(\cos^2\theta - \sin^2\theta) \qquad (4.4)$$

Resolving the resistance moments of the x and y bars, fig 4.3.2(d), and ignoring torsion, the resisting normal moment at the yield line can be expressed as the following:

$$M_n^* = M_x^*\cos^2\theta + M_y^*\sin^2\theta \qquad (4.5)$$

where the value of M_n^* must always be greater than M_n from equation 4.2, i.e.

$$M_n^* - M_n \geq 0.0 \qquad (4.6)$$

Substituting equations 4.2 and 4.5 into 4.6 leads to:

4.3.2 Yield criteria for reinforced concrete slabs

Consider an element of a slab subjected to bending and torsion moments as shown in figure 4.3.2(a). The flexural strength provided by the slab is M_x^* and M_y^* in the x and y directions respectively (fig 4.3.2(b)). The yield criterion is a mathematical relationship between the applied set of stresses and the strength of the material. Hence the yield criteria for the slab element can be written as:

$$F(M_x , M_y , M_{xy} , M_x^*, M_y^*) = 0.0 \qquad (4.1)$$

Now consider as shown in figure 4.3.2(c), at any point in the slab element a line with a normal n and a tangent t. The normal applied moment M_n must not exceed the value of the moment of resistance generated by the slab in that direction.

Taking the normal to the yield line at an angle θ to the x-axis, the equilibrium of the element in figure 4.3.2(c), results in the following:

$$M_n = M_x\cos^2\theta + M_y\sin^2\theta - 2M_{xy}\sin\theta\cos\theta \qquad (4.2)$$

$$M_t = M_x\sin^2\theta + M_y\cos^2\theta + 2M_{xy}\sin\theta\cos\theta \qquad (4.3)$$

$$M_{nt} = (M_x - M_y)\sin\theta\cos\theta + M_{xy}(\cos^2\theta - \sin^2\theta) \qquad (4.4)$$

Resolving the resistance moments of the x and y bars, fig 4.3.2(d), and ignoring torsion, the resisting normal moment at the yield line can be expressed as the following:

$$M_n^* = M_x^*\cos^2\theta + M_y^*\sin^2\theta \qquad (4.5)$$

where the value of M_n^* must always be greater than M_n from equation 4.2, i.e.

$$M_n^* - M_n \geq 0.0 \qquad (4.6)$$

Substituting equations 4.2 and 4.5 into 4.6 leads to:

$$(M_x^* - M_x)\cos^2\theta + (M_y^* - M_y)\sin^2\theta + 2M_{xy}\sin\theta\cos\theta \geq 0.0 \quad (4.7)$$

The above equation can be written in simplified from by taking:

$$A = M_x^* - M_x \quad (4.8)$$

$$B = M_y^* - M_y \quad (4.9)$$

$$C = M_{xy} \quad (4.10)$$

$$A\cos^2\theta + B\sin^2\theta + 2\cos\theta\sin\theta \geq 0.0 \quad (4.11)$$

Dividing by $\cos^2\theta$ equation 4.11 becomes:

$$F(\theta) = A + B\tan^2\theta + 2C\tan\theta \geq 0.0 \quad (4.12)$$

For optimum steel, the excess strength must be a minimum hence:

$$\frac{dF(\theta)}{d\tan\theta} = 0 \quad (4.13)$$

$$\frac{d^2F(\theta)}{d\tan^2\theta} > 0 \quad (4.14)$$

$$\frac{dF(\theta)}{d\tan^2\theta} = B\tan\theta + C = 0 \Rightarrow \tan\theta = -\frac{C}{B} \quad (4.15)$$

$$\therefore \frac{d^2F(\theta)}{d\tan^2\theta} = B > 0 \Rightarrow M_y^* > M_y \quad (4.16)$$

Substituting equation 4.15 in equation 4.11 results in:

$$A + B(-\frac{C}{B})^2 + 2C(-\frac{C}{B}) = 0 \quad (4.17)$$

$$\text{or } AB - C^2 = 0 \qquad (4.18)$$

Replacing A,B and C by their values in equation 4.18 gives:

$$-(M_x^* - M_x)(M_y^* - M_y) + M_{xy}^2 = 0 \qquad (4.19)$$

The above equation is the yield criterion for reinforced concrete slabs known as the Wood criterion. This is the yield criterion for positive steel (i.e. bottom steel). For negative (i.e. top steel) a similar procedure is adopted to give:

$$-(M_x^{*t} + M_x)(M_y^{*t} - M_y) + M_{xy}^2 = 0 \qquad (4.20)$$

Experimental work by a number of researchers such as Cardenas and Sozen (1973), Jain and Kennedy (1974) have confirmed the validity of the yield criterion for orthogonal steel. In the work by Hago and Bhatt (1986), elastic stress fields in conjunction with the Wood-Armer criterion was used for the design of orthogonally reinforced slabs. The method was found to be a highly practical procedure leading to lower bound solutions to slab design. Bensalem (1993) continued this work with the direct design of slabs using the non-linear stress-field. It was found that in many cases, design from the non-linear field helped to reduce steel congestion by 'smoothing' out the peak moments occurring at concentrated loads or supports.

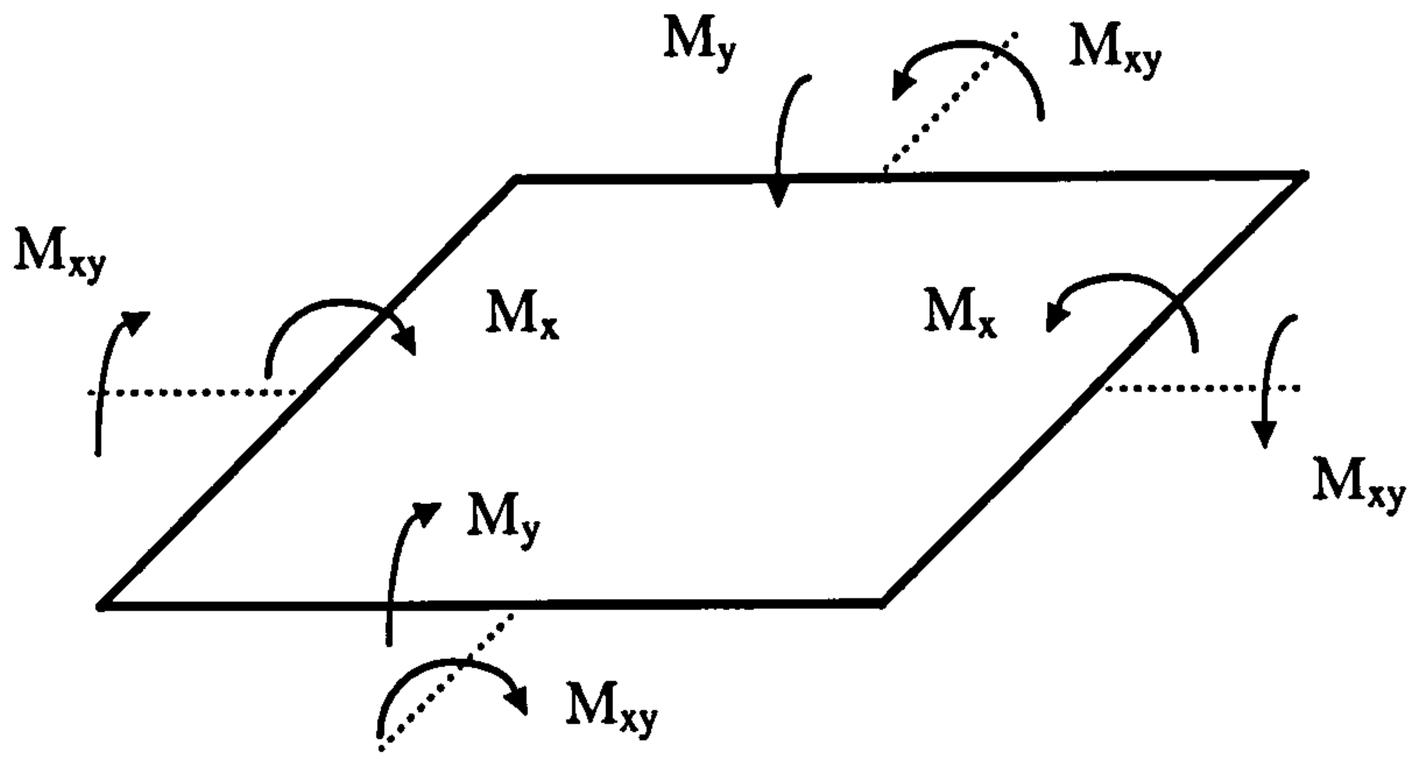

fig.4.3.2(a) +ve Moments on a slab element

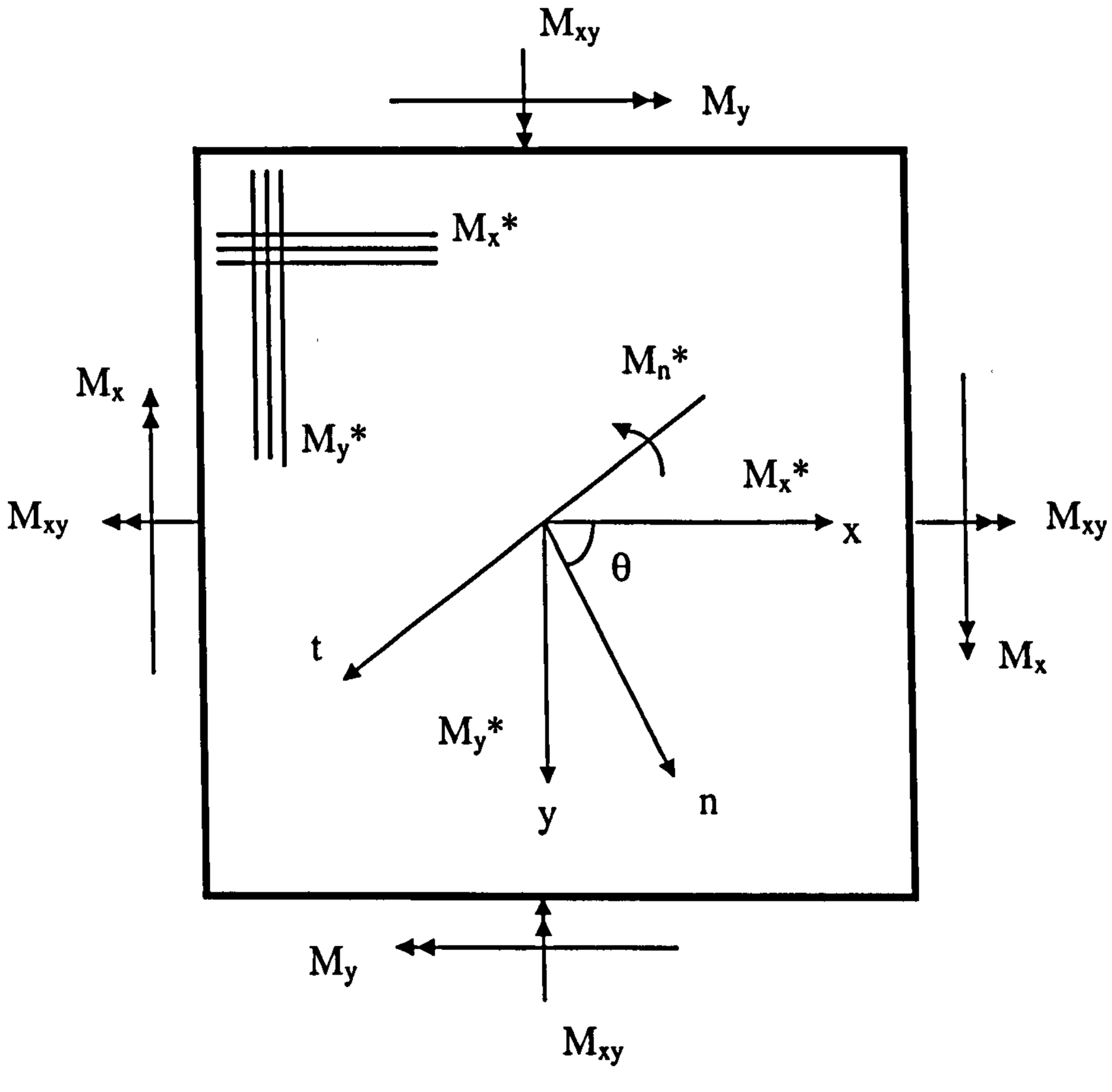

fig.4.3.2(b) Applied and resisting moments on an element

4.3.3 Design equations

The following design equations can be derived from the yield criterion described above.

i)Positive Moment Field (bottom steel)

$$M_x^* = \frac{M_{xy}^2}{M_y^* - M_y} + M_x \qquad (4.21)$$

The total amount of bottom steel providing resistance Mx* and My* is represented by the following equation:

$$M_x^* + M_y^* = \frac{M_{xy}^2}{M_y^* - M_y} + M_x + M_y^* \qquad (4.22)$$

Which implies for minimum steel: $\frac{d(M_x^* + M_y^*)}{dM_y^*} = 0$, hence $M_y^* = M_y \pm M_{xy}$, or since in equation 4.16, $M_y^* > M_y$, this reduces to:

$$M_y^* = M_y + |M_{xy}| \qquad (4.23)$$

Substitution of equation 4.23 into equation 4.19 results in :

$$M_x^* = M_x + |M_{xy}| \qquad (4.24)$$

ii)Negative Moment Field (top steel)

The same procedure as above is applied to the negative yield criterion (eq. 4.20) to obtain the following:

$$M_x^{*t} = M_x - |M_{xy}| \qquad (4.25)$$

$$M_y^{*t} = M_y - |M_{xy}| \qquad (4.26)$$

iii)Mixed Moment Field

From equations 4.21 and 4.22, if $M_y^* \leq 0.0$, is considered to be equal to zero and from the yield equation (4.19), the following is obtained:

$$M_x^* = M_x + \left| \frac{M_{xy}^{\ 2}}{M_y} \right| \tag{4.27}$$

similarly if $M_x^* \leq 0.0$, from equation (4.19) :

$$M_y^* = M_y + \left| \frac{M_{xy}^{\ 2}}{M_x} \right| \tag{4.28}$$

The same procedure as above can be applied to the negative moment fields to obtain:

$$M_x^{*t} = M_x + \left| \frac{M_{xy}^{\ 2}}{M_y} \right| \tag{4.29}$$

$$M_y^{*t} = M_y + \left| \frac{M_{xy}^{\ 2}}{M_x} \right| \tag{4.30}$$

4.3.4 Procedure for Placing of Reinforcement

Given a stress field (M_x, M_y , M_{xy}) at any point in a slab , the reinforcement in the x and y directions can be placed according to the following:

i)Bottom Steel

- Design moments $M_x^*$and M_y^* are calculated from equations 4.24 and 4.23
- If $M_x^*$and M_y^* are negative, then no bottom reinforcement is needed
- If $M_x^*$and M_y^* are positive, then the calculated values are adopted as the resistance moments
- If $M_x^* < 0.0$, then set $M_x^* = 0.0$ and calculate M_y^* from equation 4.28
- If $M_y^* < 0.0$, then set $M_y^* = 0.0$ and calculate M_x^* from equation 4.27

ii)Top Steel

- Design moments M_x^{*t} and M_y^{*t} are calculated from equations 4.25 and 4.26
- If M_x^{*t} and M_y^{*t} are positive, then no top reinforcement is needed
- If M_x^{*t} and M_y^{*t} are negative, then the calculated values are adopted as the resistance moments
- If $M_x^{*t} > 0.0$, then set $M_x^{*t} = 0.0$ and calculate M_y^{*t} from equation 4.30.
- If $M_y^{*t} > 0.0$, then set $M_y^{*t} = 0.0$ and calculate M_x^{*t} from equation 4.29.

A schematic representation of the design equations for bottom steel is given in figure 4.3.4(a).

4.3.5 Multiple Load Cases

The rules outlined so far only deal with a slab subject to a moment field resulting from a single load case. In practice, slabs such as in the case of bridge decks, can be subject to multiple load cases. For this situation, reinforcement is provided to accommodate the moment triad resulting from multiple load cases; (M_{xi}, M_{yi} , M_{xyi}) i=1,n, where n is the number of loading cases. Here a method for provision of reinforcement in multiple load case situations is presented. The procedure was used by Kemp (1971) and was also applied to skew reinforcement.

- For each load case i (i=1,n), the moments (M_{xi}, M_{yi} , M_{xyi}) are calculated . The corresponding resistance moments $M_x^{*}{}_i$ and $M_y^{*}{}_i$ are found using the procedure outlined earlier.
- At each point the maximum value of $M_x^{*}{}_i$ and $M_y^{*}{}_i$ can be found. Once the maximum values are obtained i.e. $M_x^{*}{}_{max}$ and $M_y^{*}{}_{max}$, they can be used for design. The resulting design would be safe, but not necessarily economic. Hence an optimisation procedure must be adopted
- The next step is to assume that in the x-direction, $M_x^{*}{}_{max}$ is provided for, but in the y-direction $M_y^{*}{}_i$ is provided for to satisfy the corresponding yield condition in each case. The maximum value of all these $M_y^{*}{}_i$ is found, let it be $M_y^{*}{}_{pmax}$. Using $M_x^{*}{}_{max}$ in conjunction with $M_y^{*}{}_{pmax}$, a safe design is produced.

- Using the same procedure as above, a corresponding value of $M_x{}^*{}_{pmax}$ can be found for $M_y{}^*{}_{max}$. Clearly, the optimal design would result from a set of design moments where ($M_x{}^* + M_y{}^*$) is the smallest.

Further optimisation of the design can be carried out by using a simple search technique to examine the feasible design region as shown in figure 4.3.5. For each load case, design moments at the grid points is examined in order to determine if it is a better minimum. If the search is positive, a check is made to ensure yield conditions are not violated. If the yield condition is violated, then the design moment is rejected. If not, then a check is made to see where on the grid the best minimum value of ($M_x{}^* + M_y{}^*$) is obtained.

4.4 Inplane Application

In 1964, Nielsen first proposed a yield criterion for a section with known orthogonal reinforcement, which can carry tension or compression, and placed symmetrically with respect to the section's middle surface. Equations were derived to determine orthogonal tension reinforcement to resist a given inplane force triad. In 1984, Nielsen considered the case of skew tension reinforcement. His work assumes that the concrete has sufficient compression strength without the need for compression reinforcement. When the compression strength of the concrete is reached, the section thickness must be increased. In 1976, Clark proposed a series of equations for proportioning skew or orthogonal tension and/or compression reinforcement to resist a triad of inplane forces. A number of researchers have used these equations to design deep beams. Khaskheli (1989) used these equations to derive reinforcement layouts for deep beams from the elastic stress pattern. Bensalem (1993) used the non-elastic stress patterns to derive reinforcement layouts for deep beams.

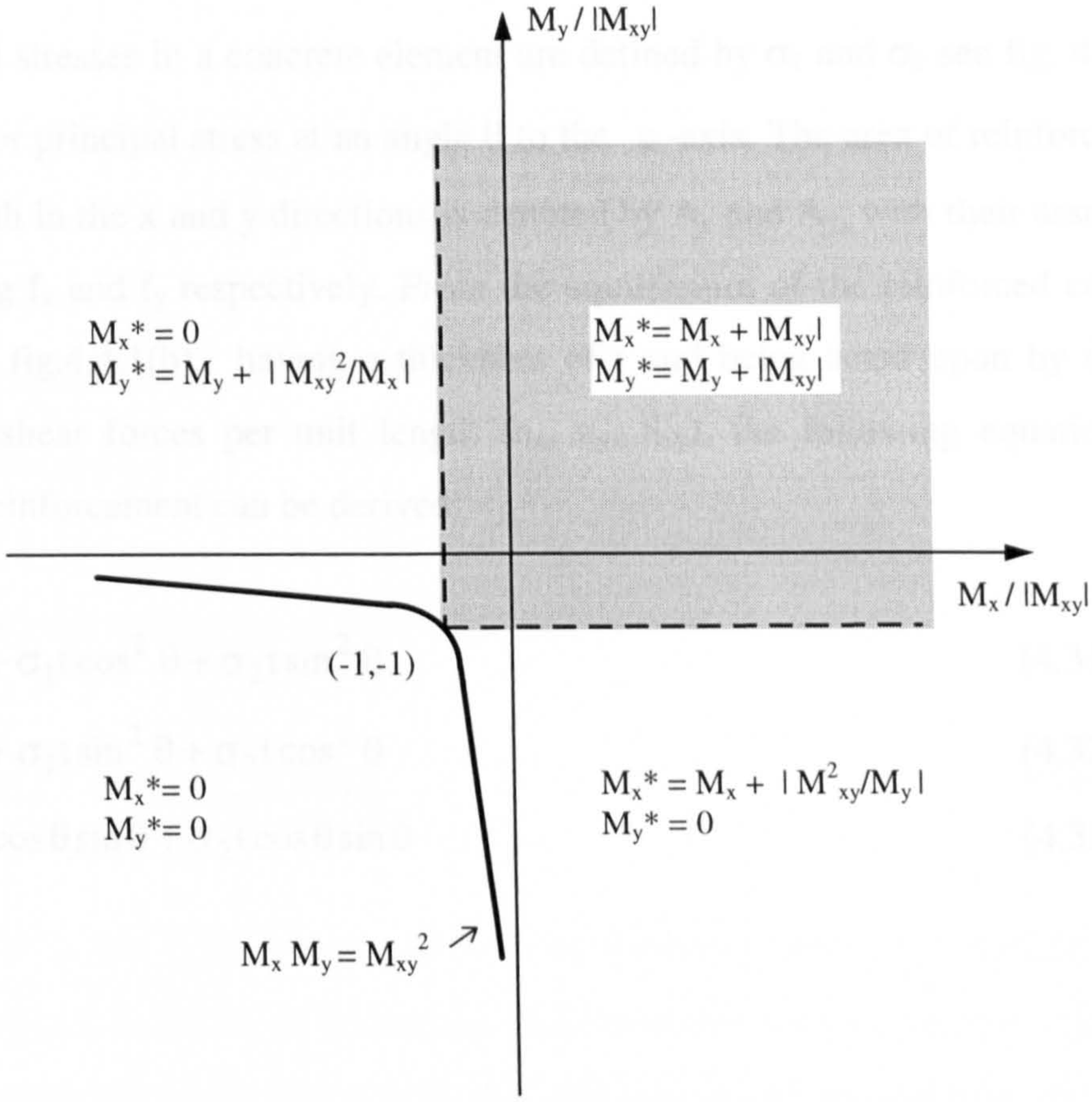

fig4.3.4(a) Design Equations for Bottom Steel

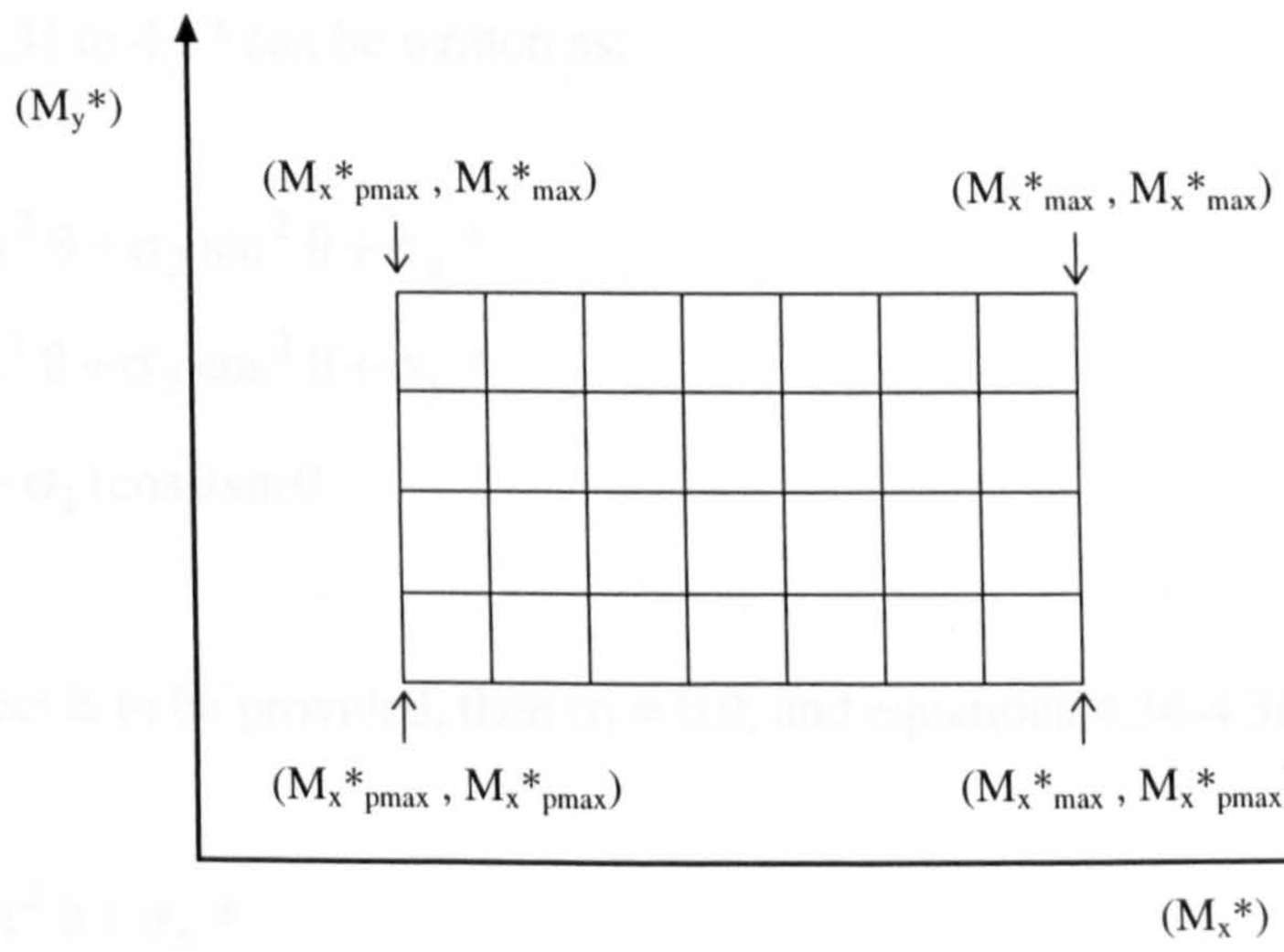

fig.4.3.5 Simple Search Technique for Use in Multiple Load Case Design

4.4.1 Yield Criteria

The principal stresses in a concrete element are defined by σ_1 and σ_2 see fig. 4.4.1(a) with the major principal stress at an angle θ to the x -axis. The area of reinforcement per unit length in the x and y directions is denoted by A_x and A_y, with their associated stresses being f_x and f_y respectively. From the equilibrium of the reinforced concrete element, see fig.4.4.1(b), having a thickness of t and being acted upon by inplane normal and shear forces per unit length (n_x, n_y, n_{xy}), the following equations for orthogonal reinforcement can be derived:

$$n_x = A_x f_x + \sigma_1 t \cos^2\theta + \sigma_2 t \sin^2\theta \quad (4.31)$$

$$n_y = A_y f_y + \sigma_1 t \sin^2\theta + \sigma_2 t \cos^2\theta \quad (4.32)$$

$$n_{xy} = -\sigma_1 t \cos\theta \sin\theta + \sigma_2 t \cos\theta \sin\theta \quad (4.33)$$

setting:

$$\sigma_x = \frac{n_x}{t}, \sigma_y = \frac{n_y}{t}, \tau_{xy} = \frac{n_{xy}}{t} \text{ and } \sigma_x^* = \frac{A_x f_x}{t}, \sigma_y^* = \frac{A_y f_y}{t}$$

where σ_x, σ_y, τ_{xy} are the normal and shear stresses, and σ_x^*, σ_y^* are the resistant stresses provided by the steel reinforcement in the x and y directions respectively. Equations 4.31 to 4.33 can be written as:

$$\sigma_x = \sigma_1 \cos^2\theta + \sigma_2 \sin^2\theta + \sigma_x^* \quad (4.34)$$

$$\sigma_y = \sigma_1 \sin^2\theta + \sigma_2 \cos^2\theta + \sigma_y^* \quad (4.35)$$

$$\tau_{xy} = (\sigma_2 - \sigma_1)\cos\theta \sin\theta \quad (4.36)$$

If tensile steel is to be provided, then $\sigma_1 = 0.0$, and equations 4.34-4.36 become:

$$\sigma_x = \sigma_2 \sin^2\theta + \sigma_x^* \quad (4.37)$$

$$\sigma_y = \sigma_2 \cos^2\theta + \sigma_y^* \quad (4.38)$$

$$\tau_{xy} = (\sigma_2)\cos\theta\sin\theta \qquad (4.39)$$

hence:

$$\sigma_x * - \sigma_x = \sigma_2 \sin^2\theta$$

$$\sigma_y * - \sigma_y = \sigma_2 \cos^2\theta$$

$$\tau_{xy} = (\sigma_2)\cos\theta\sin\theta$$

Eliminating σ_2 and θ from the above equations leads to:

$$(\sigma_x * - \sigma_x)(\sigma_y * - \sigma_y) - {\tau_{xy}}^2 = 0.0 \qquad (4.40)$$

Equation 4.40 is the yield criterion derived by Nielsen (1964) for a section having known orthogonal isotropic or orthotropic reinforcement carrying tension forces and placed symmetrically with respect to the mid-surface of the section. From this criterion, equations for four different cases of reinforcement design were proposed. As already stated, this criterion assumes that concrete strength is not violated. Clark (1976) extended this criterion for the provision of compressive reinforcement. The four cases outlined by Nielsen, were extended to nine. Table 4.4.1(a) shows the possible combinations of reinforcement (in the table ρ is the reinforcement ratio and α is the angle of the reinforcement from the x axis when skew reinforcement is considered). From this table, it can be seen that all cases can be solved by direct solution except cases 1 and 4 where minimisation of the total reinforcement in both directions of the member is necessary. The principal stress σ_1 is considered equal to zero when tension reinforcement is required and σ_2 equal to the concrete compressive strength f_c when compressive reinforcement is required. Derivation of the design equations is now described in the following section.

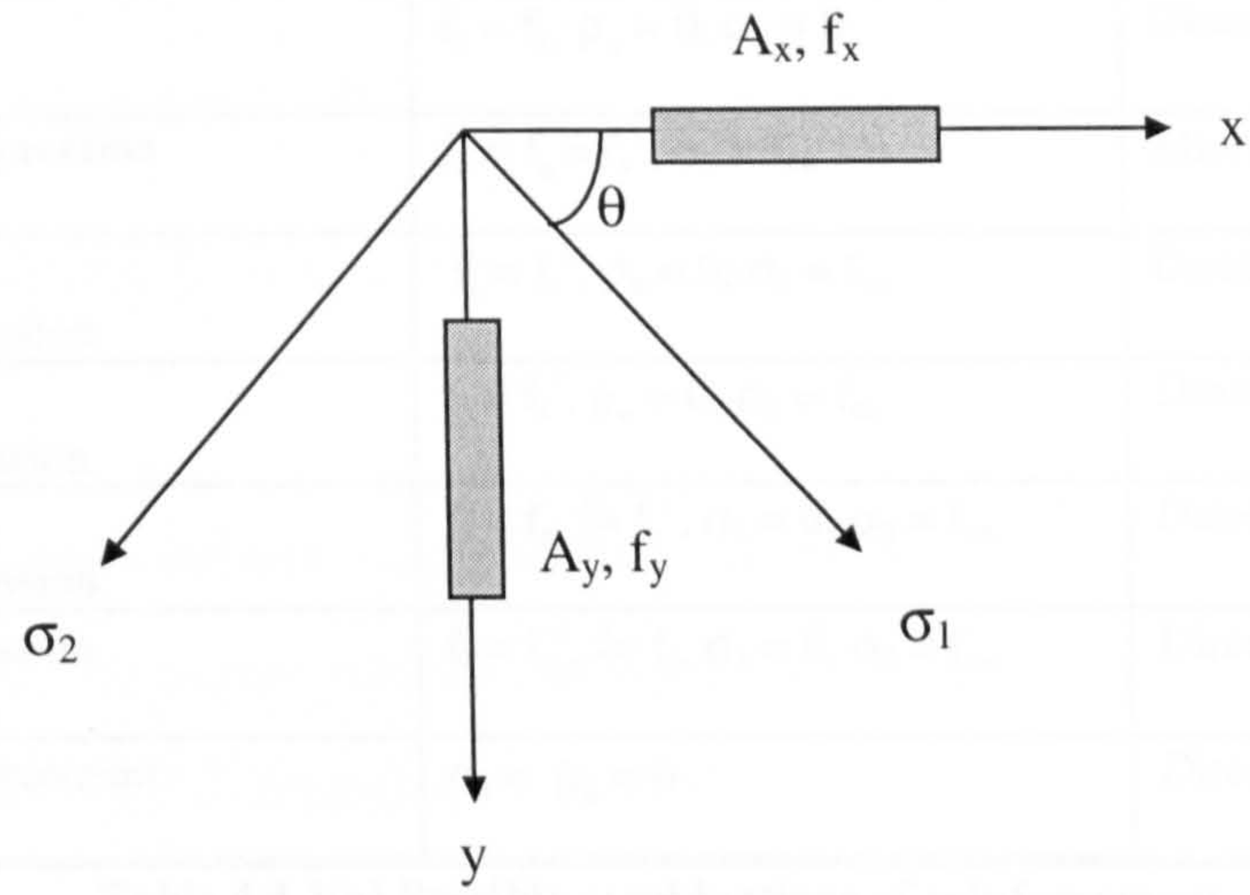

fig.4.4.1(a) Principal Concrete Stresses and Reinforcement Directions

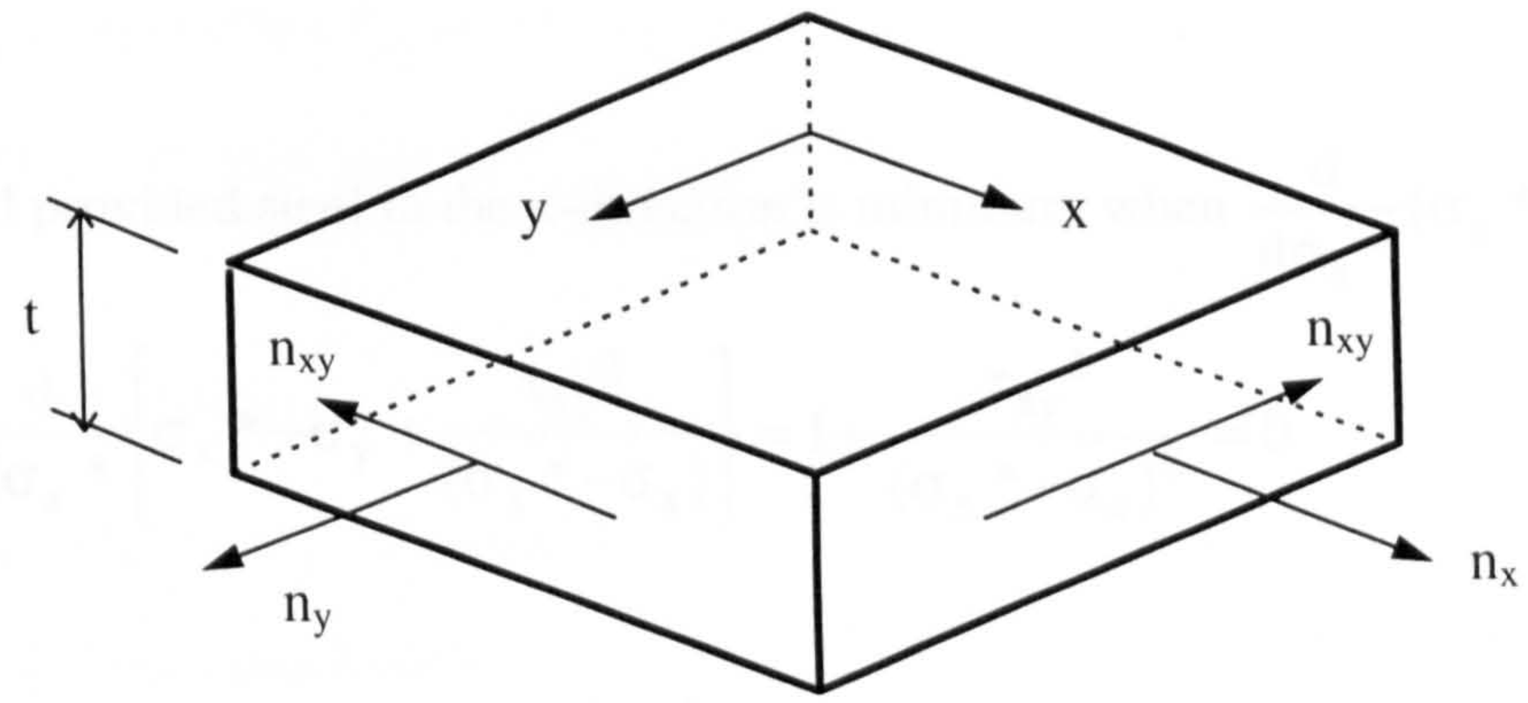

fig.4.4.1(b) Sign Convention for Inplane Normal & Shear Forces per unit length

Case	Reinforcement Description	Known Values	Method of Solution
1	Both tension	$f_x = f_\alpha = f_s$, $\sigma_1 = 0$	Minimisation of $(\rho_x + \rho_y)$
2	No x α tension	$f_\alpha = f_s$, $\rho_x = 0$, $\sigma_1 = 0$	Direct solution
3	No α x tension	$f_x = f_s$, $\rho_\alpha = 0$, $\sigma_1 = 0$	Direct solution
4	Both compression	$f_x = f_\alpha = f_s'$, $\sigma_2 = f_{cu}$	Minimisation of $(\rho_x + \rho_y)$
5	No x α compression	$f_\alpha = f_s'$, $\rho_x = 0$, $\sigma_2 = f_{cu}$	Direct solution
6	No α x compression	$f_x = f_s'$, $\rho_\alpha = 0$, $\sigma_2 = f_{cu}$	Direct solution
7	x tension α compression	$f_x = f_s$, $f = f_s'$, $\sigma_1 = 0$, $\sigma_2 = f_{cu}$	Direct solution
8	x compression α tension	$f_x = f_s'$, $f = f_s$, $\sigma_1 = 0$, $\sigma_2 = f_{cu}$	Direct solution
9	No reinforcement	$\rho_x = \rho_\alpha = 0$	Direct solution

Table 4.4.1(a) Possible combinations of reinforcement

4.4.2 Design Equation Derivation

4.4.2.1 Cases where tension steel is to be provided

- Case1: σ_x^* and $\sigma_y^* > 0$

From equation 4.40, $\sigma_y^* = \sigma_y + \dfrac{\tau_{xy}^2}{(\sigma_x^* - \sigma_x)}$,

The total provided steel in the x-direction is minimum when $\dfrac{d}{d\sigma_x^*}(\sigma_x^* + \sigma_y^*) = 0$,

Thus: $\dfrac{d}{d\sigma_x^*}\left\{\sigma_x^* + \sigma_y + \dfrac{\tau_{xy}^2}{(\sigma_x^* - \sigma_x)}\right\} = 1 - \dfrac{\tau_{xy}^2}{(\sigma_x^* - \sigma_x)^2} = 0$

$\therefore$ Since $\sigma_x^* > \sigma_x$, $\sigma_x^* = \sigma_x + |\tau_{xy}|$, the steel ratio in the x-direction is:

$\rho_x = 1/f_s(\sigma_x + |\tau_{xy}|)$, similarly in the y-direction : $\rho_y = 1/f_s(\sigma_y + |\tau_{xy}|)$,

where f_s is the yield strength of the steel.

- Case 2: $\sigma_x^* = 0$ and $\sigma_y^* > 0$

From equation 4.40, $\sigma_y^* = \sigma_y - \frac{\tau_{xy}^2}{\sigma_x}$, thus $\rho_x = 0$, and $\rho_y = 1/f_s(\sigma_y - \frac{\tau_{xy}^2}{\sigma_x})$

- Case 3: $\sigma_x^* > 0$ and $\sigma_y^* = 0$

Similar to case 2, here $\rho_y = 0$, and $\rho_x = 1/f_s(\sigma_x - \frac{\tau_{xy}^2}{\sigma_y})$

4.4.2.2 Cases where compression steel is needed

For this situation, the minor principal stress in the concrete reaches ultimate strength, i.e. $\sigma_2 = -f_{cu}$ and $\sigma_1 < 0.0$. Equations 4.34-4.36 can be written as

$$\sigma_x = \sigma_1 \cos^2\theta - f_{cu}\sin^2\theta + \sigma_x^* \quad (4.41)$$

$$\sigma_y = \sigma_1 \sin^2\theta - f_{cu}\cos^2\theta + \sigma_y^* \quad (4.42)$$

$$\tau_{xy} = (-f_{cu} - \sigma_1)\cos\theta\sin\theta \quad (4.43)$$

thus:

$$\sigma_x + f_{cu} = \sigma_1 \cos^2\theta + f_{cu}\cos^2\theta + \sigma_x^* \quad (4.44)$$

$$\sigma_y + f_{cu} = \sigma_1 \sin^2\theta + f_{cu}\sin^2\theta + \sigma_y^* \quad (4.45)$$

$$\tau_{xy} = (-f_{cu} - \sigma_1)\cos\theta\sin\theta \quad (4.46)$$

and:

$$\sigma_x + f_{cu} - \sigma_x^* = (\sigma_1 + f_{cu})\cos^2\theta$$

$$\sigma_y + f_{cu} - \sigma_y^* = (\sigma_1 + f_{cu})\sin^2\theta$$

$$\tau_{xy} = -(f_{cu} + \sigma_1)\cos\theta\sin\theta$$

$$\therefore -(\sigma_x + f_{cu} - \sigma_x^*)(\sigma_y + f_{cu} - \sigma_y^*) + \tau_{xy}^2 = 0.0 \quad (4.47)$$

For the following sections, $\sigma_{xf} = \sigma_x + f_{cu}$ and $\sigma_{yf} = \sigma_y + f_{cu}$

- Case 4: $\sigma_x^* < 0$ and $\sigma_y^* < 0$

From equation 4.47, $\sigma_y^* = +\sigma_{yf} - \dfrac{\tau_{xy}^2}{(\sigma_{xf} - \sigma_x^*)}$

provided steel is minimum when: $\dfrac{d}{d\sigma_x^*}(\sigma_x^* + \sigma_y^*) = 0$,

Thus: $1 - \dfrac{\tau_{xy}^2}{(\sigma_{xf} - \sigma_x^*)^2} = 0$,

$\therefore$ Since $\sigma_x^* < \sigma_{xf}$, $\sigma_x^* = \sigma_{xf} - |\tau_{xy}|$, the steel ratio in the x-direction is:

$\rho_x = 1/f_s'(\sigma_{xf} - |\tau_{xy}|)$, similarly in the y-direction : $\rho_y = 1/f_s'(\sigma_{yf} - |\tau_{xy}|)$

- Case 5: $\sigma_x^* = 0$ and $\sigma_y^* < 0$

From equation 4.47, $\sigma_y^* = \sigma_{yf} - \dfrac{\tau_{xy}^2}{\sigma_{xf}}$, thus:

$\rho_x = 0$, and $\rho_y = 1/f_s'(\sigma_{yf} - \dfrac{\tau_{xy}^2}{\sigma_{xf}})$

- Case 6: $\sigma_x^* < 0$ and $\sigma_y^* = 0$

similar to case 5, $\rho_y = 0$, and $\rho_x = 1/f_s'(\sigma_{xf} - \dfrac{\tau_{xy}^2}{\sigma_{yf}})$

4.4.2.3 Mixed Cases:

where σ_x^* and σ_y^* are of different signs:

- Case 7: $\sigma_x^* > 0$ and $\sigma_y^* < 0$

$\sigma_1 = 0$ and $\sigma_1 = f_c$, thus equations 4.34-4.36 become:

$$\sigma_x = f_{cu}\sin^2\theta + \sigma_x^* = [f_{cu}/2.0](1-\cos 2\theta) + \sigma_x^* \qquad (4.48)$$

$$\sigma_y = f_{cu}\cos^2\theta + \sigma_y^* = [f_{cu}/2.0](1+\cos 2\theta) + \sigma_y^* \quad (4.49)$$

$$\tau_{xy} = f_{cu}\sin\theta\cos\theta = [f_{cu}/2.0]\sin 2\theta \quad (4.50)$$

From equation 4.44, $\beta = \cos 2\theta = [1 - \frac{2\tau_{xy}^2}{f_{cu}}]^{1/2}$

Eliminating θ from equations 4.48 and 4.49 gives:

$$\sigma_x^* = \sigma_x - (f_{cu}/2.0)(1-\beta)$$

$$\sigma_y^* = \sigma_y - (f_{cu}/2.0)(1+\beta)$$

The steel ratios are:

$$\rho_x = 1/f_s[\sigma_x - (f_{cu}/2)(1-\beta)]$$

$$\rho_y = 1/f_s'[\sigma_y - (f_{cu}/2)(1+\beta)]$$

- Case 8: $\sigma_x^* < 0$ and $\sigma_y^* > 0$

Similar to case 7;

$$\rho_x = 1/f_s'[\sigma_x - (f_{cu}/2)(1+\beta)]$$

$$\rho_y = 1/f_s[\sigma_y - (f_{cu}/2)(1-\beta)]$$

- Case 9: No steel required, $\rho_x = \rho_y = 0$

4.4.3 Boundary Curves

Given the stresses (σ_x, σ_y, τ_{yx}) at any point, it is necessary to find out which design equations are to be used. The boundary between each case surface on a horizontal axis of ($\sigma_x/|\tau_{xy}|$) and vertical axes of ($\sigma_x/|\tau_{xy}|$), can be constructed to define the required case, see figure 4.4.3. In figure 4.4.3, the circled numbers represent the cases. The

boundary curves were derived by equating the design equations for two cases. The following describes the derivation of the curve separating cases 1 and 2:

$$\rho_{x1} = \rho_{x2} \Rightarrow \sigma_x = -|\tau_{xy}| \Rightarrow \frac{\sigma_x}{|\tau_{xy}|} = -1.0$$

The same equation can be derived by equating the expressions for steel ratios in the y-direction.

$$\rho_{y1} = \rho_{y2} \Rightarrow \sigma_y + |\tau_{xy}| = \sigma_y - \frac{\tau_{xy}^2}{\sigma_x} \Rightarrow \frac{\sigma_x}{|\tau_{xy}|} = -1.0$$

This is the equation of a straight line and is shown as line number 8 in figure 4.4.3.

Table 4.4.3 shows the boundary equations for the intersections between each case.

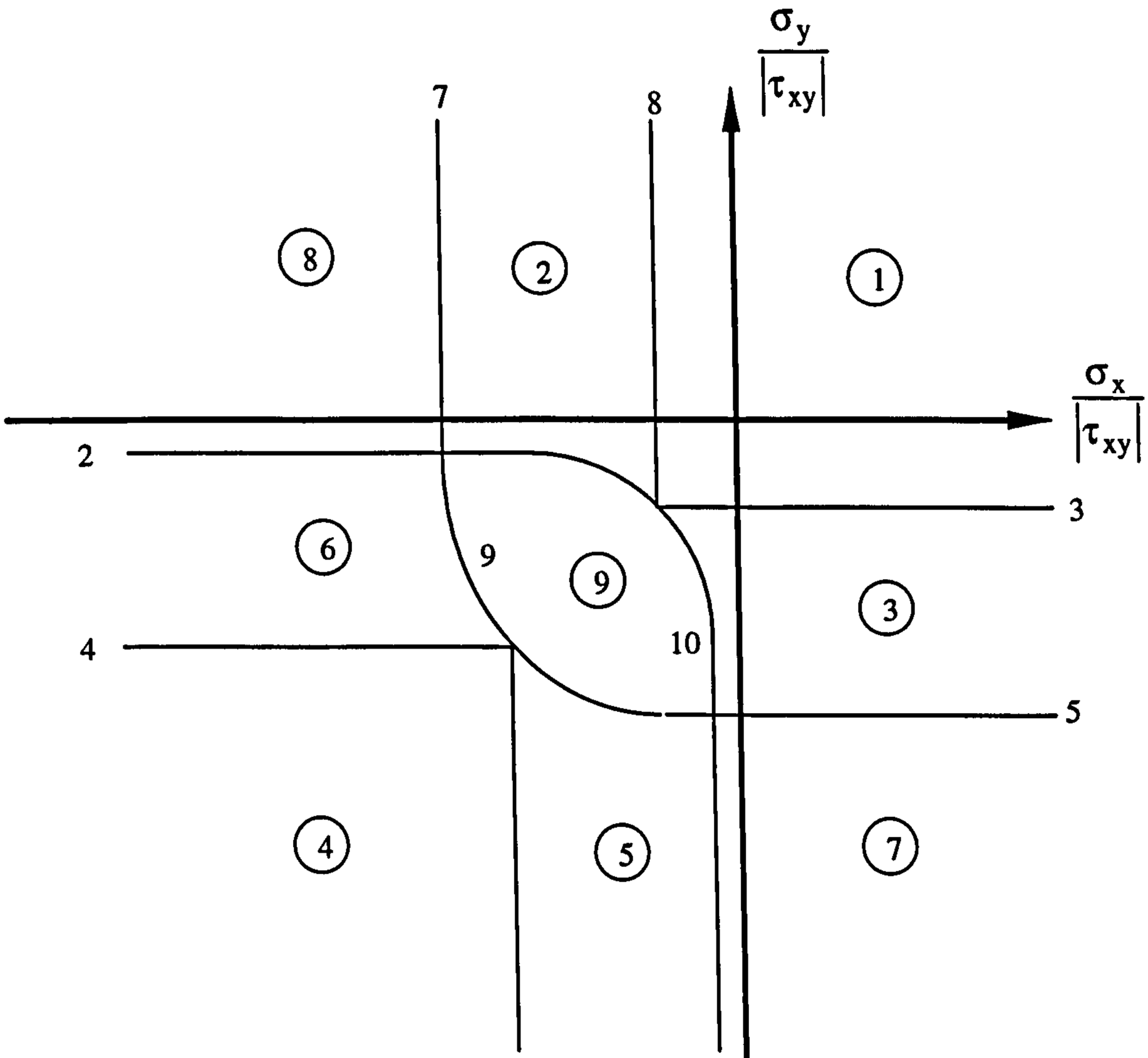

fig.4.4.3 Boundary Curves for Orthogonal Reinforcement, $f_{cu} = -4|\tau_{xy}|$

Curve	Equation	Curve	Equation
1	$\frac{\sigma_y}{\lvert\tau_{xy}\rvert} = +\infty$	7	$\frac{\sigma_x}{\lvert\tau_{xy}\rvert} = \frac{1}{2}\left(\frac{f_{cu}}{\lvert\tau_{xy}\rvert} - \left[\left(\frac{f_{cu}}{\lvert\tau_{xy}\rvert}\right)^2 - 4\right]^{1/2}\right)$
2	$\frac{\sigma_y}{\lvert\tau_{xy}\rvert} = \frac{1}{2}\left(\frac{f_{cu}}{\lvert\tau_{xy}\rvert} + \left[\left(\frac{f_{cu}}{\lvert\tau_{xy}\rvert}\right)^2 - 4\right]^{1/2}\right)$	8	$\frac{\sigma_x}{\lvert\tau_{xy}\rvert} = -1$
3	$\frac{\sigma_y}{\lvert\tau_{xy}\rvert} = -1$	9	$\frac{\sigma_{xf}}{\lvert\tau_{xy}\rvert}\frac{\sigma_{yf}}{\lvert\tau_{xy}\rvert} = 1$
4	$\frac{\sigma_y}{\lvert\tau_{xy}\rvert} = \frac{f_{cu}}{\lvert\tau_{xy}\rvert} + 1$	10	$\frac{\sigma_x}{\lvert\tau_{xy}\rvert}\frac{\sigma_y}{\lvert\tau_{xy}\rvert} = 1$
5	$\frac{\sigma_y}{\lvert\tau_{xy}\rvert} = \frac{1}{2}\left(\frac{f_{cu}}{\lvert\tau_{xy}\rvert} - \left[\left(\frac{f_{cu}}{\lvert\tau_{xy}\rvert}\right)^2 - 4\right]^{1/2}\right)$	11	$\frac{\sigma_x}{\lvert\tau_{xy}\rvert} = \frac{f_{cu}}{\lvert\tau_{xy}\rvert} + 1$
6	$\frac{\sigma_y}{\lvert\tau_{xy}\rvert} = -\infty$	12	$\frac{\sigma_x}{\lvert\tau_{xy}\rvert} = \frac{1}{2}\left(\frac{f_{cu}}{\lvert\tau_{xy}\rvert} + \left[\left(\frac{f_{cu}}{\lvert\tau_{xy}\rvert}\right)^2 - 4\right]^{1/2}\right)$

Table 4.4.3: Boundary Curve Equations for Orthogonal Reinforcement

Chapter 5

Material Behaviour & Numerical Modelling

5.1 Introduction

In the analysis of reinforced concrete structures, the development of an adequate model for the mechanical behaviour of concrete presents the most difficult challenge. In order to model the complete response of concrete and steel, a number of non-linear effects have to be considered. The most important of these effects are:

- tensile cracking
- yielding of the steel
- non-linear material behaviour
- crushing of the concrete
- aggregate interlock
- bond between concrete and reinforcement
- dowel action of reinforcing bars

The fundamental requirement is to develop a set of constitutive laws which adequately describe the multidimensional stress-strain relationships within the reinforced concrete. These constitutive laws are mathematical expressions which approximate the constituent material behaviour. These laws are based upon experimental data. The complexity of concrete behaviour involving some of the phenomenon outlined above, has led to difficulty in being able to fully develop accurate constitutive models. There is at present no universally accepted constitutive law which fully describes concrete behaviour in combined stress conditions (Buyukozturk et. al (1985)). However, much

work on this problem has been carried out over the years in the development of material models for cracked and uncracked concrete and subsequently several numerical models exist, (Chen 1982).

5.2 Concrete Constituent Behaviour

Concrete being a brittle material, there exists within the results of concrete tests, a marked statistical scatter. Figures 5.2(a-b) shows examples of this for Young's modulus and the stress-strain behaviour of concrete in tension. Variation in one of three test variables can account for this scatter, namely:

- materials tested
- test method used
- loading systems

The presence of this scatter suggests that a perfect match between analytical and experimental data is neither possible nor necessary. The following sections describe the behaviour of concrete and steel as well as detailing the model adopted for the numerical analysis of plate bending and inplane problems in this study.

5.2.1 Uni-axial Compression

Uni-axial compressive strength is the most widely used variable for assessing concrete quality. In the UK, the uniaxial cube strength f_{cu} is determined by testing 150mm cube strengths after say 28 days. In the U.S, the uniaxial cylinder strength f_c' is derived from testing 152x305 mm cylinders. The cylinder strength is usually around 70-90% of the cube strength. This difference can be attributed to the friction forces which are generated between the contact face of the cube specimen and the testing machine platens. Such forces result in the formation of a multi-axial stress state and result in an increase in the cube compressive strength. These multi-axial effects are reduced in the cylinder specimens due to the increased width to height ratio of the specimens.

The study of concrete under uniaxial compression provides a good premise from which to detail its behaviour under more complex stress states.

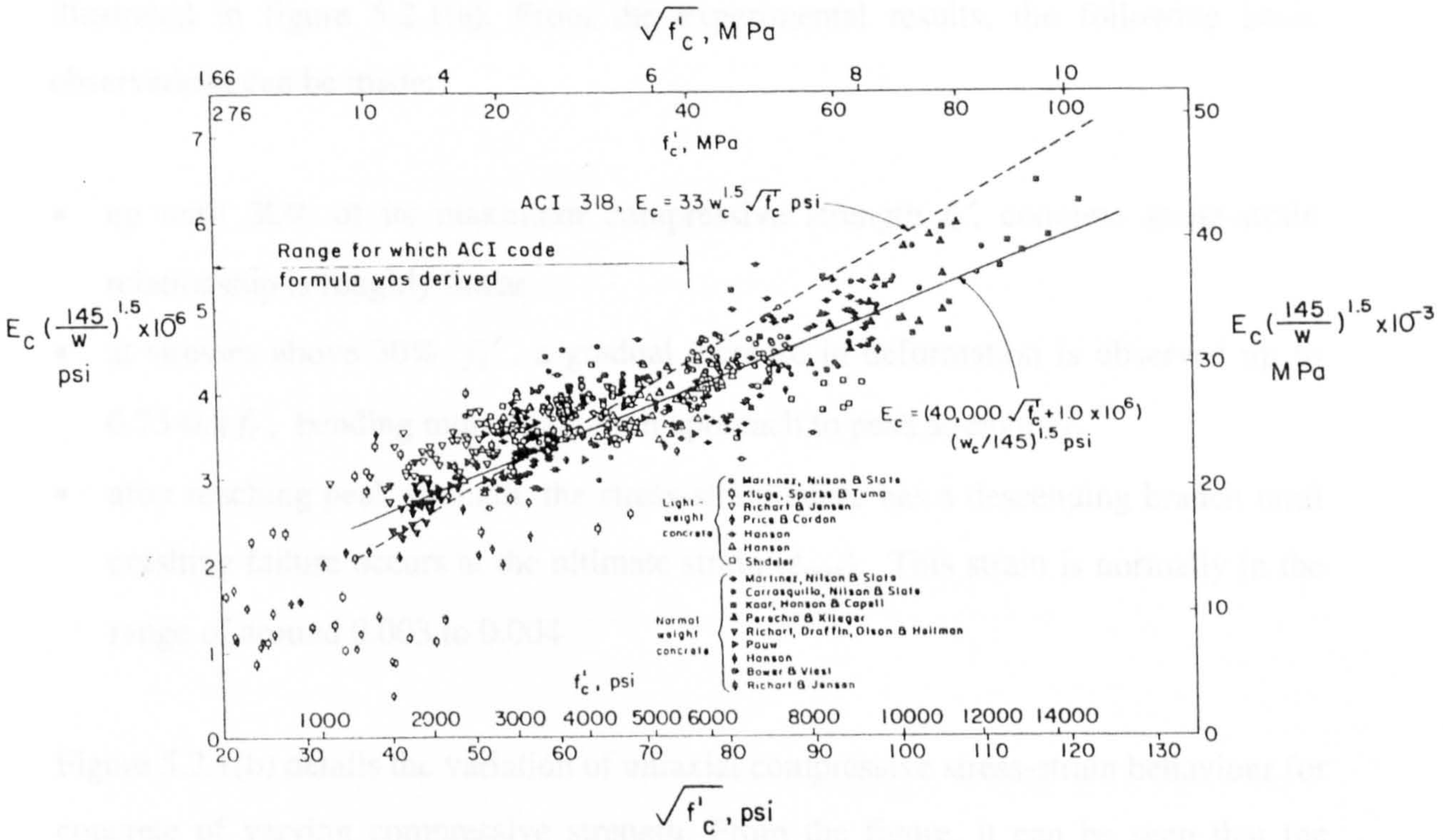

fig. 5.2(a) Young's modulus E_c vs. cylinder compressive strength f_c',
(w = concrete unit weight, ACI-Committee-363 1984)

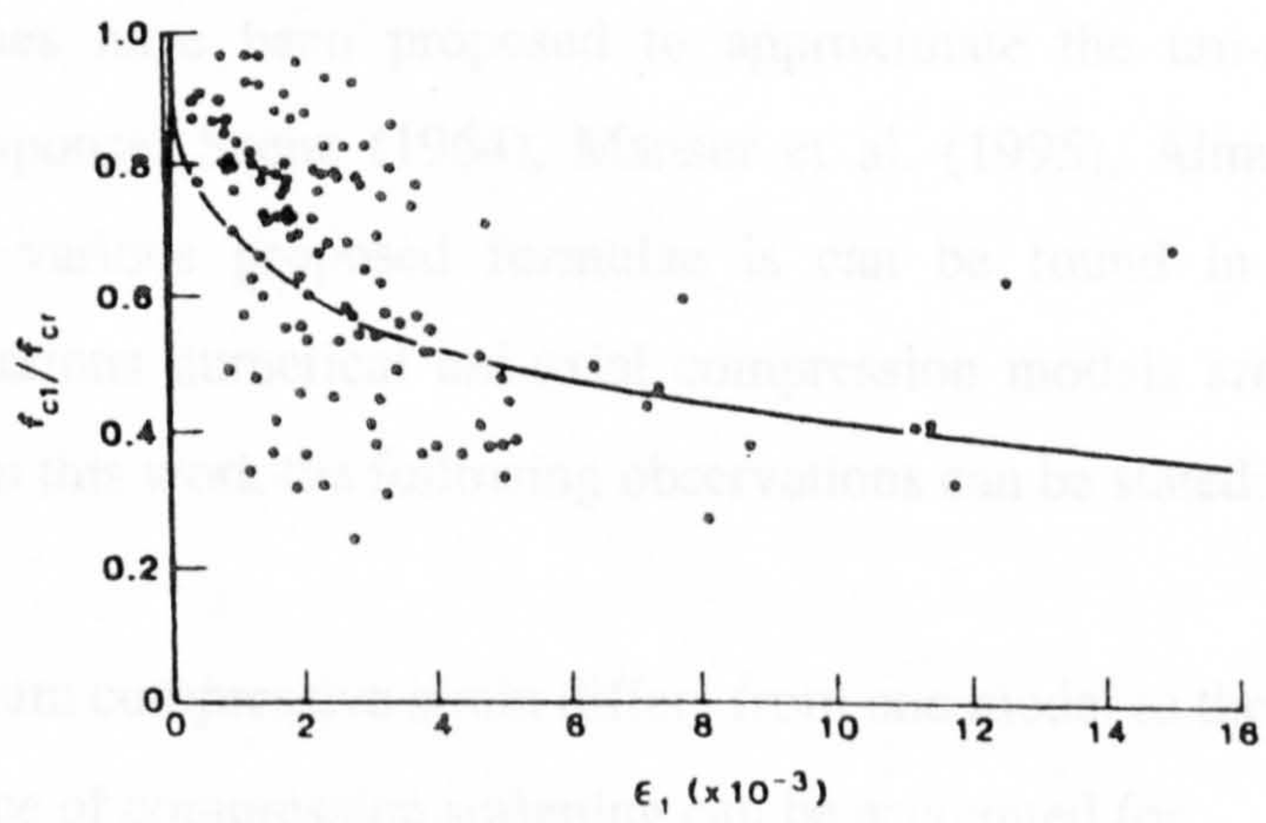

fig. 5.2(b) Test data for cracked concrete in tension,

(f_{c1} = principal tensile stress, f_{cr} = stress at cracking, Vecchio & Collins 1986)

The typical stress-strain relationship for concrete under multi-axial compression is illustrated in figure 5.2.1(a). From the experimental results, the following basic observations can be made:

- up until 30% of its maximum compressive strength f_c', concrete stress-strain relationship is roughly linear
- at stresses above 30% f_c', a gradual increase in deformation is observed up to 0.75-0.9 f_c', bending more sharply on approach to peak strength f_c'
- after reaching peak strength, the stress-strain curve has a descending branch until crushing failure occurs at the ultimate strain (ε_{max}). This strain is normally in the range of around 0.003 to 0.004

Figure 5.2.1(b) details the variation of uniaxial compressive stress-strain behaviour for concrete of varying compressive strength. From the figure, it can be seen that the initial modulus of elasticity is dependent upon the specific compressive strength of the concrete. It is observed that concrete behaves in an increasingly linear fashion up to peak strength the greater the compressive strength. All peak stress points occur at around 0.002 strain. A decrease in the ductile nature of unloading is observed in the descending branch of the stress-strain plot as the compressive strength is increased.

Numerous formulae derived from standard mathematical functions or from curve fitting techniques have been proposed to approximate the uni-axial compressive stress-strain response; Saenz (1964), Mansur et al. (1995), Almusallam (1995). A review of the various proposed formulae is can be found in Popovics (1970). Examples of various numerical uni-axial compression models are presented in figs 5.2.1(c-e). From this work the following observations can be stated:

- The maximum compressive strain differs from one model to the next
- The presence of compression softening can be accounted for.
- There is no unique model for the uni-axial compressive stress-strain response that has been agreed by the majority of researchers.

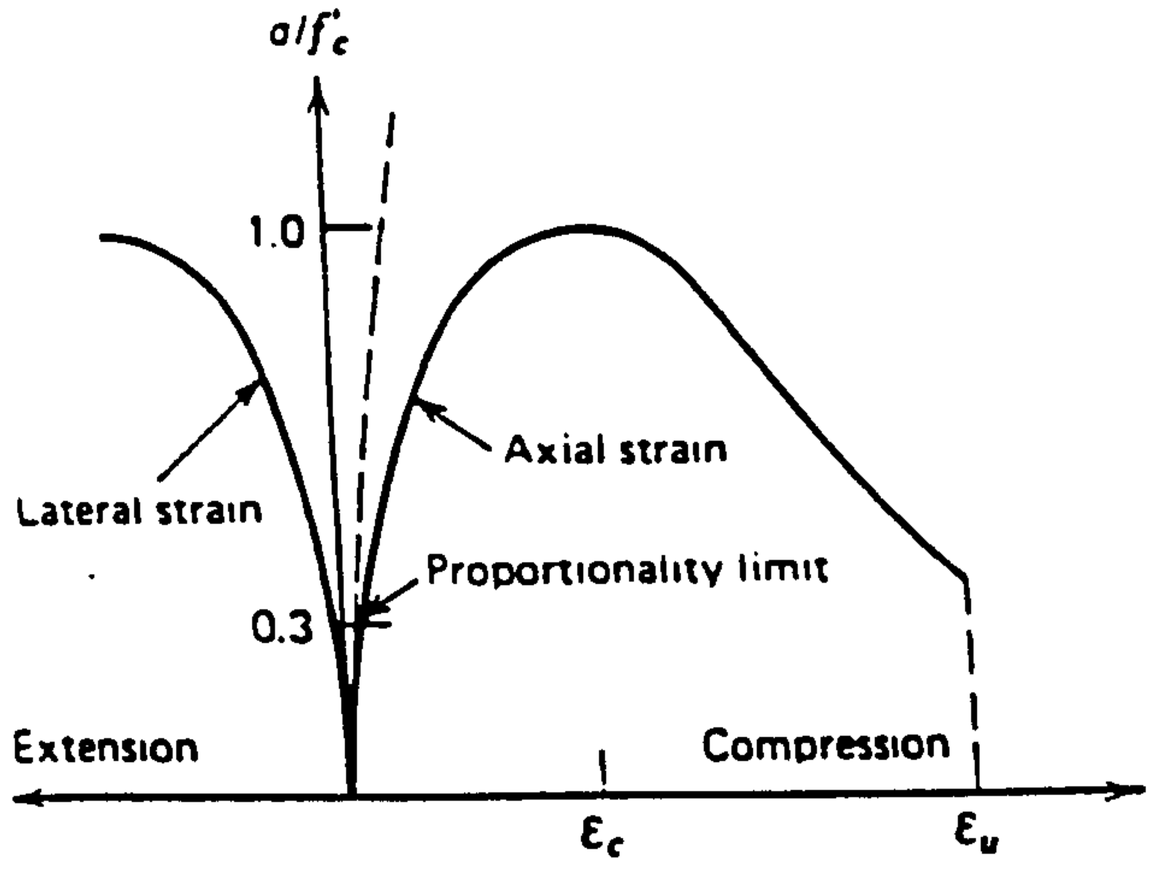

fig 5.2.1 (a) Uni-axial compressive stress-strain response of concrete (Chen 1982)

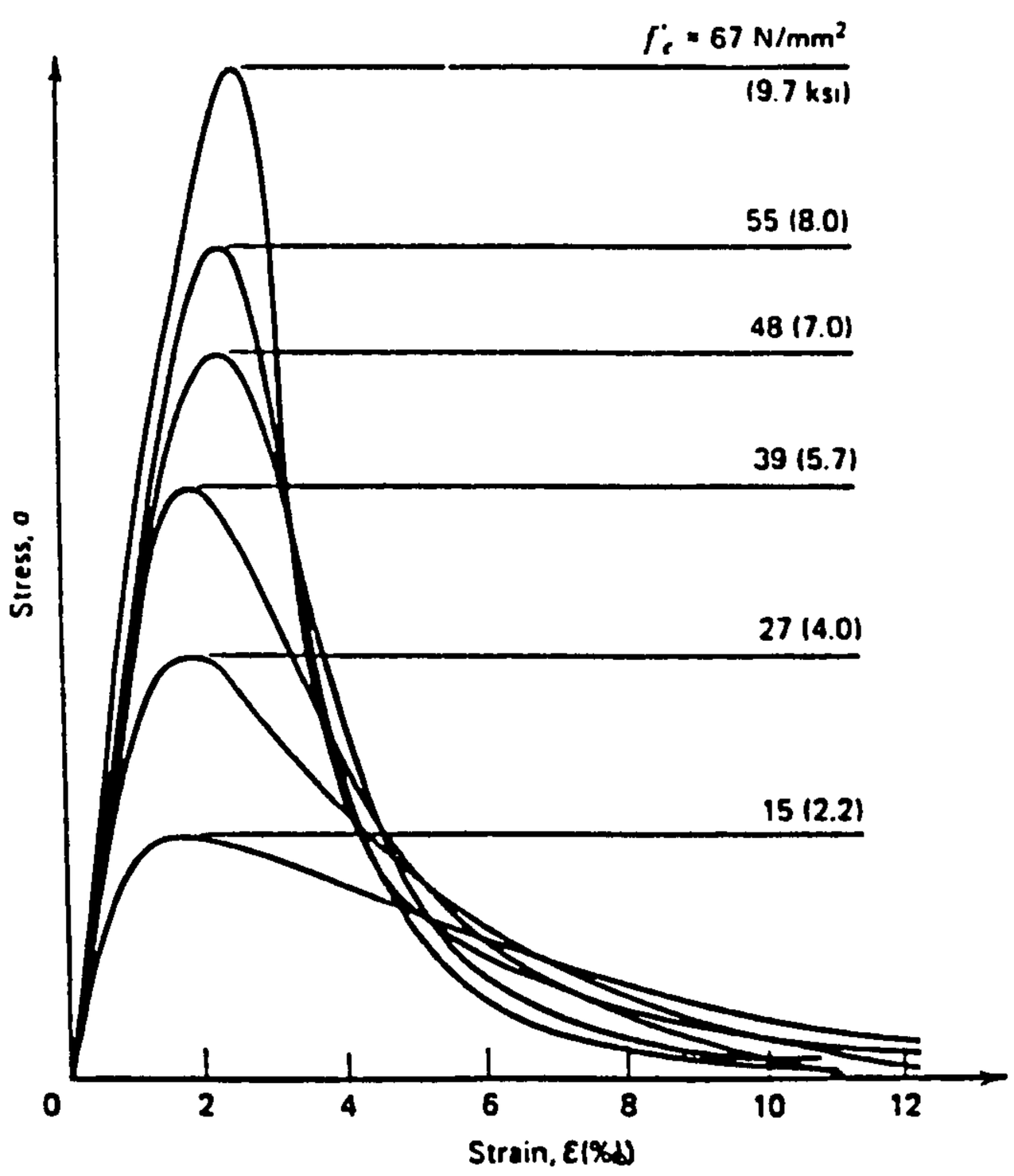

fig. 5.2.1(b) Compressive stress-strain curves for concrete with different f_c' (Chen 1982)

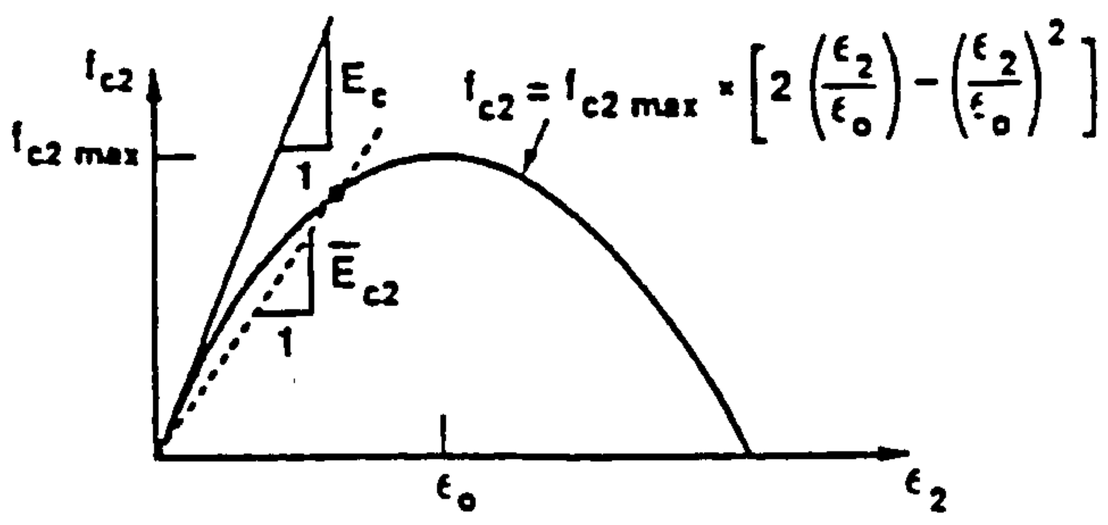

c) Vecchio (1989), f_{c2} = max compressive principal stress

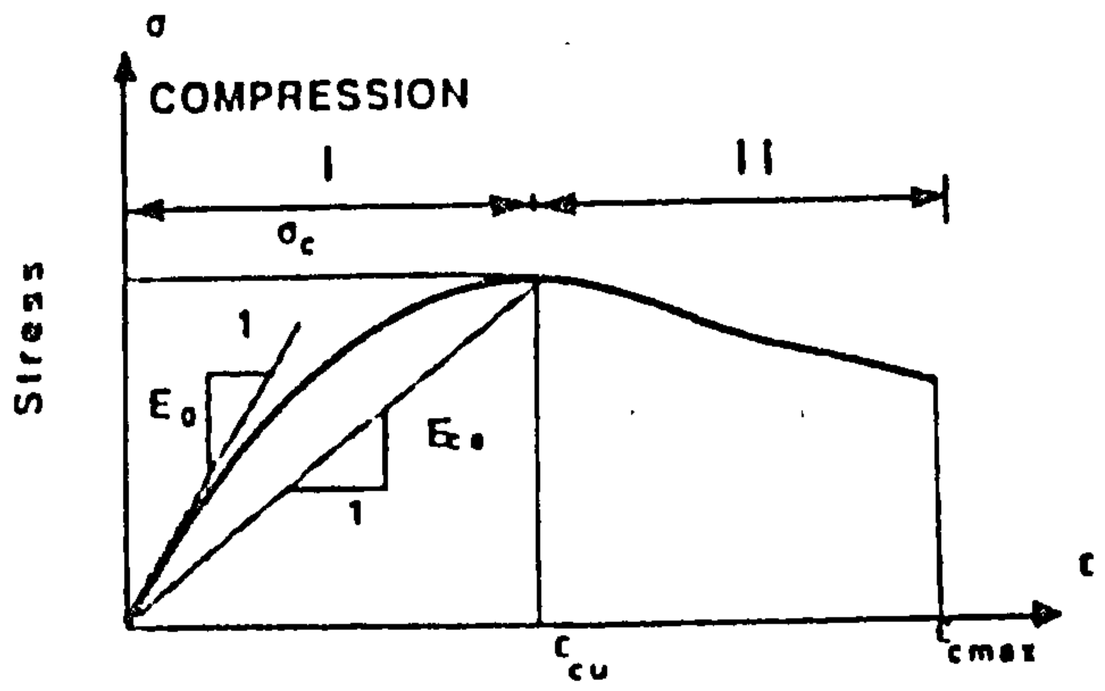

d) Razaqpur & Nofal (1990)

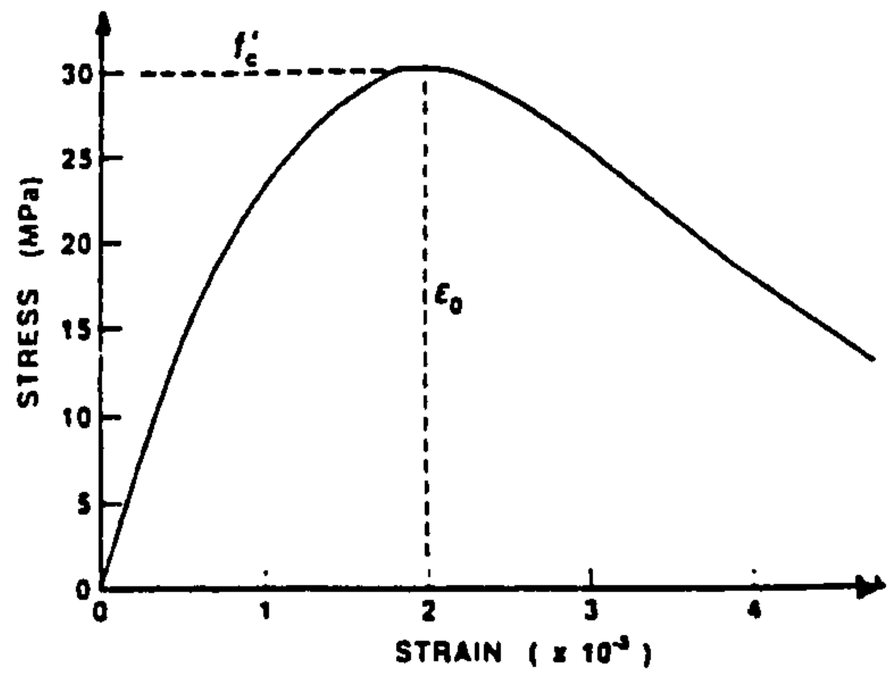

e) Vecchio & Nieto (1991)

fig 5.2.1(c-e) Numerical Compressive Stress-Strain Curves for Concrete

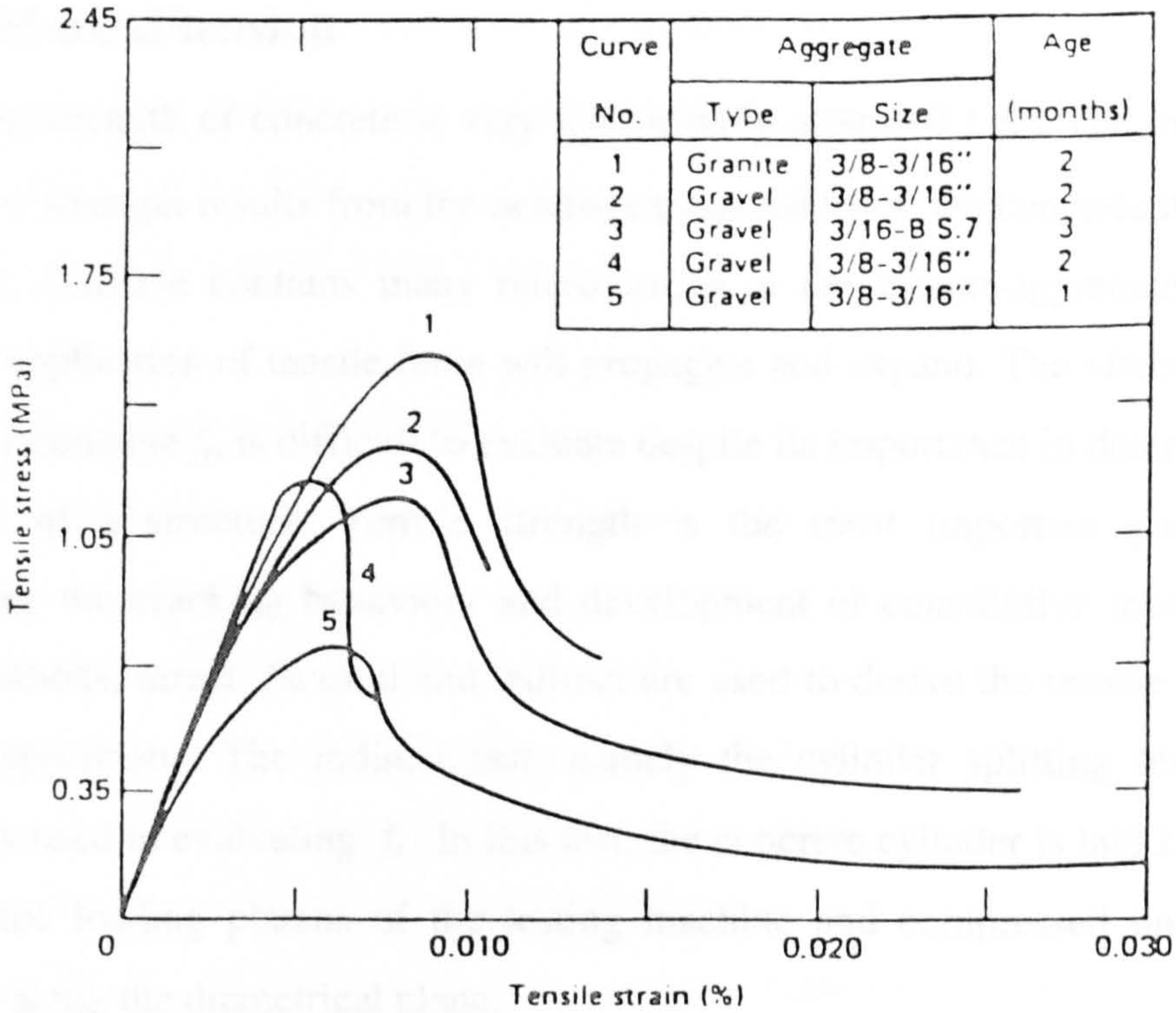

Curve No.	Aggregate Type	Aggregate Size	Age (months)
1	Granite	3/8-3/16"	2
2	Gravel	3/8-3/16"	2
3	Gravel	3/16-8 S.7	3
4	Gravel	3/8-3/16"	2
5	Gravel	3/8-3/16"	1

fig 5.2.2(a) Uni-axial tensile stress-strain curves for concrete (Chen 1982)

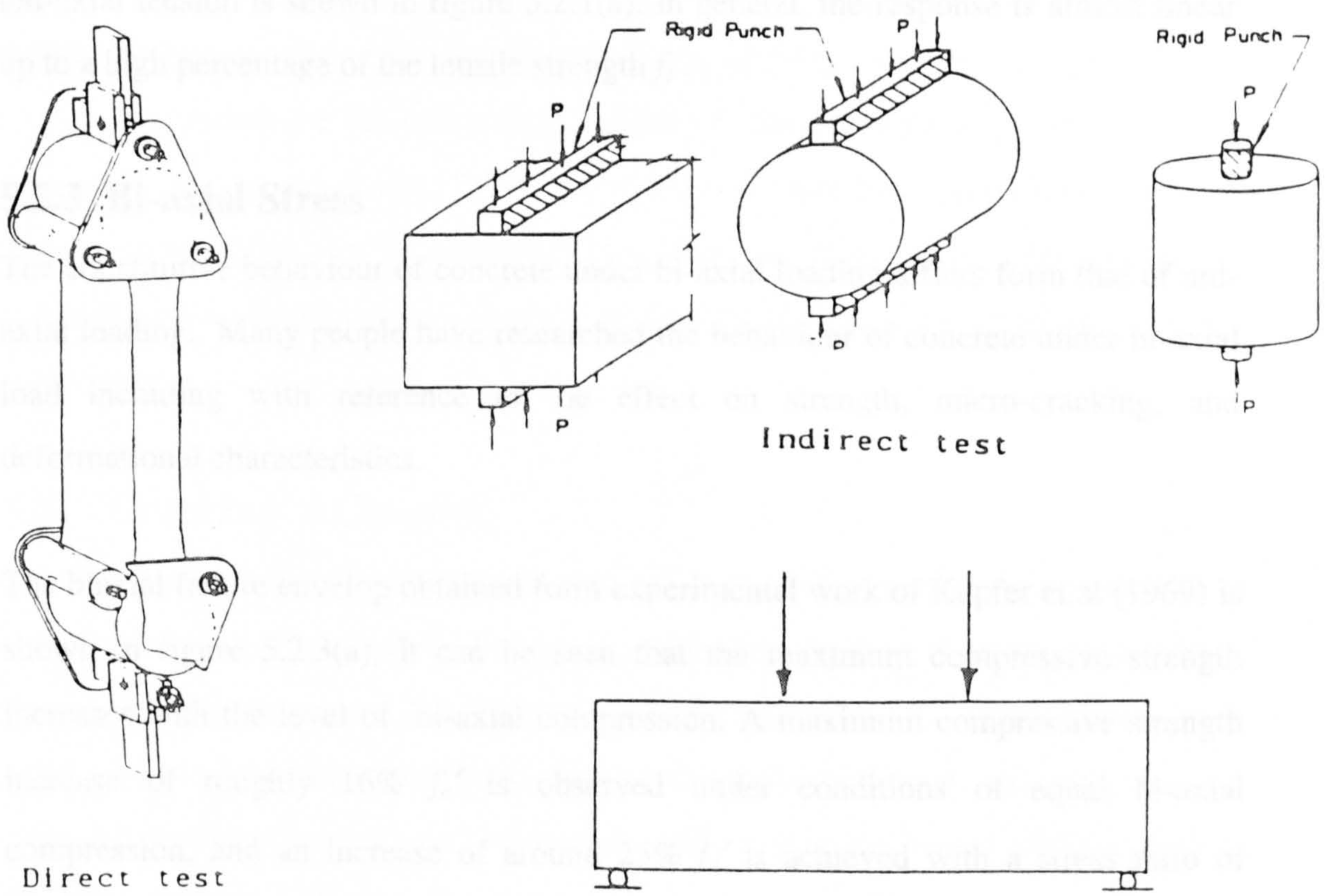

fig 5.2.2(b) Test methods used for measuring the tensile strength of concrete

5.2.2 Uni-axial tension

The tensile strength of concrete is very low, usually around 0.1 f_c'. The main reason for this low strength results from the heterogeneous nature of the concrete itself. From the outset, concrete contains many micro-cracks at the mortar-aggregate interface, which on application of tensile force will propagate and expand. The effective tensile strength of concrete f_t, is difficult to evaluate despite its importance in determining the behaviour of a structure. Tensile strength is the most important parameter in determining the cracking behaviour and development of constitutive models. Three testing methods; direct, flexural and indirect are used to derive the tensile strength of concrete specimens. The indirect test, namely the cylinder splitting test, is most commonly used in evaluating f_t. In this test, the concrete cylinder is laid horizontally between the loading platens of the testing machine and compressed until it splits vertically along the diametrical plane.

The stress-strain relationship for a number of different concrete specimens tested in uni-axial tension is shown in figure 5.2.1(a). In general, the response is almost linear up to a high percentage of the tensile strength f_t.

5.2.3 Bi-axial Stress

The constitutive behaviour of concrete under bi-axial loading differs form that of uni-axial loading. Many people have researched the behaviour of concrete under bi-axial load including with reference to the effect on strength, micro-cracking, and deformational characteristics.

The biaxial failure envelop obtained form experimental work of Kupfer et.al (1969) is shown in figure 5.2.3(a). It can be seen that the maximum compressive strength increases with the level of bi-axial compression. A maximum compressive strength increase of roughly 16% f_c' is observed under conditions of equal bi-axial compression, and an increase of around 25% f_c' is achieved with a stress ratio of $\sigma_1/\sigma_2 = 0.5$. An increased initial stiffness in bi-axial compression is also observed which may be due to Poisson's effect, i.e. a reduction in lateral tensile strain, see figure 5.2.3(b).

In the case of bi-axial tension , a tensile strength similar to uni-axial tension is achieved. The stress-strain curves for bi-axial and uni-axial compression are similar. For the tension-compression case (fig.5.2.3(c)), the compressive strength decreases almost linearly as the tensile stress increases.

5.2.4 Compression Softening

As shown in the uni-axial compression curves, once the peak stress is reached, the concrete begins to unload while the strain increases. The term strain softening is used to describe the response of a material where the slope of the stress-strain curve becomes negative. There exists considerable variation in the experimentally obtained unloading branch of the stress-strain curve. Compression softening behaviour of concrete is dependent upon the boundary conditions and the size of the specimen, see (Van Mier (1984), Vonk (1992)). Post crushing behaviour of the concrete has a definite effect on the failure mode of the structure. Work carried out by Kent & Park (1971), has shown that the level of confinement plays an important role in post crushing behaviour. As expected, the greater the level of confinement, the more ductile the post crushing response, (Issa & Tobaa (1994)). As shown in figs. 5.2.1.(c-e), various models for the descending portion of the stress-strain curve have been proposed. Meyer and Bathe (1982), suggested a straight line approximation with a free parameter to account for confinement of steel was sufficient for most analysis. A concrete post-crushing residual strength of 10-40% of f_c' has been proposed by many researchers.

5.3 Cracking of Concrete

The low tensile strength of concrete will result in early cracking of members in a tension zone at low load levels before the steel starts yielding. Cracking is therefore, one of the most important non-linear phenomena displayed by concrete. Three main approaches to cracking have been developed in finite element analysis; *discrete cracking* models, *smeared cracking* models, and *fracture mechanics* models. Each of the three methods will be briefly described in the following:

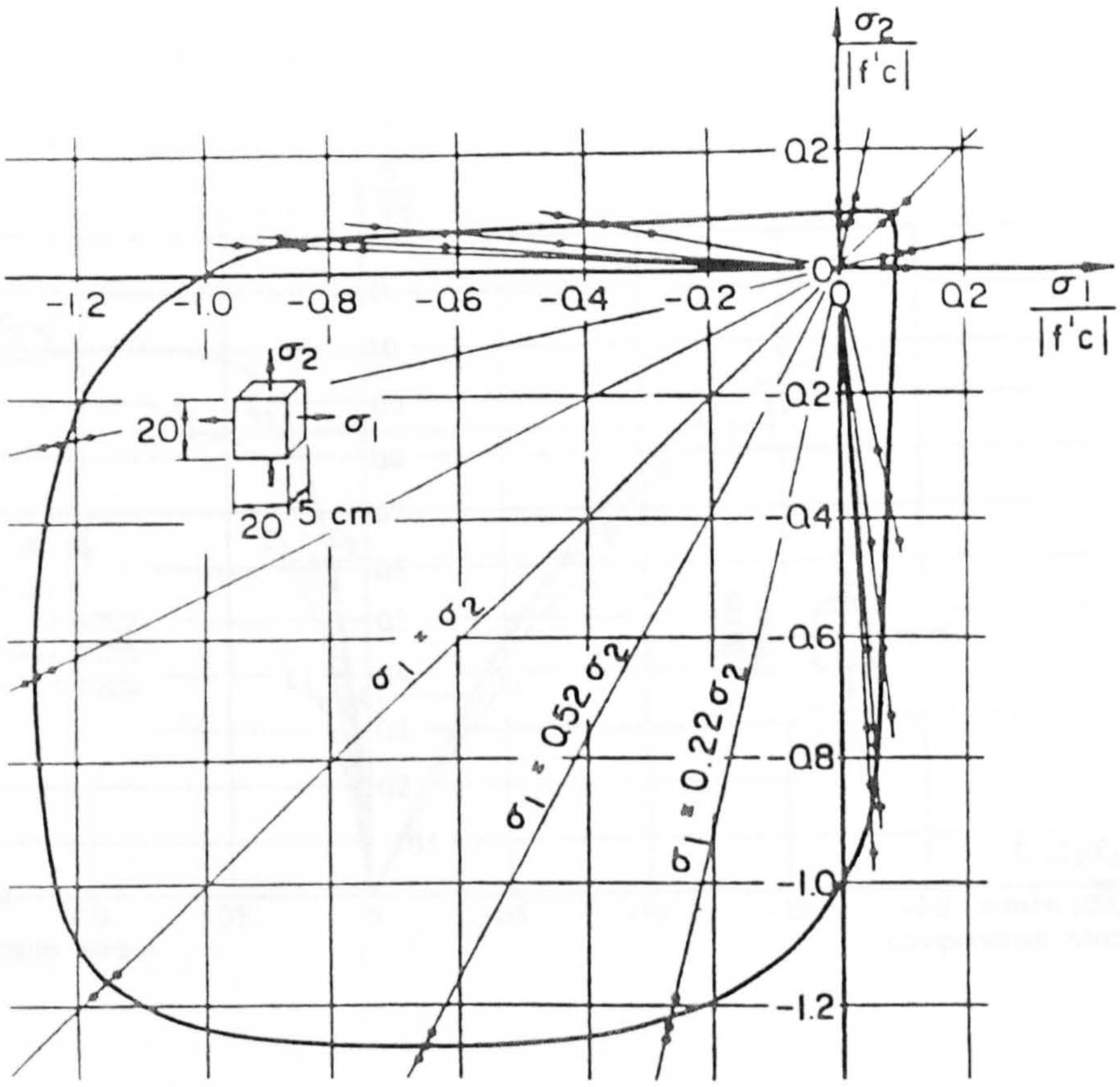

fig 5.2.3(a) Bi-axial strength envelope of concrete (Kupfer et al.1969)

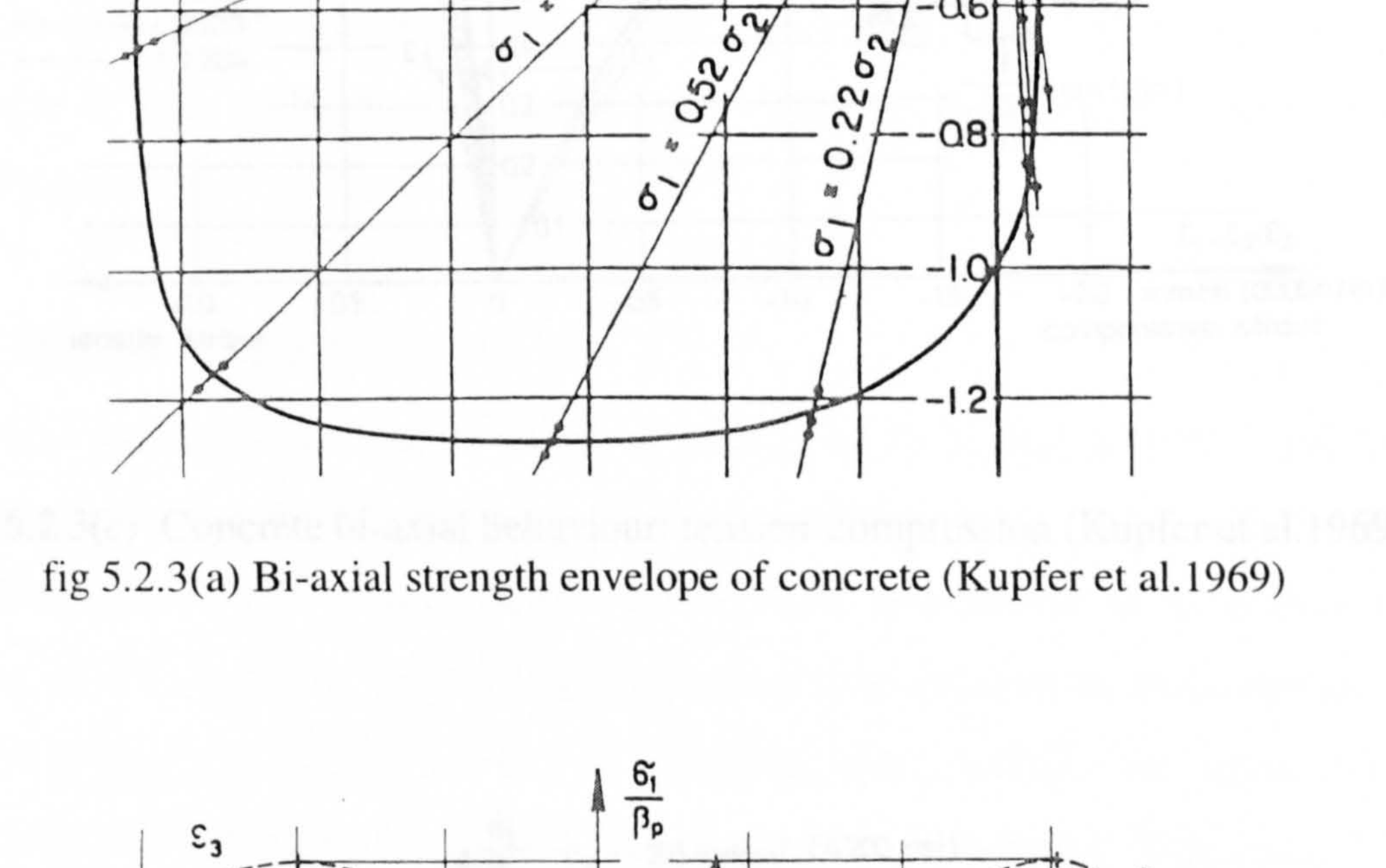

fig 5.2.3(b) Concrete bi-axial behaviour: compression-compression (Kupfer et al.1969)

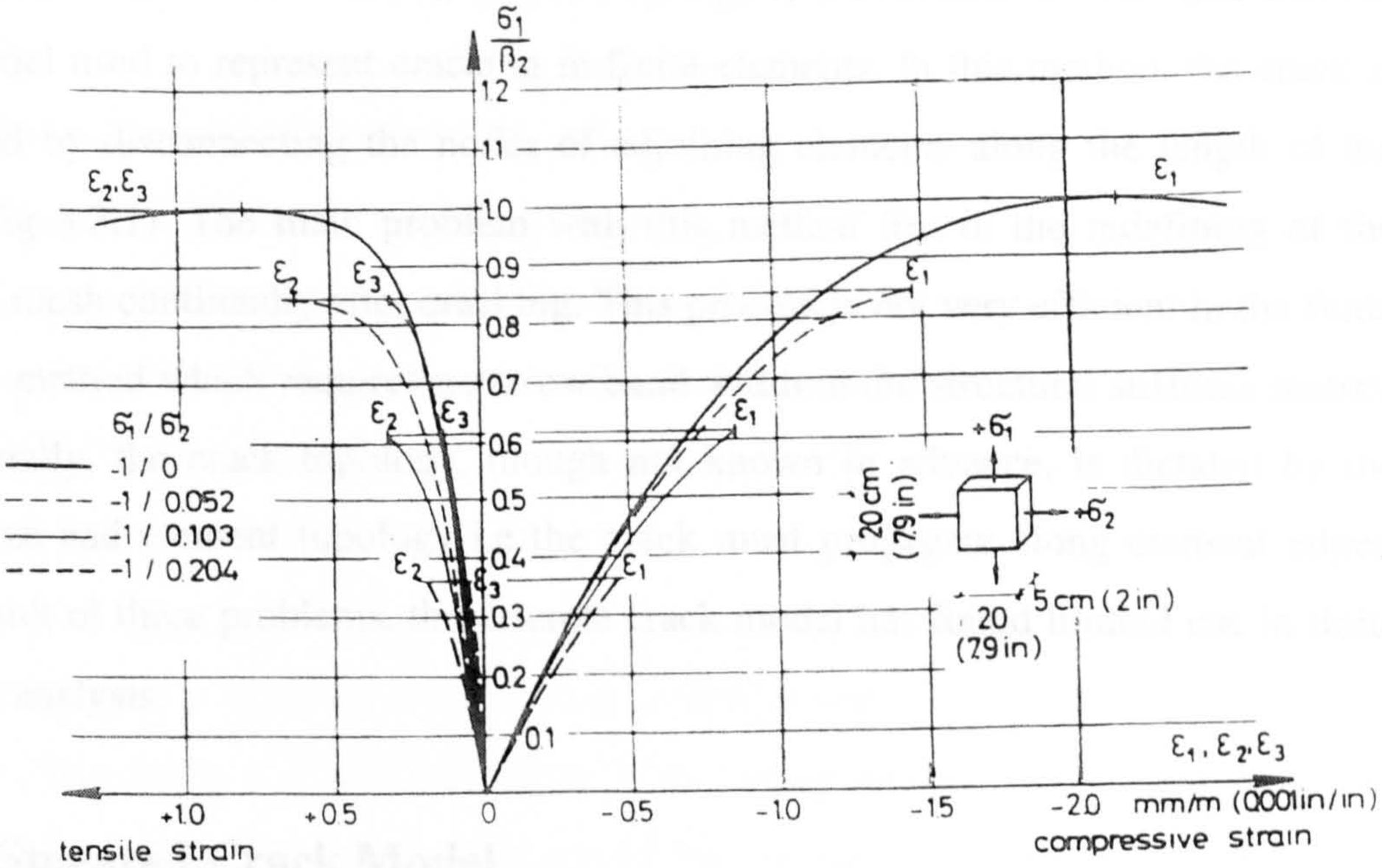

fig 5.2.3(c) Concrete bi-axial behaviour: tension-compression (Kupfer et al.1969)

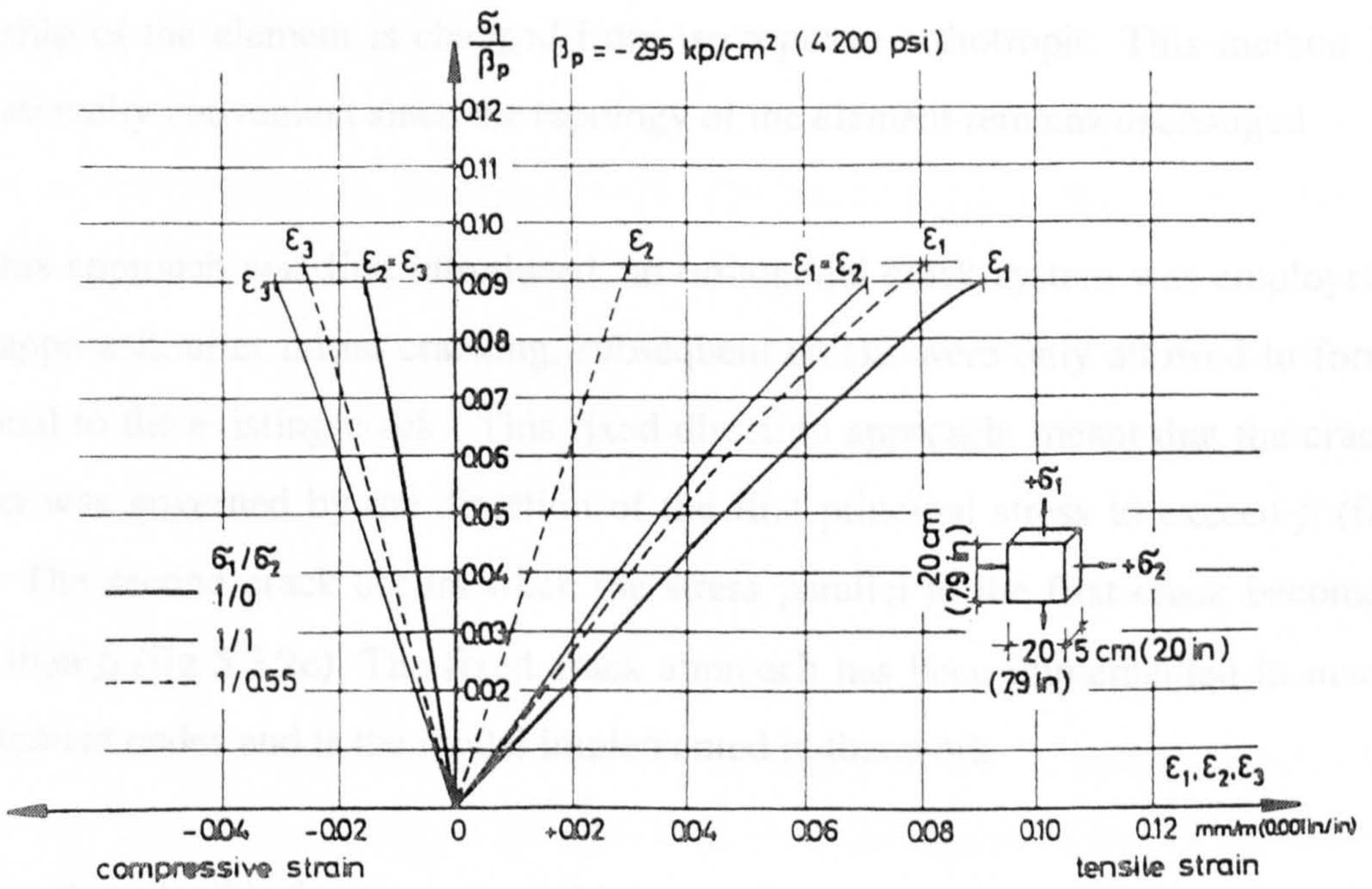

fig 5.2.3(d) Concrete bi-axial behaviour: tension-tension (Kupfer et al.1969)

5.3.1 Discrete Crack Model

The discrete crack model was introduced by Ngo and Scordelis in 1967 and was the first model used to represent cracking in finite elements. In this method, the crack is modelled by disconnecting the nodes of adjoining elements along the length of the crack (fig 5.3.1). The main problem with this method lies in the redefining of the element mesh continually after cracking. This process is not very efficient in the finite element method which requires a narrow band width in the structural stiffness matrix. Additionally, the crack topology, though not known in advance, is dictated by the mesh size and element topology i.e the crack must propagate along element edges. As a result of these problems, the discrete crack model has found limited use in finite element analysis.

5.3.2 Smeared Crack Model

A practical smeared crack model was first introduced by Rashid in 1968. Further enhancements to this model were made by Suidan & Schnobrich (1973) and Phillips & Zienkiewicz (1976). In this model, the concrete is idealised as a continuum, isotropic prior to cracking. On cracking, it is possible to describe its behaviour from the stress-strain relationship. Once the concrete has cracked, the stress-strain relationship of the element is changed from isotropic to orthotropic. This method is computationally convenient since the topology of the element remains unchanged

When this approach was first introduced, an orthogonal crack system was employed. In this approach, after initial cracking, subsequent cracks were only allowed to form orthogonal to the existing crack. This fixed direction approach, meant that the crack direction was governed by the direction of the first principal stress to exceed f_t (fig 5.3.2b). The second crack occurs when the stress parallel to the first crack becomes greater than f_t (fig 5.3.2c). The fixed crack approach has been implemented in many finite element codes and is the model implemented in this work

In reality, it is possible for the post cracking principal strains to deviate from the crack orientation due to the presence of shear strain on a cracked plane. The principal post cracking tensile stress may reach peak on a plane other than the initial crack plane.

The subsequent development of the rotating crack model allowed the co-rotation of the crack with the principal strain axes.

5.3.3 Fracture Mechanics Model

Fracture mechanics theory has been applied successfully in the past to cracking problems involving metals, ceramics and rocks. Some research has been carried out on the applicability of fracture mechanics theory to reinforced concrete; Bazant & Cedolin (1980). It was concluded by Chen(1982), that the use of fracture mechanics in reinforced concrete is still questionable.

The smeared crack approach was adopted for the present study. The simplicity of this approach has made it a popular choice with many analysts. The smeared crack approach provides a good approximation of the load-displacement relationship but is unable in many cases to realistically model exact crack patterns. In cases where this is desired, a fracture mechanics based model is more suitable.

5.4 Present Concrete Model

Recent research into the applicability of various concrete models has found that the level of complexity of the model is not necessarily linked to the level of accuracy. It has been found that simple models can be just as effective, or ineffective as more complex models, Collins & Vecchio (1985). The model used in this work although simple, is capable of adequately predicting the non-linear behaviour of reinforced concrete structures. It has been adapted from models successfully used by Bensalem (1993) and Abdel Kader (1993) to account for compression softening and non-orthogonal steel.

5.4.1 Yield Criterion

The yield criterion defines the combination of stresses which will initiate plastic flow at any point. With regards to the definition of an ideal failure criterion which modeled the exact behaviour of concrete under all conditions, Chen (1982) concluded that such a criterion would be so complex as to make its use in numerical analysis impractical.

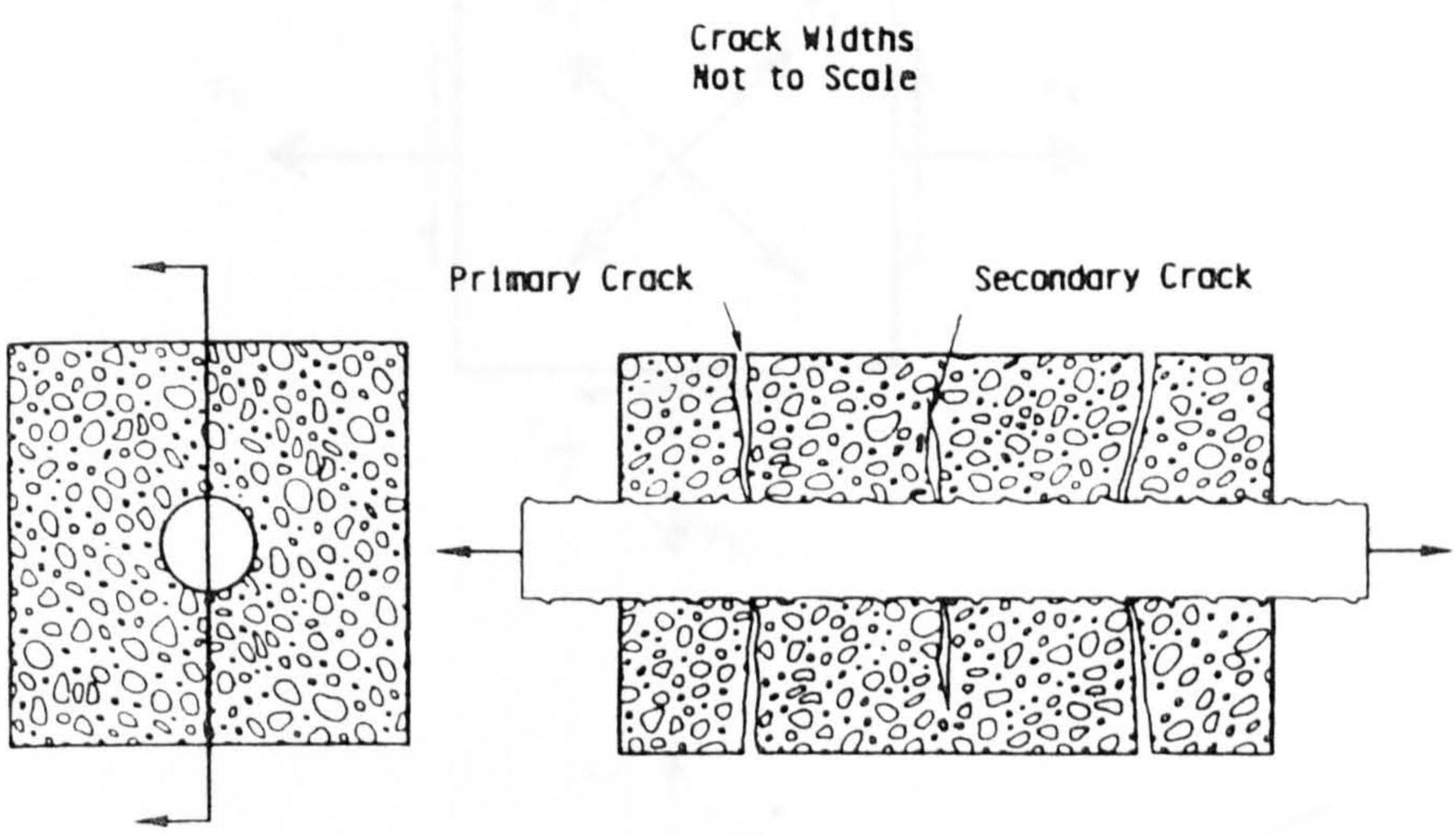

fig 5.3 Cracking of Concrete

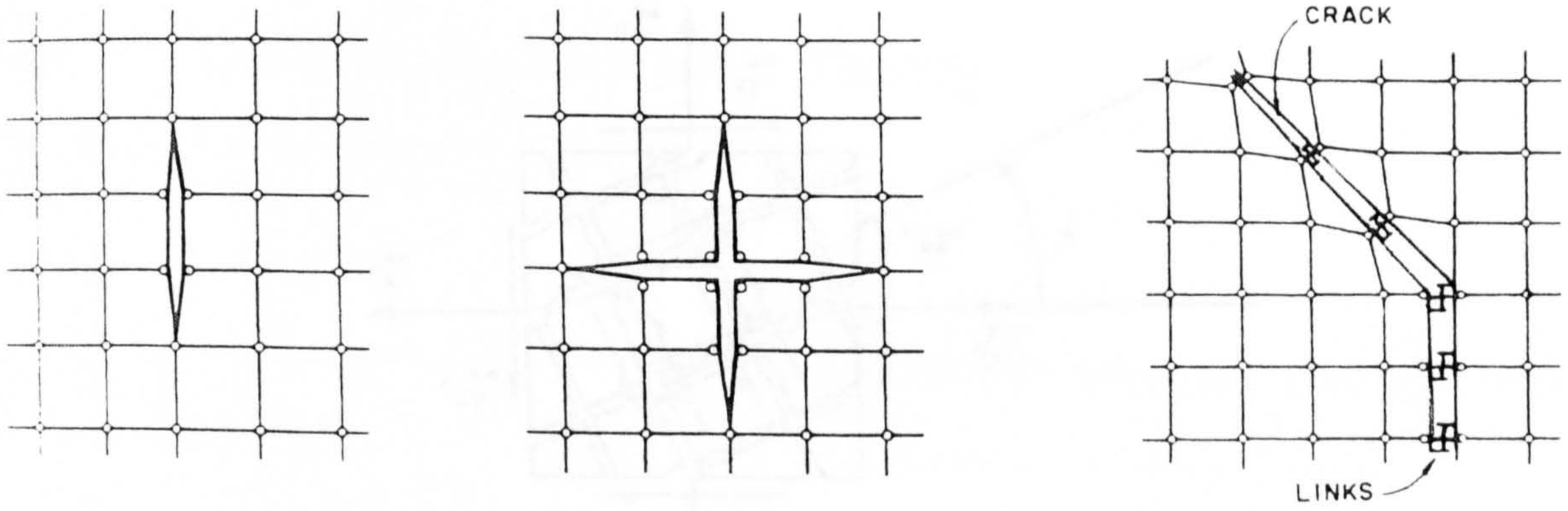

Single crack

Double crack

Crack and aggrgate interlock

fig 5.3.1 Discrete Crack Model

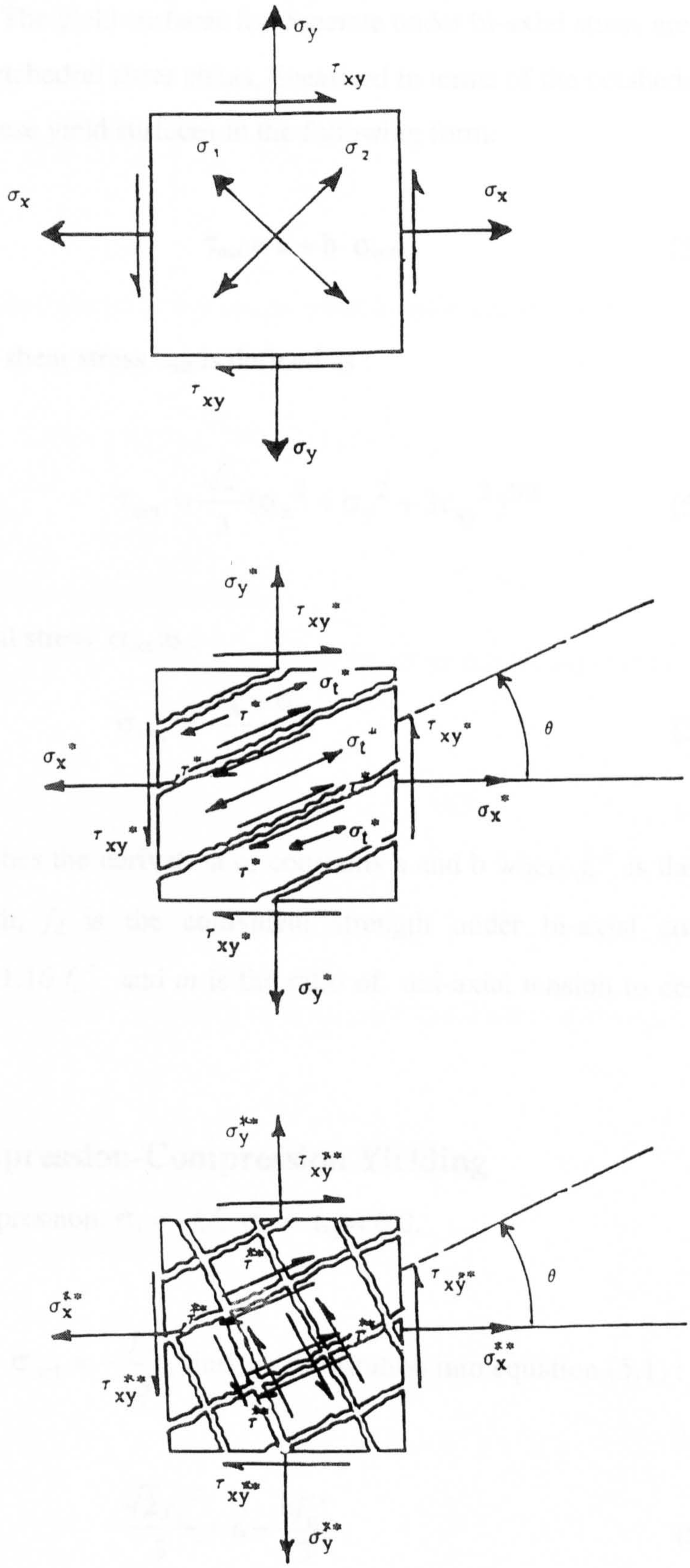

figs 5.3.2 (a-c) Smeared Crack Model

The bi-axial yield criterion used in this work is based upon the experimental work of Kupfer et al (1969). The yield surfaces for concrete under bi-axial stress are shown in figure (5.4.1). The octahedral shear stress, linearised in terms of the octahedral normal stress is used to fit these yield surfaces in the following form:

$$\tau_{oct} = a + b\ \sigma_{oct} \tag{5.1}$$

where the octahedral shear stress τ_{oct} is defined as :

$$\tau_{oct} = \frac{\sqrt{2}}{3}(\sigma_x{}^2 + \sigma_y{}^2 + 3\tau_{xy}{}^2)^{1/2} \tag{5.2}$$

and octahedral normal stress σ_{oct} as :

$$\sigma_{oct} = \frac{\sigma_x + \sigma_y}{3} \tag{5.3}$$

The following describes the derivation of constants a and b where f_c' is the uni-axial compression strength, f_d is the equivalent strength under bi-axial compression previously stated as $1.16\,f_c'$ and m is the ratio of uni-axial tension to compression strength (f_t / f_c').

5.4.1.1 Compression-Compression Yielding

a) For uni-axial compression: $\sigma_x = -f_c'$, $\sigma_y = \tau_{xy} = 0.0$,

$\tau_{oct} = \frac{\sqrt{2}}{3} f_c'$ and $\sigma_{oct} = -\frac{f_c'}{3}$, thus on substitution into equation (5.1) :

$$\frac{\sqrt{2} f_c'}{3} = a - \frac{b f_c'}{3} \tag{5.4}$$

b) For bi-axial compression: $\sigma_x = \sigma_y = -f_d = -1.16\,f_c'$, $\tau_{xy} = 0.0$,

$\tau_{oct} = 1.16\frac{\sqrt{2}}{3} f_c'$ and $\sigma_{oct} = -1.16\frac{2 f_c'}{3}$, after substitution into equation (5.1) :

$$1.16\left(\frac{\sqrt{2} f_c'}{3}\right) = a - 1.16\left(\frac{2b f_c'}{3}\right) \tag{5.5}$$

Solving for a and b, the bi-axial compression yield equation is given by:

$$\frac{\tau_{oct}}{f_c'} + \left(0.1714\frac{\sigma_{oct}}{f_c'} - 0.4143\right) = 0.0 \tag{5.6}$$

5.4.1.2 Tension-Compression

In this case $\sigma_x = -f_c'$, $\sigma_y = f_t = m f_c'$, following the same procedure leads to:

$$\frac{\tau_{oct}}{f_t} + \frac{\sqrt{2}(1-m)}{(1+m)}\frac{\sigma_{oct}}{f_c'} - \frac{2\sqrt{2}}{3}\frac{m}{(1+m)} = 0.0 \tag{5.7}$$

5.4.1.3 Tension-Tension

For biaxial tension the following simple circular yield criterion is implemented:

$$\left(\frac{\sigma_1}{f_t}\right)^2 + \left(\frac{\sigma_2}{f_t}\right)^2 - 1.0 = 0.0 \tag{5.8}$$

where σ_1 and σ_2 are the principal stresses.

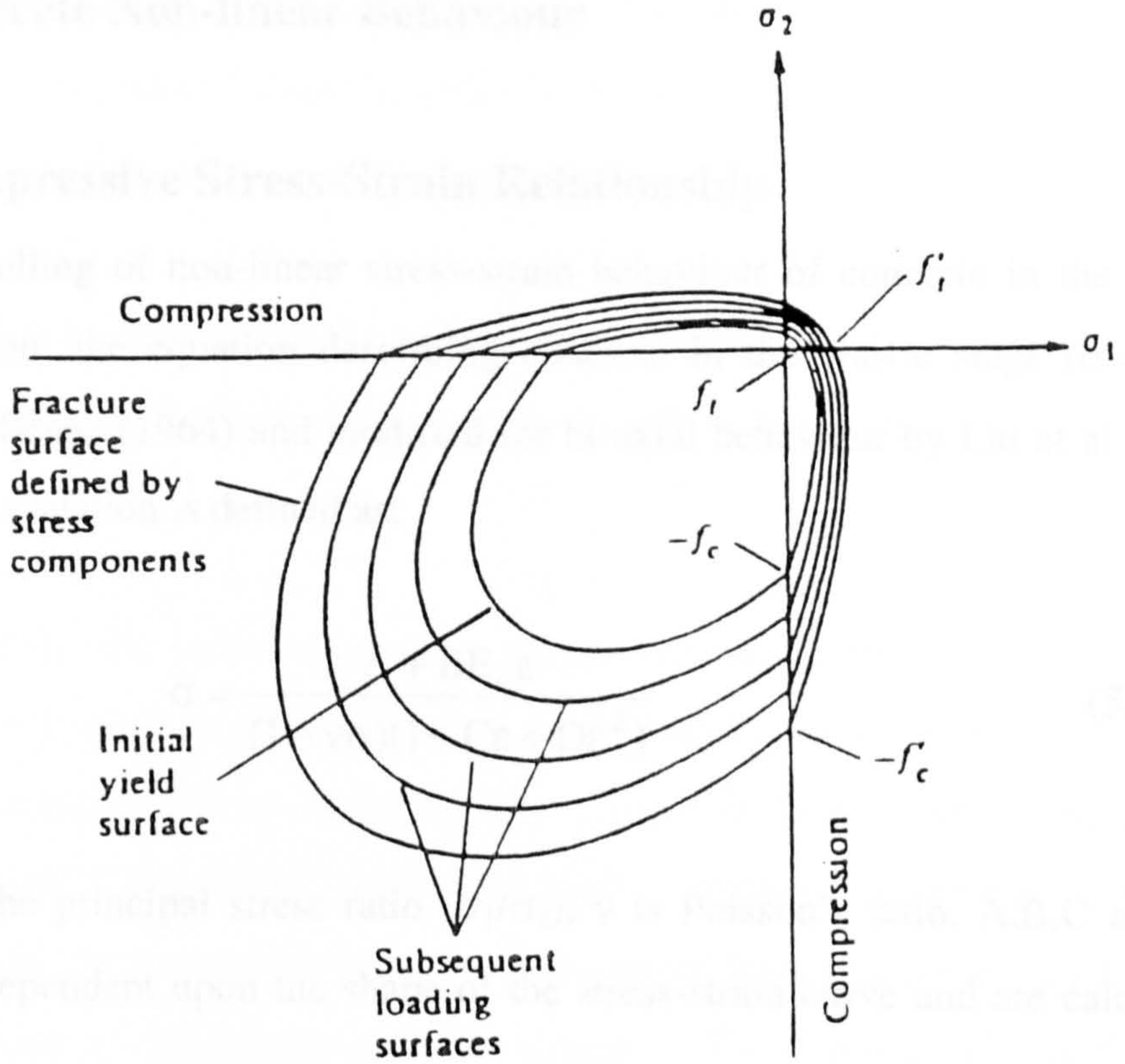

fig 5.4.1 Yield Surfaces of Concrete under Bi-axial Stress (Chen 1982)

5.5 Concrete Non-linear Behaviour

5.5.1 Compressive Stress-Strain Relationship

For the modelling of non-linear stress-strain behaviour of concrete in the principal stress direction, the equation describing concrete in the elastic stage ($\sigma=D\varepsilon$) first proposed by Seanz (1964) and modified for bi-axial behaviour by Liu et al (1972) is applied. This equation is defined as:

$$\sigma = \frac{A + BE_c\varepsilon}{(1-\nu\alpha)(1+C\varepsilon+D\varepsilon^2)} \tag{5.9}$$

where α is the principal stress ratio (σ_1/σ_2), ν is Poisson's ratio. A,B,C and D are parameters dependent upon the shape of the stress-strain curve and are calculated as follows:

1. At initial loading $\varepsilon = 0.0, \sigma = 0.0$

$$\frac{d\sigma}{d\varepsilon} = \frac{E_c}{(1-\nu\alpha)} \quad \text{and } \sigma = 0.0$$

2. On reaching the peak stress σ_p at strain ε_p, the slope of the stress strain curve becomes zero. Therefore at:

$$\frac{d\sigma}{d\varepsilon} = 0.0 \quad \text{and} \quad \sigma = \sigma_p$$

From the four conditions described above, the unknown parameters A, B, C and D of equation 5.9 can be evaluated. Solving for these constants leads to the following equation:

$$\sigma = \frac{E_c\varepsilon}{(1-\nu\alpha)\left[1+\left(\frac{1}{1-\nu\alpha}\frac{E_c}{E_s}-2\right)\frac{\varepsilon}{\varepsilon_p}+\left(\frac{\varepsilon}{\varepsilon_p}\right)^2\right]} \tag{5.10}$$

where:

E_c is the initial modulus of elasticity of concrete for uni-axial loading

E_s is the secant modulus of elasticity at the peak stress (σ_p / ε_p)

σ and ε are the stress and strain in biaxial load

This equation is used to model the stress-strain relationship for concrete under biaxial compression up to peak strain at which point the equation ceases to become valid due to softening.

Early changes in the stiffness of the concrete are accounted for by incrementally linearizing equation 5.10 during loading. This process is carried out by assuming intermediate surfaces shown in figure 5.4.1 similar to those proposed by Bell and Elms (1971) and Chen (1982). The first loading surface corresponds to the initial discontinuity in the stress-strain diagram. Subsequent loading surfaces are assumed to have the shape of the limiting yield surface. The intermediate surfaces are represented by equation 5.1 but with an intermediate concrete strength f_{cc} replacing the ultimate strength f_c'. The following equation was proposed by Johnarry (1979):

$$f_{cc} = f_{co} - f_t + \frac{E_c}{E_i} f_t \qquad (5.11)$$

where f_{cc} = intermediate compressive strength, $f_{co} = 0.5\, f_c'$, f_t = tensile strength, E_c = concrete elastic modulus, E_i = instantaneous elastic modulus. The instantaneous elastic modulus is calculated up to peak strain ε_p using equation 5.11. For strains above this value the following expression is used until the assumed crushing strain of 0.0035 is reached:

$$E_i = f_c' / \varepsilon_i \qquad (5.12)$$

If the principal compressive strain exceeds 0.0035 or if the failure criteria is violated, then concrete is assumed to be crushed.

5.5.2 Tensile Behaviour

The tensile behaviour of concrete, most notably cracking, accounts for the main source of non-linearity in concrete structures. The present concrete model is able to generate the main features of concrete in tension; cracking in one or two directions, shear transfer to account for aggregate interlock and tension stiffening.

5.5.2.1 Single Cracking

If the yield equations 5.7 or 5.8 in tension-tension or tension-compression, are violated then the material is said to be cracked. The direction of the cracked is taken as normal to the major principal tensile stress direction. The stiffness perpendicular to the crack is assumed equal to zero when tension stiffening is neglected. The material parallel to the crack is still able to carry stress. In addition some shear force is transmitted along the rough surfaces of the crack. The material stiffness matrix of the concrete in the local coordinate system is given below:

$$[D']_{cr} = \begin{bmatrix} E_c & 0 & 0 \\ 0 & 0 & 0 \\ 0 & 0 & \beta G \end{bmatrix} \qquad (5.13)$$

The shear modulus G is reduced ($0 \le \beta \le 1$) to account for aggregate interlock. The Poisson effect is neglected since it is assumed that there is no interaction between the two principal directions once the concrete has cracked. The following describes the process of defining the crack direction:

a: The principal stresses are calculated according to the following:

$$\sigma_{1,2} = \frac{\sigma_x + \sigma_y}{2} \pm \left[\left(\frac{\sigma_x - \sigma_y}{2} \right)^2 + \tau_{xy}{}^2 \right]^{\overline{2}} \qquad (5.14)$$

b. The principal angle θ, with respect to the x-axis from:

$$\tan 2\theta = -\frac{2\tau_{xy}}{\sigma_x - \sigma_y} \qquad (5.15)$$

c. Since $-45 \leq \theta \leq 45$, it may lead to confusion about the major principal direction. It is necessary to calculate the normal stress σ_n associated with angle θ from the following.

$$\sigma_n = \sigma_x \cos^2\theta + \sigma_y \sin^2\theta + 2\tau_{xy} \sin\theta\cos\theta \qquad (5.16)$$

d. It is then necessary to compare the values of σ_1 and σ_2 with the normal stress σ_n calculated from the above equation.

- if $\sigma_n = \sigma_1$, then σ_1 is at θ and hence the crack angle is inclined $\theta + 90^o$ to the x-axis.
- if $\sigma_n = \sigma_2$, then σ_1 is at $\theta + 90^o$ and hence the crack angle is inclined θ to the x-axis.

5.5.2.2 Double Cracking

Subsequent cracking and changes in crack orientation are due to the presence of shear retention and tension stiffening. These subsequent or secondary cracks in reality may not be orthogonal to the original crack direction since aggregate interlock implies that the primary crack direction does not coincide with the principal direction. Vecchio and Collins (1982), found from experiments on shear panels, that changes in crack orientation do take place, especially in unequally reinforced panels.

In the case of previously uncracked concrete, a double crack will occur when both principal stresses exceed the tensile strength f_t . The material stiffness matrix in local coordinates for this case is given as:

$$[D']_{cr} = \begin{bmatrix} 0 & 0 & 0 \\ 0 & 0 & 0 \\ 0 & 0 & \beta G \end{bmatrix} \qquad (5.17)$$

When tension stiffening is considered in the analysis, then the first two diagonal terms of the above matrix may be updated accordingly. The material stiffness matrix $[D']_{cr}$

is expressed in terms of the local coordinates (x′,y′), it is therefore necessary to carry out a transformation into global coordinates via the transformation matrix [T]:

$$[D]_{cr} = [T]^T [D']_{cr} [T] \tag{5.18}$$

and $$[T] = \begin{bmatrix} C^2 & S^2 & CS \\ S^2 & C^2 & -CS \\ -2CS & 2CS & -S^2C^2 \end{bmatrix} \tag{5.19}$$

where $C = \cos\theta$, $S = \sin\theta$

5.5.2.3 Tension Stiffening

Cracking in a reinforced concrete member usually occurs at discrete sections. On cracking, the concrete tensile strength at the crack reduces to zero. However, the uncracked concrete between the cracks is still able to carry tension and thus contribute to stiffness. This phenomenon is known as tension stiffening (fig 5.5.2.3a). Modelling of tension stiffening is important for the prediction of a structure's load-deformation characteristics in the post cracking stage.

Numerically, there are two ways in which to model the tension stiffening effect. The first method is to modify the tensile stress-strain curve for concrete. The second method involves modifying the stress-strain curve for steel. The first method is the most popular and was introduced by Scanlon and Murray (1974). In this model, a strain softening branch is added to the stress-strain curve after the cracking strain has been exceeded. In experiments on the tensile strength of plain concrete, the presence of a softening branch of the stress strain curve has been confirmed, Reinhardt (1985), Gopalaratnam and Shah (1985). Thus, the inclusion of this tension softening behaviour in the model is closer to reality.

Experiments by Clark and Speirs (1978) on one-way spanning slabs with different steel ratios have shown that the effect of tension stiffening decreases with increasing

steel strains and steel ratios. They suggested that tension stiffening could be ignored if the steel ratio exceeds 1.5% or the steel strains exceed 0.0016.

For the model used in this study, the tension stiffening regime shown in fig 5.5.2.3(b) was adopted. Tension stiffening was modelled as a linear softening in the post cracking regime.

when $\varepsilon_i < \varepsilon_{cr}$ then $\sigma = E_i \varepsilon_i$

if $\varepsilon_{cr} \leq \varepsilon_i \leq C2\,\varepsilon_{cr}$ then $\sigma = C1\, f_t \left[\dfrac{(C2\varepsilon_{cr} - \varepsilon_i)}{\varepsilon_{cr}(C2-1)} \right]$

if $C2\varepsilon_i > C2\varepsilon_{cr}$ then $\sigma = 0$

where σ and ε_i are the local stresses and strains orthogonal to the crack, the cracking strain $\varepsilon_{cr} = f_t/E_c$, and f_t is the tensile strength of the concrete. The value of coefficients C1 and C2 can vary between the following range: $0.5 \leq$ C1 ≤ 1.0 and $10.0 \leq$ C2 $\leq$ 20.0

5.5.2.4 Shear Retention

In a cracked structure, shear can be transmitted along the cracked interface by one of two mechanisms. The first mechanism, aggregate interlock, results from the uneven fracture surface and works in combination with friction to provide resistance along the fracture plane (fig. 5.5.2.4(a)). The second, dowel action of the bars, is caused by reinforcement crossing the crack (fig. 5.5.2.4(b)). The resistance provided by these effects can be quite significant in structures under high direct shear, where the strength may be dictated by behaviour along a single dominant plane or fracture zone. Both these mechanisms are governed by the width of the crack, i.e. as crack width increases, shear resistance decreases. Aggregate interlock has been found experimentally to provide more shear resistance than dowel action, Millar & Jonson (1985). It is not possible to implement directly the above mentioned mechanisms when using the smeared crack approach. For this purpose, the reduction in shear modulus across

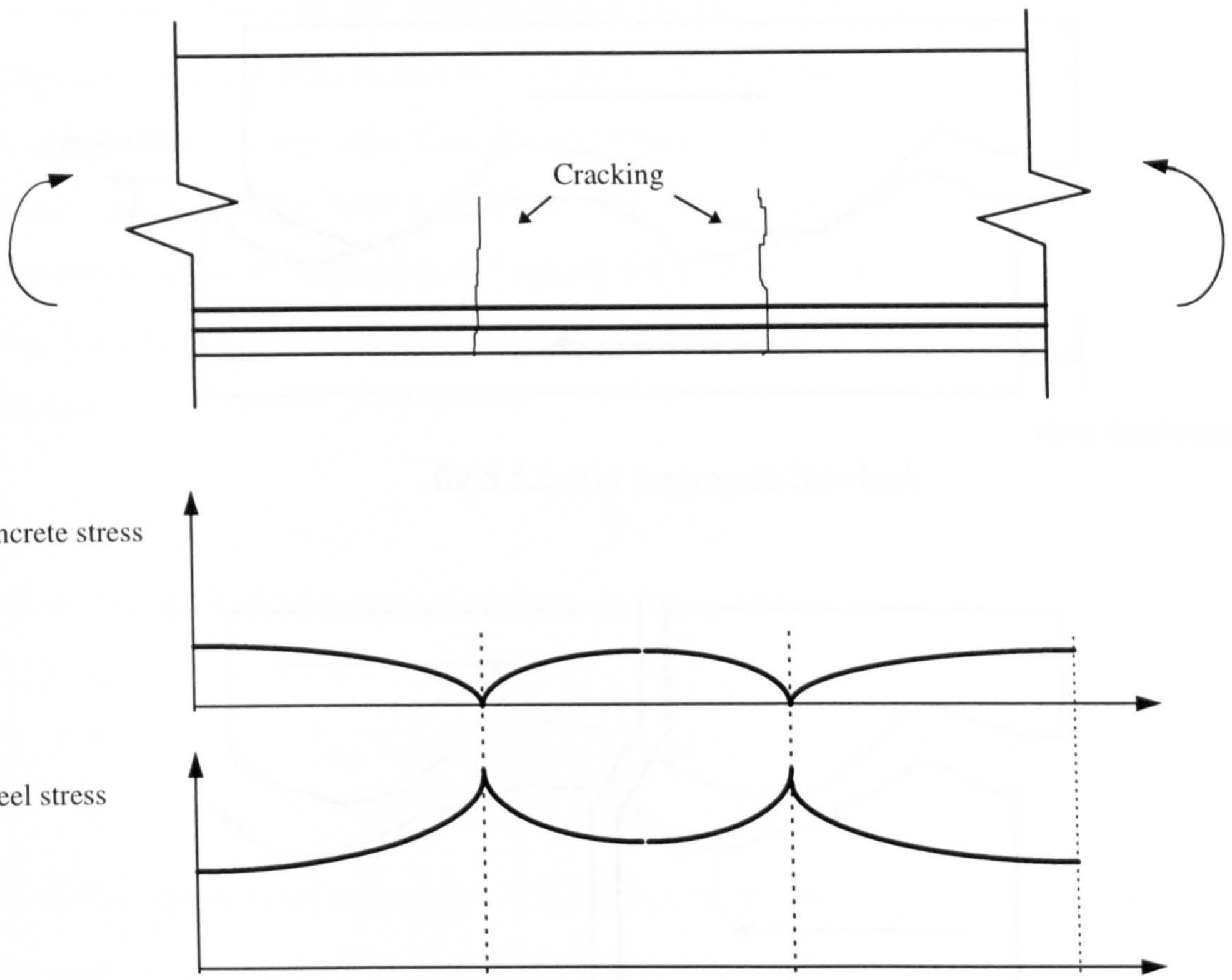

fig.5.5.2.3(a) Stress distribution in a cracked reinforced concrete beam

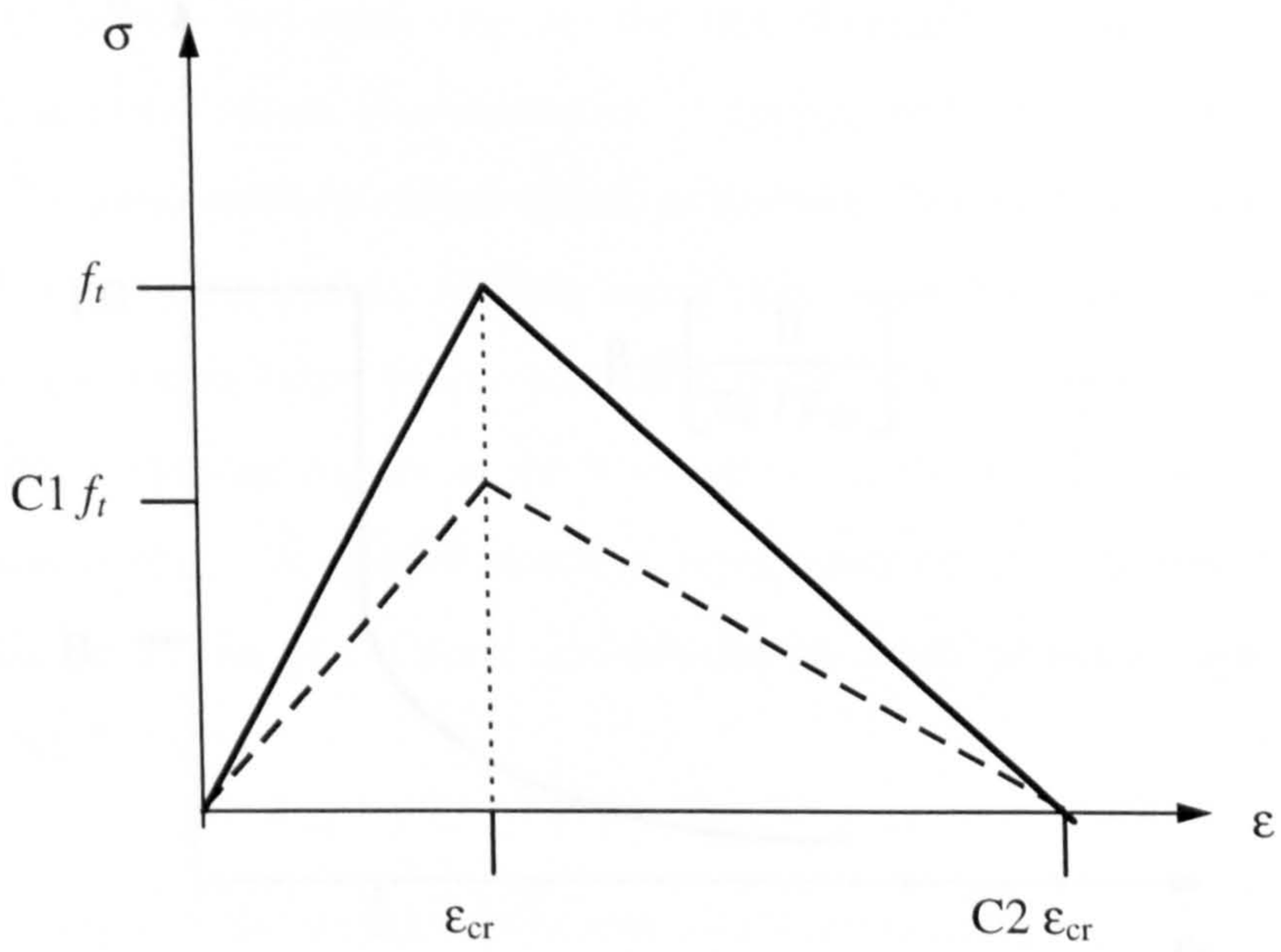

fig.5.5.2.3(b) Tension stiffening idealisation

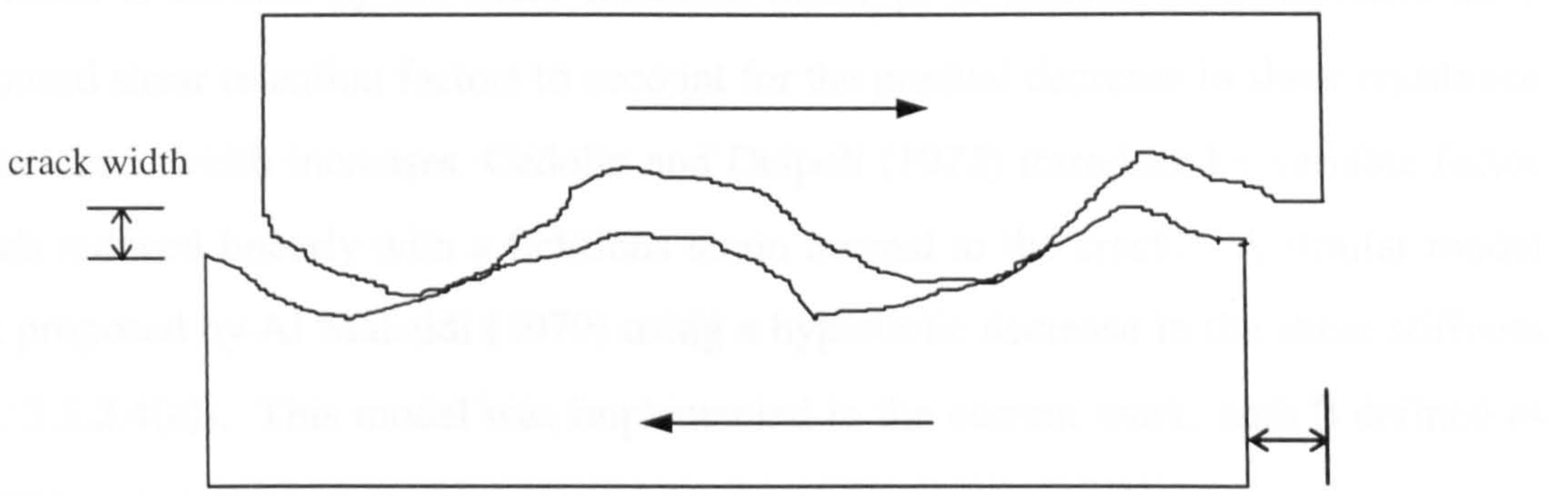

fig.5.5.2.4(a) Aggregate interlock

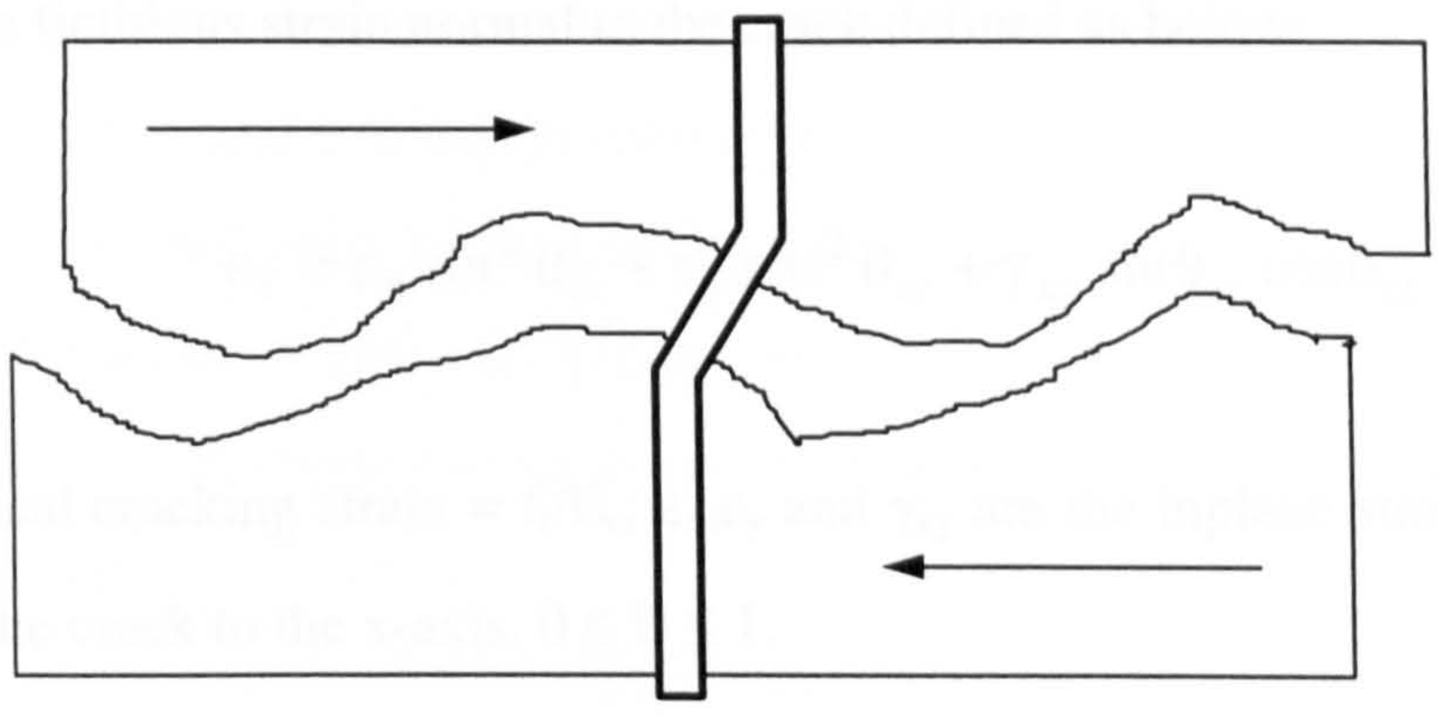

fig.5.5.2.4(b) Dowel action of reinforcing bar

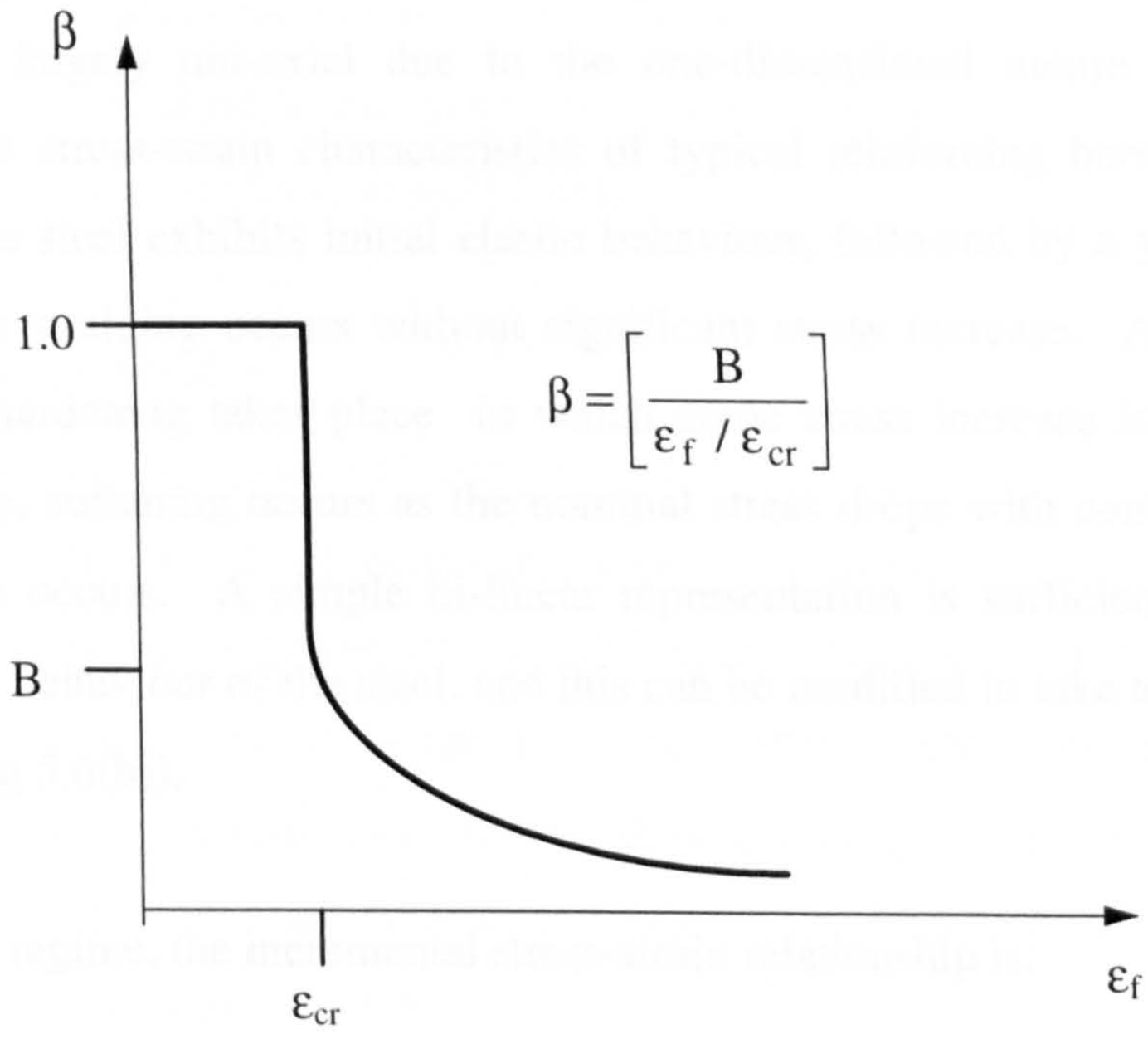

fig.5.5.2.4(c) shear retention factor

the crack is defined by the shear retention factor β. A number of researchers have proposed shear retention factors to account for the gradual decrease in shear resistance as the crack width increases. Cedolin and Deipoli (1972) introduced a variable factor which reduced linearly with a fictitious strain normal to the crack. A similar model was proposed by Al Mahaidi (1979) using a hyperbolic decrease in the shear stiffness (fig. 5.5.2.4(c)). This model was implemented in the current work, with β defined as follows.

$$\beta = \frac{B}{(\varepsilon_f / \varepsilon_{cr})} \tag{5.20}$$

where ε_f is the fictitious strain normal to the crack defined as below:

$$\varepsilon_f = \varepsilon_x \sin^2\theta_{cr} + \varepsilon_y \cos^2\theta_{cr} + \gamma_{xy} \sin\theta_{cr} \cos\theta_{cr} \tag{5.21}$$

ε_{cr} is the critical cracking strain = f_t/E_c, ε_x,ε_y and γ_{xy} are the inplane strains and θ_{cr} is the angle of the crack to the x-axis, $0 \leq B \leq 1$.

5.6 Modelling of Reinforcement

The modelling of steel bar behaviour is less complicated than that of concrete since its behaviour is largely uni-axial due to the one-dimensional nature of reinforcing elements. The stress-strain characteristics of typical reinforcing bars are shown in fig.5.6(a). The steel exhibits initial elastic behaviour, followed by a yield plateau in which further straining occurs without significant stress increase. After this point, some strain hardening takes place in which some stress increase is observed with strain. Finally, softening occurs as the nominal stress drops with continued straining until fracture occurs. A simple bi-linear representation is sufficient to model the elasto-plastic behaviour of the steel. and this can be modified to take account of strain hardening (fig 5.6(b)).

In the elastic regime, the incremental stress-strain relationship is:

$$\Delta\sigma = E_s \Delta\varepsilon$$

On reaching the yield stress f_y, the incremental stress relationship becomes:

$$\Delta\sigma = E_s(1 - E_s / (E_s + H))\Delta\varepsilon$$

where H is the hardening parameter and E_s is the Young's modulus of the steel. There are three main types of models used for reinforcing steel; smeared, embedded and discrete model (figs 5.6(c-e))

5.6.1 Smeared Model

Here the reinforcements are assumed to be spread in a steel layer over the concrete element. Hence, this model is widely used in structures where there is a large number of closely spaced bars such as in plate and shell structures. This model was first devised by Wegmuller (1974) and further adapted by Cope & Rao (1977). In this model, the structure is divided in to layers and the stress-strain relationship for each layer is defined as:

$$\{\sigma\} = [D_s']\{\varepsilon\} \qquad (5.22)$$

where $[D_s']$ is the material matrix for steel. The behaviour of the steel layer is described in the local coordinate direction of the reinforcement and hence the bars can be orientated at any angle to the global axes (x,y). The constitutive relationship can then be transformed from local to global axes

5.6.2 Discrete Model

Here, a one dimensional bar element, representing the reinforcing bar, is superimposed on the parent concrete element by assuming that the bar is pin connected (two degrees of freedom) at nodal points. This model was first introduced by Ngo and Scordelis (1967). In addition to this, beam elements can be used in place of the bars to accommodate axial forces, shear forces and bending moments. Such idealisation may be necessary in structures where very large bars are used and hence bending becomes a significant effect.

In this method, it is possible to model the steel-concrete interaction by means of linkage elements which can account for bond slip. This model also allows the bar stiffness and strains to be calculated exactly on the bar position. The main disadvantage of this approach is that the mesh geometry is restricted by the reinforcement positions i.e. bar elements must pass through element nodes and hence mesh sizes can often become large which in turn results in greater computation time. To overcome this problem, El-Mezaini and Citipitoglu (1991) developed a technique which allows the discrete reinforcement to be modelled independent of the mesh geometry. In this method, the desired concrete mesh is set up independent of any reinforcement. Then, the edge nodes of the concrete elements are moved to the points of intersection of the reinforcing bars. This system can cause distortion of the concrete element and a correction technique is necessary to avoid this. In addition, this model does not account for non-linear behaviour such as cracking and dowel action.

5.6.3 Embedded Model

The embedded model was developed to overcome the mesh dependency problems of the discrete model. This method was first developed by Phillips & Zienkiewicz (1976). Bars are treated as special line elements which are positioned or embedded within the concrete element boundaries (fig.5.6(e)). In its original formulation, the bar had to be aligned to one of the local iso-parametric axes and hence the method was only applicable to orthogonal reinforcement. Full compatibility between the steel and the concrete is assumed. The line of the bar is defined using the same shape functions as the main concrete element and because of compatibility, the displacements of the bar are obtainable form the displacement field of the embedding concrete element. The stiffness contribution of the bar is assumed to be only in the longitudinal direction.

Further development of the embedded method was carried out by Ranjbaran (1991) to allow for inclined bars. Elwi & Hrudley (1989) and Phillips and Wu (1990) developed a method for embedded curved reinforcement. The main advantage of this method is that there are no limitations to representing the reinforcement layouts. In addition, the

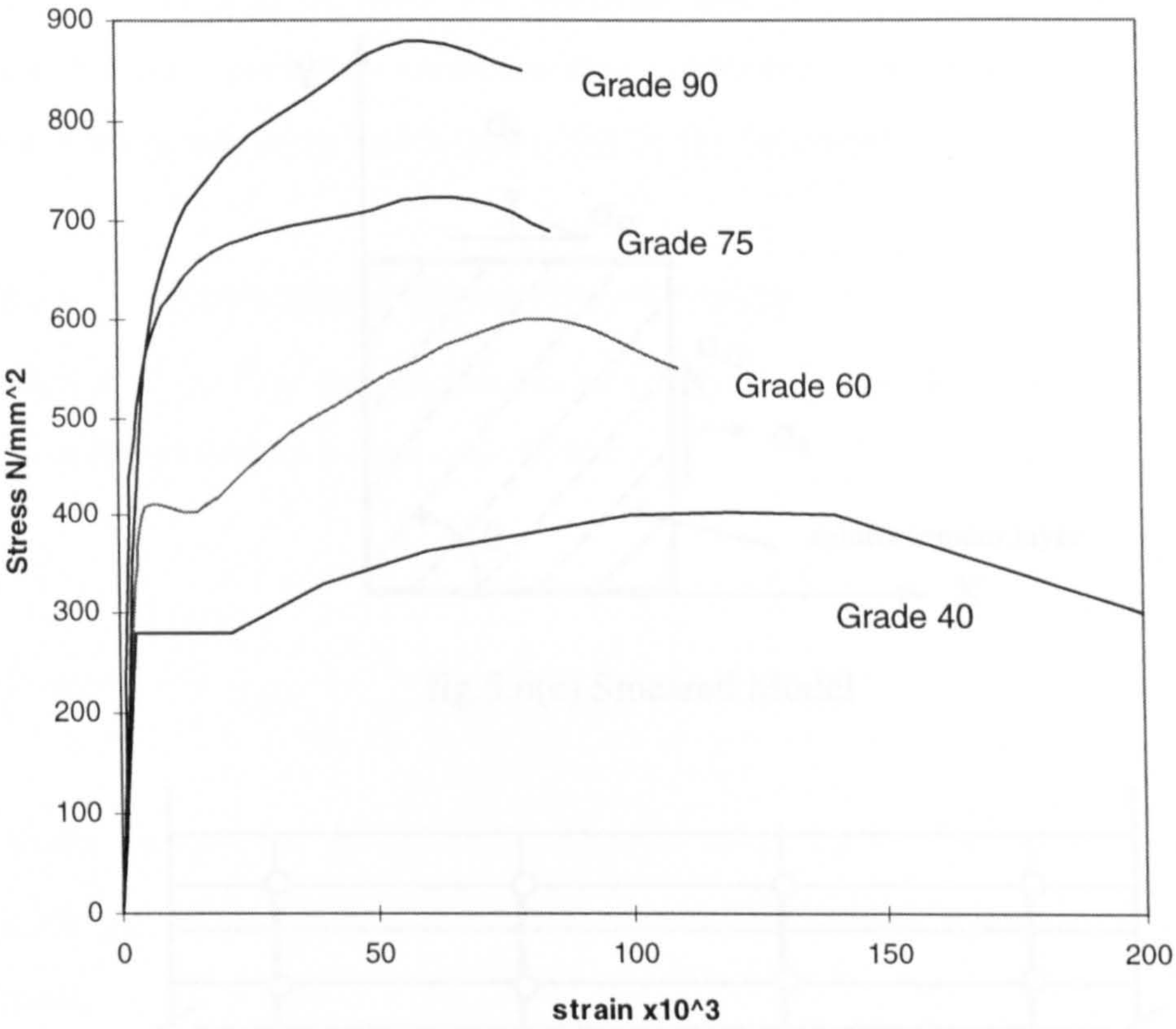

fig.5.6(a) Stress-strain Relationship of Typical Reinforcing Bars

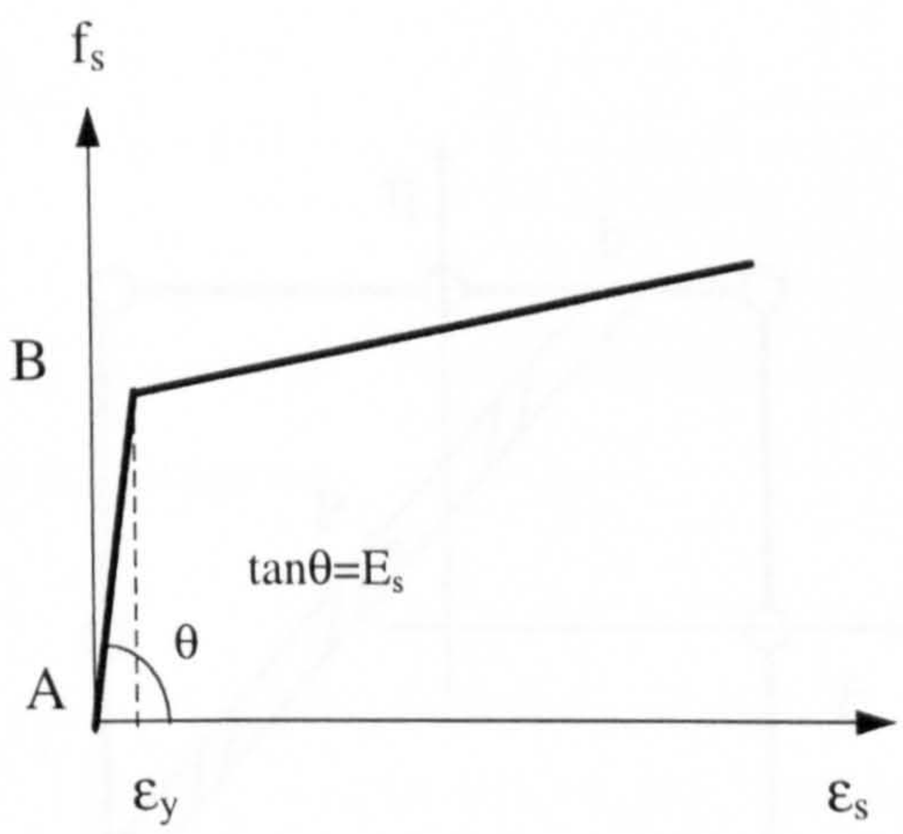

i) Bi-linear (hardening)

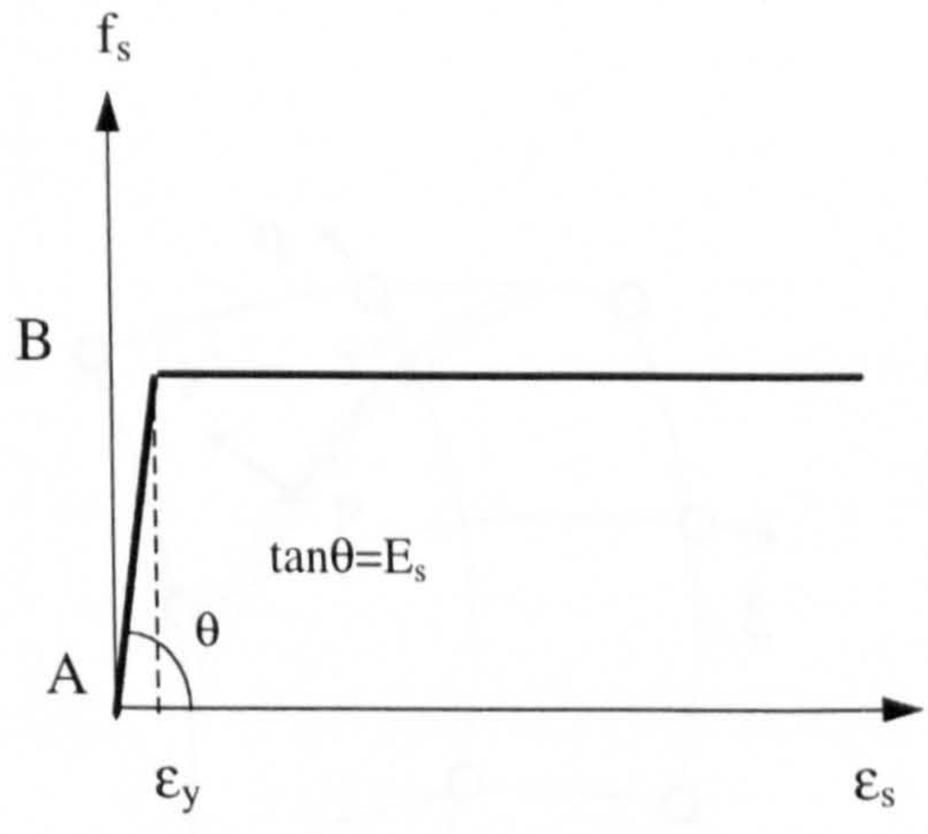

ii) Elastic-Perfectly Plastic

fig.5.6(b) Idealisation of Steel Stress-Strain Relationship

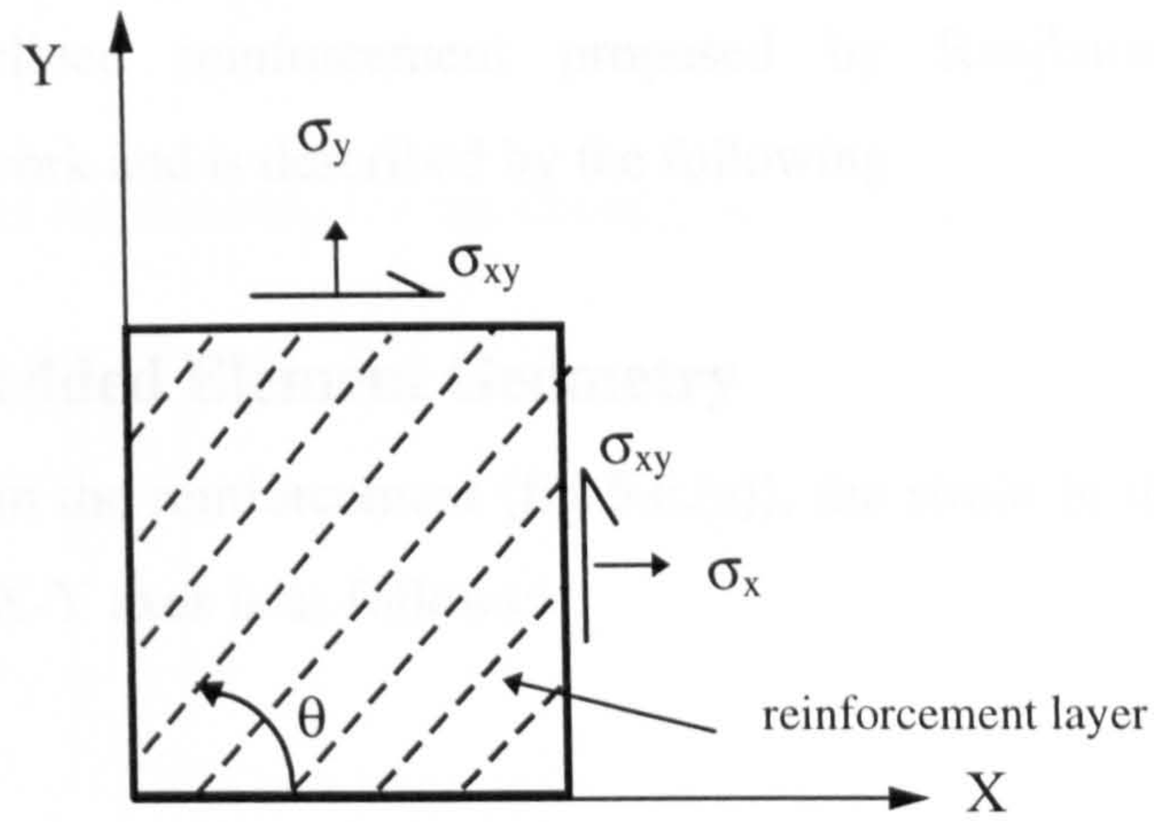

fig.5.6(c) Smeared Model

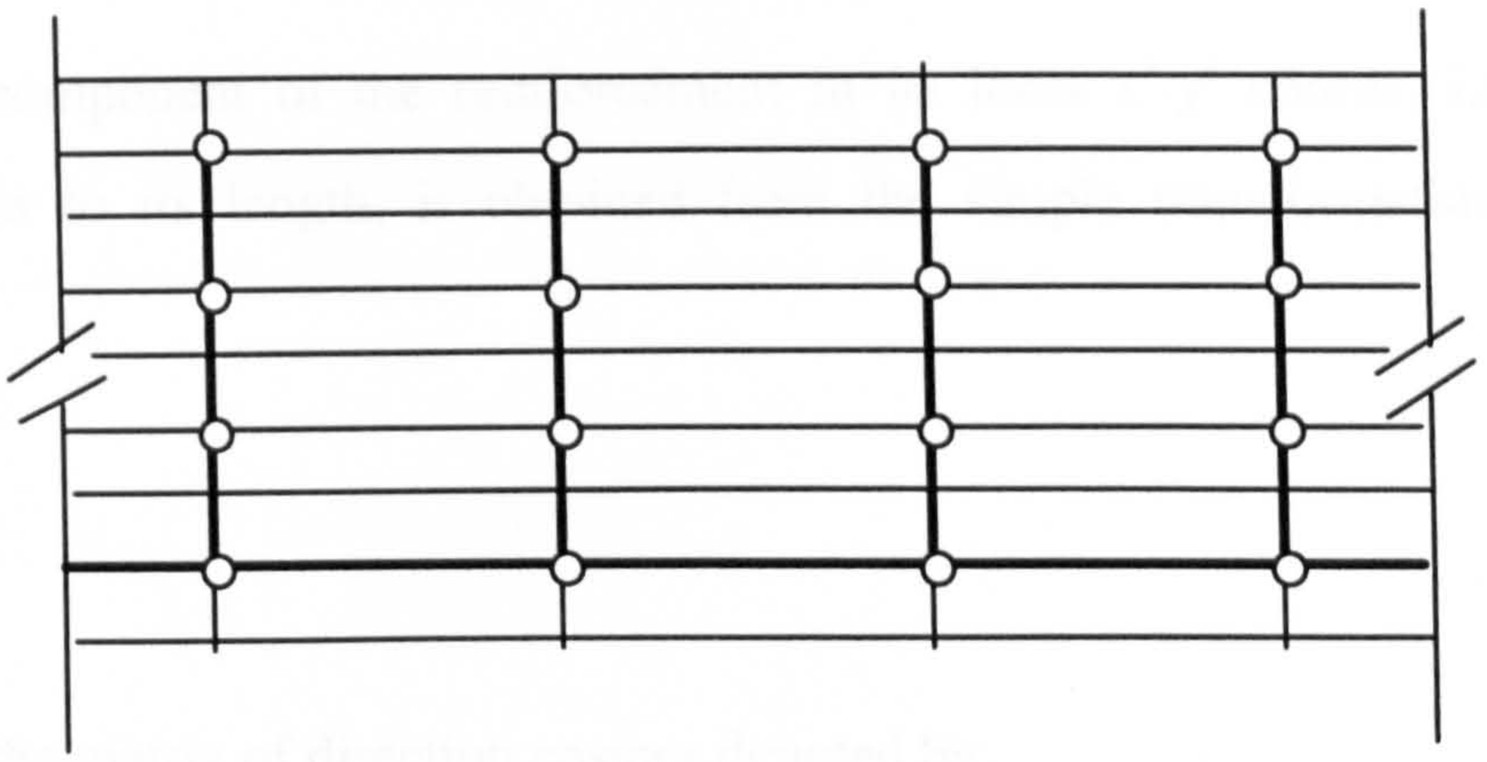

fig.5.6(d) Discrete Model

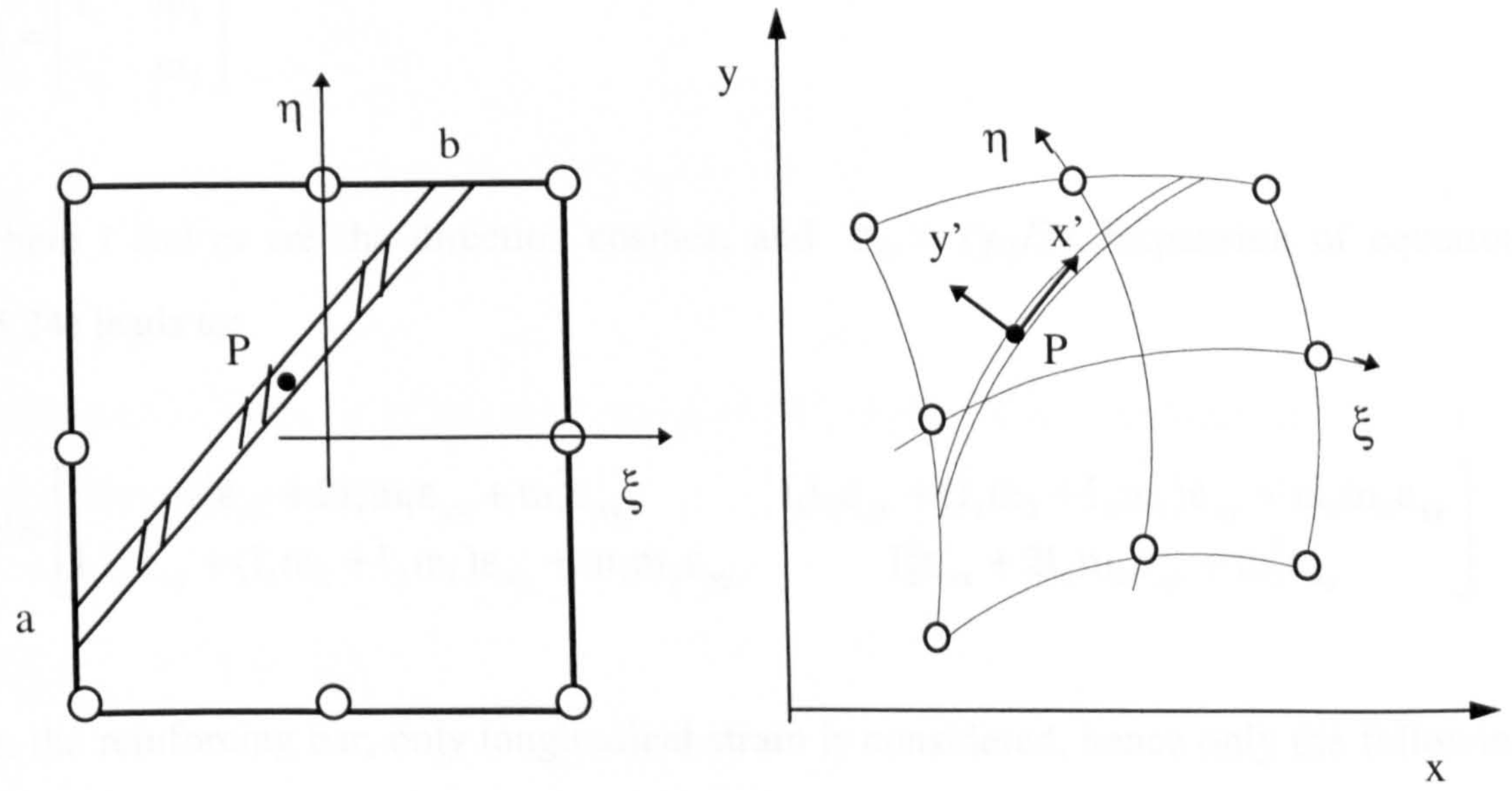

fig.5.6(e) Embedded formulation

stiffness contribution of each bar element can be evaluated independently. The formulation for inclined reinforcement proposed by Ranjbaran (1991) was implemented in this work and is described by the following

5.6.3.1 Embedded Element Geometry

At a typical point P in the reinforcement (fig 5.6.(e)), the strain in the concrete with respect to the global X-Y axes is as follows:

$$\varepsilon = \begin{bmatrix} \varepsilon_{xx} & \gamma_{xy/2} \\ \gamma_{xy/2} & \varepsilon_{yy} \end{bmatrix} \tag{5.23}$$

The strain component of the reinforcement in its local x′-y′ coords, i.e. along or perpendicular to its length, is obtained from the simple transformation described previously:

$$\varepsilon' = R\varepsilon R^{T} \tag{5.24}$$

where R is the matrix of direction cosines denoted by:

$$R = \begin{bmatrix} l_1 & m_1 \\ l_2 & m_2 \end{bmatrix}$$

where l and m are the direction cosines, and $\varepsilon_{xy} = (\gamma_{xy}/2)$. Expansion of equation (5.24) leads to:

$$\varepsilon' = \begin{bmatrix} l_1^2\varepsilon_{xx} + 2l_1m_1\varepsilon_{xy} + m_1^2\varepsilon_{xy} & l_1l_2\varepsilon_{xx} + (l_1m_2 + l_2m_1)\varepsilon_{xy} + m_1m_2\varepsilon_{yy} \\ l_1l_2\varepsilon_{xx} + (l_1m_2 + l_2m_1)\varepsilon_{xy} + m_1m_2\varepsilon_{yy} & l_2^2\varepsilon_{xx} + 2l_2m_2\varepsilon_{xy} + m_2^2\varepsilon_{xy} \end{bmatrix}$$

In the reinforcing bar, only longitudinal strain is considered, hence only the following equation is required:

$$\varepsilon_{xx}' = l_1^2\varepsilon_{xx} + 2l_1m_1\varepsilon_{xy} + m_1^2\varepsilon_{yy} \tag{5.25}$$

The stain displacement relationship for the element is expressed as follows:

$$\varepsilon_{xx} = \frac{\partial U}{\partial x} = \sum_{i=1}^{n}\left[\frac{\partial N_i}{\partial x}, 0\right]\begin{Bmatrix}\overline{U}_i \\ \overline{V}_i\end{Bmatrix}$$

$$\varepsilon_{yy} = \frac{\partial U}{\partial y} = \sum_{i=1}^{n}\left[0, \frac{\partial N_i}{\partial y}\right]\begin{Bmatrix}\overline{U}_i \\ \overline{V}_i\end{Bmatrix}$$

$$\varepsilon_{xy} = \frac{1}{2}\left(\frac{\partial V}{\partial x} + \frac{\partial U}{\partial y}\right) = \frac{1}{2}\sum_{i=1}^{n}\left[\frac{\partial N_i}{\partial y}, \frac{\partial N_i}{\partial x}\right]\begin{Bmatrix}\overline{U}_i \\ \overline{V}_i\end{Bmatrix} \tag{5.26}$$

in which N_i is the shape function of the element at node i and n is the number of nodes in the concrete element. Substituting the above into equation (5.25) leads to

$$\varepsilon_{xx}' = \sum_{i=1}^{n}\left[B_U^i B_V^i\right]\begin{Bmatrix}U_i \\ V_i\end{Bmatrix} = \sum_{i=1}^{n}\left[B^i\right]\begin{Bmatrix}U_i \\ V_i\end{Bmatrix} \tag{5.27}$$

where

$$B_U^i = l_1^2\frac{\partial N_i}{\partial x} + l_1m_1\frac{\partial N_i}{\partial y}$$

$$B_V^i = l_1m_1\frac{\partial N_i}{\partial x} + m_1^2\frac{\partial N_i}{\partial y}$$

With the strain matrix of the reinforcement $[B^i]$ obtained, it's stiffness contribution to the element is defined as:

$$K_{ij}^r = \int_{\Omega_r} B^{iT}DB^j.d\Omega$$

$$= \begin{bmatrix} \int_{\Omega_r} B_U^{iT} D B_U^j . d\Omega & \int_{\Omega_r} B_U^{iT} D B_V^j . d\Omega \\ \int_{\Omega_r} B_V^{iT} D B_U^j . d\Omega & \int_{\Omega_r} B_V^{iT} D B_V^j . d\Omega \end{bmatrix} \quad (5.28)$$

The equivalent nodal forces can be evaluated from

$$F_r^i = \int_{\Omega_r} B^{iT} \sigma_r . d\Omega \quad (5.29)$$

The element of volume (or in this case length) is evaluated in terms of the dimensionless natural coordinates ξ,η of the parent element. Dimensionless coordinate *r* defines the position along the reinforcement in the parent element where (-1<r<1) . The direction cosines can now be expressed in terms of *r*:

$$l_1 = \frac{\partial x}{\partial x'} = \frac{\partial x}{\partial r}\frac{\partial r}{\partial x'} = \frac{1}{C}\frac{\partial x}{\partial r} \ , \quad m_1 = \frac{\partial y}{\partial x'} = \frac{\partial y}{\partial r}\frac{\partial r}{\partial x'} = \frac{1}{C}\frac{\partial y}{\partial r} \quad (5.30)$$

where $C = \sqrt{\left[\left(\frac{\partial x}{\partial r}\right)^2 + \left(\frac{\partial y}{\partial r}\right)^2\right]}$ from $l_1^2 + m_1^2 = 1$

Substituting (5.30) into (5.27) leads to :

$$B_U^i = (C_1 \frac{\partial N^i}{\partial x} + C_2 \frac{\partial N^i}{\partial y}) / C^2$$

$$B_V^i = (C_2 \frac{\partial N^i}{\partial x} + C_3 \frac{\partial N^i}{\partial y}) / C^2 \quad (5.31)$$

where

$$C_1 = \left(\frac{\partial x}{\partial r}\right)^2 , C_2 = \left(\frac{\partial x}{\partial r}\right)\left(\frac{\partial y}{\partial r}\right) , C_3 = \left(\frac{\partial y}{\partial r}\right)^2$$

The Jacobian of transformation can then be evaluated from:

$$\left|J^r\right| = \left|\frac{dx}{dr}\right| = C \quad (5.32)$$

noting that the relevant partial derivatives can be found from;

$$\frac{\partial x}{\partial r} = \frac{\partial x}{\partial \xi}\frac{\partial \xi}{\partial r} + \frac{\partial x}{\partial \eta}\frac{\partial \eta}{\partial r} = J_{11}\frac{\partial \xi}{\partial r} + J_{21}\frac{\partial \eta}{\partial r}$$

$$\frac{\partial y}{\partial r} = \frac{\partial y}{\partial \xi}\frac{\partial \xi}{\partial r} + \frac{\partial y}{\partial \eta}\frac{\partial \eta}{\partial r} = J_{12}\frac{\partial \xi}{\partial r} + J_{22}\frac{\partial \eta}{\partial r} \qquad (5.33)$$

and hence:

$$\left|J^r\right| = \left[(J_{11}^2 + J_{12}^2)\left(\frac{\partial \xi}{\partial r}\right)^2 + 2(J_{11}J_{21} + J_{12}J_{22})\left(\frac{\partial \xi}{\partial r}\frac{\partial \eta}{\partial r}\right) + (J_{21}^2 + J_{22}^2)\left(\frac{\partial \eta}{\partial r}\right)^2\right]^{1/2} \qquad (5.34)$$

where the constants J_{11}, J_{12} etc. are the elements of the Jacobian matrix as defined by:

$$J = \begin{bmatrix} J_{11} & J_{12} \\ J_{21} & J_{22} \end{bmatrix} = \begin{bmatrix} \frac{\partial x}{\partial \xi} & \frac{\partial y}{\partial \xi} \\ \frac{\partial x}{\partial \eta} & \frac{\partial y}{\partial \eta} \end{bmatrix} \qquad (5.35)$$

Since it is assumed that the reinforcements are distributed through the thickness of the element, the element volume can be calculated from:

$$d_{\Omega_r} = A\,dl = \frac{A_s t}{S_r}\left|J^r\right| dr \qquad (5.36)$$

where A_s is the cross sectional area of the reinforcement, t is the thickness of the parent element, and S_r is the spacing of the reinforcements through the element. All the equations defined are evaluated in terms of the concrete or master element coordinates. It is hence necessary to define the relationship between r, ξ and η. This relationship is expressed as follows:

$$\begin{bmatrix} \xi \\ \eta \end{bmatrix} = \begin{bmatrix} [M] & 0 \\ 0 & [M] \end{bmatrix} \begin{bmatrix} \{\xi^*\} \\ \{\eta^*\} \end{bmatrix} \qquad (5.37)$$

where $\{\xi^*\}$ and $\{\eta^*\}$ are the nodal coords on the reinforcement in the parent element and M is a single variable interpolation function, defined as the Lagrangian polynomial:

$$M_i = \frac{(r - r_1)\ldots(r - r_{i-1})(r - r_{i+1})\ldots(r - r_n)}{(r_i - r_1)\ldots(r_i - r_{i-1})(r_i - r_{i+1})\ldots(r_i - r_n)} \tag{5.38}$$

Hence for a straight reinforcing element, equation (5.36) may be written as:

$$\begin{aligned} \xi &= \frac{1}{2} r(\xi_b - \xi_a) + \frac{1}{2}(\xi_b + \xi_a) \\ \eta &= \frac{1}{2} r(\eta_b - \eta_a) + \frac{1}{2}(\eta_b + \eta_a) \end{aligned} \tag{5.39}$$

and

$$\begin{aligned} \frac{\partial \xi}{\partial r} &= \frac{1}{2}(\xi_b - \xi_a) \\ \frac{\partial \eta}{\partial r} &= \frac{1}{2}(\eta_b - \eta_a) \end{aligned} \tag{5.40}$$

in which (ξ_a, η_a) and (ξ_b, η_b) are the end point coordinates of the reinforcement in the parent element (fig 5.6(e)). All of the necessary calculations can now be made to evaluate the stiffness contribution of the reinforcement to the concrete element. The calculation process can be summarised as follows:

- A gauss point coordinate r_g on the reinforcing element is selected and corresponding values of ξ, η, $\partial\xi/\partial r$, $\partial\eta/\partial r$ are calculated from eqns 5.38-5.40. These values are evaluated once in the pre-processing stage and stored.
- For the current values of ξ_g, η_g, evaluation of J, $\partial x/\partial r$, and $\partial y/dr$ is carried out from equations (5.35) and (5.33)
- $|J^r|$, $[B^r]$ and $d\Omega^r$ are calculated from equations {5.34), (5.31) and (5.36) respectively.

- K_{ij}^{r} and F_r are calculated form equations (5.28) and (5.29) respectively.
- These are then added to the corresponding values of the concrete element.

5.7 Applications of Numerical Model

In this section the performance of the current numerical model is assessed through comparison with experimental results on various types of structures. It is important to test the accuracy of the model in predicting the behaviour of in-plane and plate bending structures which will be used throughout this work. A series of structures involving different modes of failure was chosen. The main areas assessed were load-deformation response, cracking behaviour, steel yielding, ultimate load and mode of failure.

A convergence force tolerance of 4% was set for the analysis and the maximum number of iterations was set at 50 and 75 for plate bending and plane stress analysis respectively. A combined algorithm was employed whereby the stiffness matrix is updated every 2nd, 5th, 10 etc. iterations until convergence or collapse is reached. An increase in the maximum amount of iterations in plane stress structures is a result of the slow rate of redistribution of residual stresses in plane stress structures accompanied by lower deformations compared with slabs. In addition to this, small load increments were applied only to highly non-linear phases while larger increments may require more iterations. It was shown by Abdel-Hafez (1986) that the effect of increment size on the resulting solution is not significant.

5.7.1 Simply Supported Slab tested by Hago

This slab (model number 3) was chosen from a series of tests carried out by Hago (1982) and was used to asses the effect of mesh size, tension stiffening and shear retention in the numerical model. Details of the slab dimensions and reinforcement layouts are given in figures 5.7.1(a-c). The slab was simply supported on four sides and was 100 mm thick. A design load of 210 kN was applied as four point loads as shown in figure 5.7.1(a). Material properties are outlined below:

Concrete Properties	Steel Properties
E_c=21500 N/mm^2	E_s=214000 N/mm^2
f_{cu}=44.2 N/mm^2	f_y=460 N/mm^2
f_t=3.4 N/mm^2	

Table 5.7.1: Hago's Slab n.3

For numerical analysis, a symmetrical quarter of the slab was analysed. Firstly, the slab was analysed using four different mesh sizes; 2x2, 4x4, 6x6 and 8x8 elements. For comparison the load-displacement curves obtained experimentally and numerically are displayed in figure 5.7.1(d). It can be seen that a more ductile response occurred as the number of elements in the mesh increased. The minimum 2x2 element mesh was used purely for comparison. In reality, differences in reinforcement layouts may dictate a minimum density of mesh for adequate representation. A mesh of 4x4 elements was able to model the response to sufficient accuracy at a reasonable cost. As the mesh density increased, the computation time increased substantially e.g the analysis with the 8x8 element mesh was four times slower than with 4x4 elements.

Generally in flexural failure of slabs, cracking is initiated at around 20-30% of the ultimate load P_u. For the numerical analysis, a load increment of 20% of the design load P_d was used in the first increment, subsequent increments of 0.05 P_d were applied. The largest amount of iterations (26) were recorded during the 3rd increment where the onset of cracking took place. The numerical load-displacement response for each mesh size was less stiff during cracking than in the experimental model. The inclusion of tension stiffening into the model would help to increase the numerical stiffness during this stage. The next parametric study focused on the effect of tension stiffening using the model shown in fig.5.5.2.3(b), whilst varying the C2 parameter which dictates the descending branch of the tensile stress-strain curve. From figure 5.7.1(e), it can be seen that the presence of tension stiffening in the model improves the load-deflection response at the service load level.

The ultimate load achieved numerically although very close to the experimental, increases slightly with the value of C2.

In order to study the effect of shear transfer in the numerical model, analysis was carried out using four different values of shear retention factor (B=0.0, 0.4, 0.7 and 1.0). These values correspond to the transition from smooth to very rough concrete crack interfaces. The load-displacement curves resulting from each of these models are shown in figure 5.7.1(f). When shear retention is ignored, the numerical ultimate load is reduced by around 10%. When the shear retention factor B ranges from 0.4 to 1.0, no significant change in ultimate load or load-displacement characteristics is observed. The steel-strains of the bottom reinforcement at the centre of the slab are shown in fig.5.71(g). The numerical results shown were obtained using tension stiffening at C2=10 and shear retention factor B=0.4. An adequate correlation with the experimental result is obtained. The numerical crack pattern of the slab (C2=10.0, B=0.4), is shown compared with the experimental in figures 5.7.1 (h-i).

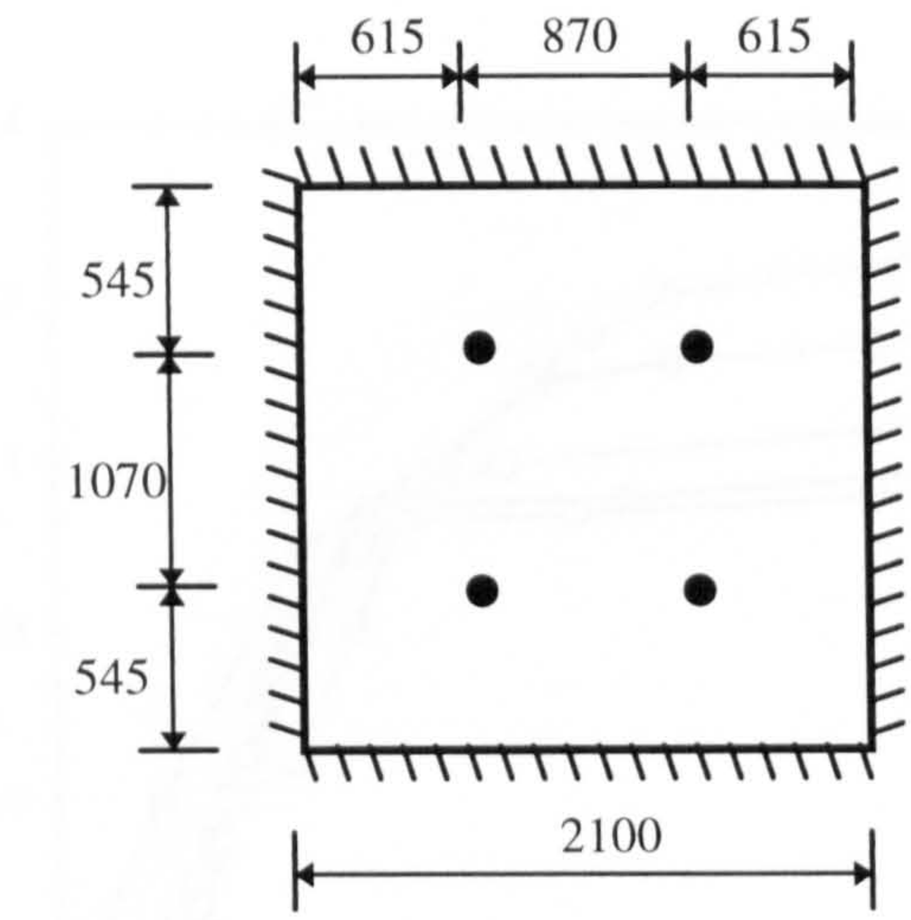

a) plan view

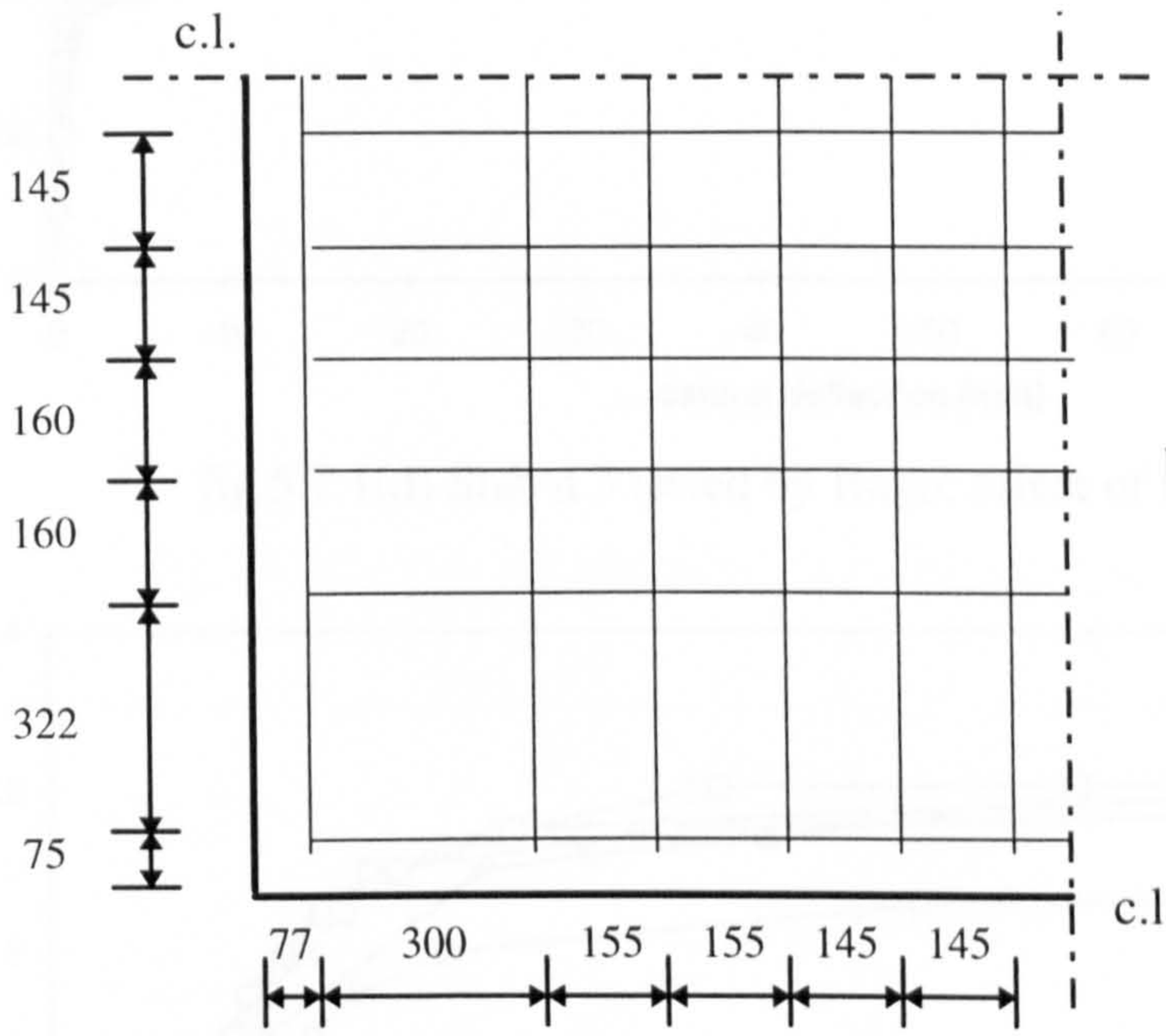

b) Bottom Steel (8mm ϕ bars)

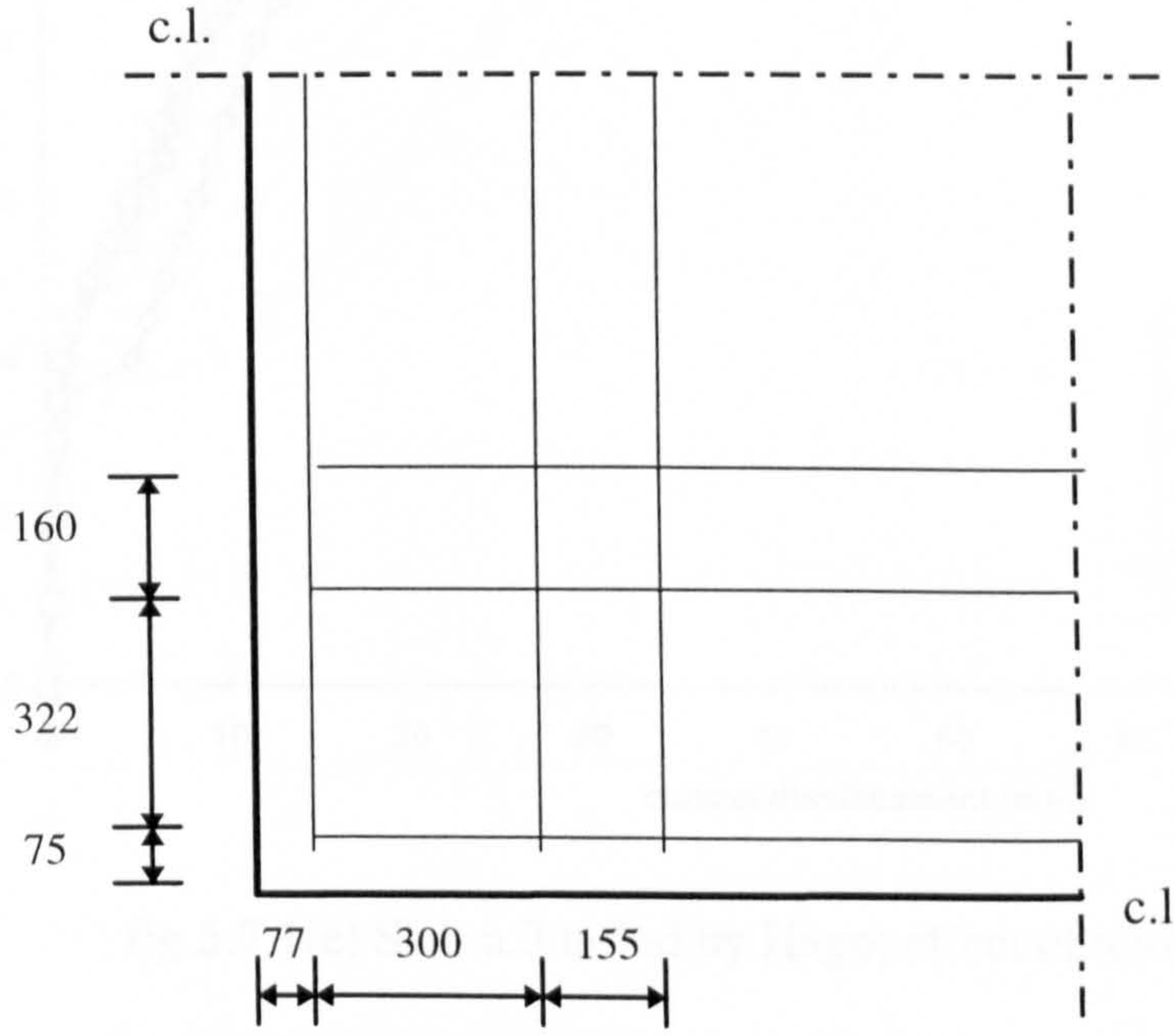

c) Top Steel (8mm ϕ bars)

figs.5.7.1 (a-c) Details of Hago's Model number 3 (all sizes in mm)

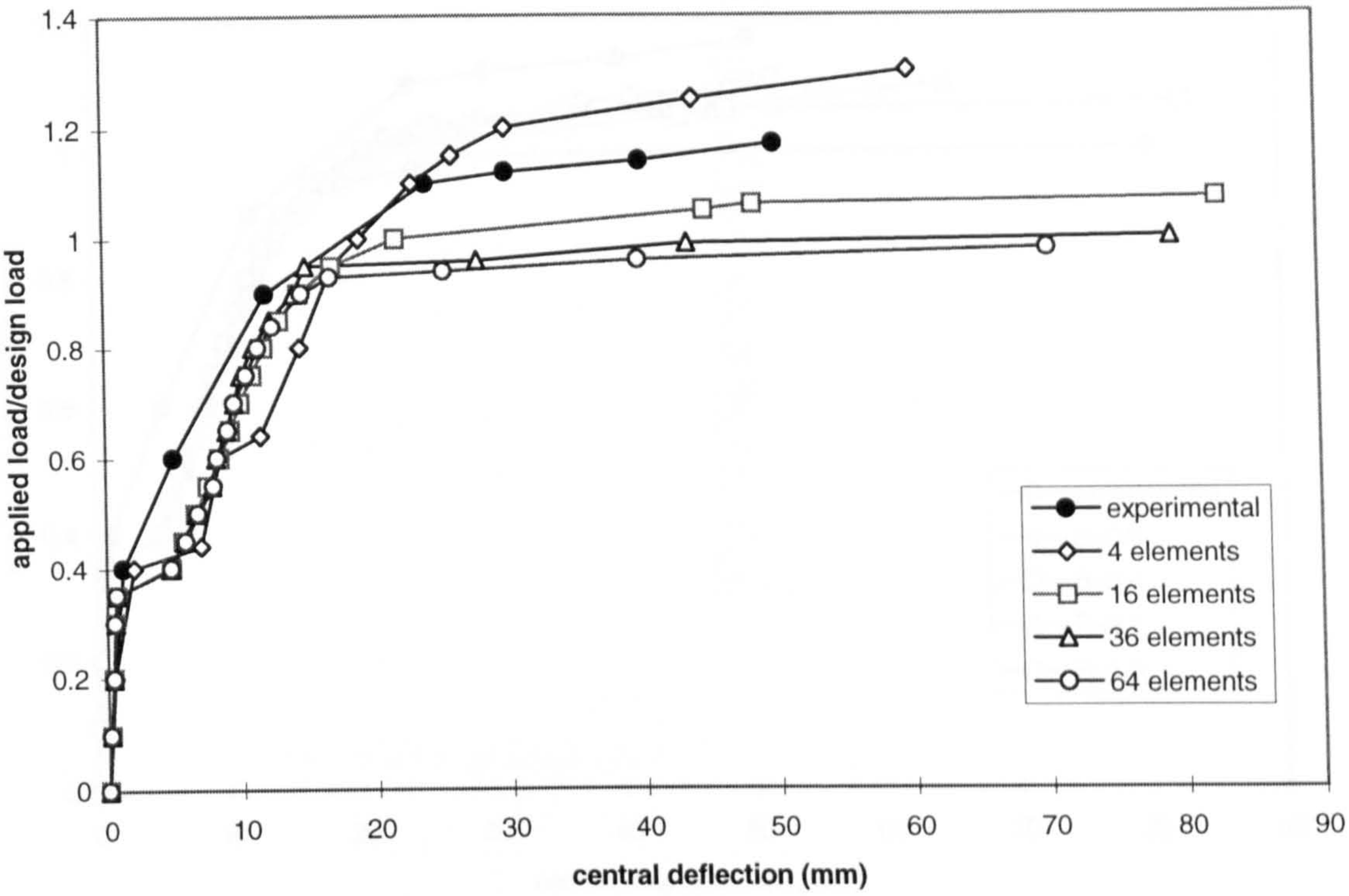

fig.5.7.1(d) Slab n.3 tested by Hago; effect of mesh size

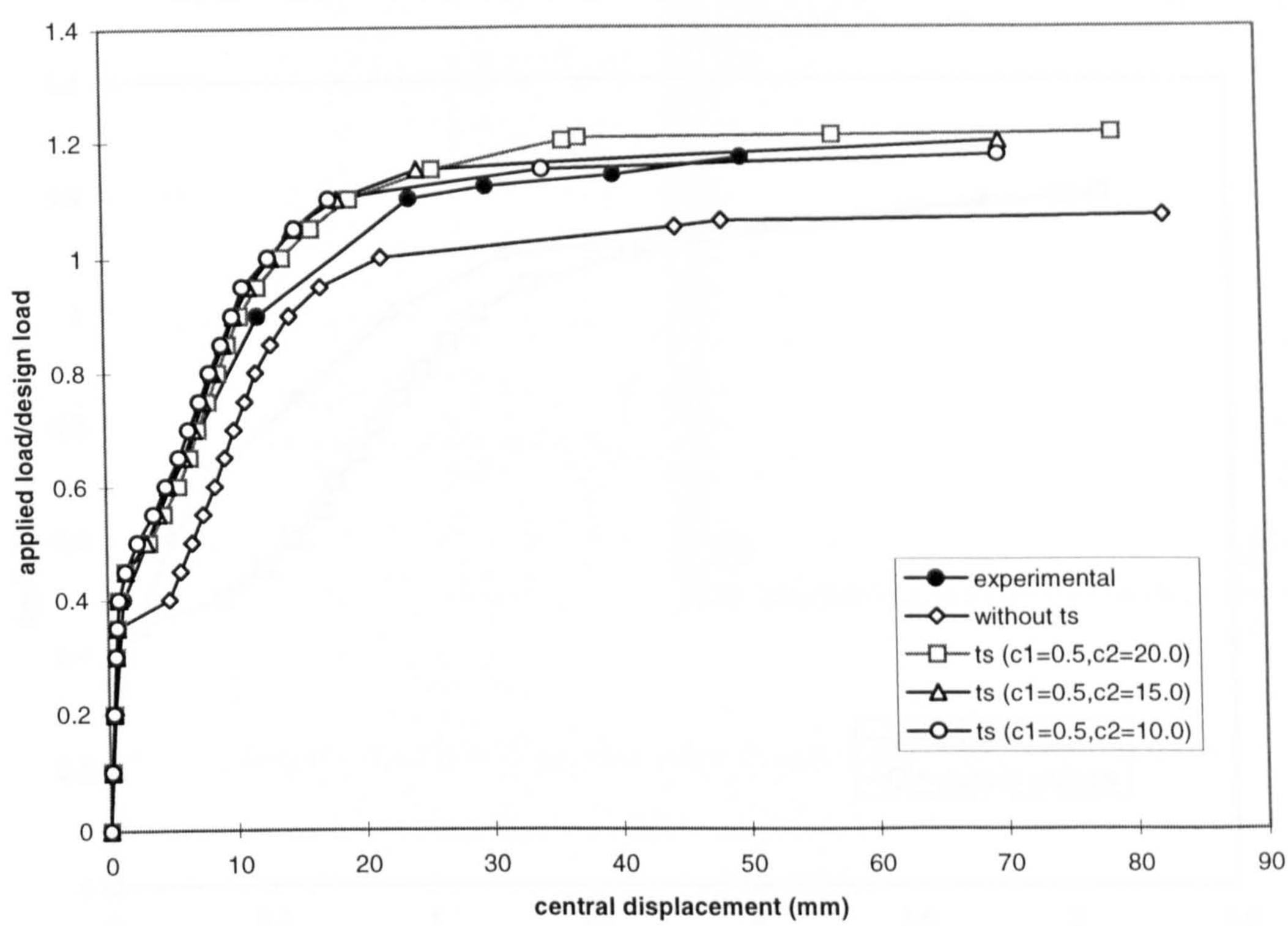

fig.5.7.1(e) Slab n.3 tested by Hago; effect of tension stiffening

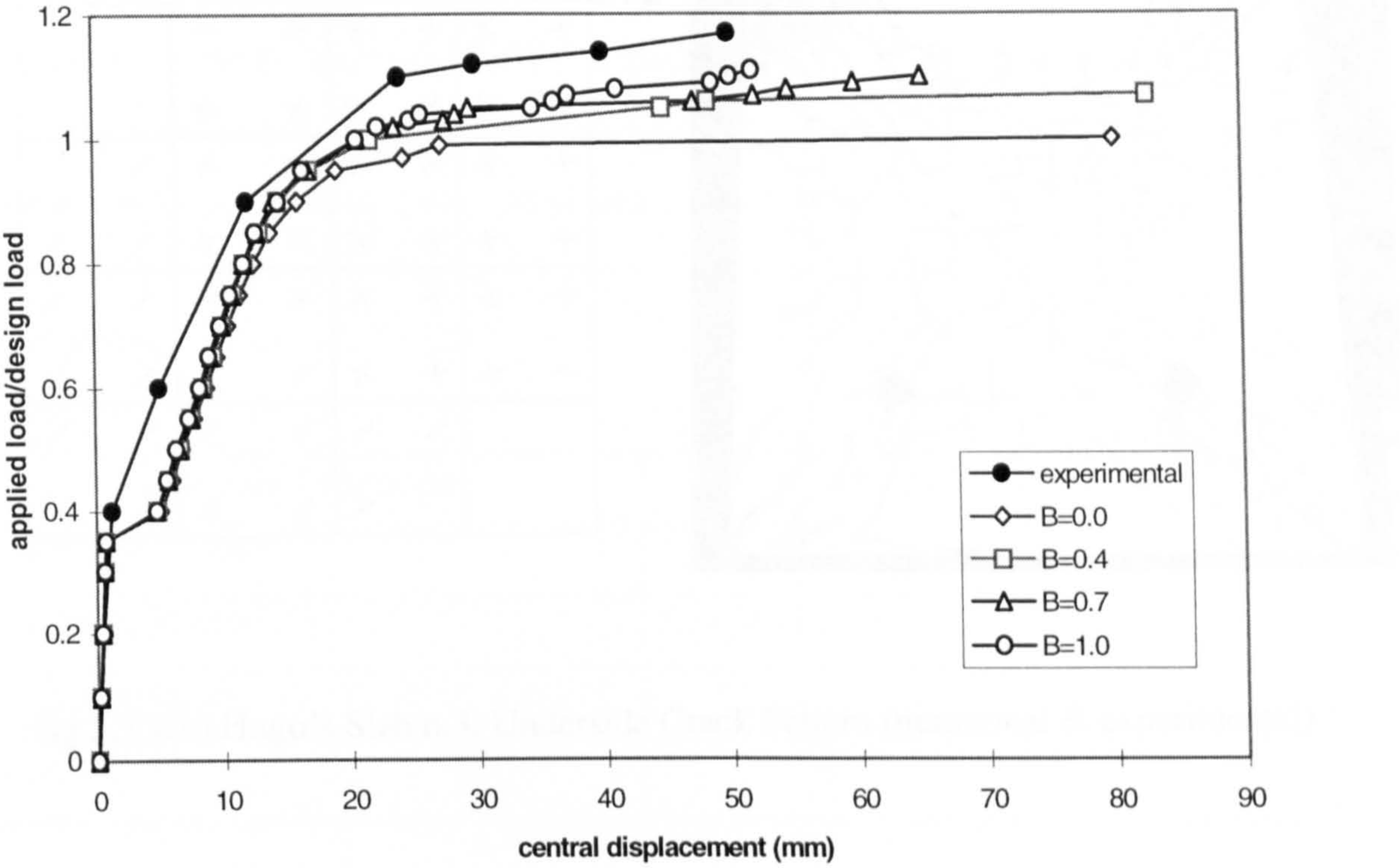

fig.5.7.1(f) Slab n.3 tested by Hago; Effect of shear retention

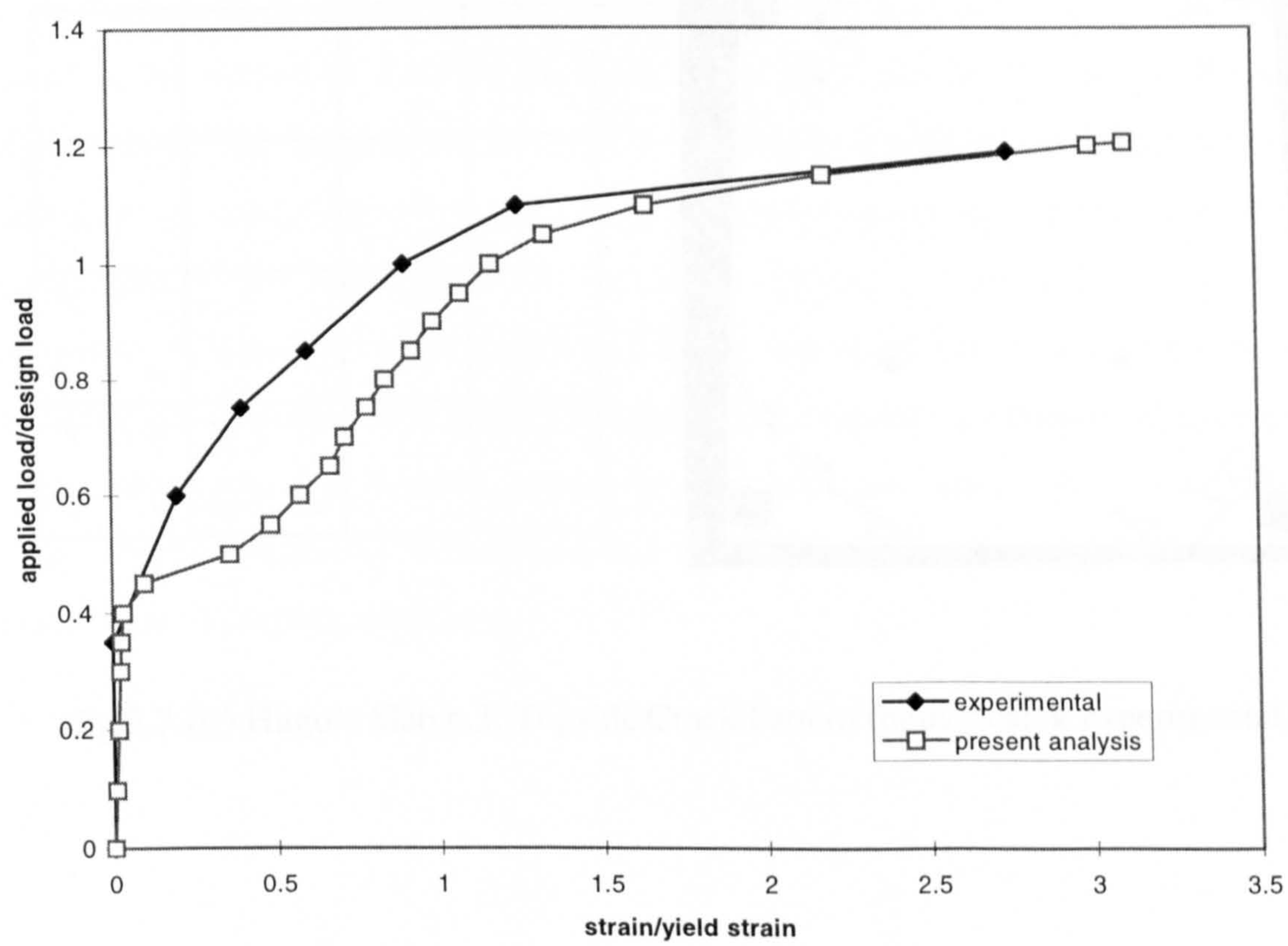

fig.5.7.1(g) Slab n.3 tested by Hago; bottom steel strains at centre

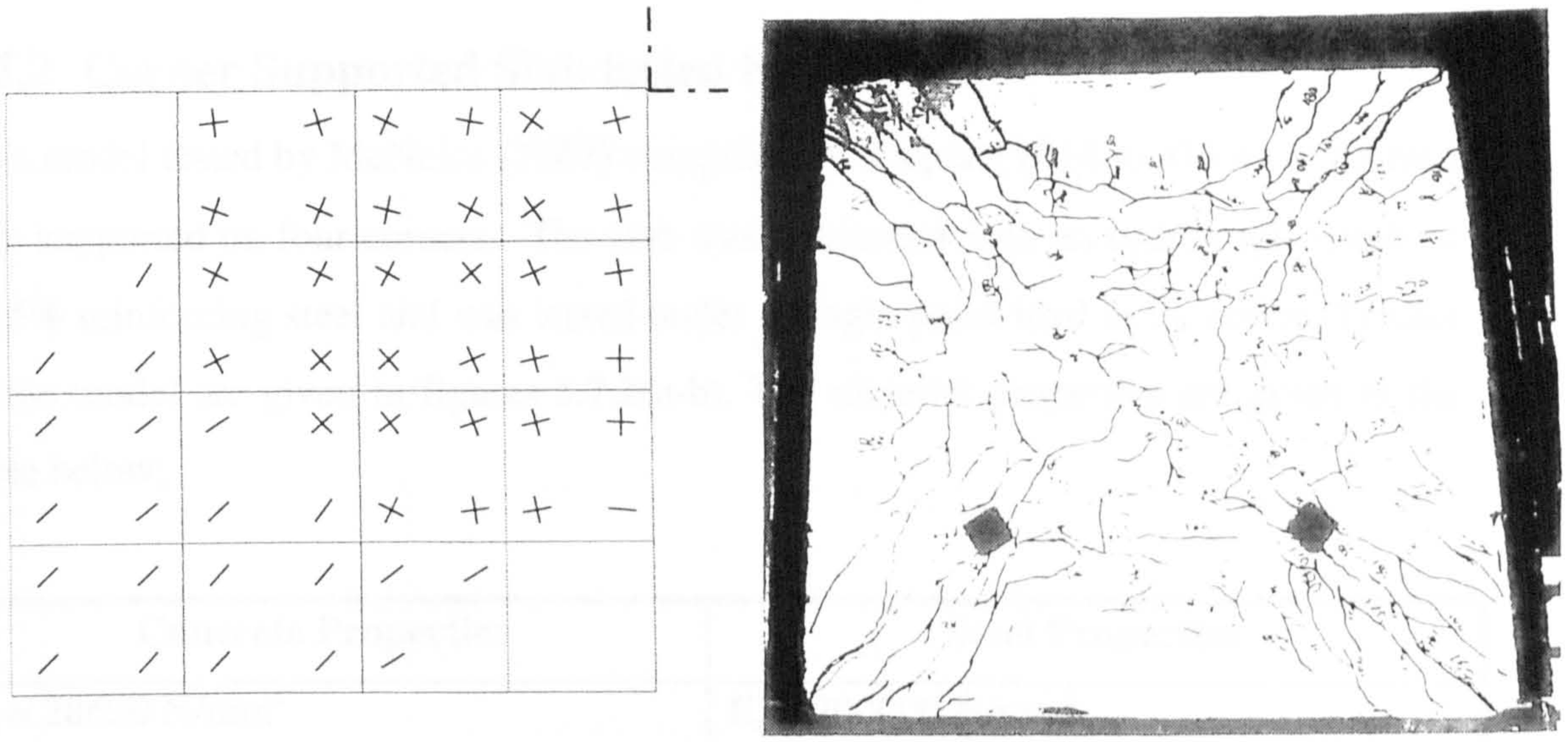

fig.5.7.1(h) Hago's Slab n.3; Underside Crack Pattern (numerical & experimental)

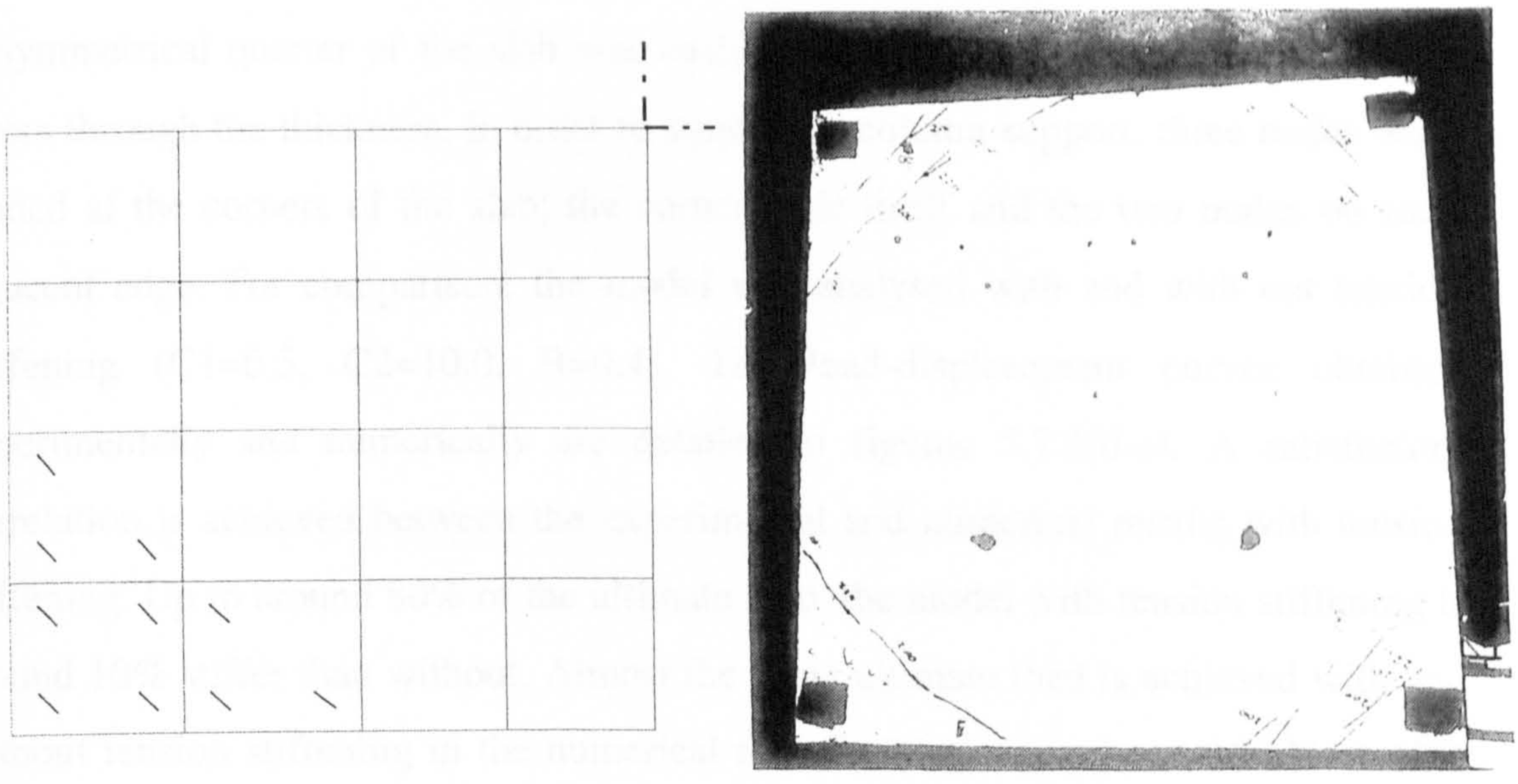

fig.5.7.1(i) Hago's Slab n.3; Topside Crack Pattern (numerical & experimental)

5.7.2 Corner Supported Slab tested by McNeice

This model tested by McNeice (1967) comprised of a square (914.4x914.4x44.45mm) slab supported on four corners. The slab was reinforced with an orthotropic mesh of 0.85% reinforcing steel and was tested under a single point load at its centre. Details of the model are given in figures 5.7.2(a-b). The material properties are given in the table below;

Concrete Properties	Steel Properties
$E_c = 28600\ N/mm^2$	$E_s = 200000\ N/mm^2$
$f_{cu} = 37.92\ N/mm^2$	$f_y = 345\ N/mm^2$
$f_t = 2.75\ N/mm^2$	
$\nu = 0.15$	

Table 5.7.2: McNeice Slab

A symmetrical quarter of the slab was analysed using a 4x4 element mesh with 10 layers through the thickness. In order to simulate a column support, three nodes were pinned at the corners of the slab; the corner node itself and the two nodes on each adjacent edge. For comparison, the model was analysed with and with out tension stiffening (C1=0.5, C2=10.0, B=0.4). The load-displacement curves obtained experimentally and numerically are detailed in figures 5.7.2(d-e). A satisfactory correlation is achieved between the experimental and numerical results with tension stiffening. Up to around 80% of the ultimate load, the model with tension stiffening is around 10% stiffer than without. Almost the same ultimate load is achieved with and without tension stiffening in the numerical model which was around 16 kN or 12% greater than the experimental load.

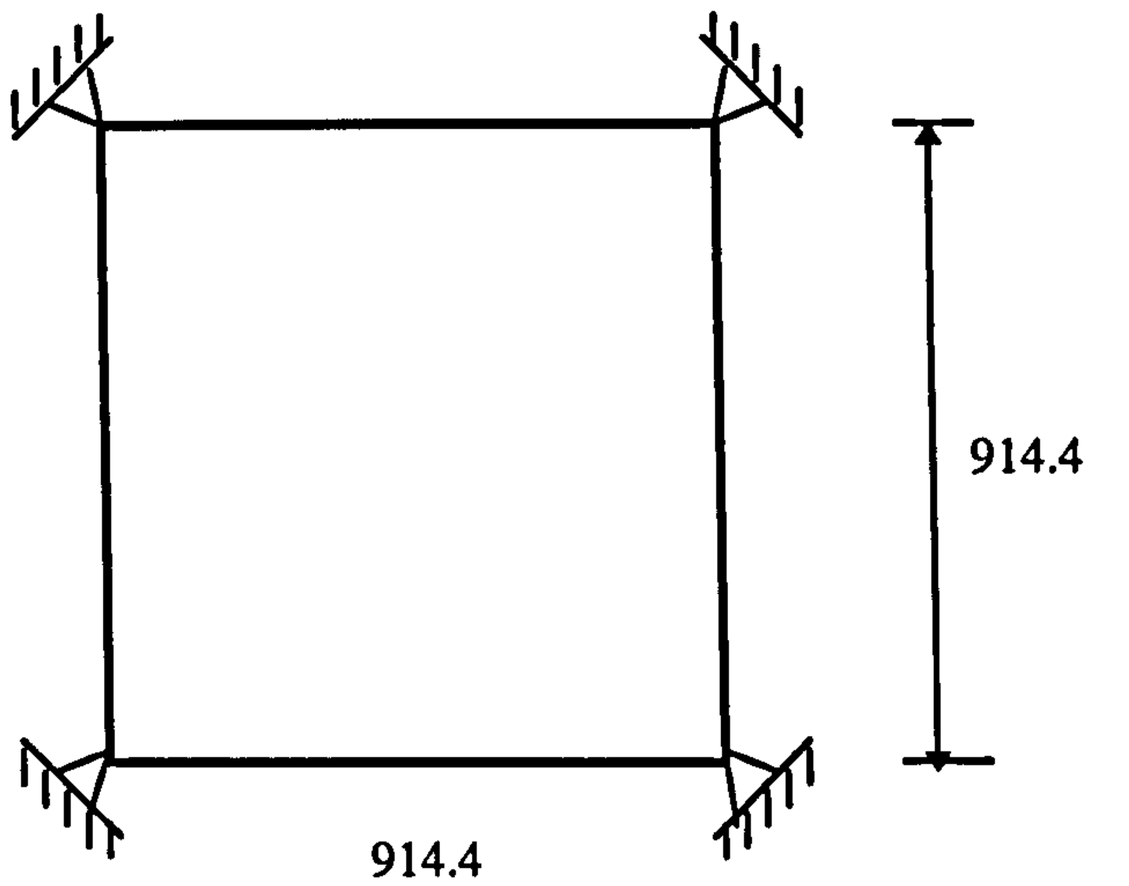

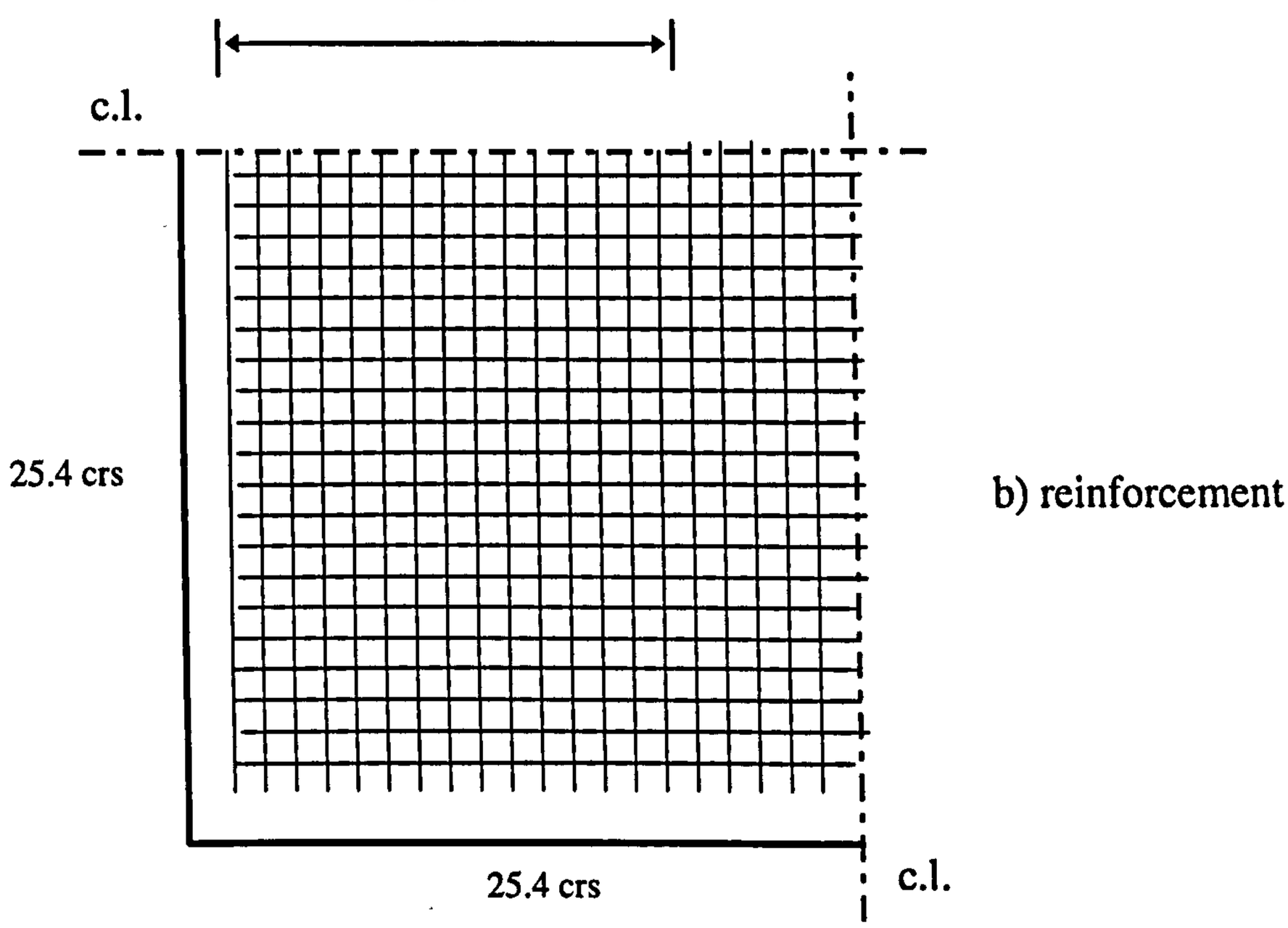

figs.5.7.2(a-b). Details of slab tested by McNeice (all sizes in mm)

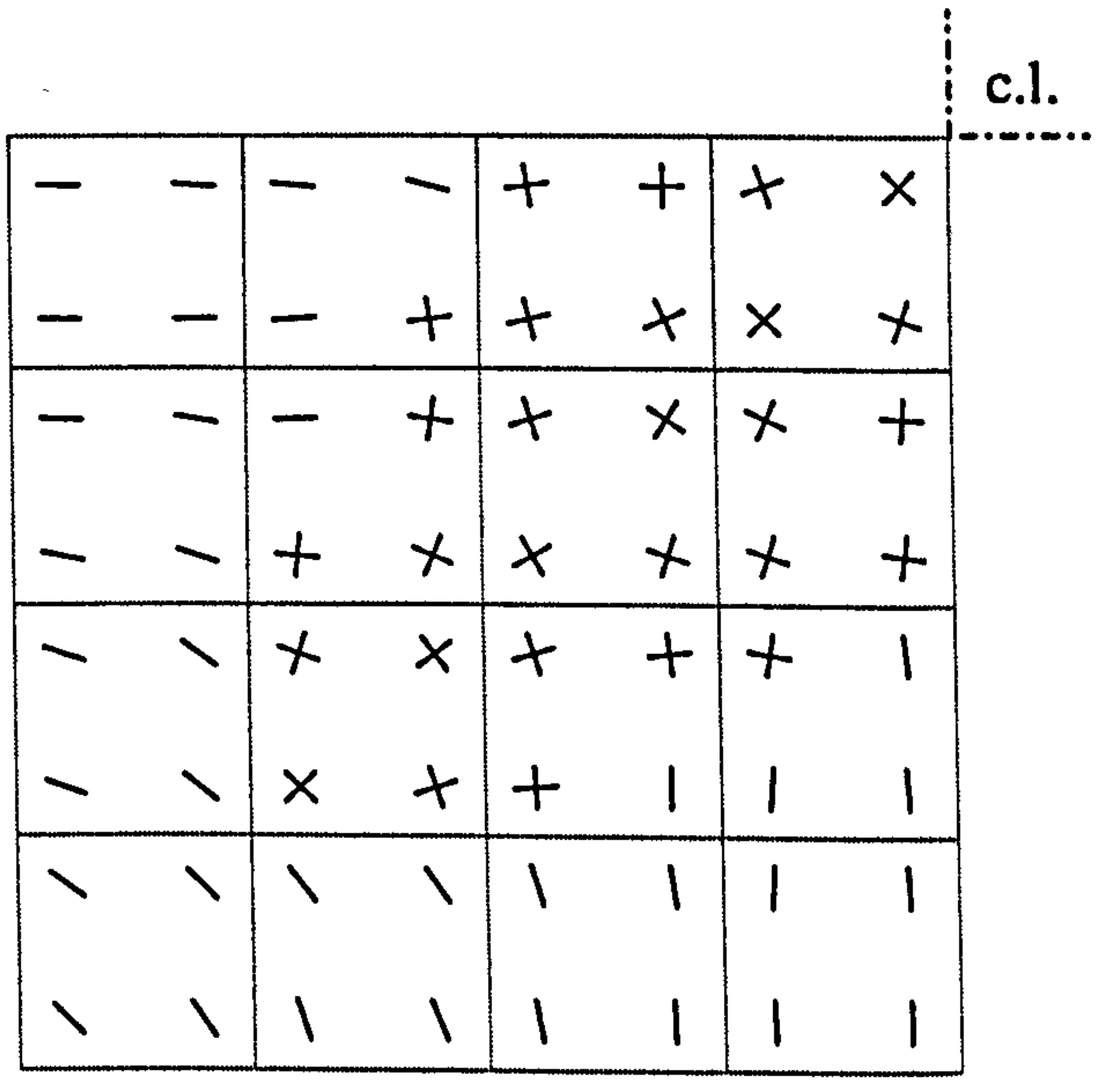

fig.5.7.2(c) Numerical Crack Pattern at failure (underside)

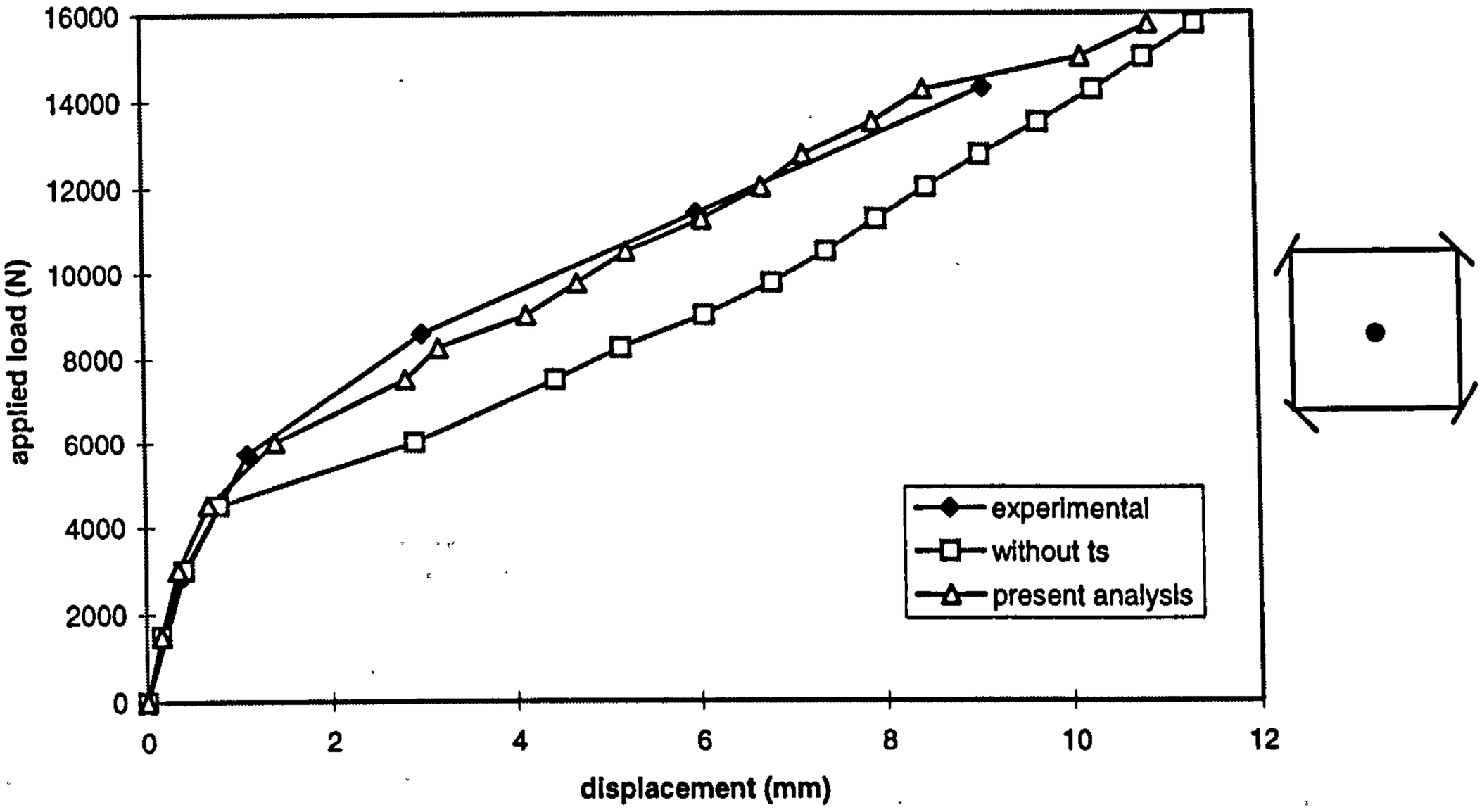

fig.5.7.2(d) Slab Tested by McNeice; load-displacement at centre

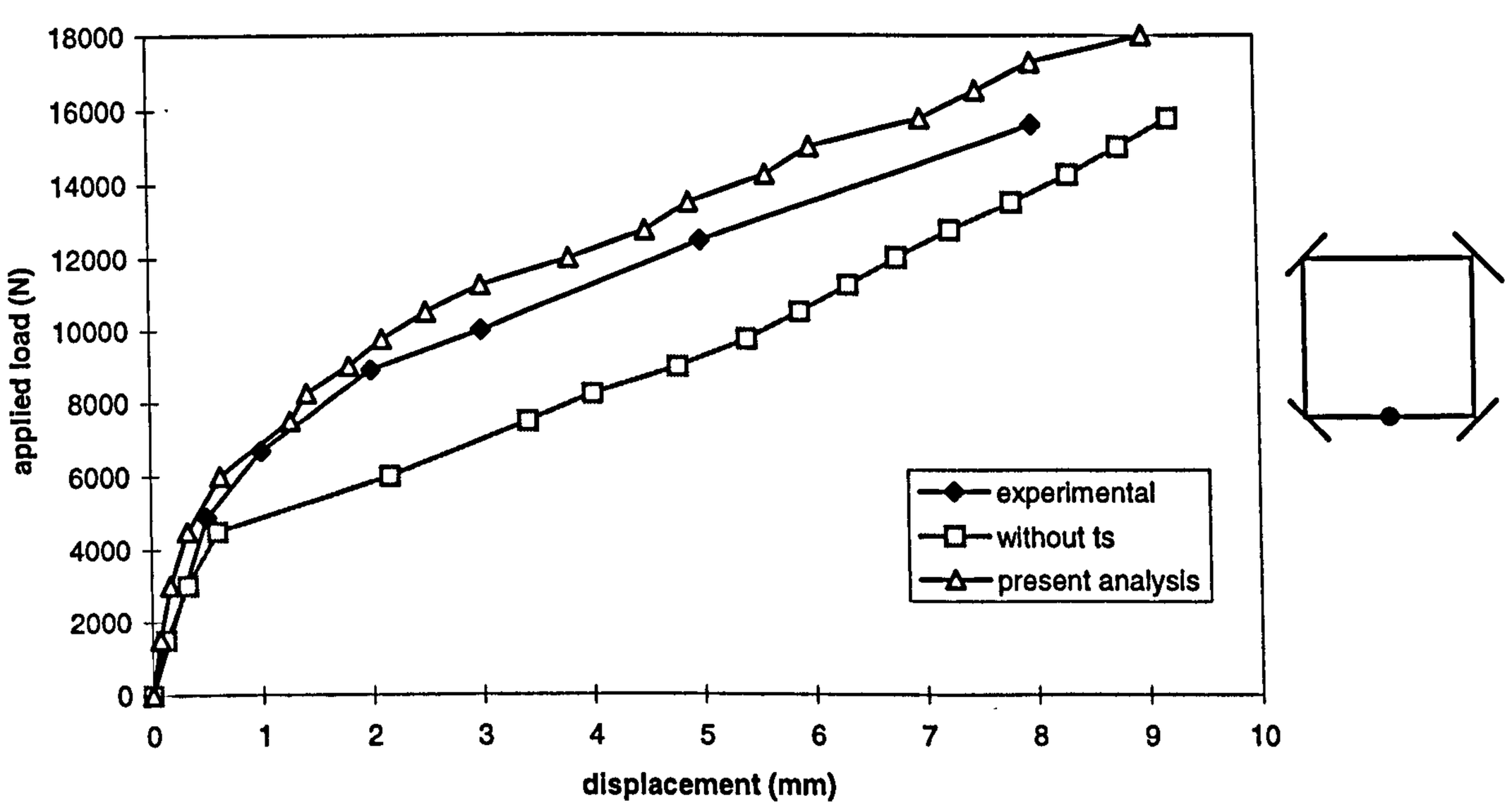

fig.5.7.2(e) Slab Tested by McNeice, load-displacement at centre of free edge

5.7.3 Slabs tested by Taylor et al.

The following models were chosen from a series of slabs tested by Taylor et al (1966). The original test program consisted of 10 two-way span, simply supported slabs with varying degrees and arrangements of reinforcement. Only bottom reinforcement was provided in each slab. All slabs were 1982.5 mm square and were simply supported along each edge to give a spans of 1830mm. For the present analysis, slabs S1, S2, S6 and S8 were chosen. Details of the reinforcement layouts for each of these slabs are given in figures 5.7.3(a-d) and the material properties are given below in table (5.7.3).

Slab	Thickness (mm)	Concrete Properties	Steel Properties
S1	50.8	$f_{cu} = 35.0$ N/mm^2	$f_y = 486.1$ N/mm^2
S2	50.8	$f_{cu} = 36.3$ N/mm^2	$f_y = 486.1$ N/mm^2
S6	50.8	$f_{cu} = 35.3$ N/mm^2	$f_y = 497.0$ N/mm^2
S8	44.45	$f_{cu} = 37.9$ N/mm^2	$f_y = 486.1$ N/mm^2

Table 5.7.3: Taylor's Slabs

All reinforcement comprised of 5 mm diameter bars. These slabs were chosen to assess the performance of the program at modelling differing layouts and orientation of reinforcement.

During testing, loads were applied by small hydraulic jacks placed at 16 uniformly spaced positions. A mesh size of 4x4 elements was chosen to model each slab. Tension stiffening with C1=0.5 and C2=10.0 was utilised in the analysis, and shear retention factor B=0.4. The load-displacement relationship for each slab is displayed in figures 5.7.3(e-h). It can be seen that a good agreement between experimental and numerical models was achieved.

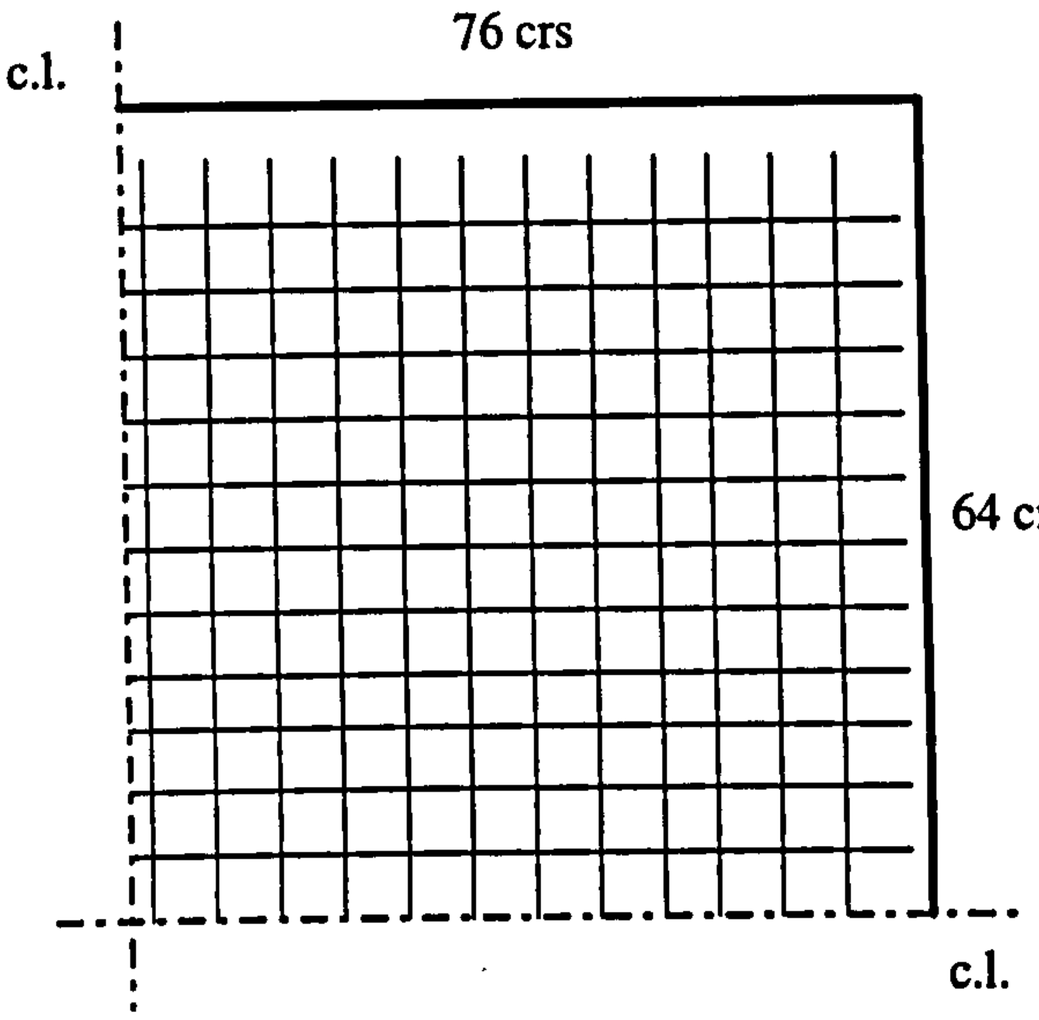

a) Model S1

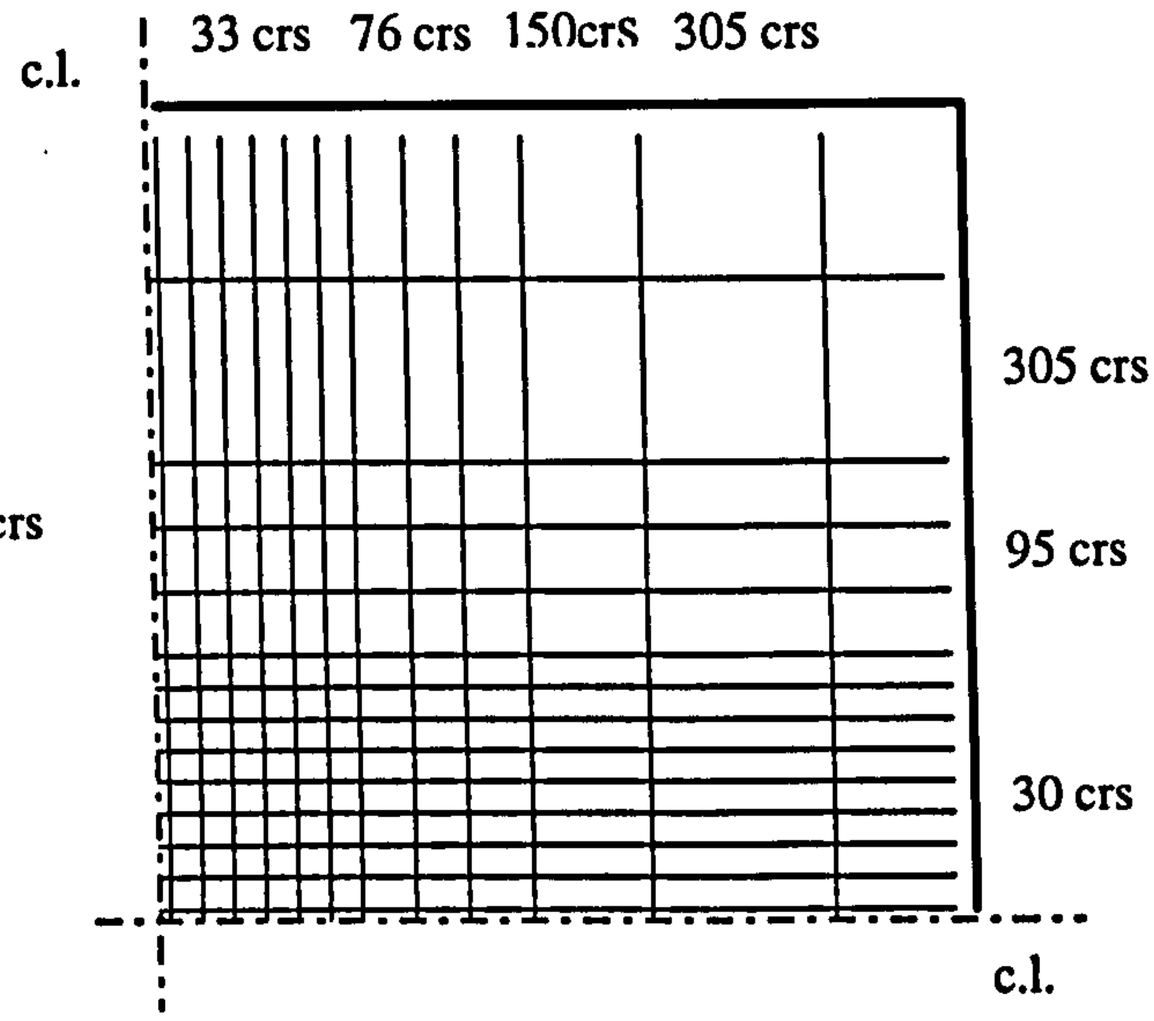

b) Model S2

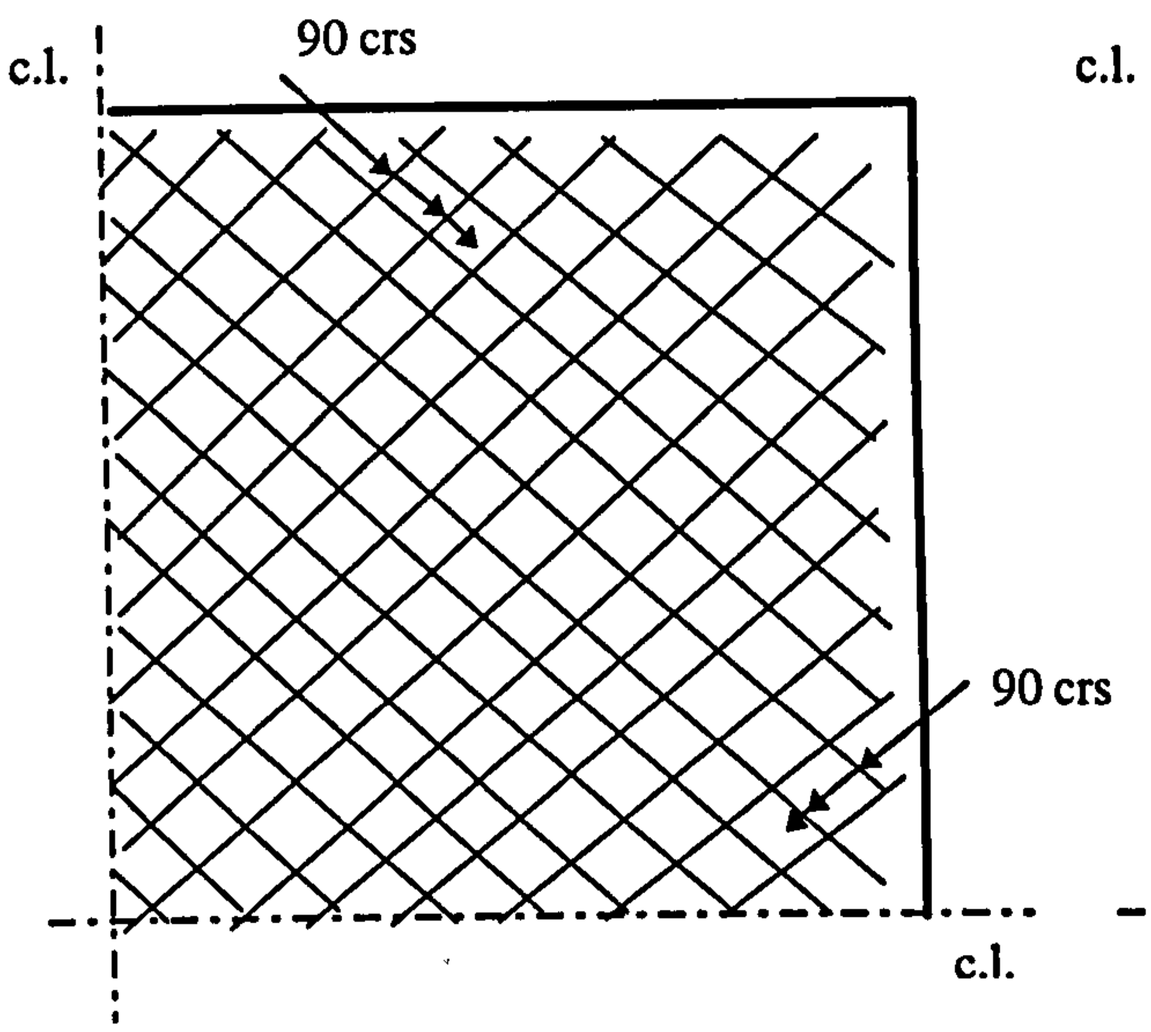

d) Model S6

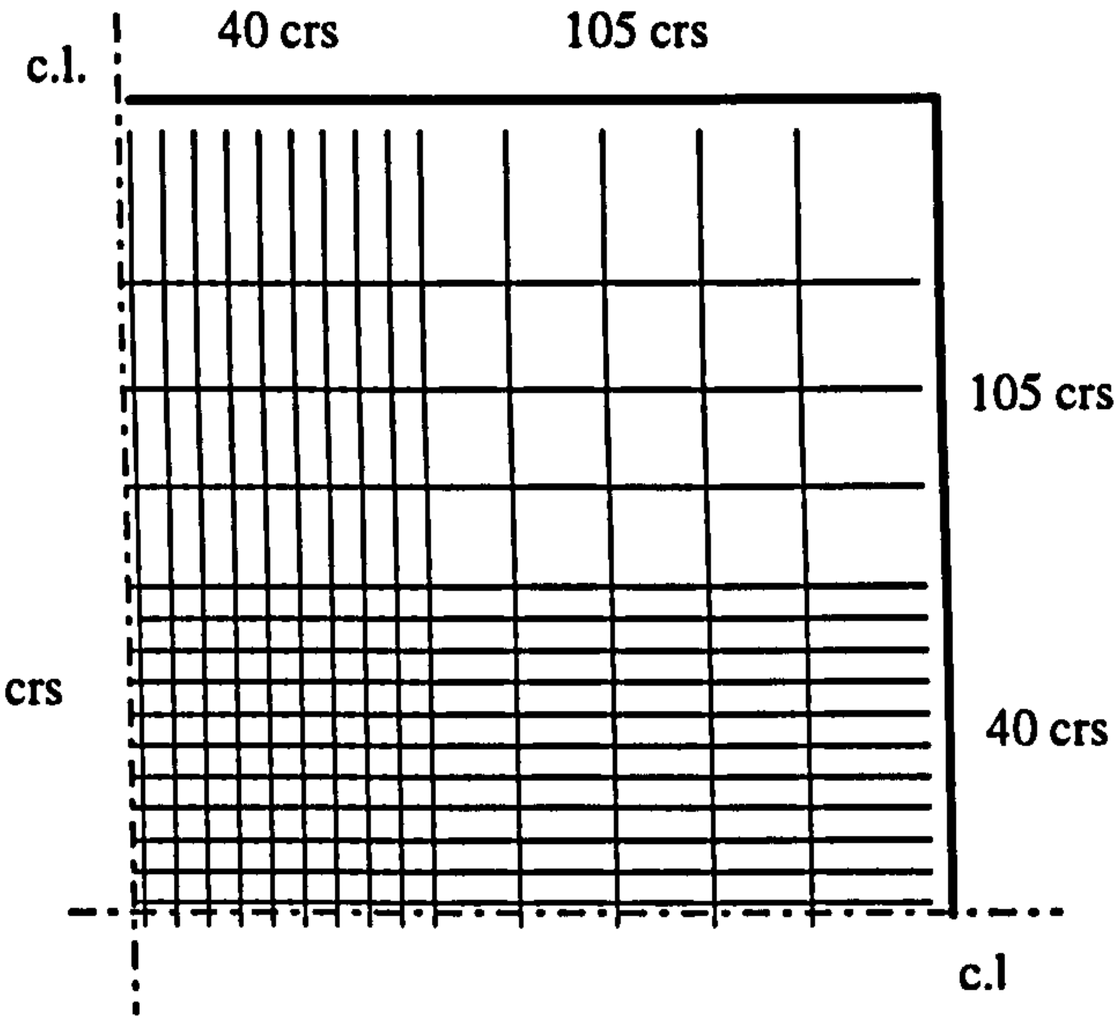

c) Model S8

figs.5.7.3(a-d) Slabs tested by Taylor et al; reinforcement details (all sizes in mm)

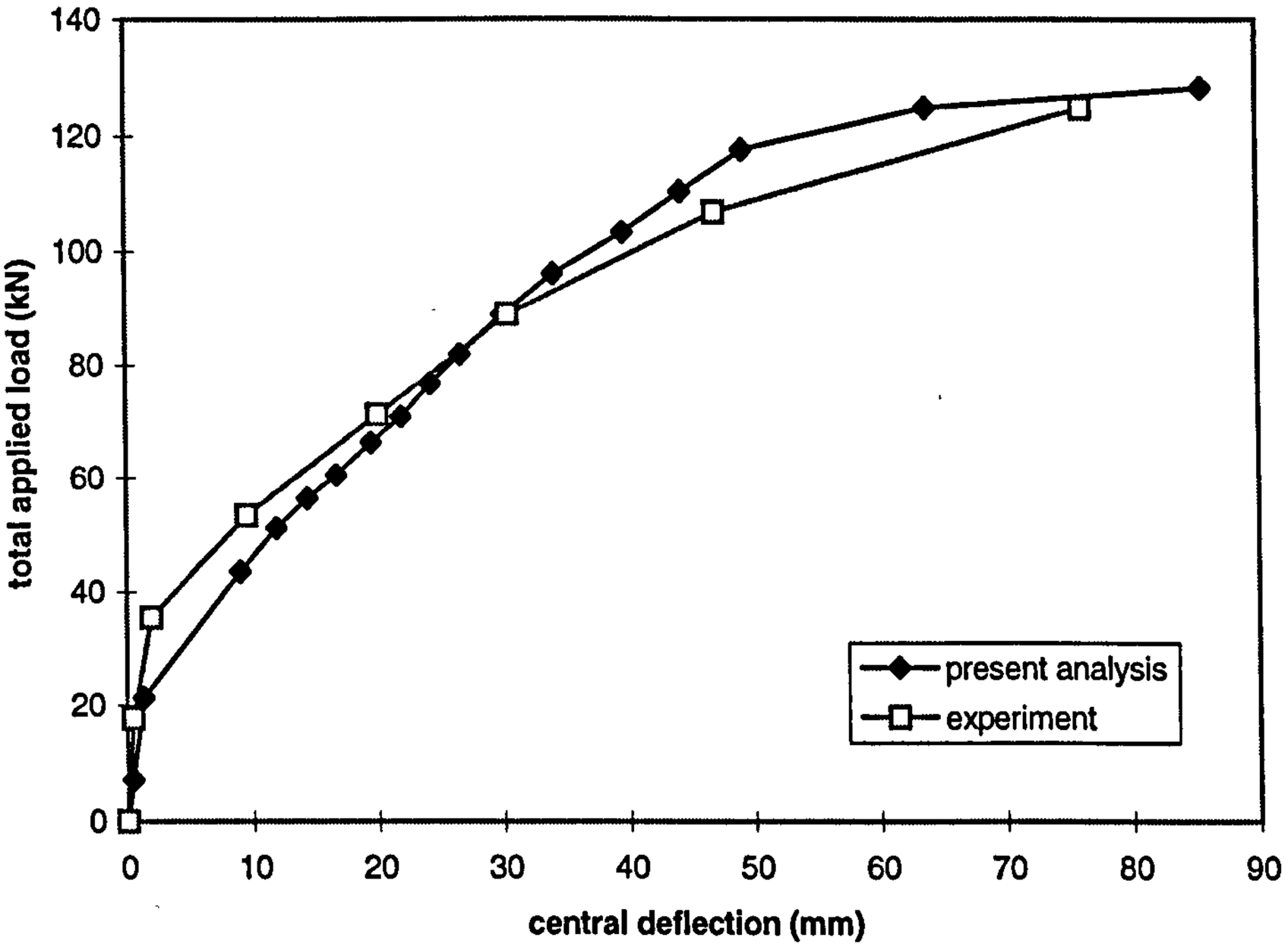

fig.5.7.3(e) Slab S1 tested by Taylor et al; load-displacement

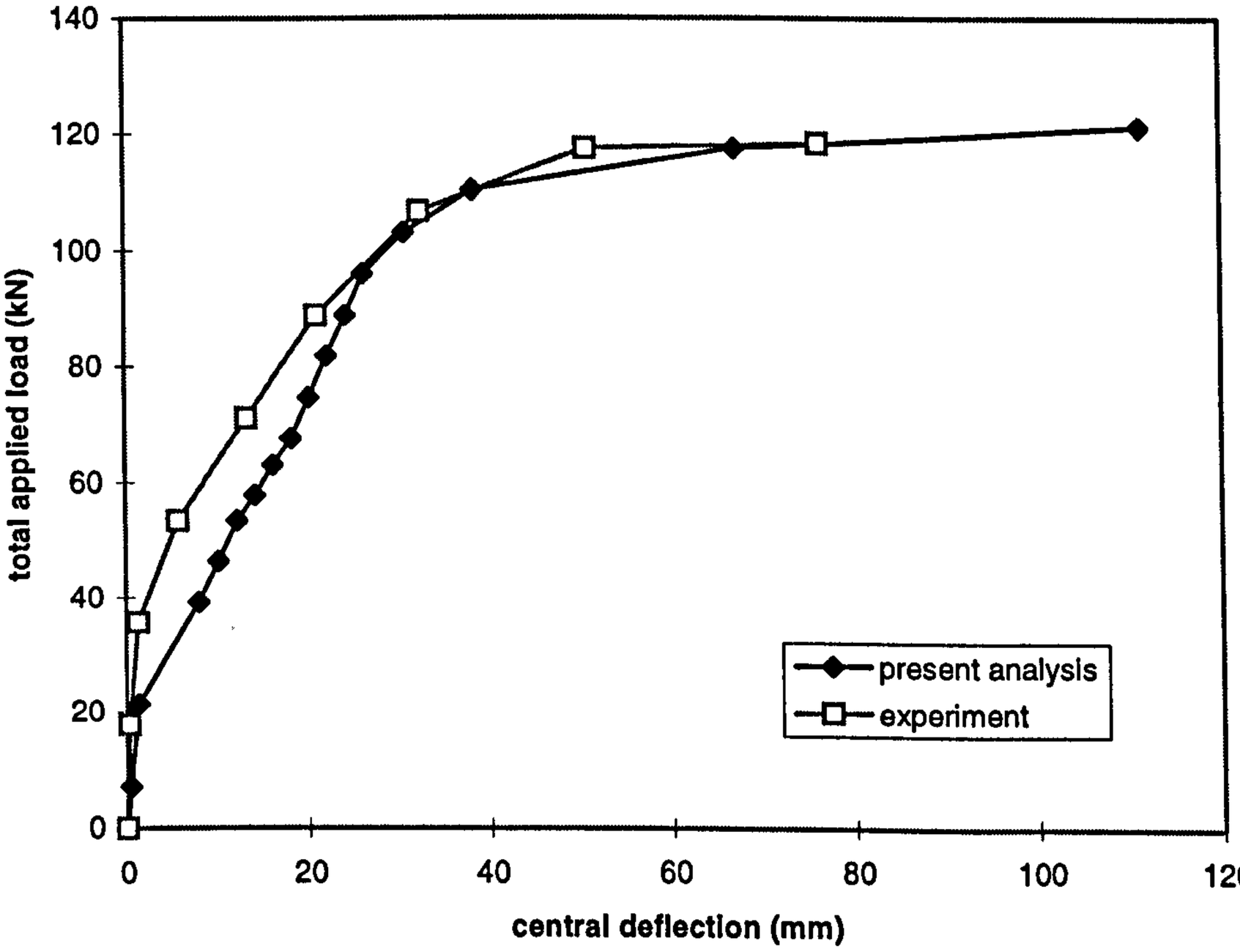

fig.5.7.3(f) Slab S2 tested by Taylor et al; load-displacement

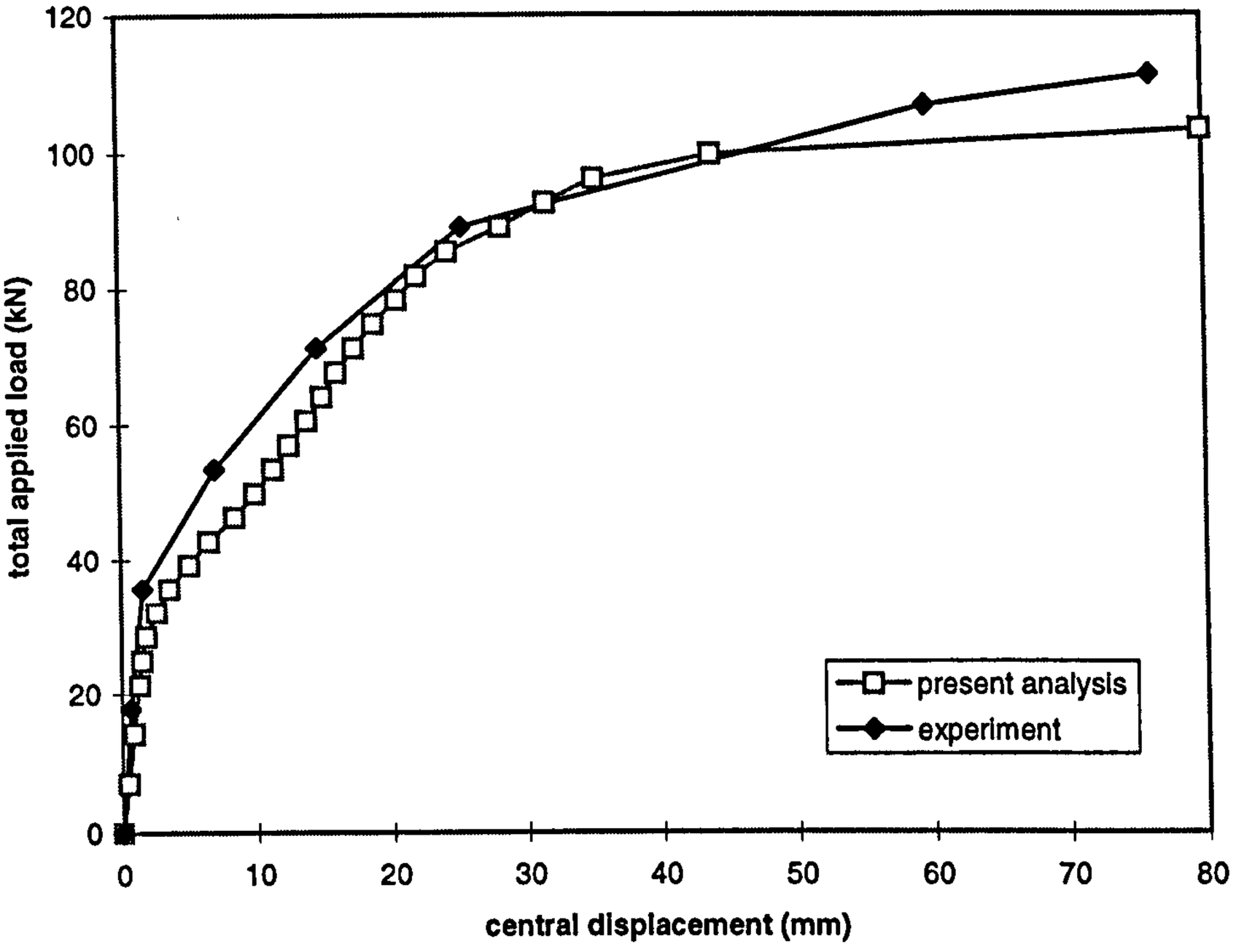

fig.5.7.3(g) Slab S6 Tested by Taylor et al; load-displacement

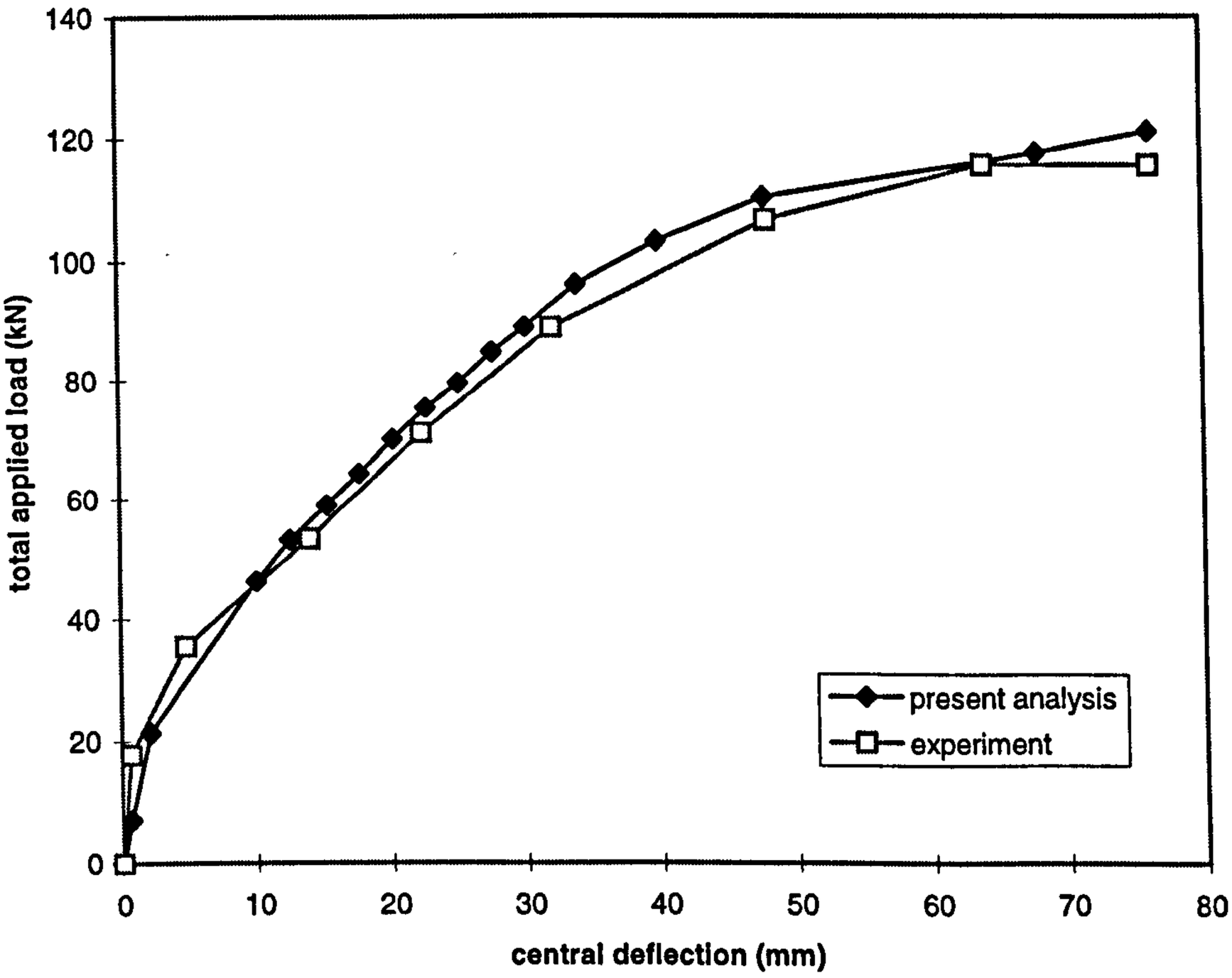

fig.5.7.3(h) Slab S8 tested by Taylor et al; load-displacement

5.7.4 Deep Beams tested by Khaskheli

Four, two-span, continuous deep beams were chosen from the experimental program carried out by Khaskheli (1989). The experimental work was mainly aimed at determining the ultimate load and serviceability performance of deep beams designed using the direct design method. Since these beams had varying reinforcement layouts and span-depth ratios, they provided a good basis on which to assess the applicability of the current numerical model in predicting the behaviour of deep beams at service and ultimate loads.

The first three beams in the series had the same span-depth ratios of 1.07 while beam TGRAS4 had an increased value of 1.61. Both TGRAS1 and TGRAS2 had the same amount of main reinforcement. Beam TGRAS1 had a greater amount of shear reinforcement than TGRAS2 and hence the failure mode would be expected to be more ductile. The shear reinforcement in TGRAS3 was the same as that for TGRAS2 but with TGRAS3 having a greater amount of main reinforcement. Details of the material properties and design load for each beam are given in table 5.7.4. The reinforcement layouts and dimensions are given in figures 5.7.4 (a-d). For numerical analysis, a symmetrical half of each beam was discretised using an 8x7 element mesh.

Concrete Properties	**TGRAS1**	**TGRAS2**	**TGRAS3**	**TGRAS4**
E_c (N/mm^2)	19300	23200	20800	19200
f_{cu} (N/mm^2)	63.0	61.0	61.0	52.0
f_t (N/mm^2)	3.2	3.7	3.4	2.6
Span/Depth Ratio	1.07	1.07	1.07	1.61
Shear-Span/Depth Ratio	0.42	0.42	0.42	0.69
Design Load P_d (kN)	810	810	1100	810
Steel Properties				
6mm ϕ bars, f_y=513 N/mm^2, Es=199000 N/mm^2				
8mm ϕ bars, f_y=520 N/mm^2, Es=195000 N/mm^2				

Table 5.7.4: Properties of Khaskheli's Beams

In the case of TGRAS1, during the experiment, initial cracking occurred at the bottom of the beam at mid-span at 0.3 P_d. In the numerical analysis, cracking was first encountered at 0.4 P_d around the same area as in the experiment. Yielding of the main longitudinal steel was recorded experimentally at the mid-span at $1.3P_d$. Numerical yielding of the main steel was recorded in this area at around $1.0P_d$. In the experiment, no yielding of the vertical stirrups was observed and this was also true for the numerical analysis. The experimental and numerical result for TGRAS1 are given in figures 5.7.4(e-f). From the load-displacement curve, the onset of significant cracking can be seen in the numerical result at around 1.05 P_d. Such a phenomenon is characterised by the sudden loss of stiffness. The numerical crack patterns at $P=1.0P_d$ and $1.05P_d$ (fig 5.7.4g-h) confirm the extensive spread of cracking in the shear span during this short load increment. This event corresponds with the opening of inclined shear cracks in the shear span of the beam during the experiment at a load level of $1.16P_d$. Good correlation between the experimental and numerical crack pattern can be seen from fig. 5.7.4(i). The ultimate load obtained from the numerical analysis was around 91% of that obtained experimentally.

The effect of the shear retention factor on the numerical behaviour was also investigated for this beam. Figure 5.7.4(k) displays the load-displacement response obtained using values of B = 0.1, 0.4, 0.7 and 1.0. When B=0.1, a low ultimate load, equal to the load where shear cracks opened in the original analysis, is obtained. This suggests that the cracks opening at $1.05P_d$ were caused by high shear stresses. A more accurate response was obtained using the higher values of B. However, no significant differences could be seen from the response at B = 0.4, 0.7, or 1.0.

Due to the reduction in shear reinforcement, the load-displacement behaviour of beams TGRAS2 and TGRAS3 is less ductile (figs 5.7.4(l-m)). Experimentally, TGRAS2 achieved a smaller ultimate load (1216kN) than TGRAS1. For TGRAS2 the load at which inclined cracks opened in the shear span was around 0.925 P_d which was lower than that for TGRAS1. The numerical failure of the beam was reached at 1.375 P_d which corresponded well with experimental failure load of around 1.43 P_d. The onset of inclined cracks in the shear span of beam TGRAS3 occurred at around

$0.8P_d$. A numerical ultimate load of $1.275P_d$ was achieved which again corresponded well with the experimental ultimate load of $1.36P_d$.

Since the span-depth ratio of beam TGRAS4 was much higher than that of the other beams, less brittle load-displacement response was anticipated. In the experiment, initial cracking occurred around the lower soffit of the beam at mid span. The first crack was recorded in this area at $0.12P_d$ while numerically, the first cracks appeared in the same area at around $0.3P_d$. This difference is due to the fact that the initial increment in the numerical analysis was $0.3P_d$. Further increases in load were accompanied by propagation of this crack towards the loading point. In the experiment cracking at the top of the beam above the internal support was initiated at $0.65P_d$ and this was recorded numerically at $0.7P_d$. The sudden appearance of diagonal cracking in the shear spans of the beam was, as for the previous models, observed numerically between 0.7 and $0.75P_d$ (figs 5.7.4(p-q)). The same phenomenon was observed experimentally at around $1.05P_d$. Beam TGRAS4 failed experimentally in shear. It is clear however, that greater ductile response was attained from the load-displacement and load-strain plots (figs 5.7.4(n-o)). Significant yielding of the main steel at the mid-span was observed in the numerical model (up to 8 times yield strain), however the strain gauge in the experiment failed once the strain surpassed 3.5 times yield strain. As in the previous beams, no yielding of the vertical reinforcement occurred experimentally or numerically. The numerical failure of the beam was reached at $1.15P_d$ which corresponded reasonably with the experimental failure at around $1.34P_d$.

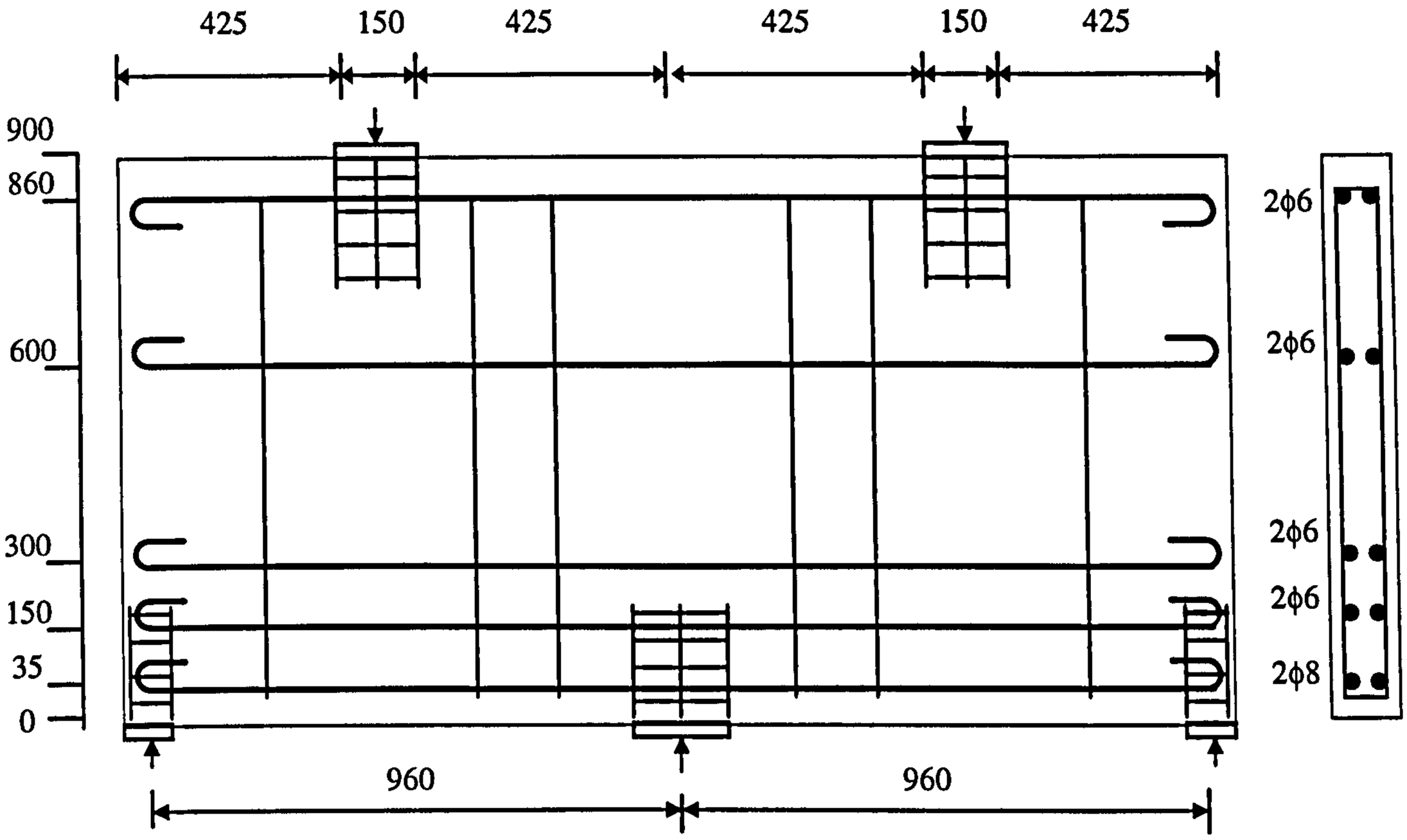

fig.5.7.4(a) Dimensions and reinforcement details for TGRAS1

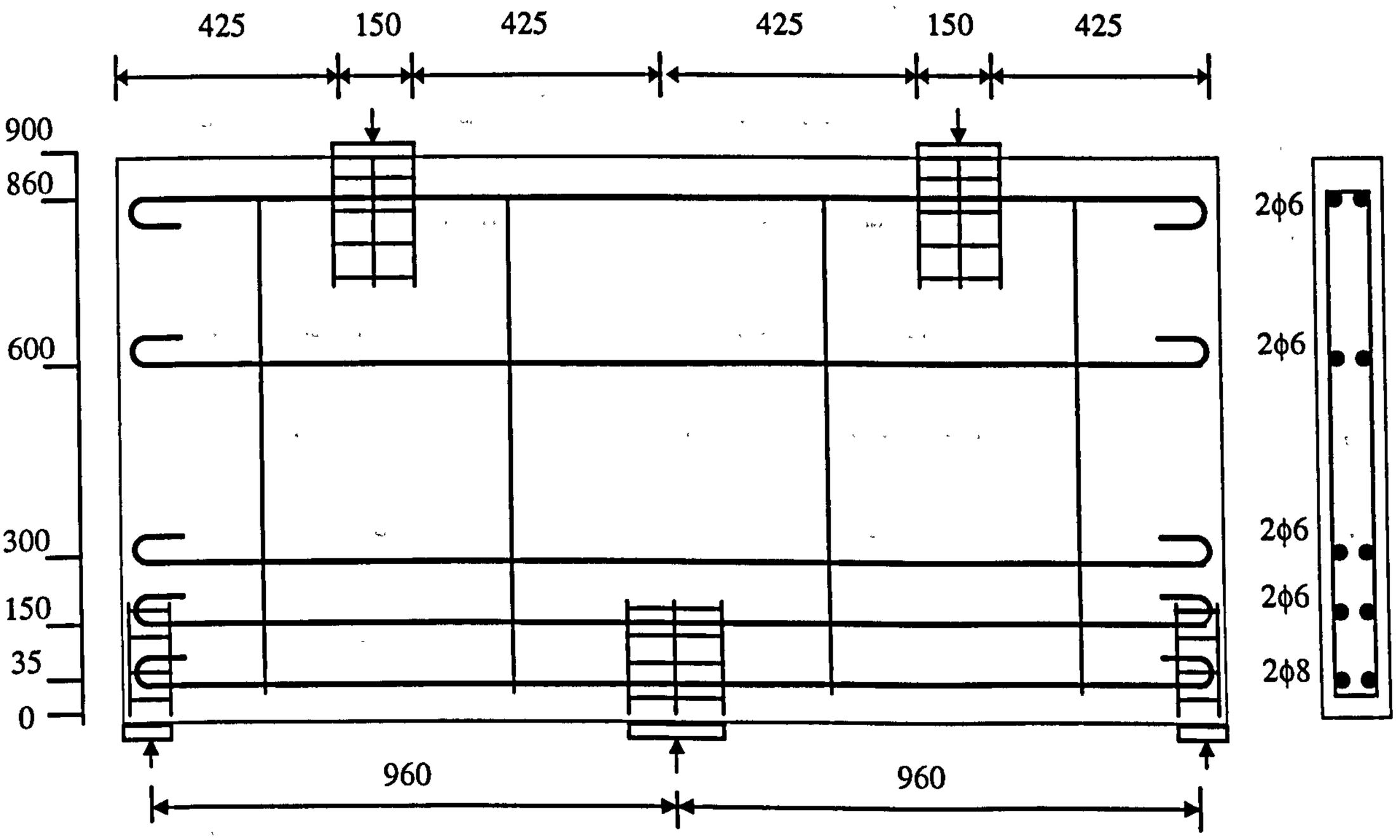

fig.5.7.4(b) Dimensions and reinforcement details for TGRAS2

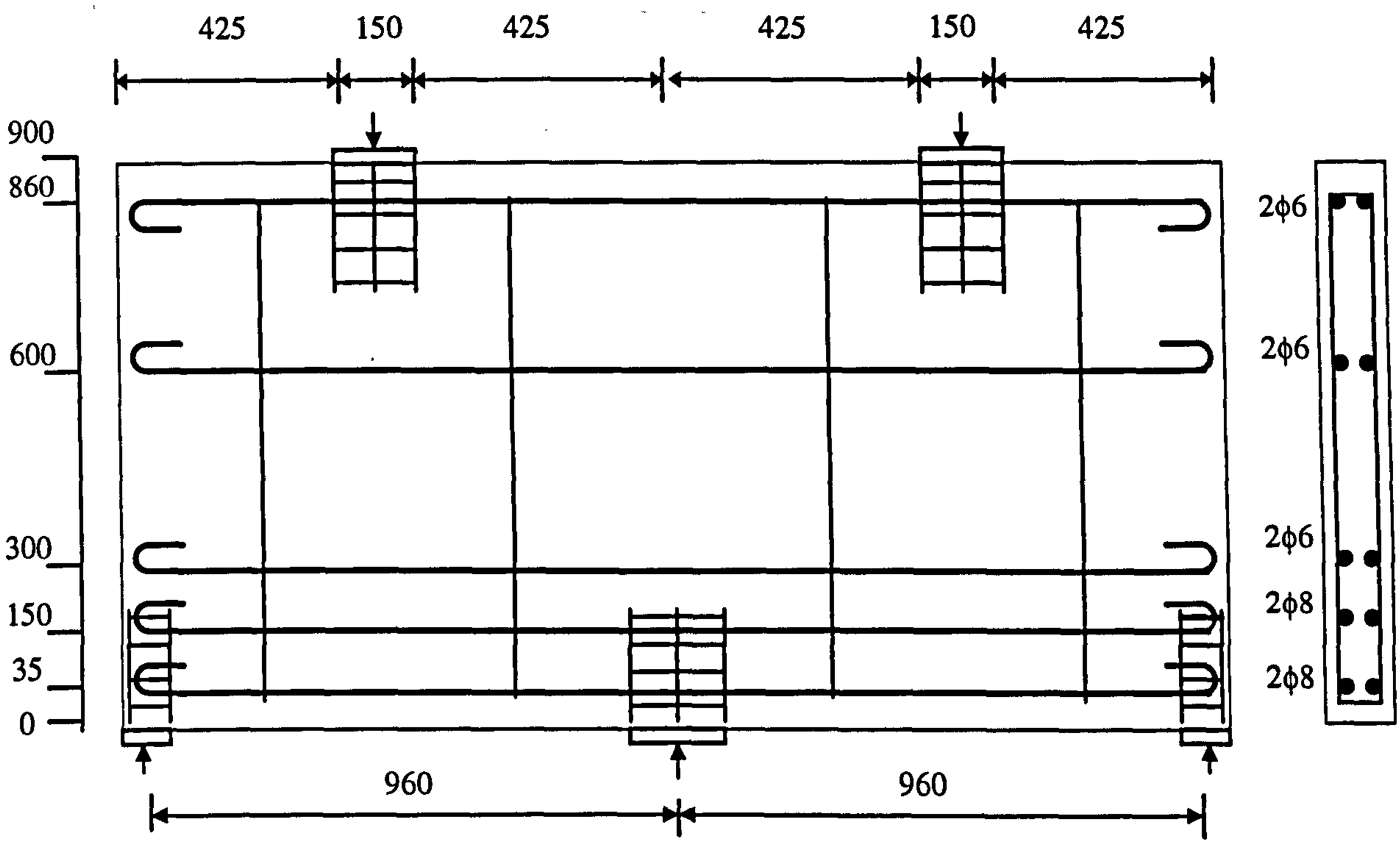

fig.5.7.4(c) Dimensions and reinforcement details for TGRAS3

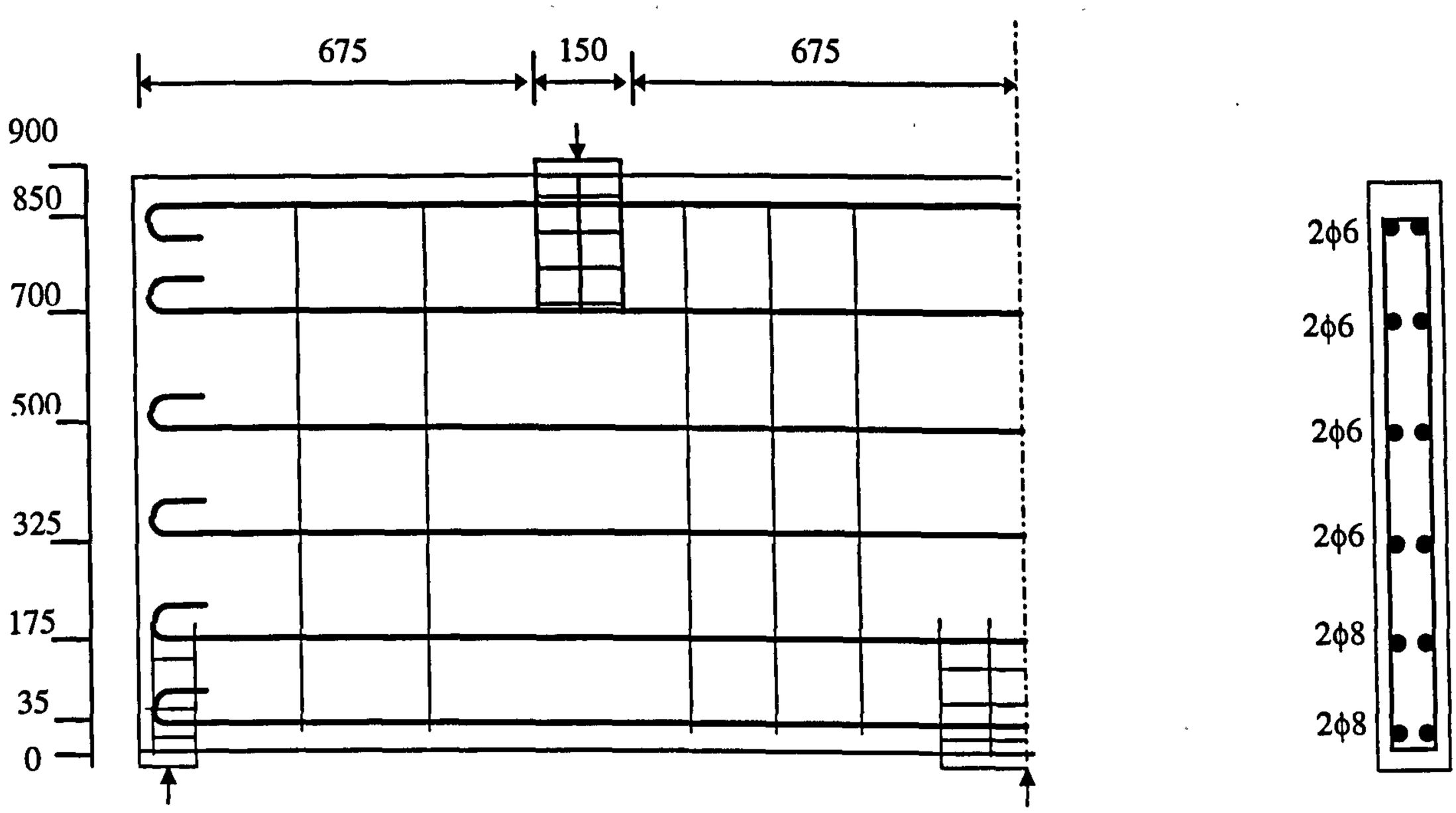

fig.5.7.4(d) Dimensions and reinforcement details for TGRAS4

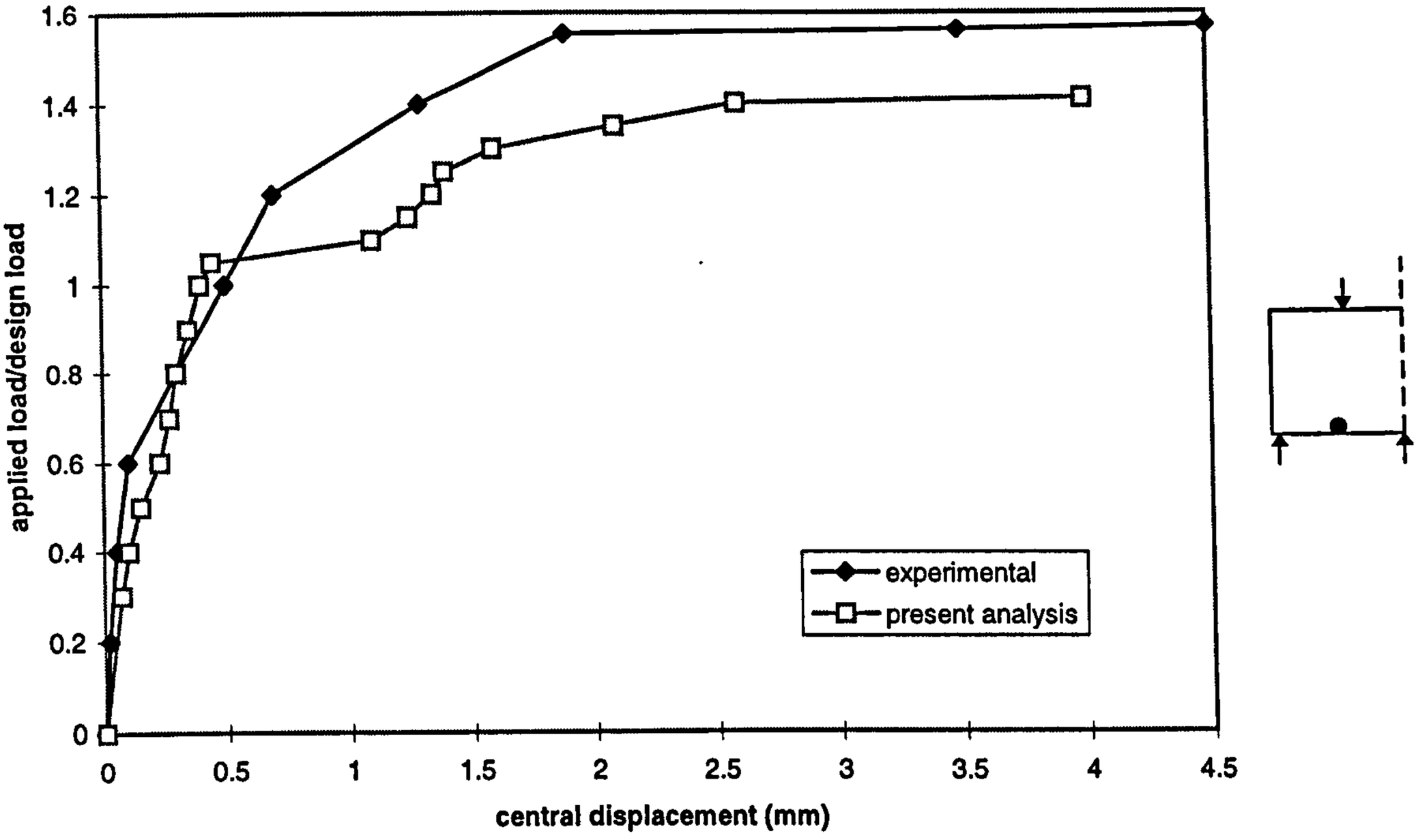

fig.5.7.4(e) Beam TGRAS 1: Load-displacement relationship

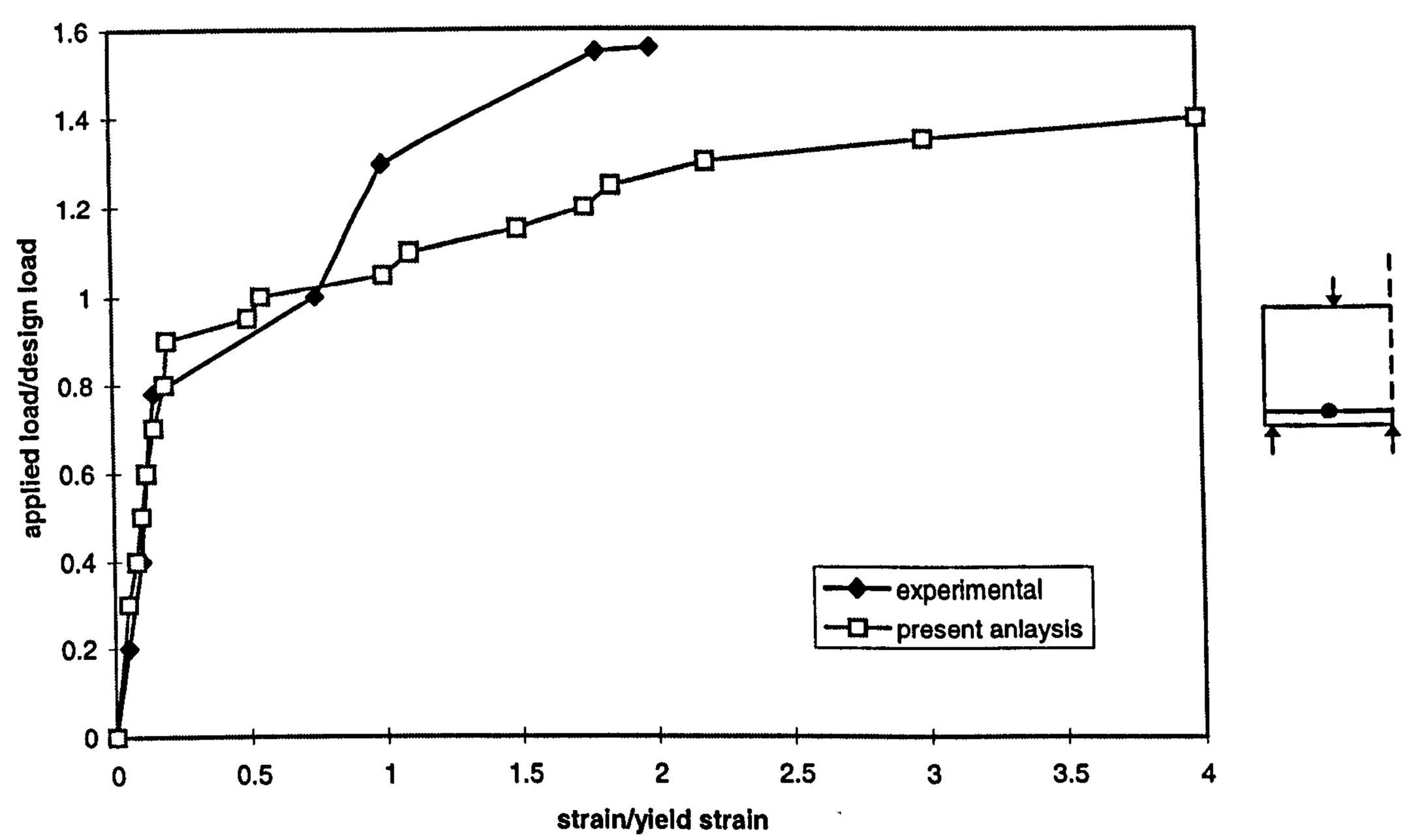

fig.5.7.4(f) Beam TGRAS 1: Main steel strains at mid-span

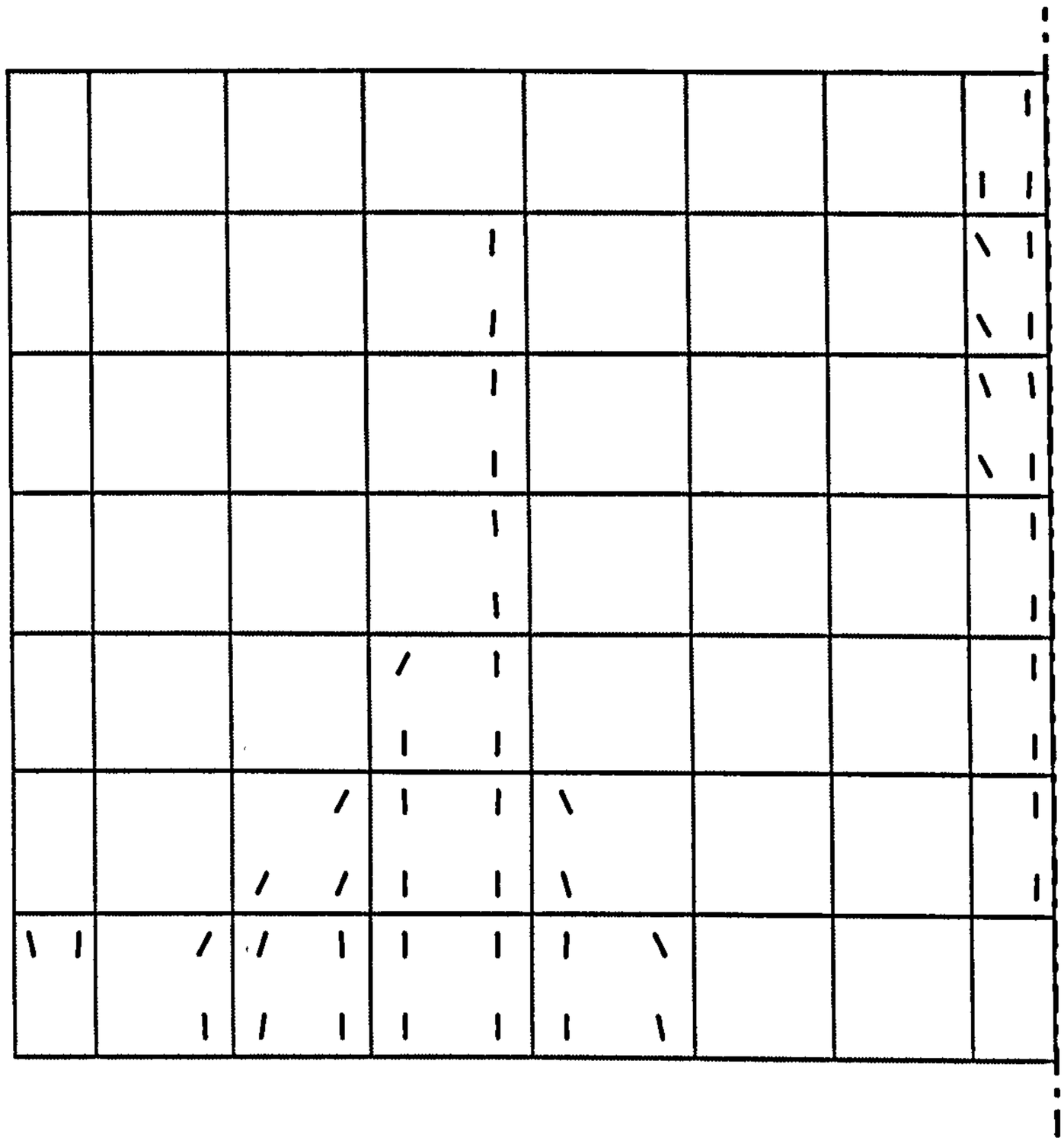

fig.5.7.4(g) Beam TGRAS1: Numerical Crack Pattern ($P=1.0P_d$)

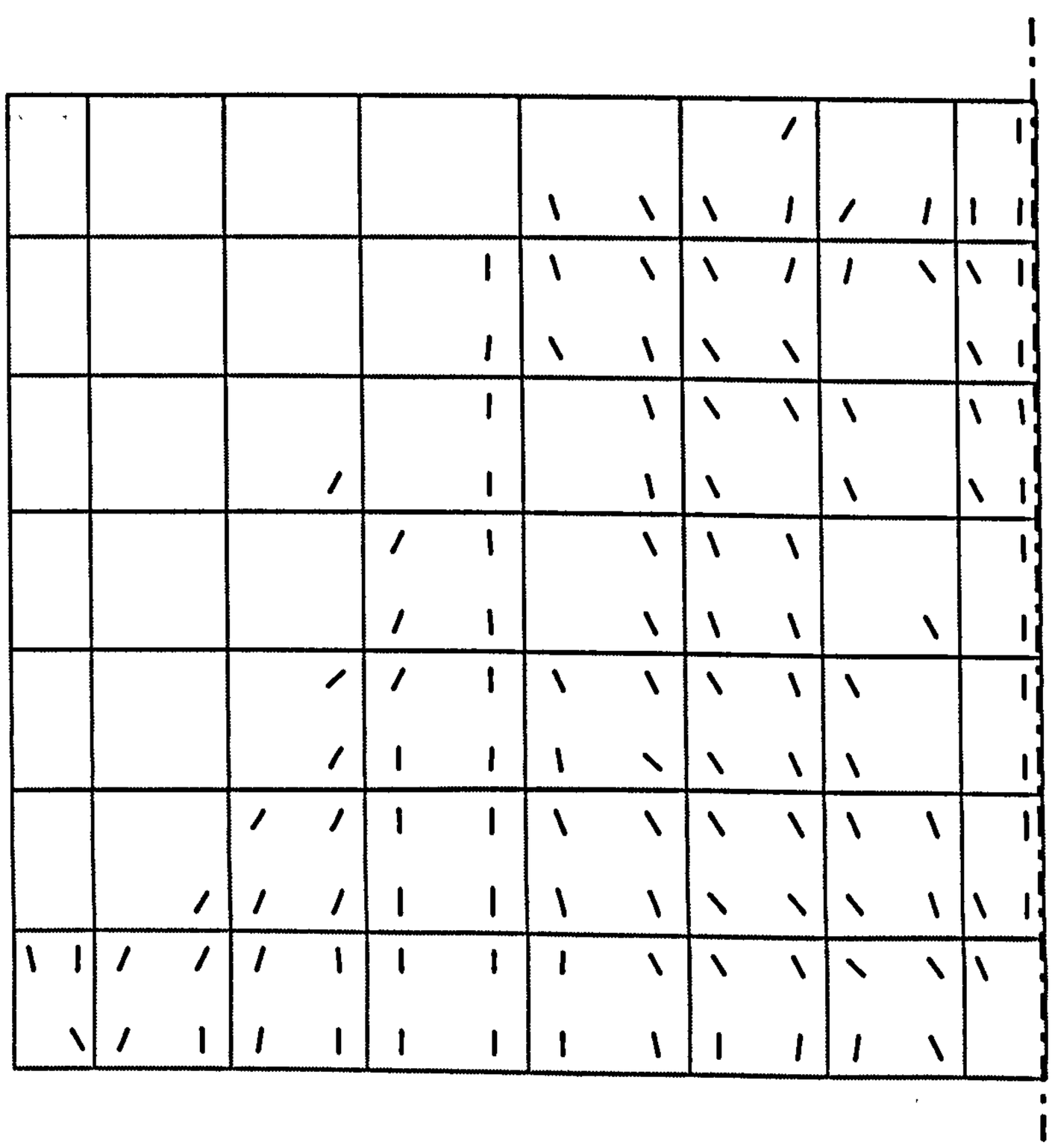

fig.5.7.4(h) Beam TGRAS1: Numerical Crack Pattern ($P=1.05P_d$)

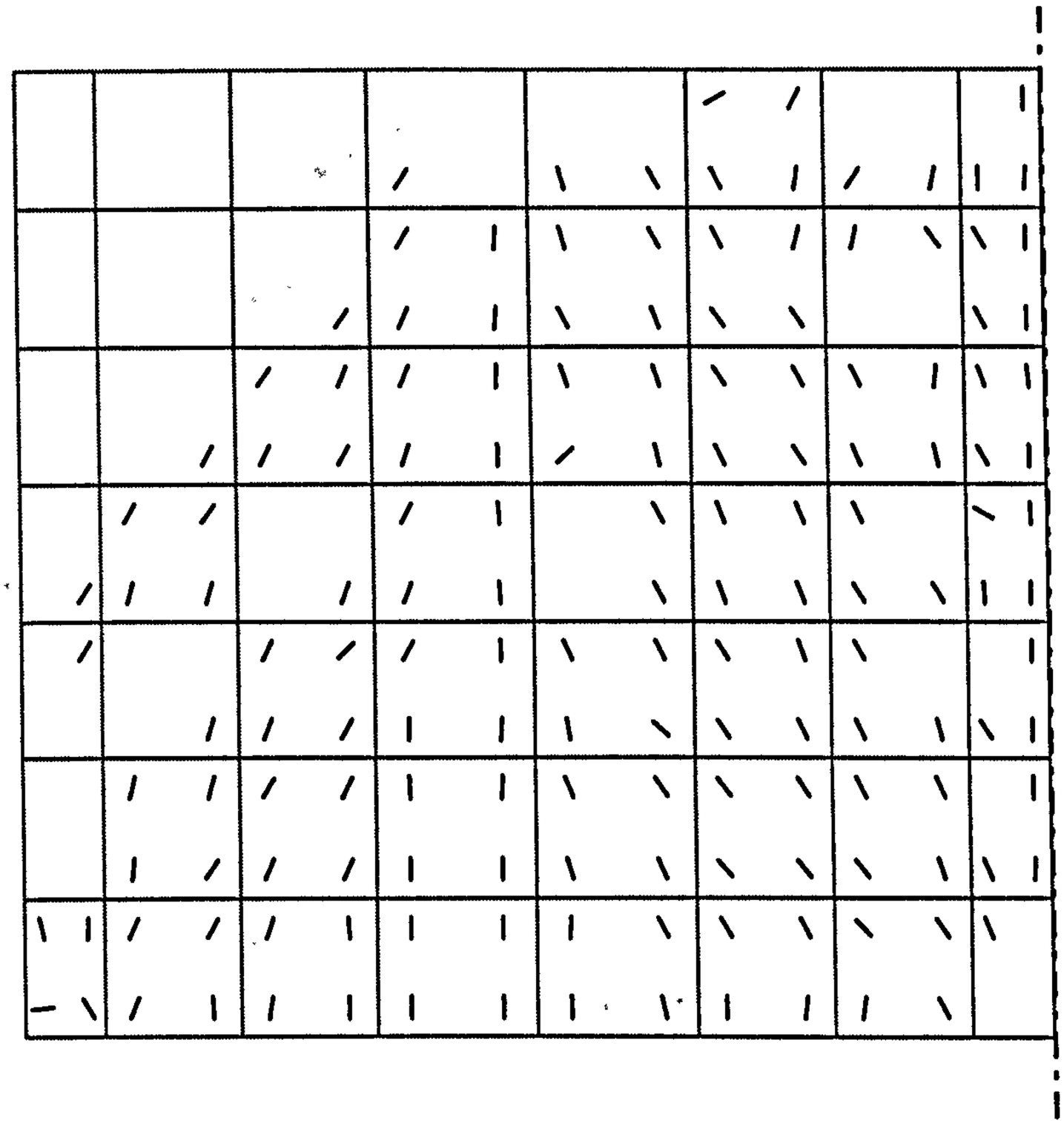

fig.5.7.4(i) Beam TGRAS1: Numerical Crack Pattern at Ultimate Load

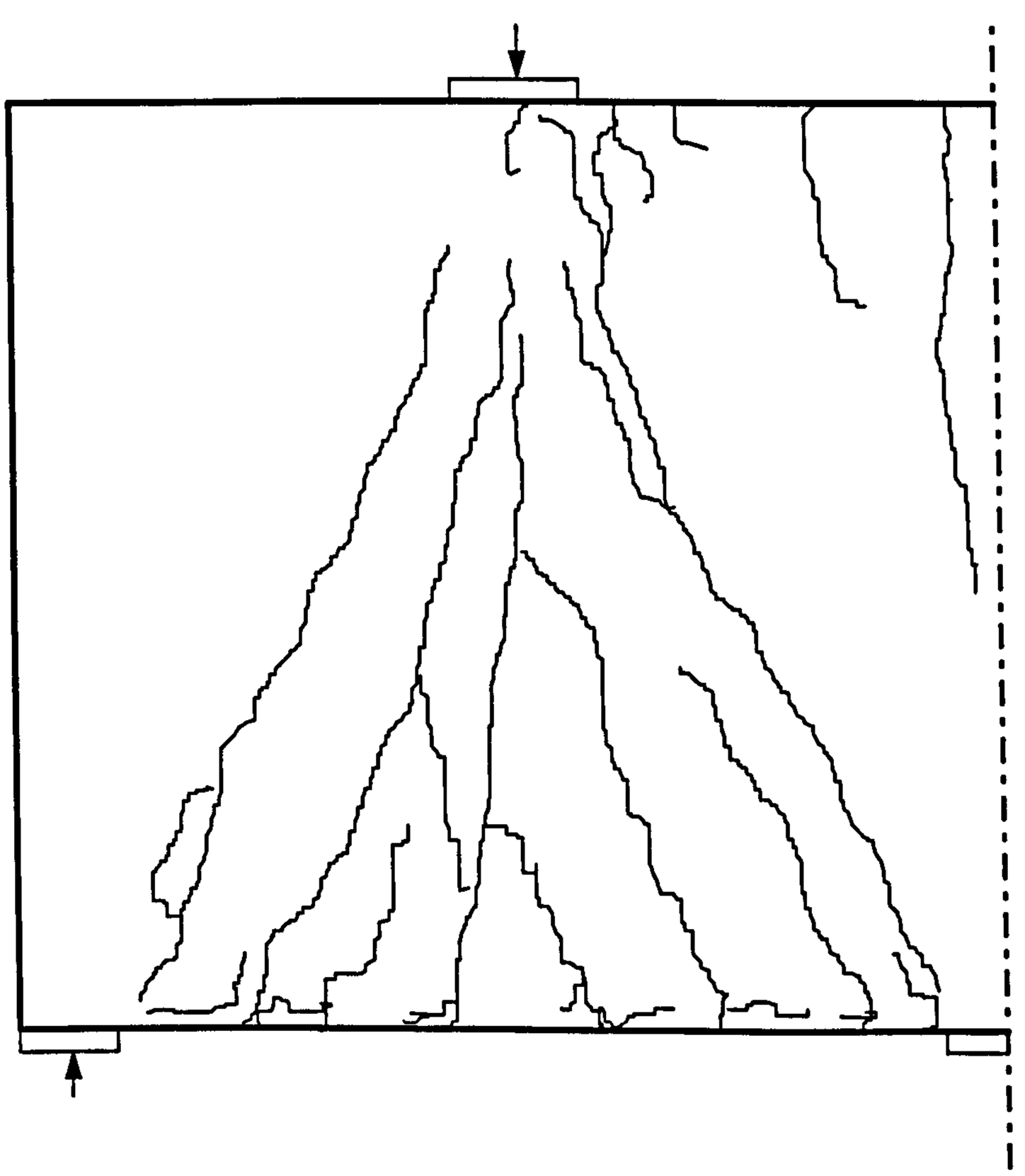

fig 5.7.4(j) Beam TGRAS 1: Experimental Crack Pattern at Ultimate Load

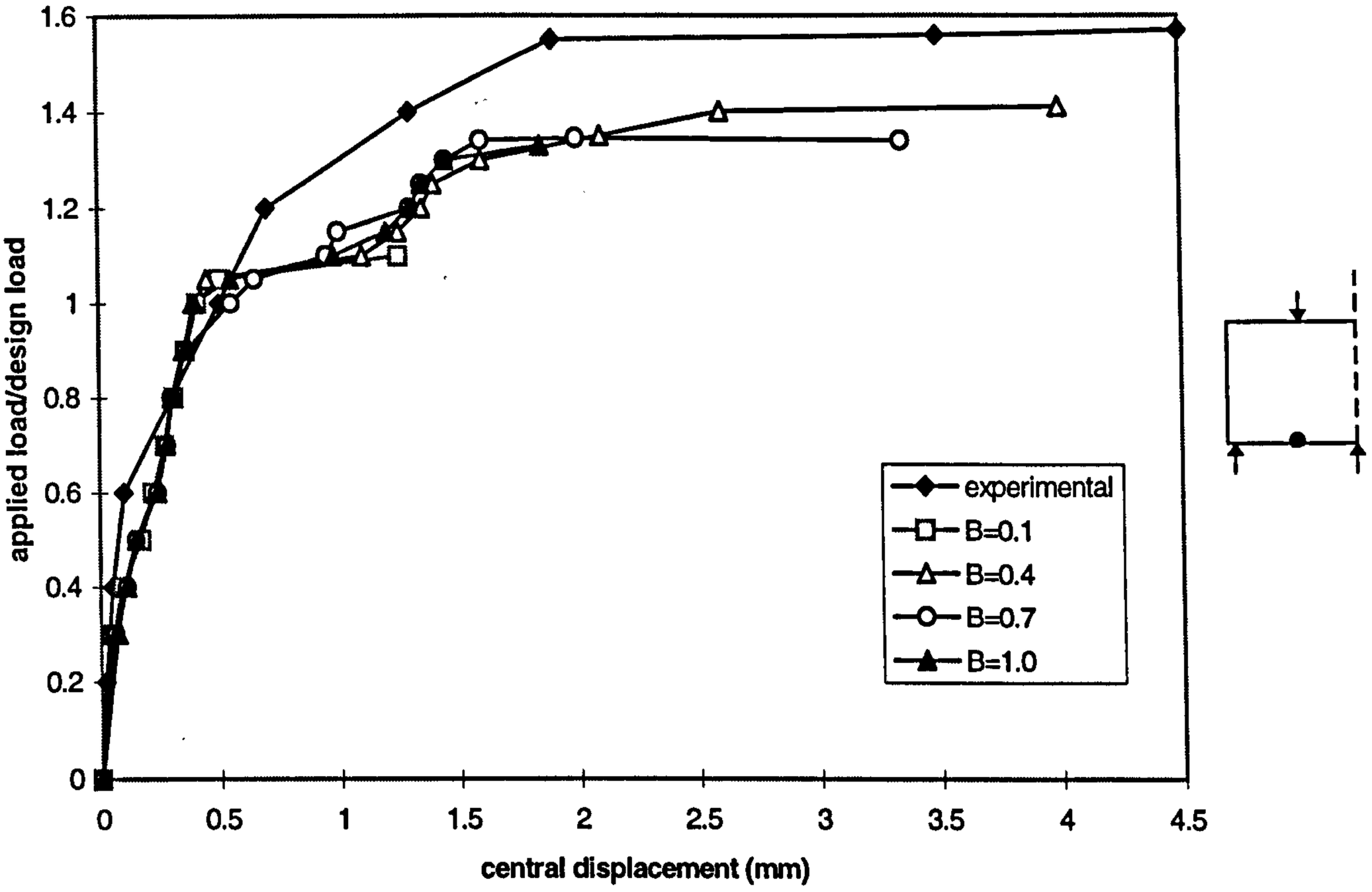

fig.5.7.4(k) Beam TGRAS1; Effect of Shear Retention Factor

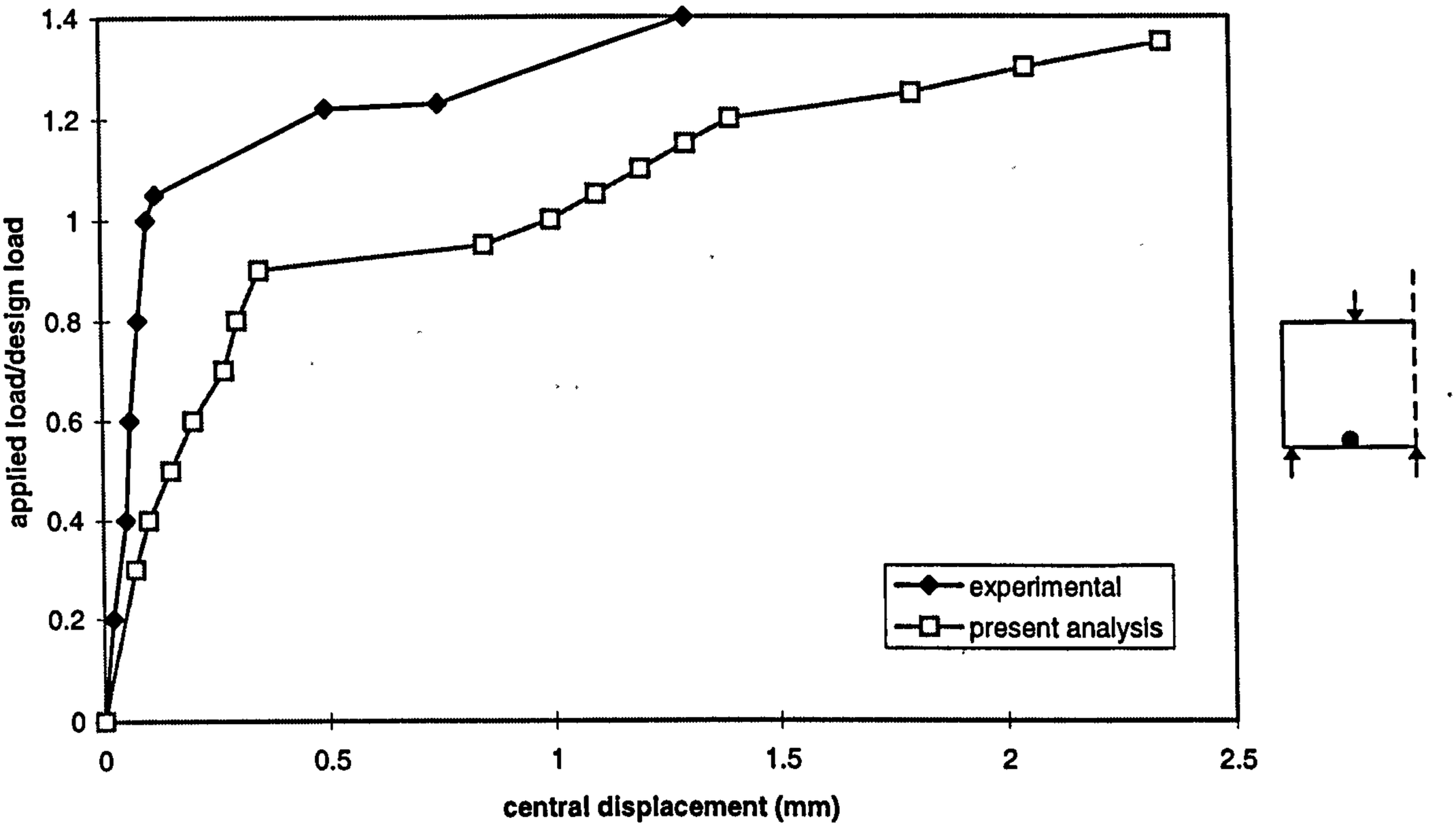

fig.5.7.4(l) Beam TGRAS 2: Load-displacement relationship

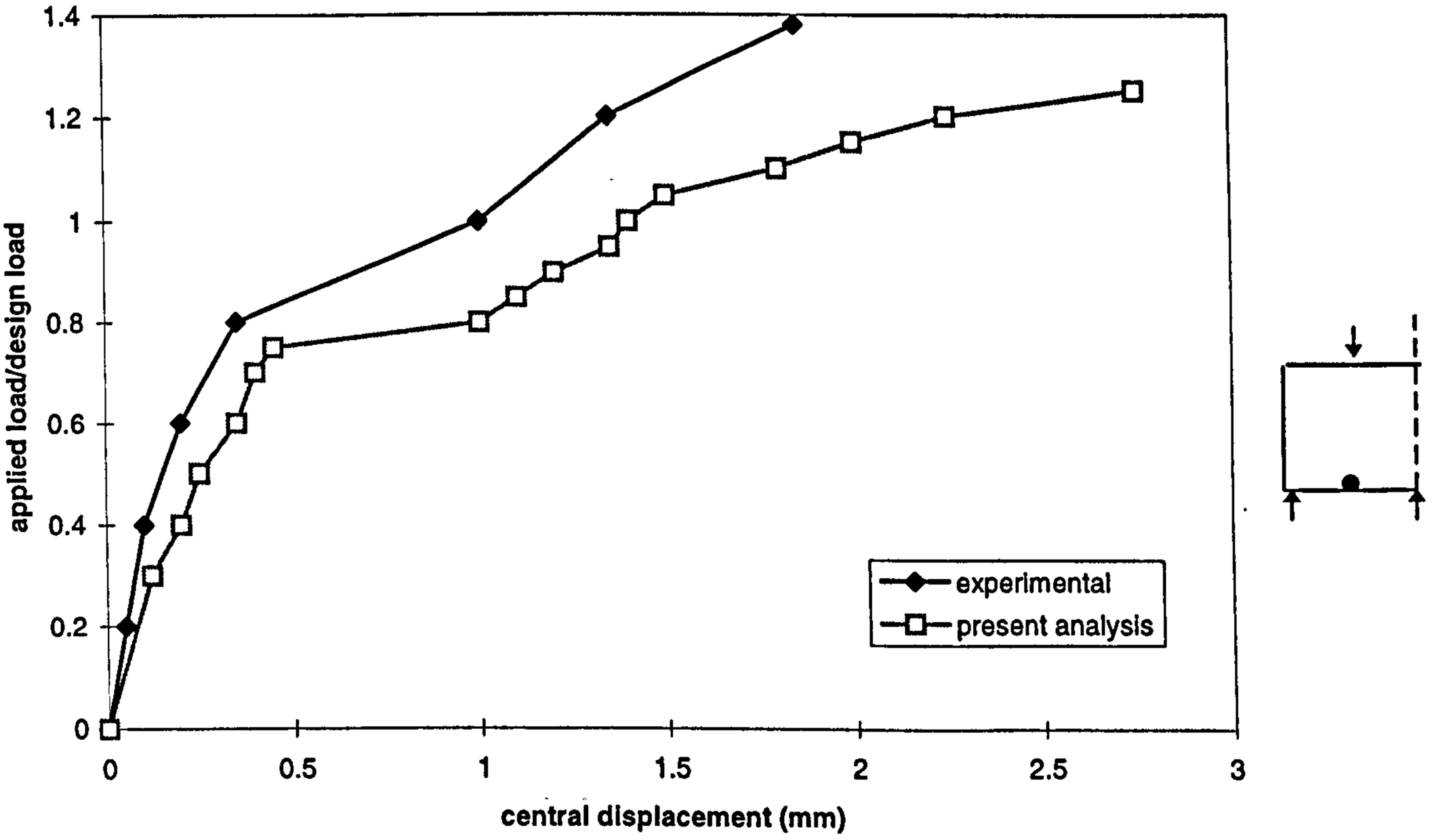

fig.5.7.4(m) Beam TGRAS 3: Load-displacement relationship

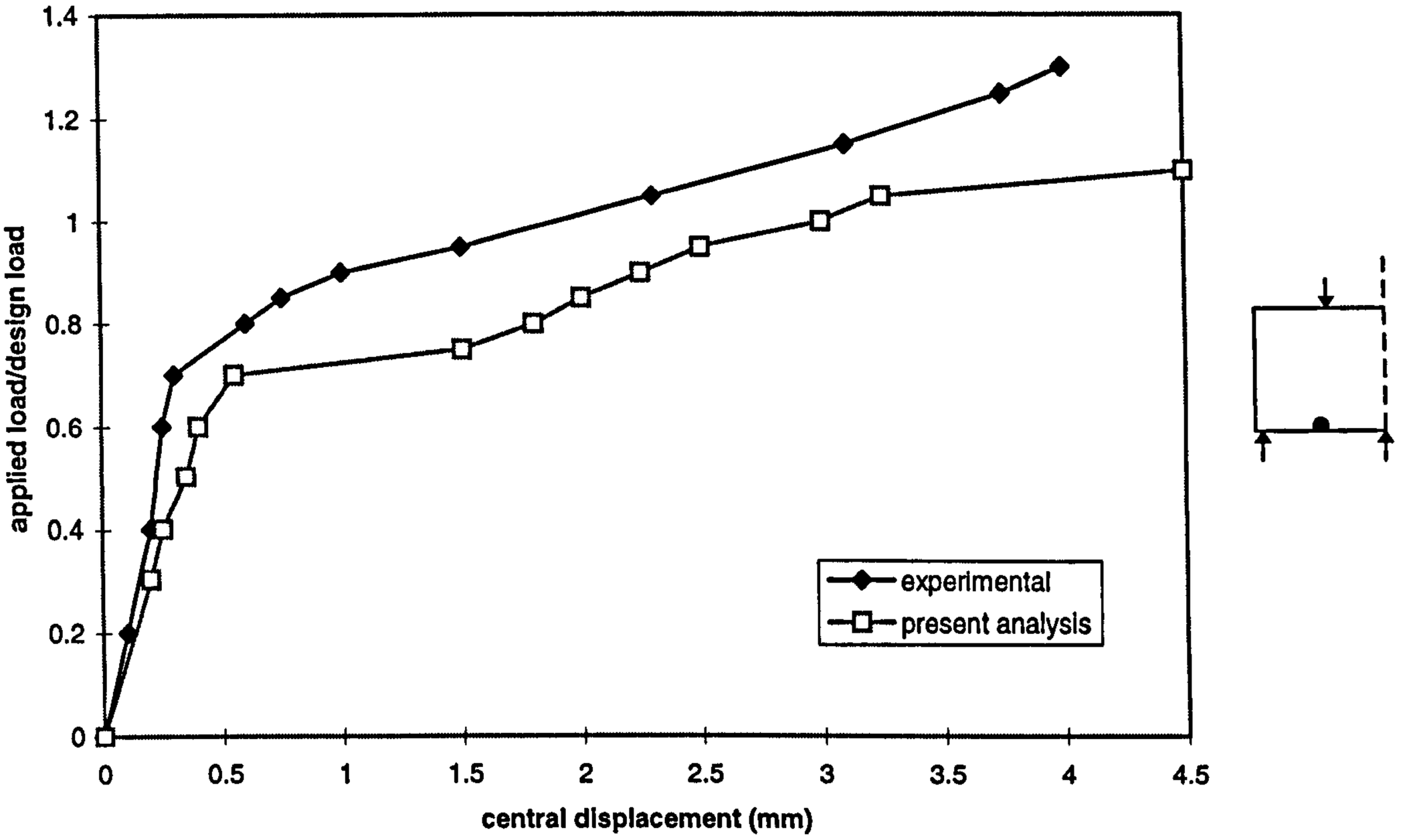

fig.5.7.4(n) Beam TGRAS 4: Load-displacement relationship

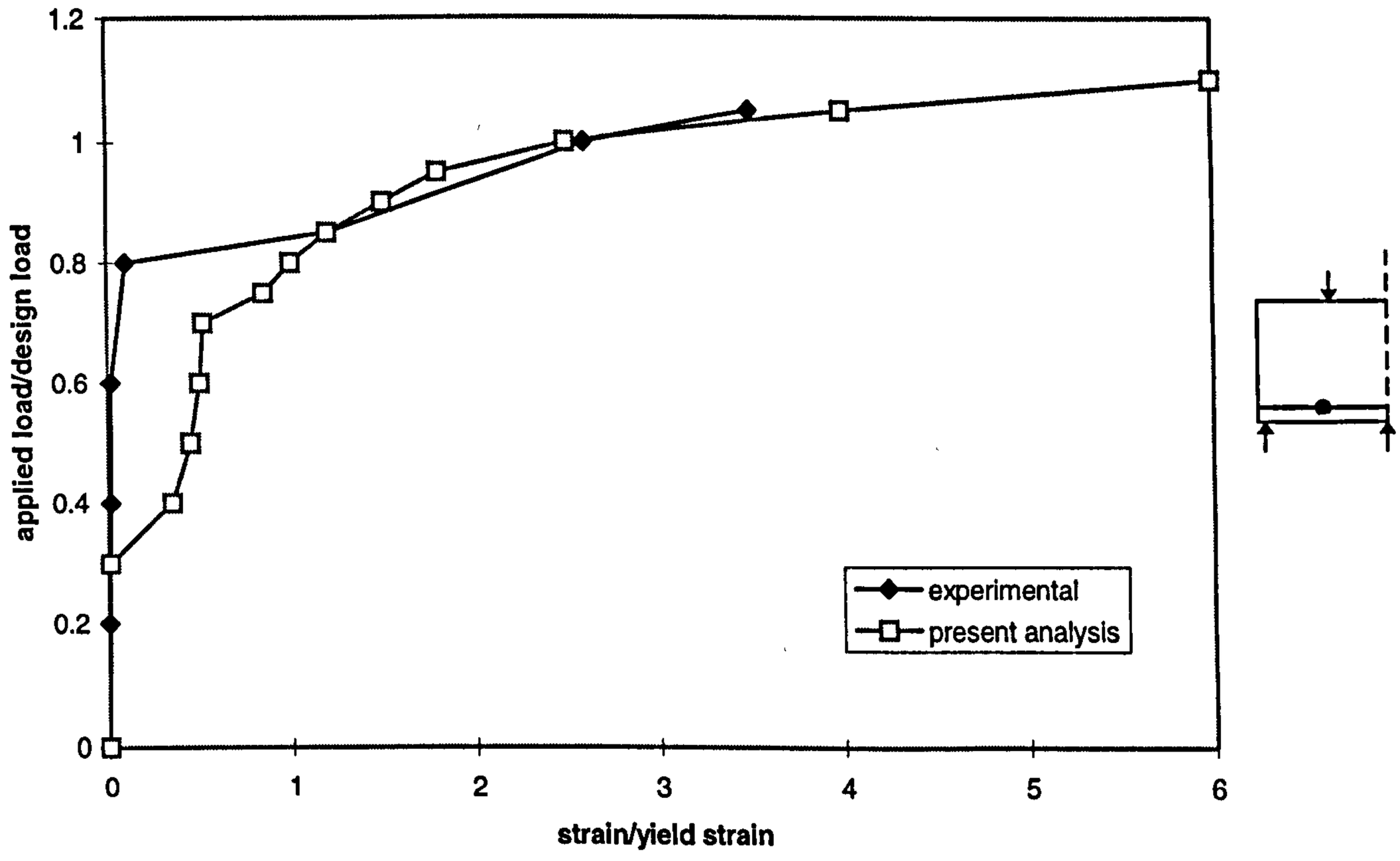

fig.5.7.4(o) Beam TGRAS 4: Main steel strains at mid-span

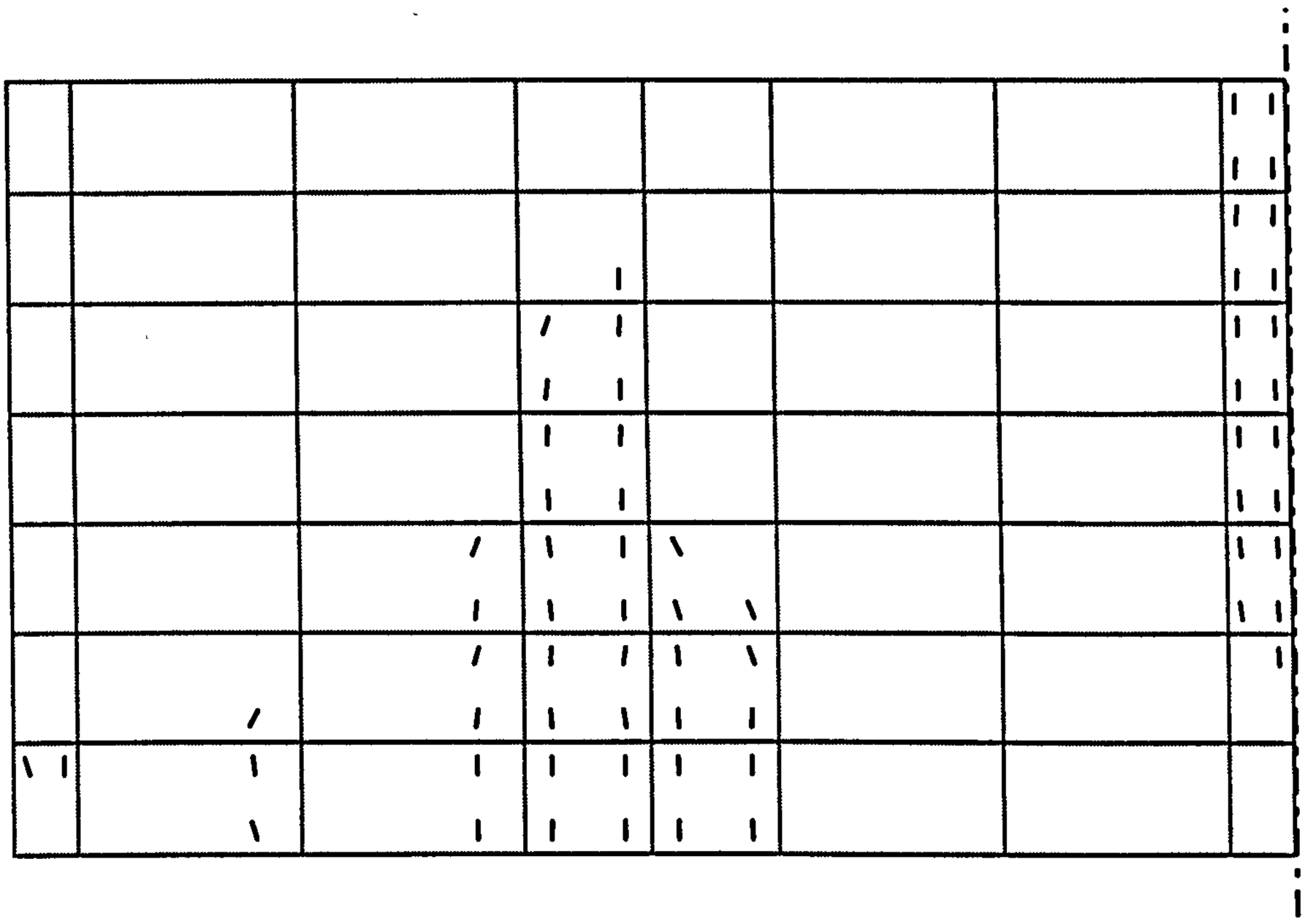

fig.5.7.4(p) Beam TGRAS4: Numerical Crack Pattern ($P=0.7P_d$)

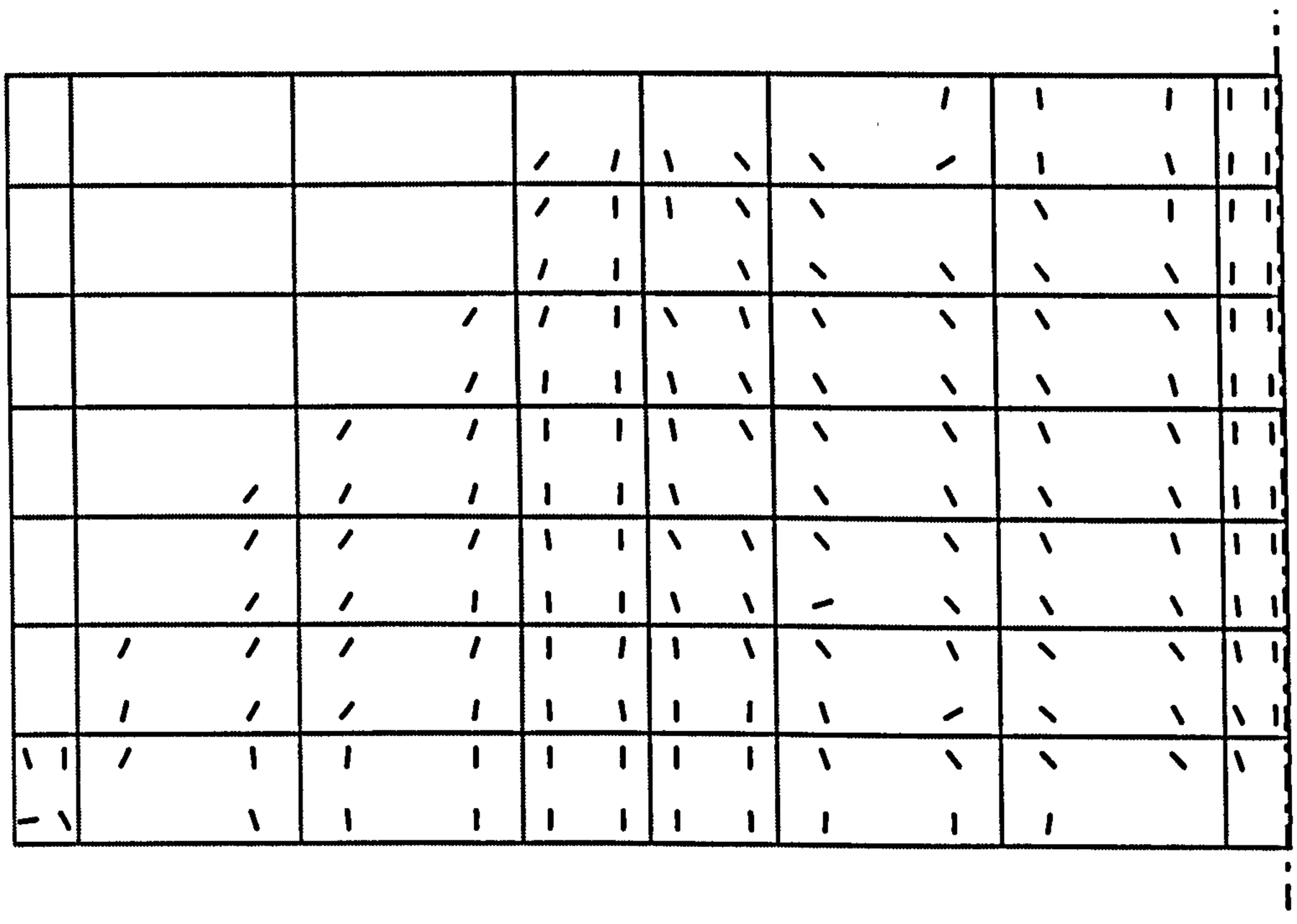

fig.5.7.4(q) Beam TGRAS4: Numerical Crack Pattern ($P=0.725P_d$)

5.7.5 Corbel Tested by Niedenhoff

In this example the analysis of a one-sided corbel is carried out. The experimental testing of one-sided corbels has been relatively scarce compared to two sided corbels (e.g. Kriz & Raths 1965). This is perhaps due to greater practical difficulties associated with testing the one-sided corbel resulting from the nature of its eccentric loading. The example chosen for this analysis was part of a series of tests carried out by Niedenhoff (1963). The original aim of these experiments was to obtain an indication of the stress distribution in these types of structures. A total of 12 corbels were tested in the program and model M2/B2 was chosen for the present numerical analysis. Numerical analysis of M2/B2 has also been carried out previously by van Mier (1987) and Prasad et. al (1993). The results obtained by the present analysis are also compared with those obtained by the above. Details of the geometry, boundary conditions and reinforcing layout are presented in figure 5.7.5(a). The material properties are shown below in table (5.7.5):

Concrete Properties	Steel Properties
$E_c = 27000\ N/mm^2$	$E_s = 210000\ N/mm^2$
$f_t = 2.42\ N/mm^2$	$f_y = 350\ N/mm^2$ (7ϕ)
$f_{cu} = 22.6\ N/mm^2$	$f_y = 282\ N/mm^2$ (12ϕ)
$\beta = 0.2$	$f_y = 300\ N/mm^2$ (14ϕ)
$\nu = 0.2$	$\nu = 0.25$

Table (5.7.5) Niedenhoff Corbel

As shown from the structural system (fig 5.7.5(b)), only the corbel was loaded. Horizontal reactions were induced as a result of this loading system. During the test, the load was applied in increments of 50 kN. In the original test, no displacements were recorded. A photo-elastic analysis was used to determine the principal stress flows and was compared with the crack pattern and behaviour of the corbel. It was found that the resultant of the principal compressive stress flows followed a diagonal path from the loading point to the lower inner corner of the corbel. The occurrence of tensile stresses perpendicular to this diagonal were also observed. Very little stress developed in the lower outside corner of the corbel.

The first crack (number1 in figure 5.7.5(h) occurred at the second load step (P=100kN). This crack then developed into a vertical crack at a load level of 150kN. At P=300kN, crack number 1 was fully developed and due to changes in the load path, crack number 2 occurred. During this time, cracking appeared in the column in addition to further cracking in the corbel. Failure of the corbel occurred at a load level of 585 kN when the main reinforcement began to yield and crack number 1 widened. Also at this stage, the compression zone at the lower column-corbel junction began to crush (crack number 3).

Figure 5.7.5(c) compares the load displacement relationship obtained from the present analysis with that obtained by van Mier (1987) and Prasad et al. (1993). In the case of the model used in van Mier's analysis, concrete was assumed to be elasto-plastic in compression and Mohr-Coulomb criterion was employed. In addition, a smeared crack model was implemented. It can be seen that that a reasonable agreement between each of the models was achieved. Numerical failure in the present analysis occurred at 485 kN which is around 83% of the experimental load. As a result of the geometry of the corbel, compressive stress concentrations occurred around the lower column corbel junction. Figures 5.7.5(d-e) show the concrete stresses in the corbel obtained from the present analysis. Observation of the concrete stresses at the lower column-corbel junction illustrates that crushing occurred at this point. In the experiment, crushing occurred at this same point towards the failure load. It can be seen from fig 5.7.5(f) that yielding of the main steel in the corbel occurred at the upper column/corbel junction. This phenomenon was also recorded in the experiment.

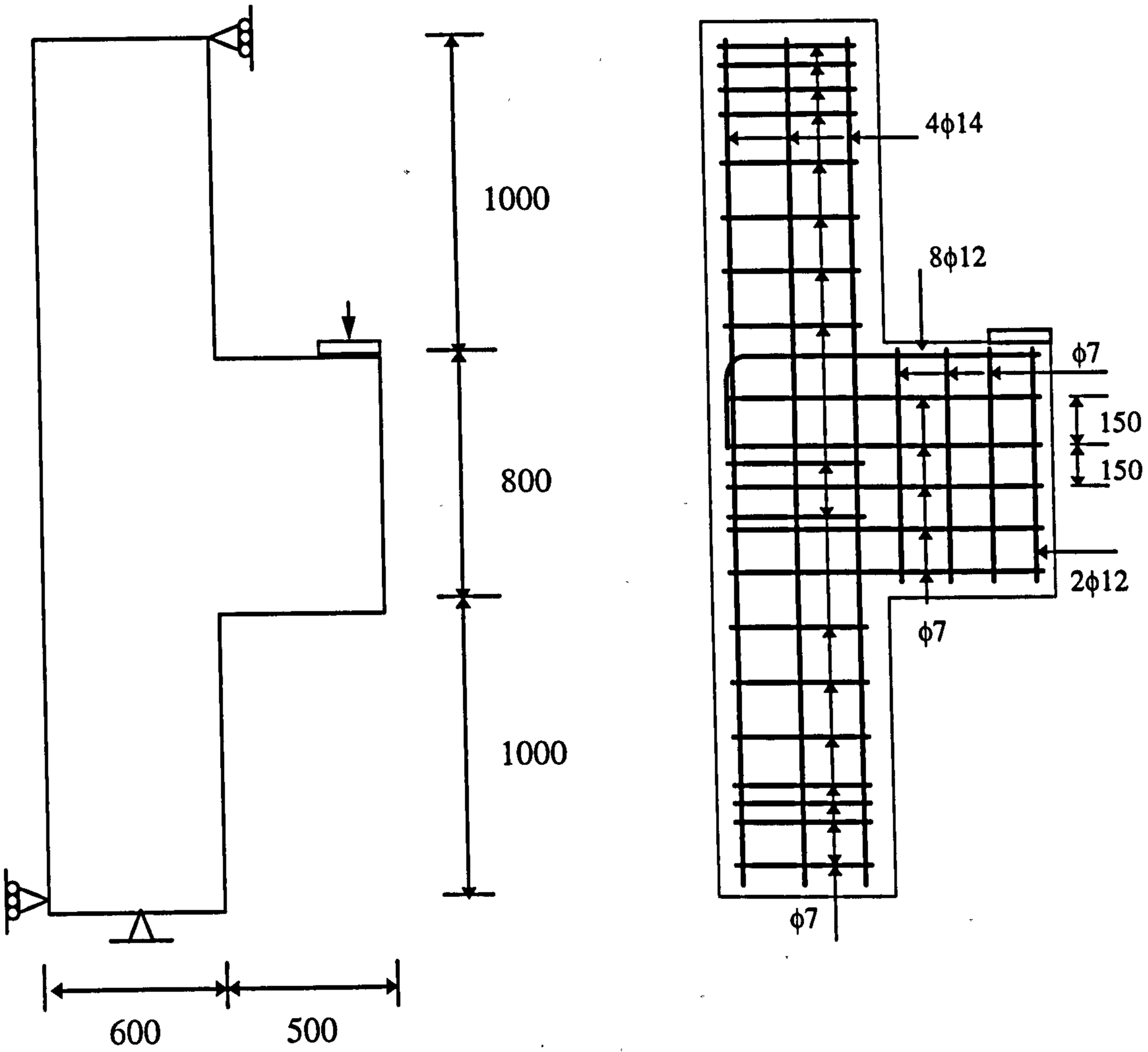

fig.5.7.5(a) Corbel dimensions and reinforcement details

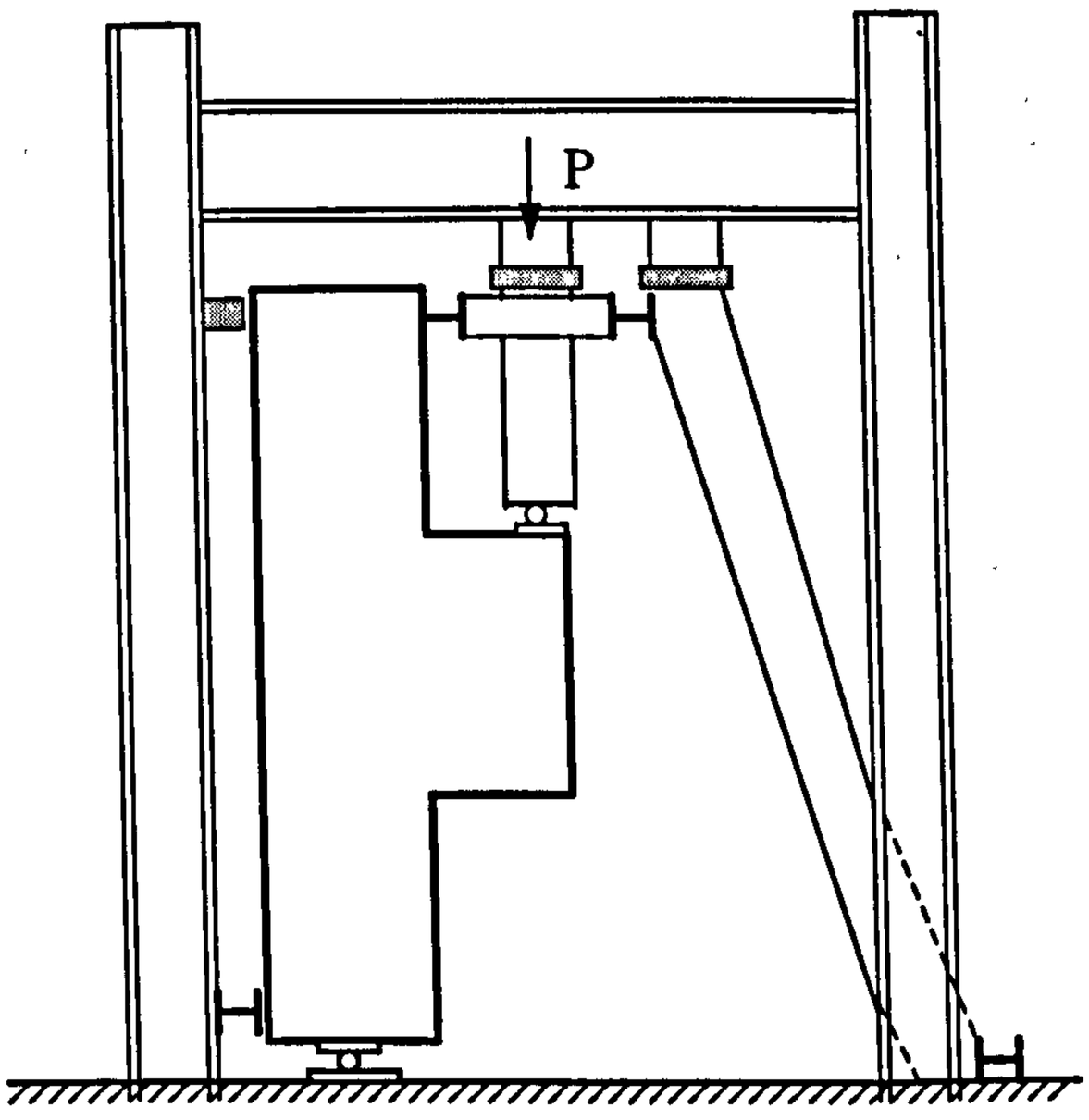

fig.5.7.5(b) Test set-up

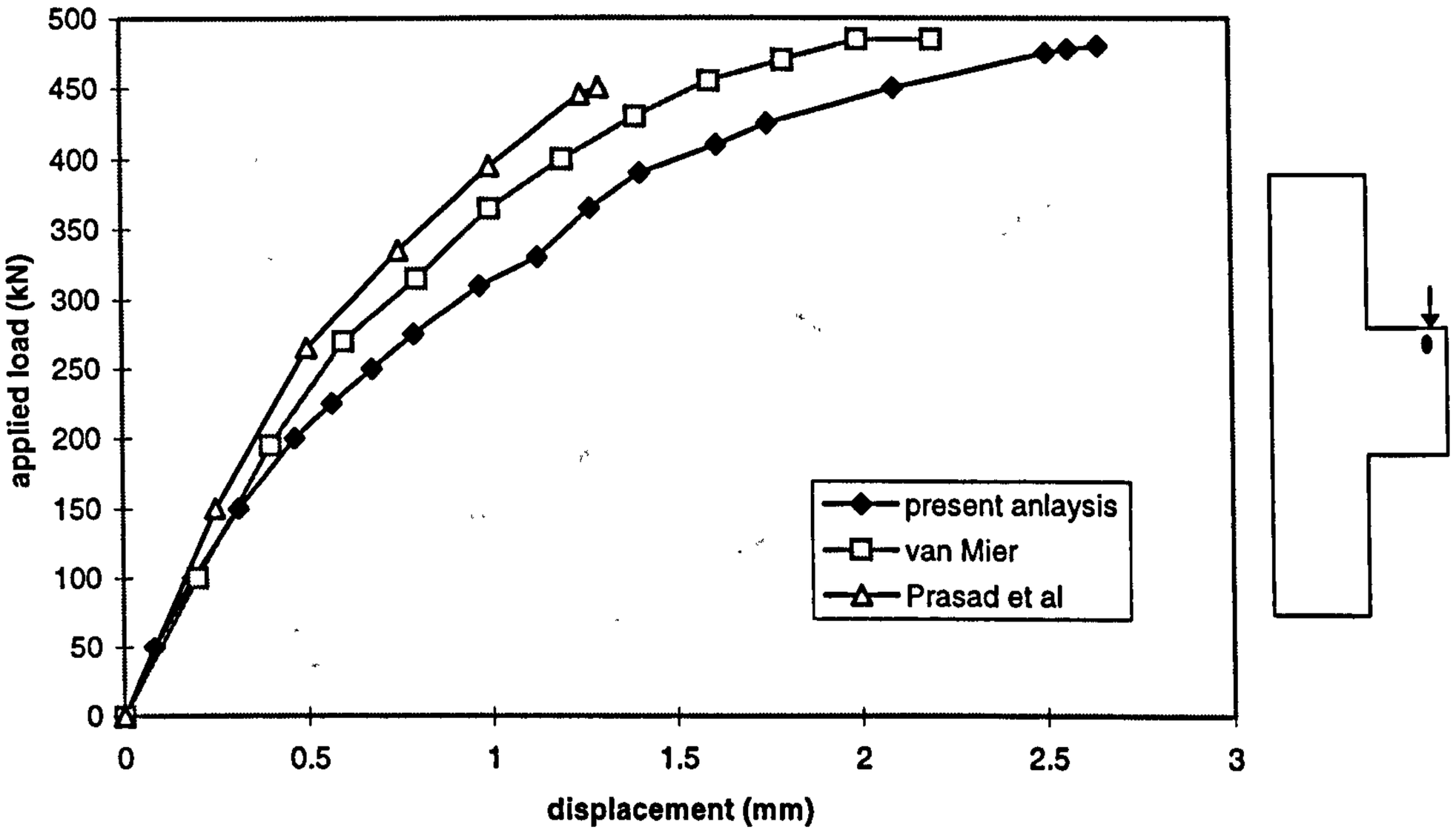

fig.5.7.5(c) Niedenhoff Corbel M2/B2 Load-Displacement

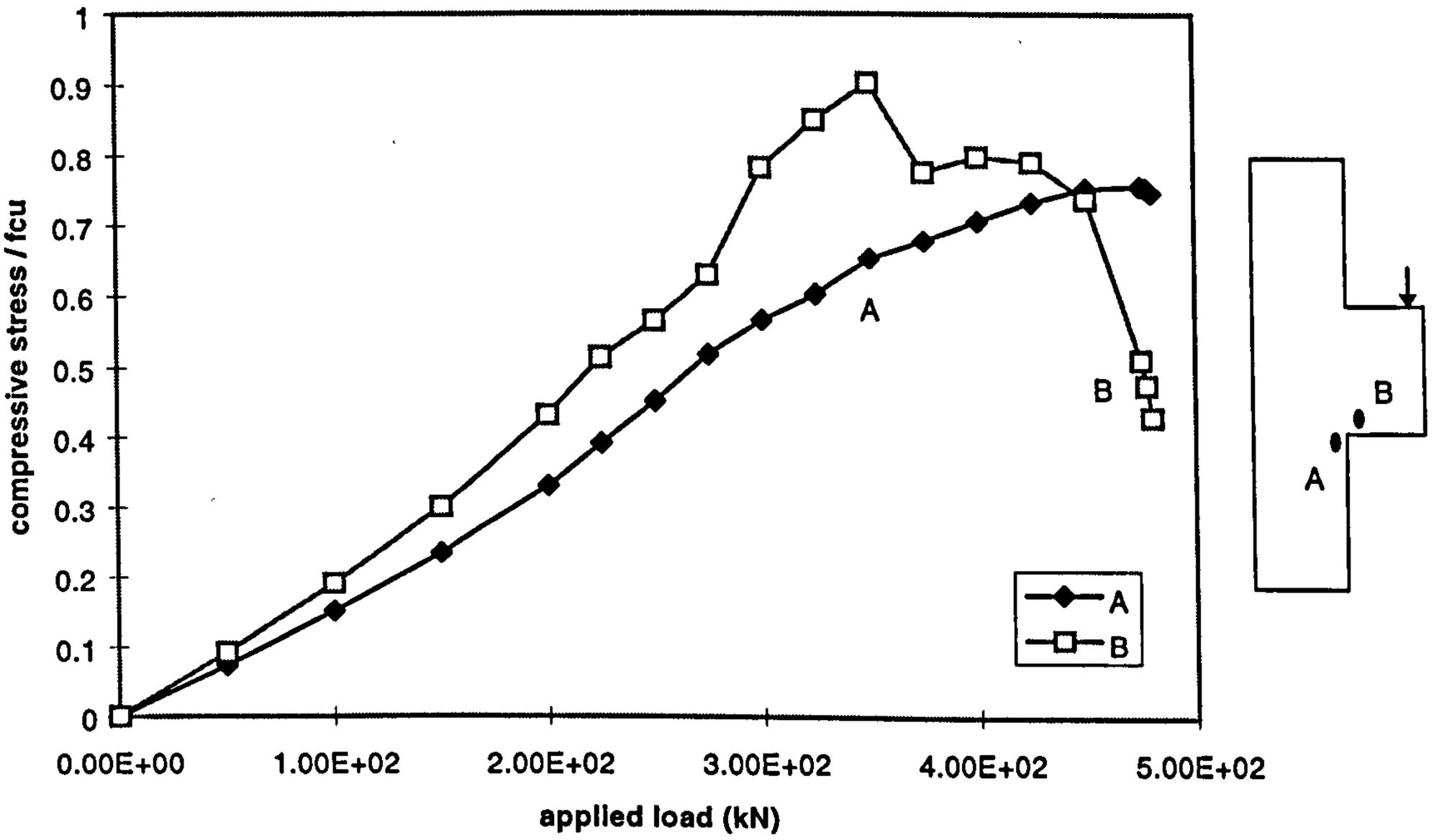

fig5.7.5(d) Niedenhoff Corbel M2/B2 Concrete Stresses

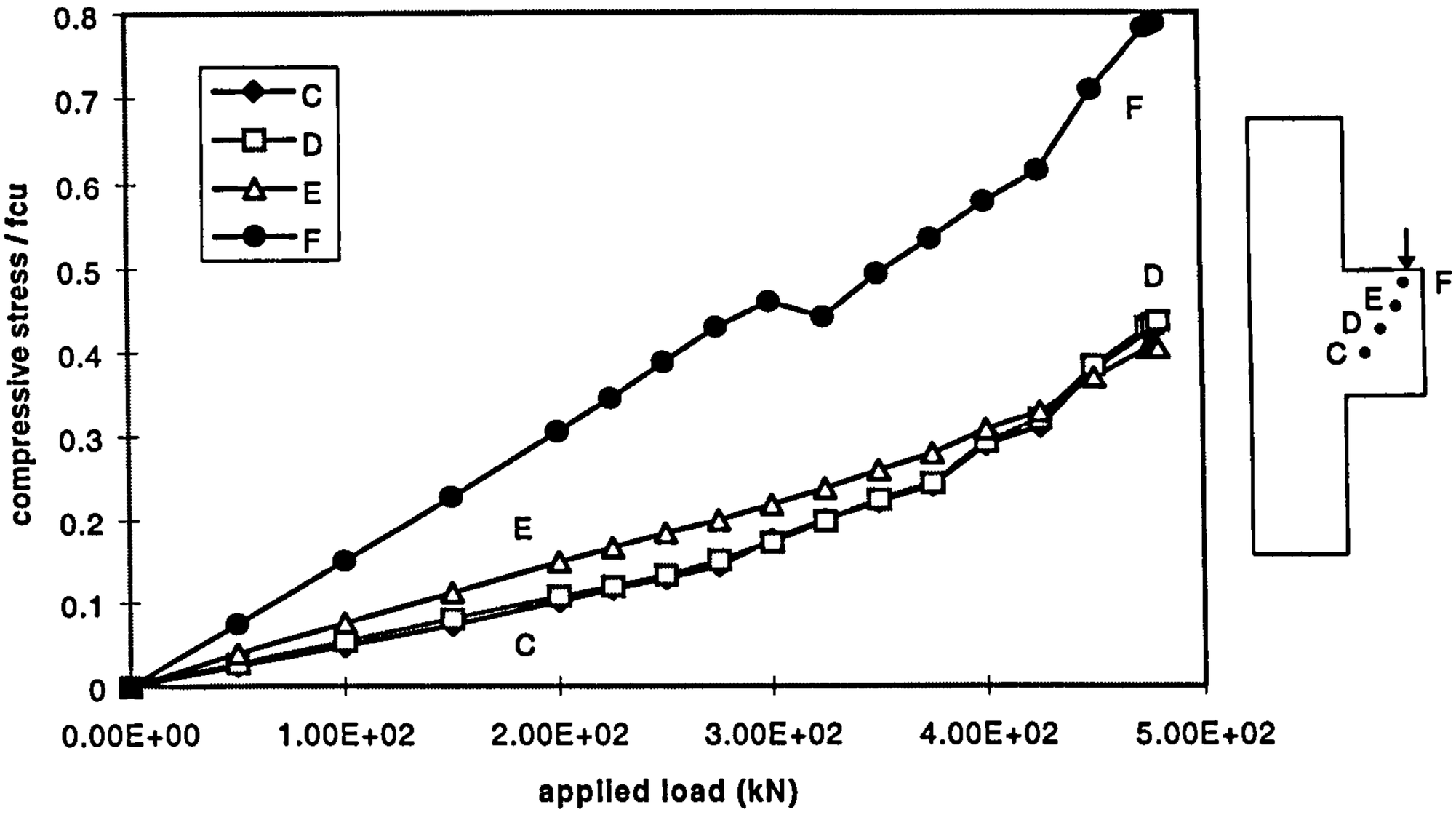

fig.5.7.5(e) Niedenhoff Corbel Concrete Stresses

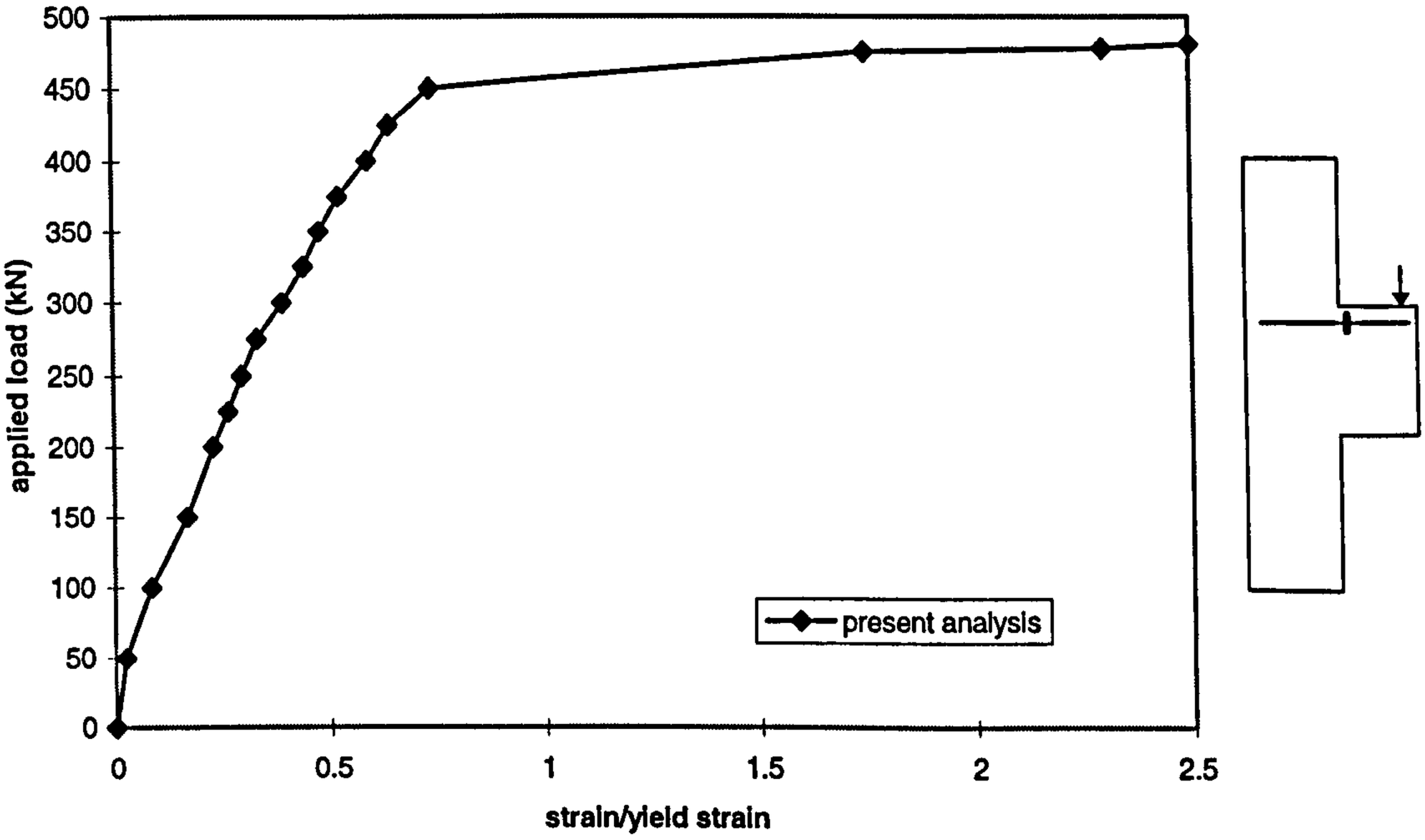

fig.5.7.5(f) Niedenhoff Corbel Main Steel Strains

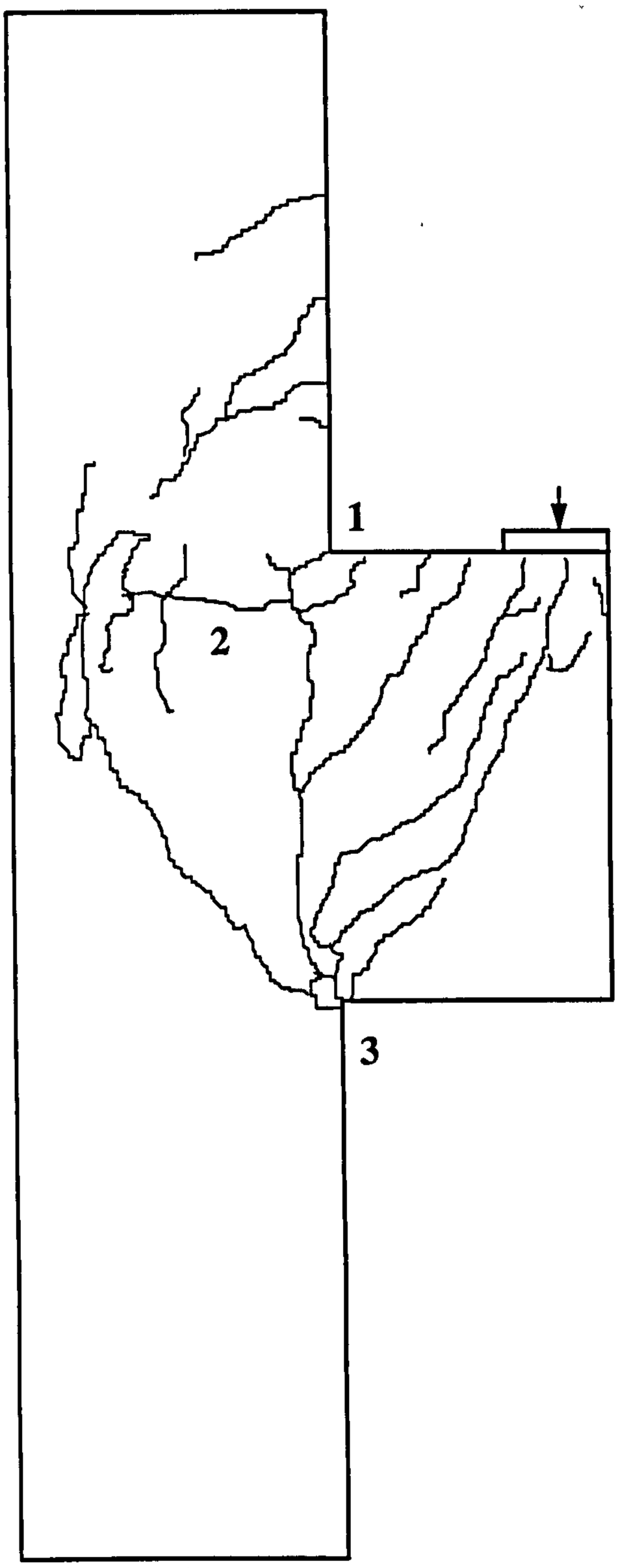

g)

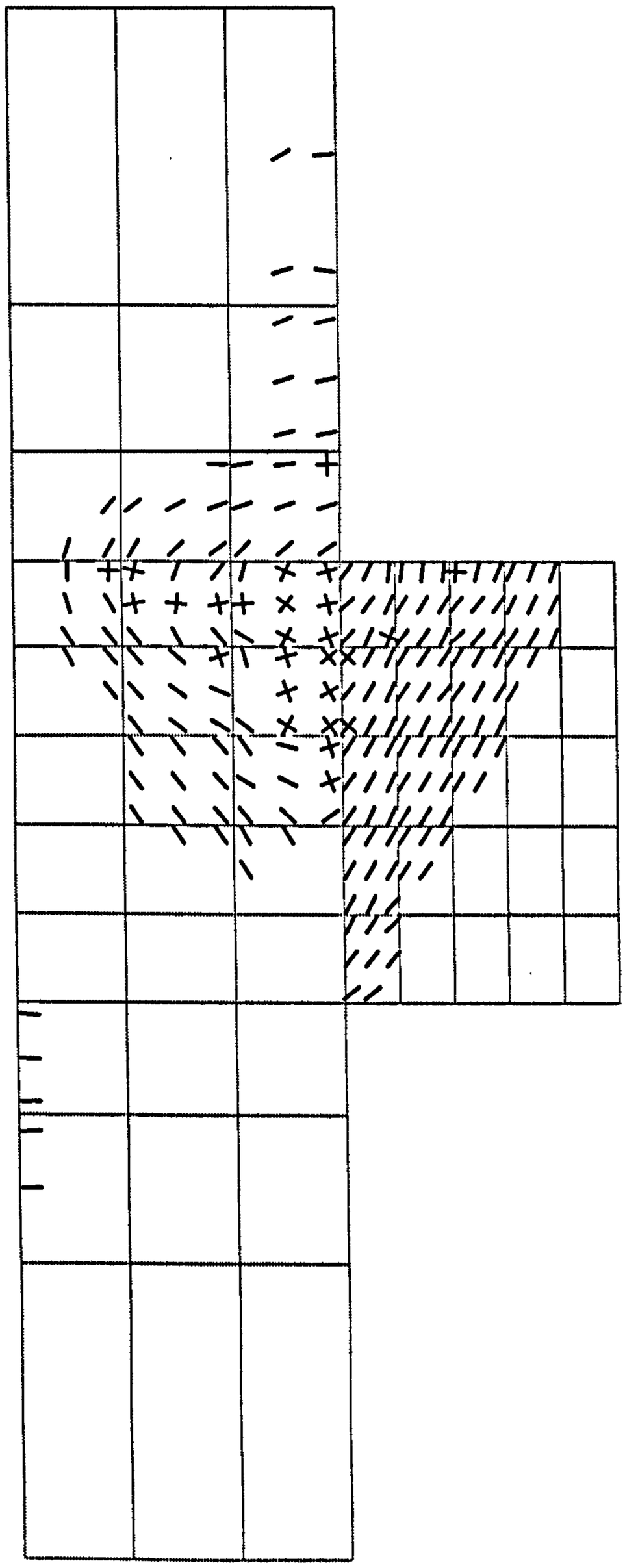

h)

figs.5.7.5(g-h) Niedenhoff Corbel M2/B2:
Comparison between experimental and numerical crack pattern

5.7.6 Frame Tested by Stroband & Kolpa

This model was part of an investigation by Storband & Kolpa (1983) studying in particular the behaviour of beam-column connections in portal frames. Likewise, a numerical study of this structure was carried out in order to test the numerical model's adequacy in predicting beam-column connection behaviour. Previous numerical analysis of this model was carried out by van Mier (1987) and Ranjbaran (1991). Work carried out by a number of researchers e.g Swann (1970), has shown that contrary to common assumption, the strength of the corner joints in portal frame structures is often less than that of the connecting members. The present model, frame A7, was tested under a negative or closing moment. Moment in the corner was generated through application of point loads in the middle thirds of the beam. The overall dimensions of frame A7 together with reinforcement details are given in fig 5.7.6(a). Material properties are presented in the table below:

Concrete Properties	Steel Properties
$E_c = 28000\ N/mm^2$	$E_s = 210000\ N/mm^2$
$f_{cu} = 26\ N/mm^2$	$f_y = 450\ N/mm^2$
$f_t = 2.1\ N/mm^2$	$\nu = 0.2$
$\nu = 0.2$	

Table 5.7.6: Stroband & Kolpa Frame

For numerical analysis, a symmetrical half of the fame was modelled. At the corner of the frame where stress concentration occurs, the mesh was refined, elsewhere in the columns and beams a coarser mesh was adopted. The curved reinforcement in the corner was modelled by dividing the arc into three equal lengths joined by successive bars, each turning 30^o in order to give an approximate radius. Van Mier (1987) analysed this model using an increased value of f_{cu} (37.5 N/mm^2) for the elements directly surrounding the inner corner of the frame. It was believed that a three-dimensional stress state would develop at the inner corner and hence a larger compressive strength in this region would result. For the present analysis, this was ignored since, although tri-axial stress may occur in very wide frames such as

retaining walls, tanks etc, the frame was only 70 mm thick and hence the generation of tri-axial stresses was believed to be negligible.

In the present analysis the frame was analysed using displacement control (chapter 4) which allowed unloading part of the load-displacement relationship to be obtained. The experimental load-displacement curve together with those obtained numerically in the present analysis and by van Mier are shown in fig 5.7.6(b). It can be seen that a good agreement between the experimental and the numerical response was achieved. During the analysis, first cracking was observed at a total load P_t=4kN. A significant increase in cracking was observed as Pt increased from 16-18 kN. This cracking caused redistribution of the stresses in the corner. The principal stress plots (fig 5.7.6(f-g)) during this stage show that increased compressive stresses form along the diagonal from the inner to outer edge. In the experiment, tensile stresses perpendicular to the reinforcement at the bend cause splitting. Significant compressive stress concentration can be observed in the inner corner at the beam column junction from the stress plots. The concrete stresses around this point are shown in figure 5.7.6(c). The stresses were calculated at the Gauss points (gp), with each gp numbered clockwise from the bottom. It can be seen that crushing of the concrete at the inner corner, in a state of bi-axial stress, occurs at a load level of 26kN. This event is accompanied by yielding of the steel in the outer face of the column near the corner at a load of 28kN (fig 5.7.6(e)). All these events were preceded by yielding of the main tension steel at mid-span at a load level of 24kN (fig 5.7.6(d)).

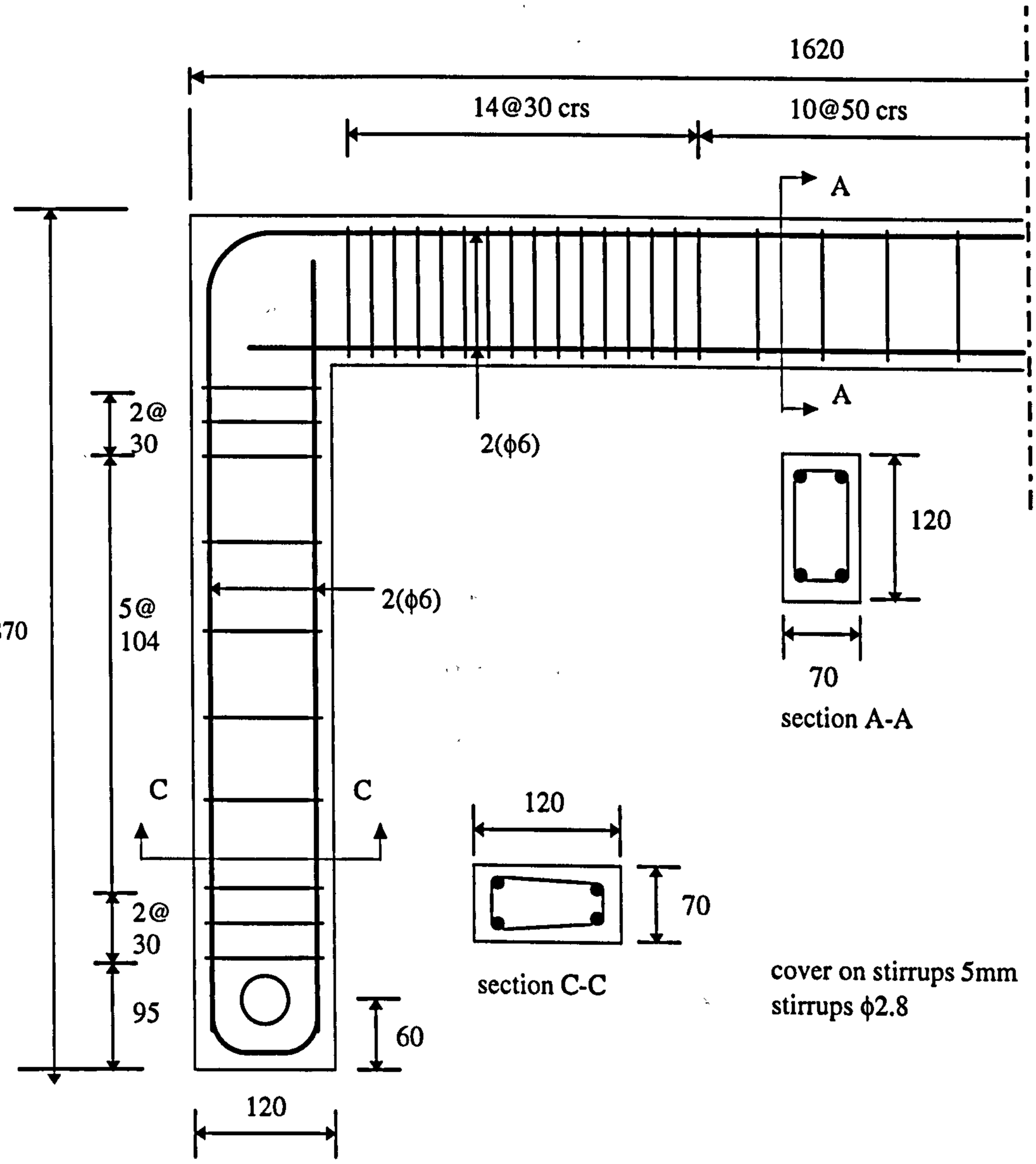

fig.5.7.6(a) Frame tested by Stroband and Kolpa

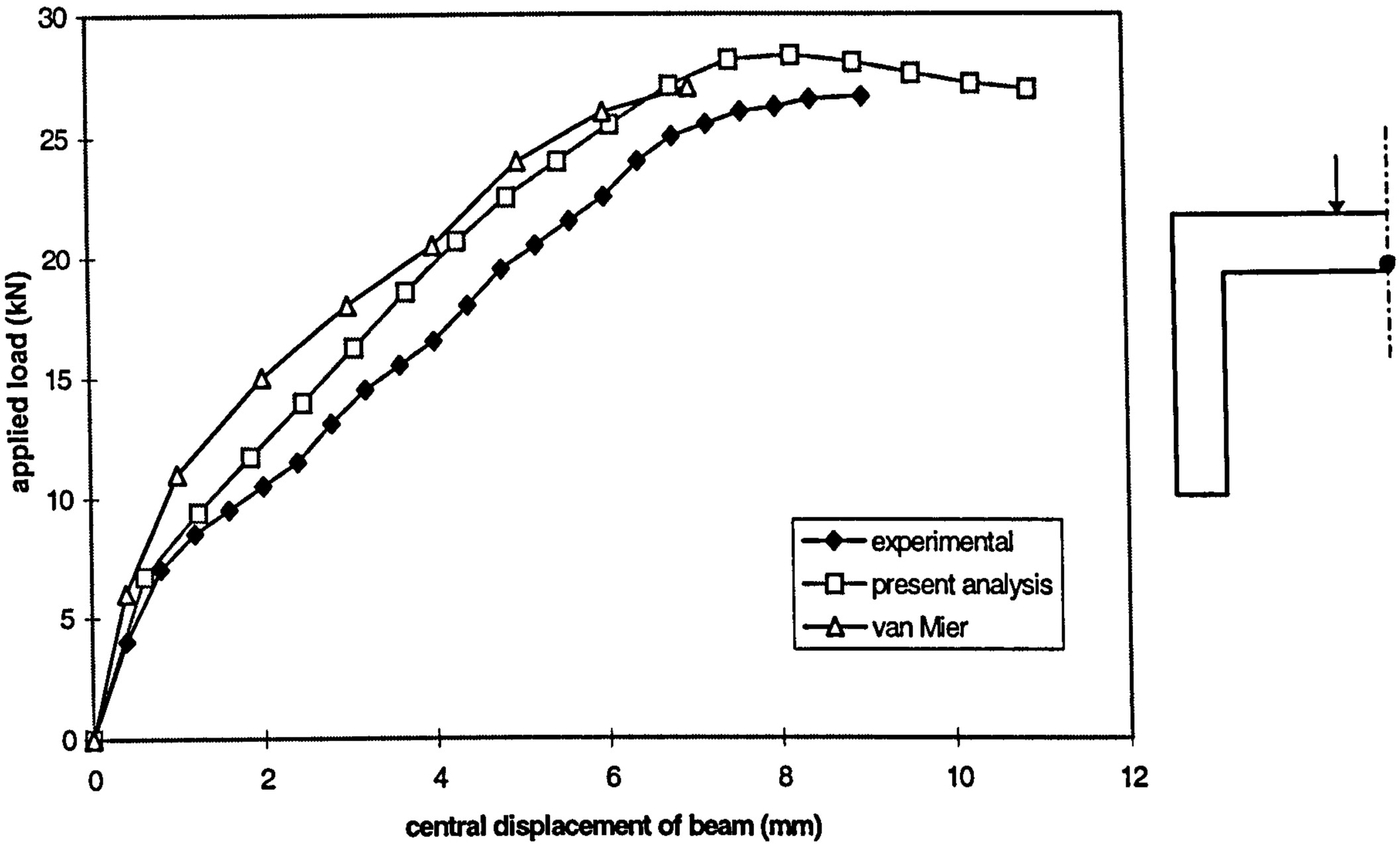

fig.5.7.6(b) Frame A7 tested by Stroband & Kolpa; Load-displacement relationship

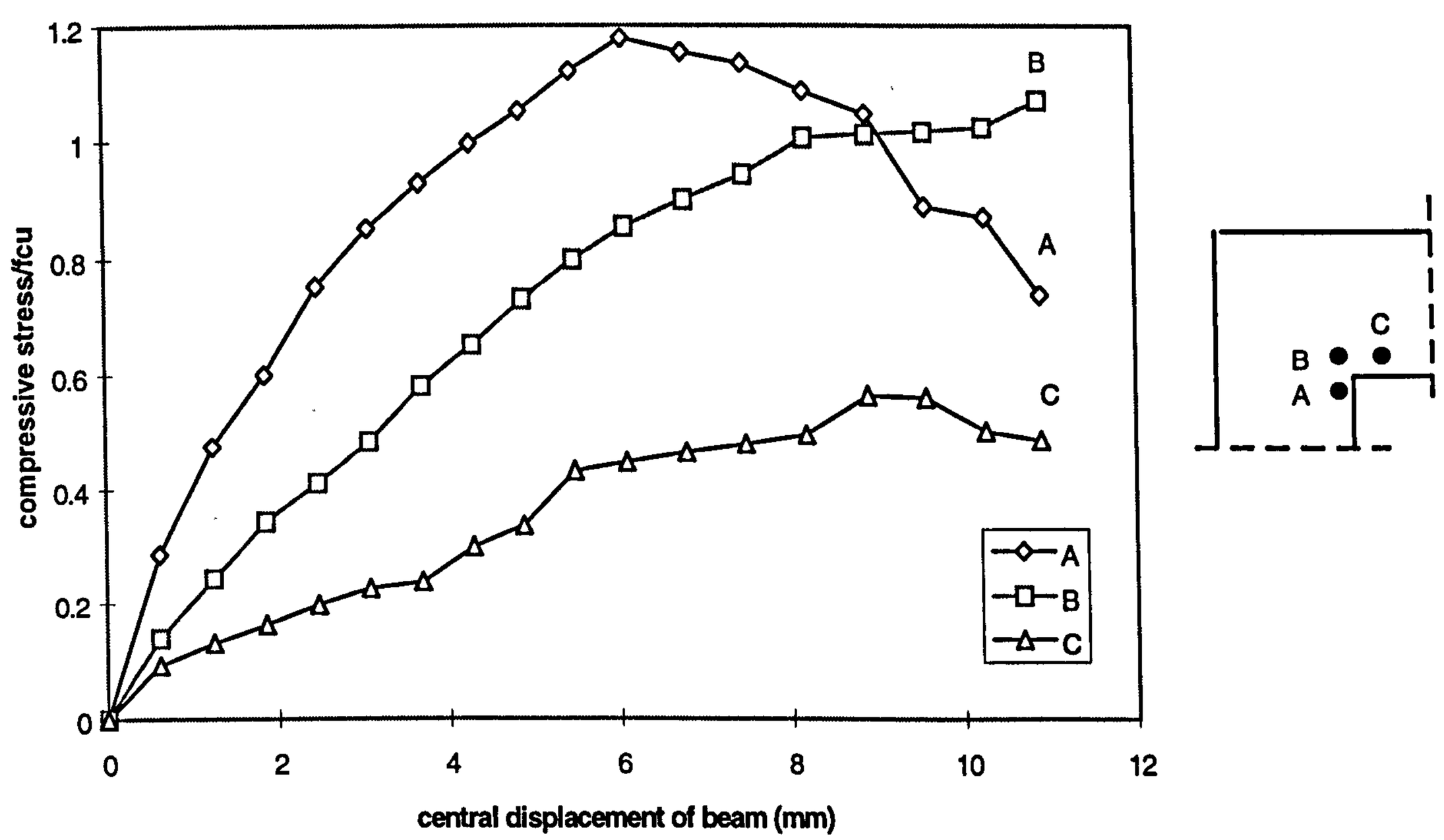

fig.5.7.6(c) Frame A7 tested by Stroband & Kolpa; Concrete stresses at inner corner

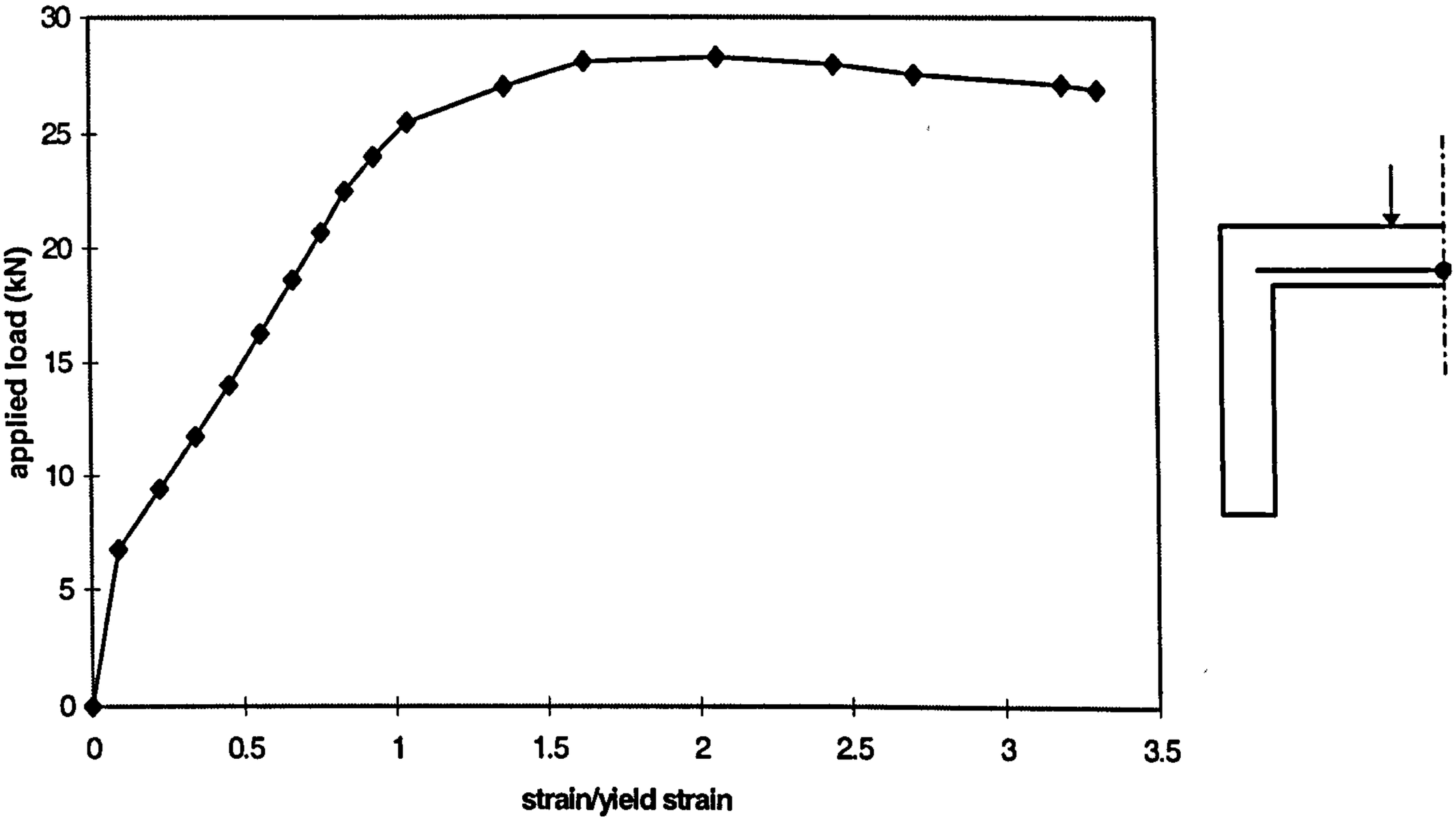

fig.5.7.6(d) Frame A7 tested by Stroband & Kolpa: Main steel in beam at mid-span

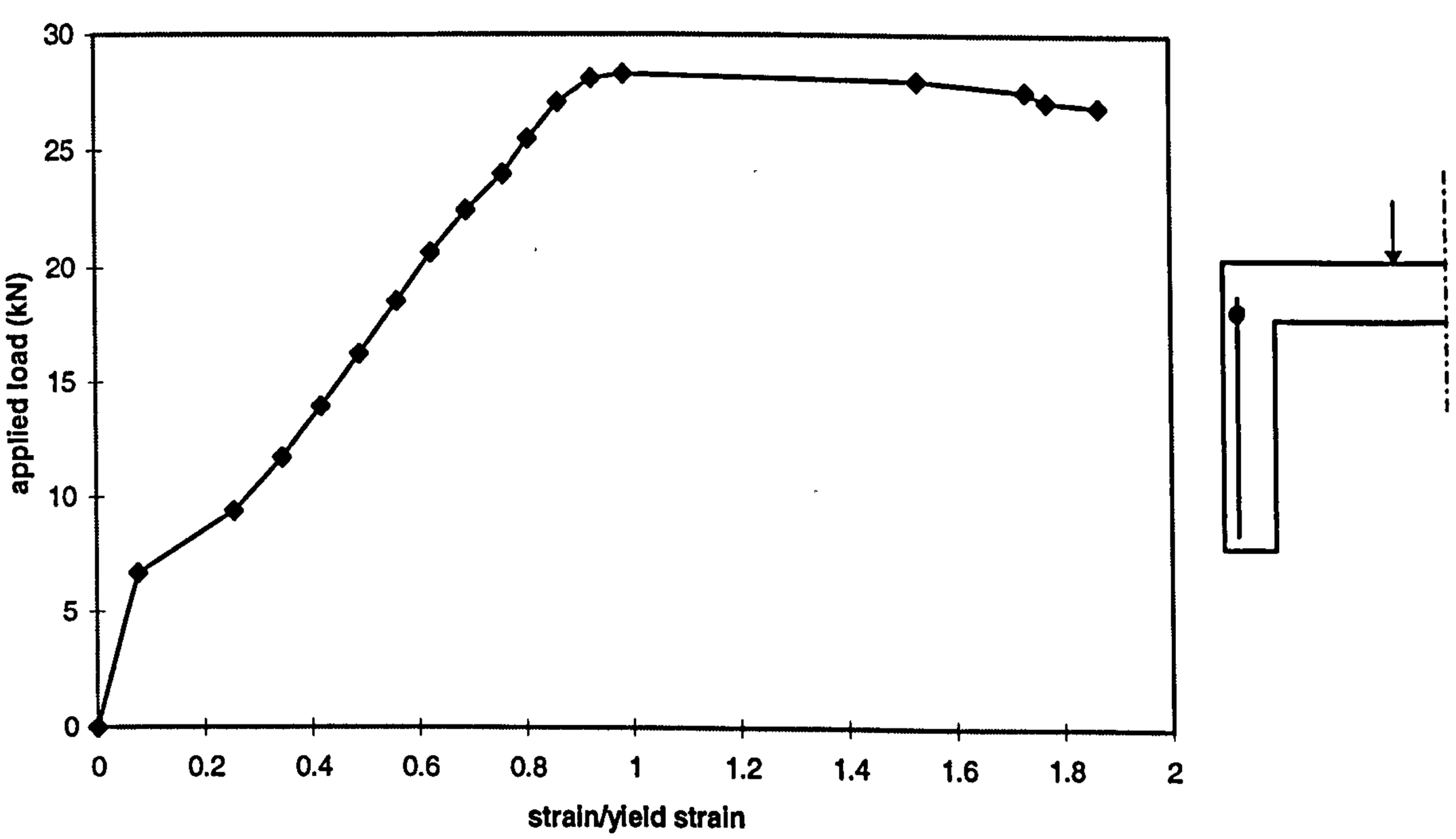

fig.5.7.6(e) Frame A7 tested by Stroband & Kolpa. Steel in outerface of column

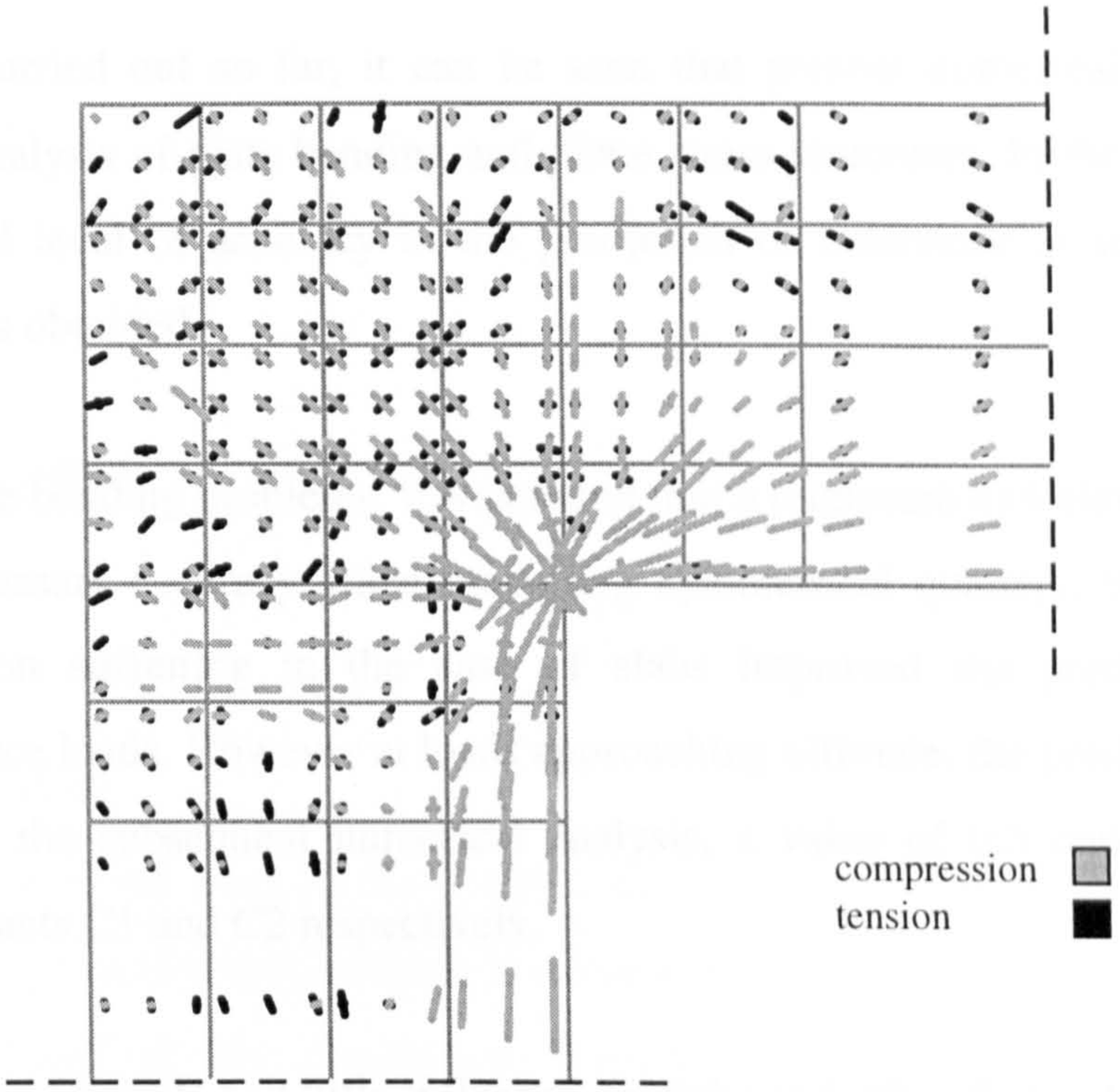

fig.5.7.6(f) Principal Stresses in Corner (P=16kN)

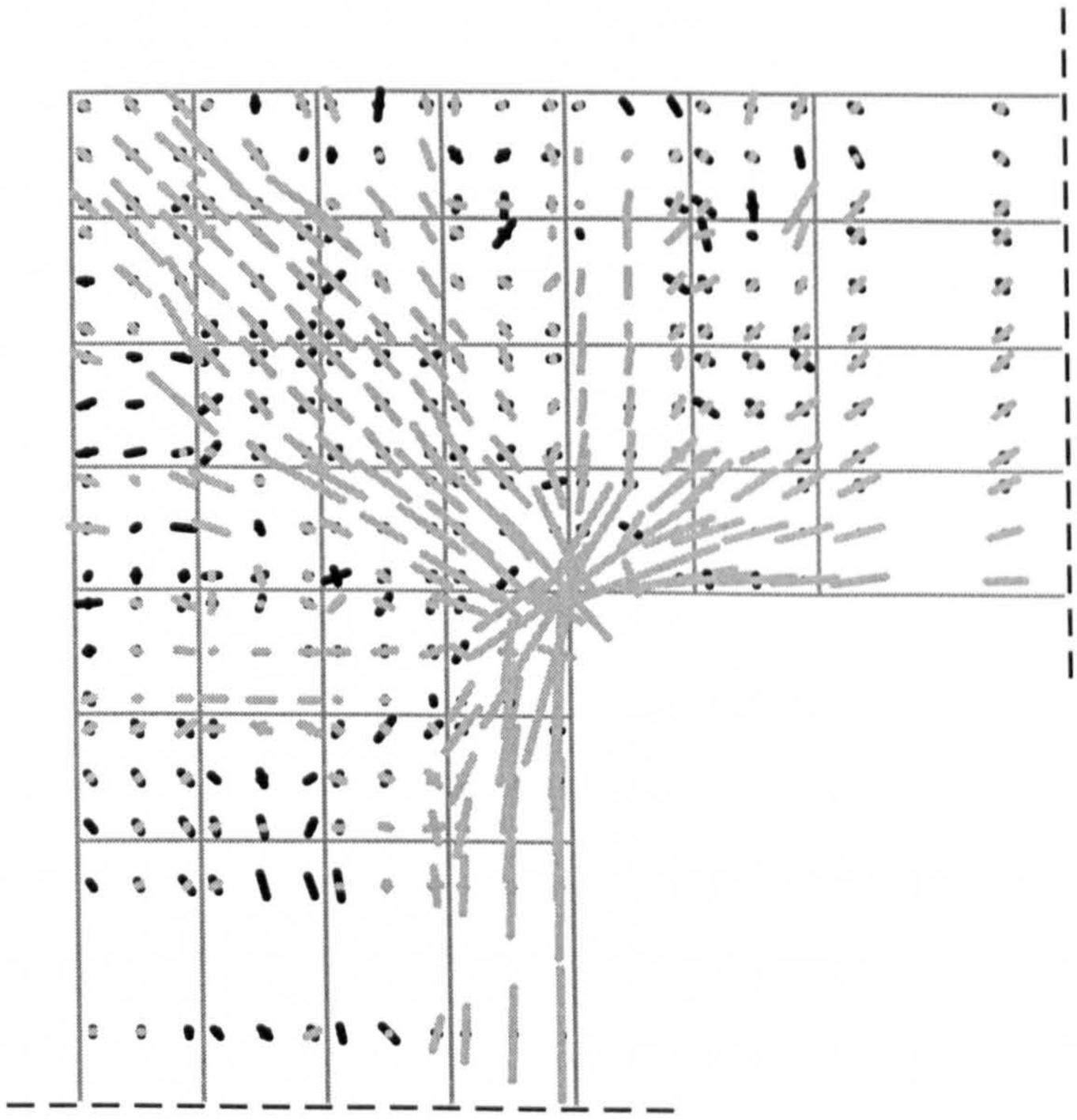

fig.5.7.6(g) Principal stresses in Corner (P=18kN)

5.8 Conclusions

From the work carried out so far, it can be seen that present numerical model is suitable for the analysis of plate bending and plane stress structures. In the examples discussed, a good level of accuracy in the prediction of behaviour at service and ultimate loads was obtained.

In the case of plate bending problems, it was found that a minimum 4x4 element mesh provided the necessary accuracy when modelling symmetrical quarters. It was also found that tension stiffening in the case of slabs improved the predictions of behaviour at service loads. However at loads approaching ultimate, the predictions are often stiffer. For the subsequent numerical analysis, a value of 0.5 and 10.0 was adopted for constants C1 and C2 respectively.

The shear retention factor B had little influence on slabs and other flexural structures. However, in the case of shear transfer members such as deep beams and corbels, low values of B, <0.1, will result in under-prediction of ultimate load. For subsequent analysis, a value of 0.4 was adopted for B.

Chapter 6

Slab Design

6.1 Introduction

The main objective of the work in this chapter was to assess the applicability of the visualisation process in deriving suitable reinforcement layouts for various types of slabs. The suitability of the reinforcing layouts is assessed in terms of the serviceability behaviour and ductility demand of the slab.

This chapter details the design and numerical analysis of 7 different types of slabs. Two slabs were simply supported, one was simply supported with a central column support, the fourth type was supported on four corners and the last type was simply supported on adjacent corners with a column support at the opposite corner. Details of the geometry and support conditions are given in table 6.1(a). Loading arrangements, design load P_d and material properties are given later. The thickness of each slab was chosen in compliance with the limiting span-depth ratios stipulated in BS8110 Part 1.

The direct design approach, described in chapter 3, was used to derive the reinforcement layouts. For slabs SM1-5, a design derived from the required numerical steel areas at (rr=0) and using the mesh evolved at the subsequent (rr) was made. The effect of using the evolved mesh on the reinforcement layout was investigated. The performance of the two designs was assessed and compared in numerical analysis. Since direct design for the slabs from the evolved mesh involves a redistribution of the stresses from the elastic pattern, it was necessary to compare the two designs and determine the effect of this re-distribution on service behaviour. The ultimate load behaviour was assessed together with service deflections and steel strains. The mid-

span service deflection limit was taken as span/250 (BS 8110). As a means of further assessing serviceability characteristics, yield strain of the steel was recorded. In order to avoid large cracking strains, a minimum load of 0.7 P_d should be reached before yielding of the main steel occurs. A minimum steel ratio of 0.13% as stipulated in BS8110 was also adopted. In the resulting steel layouts, anchorage lengths were ignored.

Slab Model	Schematic	Support conditions	Dimensions (mm)
SM1	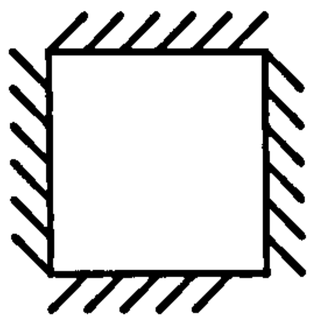	Square simply supported	2140 x 2140 x 100
SM2	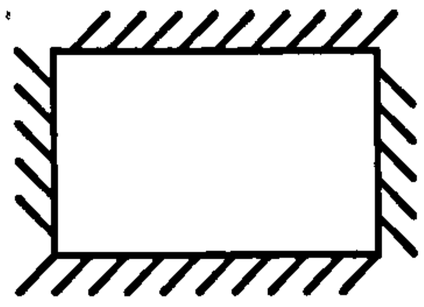	Rectangular simply supported	3140 x 2140 x 100
SM3	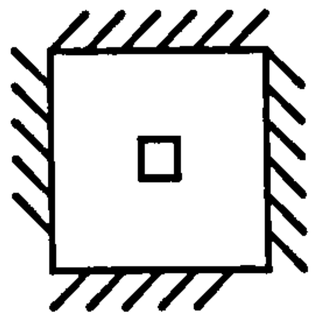	Square simply supported + central column	2140 x 2140 x 100
SM4	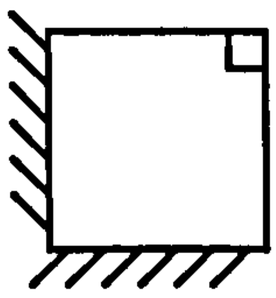	Square simply supported on adjacent sides + column support at opposite corner	2140 x 2140 x100
SM5, 6 & 7	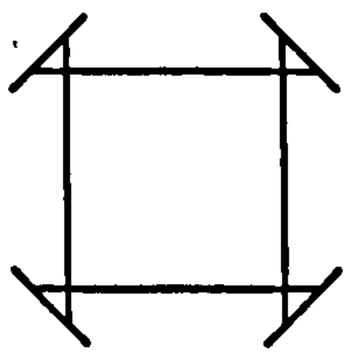	Square supported on four corners	910 x 910 x 45

Table 6.1(a): Slab Details

6.2 Effect of Mesh Size on Visualisation

Since the direct design of the reinforcement is dependent upon the stress distribution, it was necessary to assess the effect of using different mesh sizes upon the stress distribution and direct design process. To facilitate this study, three slabs with very

different moment distributions were chosen from the program; SM1, SM3 and SM5. It is necessary that the mesh density is fine enough to detail adequately the stress variation within the slab, however as the mesh density increases, the computational time increases.

The visualisation process was carried out on each slab using a symmetrical quarter discretised into a mesh of 5x5, 7x7 and 10x10 elements. The ultimate rejection ratio for each mesh size was compared along with the corresponding numerical steel volumes. The results from the comparative study are given in table 6.2. The principal moments, plotted for illustration in vector form, for each mesh size are detailed in figures 6.2.2-6.2.4. In the principal moment plots, black lines indicate negative moments, while grey lines represent positive moments.

Slab	**SM1** simply supported			**SM3** simply supported + central column			**SM5** supported on four corners		
Mesh size	5x5	7x7	10x10	5x5	7x7	10x10	5x5	7x7	10x10
Rejection ratio (rr)	40%	40%	30%	30%	30%	30%	15%	12%	10%
% area 'removed'	16%	24%	12%	48%	53%	66%	48%	57%	70%
Vol. of steel calculated cm^3	1148	1151	1112	473.7	481.1	431.8	50.2	53.5	75.9

Table 6.2 Effect of Mesh Size

Firstly, it can be observed that the rejection ratio needed to achieve a certain % area 'removal' is different for each slab. When comparing slabs SM1 and SM5, for any chosen mesh size, the ultimate rejection ratio decreases while the percentage area removed increases. This is due to the fact that the stresses are much more evenly distributed throughout the simply supported slab than in the slab supported on four corners. The average VonMises stress for each element of the 7x7 mesh is shown in figure 6.2.1 for each slab type at rr=0. As a measure of the spread of stresses within the slab, the parameter ζ is calculated. This parameter is a measure of how the average vonMises stress in an element, σ_{VMe}, differs from the maximum vonMises stress, σ_{VMmax}, considering all the elements, (N), in the slab.

The following equation defines ζ :

$$\zeta = \left(\sqrt{\frac{\sum (\sigma_{VMe} - \sigma_{VM\,max})^2}{N-1}} \right) \left(\frac{1}{\sigma_{VM\,max}} \right)$$

The closer ζ tends to zero, the less the variation in average vonMises stress from the maximum. The average vonMises stress for each element resulting from a 7x7 element mesh are detailed in fig.6.2.1. The values of ζ were equal to 0.48, 0.65 and 0.70 for slabs SM1, SM3 and SM5 respectively using a 7x7 mesh, at rr=0. Hence it would be expected that given its greater number of lowly stressed elements, a clearly evolved state would be reached at the lowest rr for Slab SM5. From this, it is clear that the visualisation process is only applicable in structures where there is a relatively wide spread of stresses. Values of ζ subsequent to visualisation were calculated as 0.40, 0.54 and 0.70 for slabs SM1, SM3 and SM5 respectively. In the first two slabs the stresses become more evenly distributed, while in the third no change is observed. The lack of change in ζ for the third slab may be attributed to the fact that while the variation in moments becomes less in the majority of the slab, a significant rise in the maximum moment at the corner support occurs, hence preserving the variation co-efficient.

For each slab, the effect of increased mesh density in most cases is to increase the percentage area removed. This is due to the fact that the spread of average elemental vonMises stresses over the mesh are wider than for a rough mesh. The form of the evolved mesh for each mesh size was similar. The resulting numerical steel areas for each mesh size was similar. For this study, a symmetrical quarter of 7x7 elements was used for each mode.

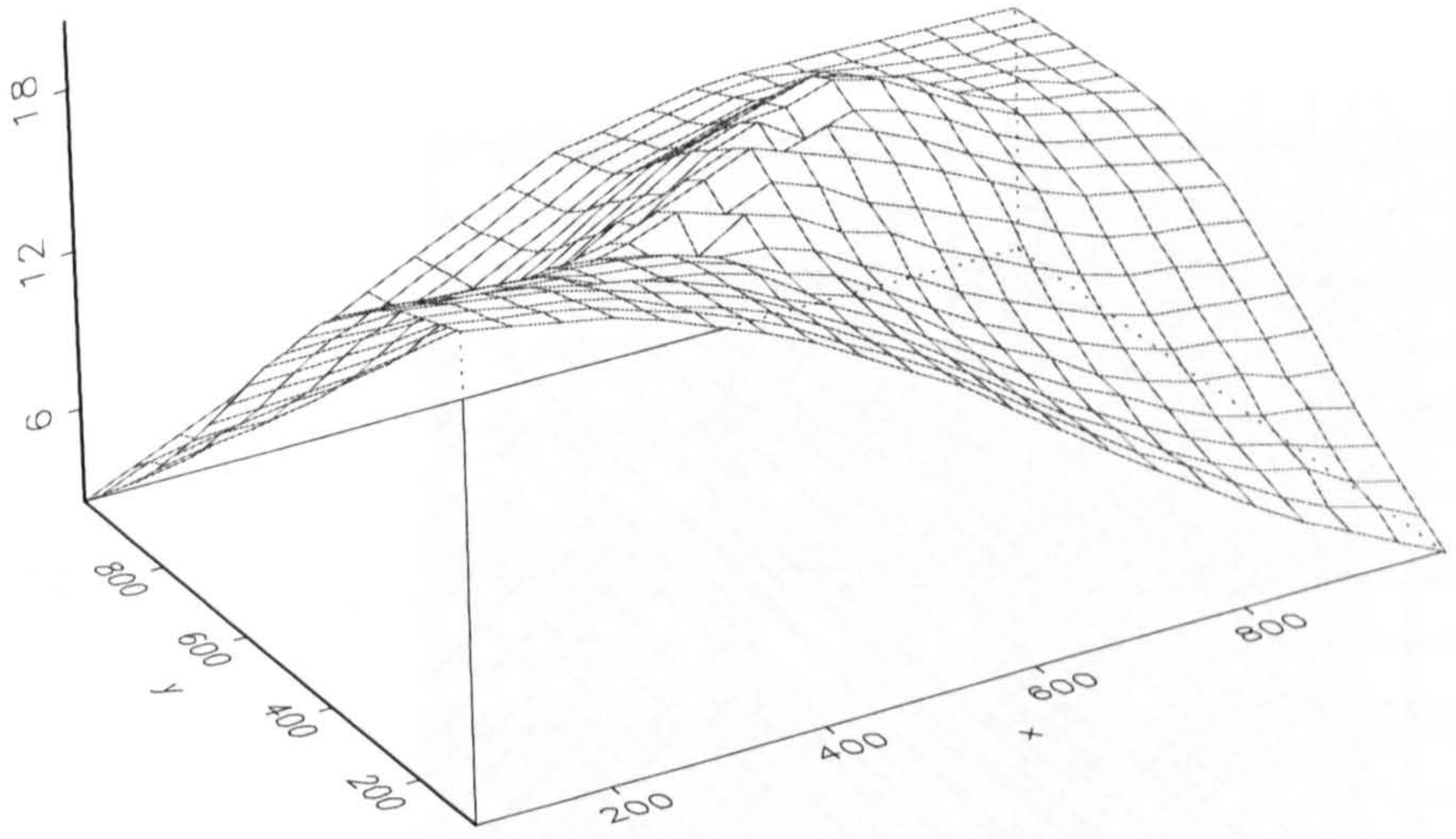

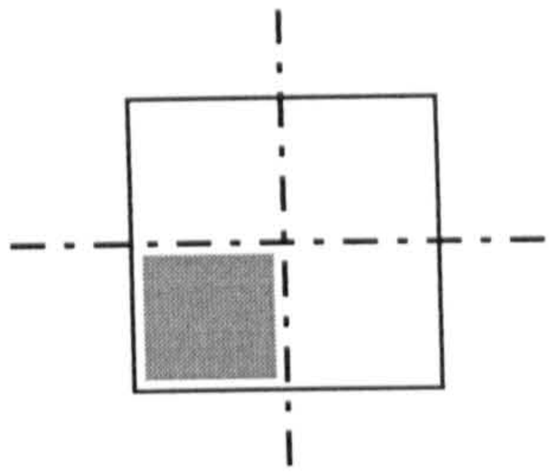

a) Slab SM1
(ζ=0.48)

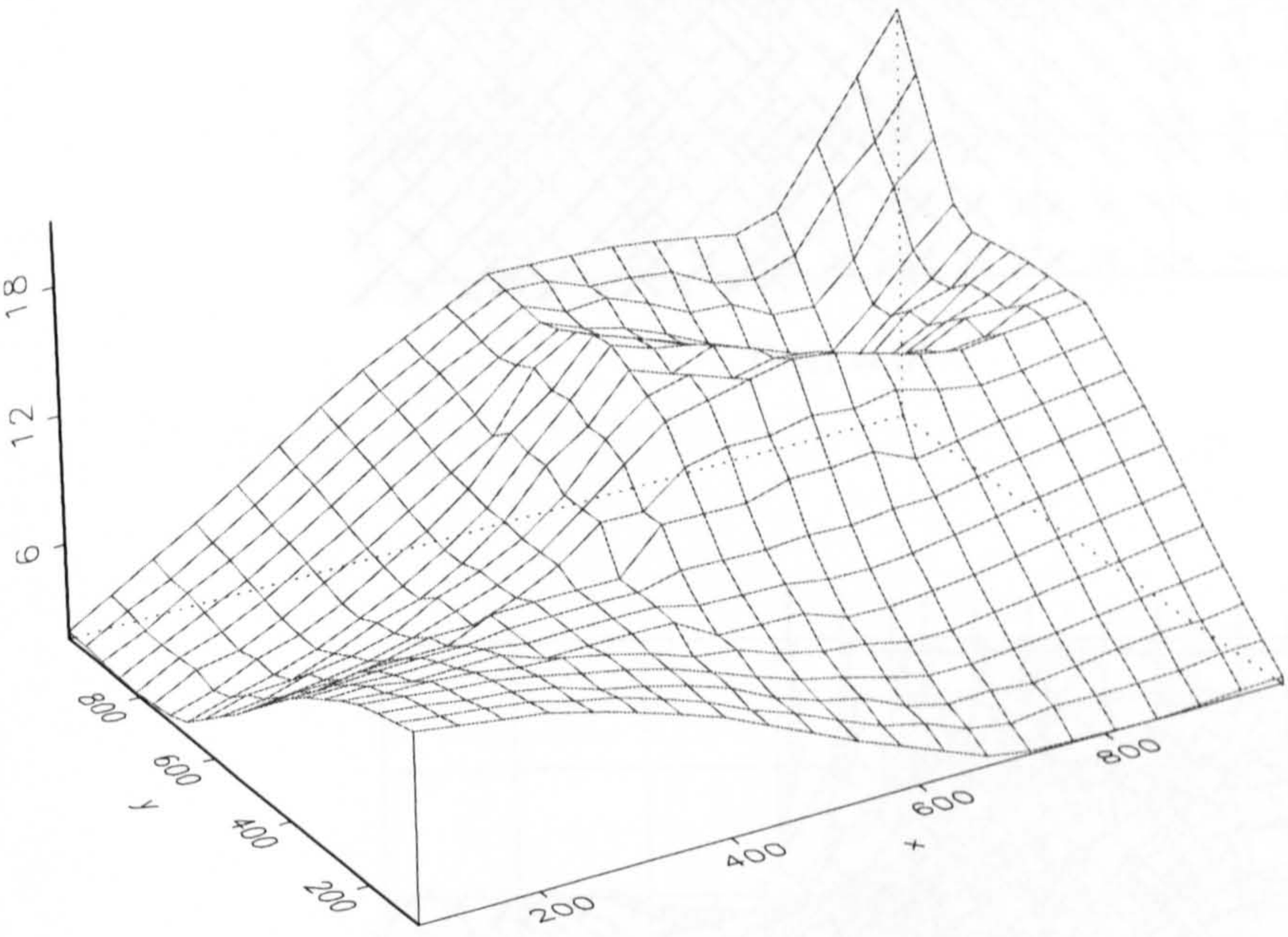

b) Slab SM3
(ζ=0.65)

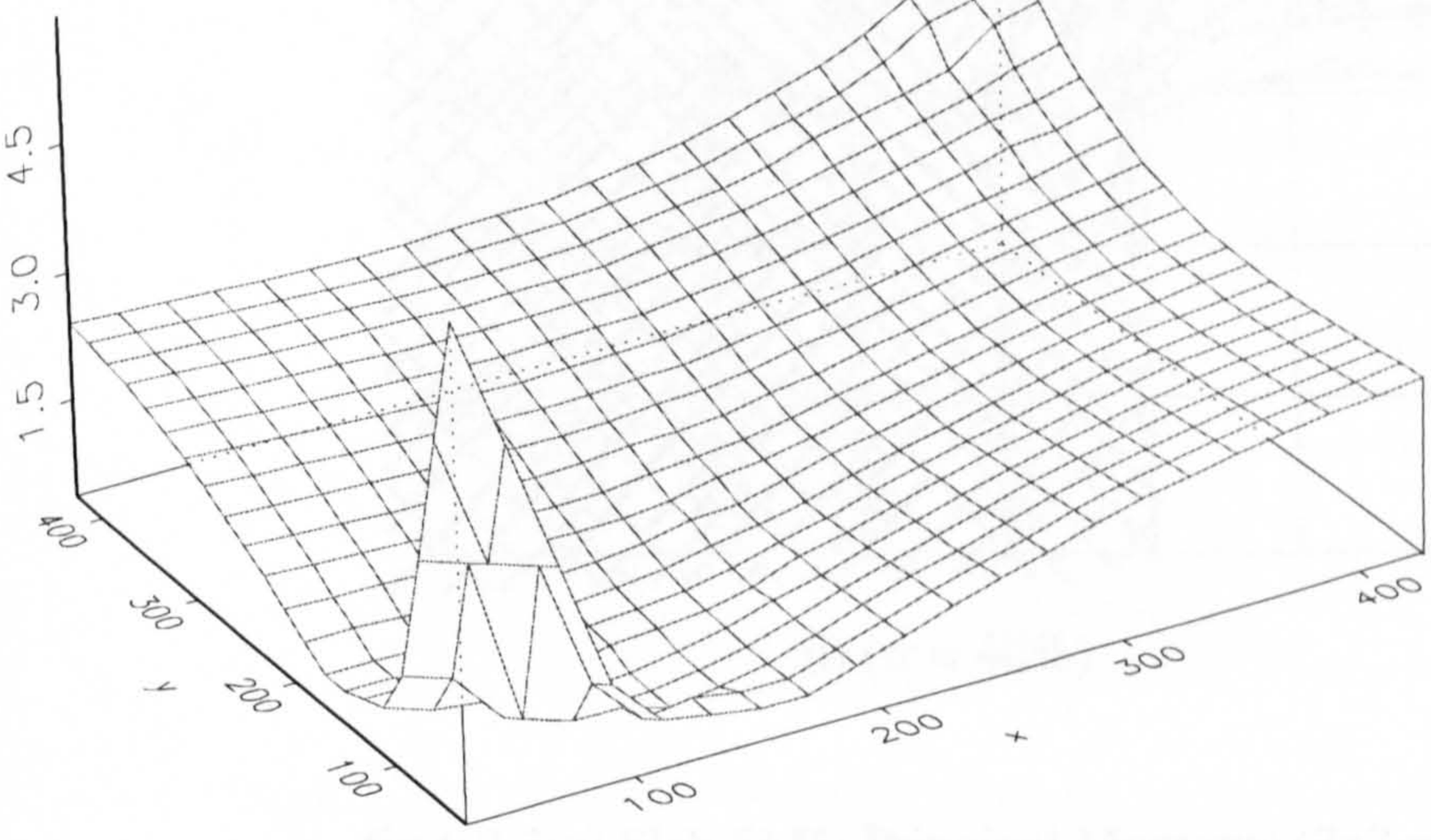

c) Slab SM5
(ζ=0.70)

fig(6.2.1) Average vonMises stress (7x7 elements), at rr=0

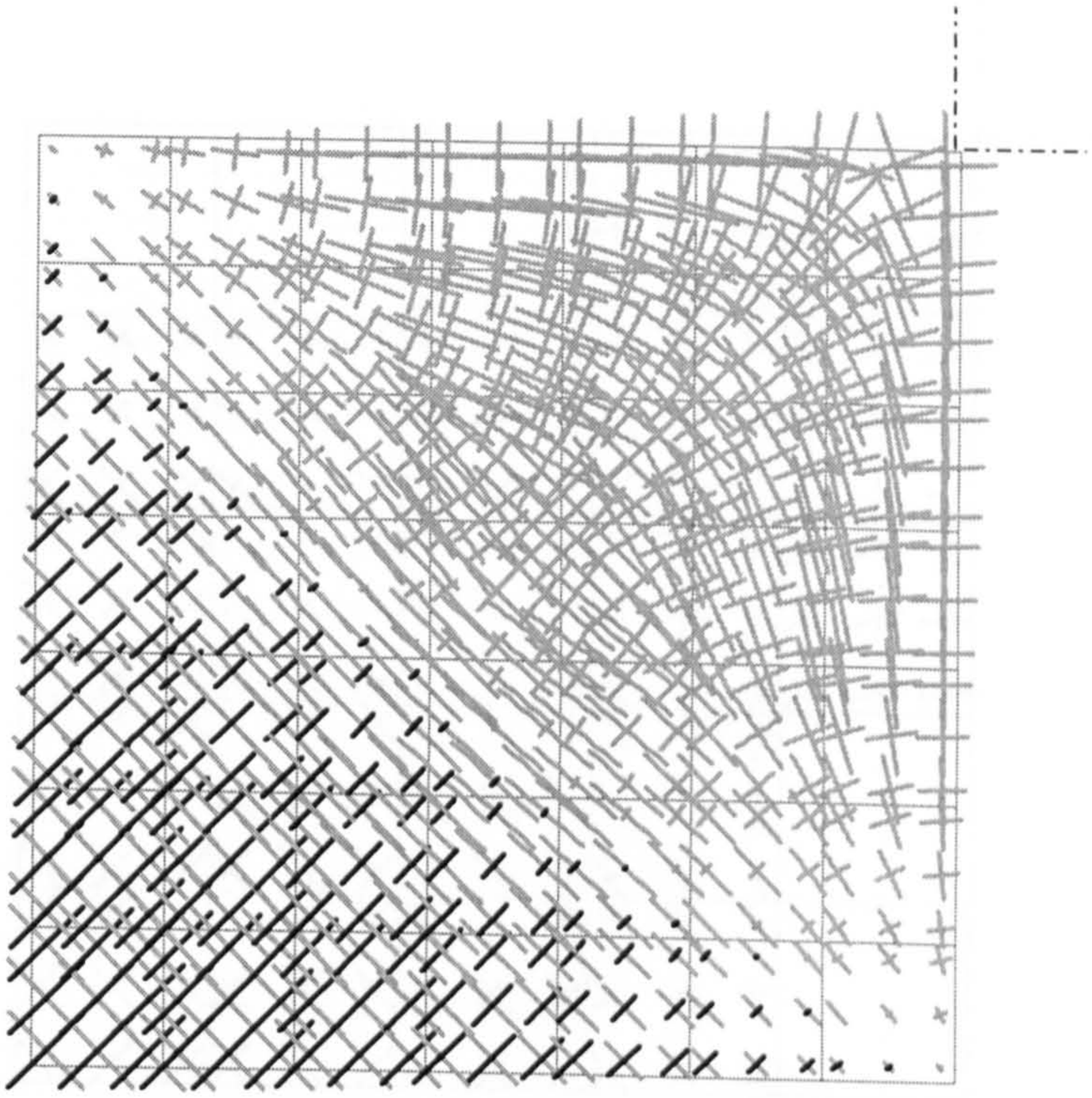

i) (rr = 0)

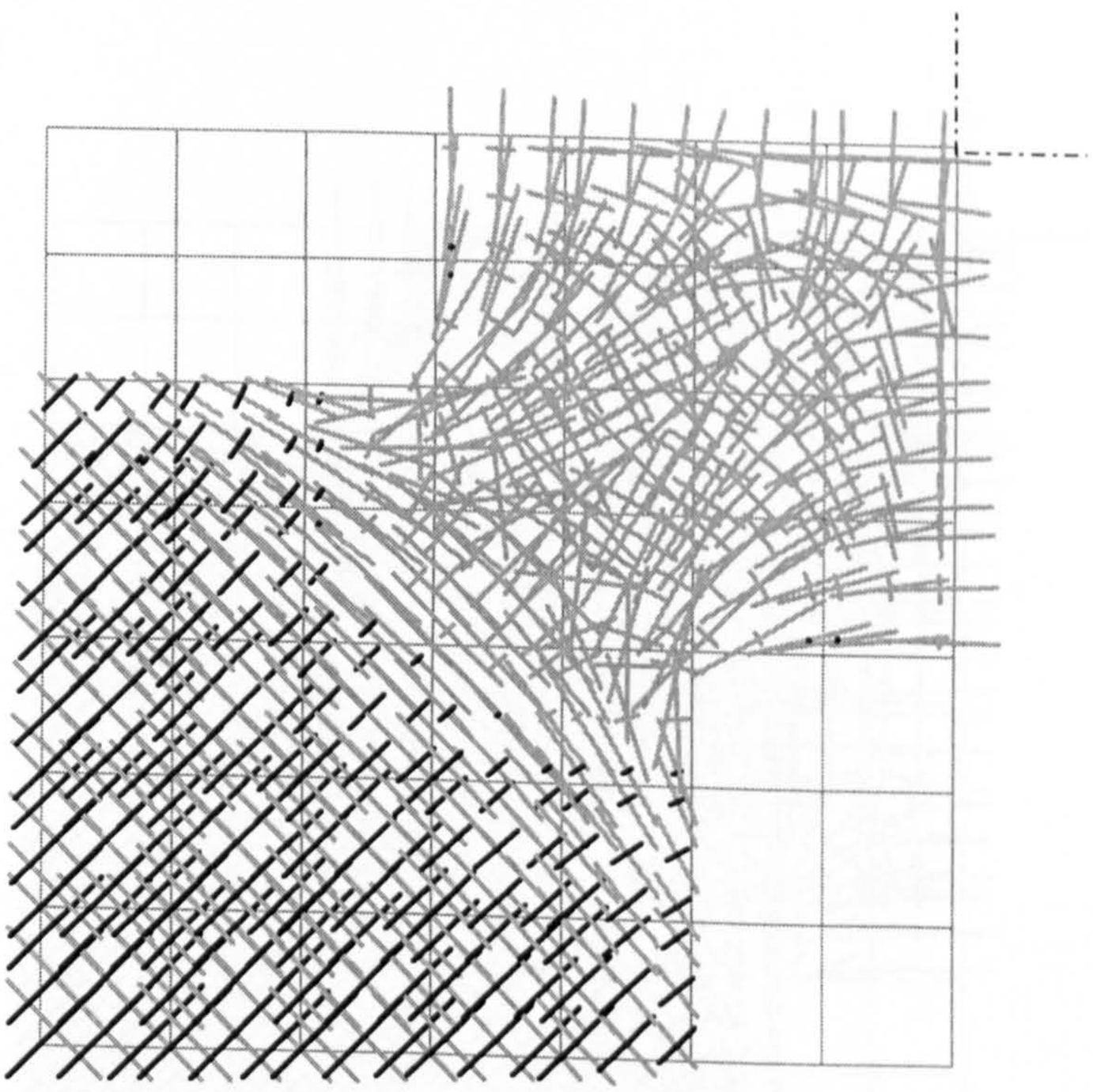

ii) (rr = 40%)

fig.6.2.2(a) Slab SM1: Principal Moments (7x7 mesh)

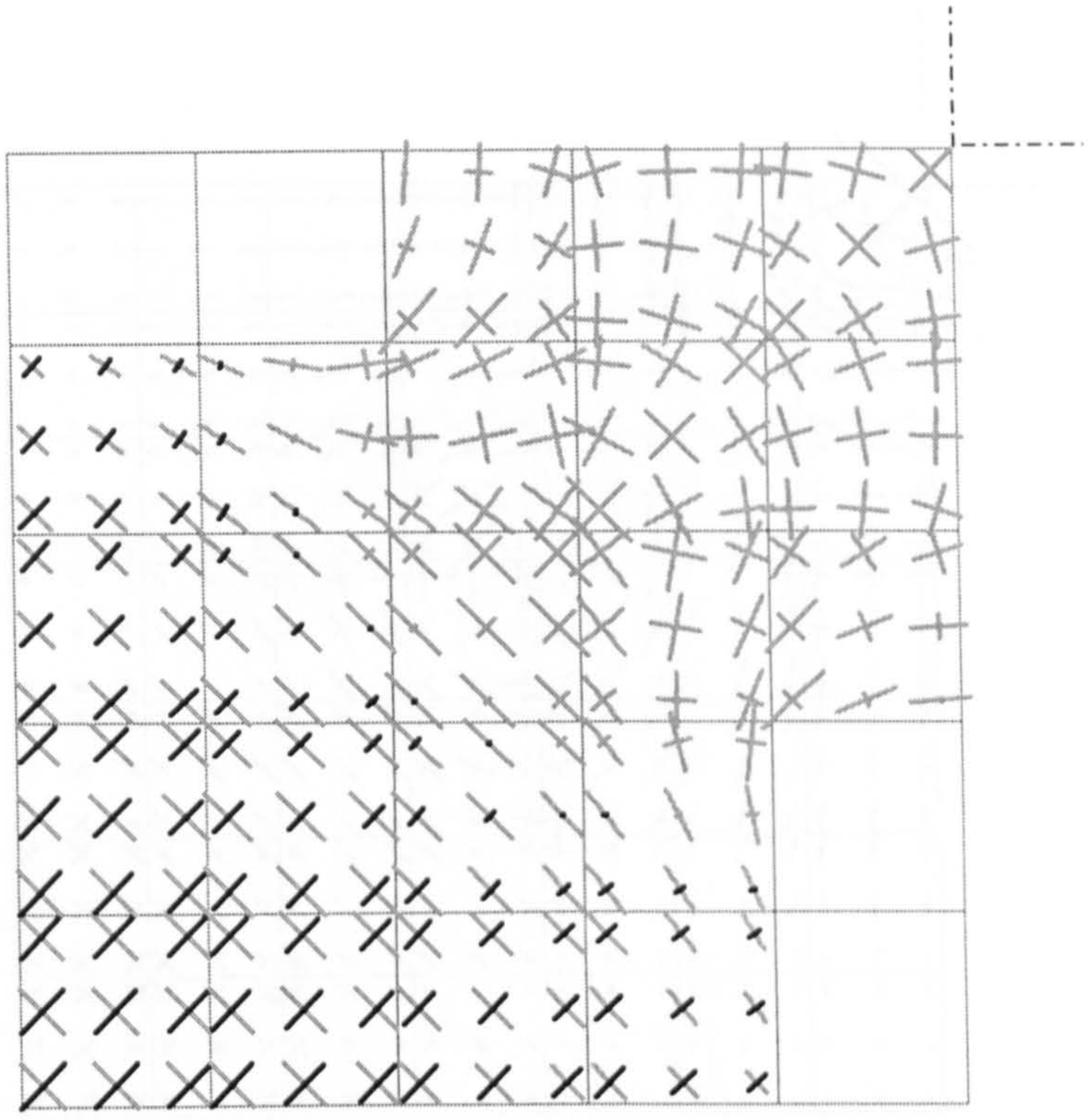

fig.6.2.2(b) Slab SM1 Principal moments, 5x5 mesh, (rr = 40%)

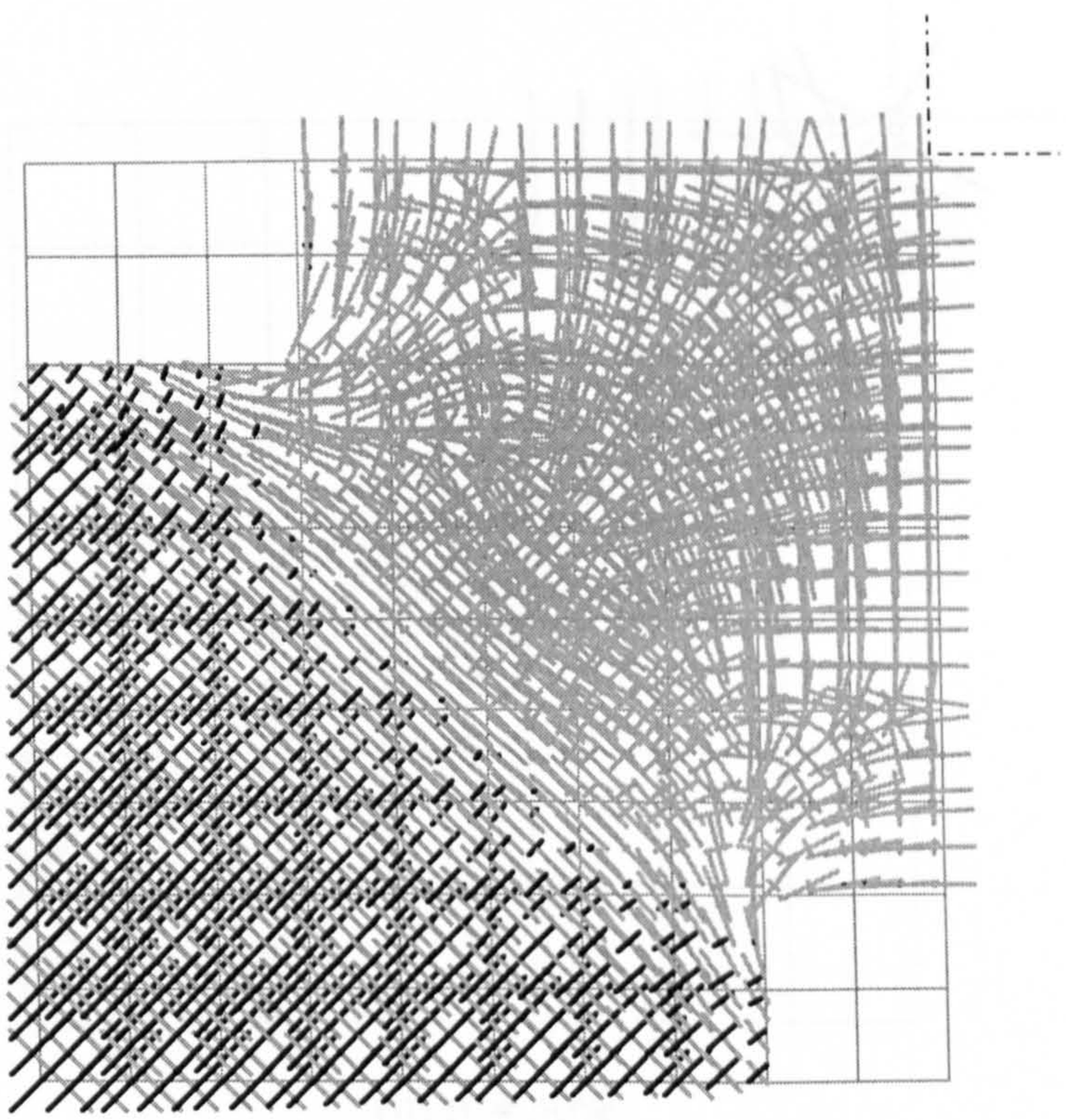

fig.6.2.2(c) Slab SM1 Principal moments, 10x10 mesh, (rr=30%)

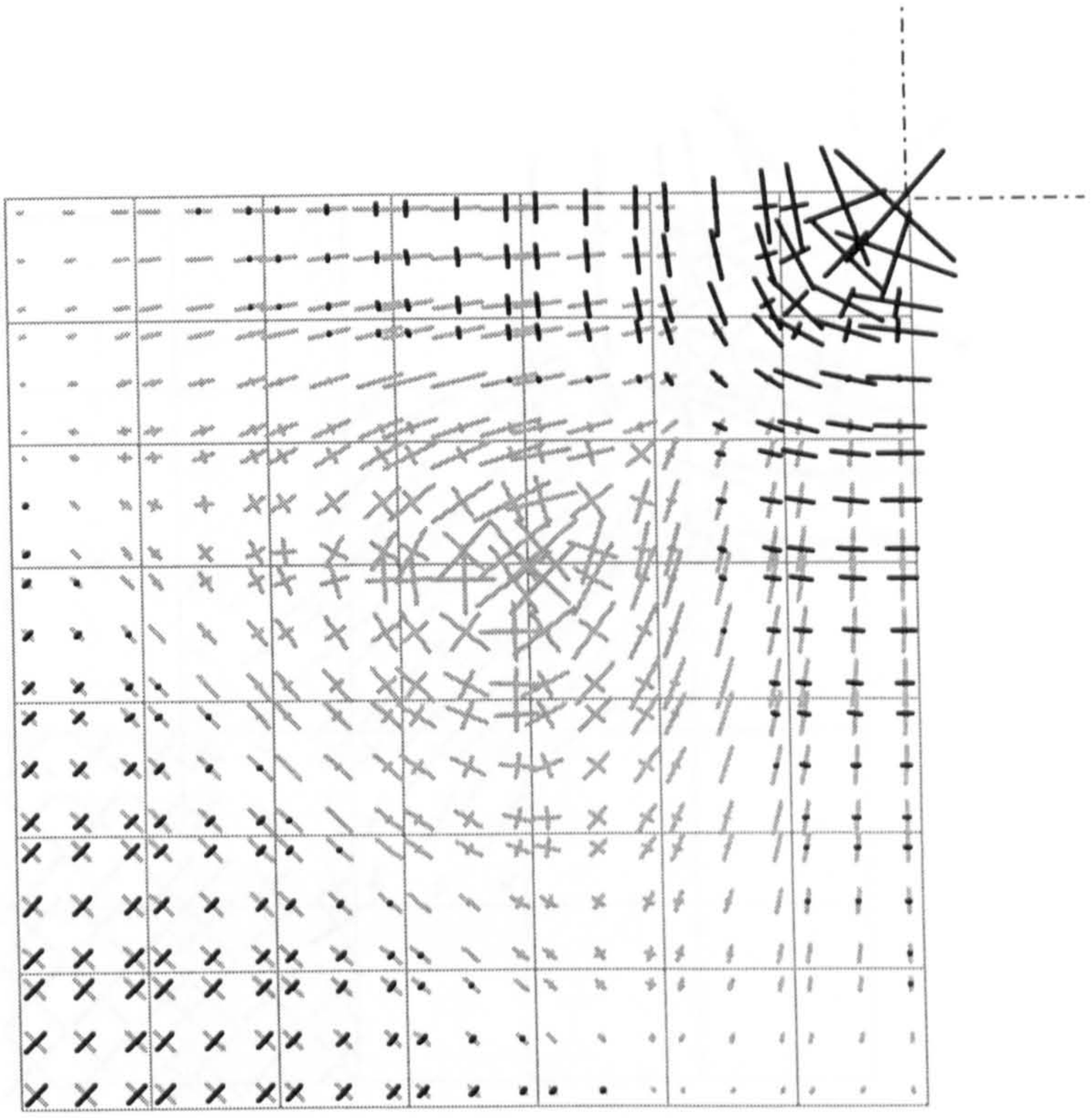

(i) rr = 0

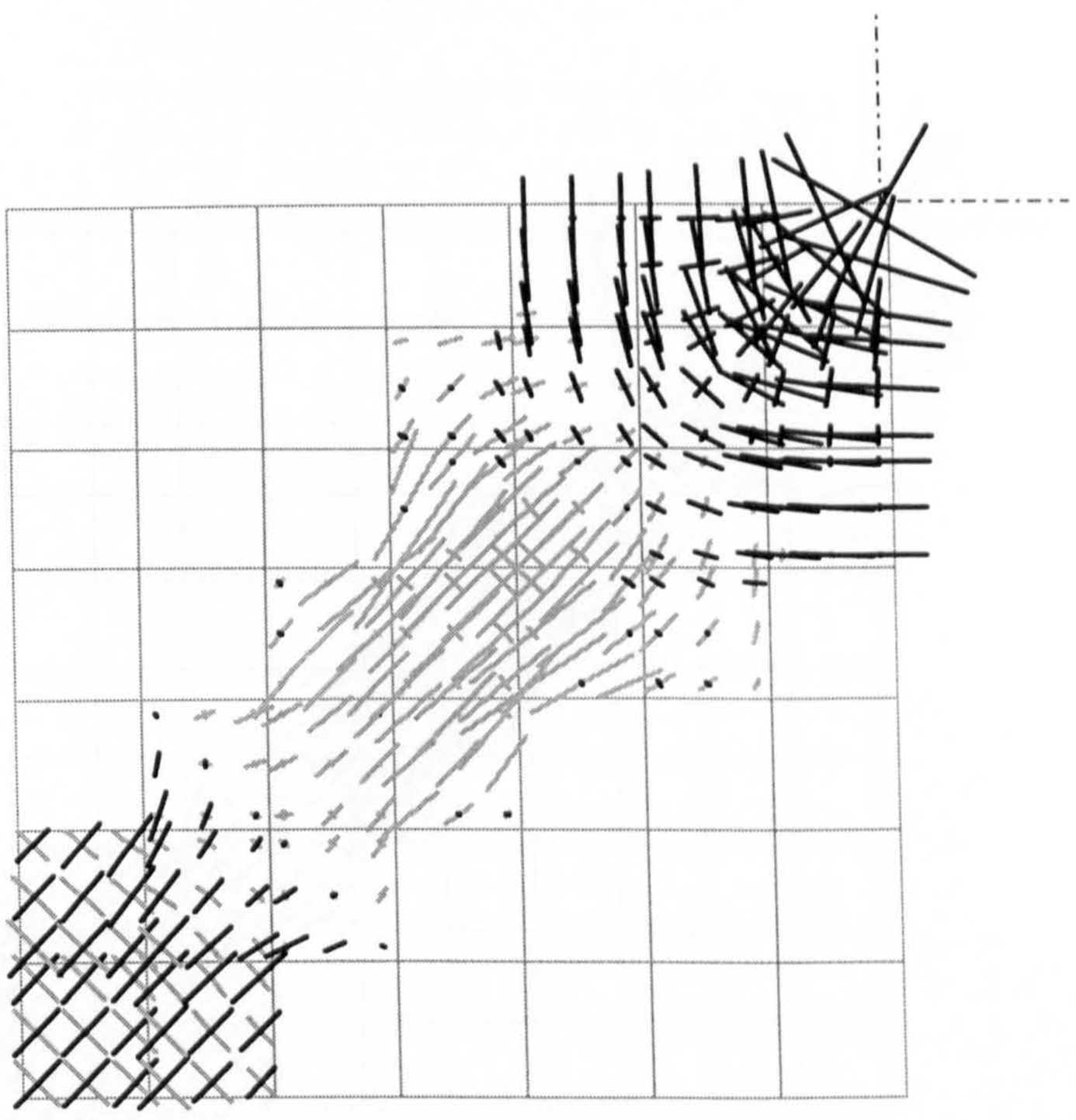

(ii) rr = 30%

fig.6.2.3(a): Slab SM3, principal moments, 7x7 mesh

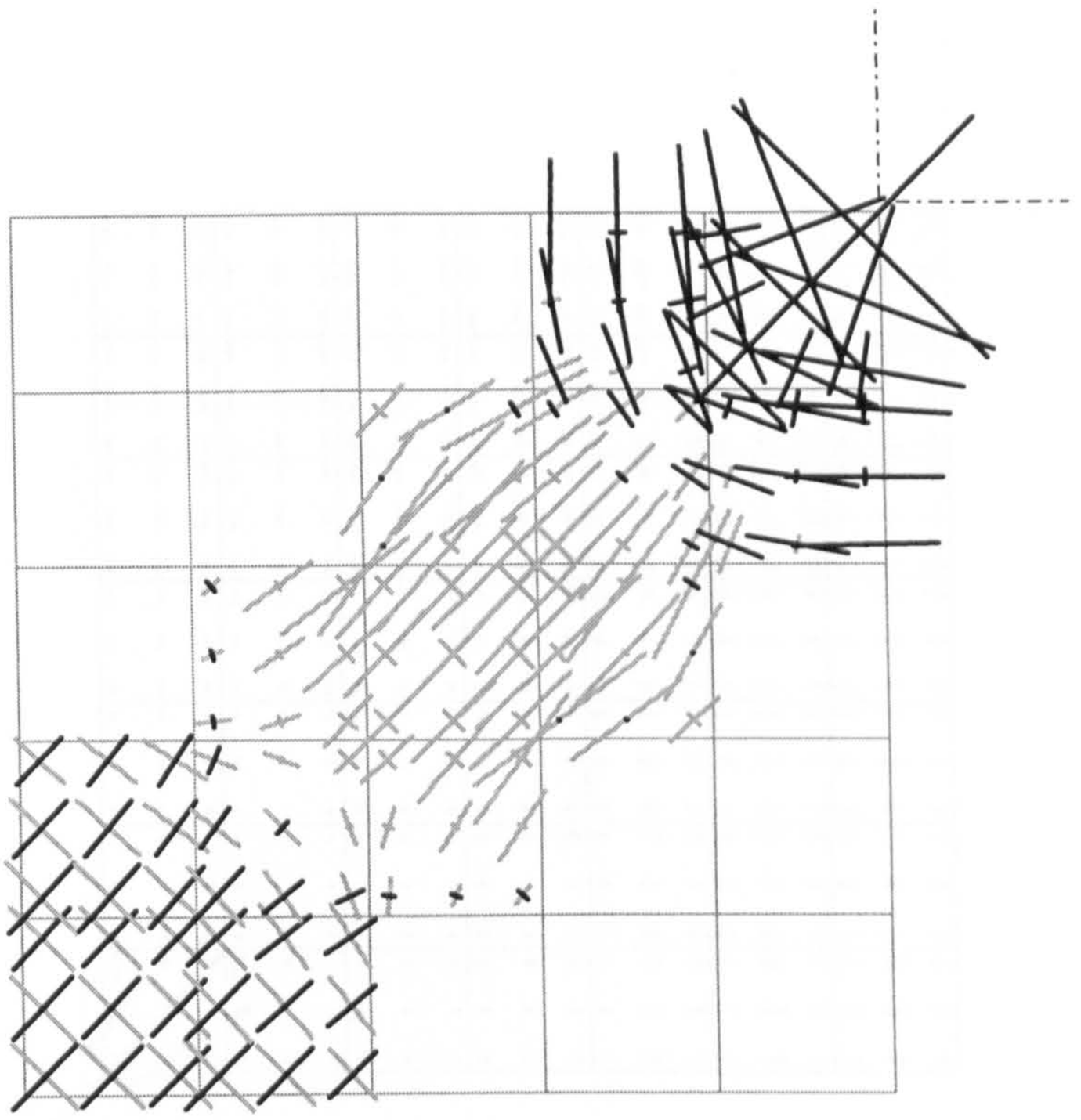

fig.6.2.3(b): Slab SM3, 5x5 mesh, (rr = 30%)

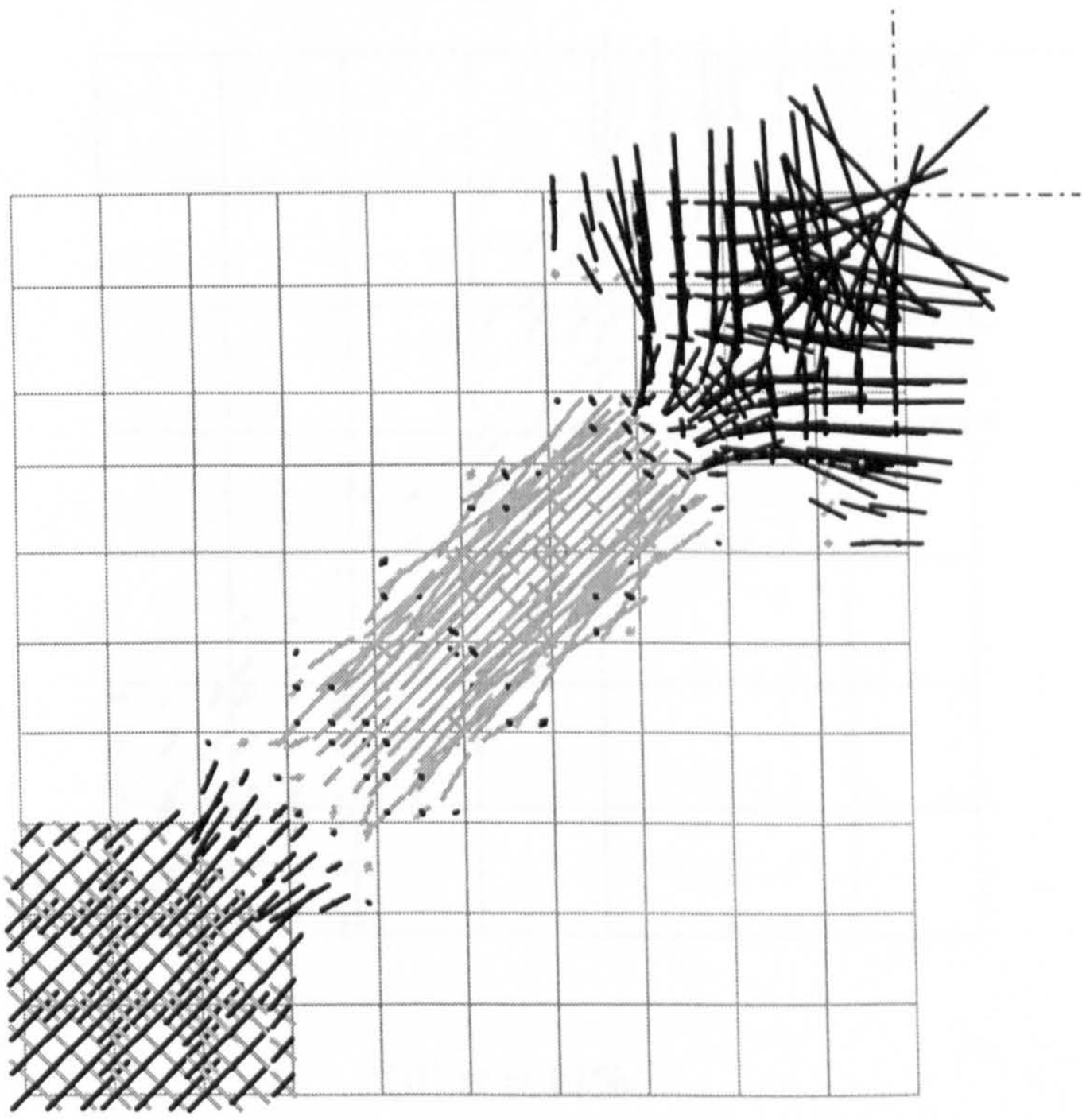

fig.6.2.3(c): Slab SM3, 10x10 mesh, (rr = 30%)

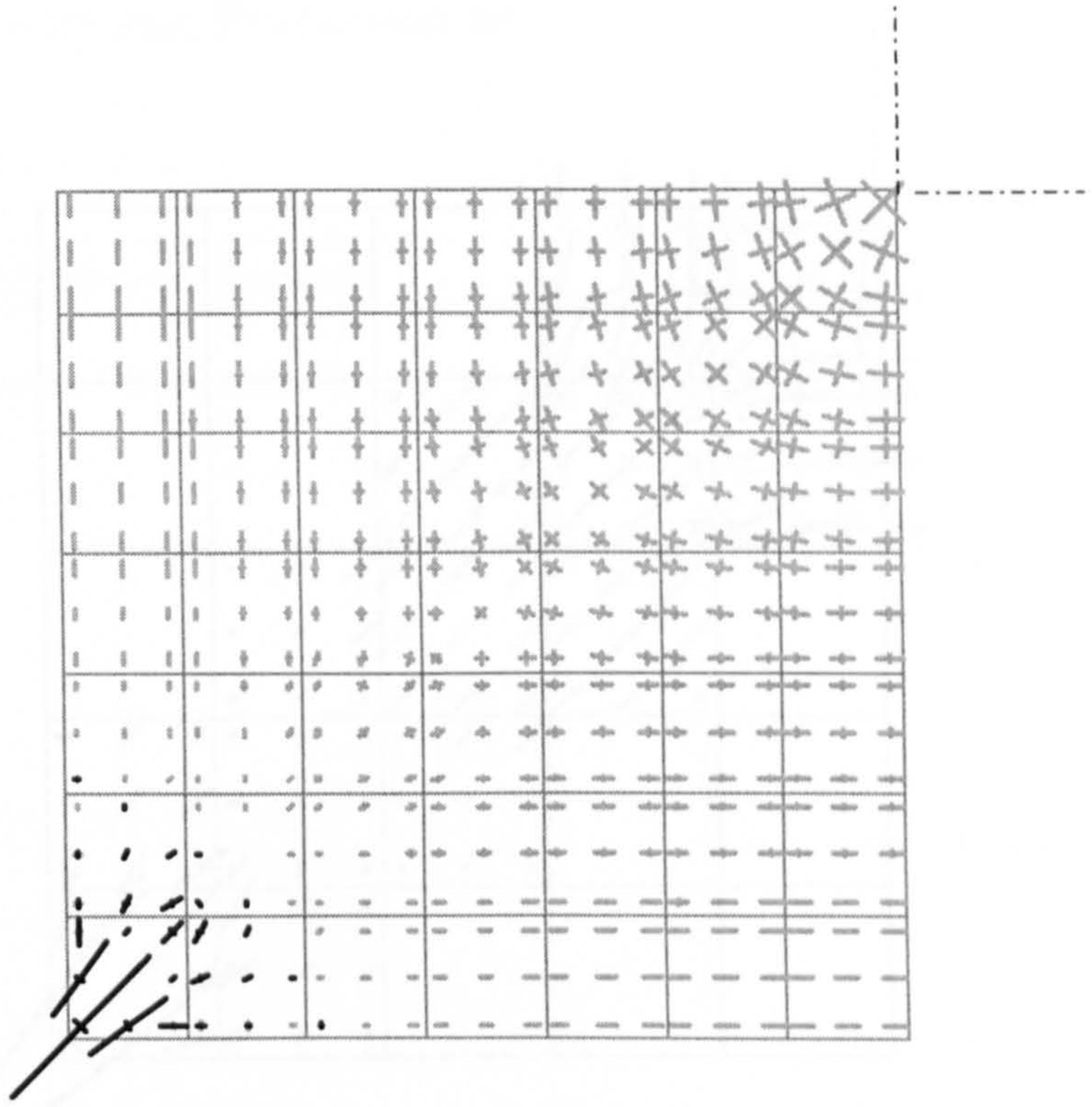

(i) rr = 0

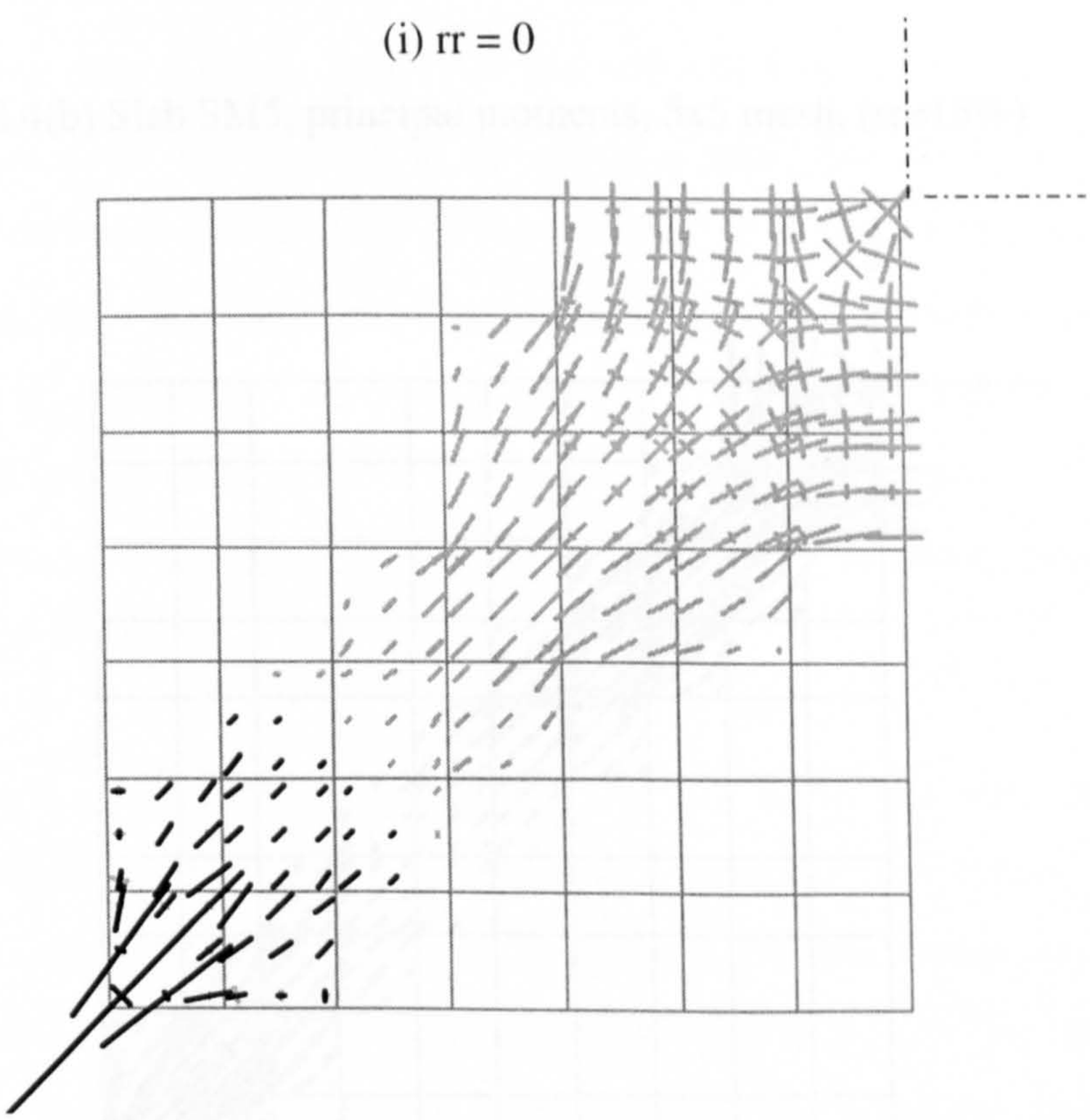

(ii) rr = 12%

fig.6.2.4(a) Slab SM5, principal moments, 7x7 mesh

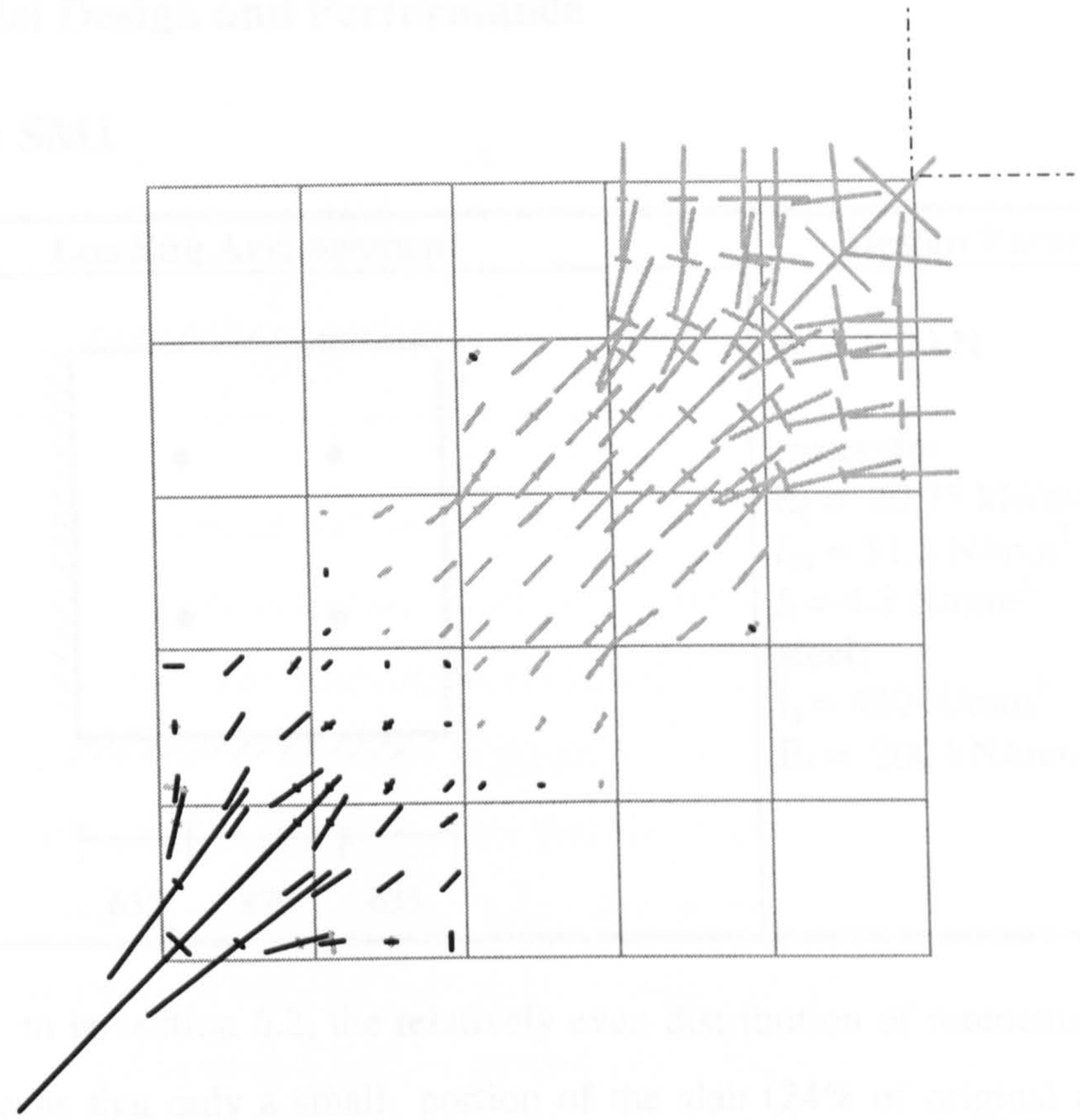

fig.6.2.4(b) Slab SM5, principal moments, 5x5 mesh, (rr=15%)

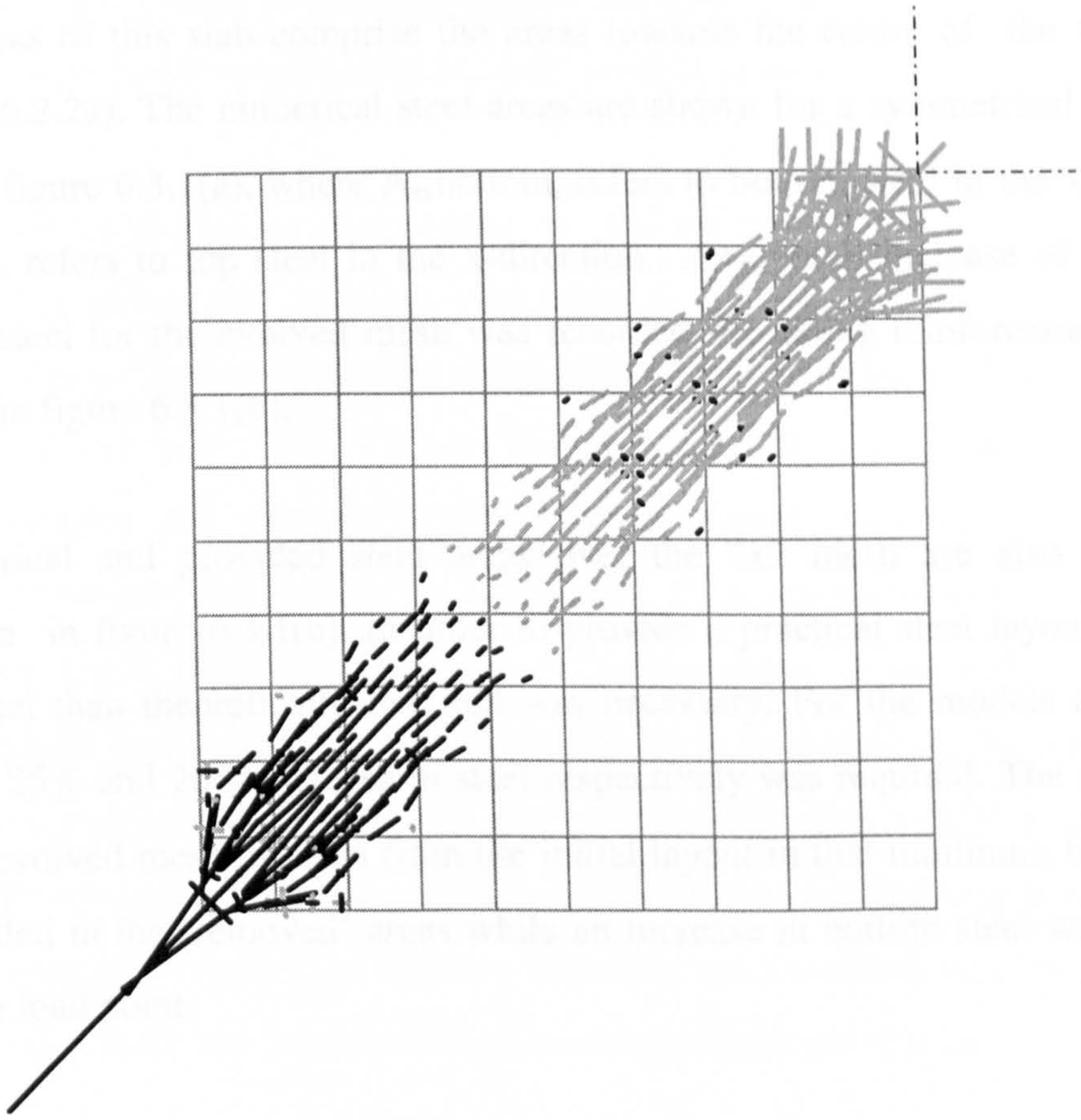

fig.6.2.4(c) Slab SM5, principal moments, 10x10 mesh, (rr=10%)

6.3 Model Design and Performance

6.3.1 Slab SM1

Loading Arrangement	Design Parameters
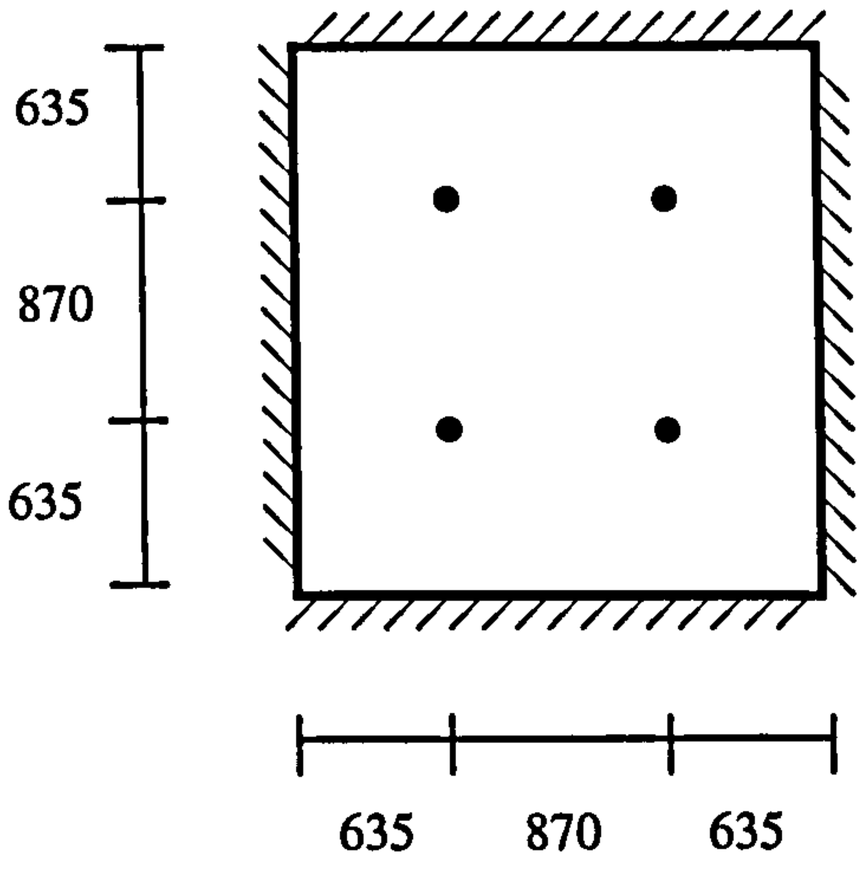	P_d = 210 kN **concrete:** E_c = 20.75 kN/mm^2 f_{cu} = 51.3 N/mm^2 f_t = 4.3 N/mm^2 **steel:** f_y = 480 N/mm^2 E_s = 200 kN/mm^2

As referred to in section 6.2, the relatively even distribution of moments throughout this slab means that only a small portion of the slab (24% of original area) has an average von Mises stress low enough to be assigned negligible stiffness. The low stressed areas of this slab comprise the areas towards the centre of the supporting edges, (fig.6.2.2a). The numerical steel areas are shown for a symmetrical quarter of the slab in figure 6.3.1(a), where A_{sx}bottom, refers to bottom steel in the x-direction, and A_{sx}top, refers to top steel in the x-direction.. An overall increase of 8% in the numerical steel for the evolved mesh was recorded. Resulting reinforcement layouts are shown in figure 6.3.1(b).

The numerical and provided steel areas over the 7x7 mesh are also shown for comparison in figure 6.3.1(b). In order to provide a practical steel layout, a greater area of steel than theoretically required was necessary. For the models at rr=0 and rr=40%, a 25% and 20% increase in steel respectively was required. The steel layout using the evolved mesh differed from the initial layout in that minimum bottom steel was provided in the 'removed' areas while an increase in bottom steel was provided around the load point.

Steel Volumes (cm^3)	(rr=0)			(rr=40%)			Total (40%) / Total (0)
	A_s bottom	A_s top	Total	A_s bottom	A_s top	Total	
Numerical	618.3	122.7	741	605.0	190.9	795.9	1.08
Provided	799.6	190.8	990.4	749.2	241.4	990.6	1.00

In the numerical analysis of each model, a total of 30 increments was used, with an initial increment of $0.1P_d$ in the elastic stage, then $0.05P_d$ during cracking and $0.01P_d$ towards ultimate load. The load-displacement relationship obtained from numerical analysis for each model is displayed in figure 6.3.1(c). The mode of failure for each model is clearly ductile. It can be seen that the behaviour of each model is very similar, both attain an ultimate load of $1.2P_d$. The service deflection limit at mid-span was reached at around $0.65P_d$ for both slabs. Yielding of the steel occurred first in the bottom steel at mid-span at a load of around $1.0P_d$, (fig.6.3.1(d)). Further significant yielding in this area occurred, reaching 6 times the yield strain at ultimate load. Similar yielding occurred in the bottom steel around the load point. Yielding of the top steel, around the corner occurred at a load level of around $1.2P_d$ (fig.6.3.1(e)).

The sectional behaviour as represented by the moment-curvature relationship is detailed at the centre and near the load point in figures 6.3.1(f-g). The moment-curvature relationship is expressed in terms of the ultimate moment of the section M_u, and the yield curvature, $1/R_y$. Values for M_u and $1/R_y$ were obtained from the numerical analysis of a one-way strip with equal reinforcement layers to that of the section being investigated. In this case, M_u and $1/R_y$ at the load point were measured as 28kNm/m and $0.0001mm^{-1}$ respectively. At the centre of the slab, M_u and $1/R_y$ were 18kNm/m and $0.0001mm^{-1}$ respectively. These values were the same for both designs since the same amount of steel was used for each case in these areas. It can be seen that the moment is still being sustained beyond the ultimate load at these points, indicating a ductile response. In addition, it is clear that no softening occurs. For both designs, as expected, the moment curvature-relationships are similar.

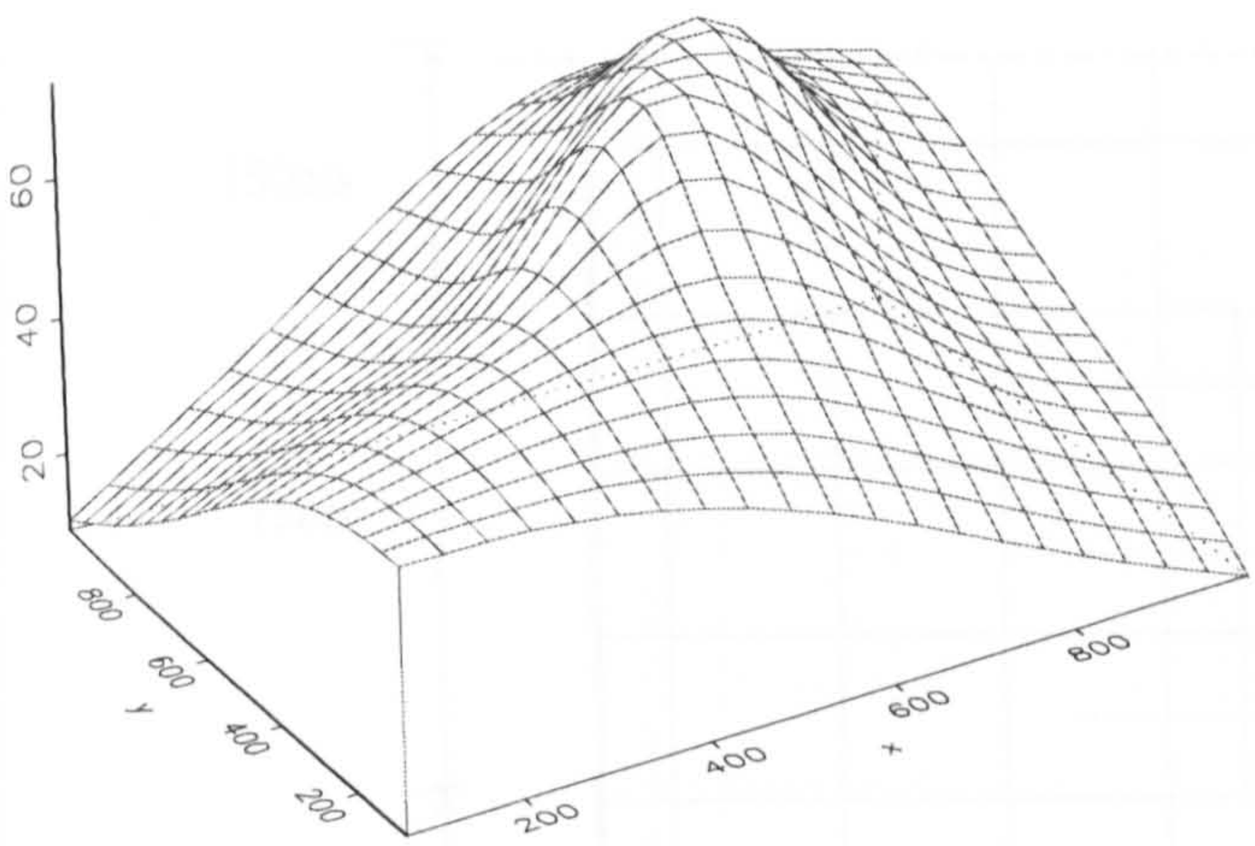

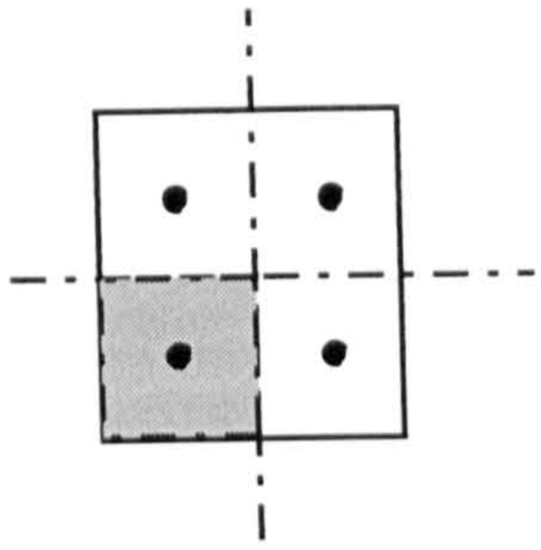

i) A_{sx}bottom (rr=0)

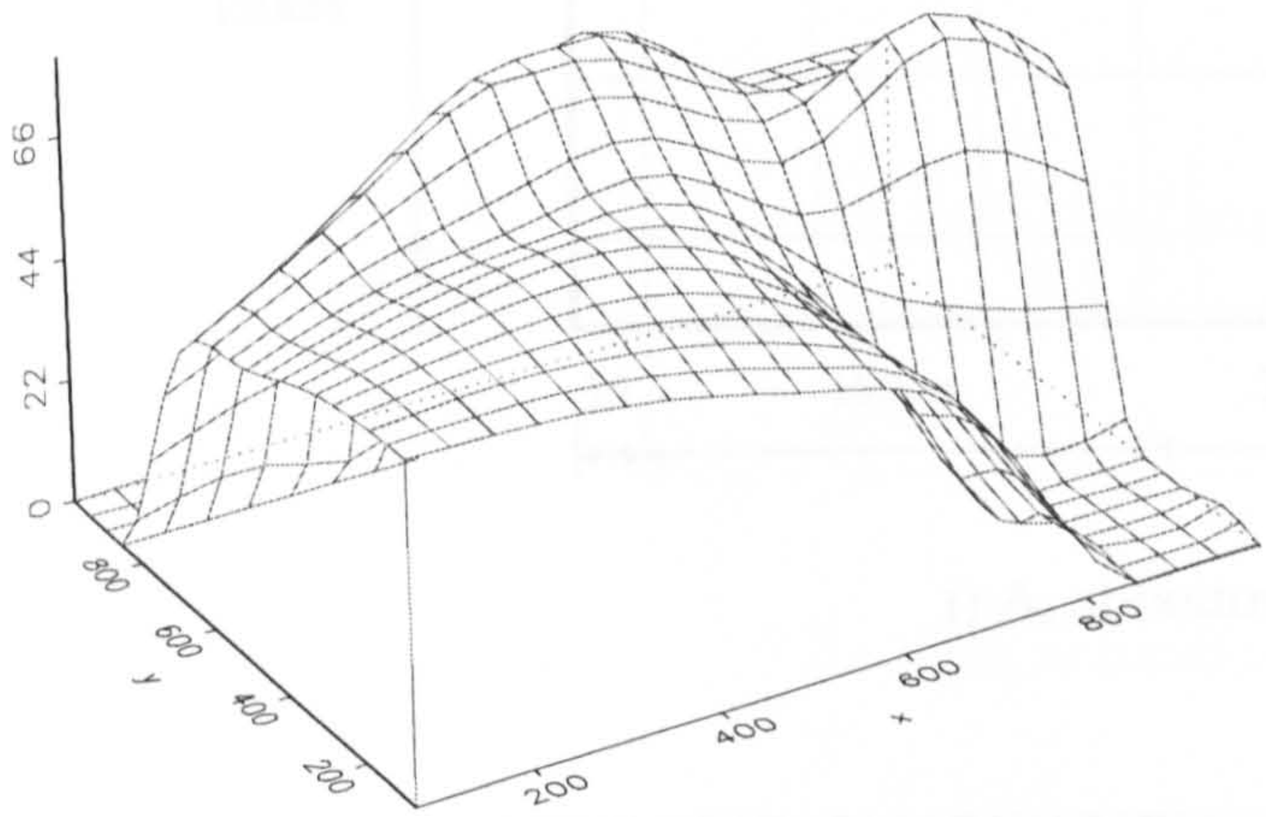

ii) A_{sx}bottom (rr=40%)

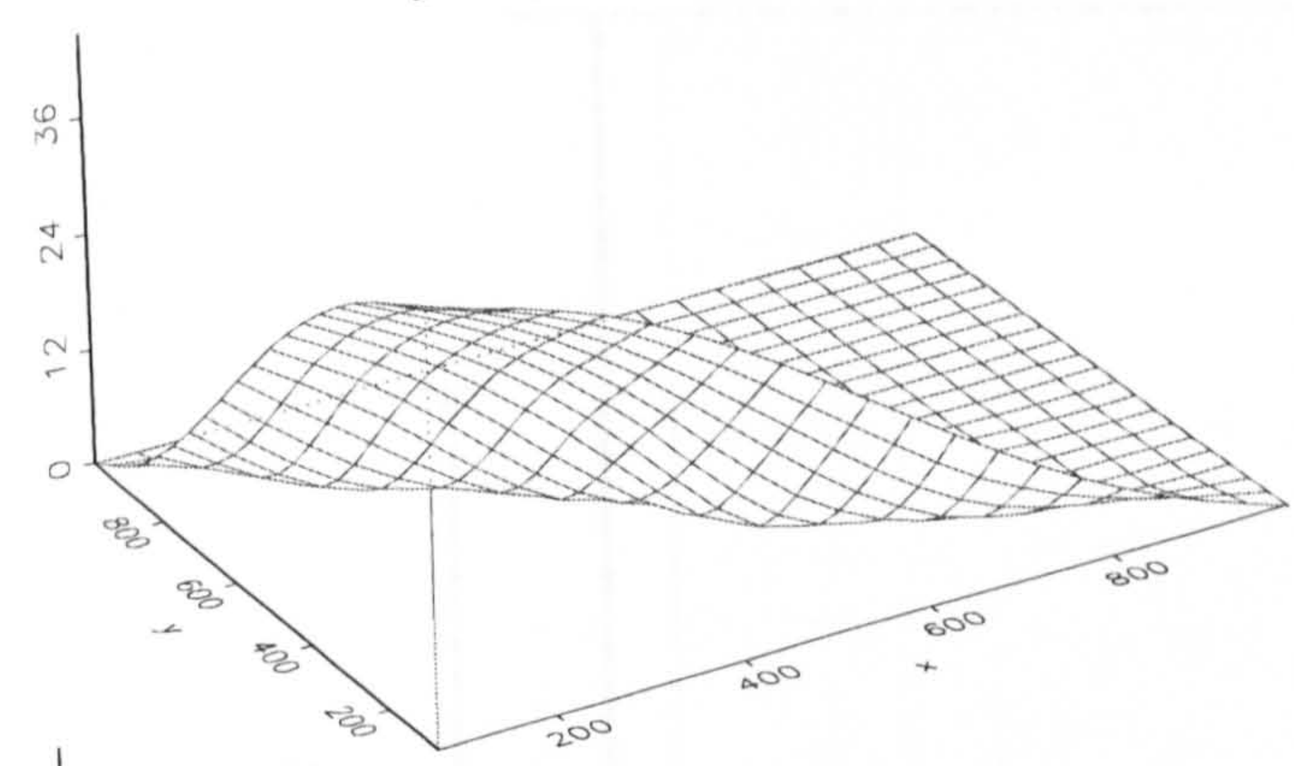

iii) A_{sx}top (rr=0)

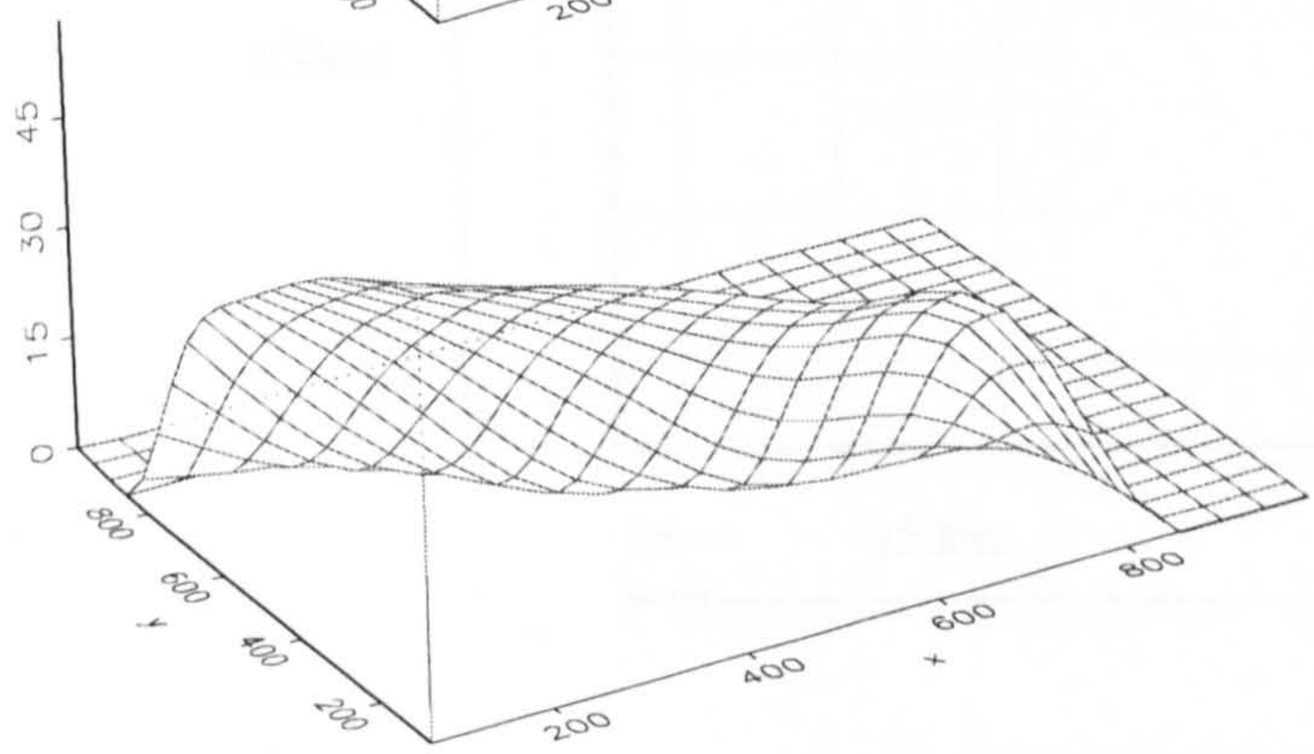

iv) A_{sx}top (rr=40%)

fig 6.3.1(a) Slab SM1: Symmetrical Quarter, Numerical Steel Areas (mm^2)

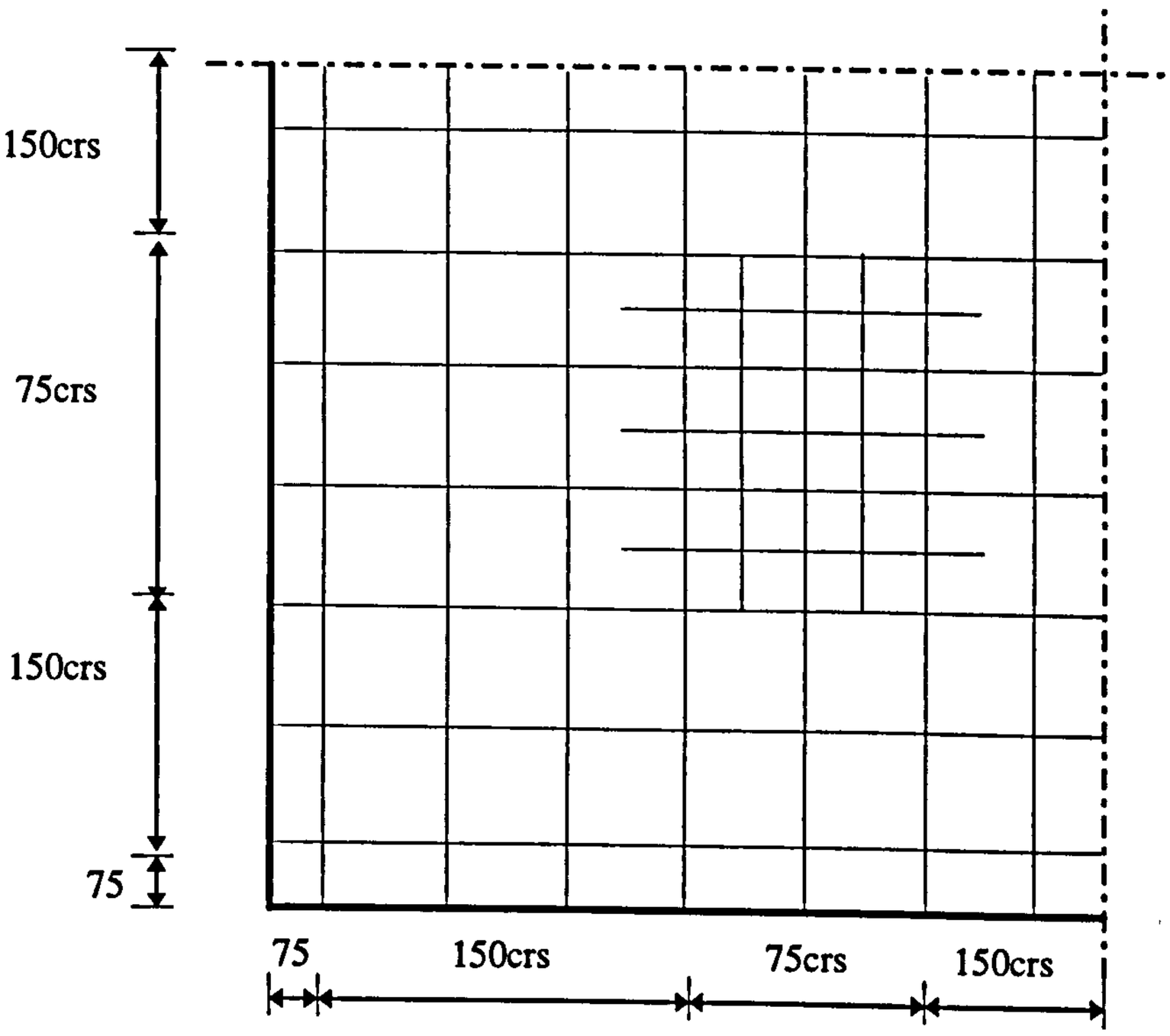

i) A_s at bottom (rr=0)

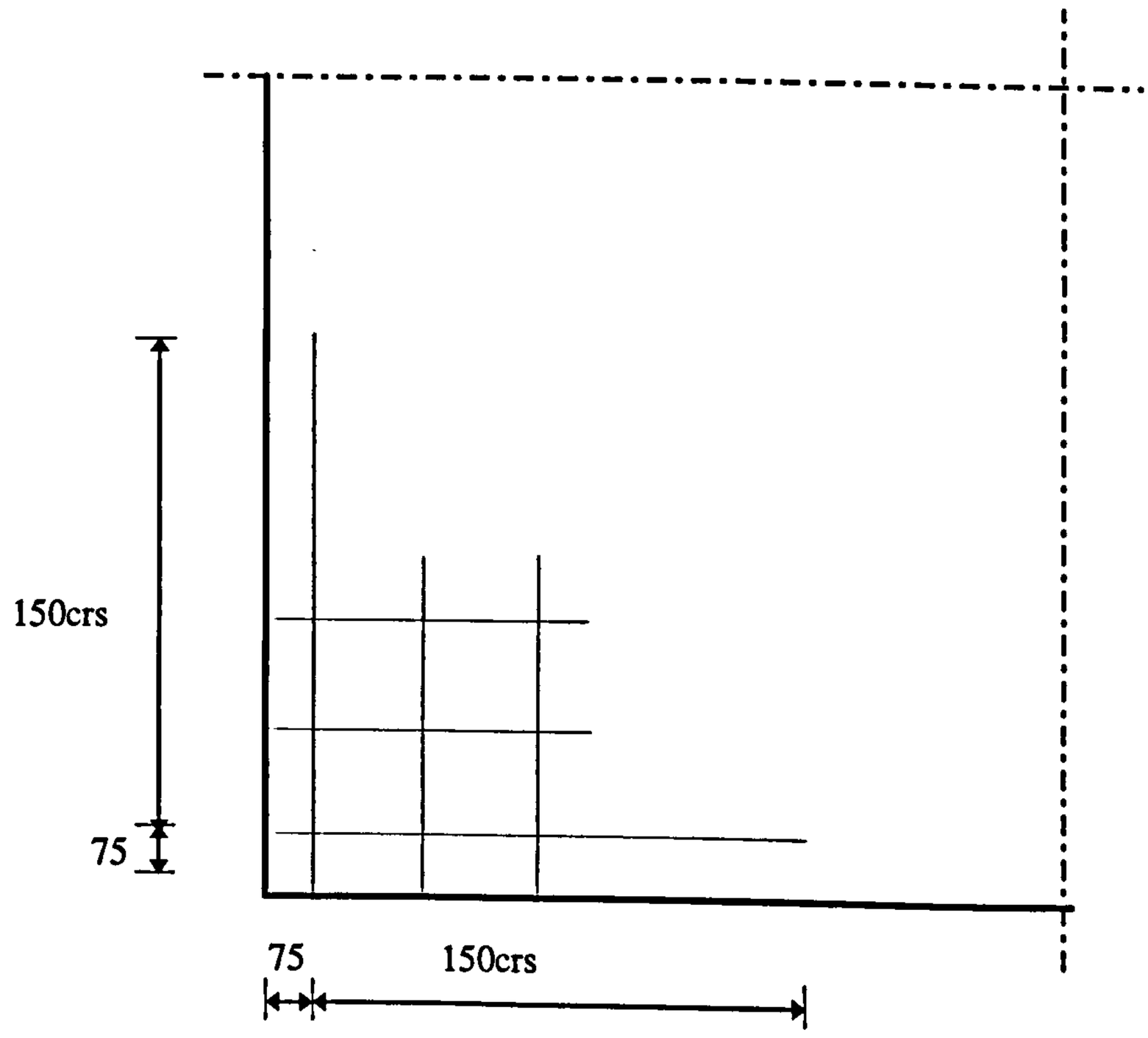

ii) A_s at top (rr=0)

fig.6.3.1(b) Slab SM1: Steel Layout, all sizes in mm, all bars 8mm diameter

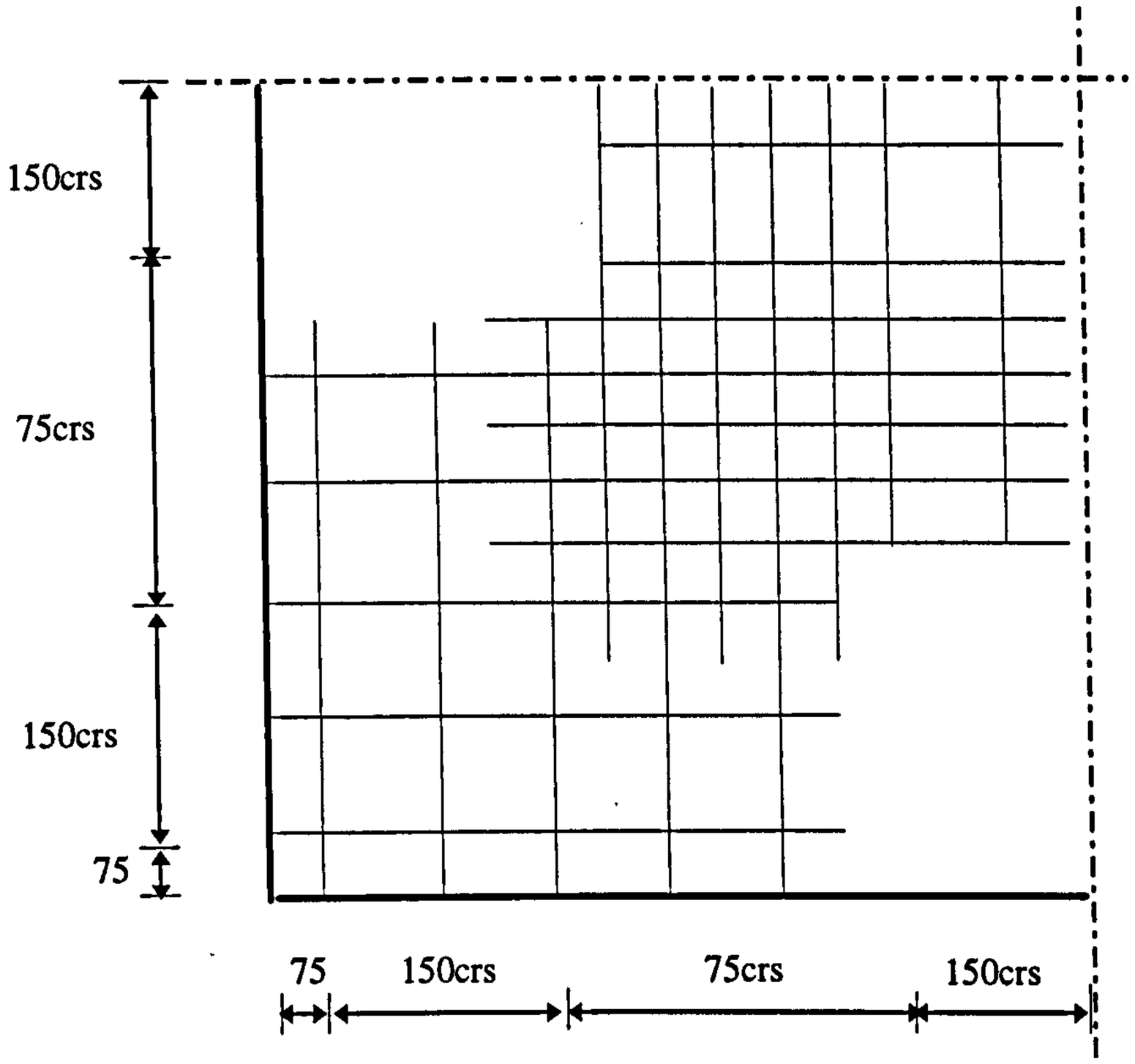

iii)A_s at bottom (rr=40%)

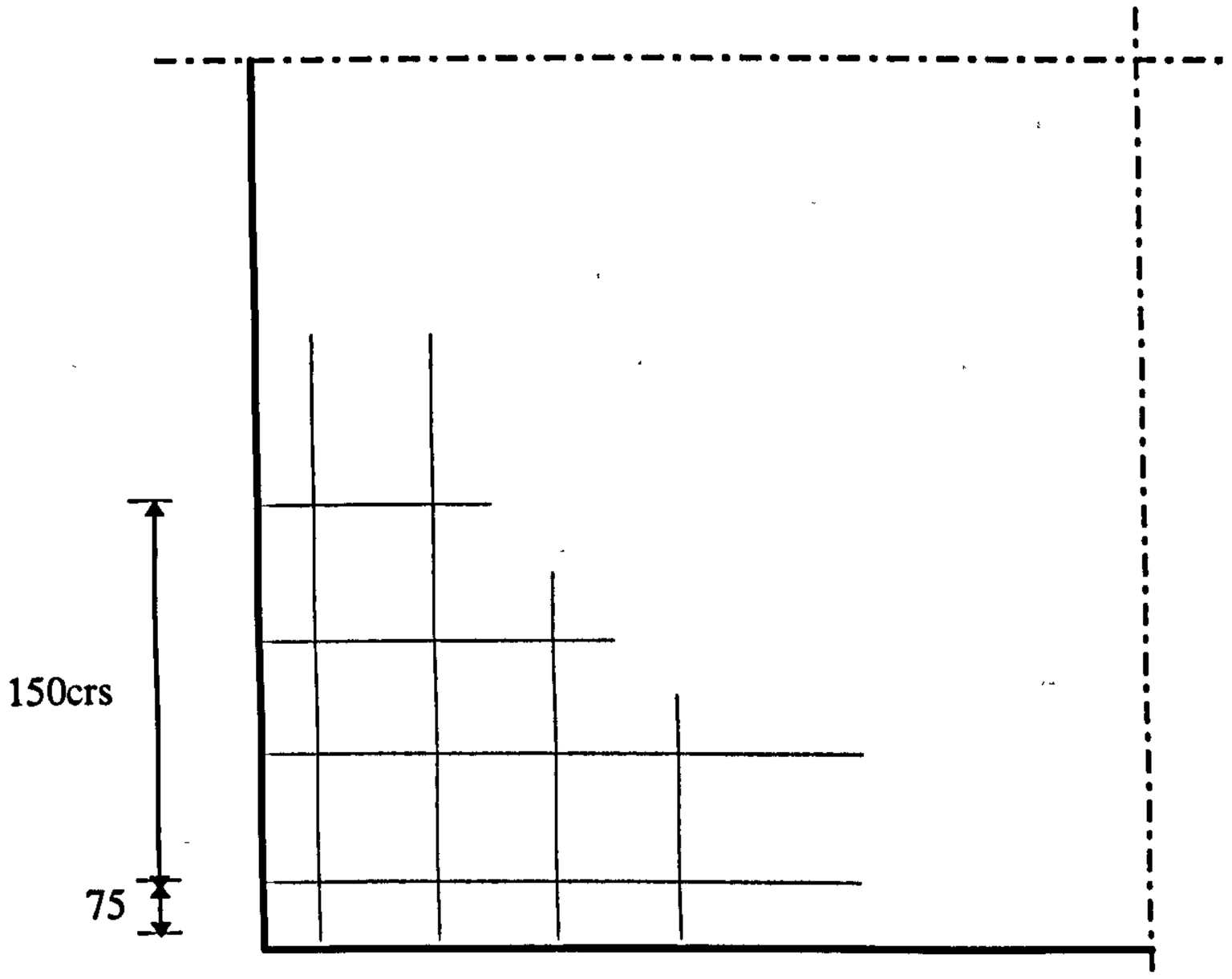

iv) A_s at top (rr=40%)

fig.6.3.1(b) Slab SM1 Steel Layout, all sizes in mm, all bars 8mm diameter

9.97 (50.3)	23.23 (50.3)	37.19 (50.3)	49.98 (50.3)	55.18 (50.3)	51.22 (50.3)	45.58 (50.3)
16.86 (50.3)	28.26 (50.3)	40.24 (50.3)	56.6 (50.3)	63.87 (50.3)	53.65 (50.3)	43.69 (50.3)
24.89 (50.3)	34.42 (50.3)	45.34 (50.3)	65.43 (100.6)	73.67 (100.6)	49.87 (50.3)	38.09 (50.3)
33.90 (50.3)	42.49 (50.3)	53.76 (50.3)	73.77 (100.6)	62.18 (100.6)	40.82 (50.3)	31.17 (50.3)
41.64 (50.3)	48.52 (50.3)	55.79 (50.3)	60.51 (50.3)	50.11 (50.3)	33.79 (50.3)	24.98 (50.3)
45.89 (50.3)	49.18 (50.3)	50.65 (50.3)	47.75 (50.3)	38.45 (50.3)	26.79 (50.3)	17.82 (50.3)
46.78 (50.3)	46.08 (50.3)	42.66 (50.3)	35.98 (50.3)	26.67 (50.3)	16.93 (50.3)	8.64 (50.3)

(v) A_{sx} at bottom (rr=0) 8mm bars

0.00 (0.00)	0.00 (0.00)	0.00 (0.00)	0.00 (0.00)	0.00 (0.00)	0.00 (0.00)	0.00 (0.00)
5.10 (0.00)	0.00 (0.00)	0.00 (0.00)	0.00 (0.00)	0.00 (0.00)	0.00 (0.00)	0.00 (0.00)
14.38 (50.3)	2.96 (0.00)	0.00 (0.00)	0.00 (0.00)	0.00 (0.00)	0.00 (0.00)	0.00 (0.00)
25.06 (50.3)	14.32 (50.3)	2.63 (0.00)	0.00 (0.00)	0.00 (0.00)	0.00 (0.00)	0.00 (0.00)
34.47 (50.3)	25.40 (50.3)	12.90 (50.3)	0.00 (0.00)	0.00 (0.00)	0.00 (0.00)	0.00 (0.00)
41.04 (50.3)	33.81 (50.3)	23.22 (50.3)	10.09 (0.00)	1.83 (0.00)	0.00 (0.00)	0.00 (0.00)
45.06 (50.3)	40.71 (50.3)	33.38 (50.3)	23.65 (50.3)	13.60 (50.3)	5.41 (0.00)	0.00 (0.00)

(vi) A_{sx} at top (rr=0) 8mm bars

fig.6.3.1(b) Slab SM1: Numerical & (Provided) Steel Areas in mm^2

0.00 (19.5)	0.00 (19.5)	0.00 (19.5)	19.24 (50.3)	39.43 (50.3)	43.15 (50.3)	42.83 (50.3)
0.00 (19.5)	0.00 (19.5)	0.00 (19.5)	57.53 (50.3)	52.89 (50.3)	45.10 (50.3)	43.03 (50.3)
42.55 (50.3)	57.03 (50.3)	74.58 (100.6)	80.42 (100.6)	64.69 (100.6)	51.13 (50.3)	46.80 (50.3)
51.79 (50.3)	61.35 (50.3)	67.29 (100.6)	69.68 (100.6)	59.00 (100.6)	72.91 (100.6)	57.87 (100.6)
56.34 (50.3)	62.79 (50.3)	65.71 (50.3)	59.88 (50.3)	34.03 (50.3)	0.00 (19.5)	0.00 (19.5)
59.64 (50.3)	62.44 (50.3)	61.92 (50.3)	55.21 (50.3)	35.47 (50.3)	0.00 (19.5)	0.00 (19.5)
60.44 (50.3)	59.65 (50.3)	56.17 (50.3)	49.92 (50.3)	36.69 (50.3)	0.00 (19.5)	0.00 (19.5)

(vii) A_{sx} at bottom (rr=40%) 8mm bars

0.00 (0.00)	0.00 (0.00)	0.00 (0.00)	0.00 (0.00)	0.00 (0.00)	0.00 (0.00)	0.00 (0.00)
0.00 (0.00)	0.00 (0.00)	0.00 (0.00)	0.00 (0.00)	0.00 (0.00)	0.00 (0.00)	0.00 (0.00)
25.87 (50.3)	6.23 (0.00)	0.00 (0.00)	0.00 (0.00)	0.00 (0.00)	0.00 (0.00)	0.00 (0.00)
39.07 (50.3)	21.60 (50.3)	3.12 (0.00)	0.00 (0.00)	0.00 (0.00)	0.00 (0.00)	0.00 (0.00)
47.58 (50.3)	35.51 (50.3)	20.32 (50.3)	5.63 (0.00)	2.23 (0.00)	0.00 (0.00)	0.00 (0.00)
54.35 (50.3)	46.50 (50.3)	36.51 (50.3)	28.18 (50.3)	22.23 (50.3)	0.00 (0.00)	0.00 (0.00)
58.65 (50.3)	54.36 (50.3)	48.02 (50.3)	41.69 (50.3)	33.39 (50.3)	0.00 (0.00)	0.00 (0.00)

(viii) A_{sx} at top (rr=40%) 8mm bars

fig.6.3.1(b) Slab SM1: Numerical & (Provided) Steel Areas in mm^2

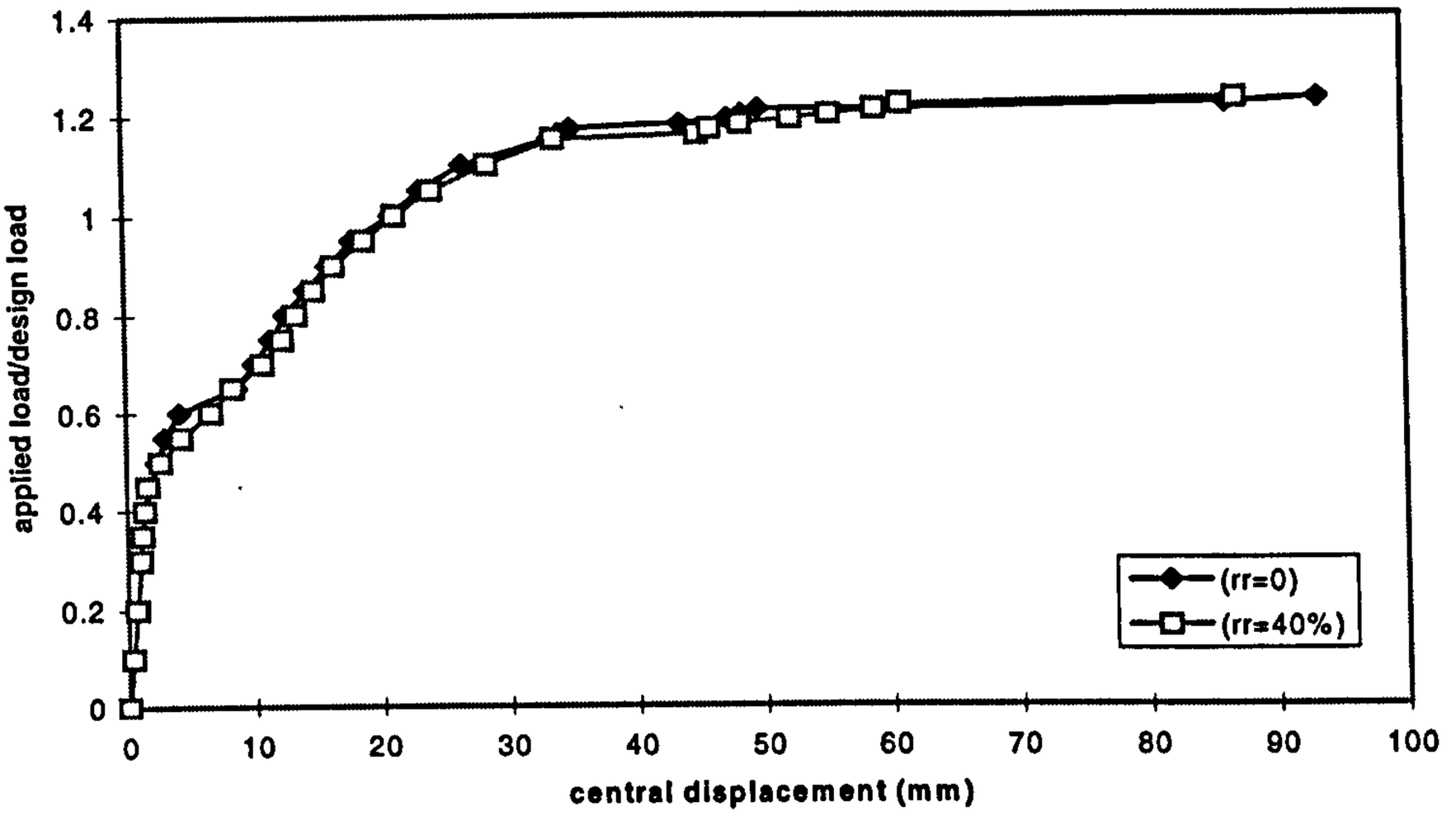

fig.6.3.1(c) Slab SM1 Load-displacement relationship

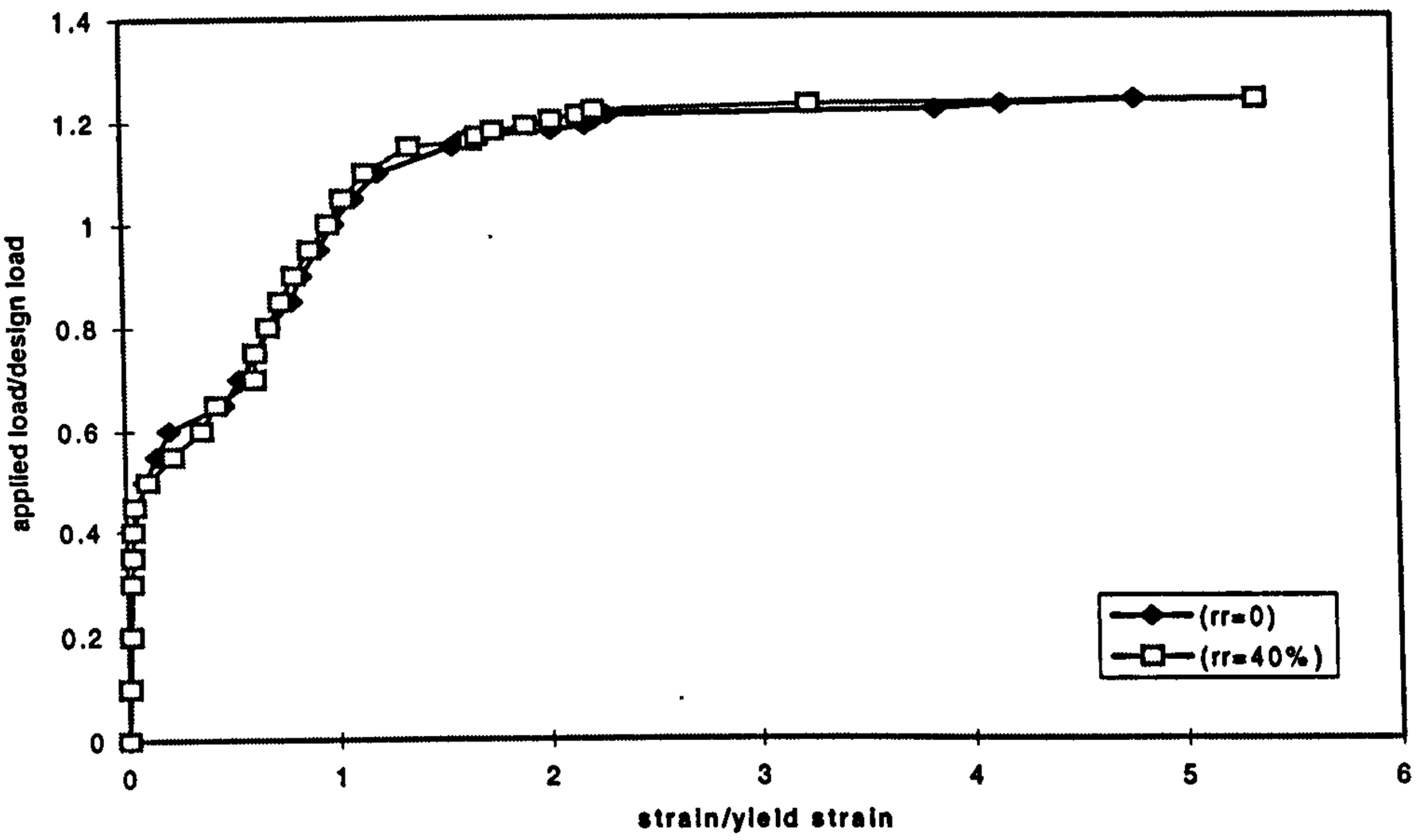

fig.6.3.1(d) Slab SM1 Bottom Steel Strains at centre

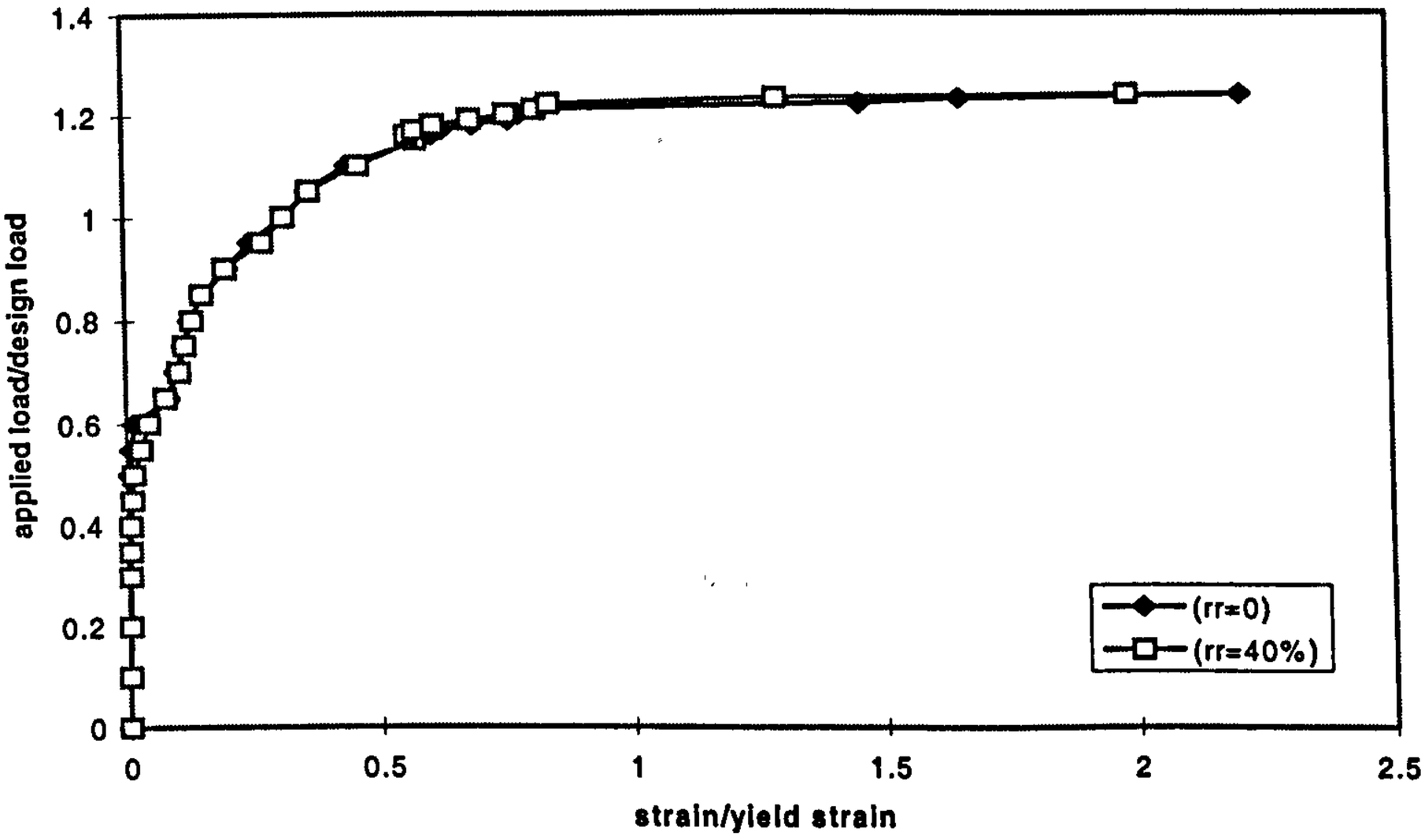

fig.6.3.1(e) Slab SM1 Top Steel Strains at corner

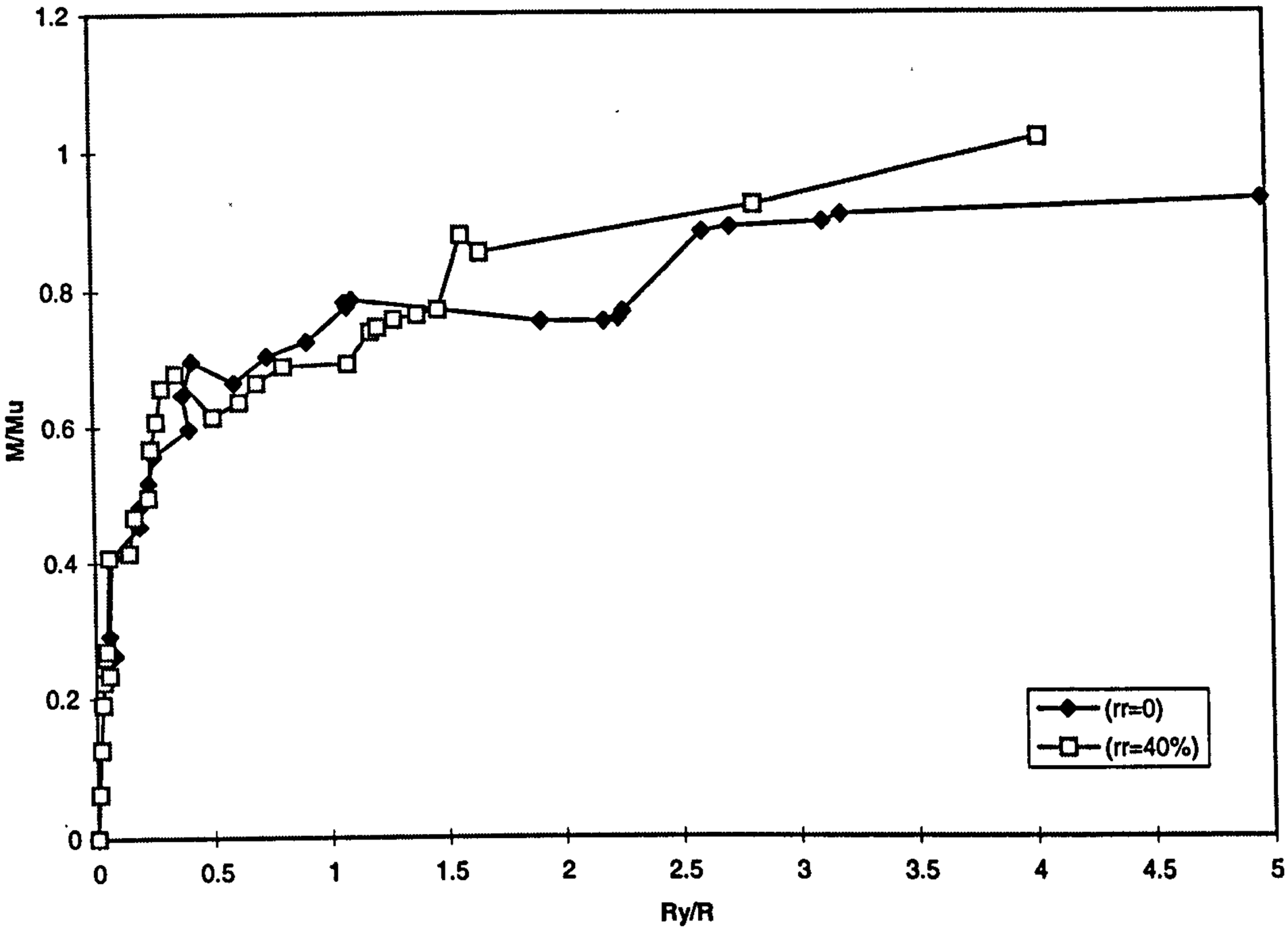

fig.6.3.1(f) Slab SM1 Principal Moment-curvature relationship near Load-point

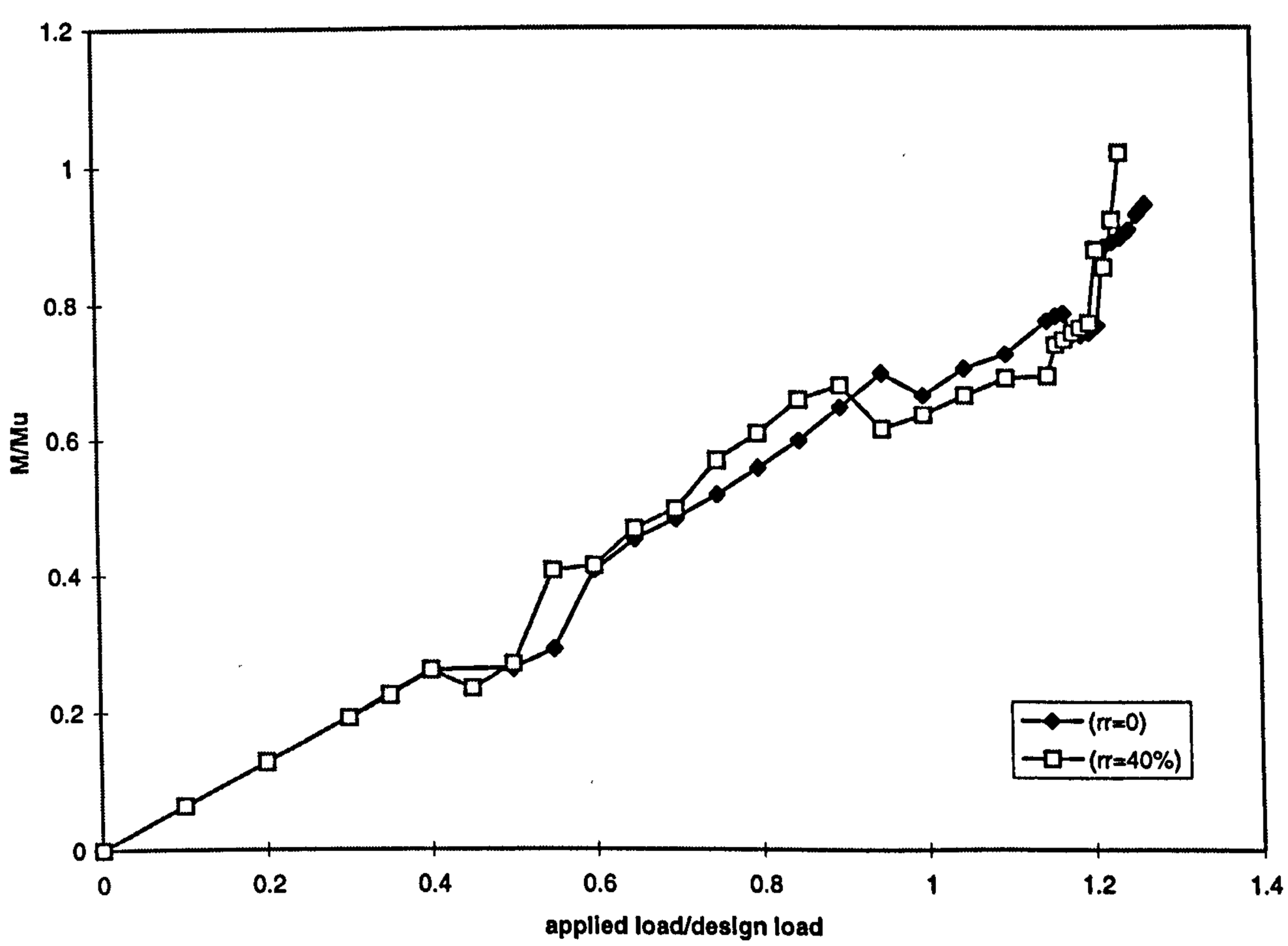

fig.6.3.1(g) Slab SM1 Principal Moment near load point vs. Load

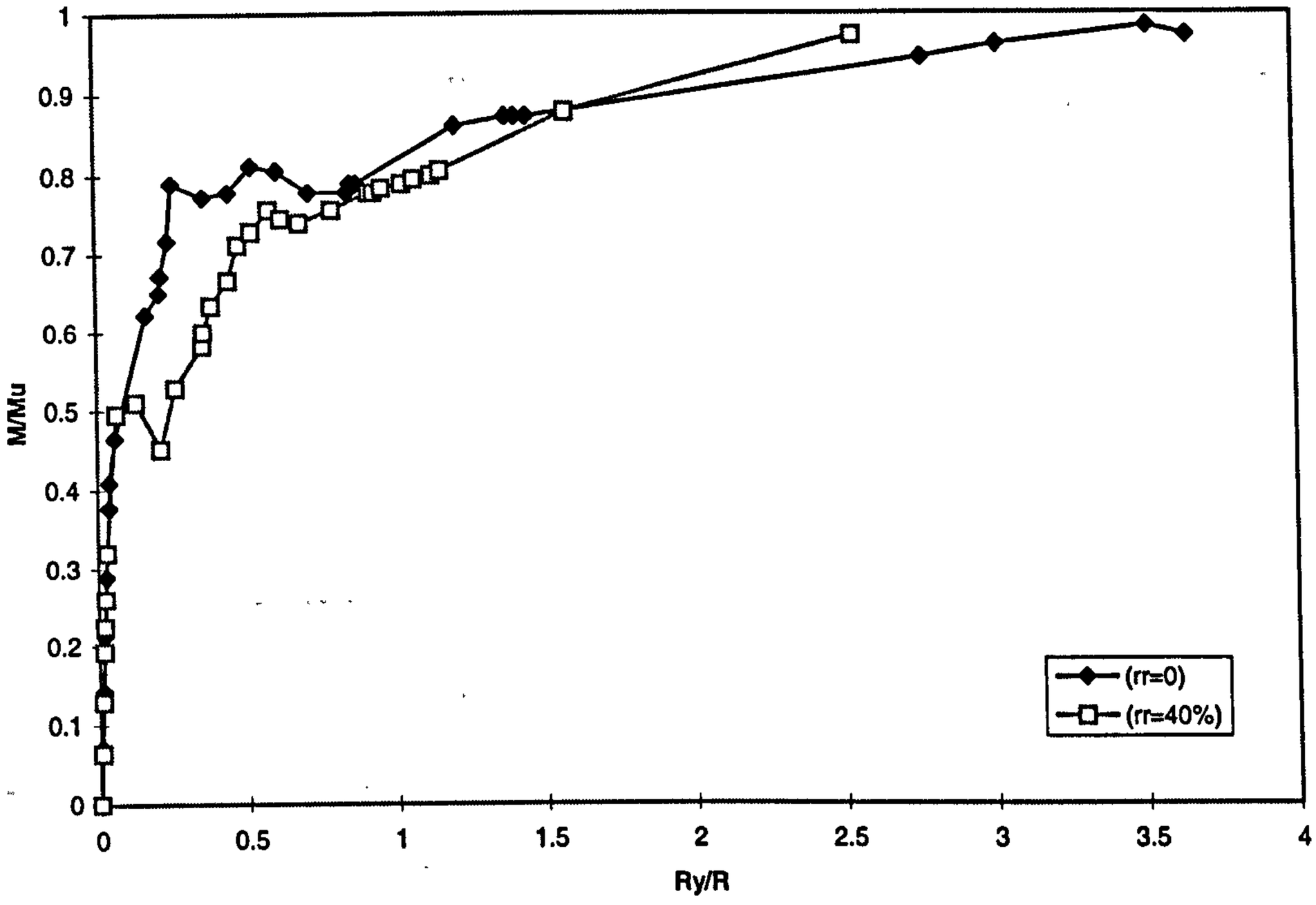

fig.6.3.1(h) Slab SM1: Principal Moment-Curvature relationship at centre

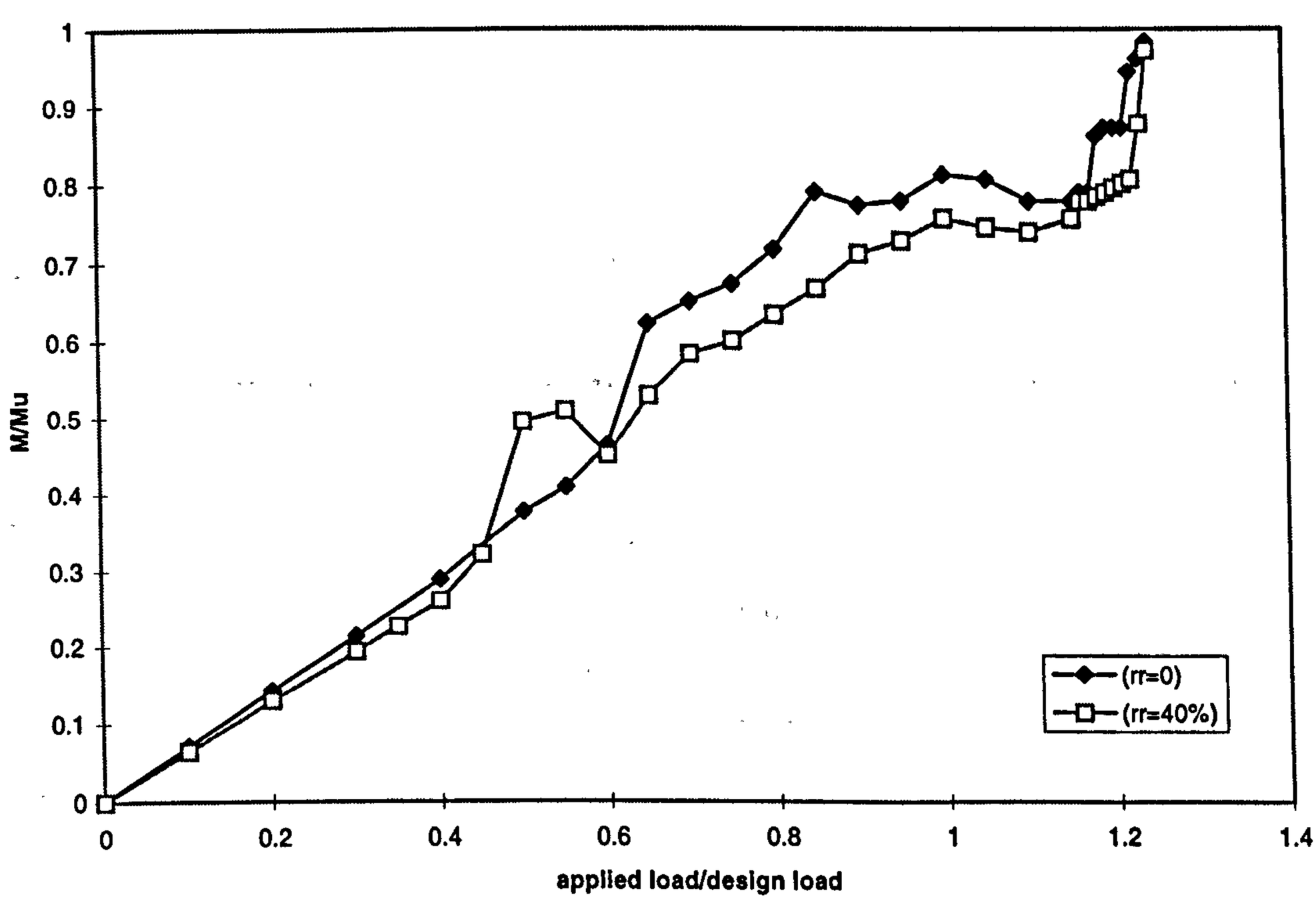

fig.6.3.1(i) Slab SM1: Principal Moment at centre vs. Load

6.3.2 Slab SM2

Loading Arrangement	Design Parameters
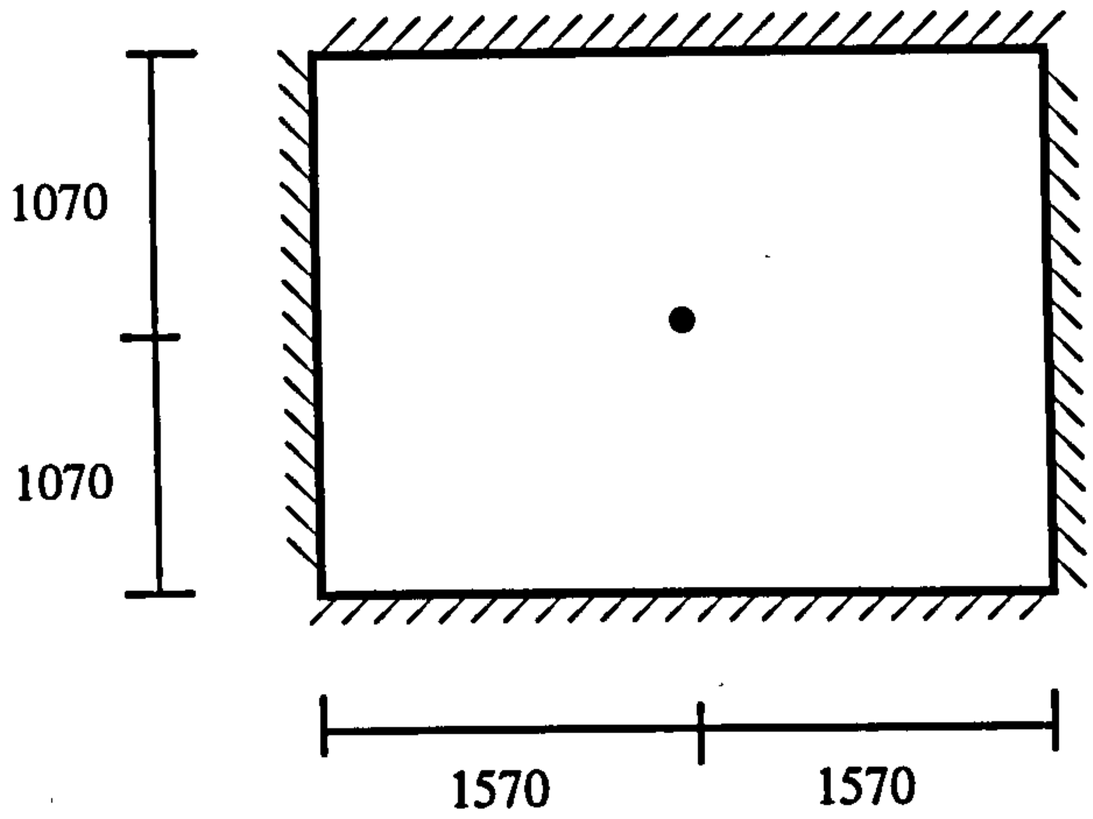	P_d = 210 kN **concrete:** E_c = 20.75 kN/mm^2 f_{cu} = 51.3 N/mm^2 f_t = 4.3 N/mm^2 **steel:** f_y = 480 N/mm^2 E_s = 200 kN/mm^2

The principal moment pattern of this slab (fig 6.3.2a), although similar to that of SM1, is less evenly distributed due to the position of the concentrated load at the centre. In common with slab SM1, the lowest stressed areas of slab occurred around the centre of the support edges. The evolved path occurring after rr=30% is shown in figure 6.3.2(a). From the numerical steel areas (fig.6.3.2b), the peak areas occurring at the centre and supporting corner of the slab can be seen to be smoothed in the evolved model. As with slab SM1, an increase of 3% and 14% in numerical and provided steel areas respectively was observed from rr=0 to rr=30%.

Steel Volumes (cm^3)	(rr=0)			(rr=30%)			Total (30%) / Total (0)
	A_s bottom	A_s top	Total	A_s bottom	A_s top	Total	
Numerical	1265.9	297.6	1563.5	1151.6	460.7	1612.3	1.03
Provided	1395.3	391.2	1786.5	1505.7	523.2	2028.9	1.14

Resulting reinforcement layouts are given in figure 6.3.2(c). For comparison, the numerical and provided steel areas in the x direction over the mesh are also shown in figure's 6.3.2(c). The main difference in the provided steel areas occurs at the 'removed' areas where minimum steel is placed, and the top corners, where more

steel is provided than for rr=0. Increases in the bottom steel around the corners can be observed from fig(6.3.2c(i)).

In the numerical analysis, a total of 20 increments were used. Initial increments of $0.1P_d$, were used in the elastic stage, subsequent increments of $0.05P_d$ were used. until ultimate load. From the load-displacement relationship (fig 6.3.2d), it can be observed that both designs perform in a similar manner. The design at rr=0, is slightly stiffer and achieves an ultimate load of $1.1P_d$ compared to $1.05P_d$ at rr=30%. The service deflection limit at mid-span for both slabs was reached at around $0.7P_d$. In both designs yielding of the bottom steel first occurred at a load of $0.7P_d$, close to the centre (fig.6.3.2e). Yielding of the top steel did not occur.

At the centre of the slab, M_u and $1/R_y$ were calculated as 58kNm/m and $0.0001mm^{-1}$ respectively, for each design. The moment-curvature relationship for the section at the centre of the slab shows that both designs behaved similarly. (fig. 6.3.2g). In each case, the ultimate moment was not reached until after the design load P_d was achieved.

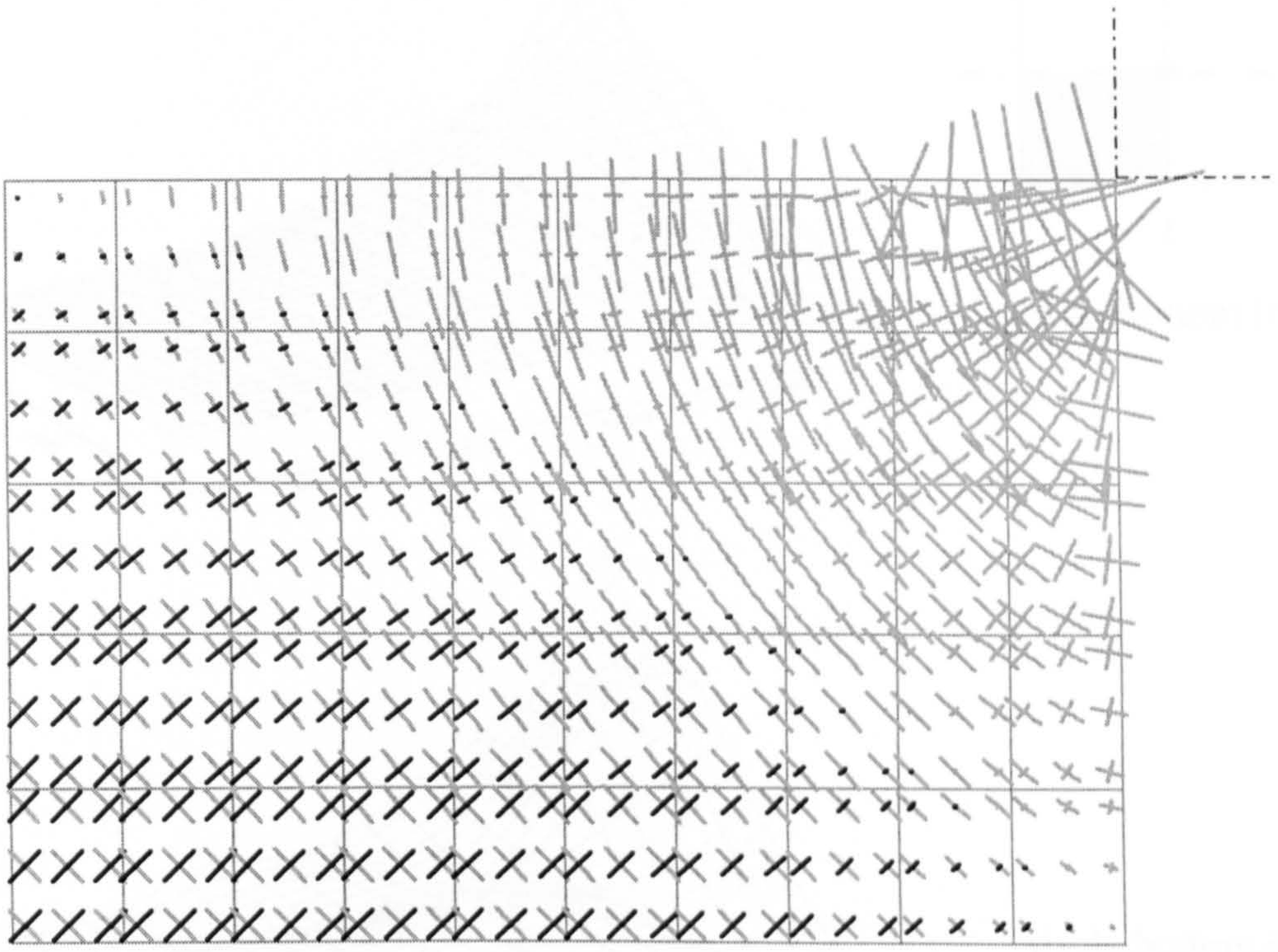

(i) rr=0

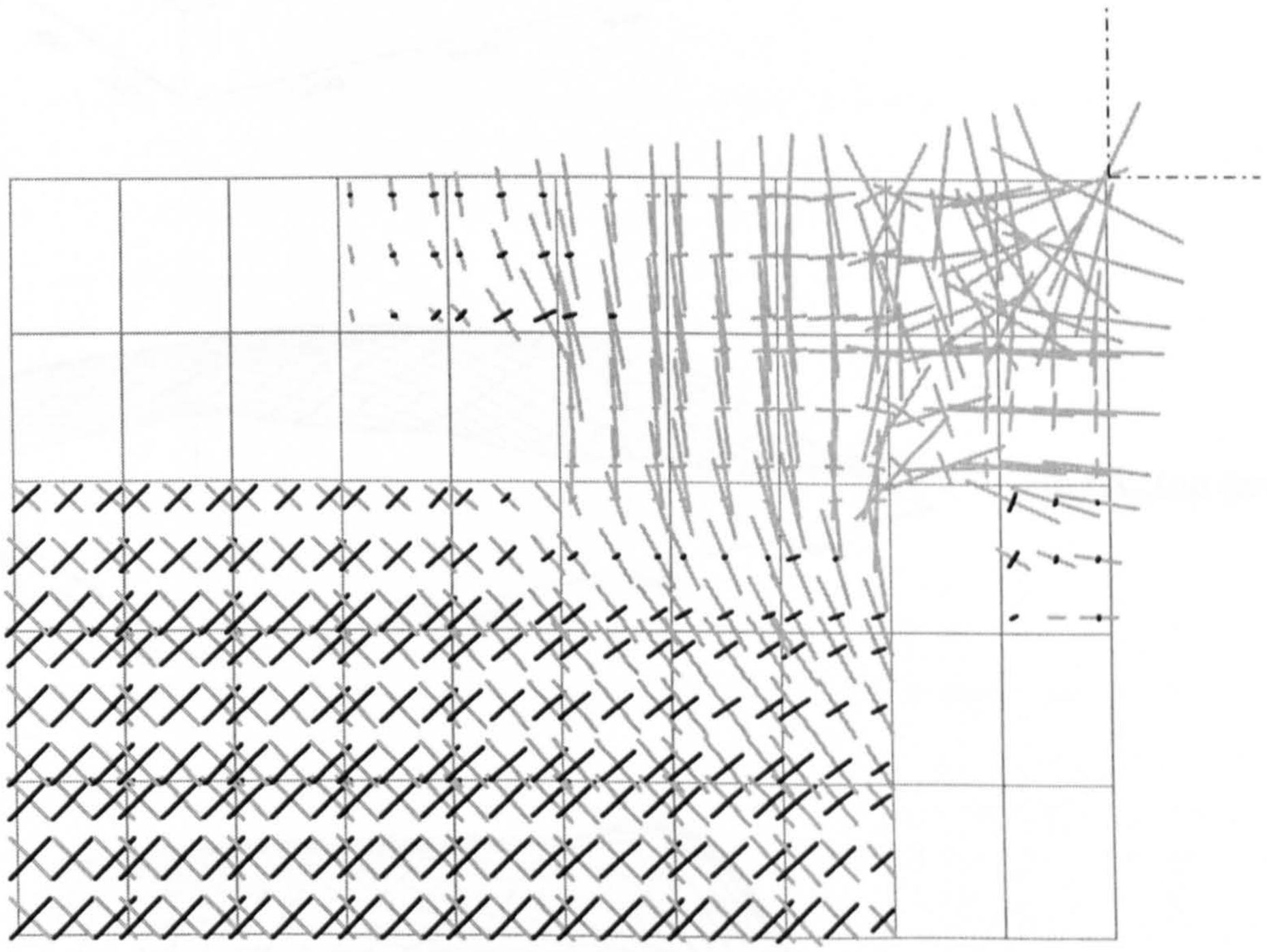

(ii) rr=30%

fig.6.3.2(a) Slab SM2, principal moments

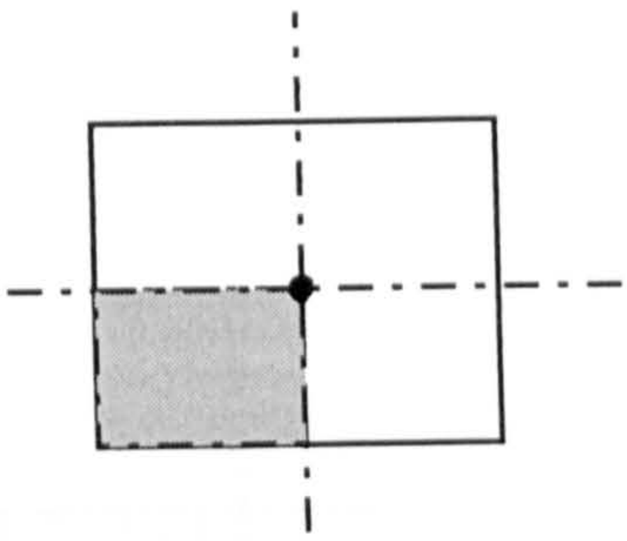

i) A_{sx}bottom (rr=0)

ii) A_{sx}bottom (rr=30%)

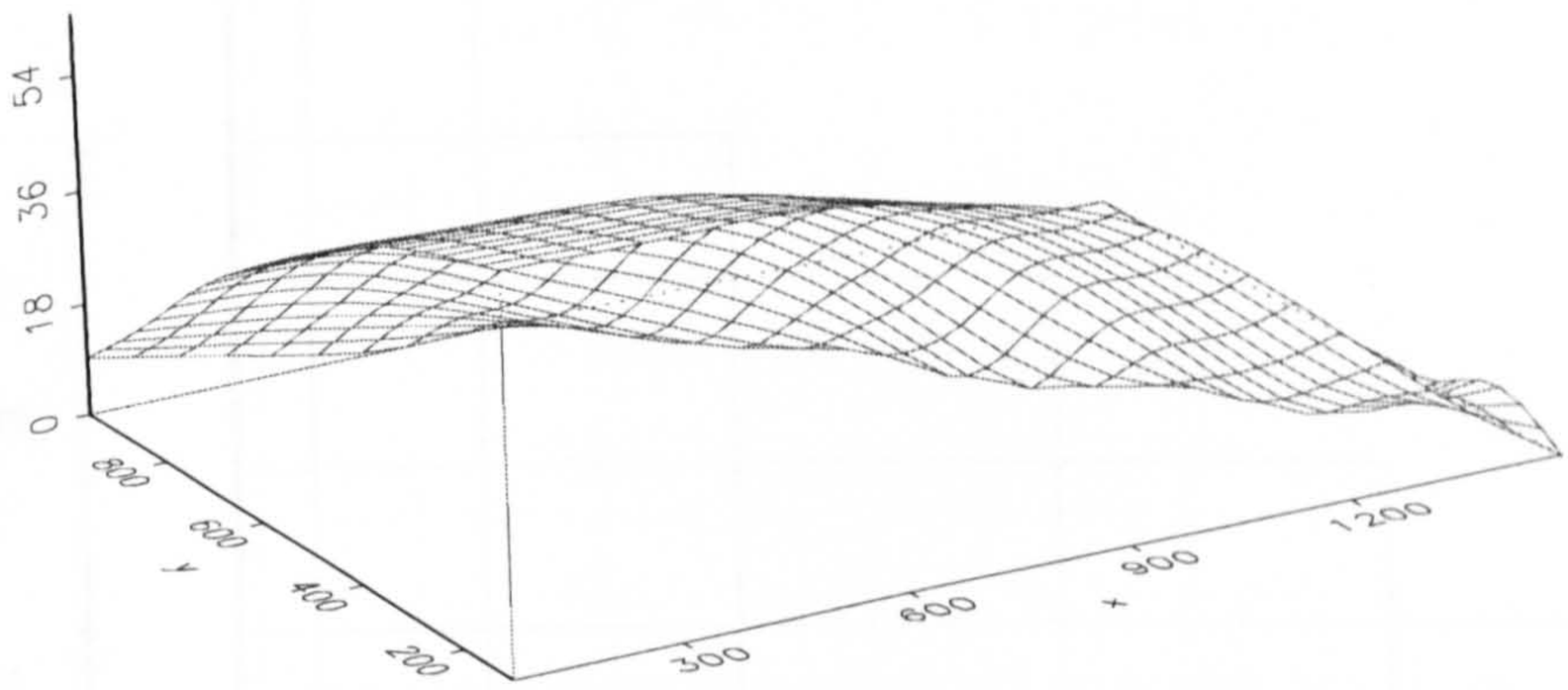

iii) A_{sx}top (rr=0)

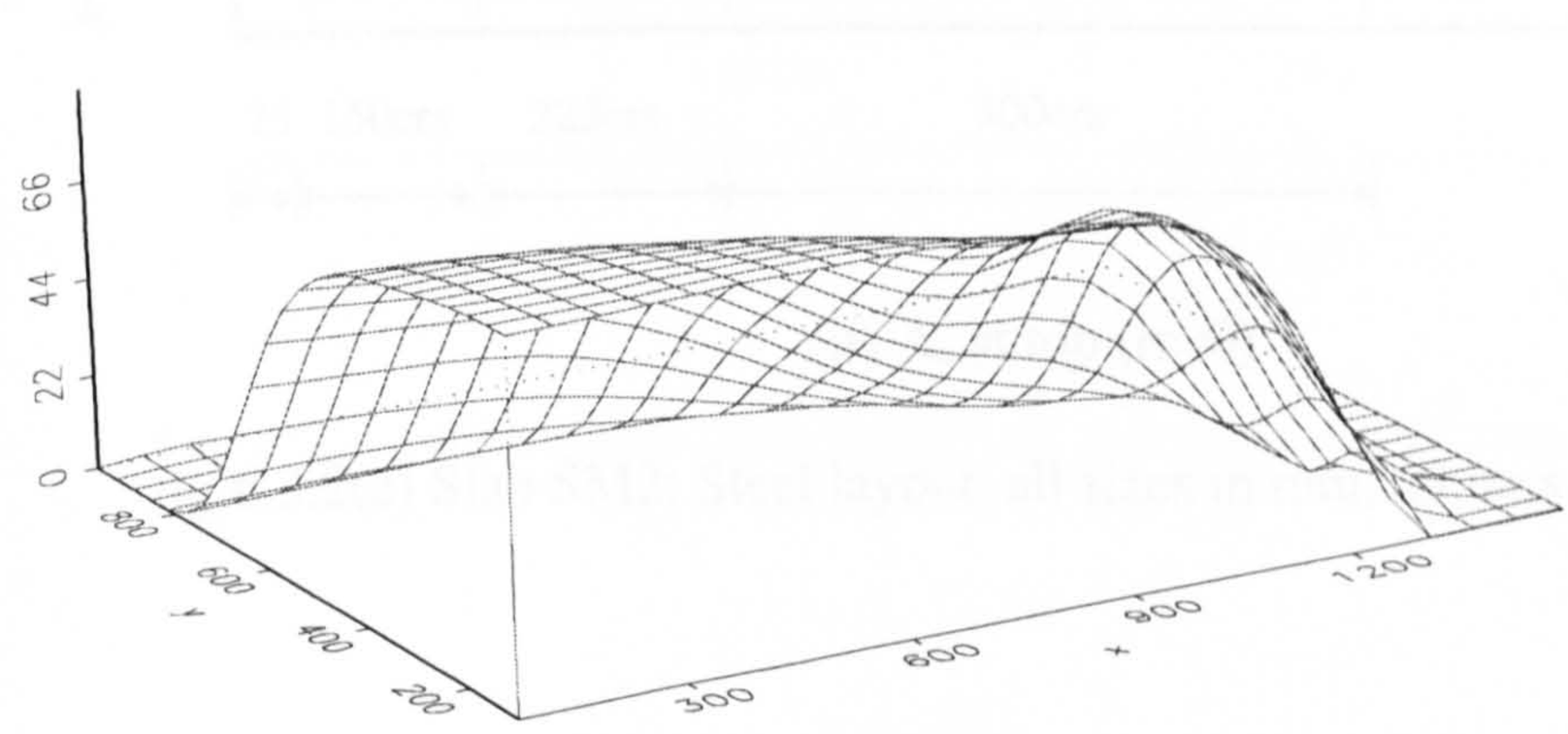

iv) A_{sx}top (rr=30%)

fig.6.3.2(b) Slab SM2, Symmetrical Quarter, Numerical Steel Areas (mm^2)

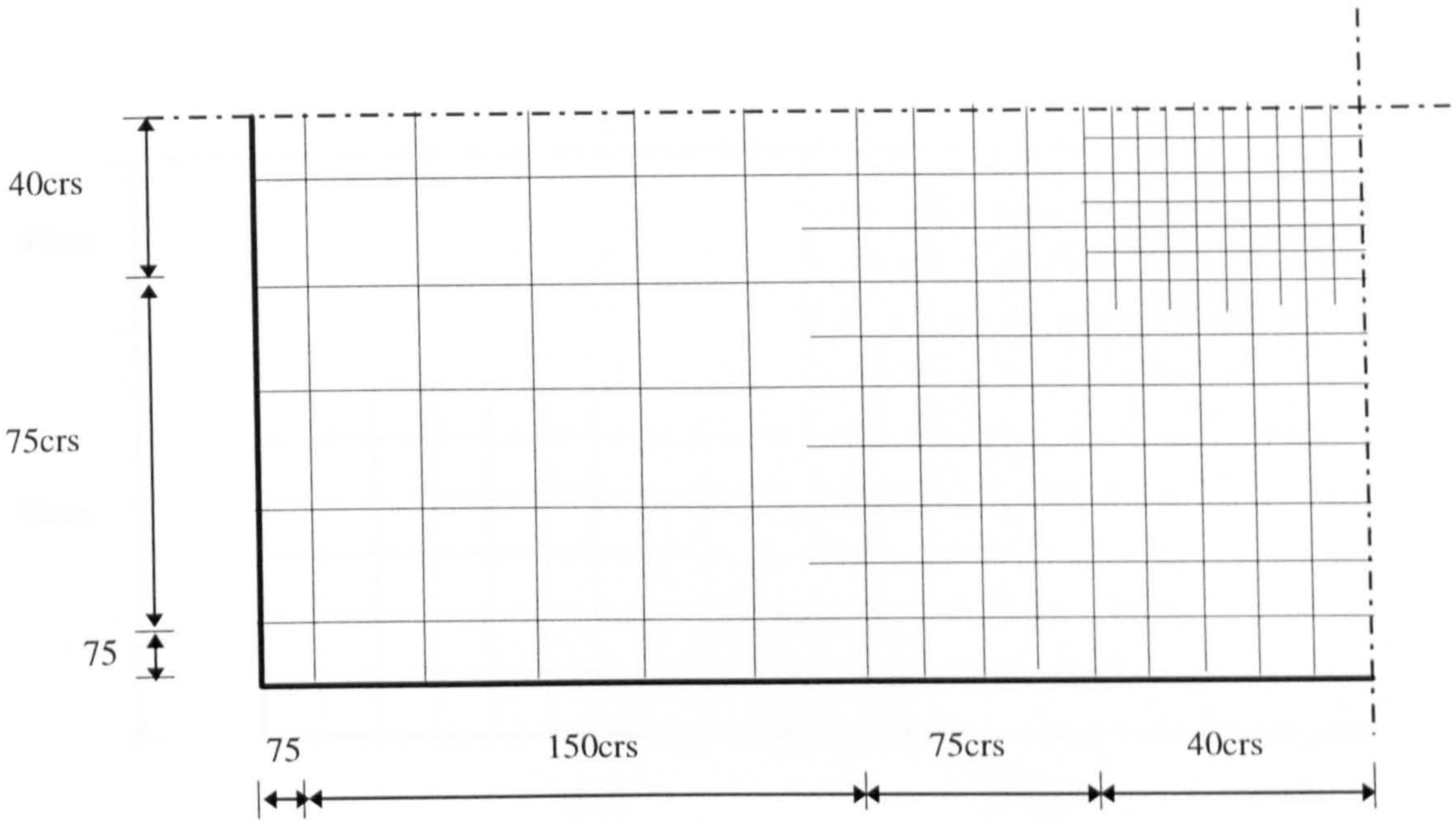

(i) A_s at bottom (rr=0)

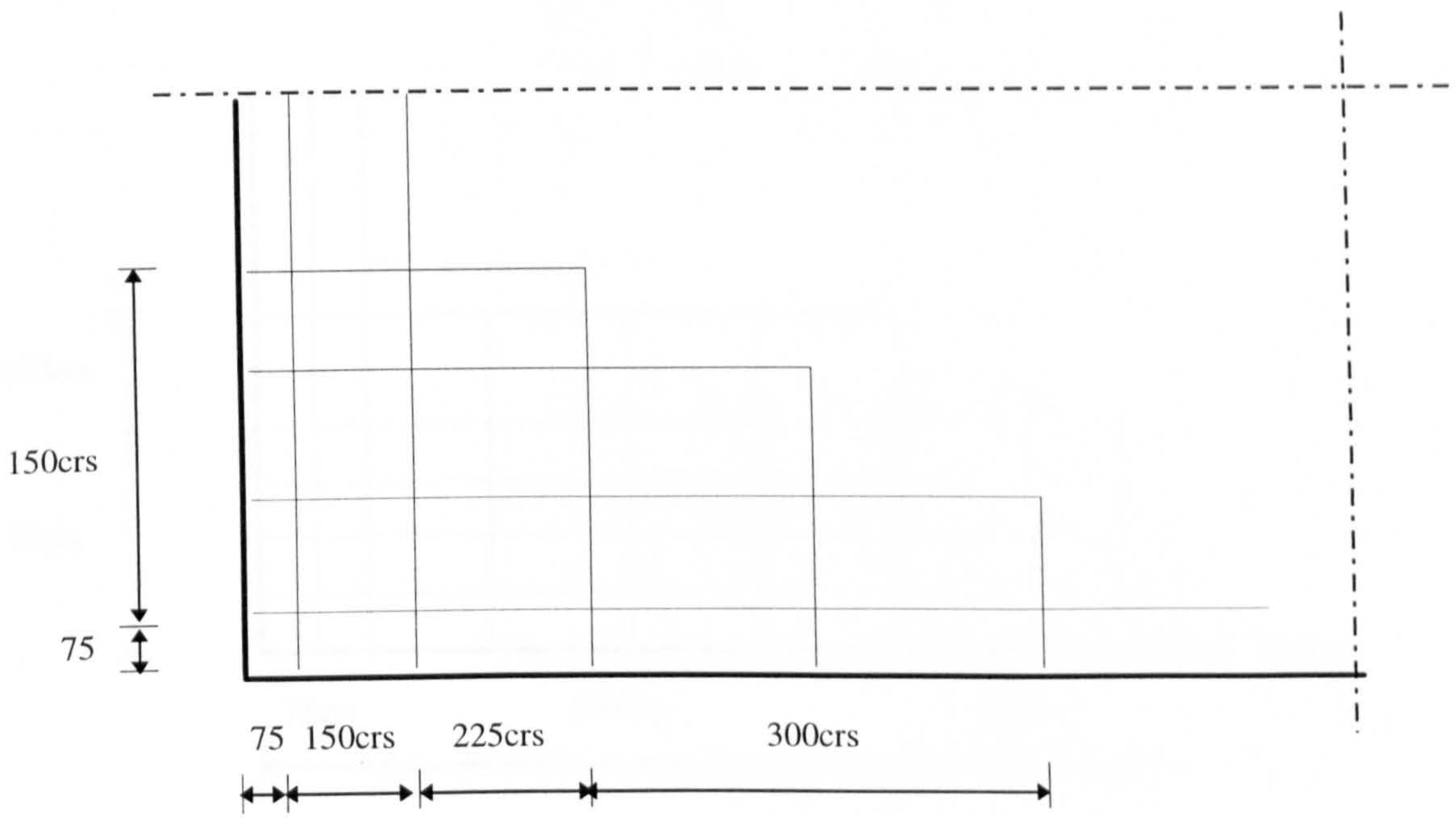

(ii) A_s at top (rr=0)

fig.6.3.2(c) Slab SM2: Steel layout, all sizes in mm, all bars 8mm diameter

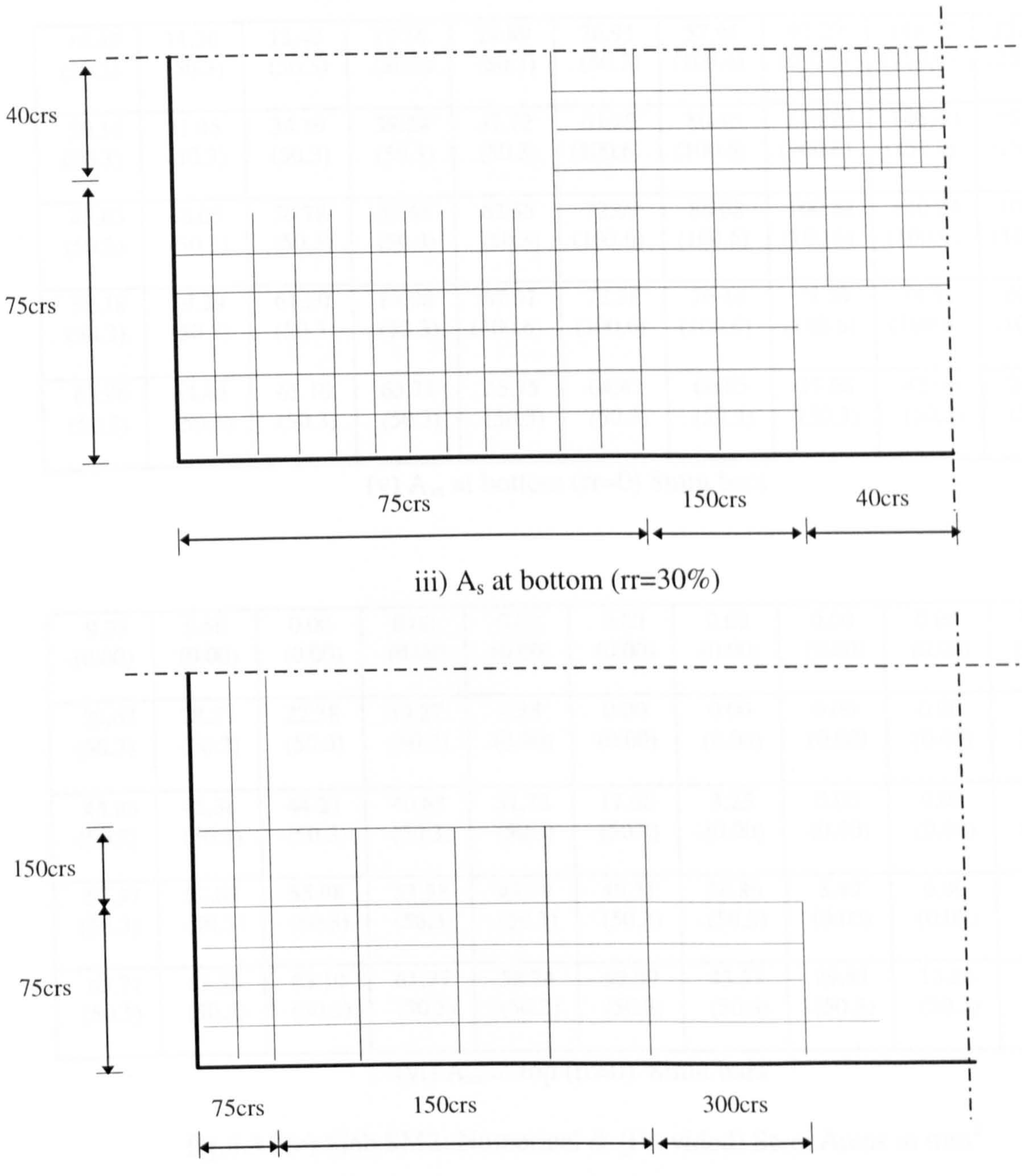

fig.6.3.2(c) Slab SM2: Steel layout, all sizes in mm, all bars 8mm diameter

10.49 (50.3)	11.36 (50.3)	13.43 (50.3)	17.56 (50.3)	24.89 (50.3)	36.91 (50.3)	57.94 (100.6)	97.27 (100.6)	149.77 (150.9)	252.24 (251.5)
30.16 (50.3)	31.45 (50.3)	34.19 (50.3)	39.24 (50.3)	47.72 (50.3)	61.29 (100.6)	80.85 (100.6)	110.29 (100.6)	146.40 (150.9)	167.34 (150.9)
46.63 (50.3)	48.05 (50.3)	50.78 (50.3)	55.41 (50.3)	62.55 (50.3)	72.69 (100.6)	86.08 (100.6)	100.52 (100.6)	110.84 (100.6)	105.62 (100.6)
58.18 (50.3)	59.29 (50.3)	61.20 (50.3)	64.08 (50.3)	67.91 (100.6)	72.38 (100.6)	76.48 (100.6)	78.29 (100.6)	74.51 (100.6)	62.10 (100.6)
63.96 (50.3)	64.43 (50.3)	65.10 (50.3)	65.71 (50.3)	65.75 (50.3)	64.47 (50.3)	60.85 (50.3)	53.68 (50.3)	42.06 (50.3)	26.01 (50.3)

(v) A_{sx} at bottom (rr=0) 8mm bars

9.33 (0.00)	5.50 (0.00)	0.00 (0.00)	0.00 (0.00)	0.00 (0.00)	0.00 (0.00)	0.00 (0.00)	0.00 (0.00)	0.00 (0.00)	0.00 (0.00)
29.62 (50.3)	28.37 (50.3)	22.38 (50.3)	13.27 (50.3)	4.88 (0.00)	0.00 (0.00)	0.00 (0.00)	0.00 (0.00)	0.00 (0.00)	0.00 (0.00)
45.93 (50.3)	45.36 (50.3)	44.21 (50.3)	40.63 (50.3)	31.78 (50.3)	17.66 (50.3)	3.25 (0.00)	0.00 (0.00)	0.00 (0.00)	0.00 (0.00)
57.57 (50.3)	57.04 (50.3)	55.98 (50.3)	53.58 (50.3)	48.79 (50.3)	40.31 (50.3)	26.80 (50.3)	8.49 (0.00)	0.00 (0.00)	0.00 (0.00)
63.71 (50.3)	63.55 (50.3)	63.10 (50.3)	61.77 (50.3)	58.74 (50.3)	52.99 (50.3)	43.53 (50.3)	29.82 (50.3)	13.06 (50.3)	0.00 (0.00)

(vi) A_{sx} at top (rr=0) 8mm bars

fig.6.3.2(c) Slab SM2: Numerical & (Provided) Steel Areas in mm^2

0.00 (25.2)	0.00 (25.2)	0.00 (25.2)	9.14 (25.2)	31.70 (25.2)	24.89 (25.2)	41.07 (50.3)	87.86 (50.3)	158.01 (251.5)	277.10 (251.5)
0.00 (25.2)	0.00 (25.2)	0.00 (25.2)	0.00 (25.2)	0.00 (25.2)	21.61 (25.2)	36.34 (50.3)	62.65 (50.3)	185.12 (201.2)	206.57 (201.2)
73.15 (100.6)	73.39 (100.6)	73.00 (100.6)	71.71 (100.6)	68.56 (100.6)	60.32 (100.6)	59.97 (100.6)	49.07 (100.6)	0.00 (100.6)	91.09 (100.6)
83.57 (100.6)	83.36 (100.6)	83.07 (100.6)	83.38 (100.6)	84.39 (100.6)	86.62 (100.6)	85.06 (100.6)	67.88 (100.6)	0.00 (25.2)	0.00 (25.2)
86.43 (100.6)	86.65 (100.6)	87.29 (100.6)	88.33 (100.6)	89.65 (100.6)	89.87 (100.6)	88.27 (100.6)	72.05 (100.6)	0.00 (25.2)	0.00 (25.2)

(vii) A_{sx} at bottom (rr=30%) 8mm bars

0.00 (0.00)	0.00 (0.00)	0.00 (0.00)	5.51 (0.00)	8.61 (0.00)	3.99 (0.00)	0.00 (0.00)	0.00 (0.00)	0.00 (0.00)	0.00 (0.00)
0.00 (0.00)	0.00 (0.00)	0.00 (0.00)	0.00 (0.00)	0.00 (0.00)	0.00 (0.00)	0.00 (0.00)	0.00 (0.00)	0.00 (0.00)	0.00 (0.00)
72.12 (50.3)	69.79 (50.3)	65.21 (50.3)	56.38 (50.3)	38.32 (50.3)	20.70 (50.3)	11.65 (50.3)	11.33 (50.3)	0.00 (0.00)	0.00 (0.00)
83.49 (100.6)	82.93 (100.6)	81.53 (100.6)	78.76 (100.6)	74.10 (100.6)	67.54 (100.6)	66.31 (100.6)	53.30 (100.6)	0.00 (0.00)	0.00 (0.00)
86.53 (100.6)	86.89 (100.6)	87.31 (100.6)	87.39 (100.6)	86.26 (100.6)	84.21 (100.6)	81.76 (100.6)	69.38 (100.6)	0.00 (0.00)	0.00 (0.00)

(viii) A_{sx} at top (rr=30%) 8mm bars

fig.6.3.2(c) Slab SM2: Numerical & (Provided) Steel Areas in mm^2

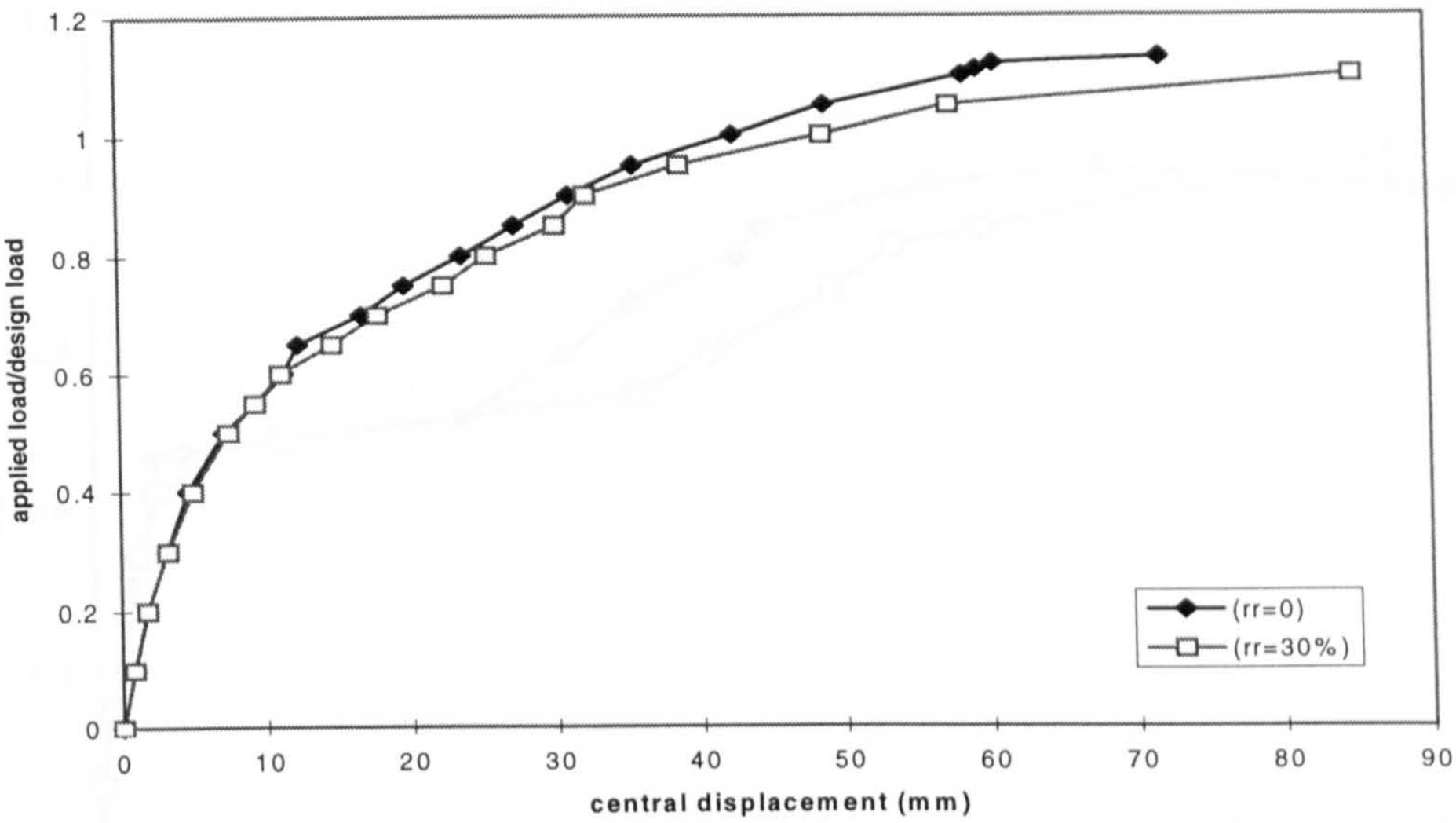

fig.6.3.2(d) Slab SM2: Load-displacement relationship

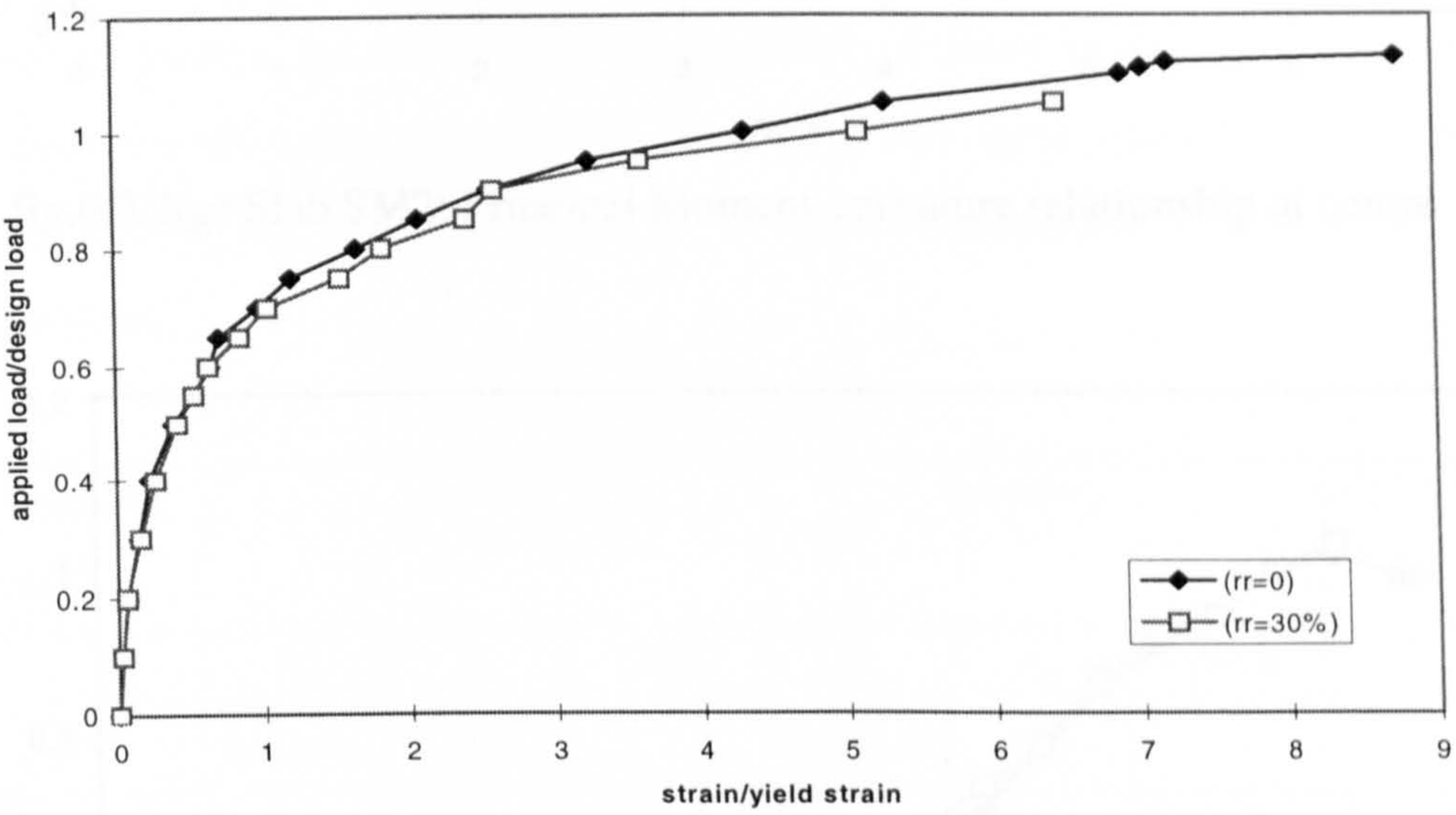

fig.6.3.2(e) Slab SM2: Bottom Steel Strains at centre

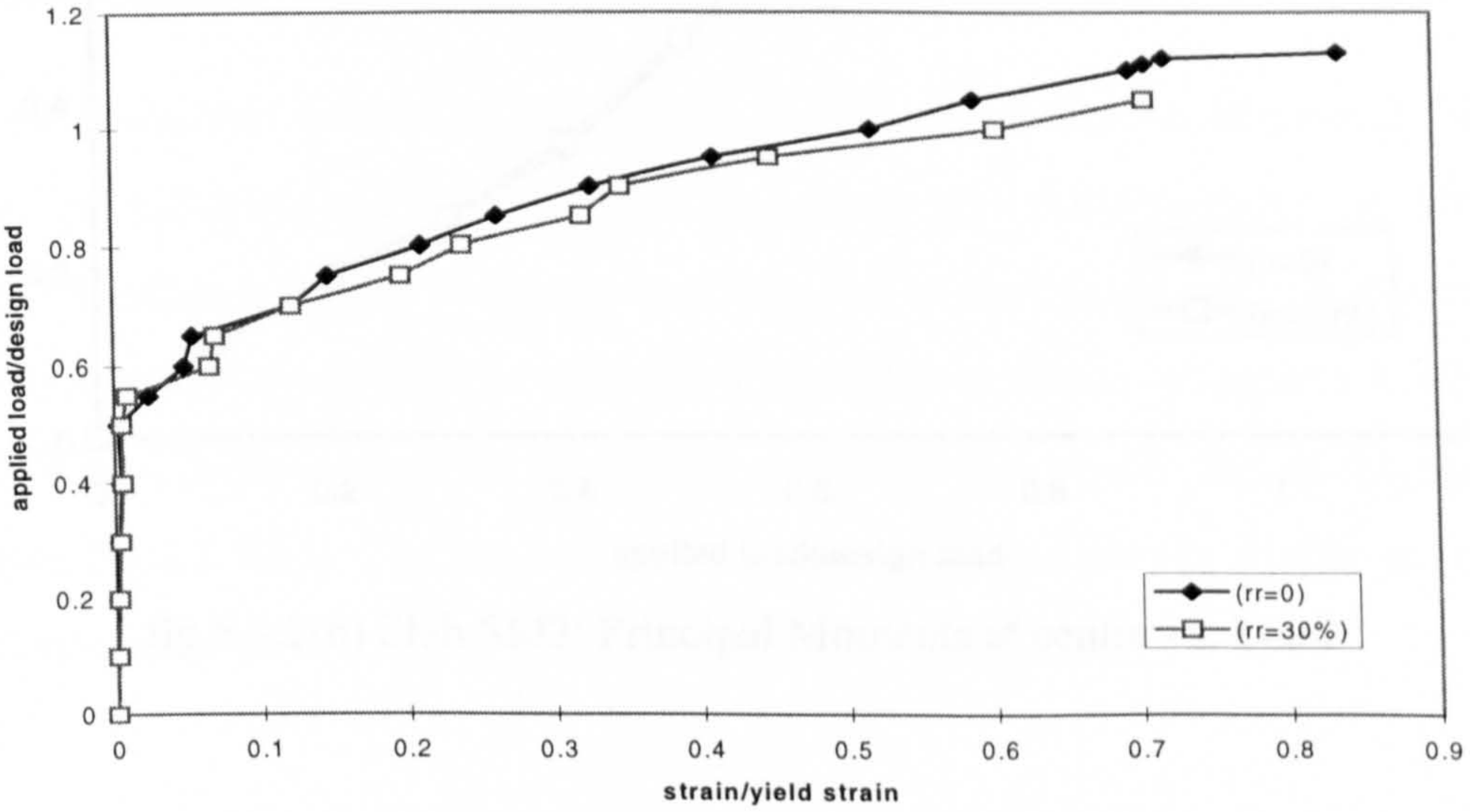

fig.6.3.2(f) Slab SM2: Top Steel Strains at corner

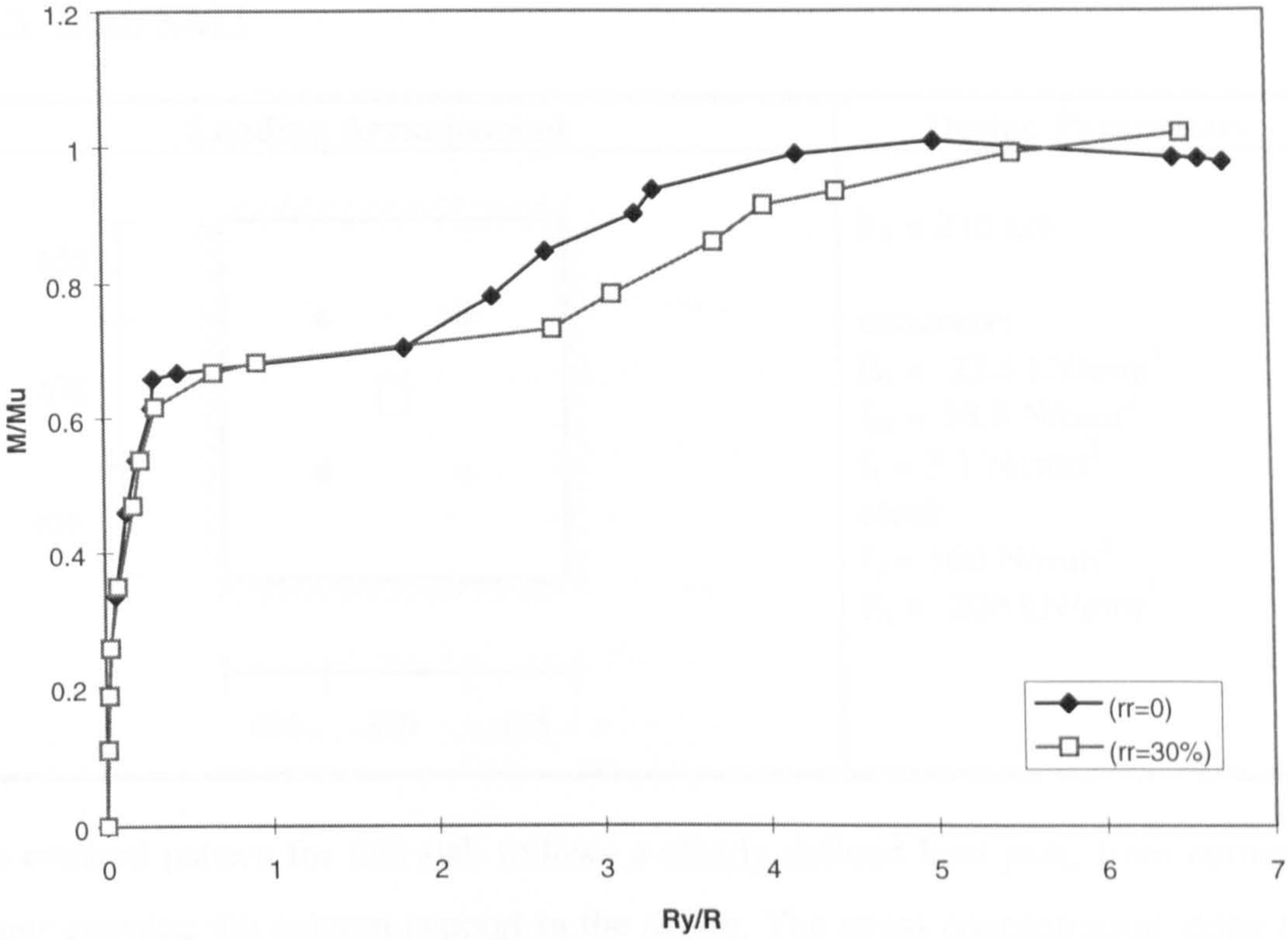

fig.6.3.2(g) Slab SM2: Principal Moment-curvature relationship at centre

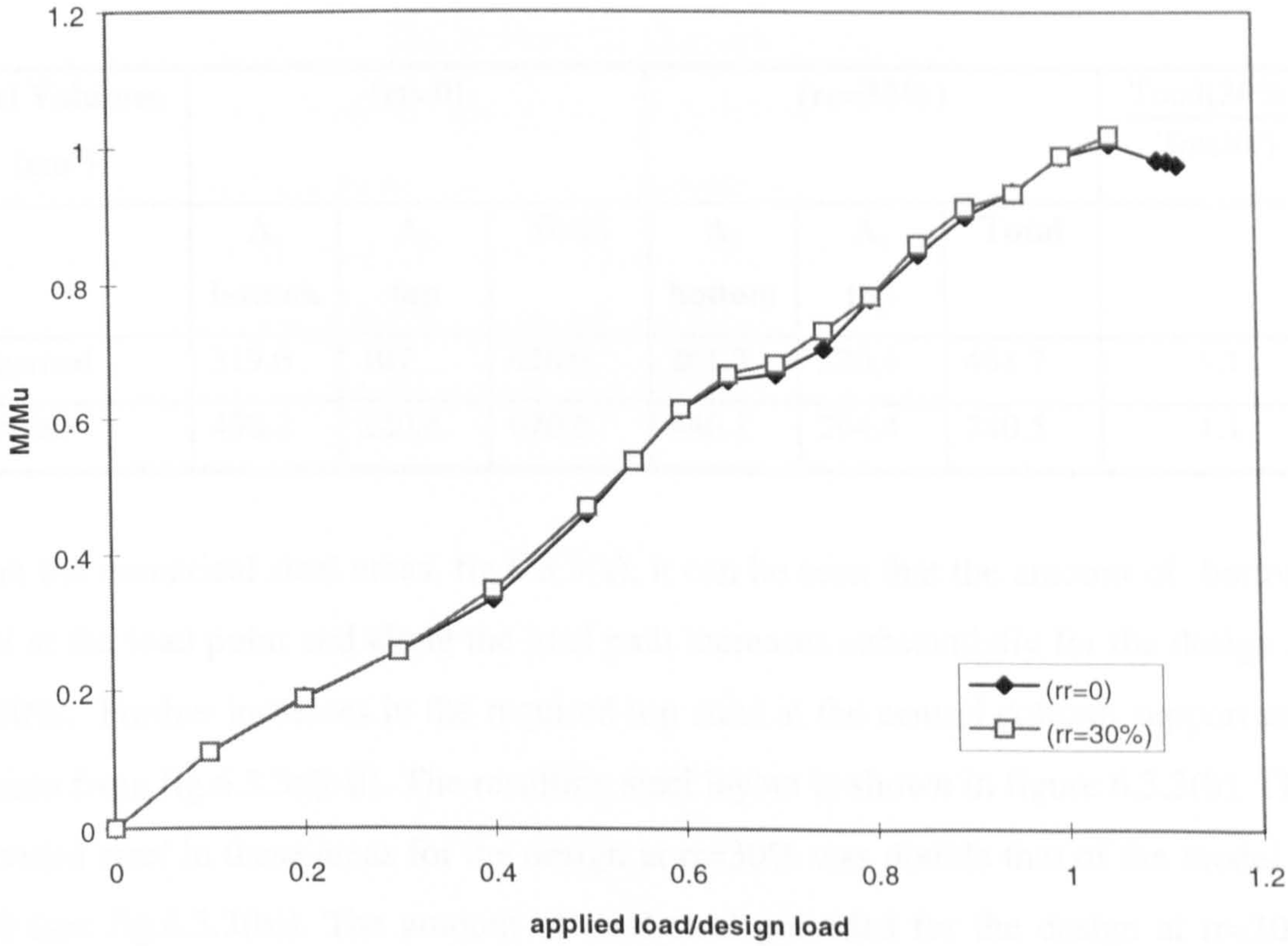

fig.6.3.2(h) Slab SM2: Principal Moments at centre vs. Load

6.3.3 Slab SM3

Loading Arrangement	Design Parameters
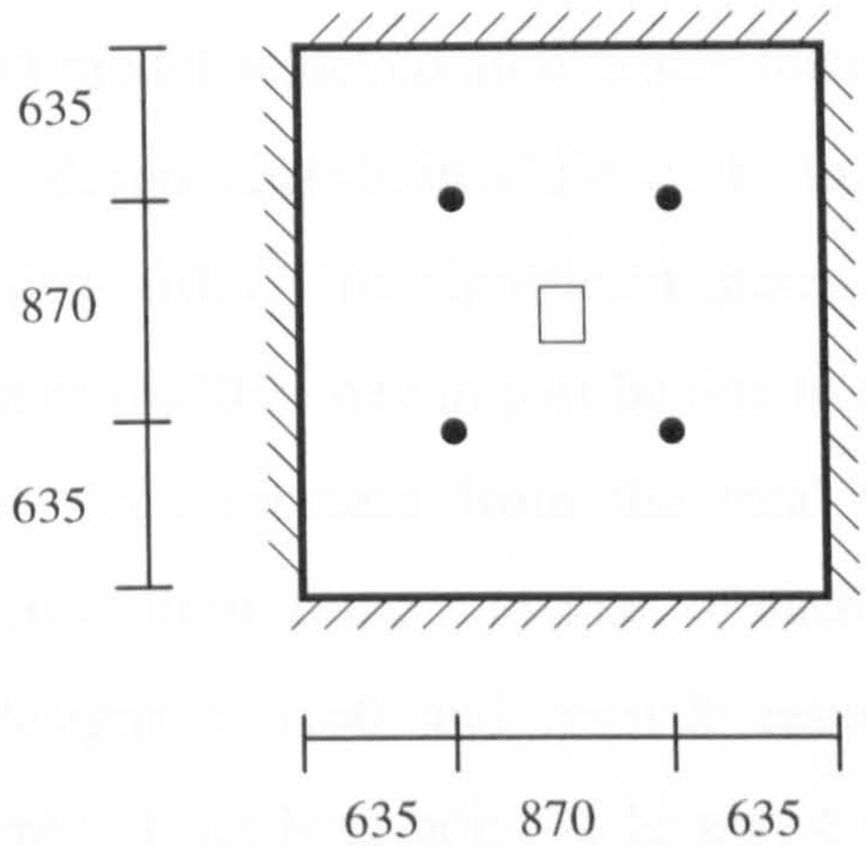	P_d = 210 kN **concrete:** E_c = 22.5 kN/mm^2 f_{cu} = 58.8 N/mm^2 f_t = 3.1 N/mm^2 **steel:** f_y = 560 N/mm^2 E_s = 200 kN/mm^2

The evolved pattern for this slab follows a clearly defined load path, from corner to corner crossing the column support in the centre. The stress concentration along this load path leads to the 'removal' of a high % area at a comparable rejection ratio to the previous slabs.

Steel Volumes (cm^3)	**(rr=0)**			**(rr=30%)**			Total(**30%**) / Total(**0**)
	A_s bottom	**A_s top**	**Total**	**A_s bottom**	**A_s top**	**Total**	
Numerical	319.6	107	426.6	261.3	220.4	481.7	1.1
Provided	450.2	220.4	670.6	446.1	294.4	740.5	1.1

From the numerical steel areas, fig.6.3.3(a), it can be seen that the amount of bottom steel at the load point and along the load path increases substantially for the design at rr=30%. Further increases in the required top steel at the central column support can be seen from fig.6.3.3a(i-ii). The resulting steel layout is shown in figure 6.3.3(b). The provided steel in these areas for the design at rr=30% was double that of the model at rr=0 (see fig.6.3.3(b)). The amount of total steel provided for the design at rr=30% was increased by 10%.

Because of the significant increase of provided steel in the critical areas, i.e along the diagonal, for the design at rr=30%, it can be expected that the ultimate load of this design would be greater. This assumption is confirmed by the numerical analysis. The second model achieved an ultimate load of $1.3P_d$ compared with an ultimate of $1.1P_d$ for the design at rr=0. In addition, the load-displacement response of the second model was also stiffer. The significant increase from design load to ultimate load for the model at rr=30% may in part be due to the fact that in order to make a practical steel layout, 35% increase from the total theoretical steel was required. The service deflection limit at the mid-span of each quarter was reached at $0.7P_d$ and $0.85P_d$ for the designs at rr=0 and rr=30% respectively. Yielding of the bottom steel first occurred at the load point at levels of $0.7P_d$ and $0.85P_d$ for the models at rr=0 and rr=30% respectively.

For the section at the load point, the values of M_u and $1/R_y$ were calculated as 18kNm/m and $0.00008mm^{-1}$ respectively, in the design at rr=0. For the second design, at rr=30%, values of M_u and $1/R_y$ were calculated as 22kNm/m and $0.00008mm^{-1}$ respectively. The increase in ultimate moment at rr=30%, is due to the increase in provided steel at this point. Inspection of the moment-applied load relationship at the load point shows that eventual softening occurred in the rr=30% design at an ultimate load of $1.2P_d$, (fig.6.3.3f-g). A similar increase in M_u was observed in the section at the corner due to the provision of more top steel at rr=30%., In this case, M_u was 27kNm/m at rr=0, and 42kNm/m at rr=30%.

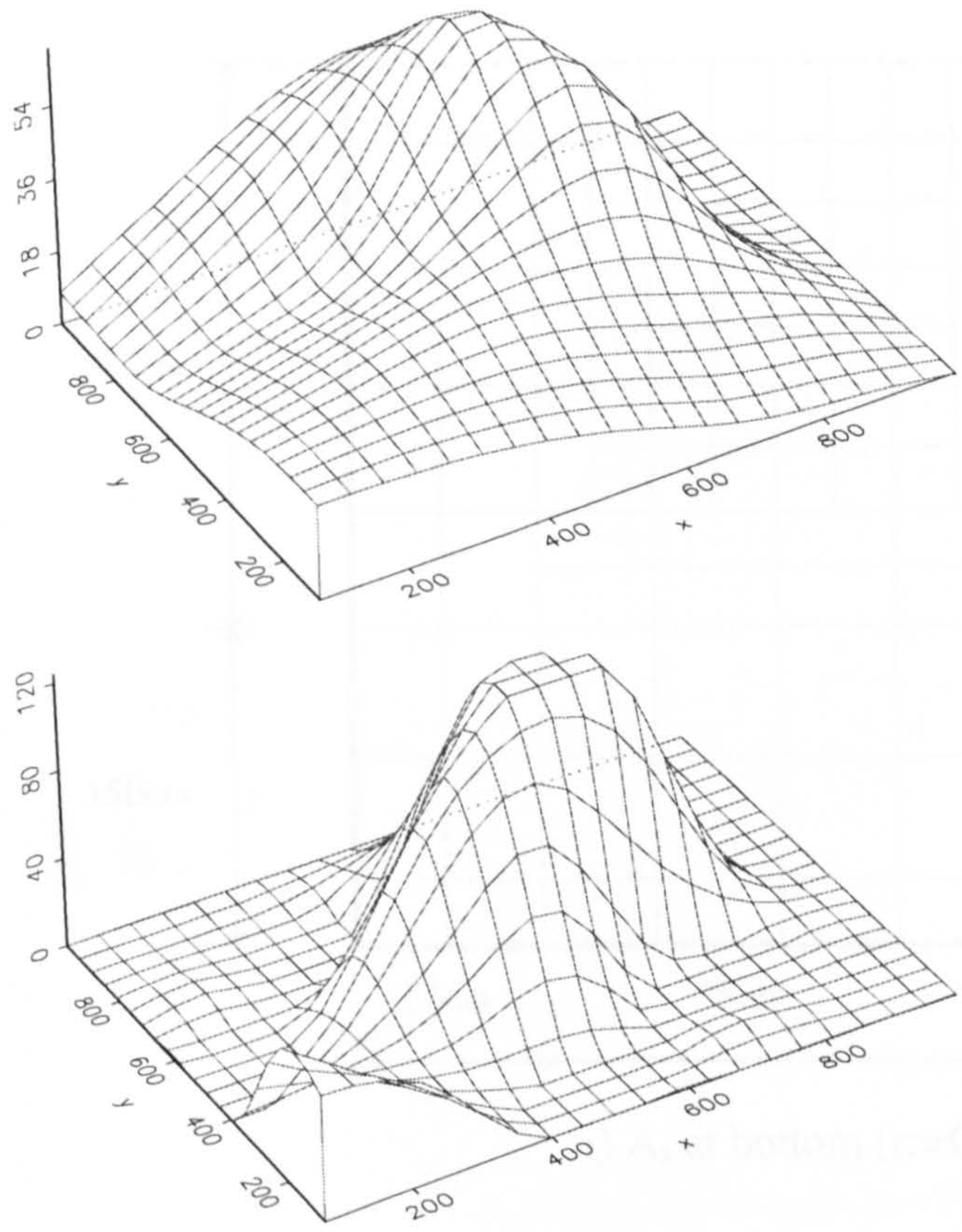

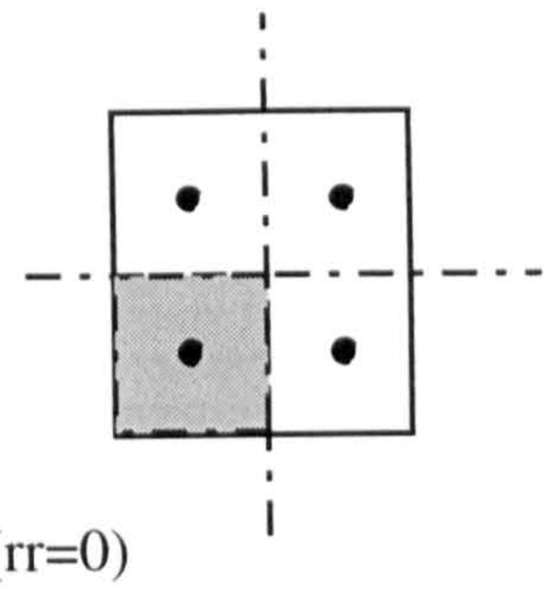

i) A_{sx}bottom (rr=0)

ii) A_{sx}bottom (rr=30%)

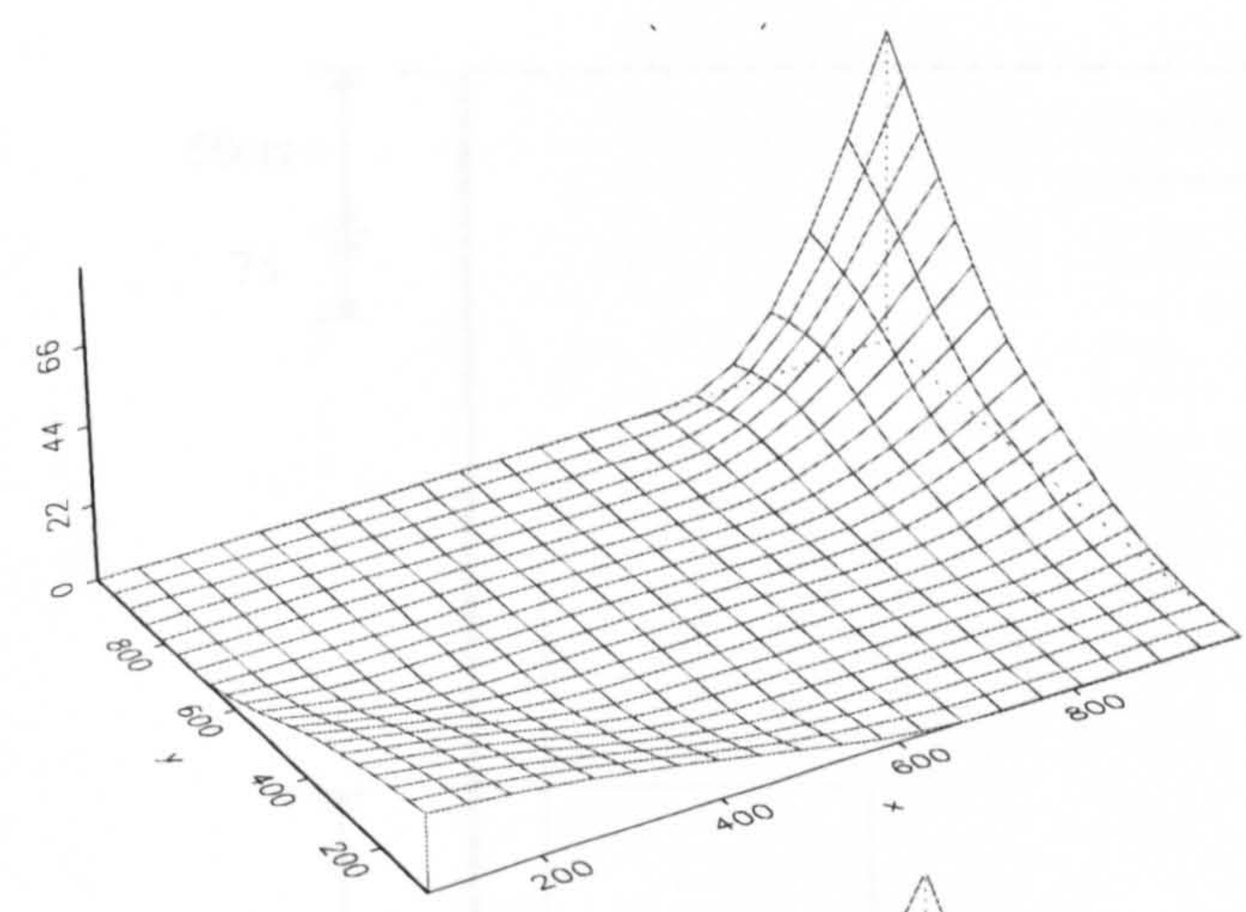

iii) A_{sx}top (rr=0)

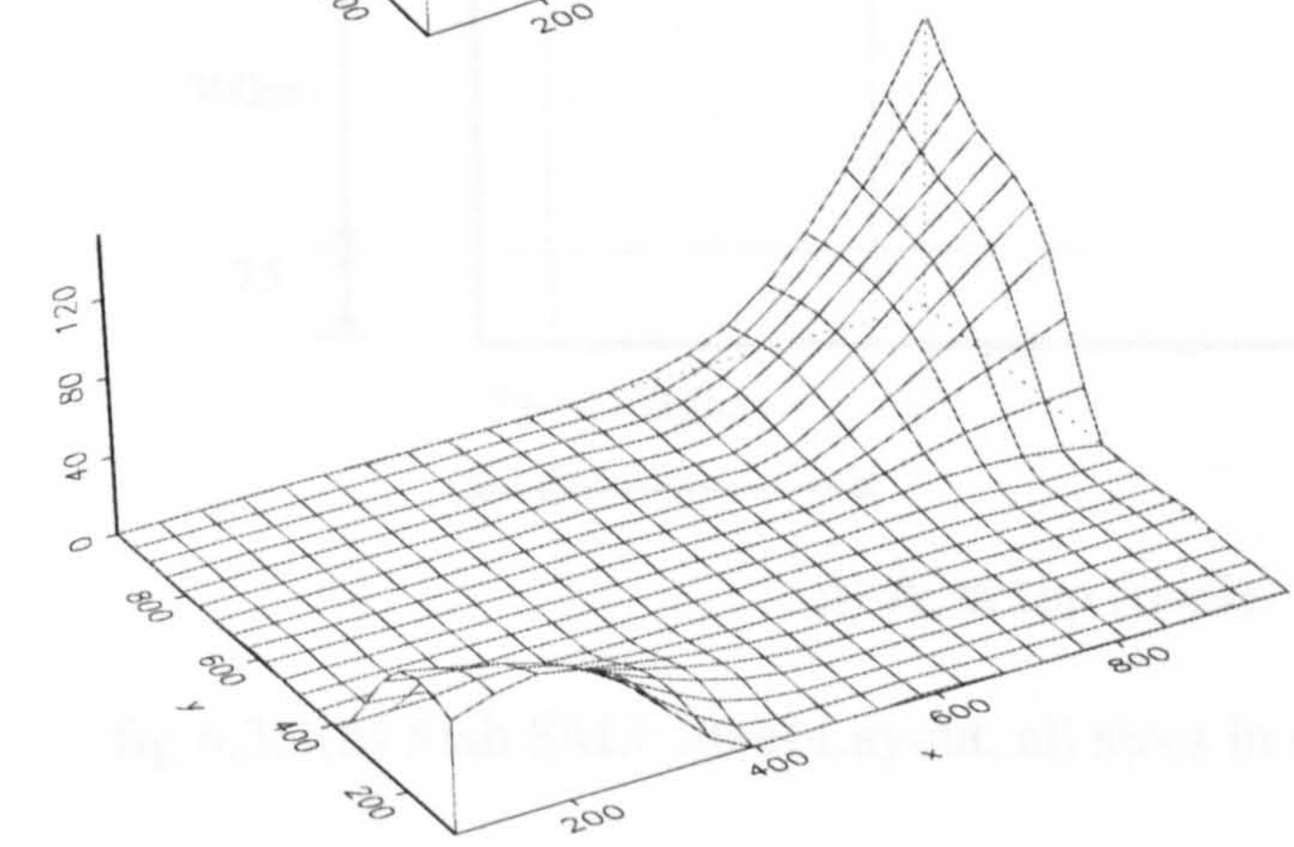

iv) A_{sx}top (rr=30%)

fig.6.3.3(a) Slab SM3, Symmetrical Quarter, Numerical Steel Areas (mm^2)

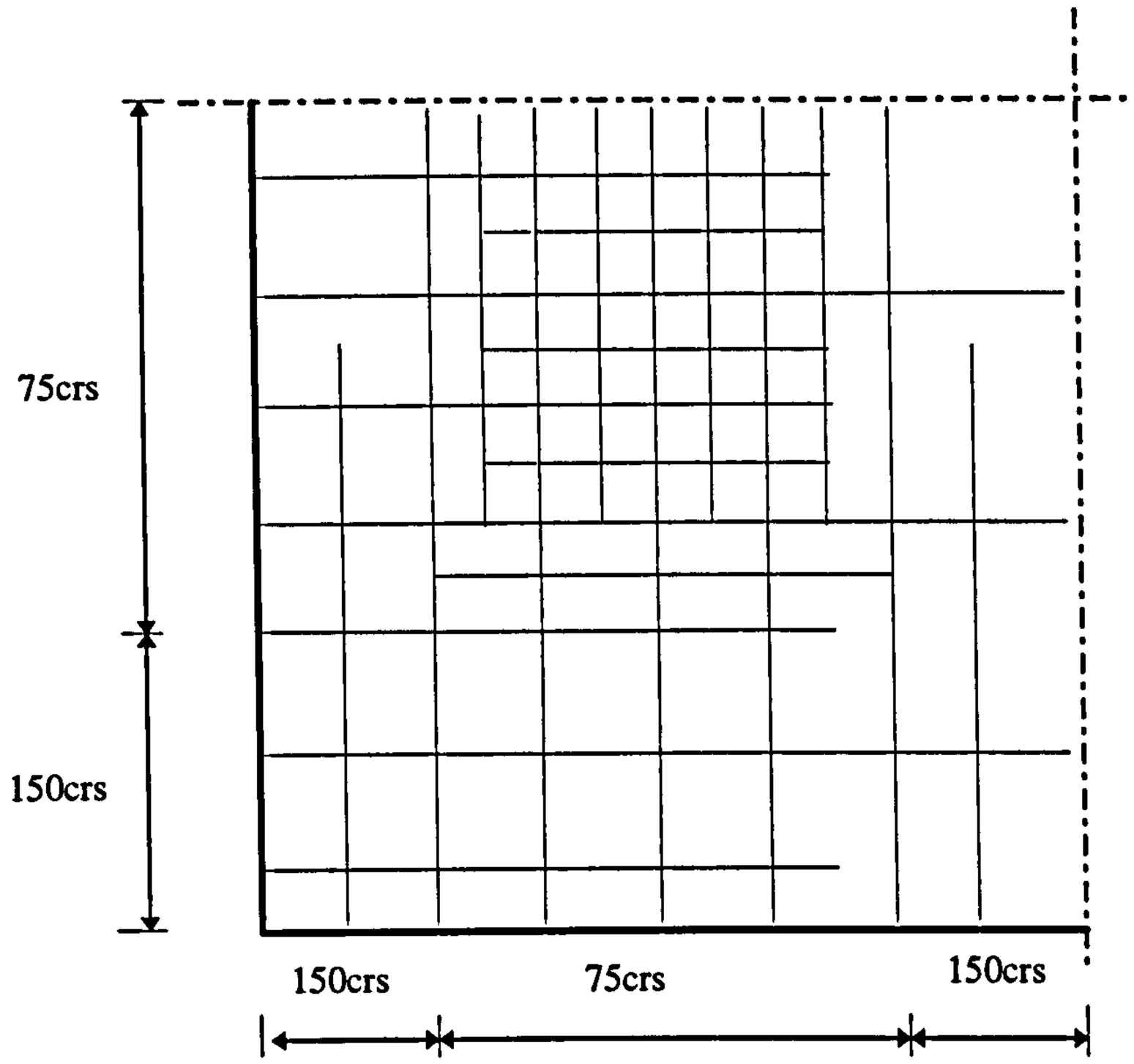

i) A_s at bottom (rr=0)

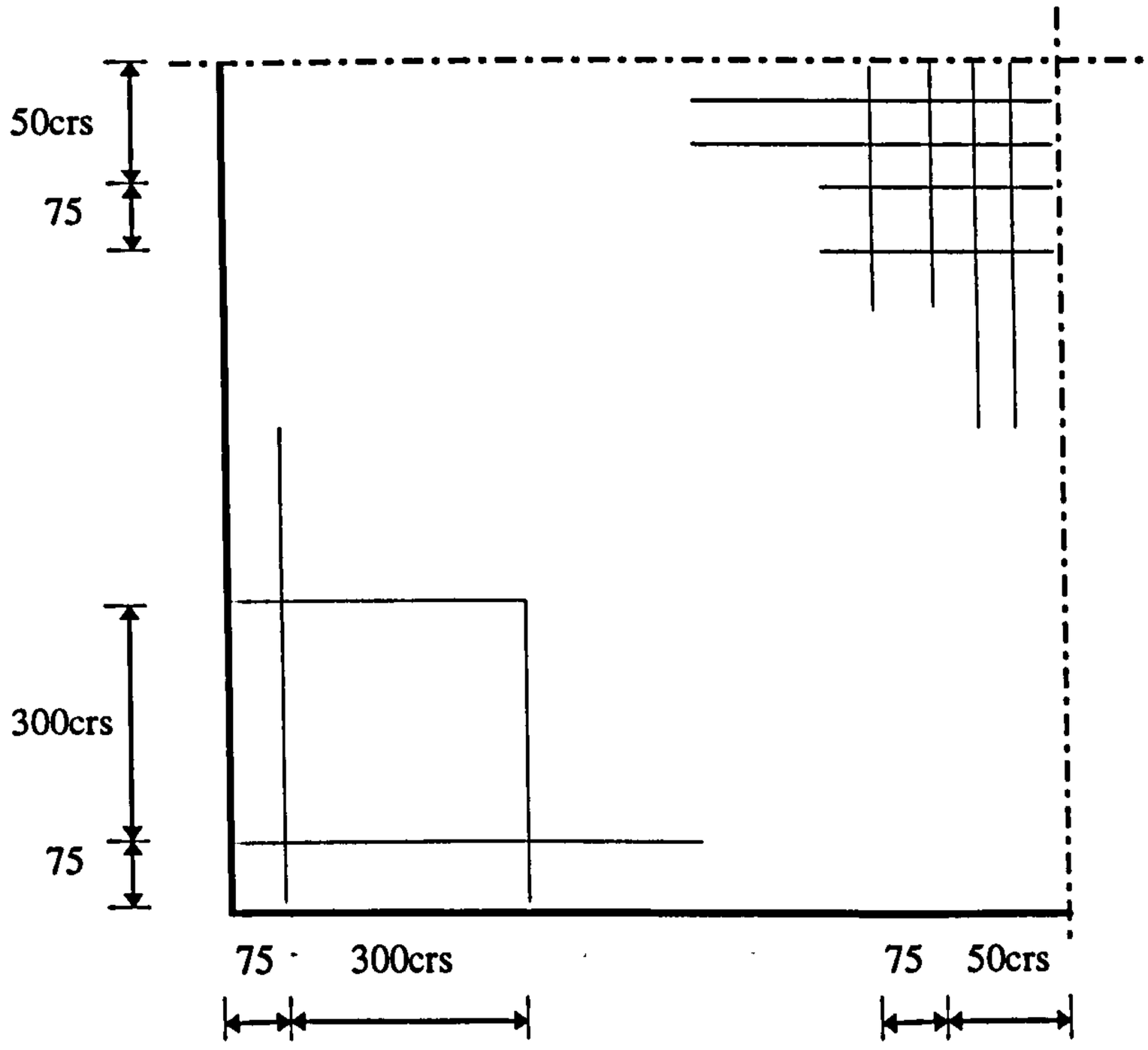

ii) A_s at top (rr=0)

fig.6.3.3(b) Slab SM3: Steel Layout, all sizes in mm, all bars 6mm diameter

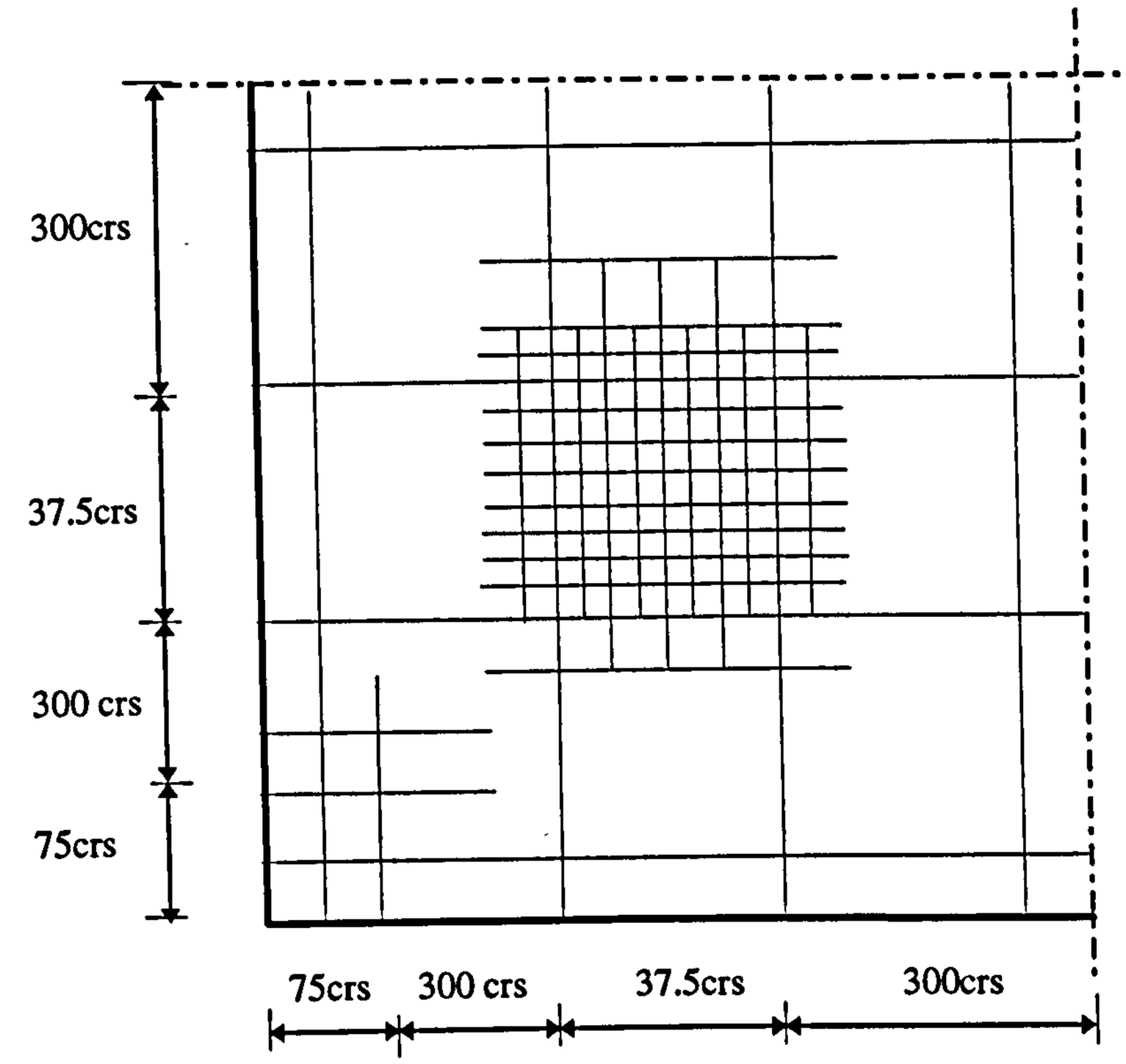

iii) A_s at bottom (rr=30%)

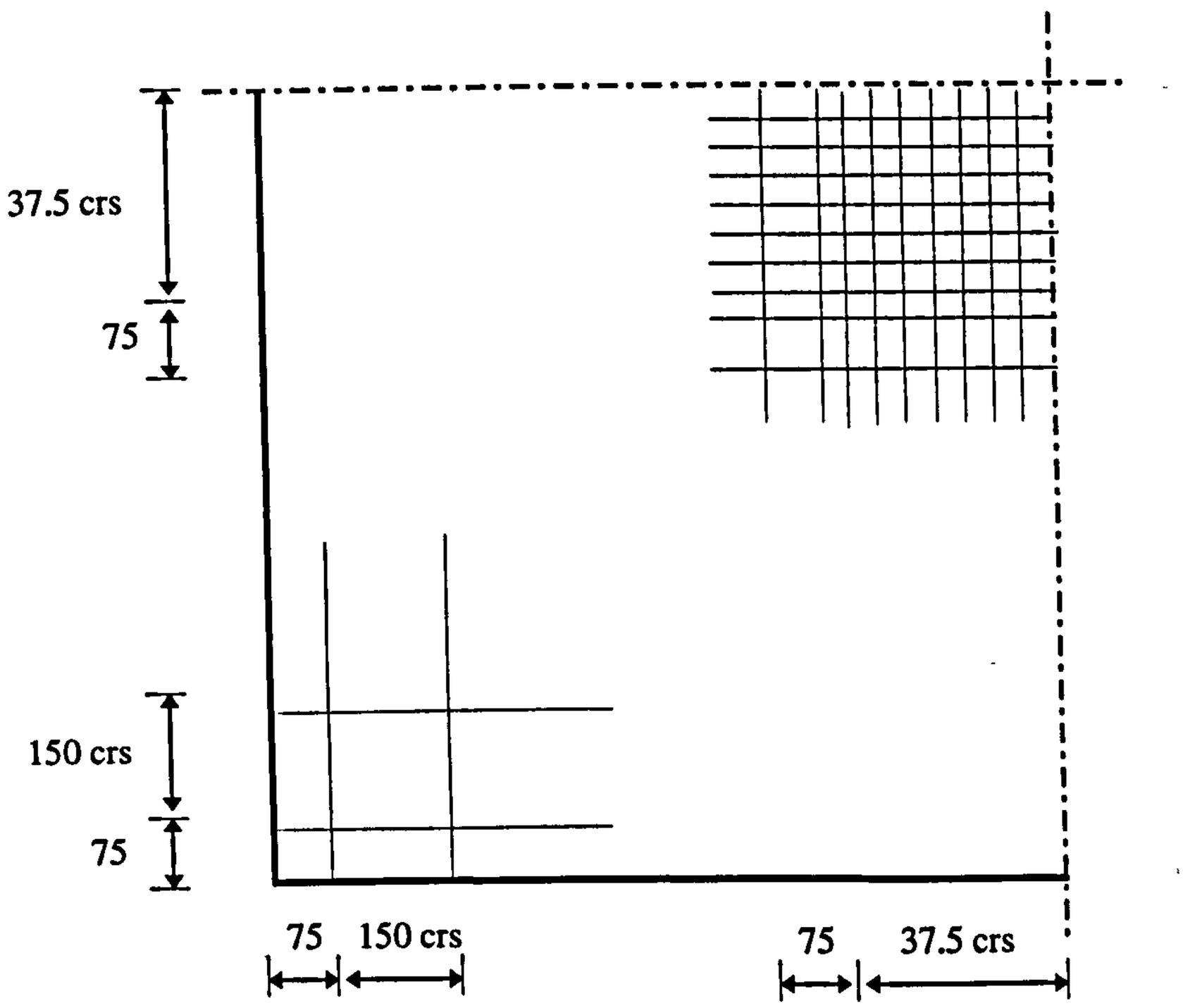

iv) A_s at top (rr=30%)

fig.6.3.3(b) Slab SM3: Steel Layout, all sizes in mm, all bars 6mm diameters

7.79 (28.3)	23.18 (28.3)	37.95 (56.6)	43.83 (56.6)	31.74 (56.6)	4.14 (14.2)	0.00 (14.2)
7.10 (28.3)	22.81 (28.3)	42.27 (56.6)	58.53 (56.6)	40.38 (56.6)	6.71 (14.2)	0.00 (14.2)
7.38 (28.3)	17.16 (28.3)	34.43 (56.6)	68.31 (56.6)	49.21 (56.6)	8.58 (14.2)	0.00 (14.2)
13.06 (28.3)	19.93 (28.3)	29.80 (28.3)	52.47 (56.6)	54.59 (56.6)	14.06 (14.2)	0.00 (14.2)
19.24 (28.3)	25.28 (28.3)	32.05 (28.3)	35.45 (28.3)	31.20 (28.3)	14.78 (14.2)	0.00 (14.2)
22.79 (28.3)	25.71 (28.3)	26.97 (28.3)	23.13 (28.3)	14.99 (28.3)	9.05 (14.2)	0.00 (14.2)
23.44 (28.3)	22.81 (28.3)	19.74 (28.3)	13.75 (28.3)	6.23 (28.3)	3.19 (14.2)	0.00 (14.2)

(v) A_{sx} at bottom (rr=0) 6mm bars

0.00 (0.00)	0.00 (0.00)	5.32 (0.00)	14.24 (0.00)	26.28 (28.3)	51.20 (56.6)	86.51 (84.9)
0.00 (0.00)	0.00 (0.00)	0.00 (0.00)	2.72 (0.00)	6.50 (0.00)	16.78 (28.3)	15.43 (28.3)
0.00 (0.00)	0.00 (0.00)	0.00 (0.00)	0.00 (0.00)	0.00 (0.00)	0.00 (0.00)	0.00 (0.00)
4.86 (0.00)	0.00 (0.00)	0.00 (0.00)	0.00 (0.00)	0.00 (0.00)	0.00 (0.00)	0.00 (0.00)
12.52 (14.2)	4.73 (0.00)	0.00 (0.00)	0.00 (0.00)	0.00 (0.00)	0.00 (0.00)	0.00 (0.00)
18.66 (14.2)	13.24 (14.2)	6.28 (0.00)	0.00 (0.00)	0.00 (0.00)	0.00 (0.00)	0.00 (0.00)
22.06 (28.3)	18.73 (28.3)	13.24 (28.3)	5.70 (28.3)	0.00 (0.00)	0.00 (0.00)	0.00 (0.00)

(vi) A_{sx} at top (rr=0) 6mm bars

fig.6.3.3(b) Slab SM3: Numerical & (Provided) Steel Areas in mm^2

0.000 (14.2)	0.000 (14.2)	0.000 (14.2)	0.000 (14.2)	2.277 (14.2)	0.000 (14.2)	0.000 (14.2)
0.000 (14.2)	0.000 (14.2)	0.000 (14.2)	33.215 (28.3)	21.579 (28.3)	0.000 (14.2)	0.000 (14.2)
0.000 (14.2)	0.000 (14.2)	0.000 (113.1)	100.151 (113.1)	63.849 (113.1)	4.147 (14.2)	0.000 (14.2)
0.000 (14.2)	0.000 (14.2)	71.844 (113.1)	124.362 (113.1)	122.283 (113.1)	22.669 (14.2)	0.000 (14.2)
0.000 (14.2)	12.387 (14.2)	40.030 (56.6)	67.130 (56.6)	0.000 (14.2)	0.000 (14.2)	0.000 (14.2)
55.834 (56.6)	23.169 (56.6)	6.372 (14.2)	0.000 (14.2)	0.000 (14.2)	0.000 (14.2)	0.000 (14.2)
56.396 (56.6)	43.444 (56.6)	0.000 (14.2)	0.000 (14.2)	0.000 (14.2)	0.000 (14.2)	0.000 (14.2)

(vii) A_{sx} at bottom (rr=30%) 6mm bars

0.000 (0.000)	0.000 (0.000)	0.000 (0.000)	0.000 (0.000)	4.922 (0.000)	46.914 (150.9)	152.496 (150.9)
0.000 (0.000)	0.000 (0.000)	0.000 (0.000)	2.675 (0.000)	4.624 (0.000)	51.292 (150.9)	111.046 (150.9)
0.000 (0.000)	0.000 (0.000)	0.000 (0.000)	0.000 (0.000)	0.000 (0.000)	36.606 (100.6)	85.961 (100.6)
0.000 (0.000)	0.000 (0.000)	0.000 (0.000)	0.000 (0.000)	1.883 (0.000)	7.241 (0.000)	0.000 (0.000)
0.000 (0.000)	3.460 (0.000)	0.000 (0.000)	0.000 (0.000)	0.000 (0.000)	0.000 (0.000)	0.000 (0.000)
55.524 (56.6)	37.761 (56.6)	12.157 (0.000)	0.000 (0.000)	0.000 (0.000)	0.000 (0.000)	0.000 (0.000)
58.099 (56.6)	61.632 (56.6)	0.000 (14.2)	0.000 (14.2)	0.000 (14.2)	0.000 (14.2)	0.000 (14.2)

(viii) A_{sx} at top (rr=30%) 6mm bars

fig.6.3.1(b) Slab SM3: Numerical & (Provided) Steel Areas in mm^2

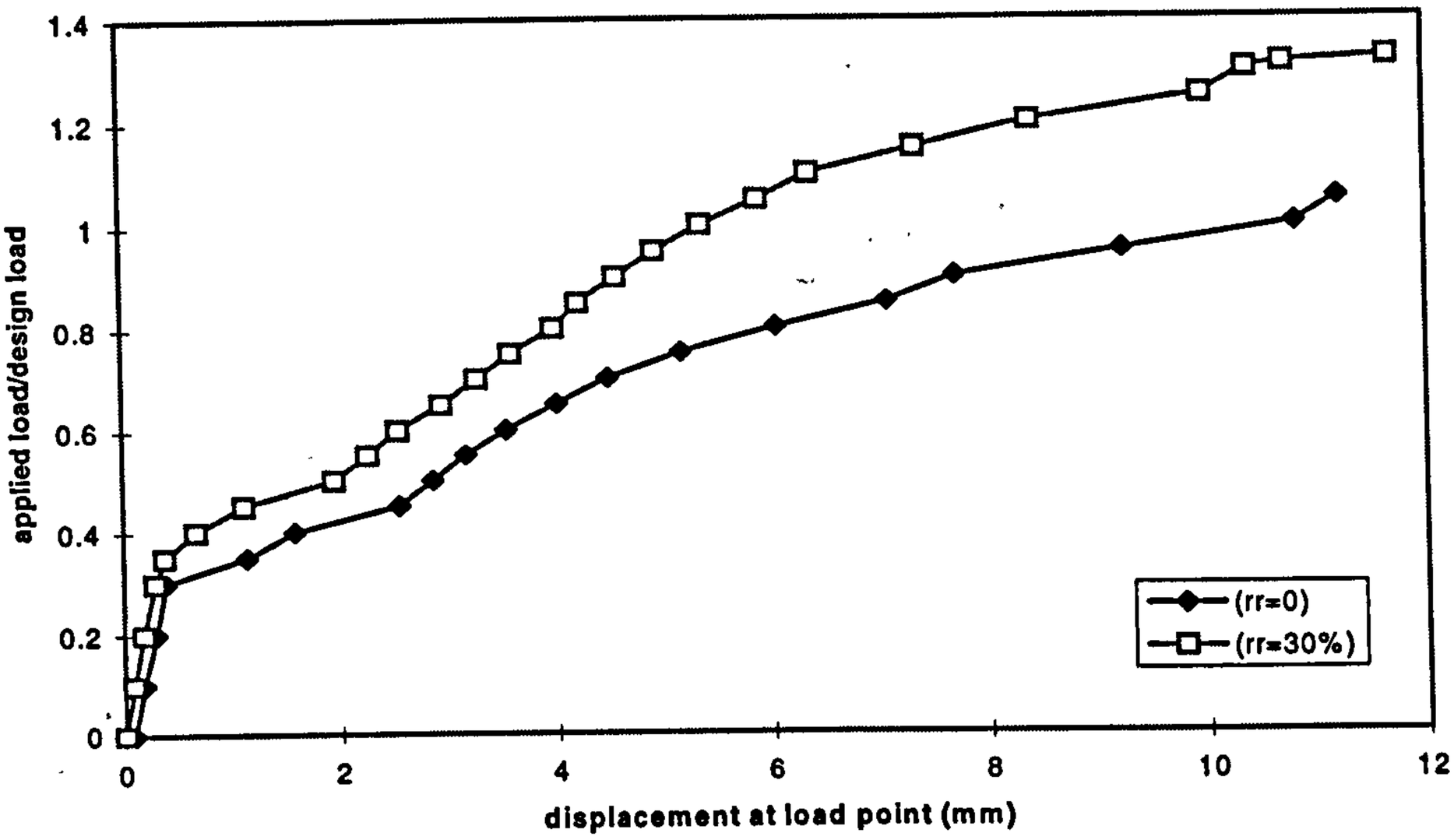

fig.6.3.3(c) Slab SM3: Load-displacement at load point

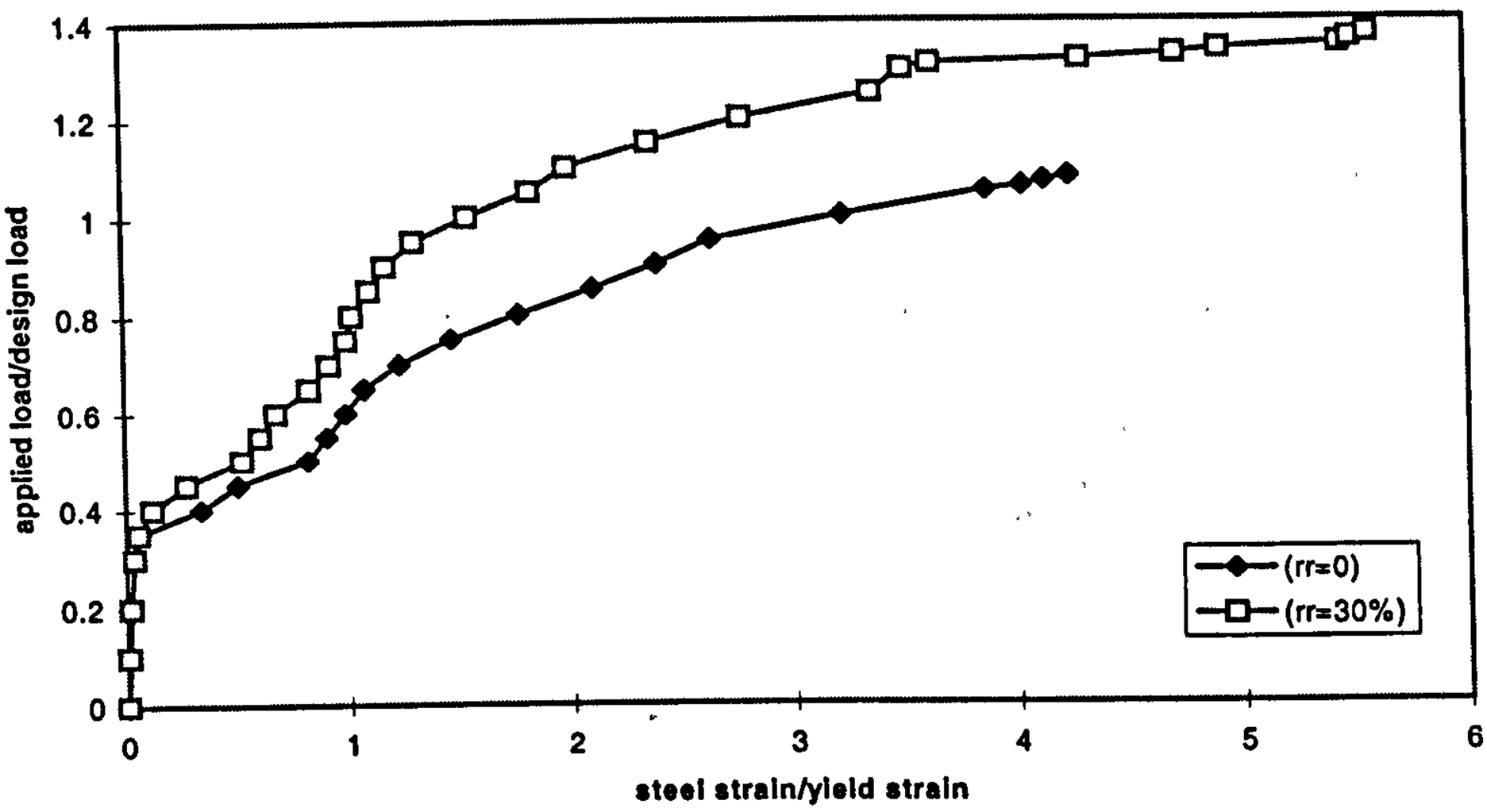

fig.6.3.3(d) Slab SM3: Bottom Steel Strains at load point

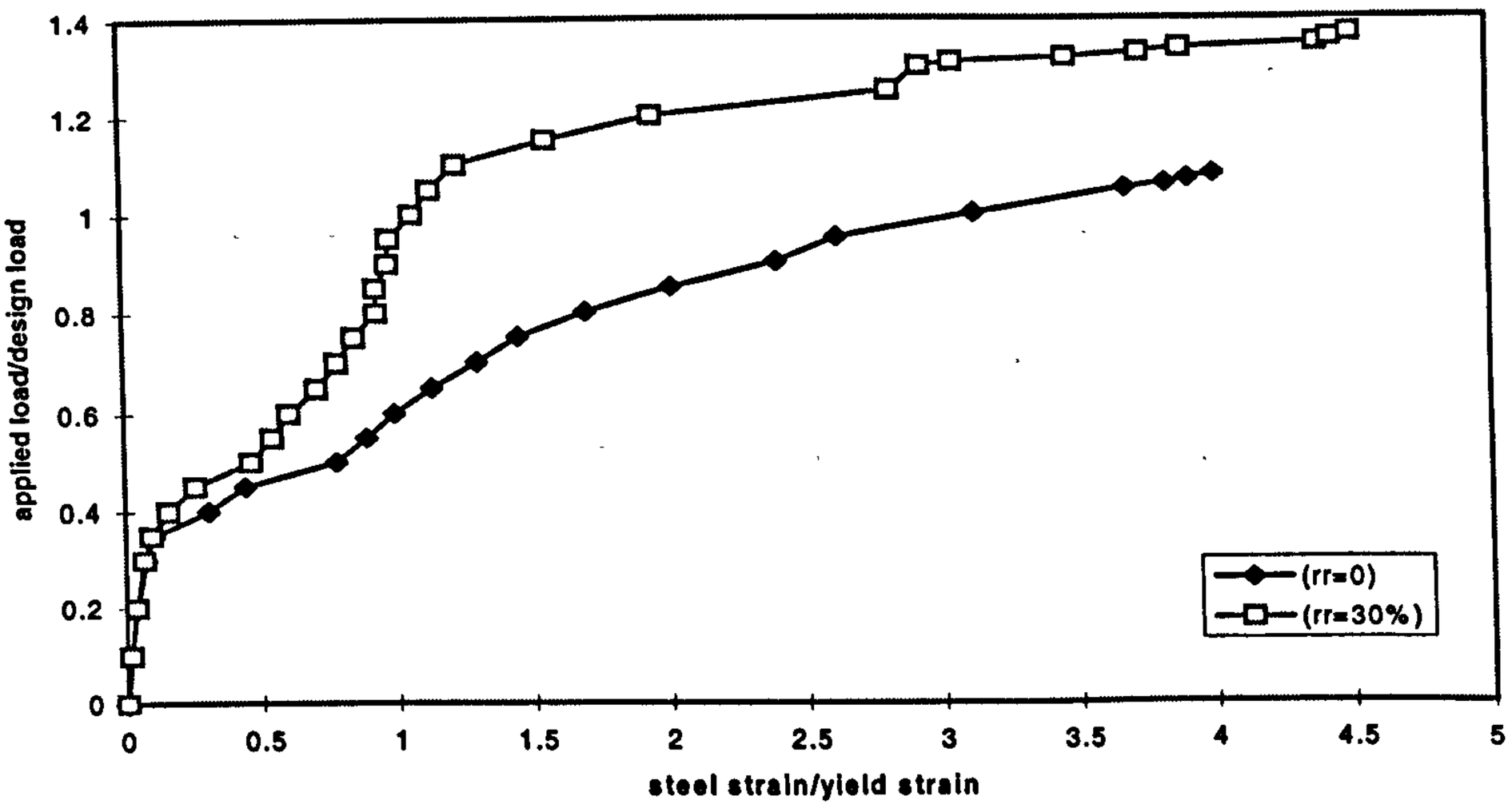

fig.6.3.3(e) Slab SM3: Top Steel Strains at column support

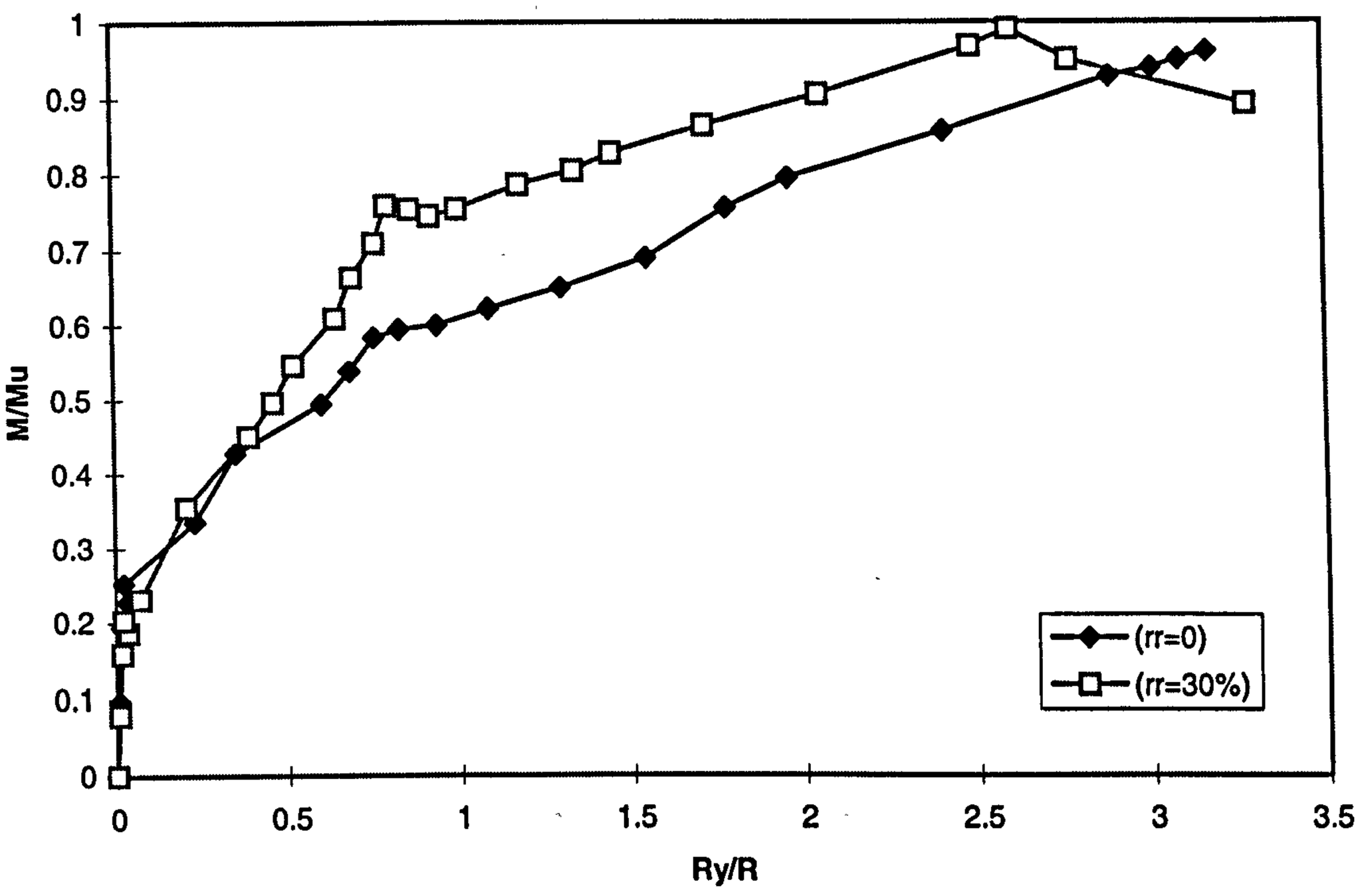

fig.6.3.3(f) Slab SM3: Principal moment-curvature relationship at load point

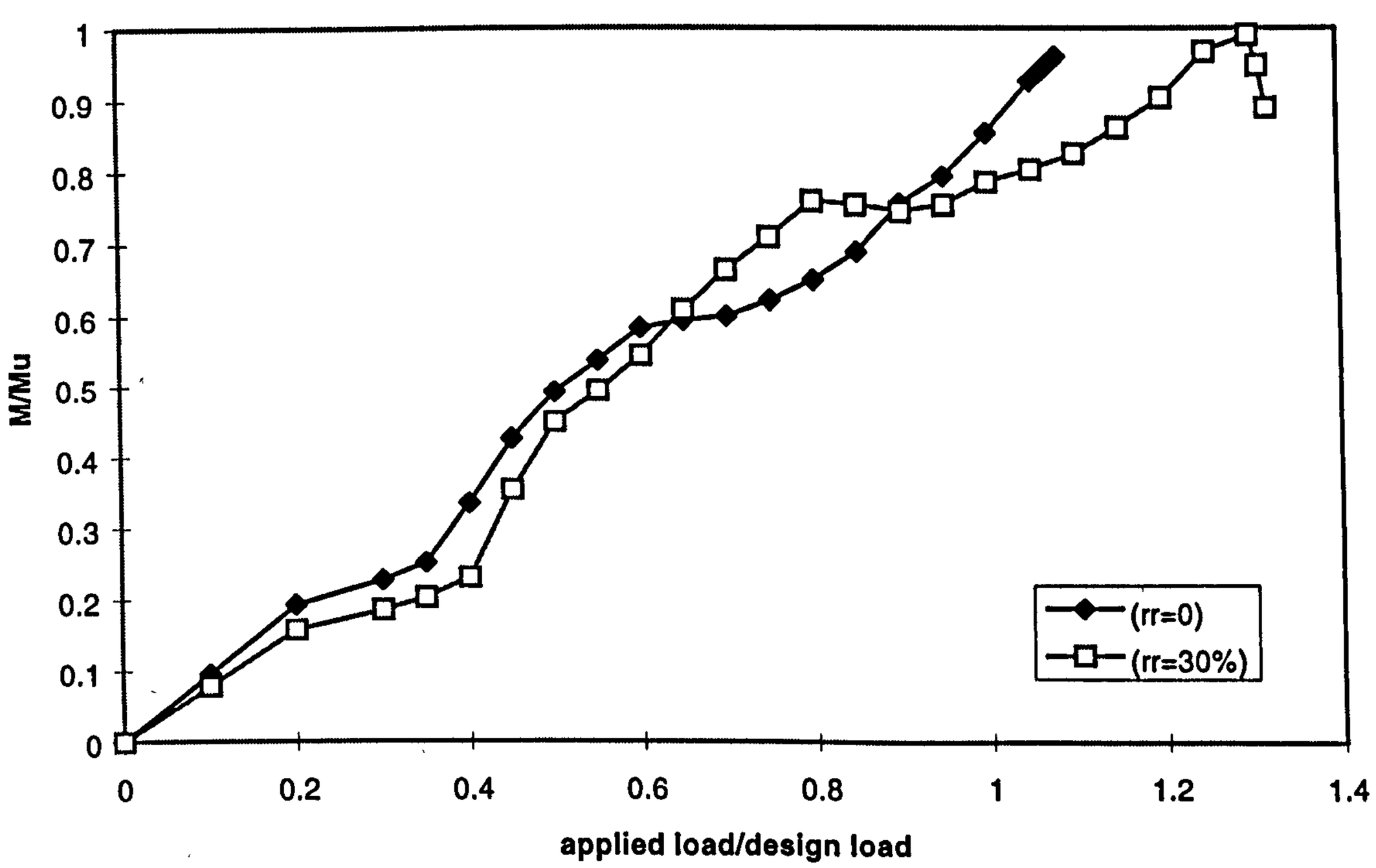

fig.6.3.3(g) Slab SM3: Principal Moments at load point vs. Load

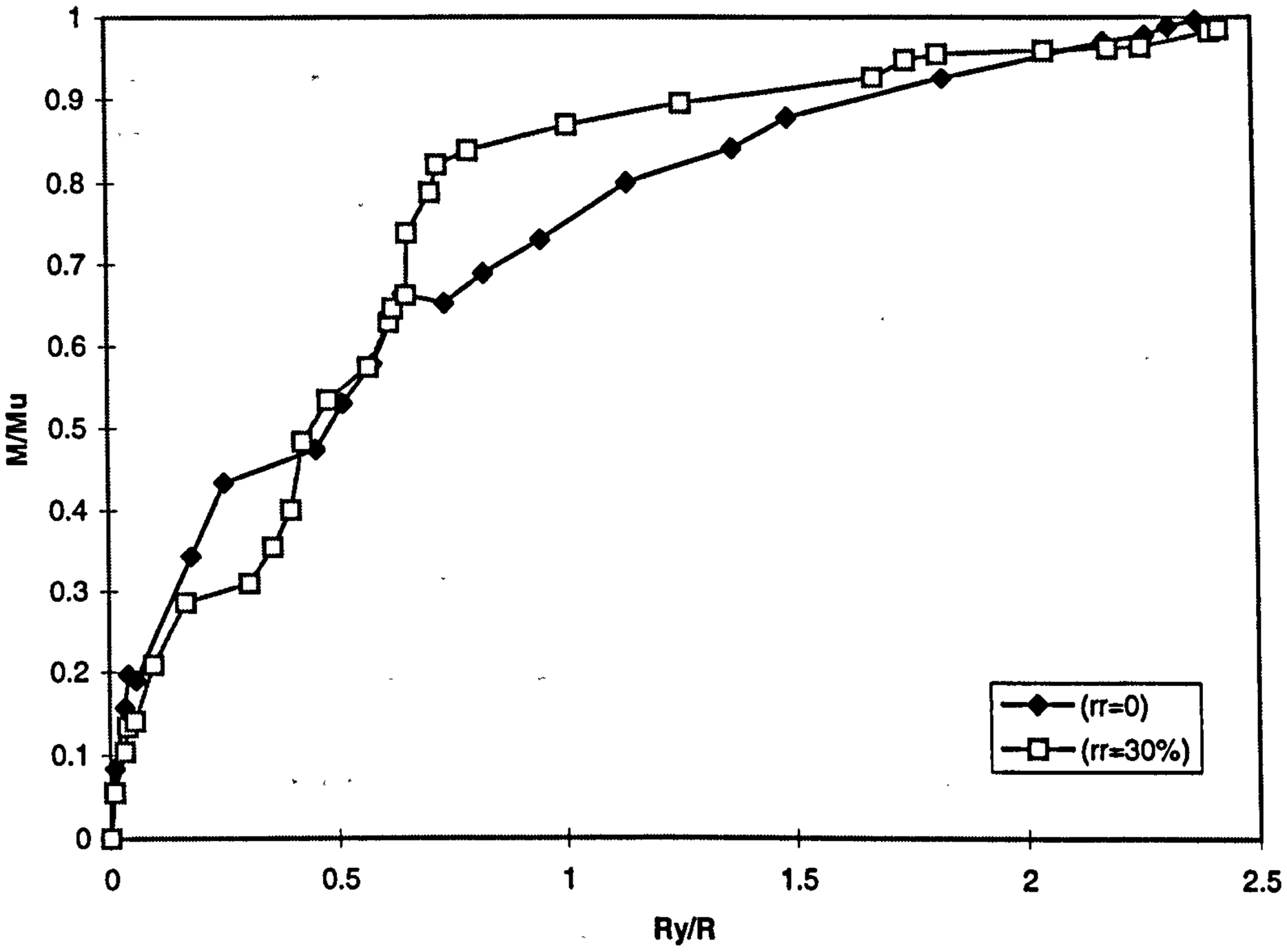

fig.6.3.3(h) Slab SM3: Principal Moment-Curvature relationship at column support

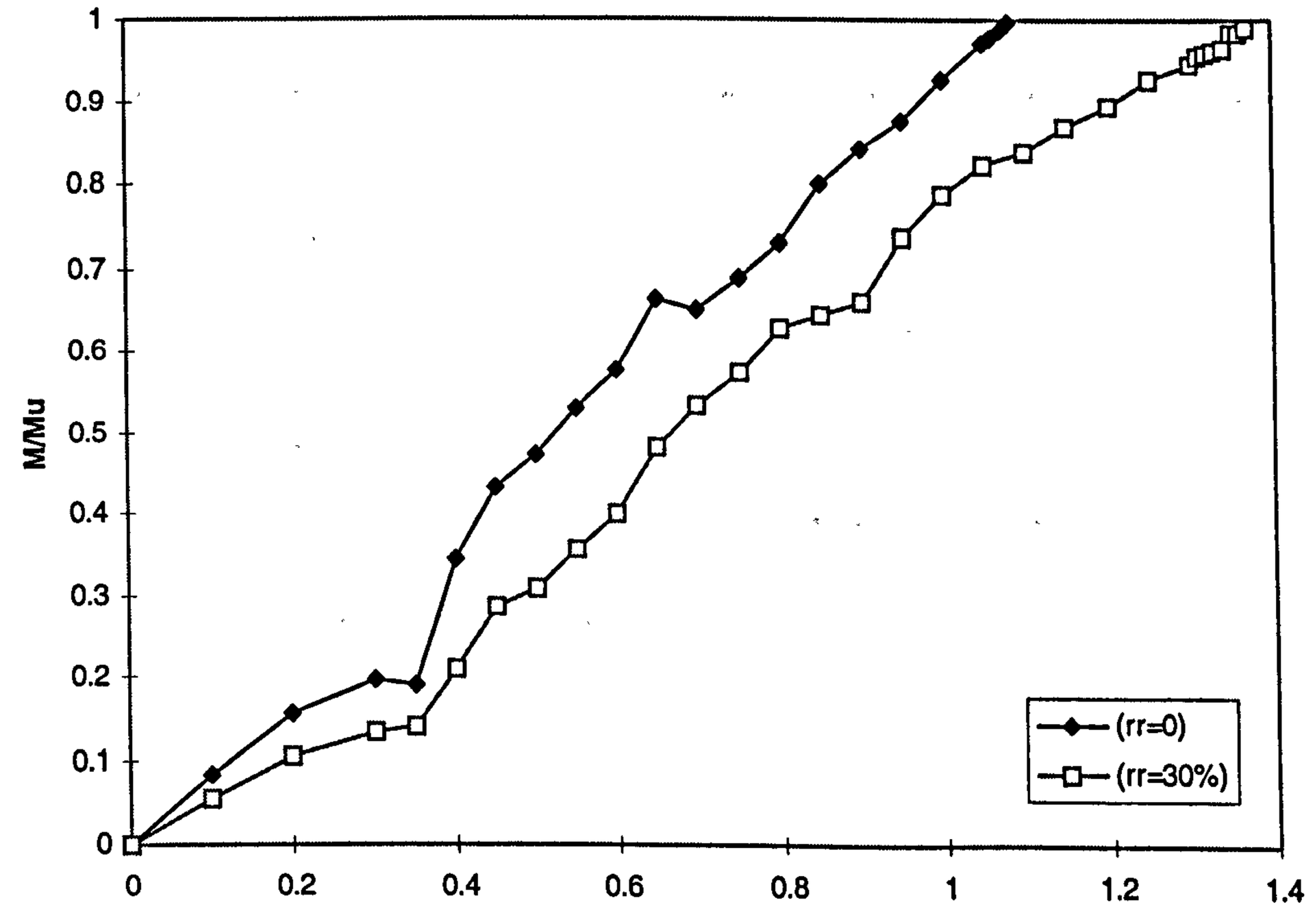

fig.6.3.3(i) Slab SM3: Principal Moments near column support vs. Load

6.3.4 Slab SM4

Loading Arrangement	Design Parameters
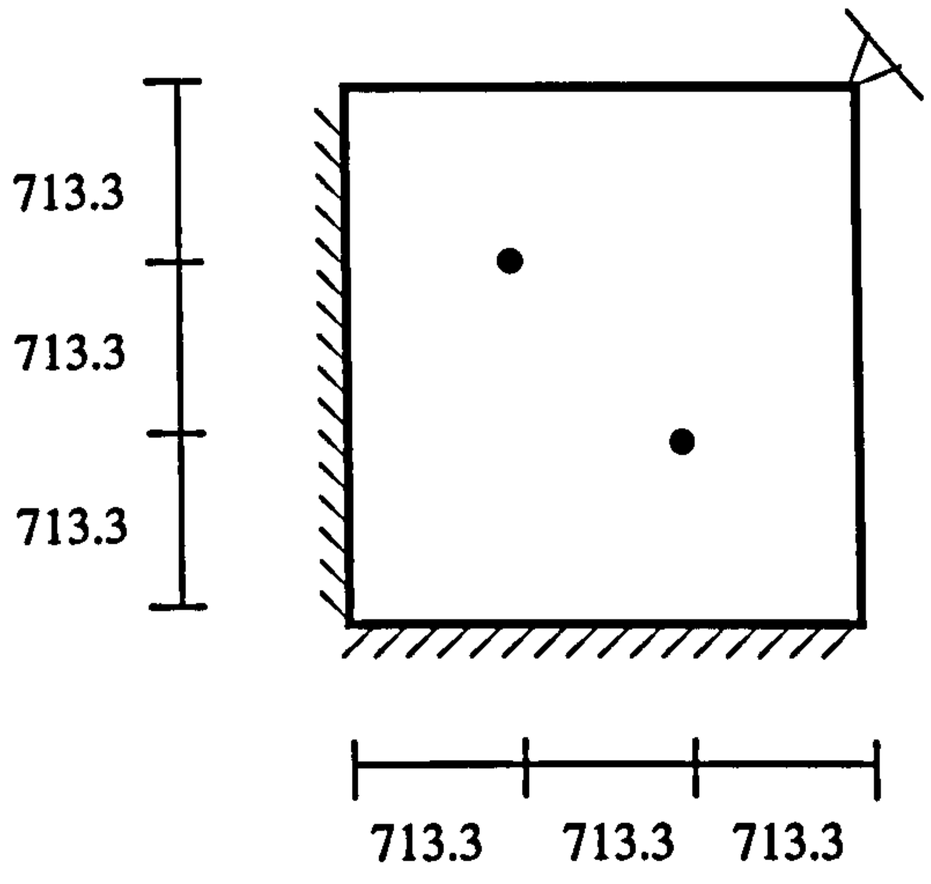	P_d = 110 kN **concrete:** E_c = 20.75 kN/mm^2 f_{cu} = 51.3 N/mm^2 f_t = 3.0 N/mm^2 **steel:** f_y = 480 N/mm^2 E_s = 200 kN/mm^2

The maximum stresses in this slab were concentrated along the main diagonal at column support. These stresses then spread out more evenly approaching the corner of the simply supported edges. A low rejection ratio of 12% resulted in a high percentage area 'removal'. The principal moments are shown at each stage in figure 6.3.4(a)

Steel Volumes (cm^3)	(rr=0)			(rr=12%)			Total(12%) / Total(0)
	A_s bottom	A_s top	Total	A_s bottom	A_s top	Total	
Numerical	3356.2	470.4	3826.6	3625.9	1093.4	4719.3	1.23
Provided	3953.6	633.8	4587.4	5297.8	1264.5	6562.3	1.43

From figure 6.3.4(b), it can be seen that some of the peak moments around the corner and load points were 'smoothed' out by the time rr=12% is reached. A 23% increase in the total numerical steel areas from rr=0 to rr=12% is observed. The main increases in numerical steel occurred around this main load path and in particular, the top steel at the column support increased by 100%. Resulting reinforcement layouts are shown in figure 6.3.4(c). The numerical and provided steel areas over the slab are also shown for comparison in figures 6.3.4(c).

The load-displacement response (fig.6.3.4d) shows that an ultimate load of $1.2P_d$ and $1.3P_d$ was achieved at rr=0 and rr=12% respectively. It can also be seen that the behaviour of the model designed at rr=0 was stiffer up until around the ultimate. After this point, the first model is more ductile as can be seen from the significant increase in displacement. Both models failed in a ductile manner. The service deflection limit at the centre of the slab was reached at a load level of $0.75P_d$ and $0.7P_d$ at rr=0 and rr=12% respectively. Yielding of the bottom steel first occurred at the centre of the slab at a load level of $1.2P_d$ for both models, (fig.6.3.4e) Yielding of the top steel was initiated at $1.1P_d$ in the first model and at $1.1P_d$ in the second model, (fig 6.3.4f).

For the section at the centre of the slab, values of M_u and $1/R_y$ were calculated as 17kNm/m and $0.00005mm^{-1}$, at rr=0. For the second design , at rr=12%, the values of M_u and $1/R_y$ for the same section were 21kNm/m and $0.00005mm^{-1}$ respectively. From the moment curvature relationship at the centre, figures 6.3.4(g-h), it can be seen that the increase in bottom steel provided at this point for the second model has led to a higher moment being sustained but with a much smaller curvature. Hence the design at rr=0, is more ductile in this area.

Although the overall behaviour of both designs was ductile, the increase in steel in some zones at rr=12% may lead to a localised loss in ductility. This can be observed from the moment-curvature plot at the centre section. Additionally, in this case, increase in required steel creates a more complicated steel layout, and may lead to congestion.

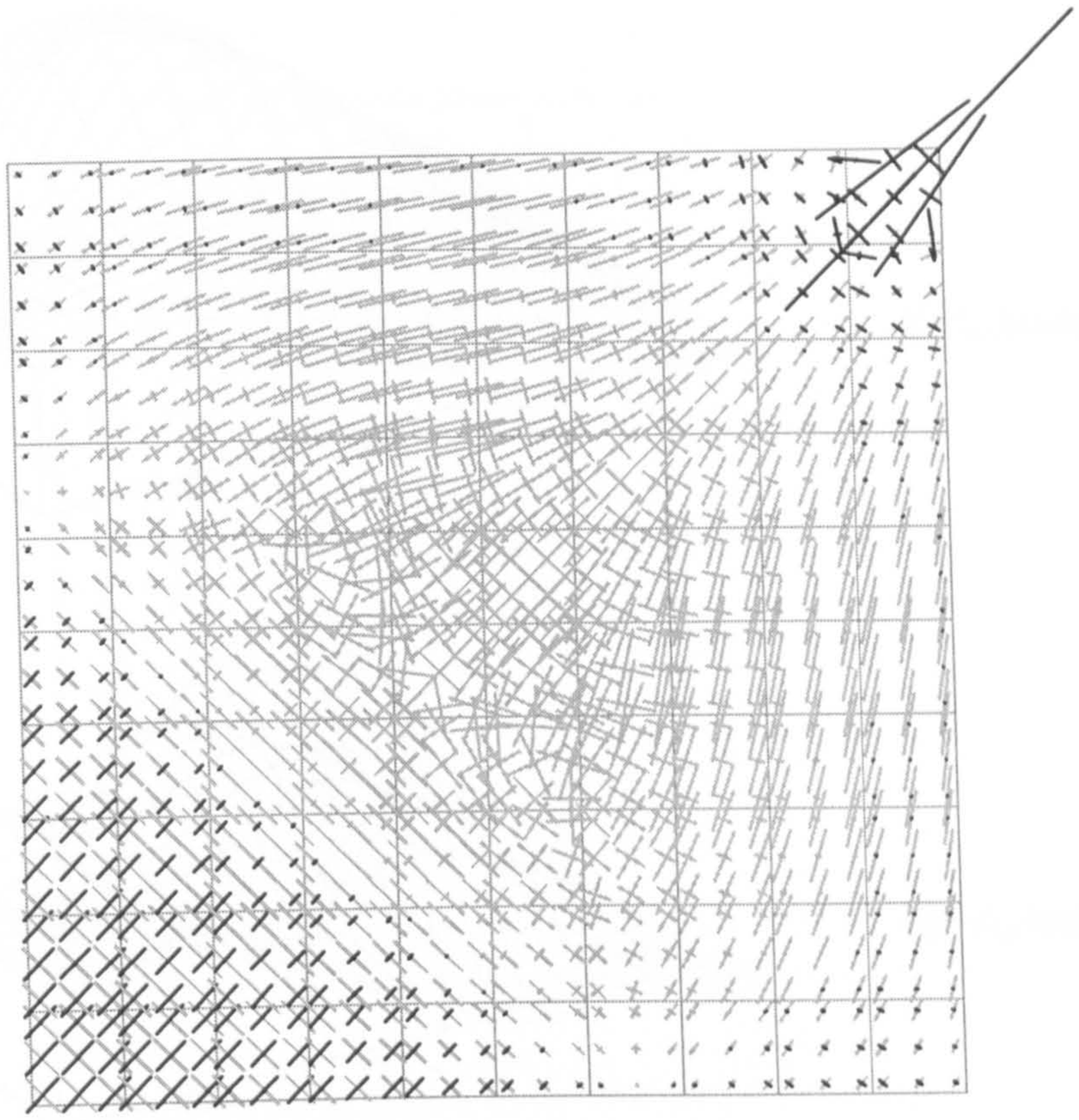

(i) rr=0

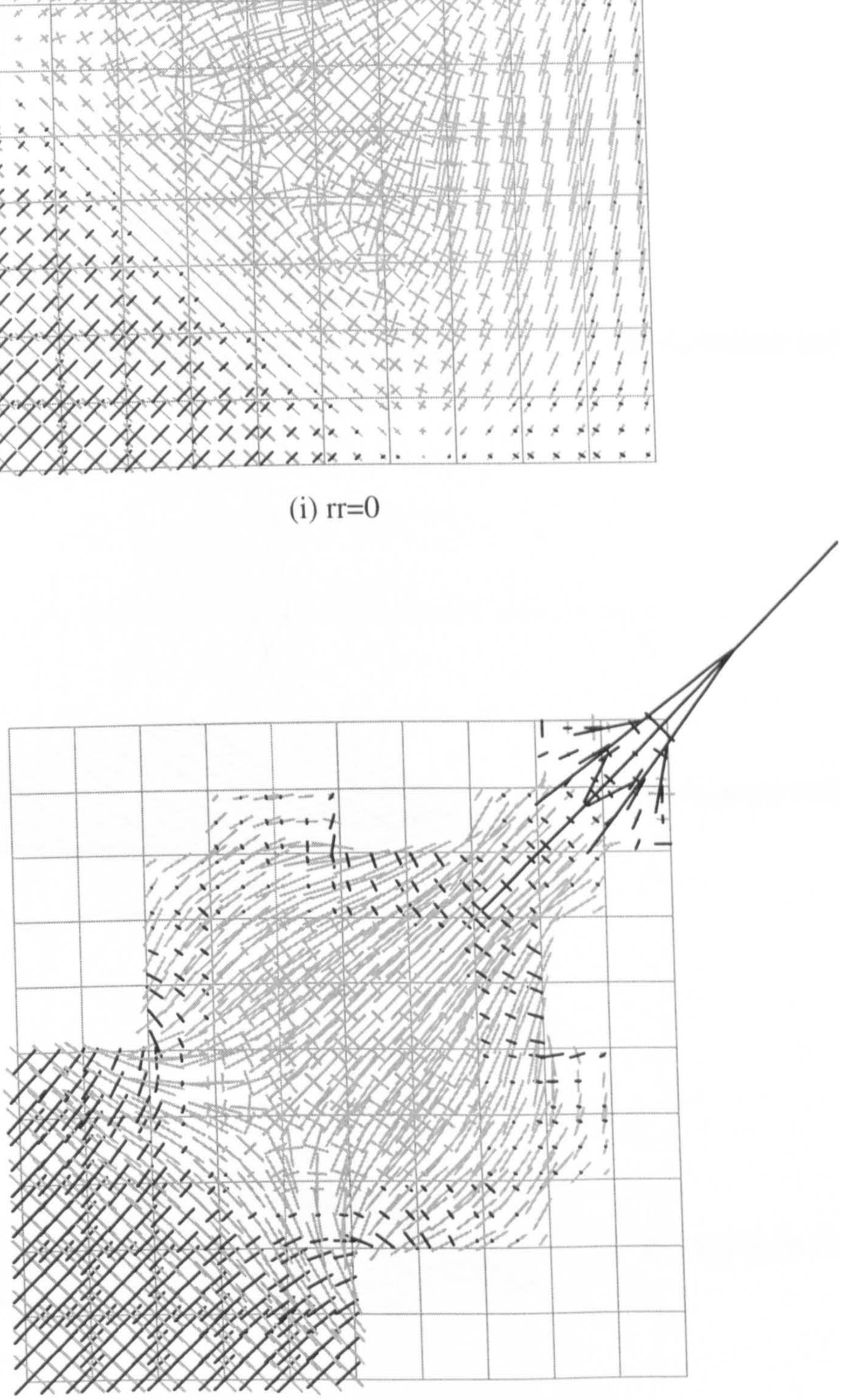

(ii) rr=12%

fig.6.3.4(a) Slab SM4, principal moments

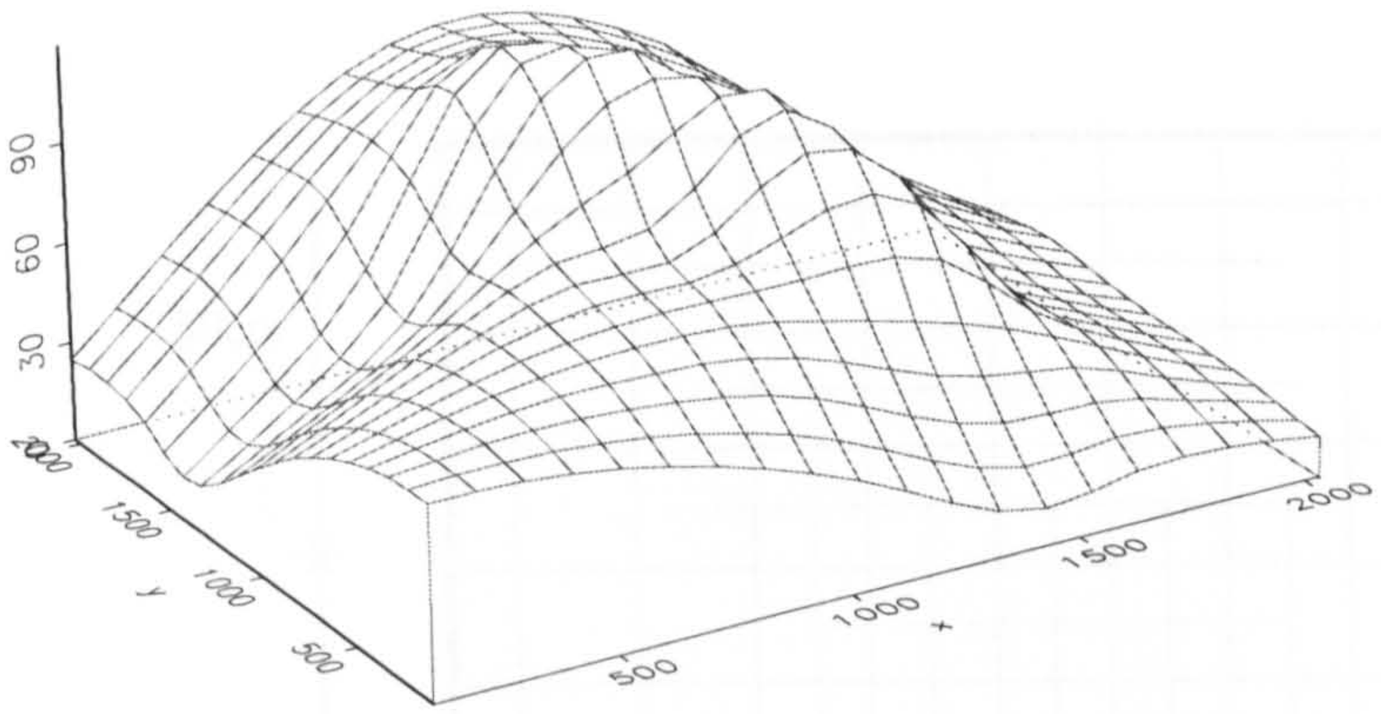

i) A_{sx}bottom (rr=0)

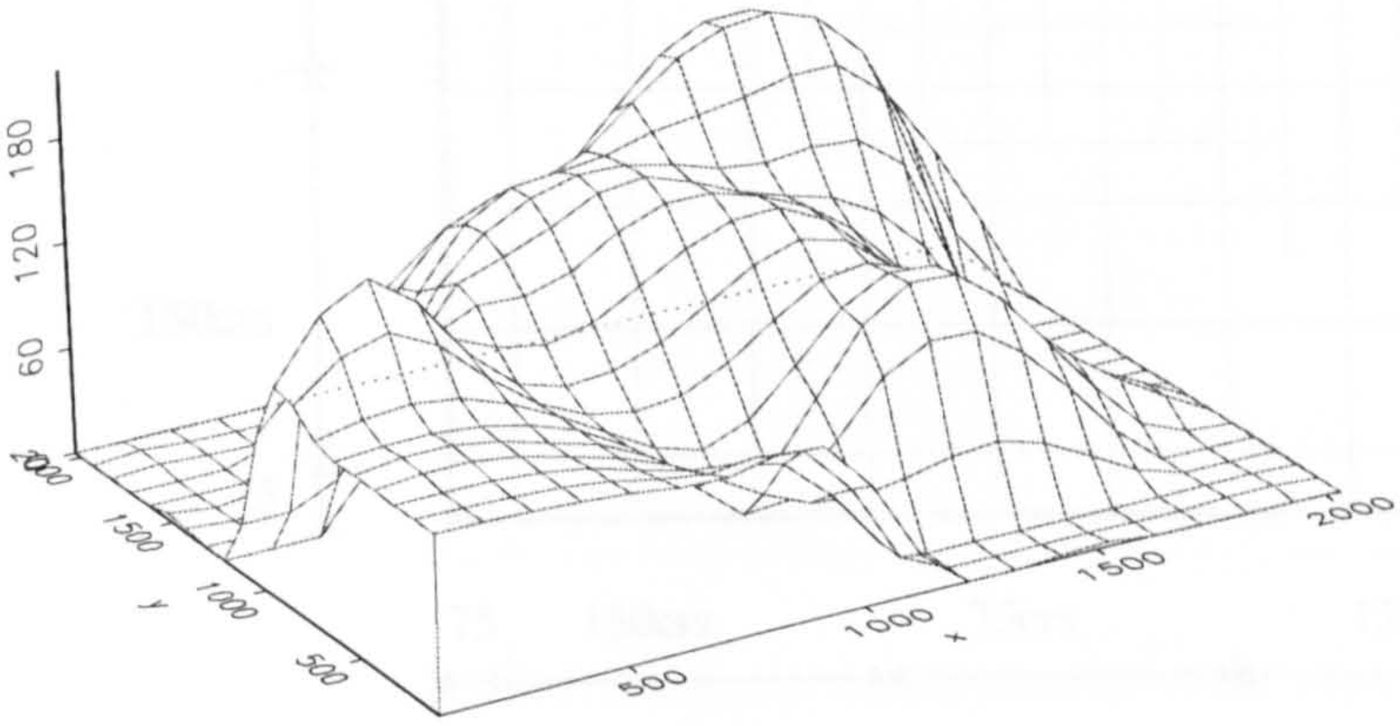

ii) A_{sx}bottom (rr=12%)

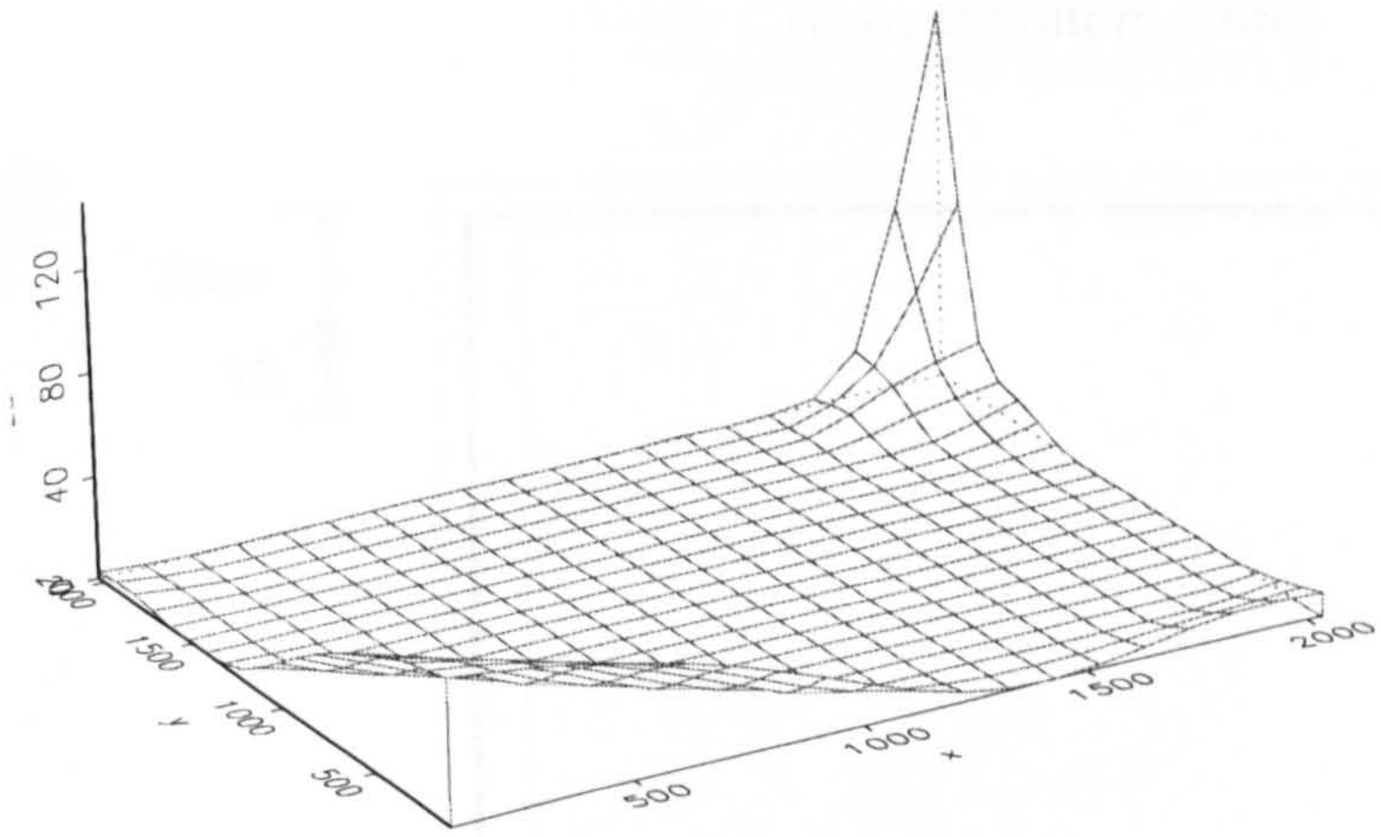

iii) A_{sx}top (rr=0)

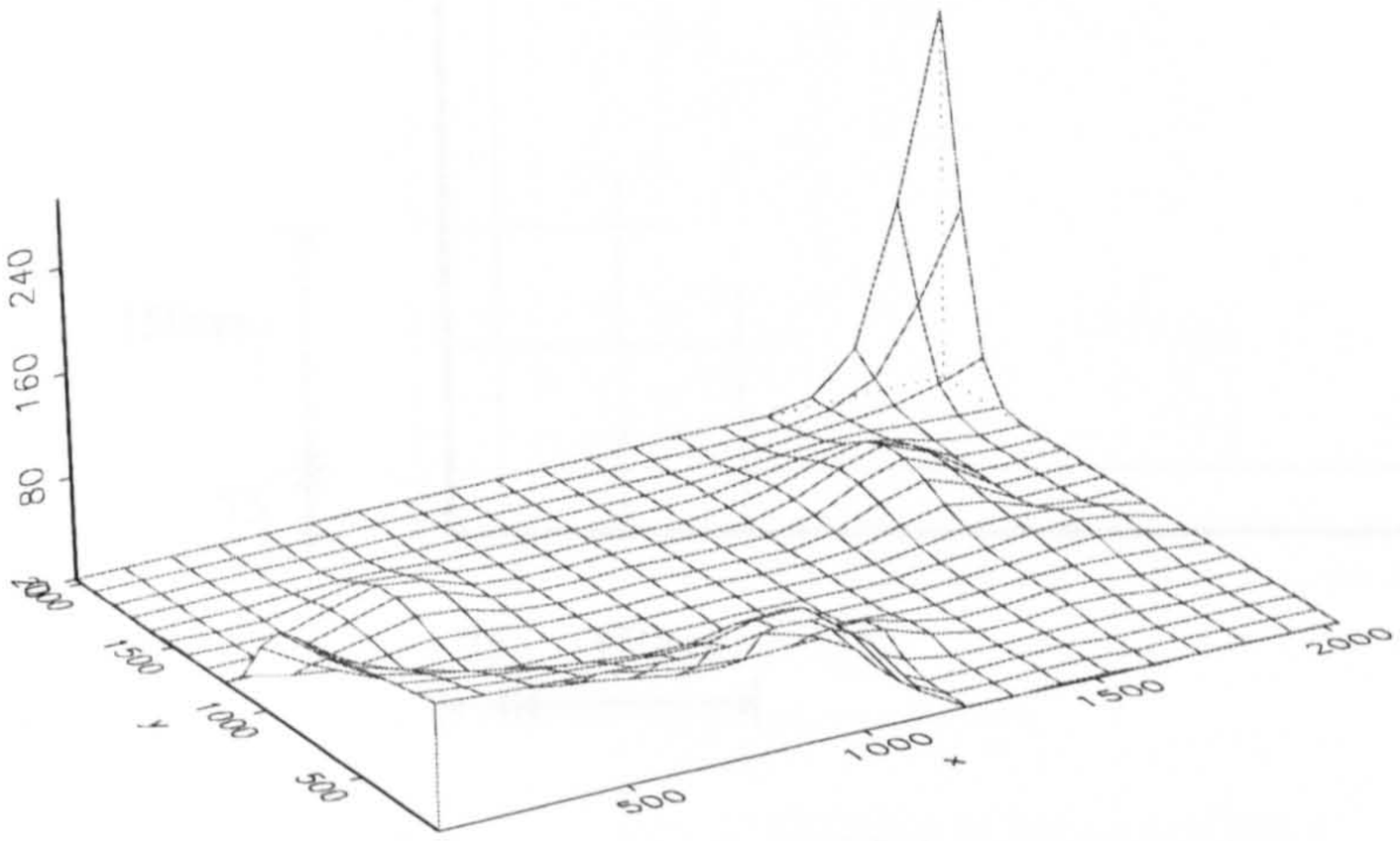

iv) A_{sx}top (rr=12%)

fig.6.3.4(b) Slab SM4: Numerical Steel Areas (mm^2)

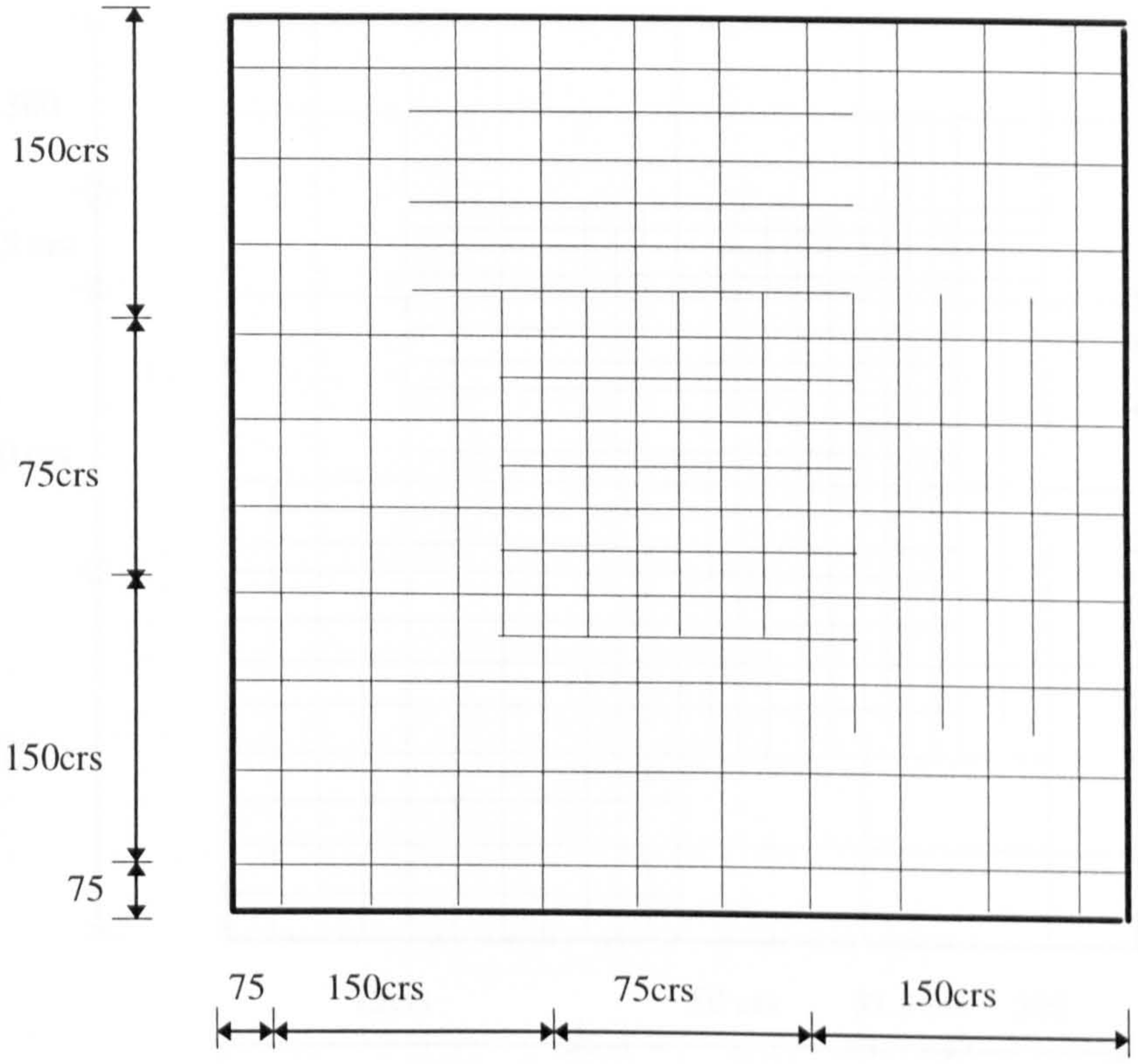

(i) A_s at bottom (rr=0)

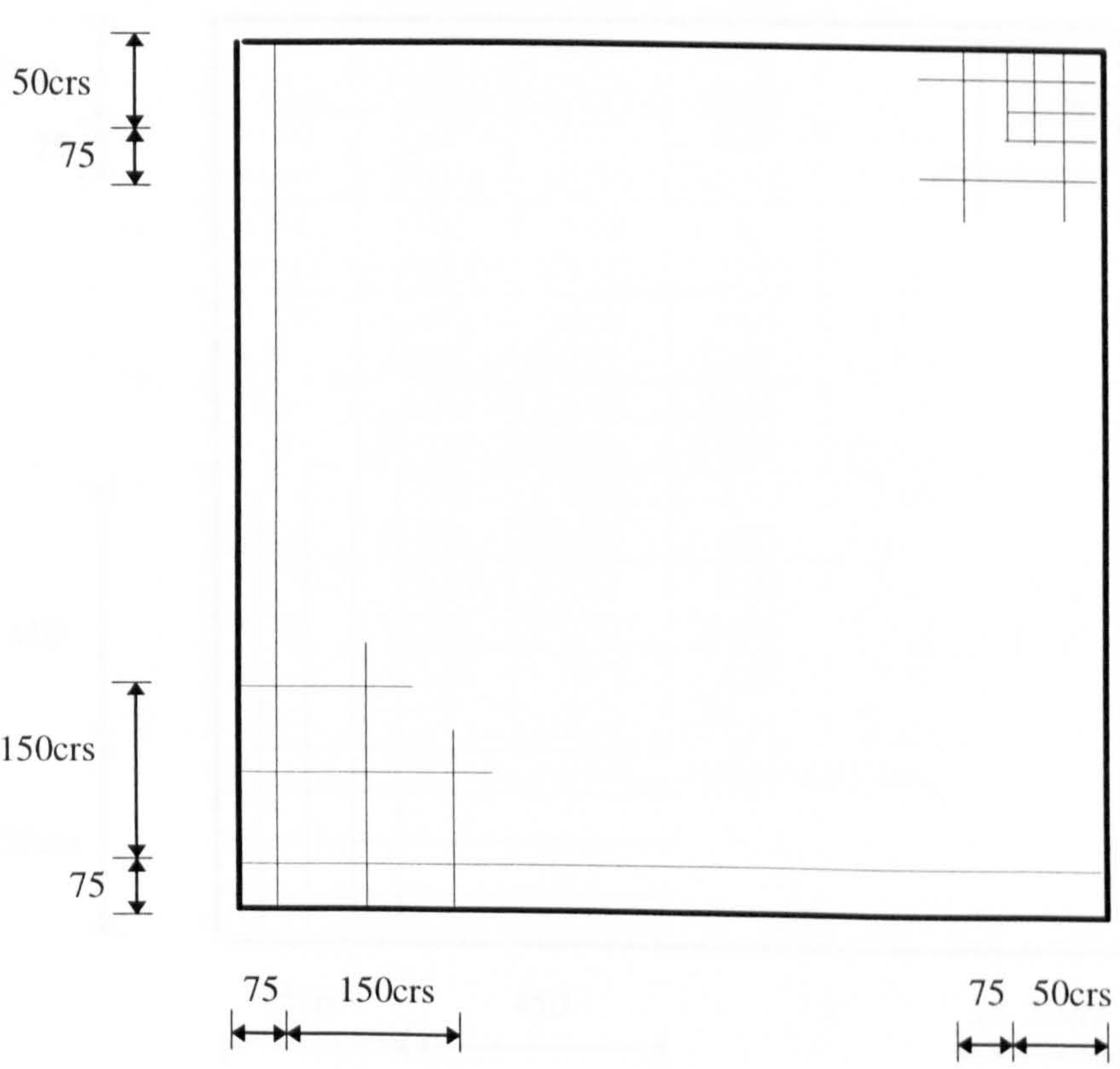

(ii) A_s at top (rr=0)

fig.6.3.4(c) Slab SM4: Steel layout, all sizes in mm, all bars 8mm diameter

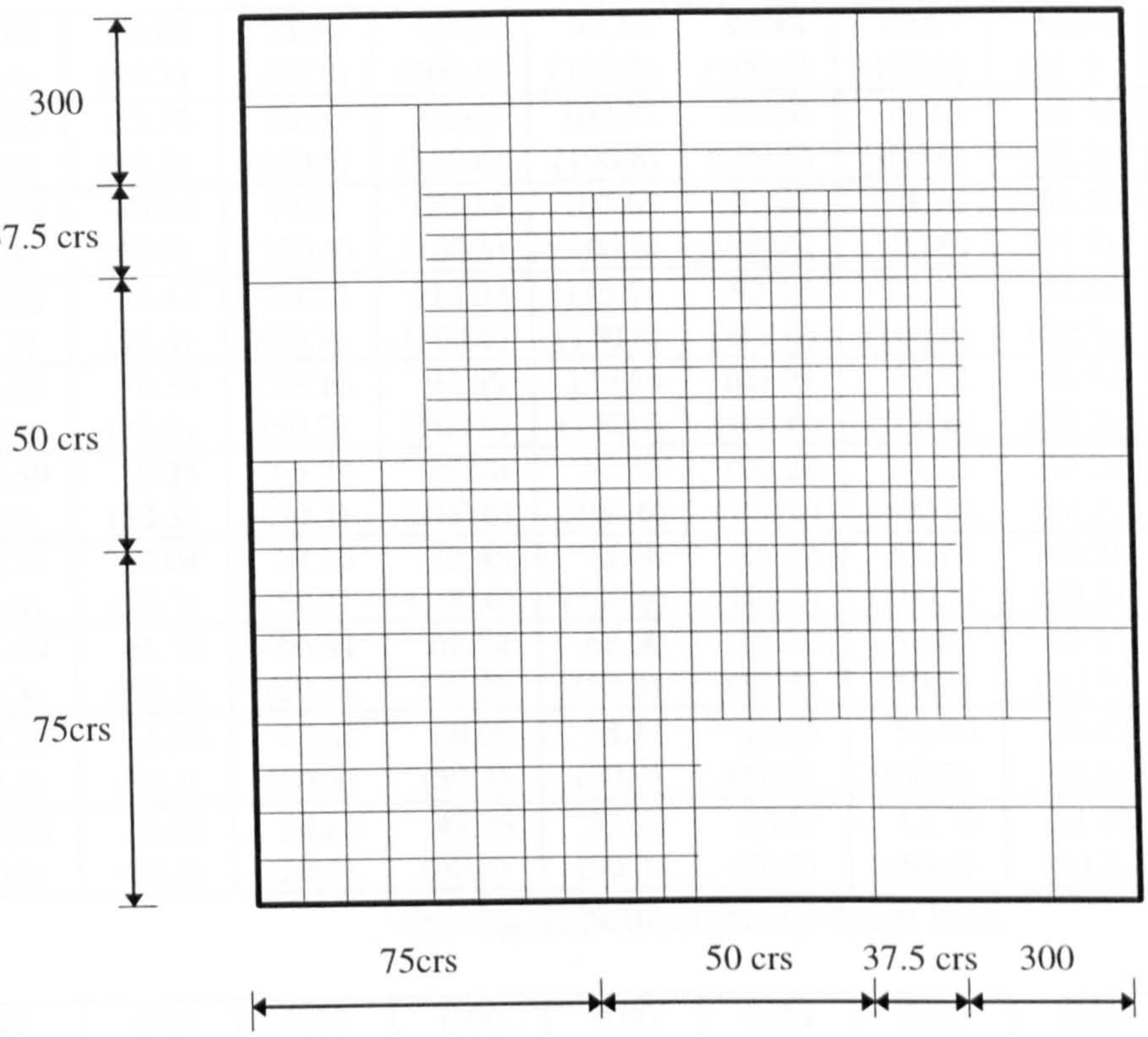

(iii) A_s at bottom (rr=12%)

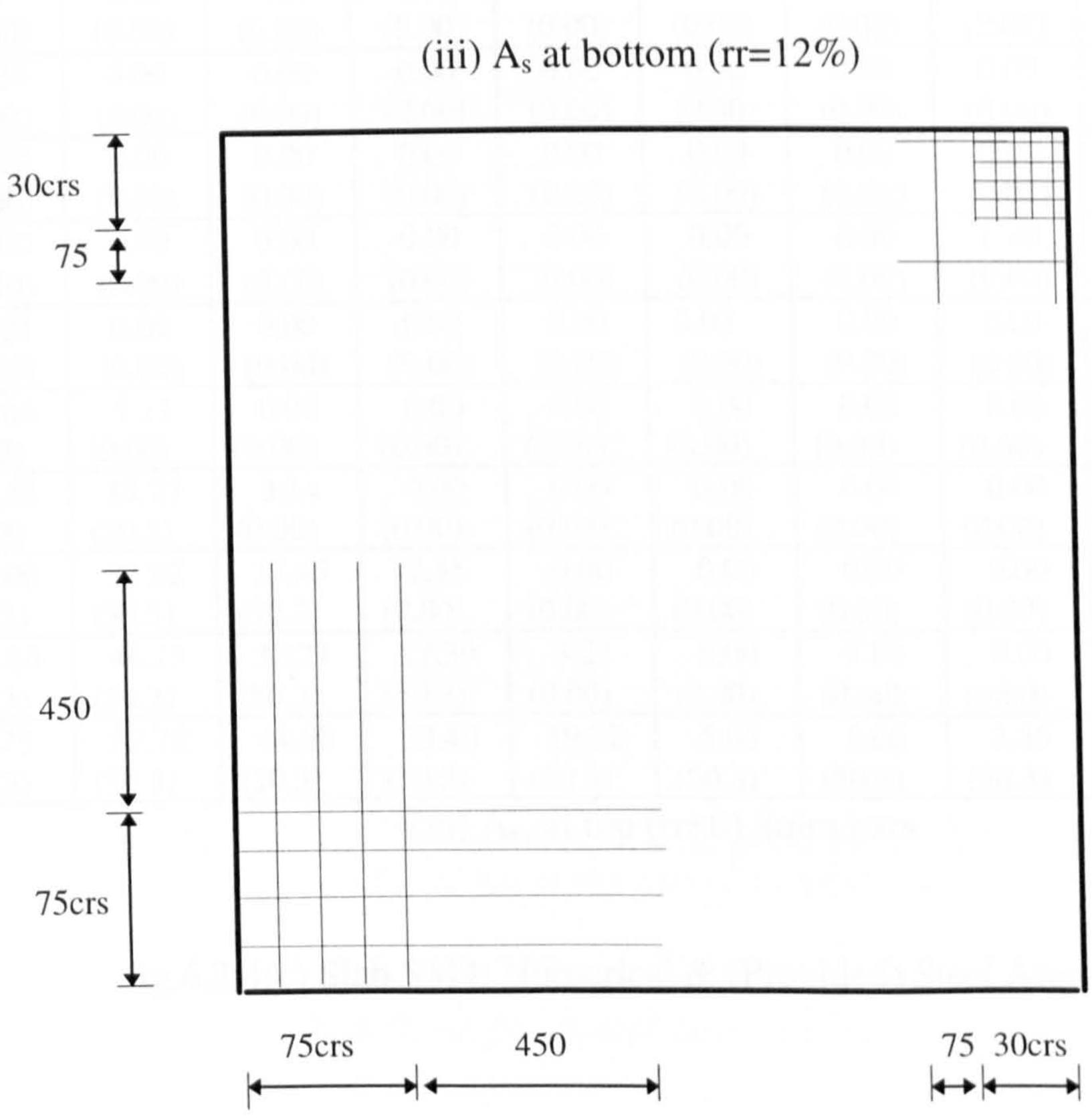

(iv) A_s at top (rr=12%)

fig.6.3.4(c) Slab SM4: Steel Layout, all sizes in mm, all bars 8mm diameter

24.70 (50.3)	50.99 (50.3)	75.55 (100.6)	93.24 (100.6)	99.63 (100.6)	94.44 (100.6)	80.07 (100.6)	56.05 (50.3)	17.33 (50.3)	0.00 (50.3)
25.89 (50.3)	52.36 (50.3)	79.07 (100.6)	98.67 (100.6)	102.93 (100.6)	94.16 (100.6)	79.10 (100.6)	58.55 (50.3)	35.16 (50.3)	15.52 (50.3)
20.78 (50.3)	46.96 (50.3)	77.51 (100.6)	105.88 (100.6)	107.68 (100.6)	91.44 (100.6)	75.50 (100.6)	56.10 (50.3)	35.16 (50.3)	18.93 (50.3)
12.83 (50.3)	34.42 (50.3)	64.52 (50.3)	113.03 (100.6)	115.28 (100.6)	93.15 (100.6)	74.13 (100.6)	52.46 (50.3)	34.01 (50.3)	20.95 (50.3)
22.05 (50.3)	38.16 (50.3)	58.16 (50.3)	94.65 (100.6)	119.54 (100.6)	103.71 (100.6)	78.52 (100.6)	48.52 (50.3)	30.68 (50.3)	18.81 (50.3)
35.59 (50.3)	50.28 (50.3)	66.28 (50.3)	79.90 (100.6)	87.82 (100.6)	109.24 (100.6)	84.76 (100.6)	47.24 (50.3)	28.82 (50.3)	17.48 (50.3)
46.79 (50.3)	58.04 (50.3)	68.05 (50.3)	73.45 (100.6)	73.68 (100.6)	85.79 (100.6)	85.74 (100.6)	49.28 (50.3)	29.43 (50.3)	17.05 (50.3)
54.49 (50.3)	61.78 (50.3)	66.81 (50.3)	68.84 (50.3)	68.00 (50.3)	62.70 (50.3)	56.02 (50.3)	43.17 (50.3)	28.35 (50.3)	16.37 (50.3)
58.72 (50.3)	61.94 (50.3)	62.45 (50.3)	60.00 (50.3)	54.11 (50.3)	42.26 (50.3)	30.90 (50.3)	29.42 (50.3)	23.04 (50.3)	14.64 (50.3)
59.73 (50.3)	58.81 (50.3)	54.88 (50.3)	47.76 (50.3)	37.28 (50.3)	23.51 (50.3)	11.79 (50.3)	15.43 (50.3)	16.43 (50.3)	12.59 (50.3)

(v) A_{sx} at bottom (rr=0) 8mm bars

2.47 (0.00)	0.00 (0.00)	0.00 (0.00)	0.00 (0.00)	0.00 (0.00)	0.00 (0.00)	0.00 (0.00)	0.00 (0.00)	13.09 (50.3)	146.7 (150.9)
3.39 (0.00)	0.00 (0.00)	0.00 (0.00)	0.00 (0.00)	0.00 (0.00)	0.00 (0.00)	0.00 (0.00)	0.00 (0.00)	12.24 (50.3)	19.11 (50.3)
0.00 (0.00)	0.00 (0.00)	0.00 (0.00)	0.00 (0.00)	0.00 (0.00)	0.00 (0.00)	0.00 (0.00)	0.00 (0.00)	0.00 (0.00)	9.92 (0.00)
0.00 (0.00)	0.00 (0.00)	0.00 (0.00)	0.00 (0.00)	0.00 (0.00)	0.00 (0.00)	0.00 (0.00)	0.00 (0.00)	0.00 (0.00)	0.00 (0.00)
6.21 (0.00)	0.00 (0.00)	0.00 (0.00)	0.00 (0.00)	0.00 (0.00)	0.00 (0.00)	0.00 (0.00)	0.00 (0.00)	0.00 (0.00)	0.00 (0.00)
20.86 (50.3)	5.12 (0.00)	0.00 (0.00)	0.00 (0.00)	0.00 (0.00)	0.00 (0.00)	0.00 (0.00)	0.00 (0.00)	0.00 (0.00)	0.00 (0.00)
34.33 (50.3)	19.27 (50.3)	3.14 (0.00)	0.00 (0.00)	0.00 (0.00)	0.00 (0.00)	0.00 (0.00)	0.00 (0.00)	0.00 (0.00)	0.00 (0.00)
45.06 (50.3)	32.92 (50.3)	17.45 (50.3)	2.85 (0.00)	0.00 (0.00)	0.00 (0.00)	0.00 (0.00)	0.00 (0.00)	0.00 (0.00)	0.00 (0.00)
52.86 (50.3)	44.13 (50.3)	32.27 (50.3)	17.39 (50.3)	3.21 (0.00)	0.00 (0.00)	0.00 (0.00)	0.00 (0.00)	0.00 (0.00)	3.26 (0.00)
57.75 (50.3)	52.78 (50.3)	44.69 (50.3)	33.40 (50.3)	19.22 (50.3)	5.65 (50.3)	0.00 (50.3)	3.85 (50.3)	9.89 (50.3)	9.54 (50.3)

(vi) A_{sx} at top (rr=0) 8mm bars

fig.6.3.4(c) Slab SM4: Numerical & (Provided) Steel Areas in mm^2

0.00 (25.2)	0.00 (25.2)	0.00 (25.2)	0.00 (25.2)	0.00 (25.2)	0.00 (25.2)	0.00 (25.2)	0.00 (25.2)	0.00 (25.2)	0.00 (25.2)
0.00 (25.2)	0.00 (25.2)	0.00 (25.2)	61.52 (100.6)	47.09 (100.6)	0.00 (100.6)	0.00 (100.6)	81.38 (100.6)	41.71 (100.6)	10.23 (25.2)
0.00 (25.2)	0.00 (25.2)	69.30 (201.2)	118.57 (201.2)	130.51 (201.2)	191.95 (201.2)	220.06 (201.2)	180.48 (201.2)	100.01 (201.2)	0.00 (25.2)
0.00 (25.2)	0.00 (25.2)	73.42 (150.9)	144.68 (150.9)	155.81 (150.9)	156.67 (150.9)	158.60 (150.9)	160.71 (150.9)	0.00 (25.2)	0.00 (25.2)
0.00 (25.2)	0.00 (25.2)	108.42 (150.9)	127.46 (150.9)	156.38 (150.9)	145.88 (150.9)	123.45 (150.9)	74.25 (150.9)	0.00 (25.2)	0.00 (25.2)
111.44 (150.9)	161.20 (150.9)	107.67 (150.9)	87.85 (150.9)	110.16 (150.9)	138.80 (150.9)	114.03 (150.9)	41.49 (150.9)	3.64 (25.2)	0.00 (25.2)
108.29 (100.6)	120.06 (100.6)	98.39 (100.6)	66.74 (100.6)	58.39 (100.6)	100.29 (100.6)	121.18 (100.6)	74.43 (100.6)	34.09 (25.2)	0.00 (25.2)
101.72 (100.6)	104.95 (100.6)	91.76 (100.6)	65.73 (100.6)	21.14 (100.6)	80.04 (100.6)	108.77 (100.6)	65.59 (100.6)	0.00 (25.2)	0.00 (25.2)
100.27 (100.6)	100.69 (100.6)	92.64 (100.6)	77.78 (100.6)	60.41 (100.6)	0.00 (25.2)	0.00 (25.2)	0.00 (25.2)	0.00 (25.2)	0.00 (25.2)
100.39 (100.6)	98.96 (100.6)	95.17 (100.6)	92.56 (100.6)	87.93 (100.6)	0.00 (25.2)	0.00 (25.2)	0.00 (25.2)	0.00 (25.2)	0.00 (25.2)

(vii) A_{sx} at bottom (rr=12%) 8mm bars

0.00 (0.00)	0.00 (0.00)	0.00 (0.00)	0.00 (0.00)	0.00 (0.00)	0.00 (0.00)	0.00 (0.00)	0.00 (0.00)	29.83 (50.3)	293.50 (301.8)
0.00 (0.00)	0.00 (0.00)	0.00 (0.00)	0.00 (0.00)	0.00 (0.00)	0.00 (0.00)	0.00 (0.00)	5.15 (0.00)	10.97 (0.00)	25.98 (50.3)
0.00 (0.00)	0.00 (0.00)	4.93 (0.00)	0.00 (0.00)	0.00 (0.00)	0.00 (0.00)	6.66 (0.00)	20.68 (0.00)	3.99 (0.00)	0.00 (0.00)
0.00 (0.00)	0.00 (0.00)	21.84 (0.00)	0.00 (0.00)	0.00 (0.00)	0.00 (0.00)	4.75 (0.00)	39.51 (0.00)	0.00 (0.00)	0.00 (0.00)
0.00 (0.00)	0.00 (0.00)	13.28 (0.00)	0.00 (0.00)	0.00 (0.00)	0.00 (0.00)	0.00 (0.00)	26.25 (0.00)	0.00 (0.00)	0.00 (0.00)
63.63 (100.3)	11.09 (0.00)	0.00 (0.00)	0.00 (0.00)	0.00 (0.00)	0.00 (0.00)	0.00 (0.00)	7.84 (0.00)	14.15 (0.00)	0.00 (0.00)
76.19 (100.3)	29.91 (100.3)	5.22 (0.00)	0.00 (0.00)	0.00 (0.00)	0.00 (0.00)	0.00 (0.00)	4.75 (0.00)	6.78 (0.00)	0.00 (0.00)
83.57 (100.3)	59.64 (100.3)	38.89 (100.3)	21.40 (100.3)	16.49 (0.00)	22.75 (0.00)	0.00 (0.00)	4.88 (0.00)	0.00 (0.00)	0.00 (0.00)
92.22 (100.3)	80.66 (100.3)	71.65 (100.3)	70.29 (100.3)	72.29 (100.3)	0.00 (0.00)	0.00 (0.00)	0.00 (0.00)	0.00 (0.00)	0.00 (0.00)
98.15 (100.3)	93.54 (100.3)	90.11 (100.3)	91.81 (100.3)	86.80 (100.3)	0.00 (0.00)	0.00 (0.00)	0.00 (0.00)	0.00 (0.00)	0.00 (0.00)

(viii) A_{sx} at top (rr=12%) 8mm bars

fig.6.3.4(c) Slab SM4: Numerical & (Provided) Steel Areas in mm^2

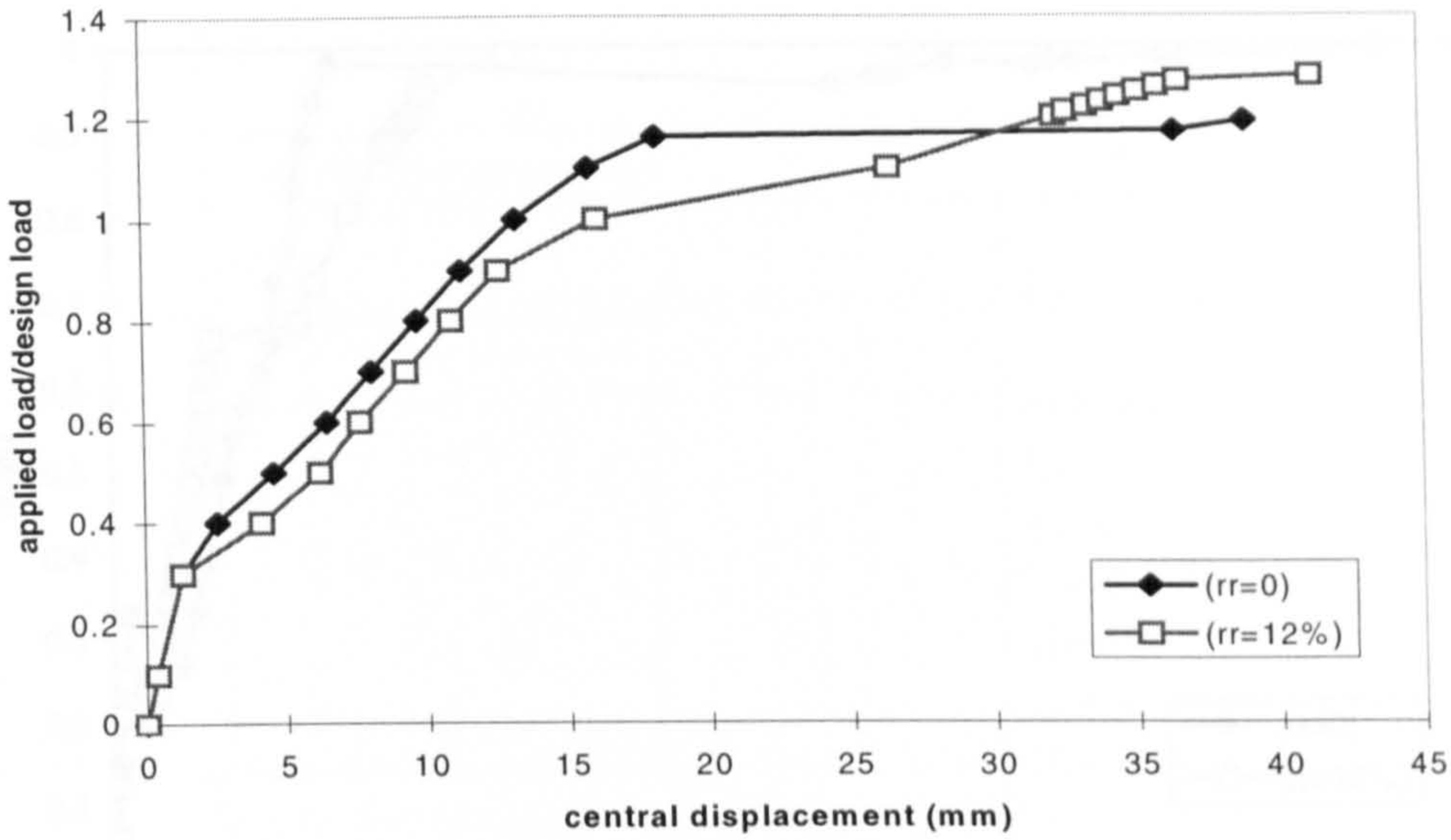

fig.6.3.4(d) Slab SM4: Load-displacement relationship at centre

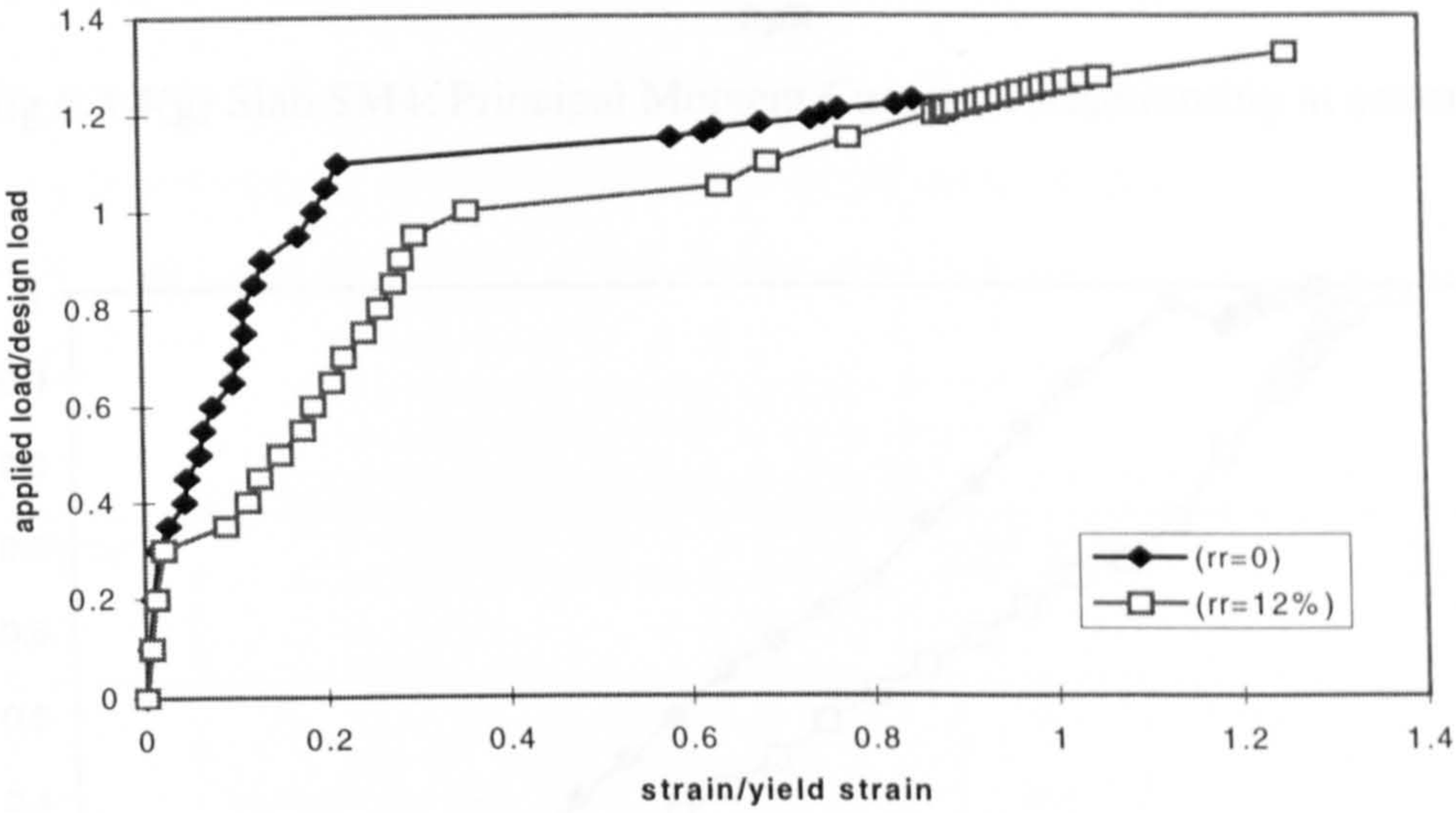

fig.6.3.4(e) Slab SM4: Bottom Steel Strain at centre

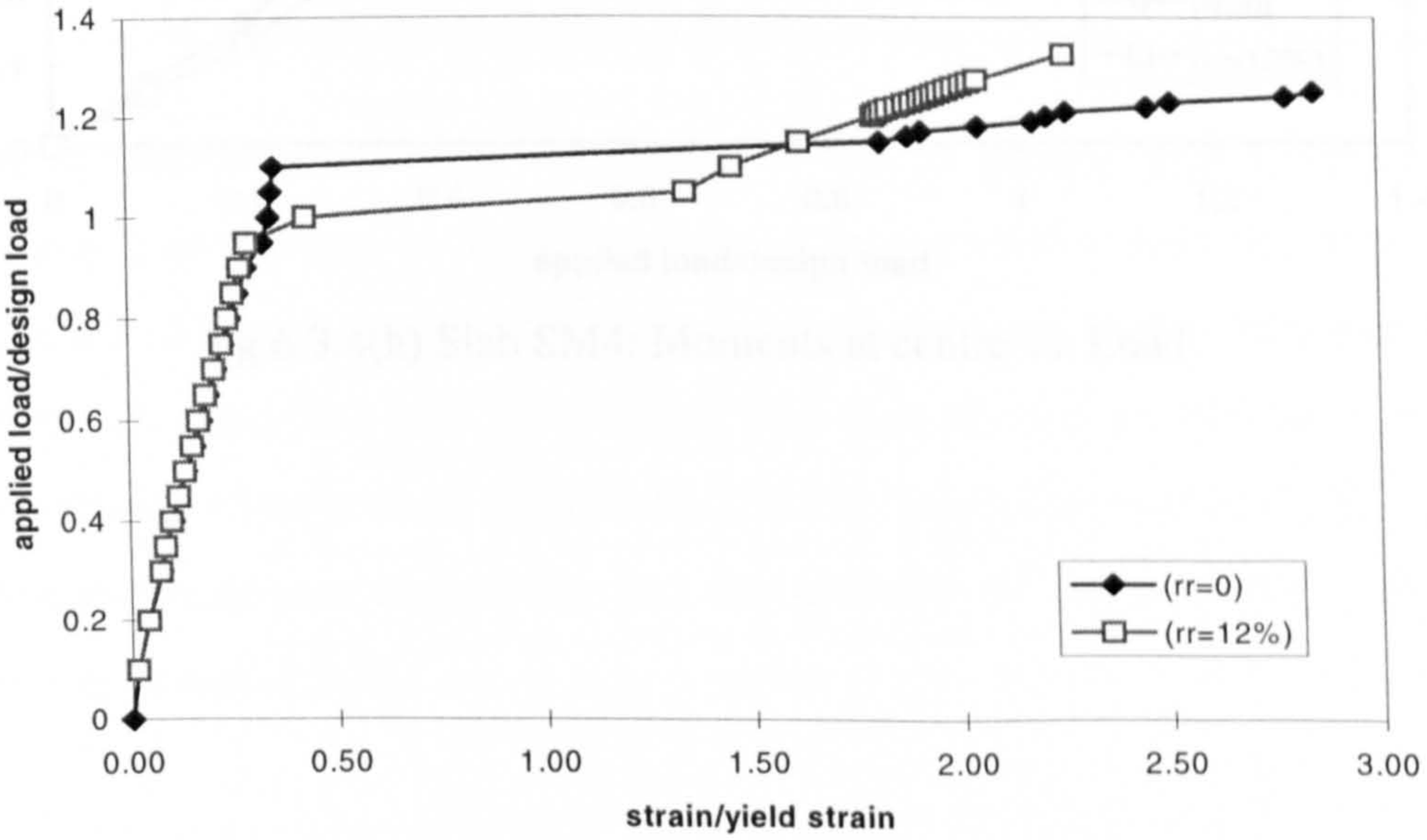

fig.6.3.4(f) Slab SM4: Top Steel Strains near column support

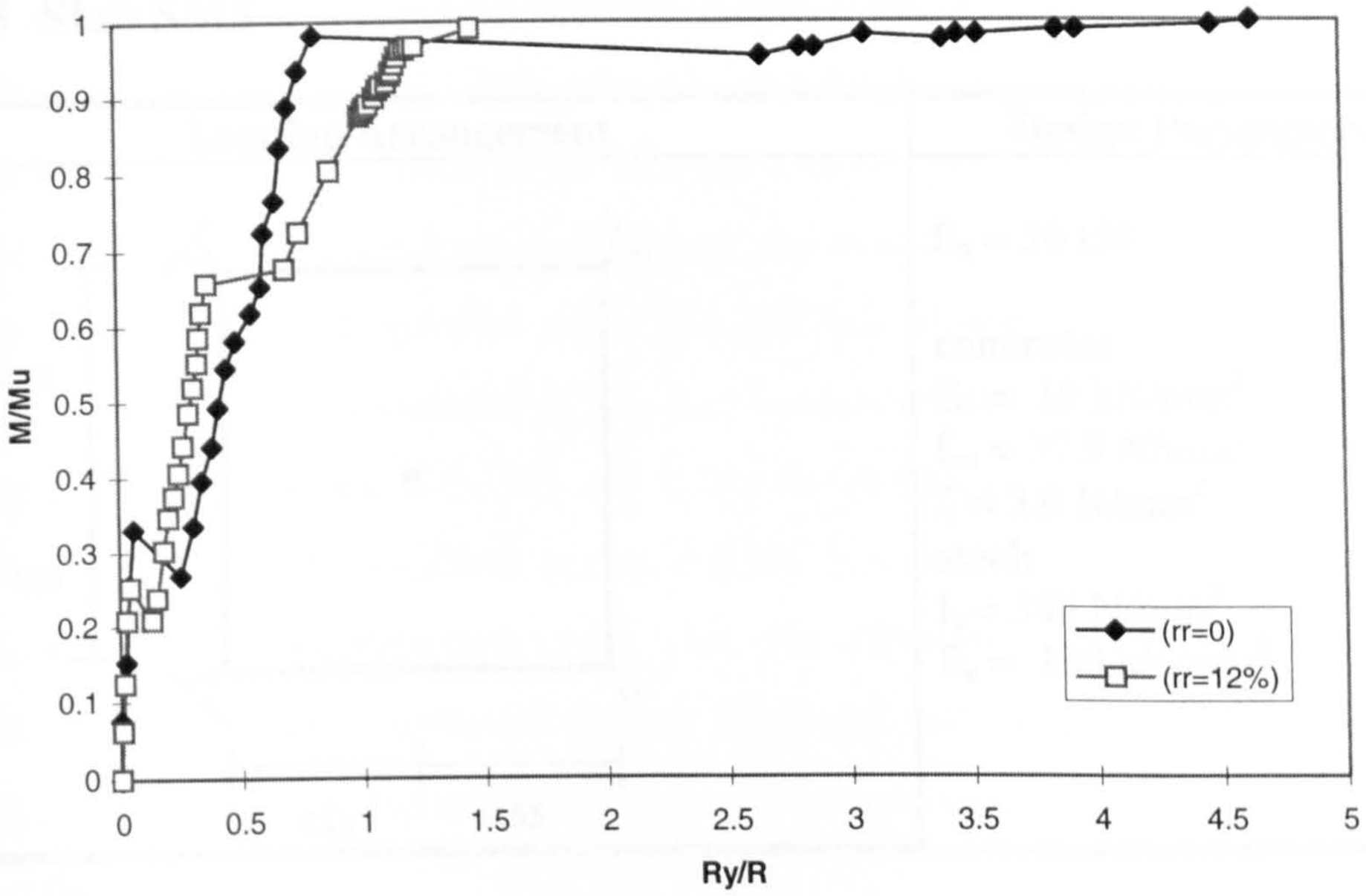

fig.6.3.4(g) Slab SM4: Principal Moment Curvature Relationship at centre

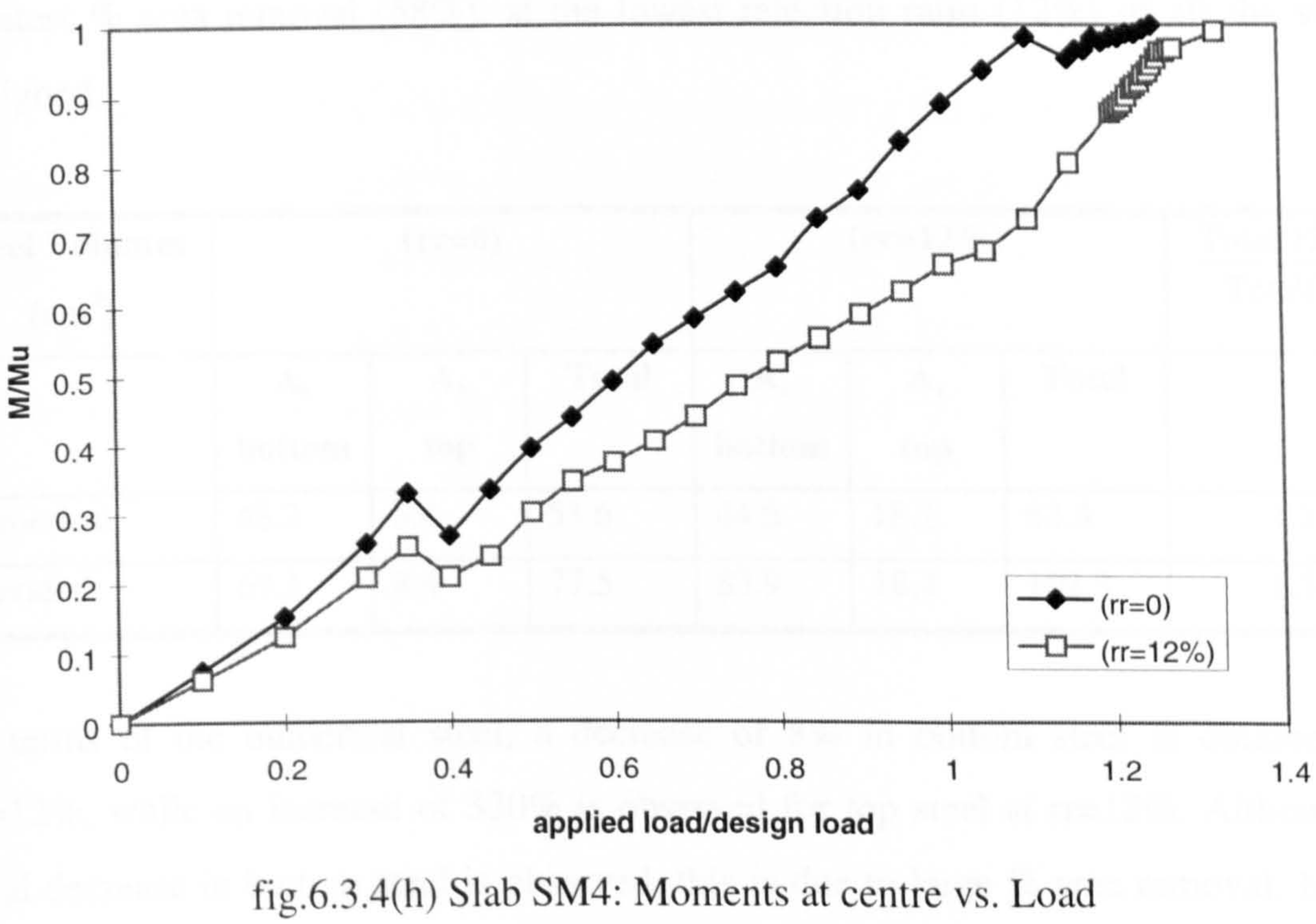

fig.6.3.4(h) Slab SM4: Moments at centre vs. Load

6.3.5 Slab SM5

Loading Arrangement	Design Parameters
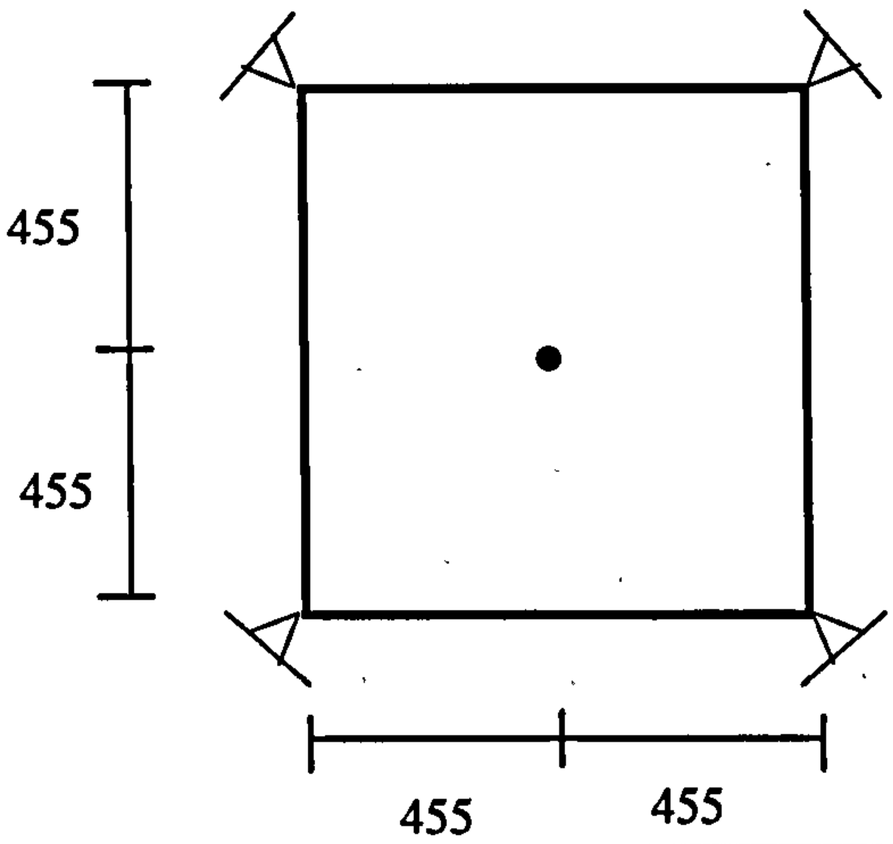	$P_d = 50$ kN **concrete:** $E_c = 19$ kN/mm^2 $f_{cu} = 37.9$ N/mm^2 $f_t = 3.0$ N/mm^2 **steel:** $f_y = 345$ N/mm^2 $E_s = 180$ kN/mm^2

This slab was centrally loaded and pin-supported at its four corners. Since this slab has the most pronounced and direct load path of all those considered, it resulted in the greatest % area removal (58%), at the lowest rejection ratio (12%) of all the slabs designed.

Steel Volumes (cm^3)	(rr=0)			(rr=12%)			Total(12%) / Total(0)
	A_s bottom	A_s top	Total	A_s bottom	A_s top	Total	
Numerical	48.2	5.4	53.6	44.6	18.2	62.8	1.2
Provided	69.1	8.4	77.5	83.9	18.4	102.3	1.3

In terms of the numerical steel, a decrease of 8% in bottom steel is obtained at rr=12%, while an increase of 330% is observed for top steel at rr=12%. Although a total decrease in bottom steel is observed, this is due to large % area removal. In the area around the main load path, much larger quantities of steel, an increase of around 50%, are required than at rr=0, (fig.6.3.5a). This is clearly observed in fig(6.3.5a(ii)). The resulting reinforcement layout and the element by element steel areas are displayed in figure 6.3.5(b).

The numerical load-displacement response of each model is shown in figure 6.3.5(c). An ultimate load of 1.1 and $1.35P_d$ was achieved for the designs at rr=0 and rr=12% respectively. The larger increase in the ultimate load of the second model is due to the fact that in order to obtain a practical layout, the total provided bottom steel was in excess of the numerical provided steel. The stiffness of both models was relatively similar up until P_d. Both models fail in a ductile manner. The service deflection limit at mid-span was reached at $0.65P_d$ and $0.7P_d$ for design one and two respectively. Yielding of the bottom steel first occurred at the centre of the slab in design one at $0.8P_d$, and at $1.2P_d$ in design two, (fig.6.3.5c). The difference in these loads is caused by the large increase in provided bottom steel and numerical steel in the second design. Yielding of the top steel first occurred in both slabs at the corner support at $0.8P_d$ (fig.6.3.5d).

For the section at the centre of the slab, M_u and $1/R_y$ were calculated as 5.2kNm/m and $0.0002mm^{-1}$ respectively, at rr=0. In the second design, at the same section, of M_u and $1/R_y$ were 8.5kNm/m and $0.0002mm^{-1}$ respectively. From the moment curvature relationship at the centre of the slab, figure 6.3.5(f), it can be seen that the second design, due to its large increase in steel area at this point, is sustaining a larger moment and is slightly less ductile than the first design. Softening is initiated at this section in the second design at around $1.35P_d$, (fig.6.3.5g). For the section at the corner support, M_u and $1/R_y$ were 6kNm/m and $0.0002mm^{-1}$ respectively, at rr=0. In the second design at this area, M_u and $1/R_y$ were 8.5kNm/m and $0.0002mm^{-1}$ respectively.

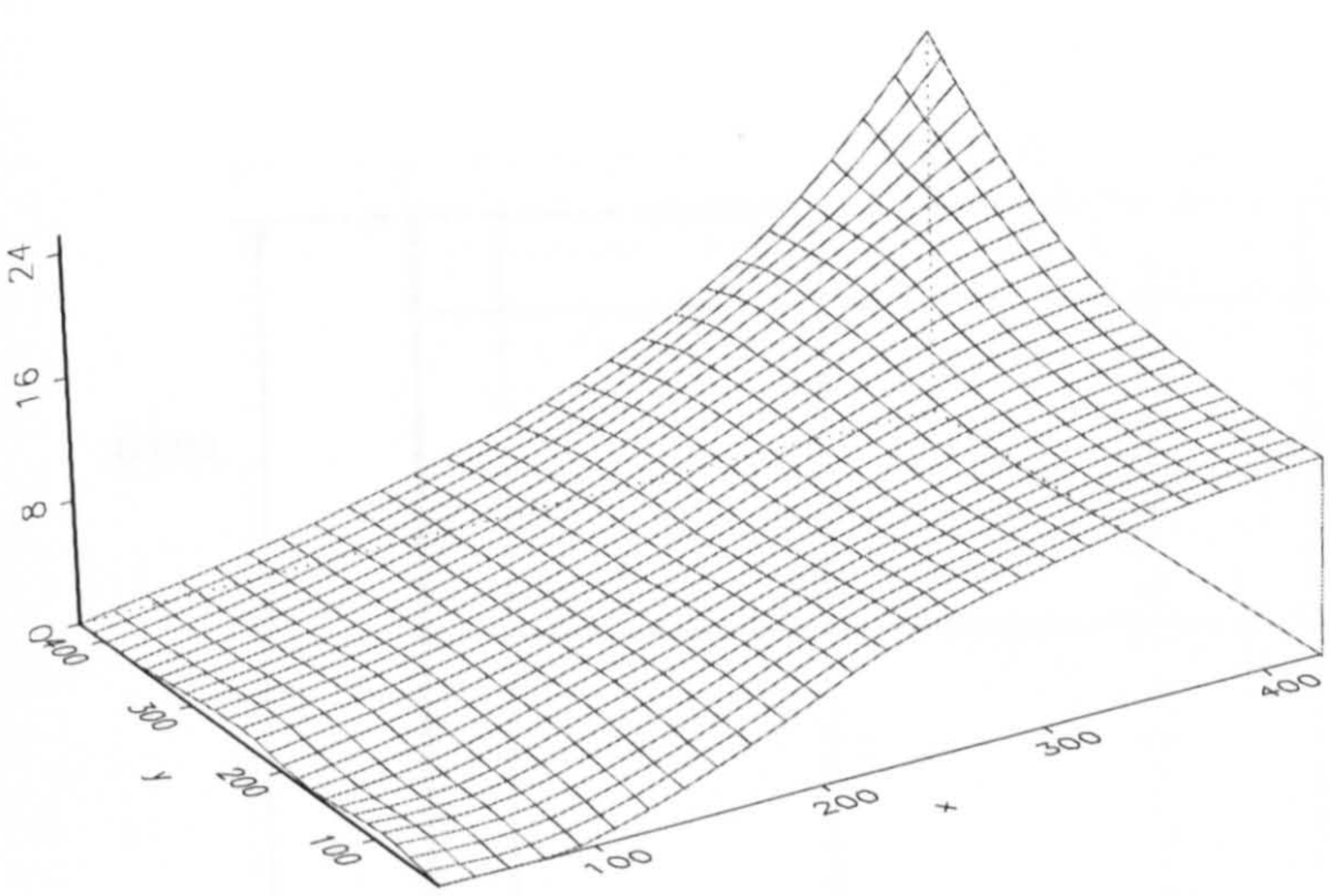

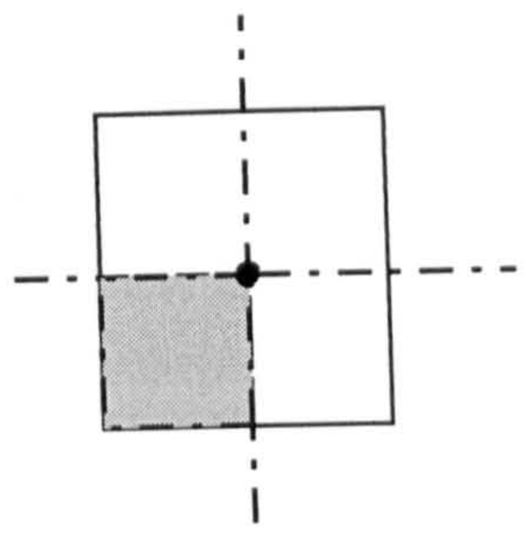

i) A_{sx}bottom (rr=0)

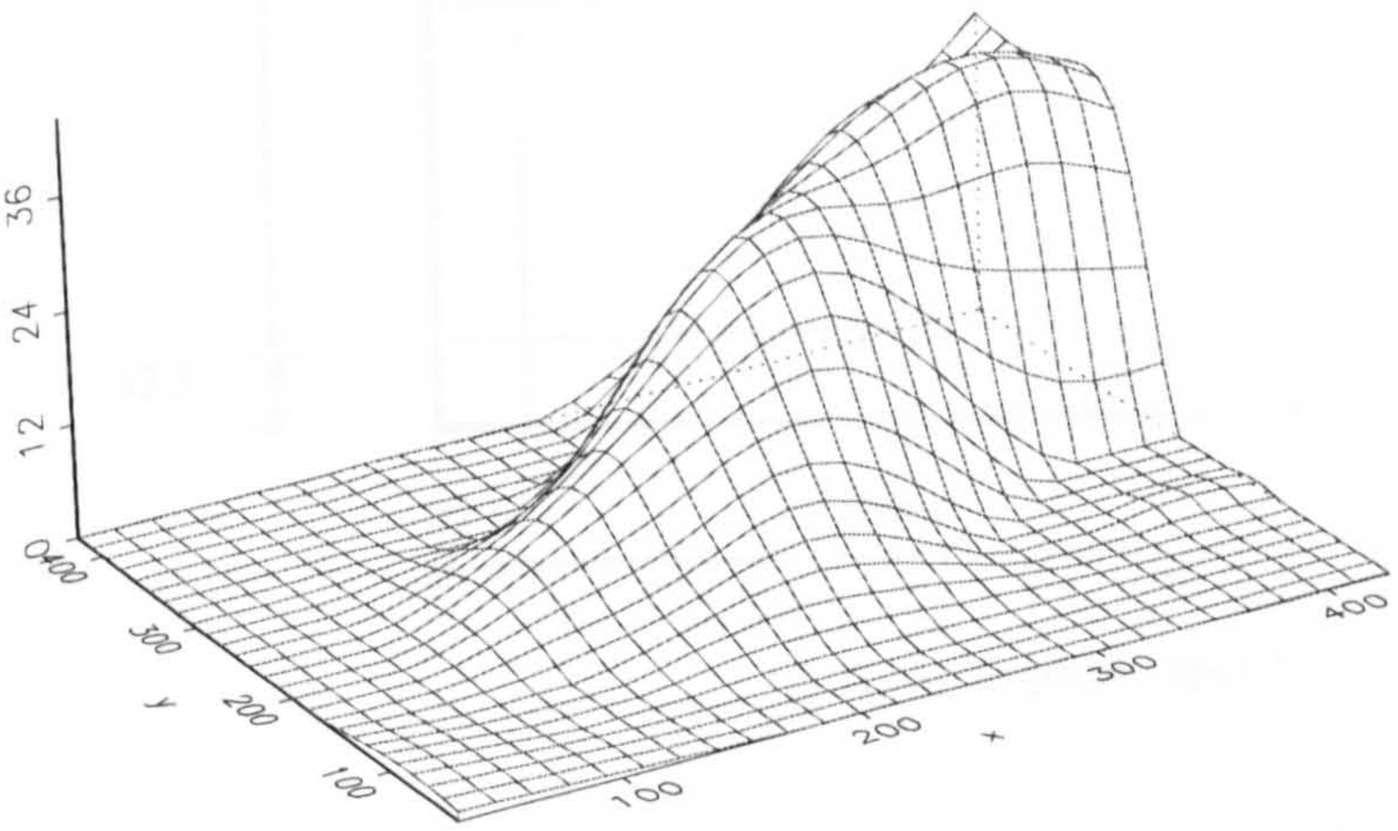

ii) A_{sx}bottom (rr=12%)

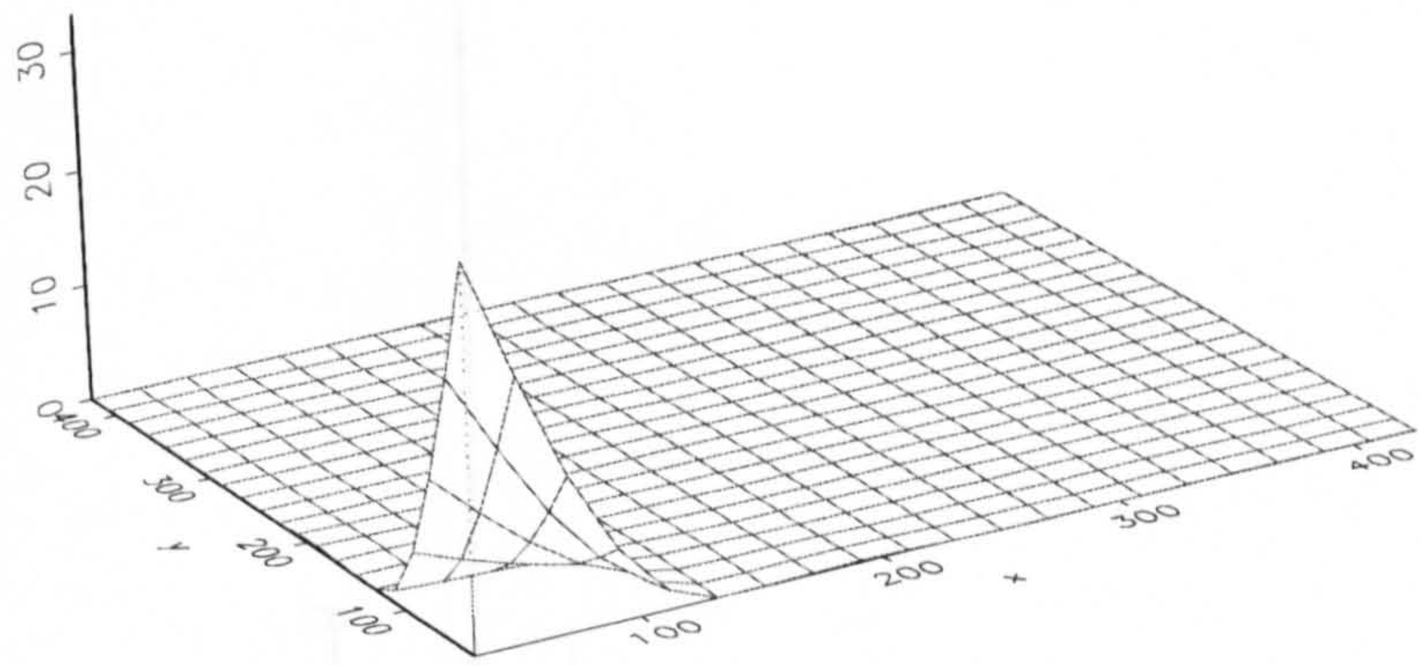

iii) A_{sx}top (rr=0)

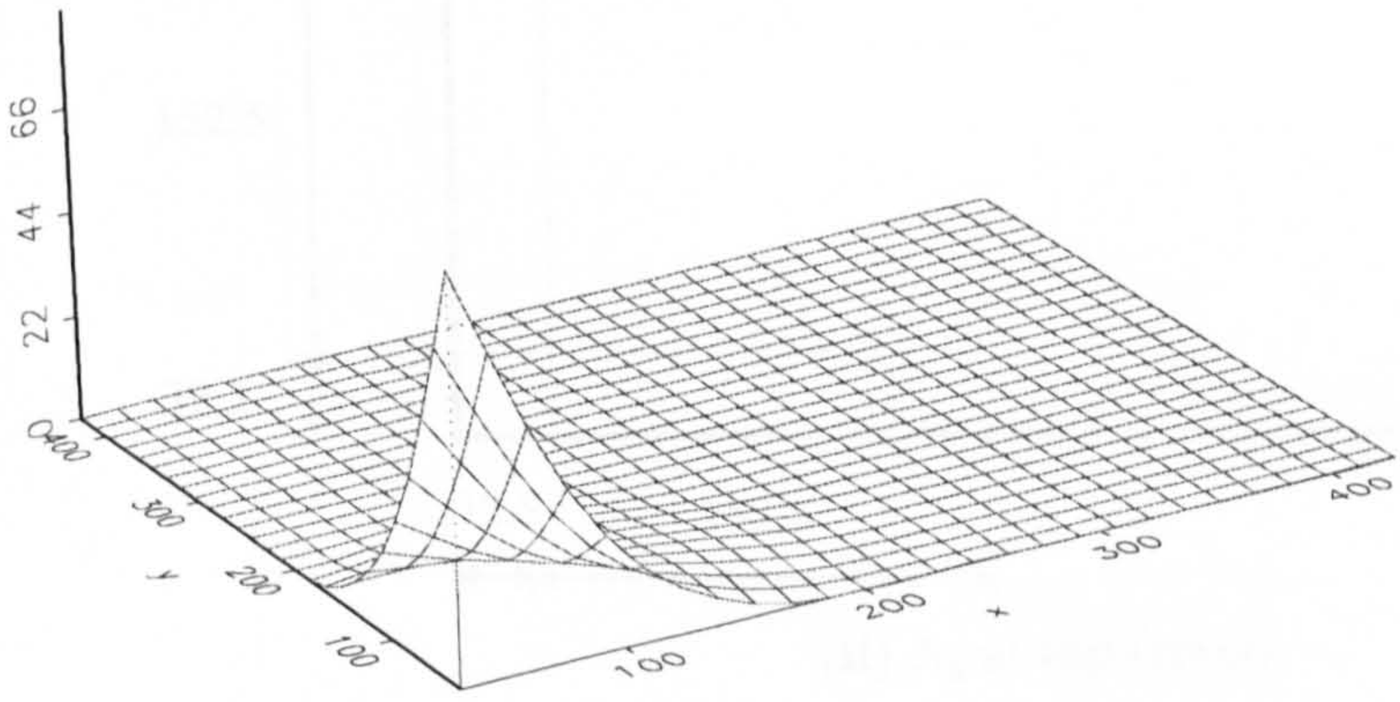

iv) A_{sx}top (rr=12%)

fig6.3.5(a) Slab SM5, Symmetrical Quarter, Numerical Steel Areas (mm^2)

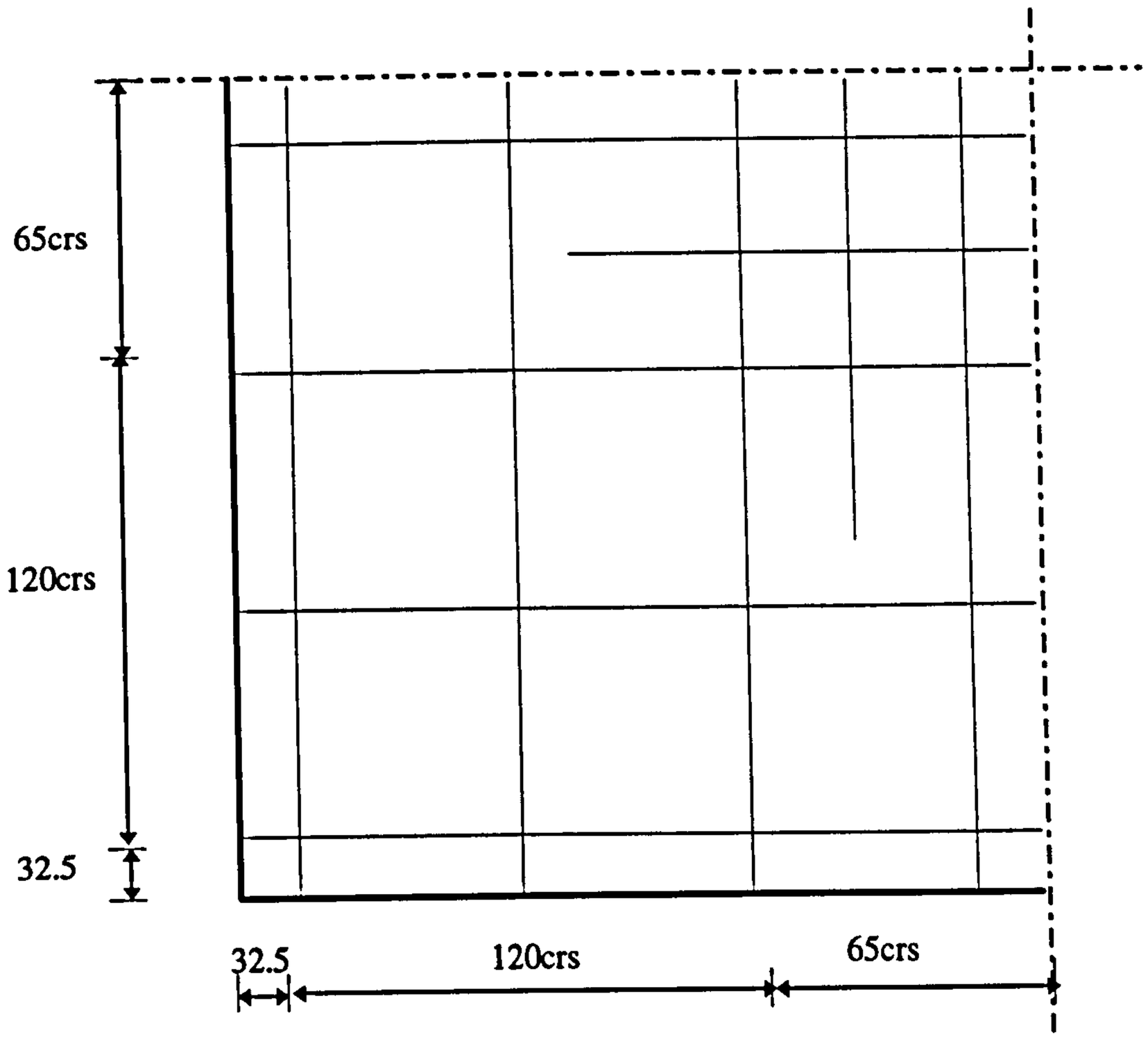

i) A_s at bottom (rr=0)

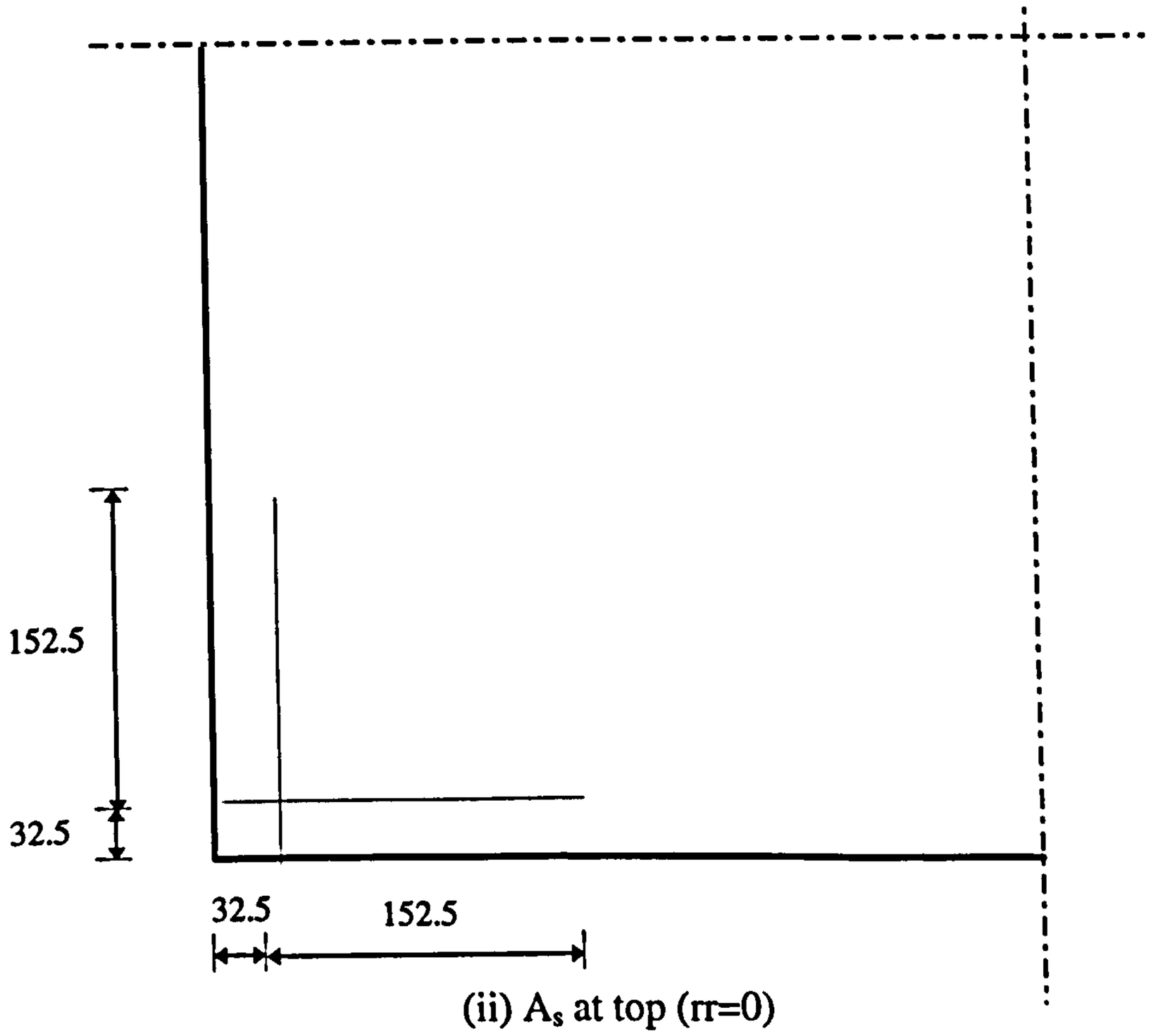

(ii) A_s at top (rr=0)

fig.6.3.5(b) Slab SM5: Steel Layout, all sizes in mm, all bars 6mm diameter

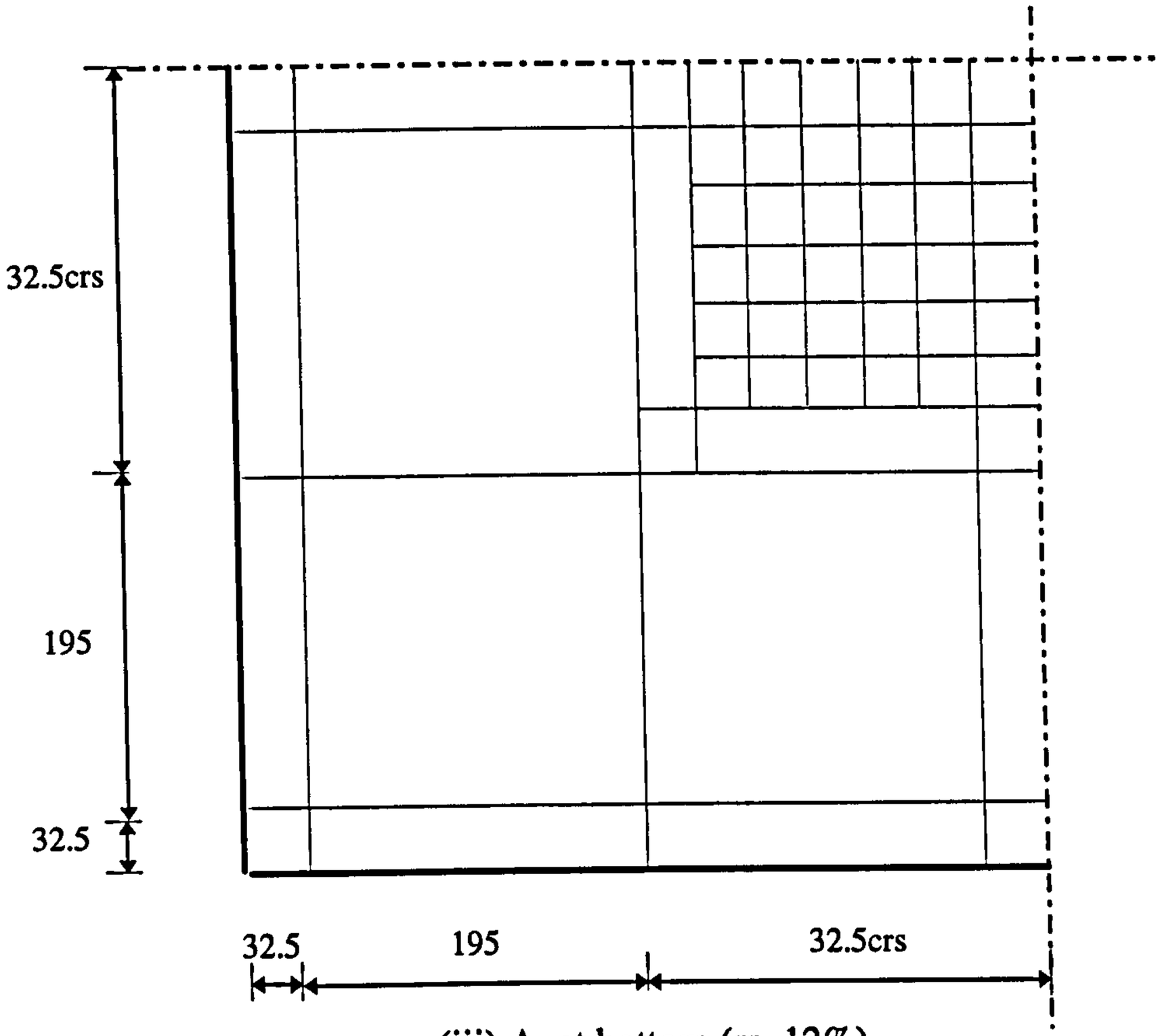

(iii) A_s at bottom (rr=12%)

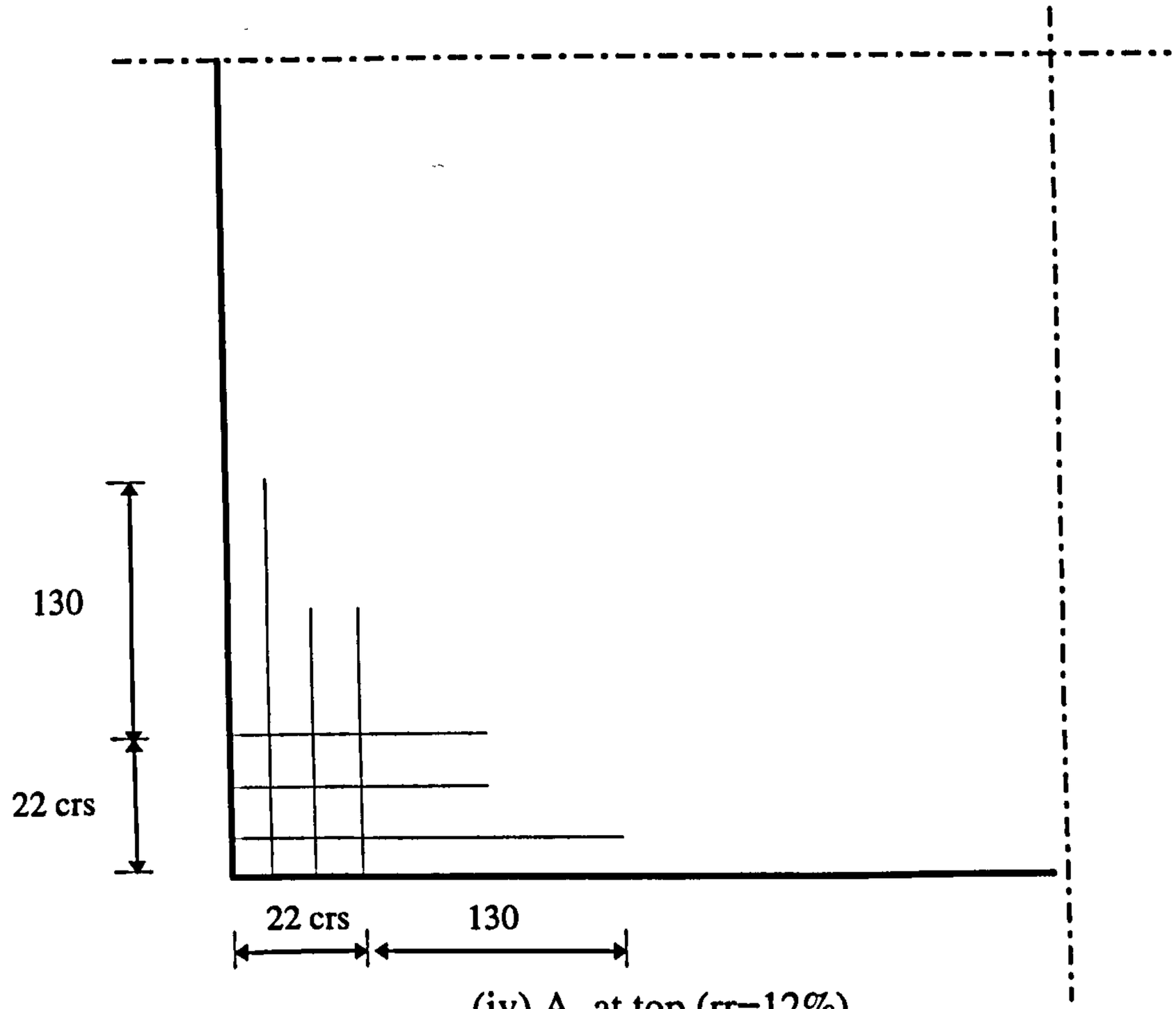

(iv) A_s at top (rr=12%)

fig.6.3.5(b) Slab SM5: Steel Layout, all sizes in mm, all bars 6mm diameter

0.000 (3.8)	1.476 (3.8)	3.411 (3.8)	6.112 (14.2)	9.733 (14.2)	15.182 (28.3)	25.174 (28.3)
0.000 (3.8)	1.611 (3.8)	3.728 (3.8)	6.862 (14.2)	10.984 (14.2)	16.028 (28.3)	20.362 (28.3)
0.705 (3.8)	1.825 (3.8)	3.835 (3.8)	7.101 (14.2)	10.980 (14.2)	14.760 (14.2)	16.691 (14.2)
0.798 (3.8)	2.028 (3.8)	4.066 (3.8)	6.903 (14.2)	10.362 (14.2)	13.252 (14.2)	14.559 (14.2)
0.000 (3.8)	1.623 (3.8)	4.385 (3.8)	7.080 (14.2)	9.787 (14.2)	12.185 (14.2)	13.358 (14.2)
0.894 (3.8)	0.854 (3.8)	4.159 (3.8)	7.444 (14.2)	9.884 (14.2)	11.757 (14.2)	12.804 (14.2)
0.000 (3.8)	0.000 (3.8)	3.504 (3.8)	7.461 (14.2)	10.116 (14.2)	11.888 (14.2)	12.755 (14.2)

(v) A_{sx} at bottom (rr=0) 6mm bars

0.000 (0.00)	0.000 (0.00)	0.000 (0.00)	0.000 (0.00)	0.000 (0.00)	0.000 (0.00)	0.000 (0.00)
0.000 (0.00)	0.000 (0.00)	0.000 (0.00)	0.000 (0.00)	0.000 (0.00)	0.000 (0.00)	0.000 (0.00)
0.000 (0.00)	0.000 (0.00)	0.000 (0.00)	0.000 (0.00)	0.000 (0.00)	0.000 (0.00)	0.000 (0.00)
0.000 (0.00)	0.000 (0.00)	0.000 (0.00)	0.000 (0.00)	0.000 (0.00)	0.000 (0.00)	0.000 (0.00)
0.000 (0.00)	0.000 (0.00)	0.000 (0.00)	0.000 (0.00)	0.000 (0.00)	0.000 (0.00)	0.000 (0.00)
3.491 (3.8)	0.758 (3.8)	0.000 (0.00)	0.000 (0.00)	0.000 (0.00)	0.000 (0.00)	0.000 (0.00)
33.127 (28.3)	4.167 (28.3)	0.000 (0.00)	0.000 (0.00)	0.000 (0.00)	0.000 (0.00)	0.000 (0.00)

(vi) A_{sx} at top (rr=0) 6mm bars

fig.6.3.5(b) Slab SM5: Numerical & (Provided) Steel Areas in mm^2

0.000 (3.8)	0.000 (3.8)	0.000 (3.8)	0.000 (3.8)	7.371 (42.4)	18.464 (42.4)	32.024 (42.4)
0.000 (3.8)	0.000 (3.8)	0.000 (3.8)	0.000 (3.8)	22.907 (42.4)	27.200 (42.4)	30.795 (42.4)
0.000 (3.8)	0.000 (3.8)	0.000 (3.8)	23.394 (42.4)	36.038 (42.4)	43.952 (42.4)	35.811 (42.4)
0.000 (3.8)	0.000 (3.8)	9.310 (28.3)	19.025 (28.3)	23.042 (28.3)	0.000 (3.8)	0.000 (3.8)
0.000 (3.8)	0.000 (3.8)	2.929 (3.8)	8.101 (3.8)	0.000 (3.8)	0.000 (3.8)	0.000 (3.8)
1.576 (3.8)	0.000 (3.8)	0.000 (3.8)	0.000 (3.8)	0.000 (3.8)	0.000 (3.8)	0.000 (3.8)
0.962 (3.8)	0.659 (3.8)	0.000 (3.8)	0.000 (3.8)	0.000 (3.8)	0.000 (3.8)	0.000 (3.8)

(vii) A_{sx} at bottom (rr=12%) 6mm bars

0.000 (0.000)	0.000 (0.000)	0.000 (0.000)	0.000 (0.000)	0.000 (0.000)	0.000 (0.000)	0.000 (0.000)
0.000 (0.000)	0.000 (0.000)	0.000 (0.000)	0.000 (0.000)	0.000 (0.000)	0.000 (0.000)	0.000 (0.000)
0.000 (0.000)	0.000 (0.000)	0.000 (0.000)	0.000 (0.000)	0.000 (0.000)	0.000 (0.000)	0.000 (0.000)
0.000 (0.000)	0.000 (0.000)	0.000 (0.000)	0.000 (0.000)	0.000 (0.000)	0.000 (0.000)	0.000 (0.000)
0.000 (0.000)	4.137 (0.000)	0.000 (0.000)	0.000 (0.000)	0.000 (0.000)	0.000 (0.000)	0.000 (0.000)
15.030 (14.2)	11.760 (14.2)	5.165 (0.000)	0.000 (0.000)	0.000 (0.000)	0.000 (0.000)	0.000 (0.000)
86.860 (84.8)	17.026 (84.8)	0.000 (0.000)	0.000 (0.000)	0.000 (0.000)	0.000 (0.000)	0.000 (0.000)

(viii) A_{sx} at top (rr=12%) 6mm bars

fig.6.3.5(b) Slab SM5: Numerical & (Provided) Steel Areas in mm^2

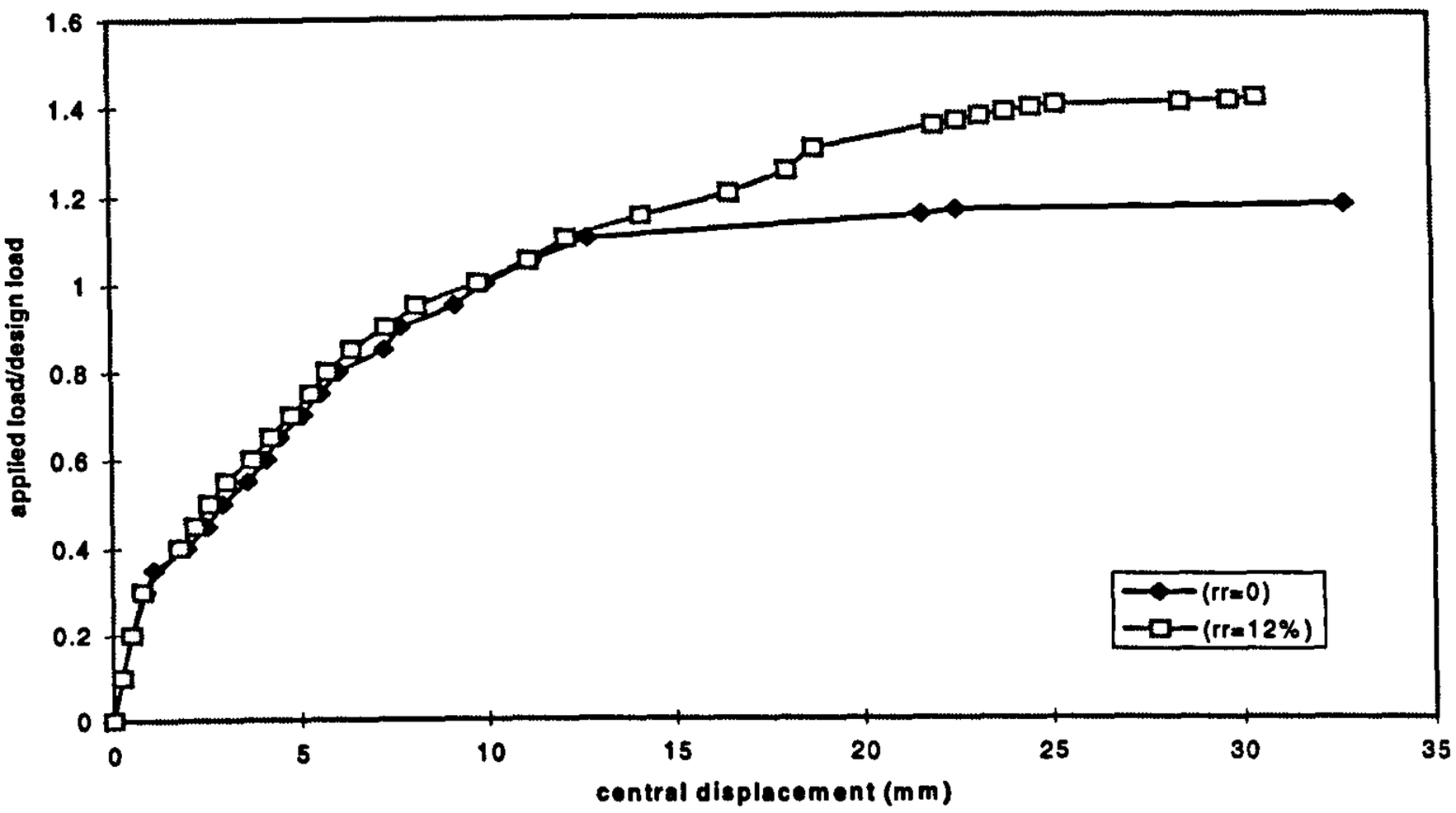

fig.6.3.5(c) Slab SM5: Load-displacement relationship

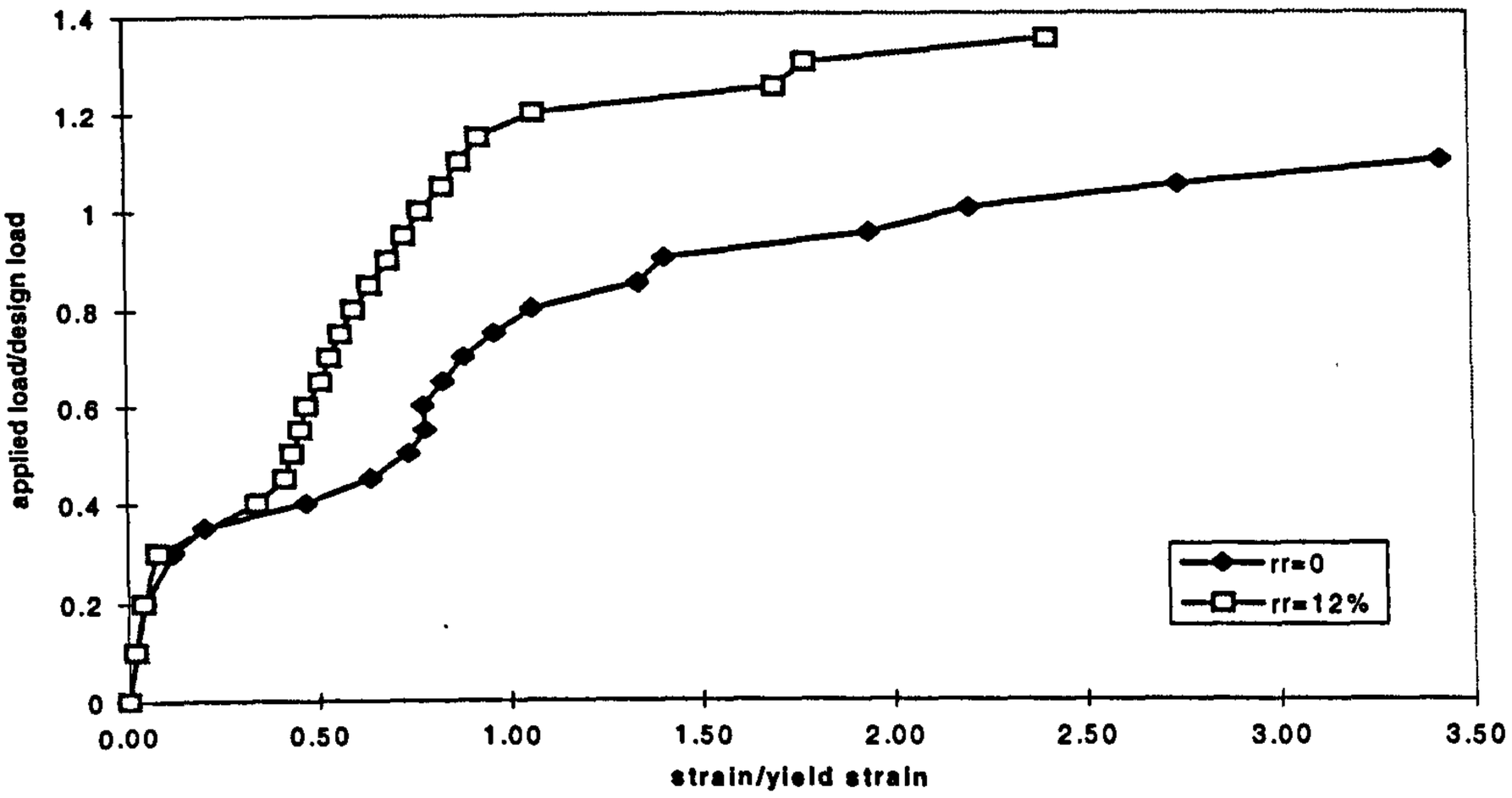

fig.6.3.5(d) Slab SM5: Bottom Steel Strains at centre

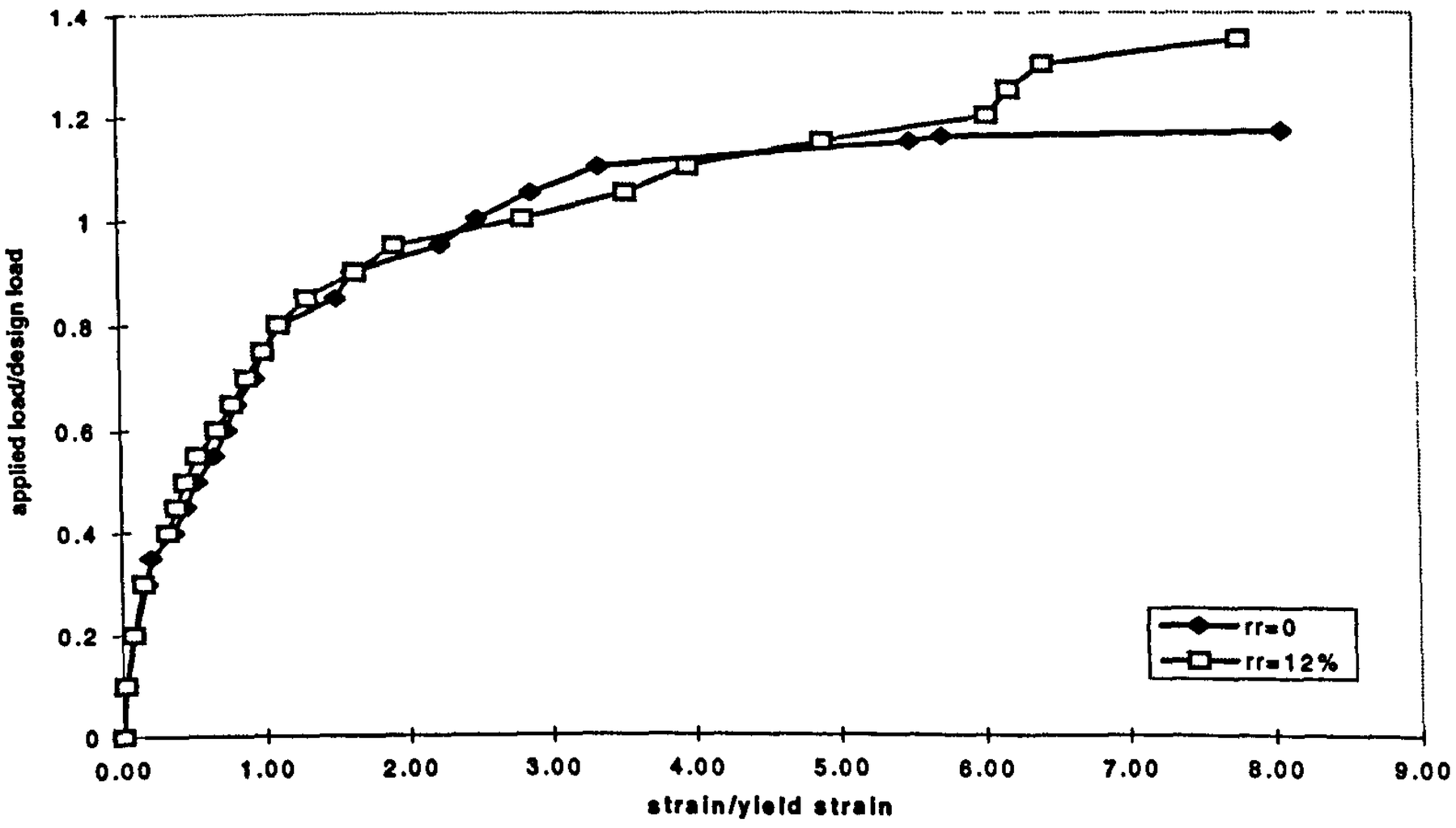

fig.6.3.5(e) Slab SM5: Top Steel Strains near corner

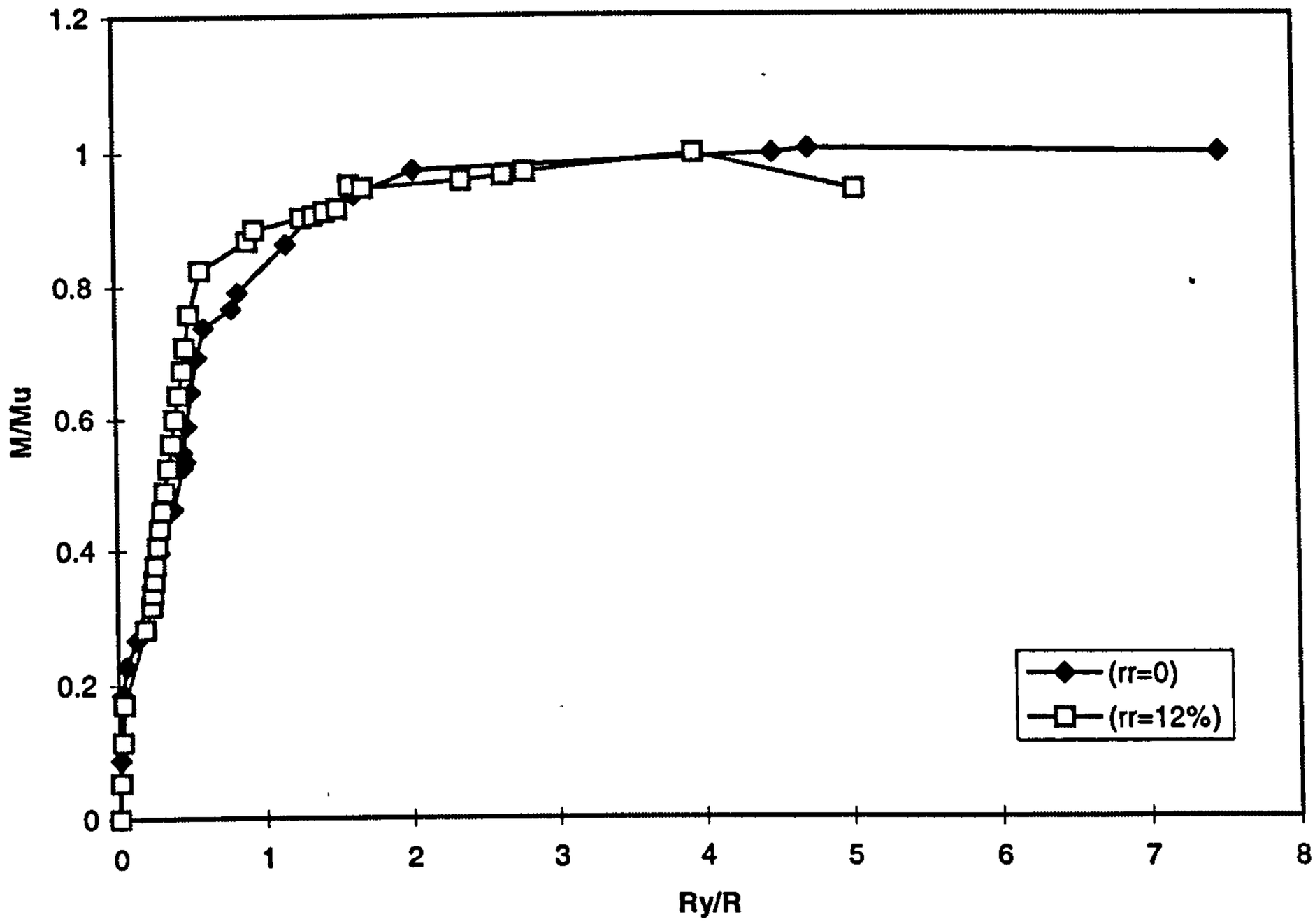

fig.6.3.5(f) Slab SM5: Principal Moment-curvature relationship at centre

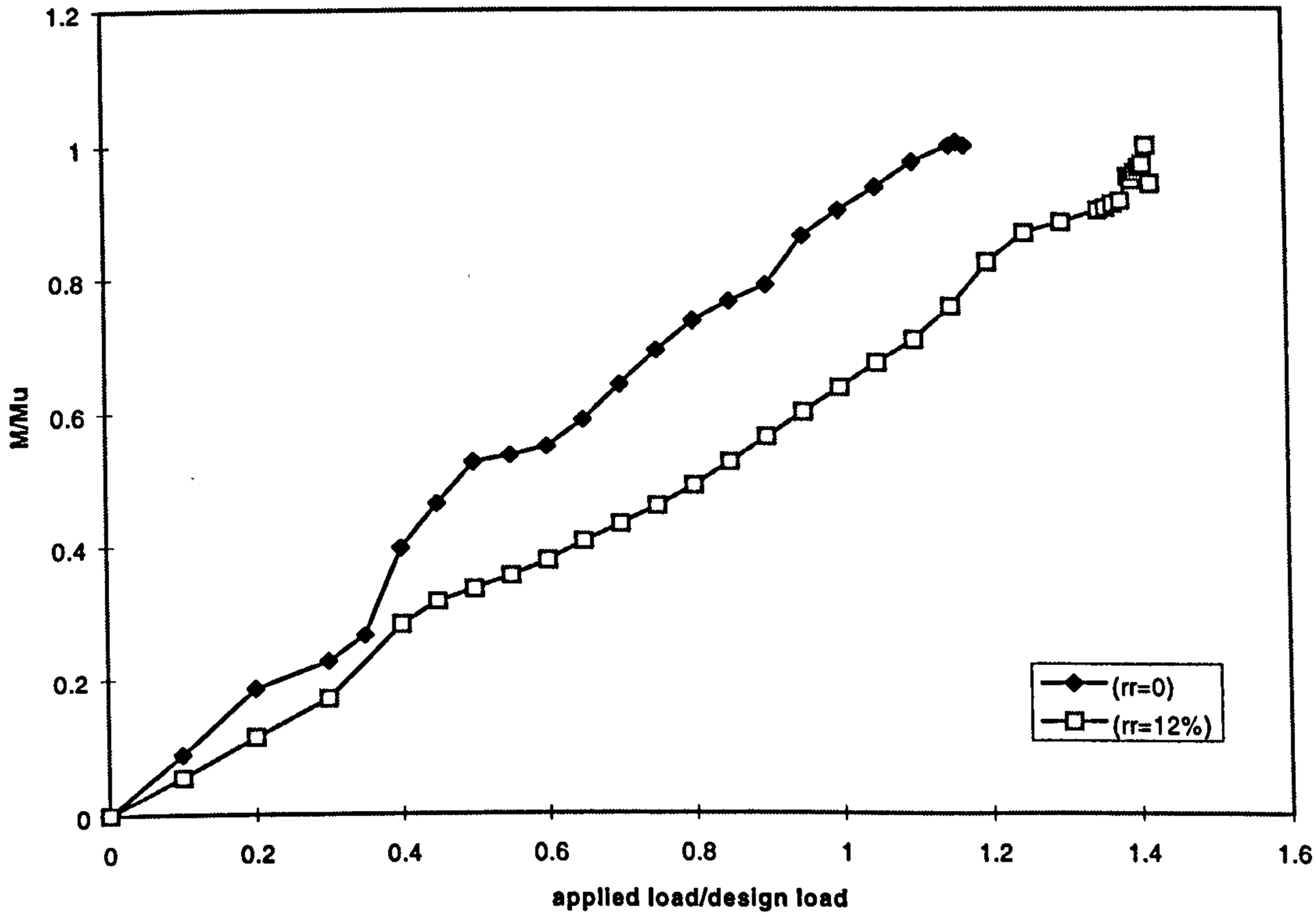

fig.6.3.5(g) Slab SM5: Principal Moment at centre vs. Load

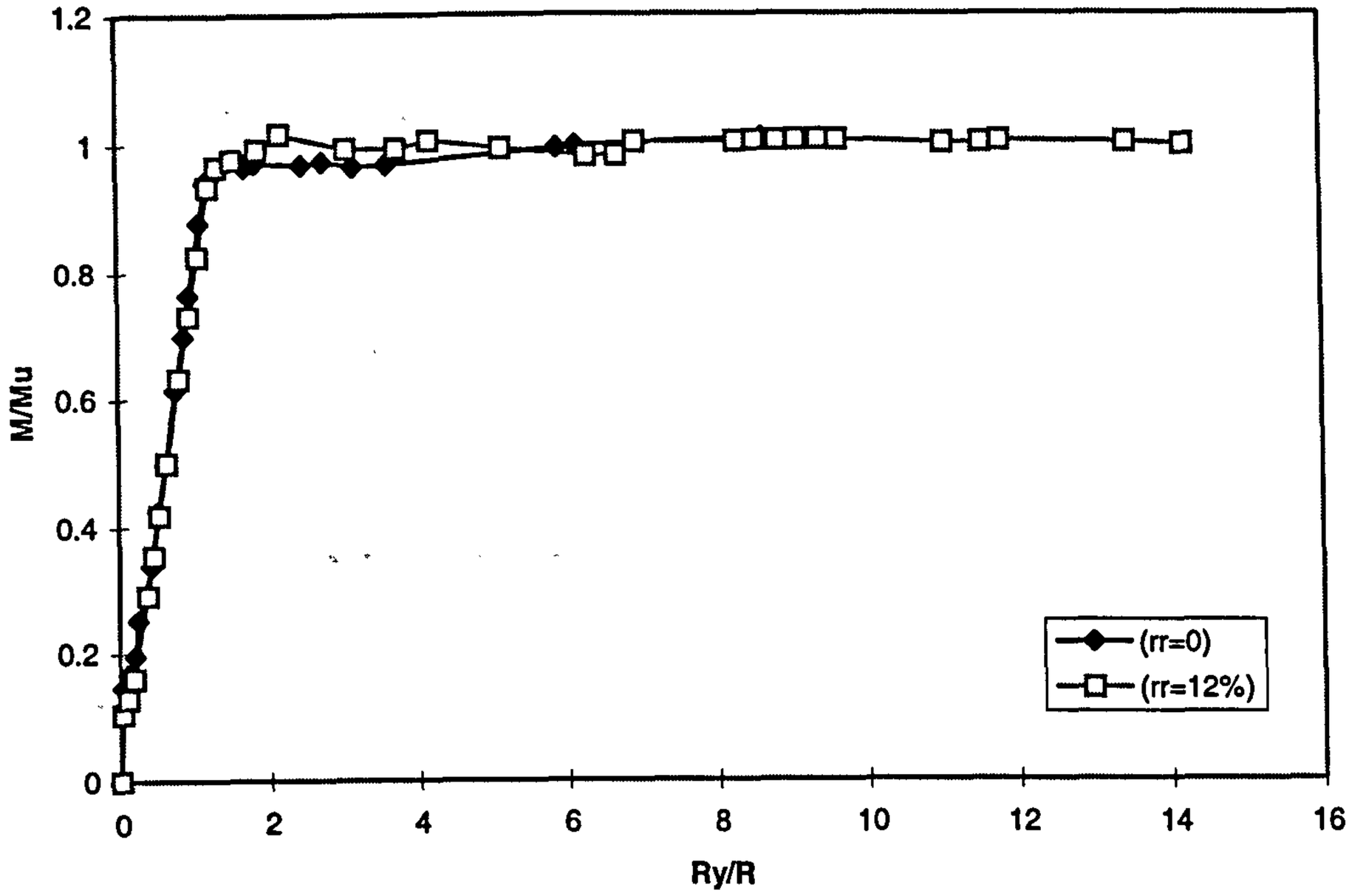

fig.6.3.5(h) Slab SM5: Moment-curvature relationship at corner support

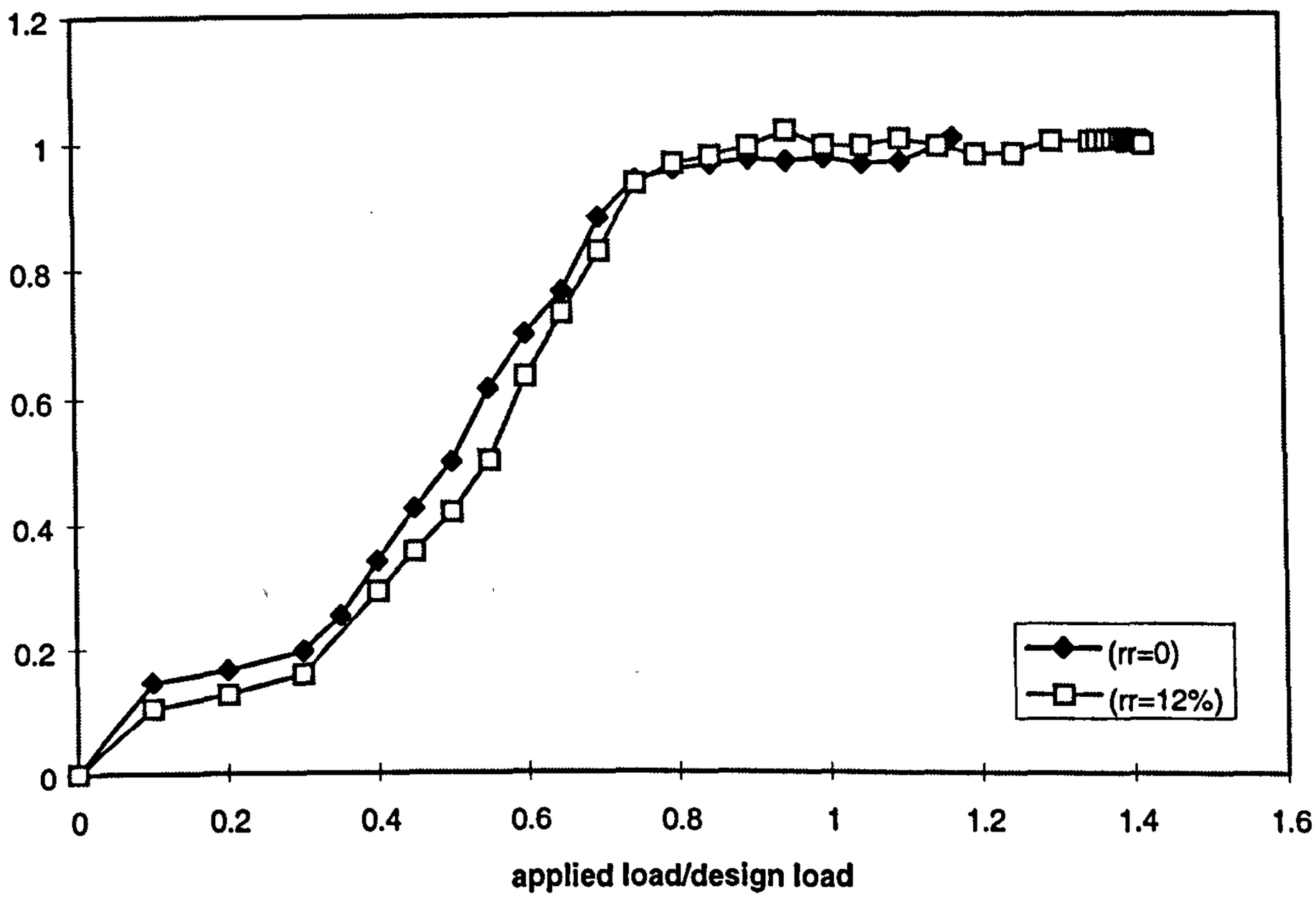

fig.6.3.5(i) Slab SM5: Moments at corner support

6.3.6 Slab SM6

For all the designs so far, only steel orthogonal to the slab edges has been considered. In some cases, this may not be the most efficient orientation for the steel layout. In slab SM5, the maximum principal moments are orientated along the main diagonal at roughly 45° to the x-axis (fig.6.2.4). In view of this fact, slab SM5 was redesigned by providing orthogonal steel transformed 45° from the horizontal.

Steel Volumes (cm^3)	**(rr=0)**			**(rr=12%)**			**Total(12%) / Total(0)**
	A_s bottom	**A_s top**	**Total**	**A_s bottom**	**A_s top**	**Total**	
Numerical	48.2	5.4	53.6	41.4	12.2	53.6	1.0
Provided	69.1	8.4	77.5	64.1	15.6	79.7	1.03

In this case, the numerical steel areas at rr=0 and 12% are equal, which is in contrasts with slab SM5 where a 20% increase was observed at rr=12%. The resulting reinforcement layout is shown in figure 6.3.6(a). The numerical load-displacement relationship is shown in figure 6.3.6(b). An ultimate load of $1.1P_d$ was obtained for this design. The service deflection limit was reached at around $0.7P_d$. Yielding of the bottom steel first occurred at the centre of the slab at a load level of $0.9P_d$. Yielding of the top steel at the corner support began at the same load level, (fig.6.3.6c-d). Inspection of the moment curvature relationship at the corner support shows that softening occurs just after $1.05P_d$, (fig.6.3.6e-f). This is due to the fact that once yielding of the top steel commences prior to this softening, unlike slab SM5 where equal steel is provided in x and y directions, redistribution of stress is more difficult since much less steel is provided orthogonal to the main steel. At the centre of the slab, the moment is sustained beyond the design load and softening is not present, (fig.6.3.6g-h).

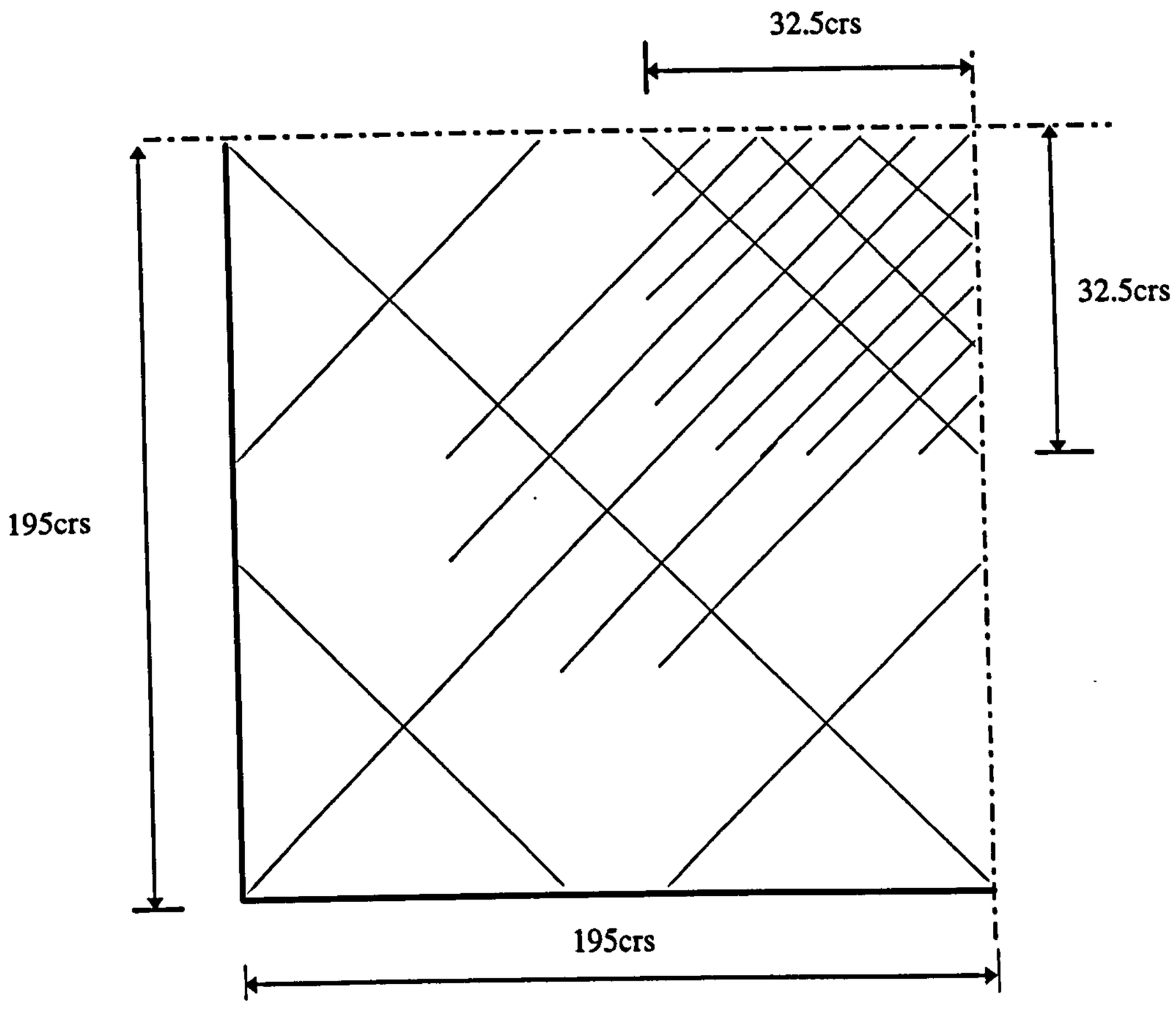

(i) A_s at bottom (rr=12%)

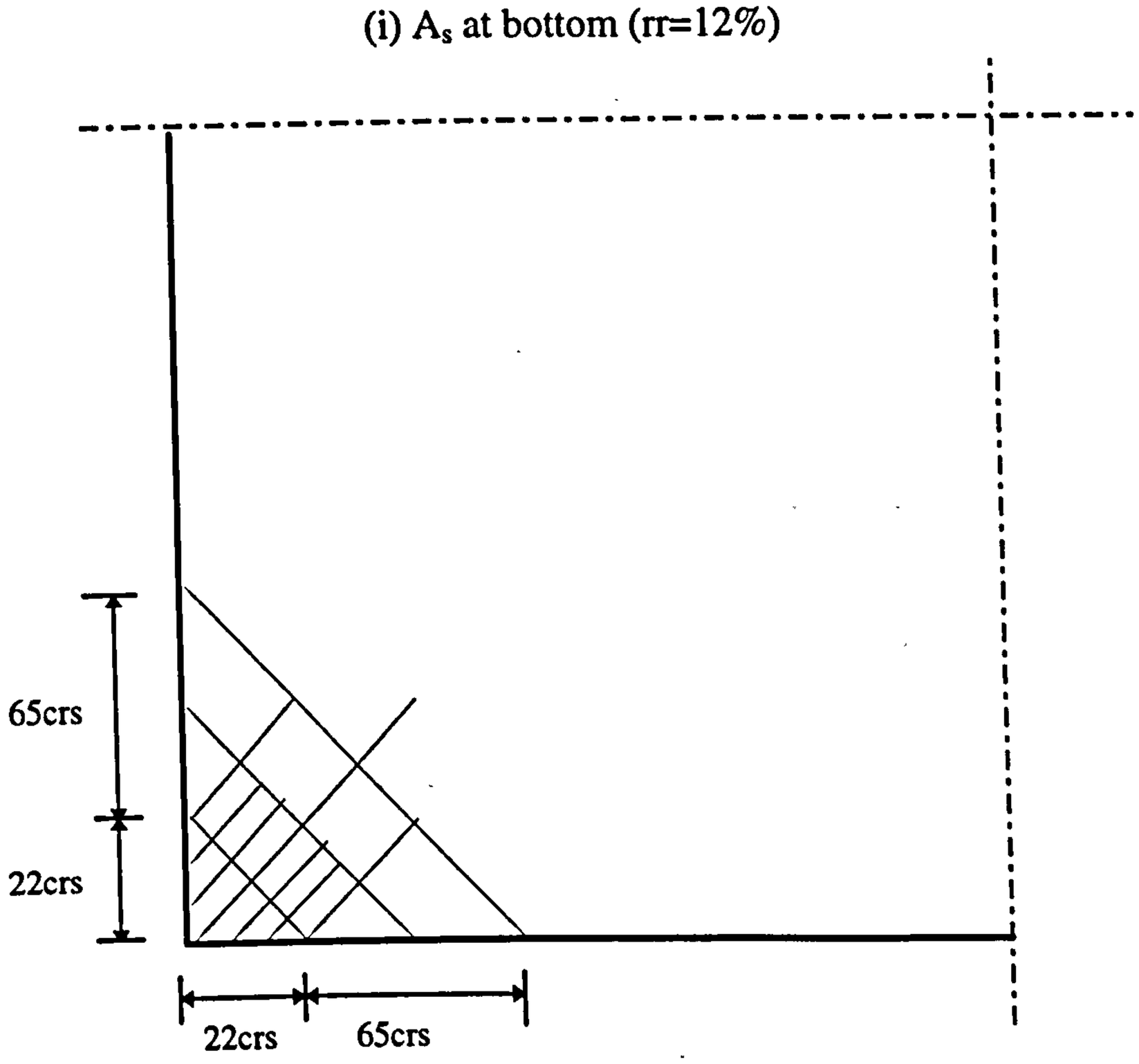

(ii) A_s at top (rr=12%)

fig.6.3.6(a) Slab SM6: Steel Layout, all sizes in mm, all bars 6mm diameter

0.00 (3.76)	0.00 (3.76)	0.00 (3.76)	0.00 (3.76)	35.76 (42.41)	30.70 (42.41)	31.70 (42.41)
0.00 (3.76)	0.00 (3.76)	0.00 (3.76)	0.00 (3.76)	43.95 (42.41)	30.11 (42.41)	30.71 (42.41)
0.00 (3.76)	0.00 (3.76)	0.00 (3.76)	24.77 (28.27)	37.03 (42.41)	43.95 (42.41)	35.77 (42.41)
0.00 (3.76)	0.00 (3.76)	9.45 (14.14)	19.52 (28.27)	24.77 (28.27)	0.00 (3.76)	0.00 (3.76)
0.00 (3.76)	0.00 (3.76)	3.32 (3.76)	9.45 (14.14)	0.00 (3.76)	0.00 (3.76)	0.00 (3.76)
1.15 (3.76)	0.00 (3.76)	0.00 (3.76)	0.00 (3.76)	0.00 (3.76)	0.00 (3.76)	0.00 (3.76)
0.00 (3.76)	1.15 (3.76)	0.00 (3.76)	0.00 (3.76)	0.00 (3.76)	0.00 (3.76)	0.00 (3.76)

(iii) A_{sx} at bottom (rr=12%) 6mm bars

0.00 (3.76)	0.00 (3.76)	0.00 (3.76)	0.00 (3.76)	29.94 (28.27)	28.67 (28.27)	34.30 (28.27)
0.00 (3.76)	0.00 (3.76)	0.00 (3.76)	0.00 (3.76)	18.27 (28.27)	18.64 (28.27)	28.68 (28.27)
0.00 (3.76)	0.00 (3.76)	0.00 (3.76)	1.83 (3.76)	4.49 (3.76)	18.27 (28.27)	29.95 (28.27)
0.00 (3.76)	0.00 (3.76)	0.89 (3.76)	1.23 (3.76)	1.83 (3.76)	0.00 (3.76)	0.00 (3.76)
0.00 (3.76)	0.00 (3.76)	0.00 (3.76)	0.89 (3.76)	0.00 (3.76)	0.00 (3.76)	0.00 (3.76)
2.43 (3.76)	0.00 (3.76)	0.00 (3.76)	0.00 (3.76)	0.00 (3.76)	0.00 (3.76)	0.00 (3.76)
0.79 (3.76)	2.43 (3.76)	0.00 (3.76)	0.00 (3.76)	0.00 (3.76)	0.00 (3.76)	0.00 (3.76)

(iv) A_{sy} at bottom (rr=12%) 6mm bars

fig.6.3.6(a) Slab SM6: Numerical & (Provided) Steel Areas in mm^2

0.00 (0.00)	0.00 (0.00)	0.00 (0.00)	0.00 (0.00)	0.00 (0.00)	0.00 (0.00)	0.00 (0.00)
0.00 (0.00)	0.00 (0.00)	0.00 (0.00)	0.00 (0.00)	0.00 (0.00)	0.00 (0.00)	0.00 (0.00)
0.00 (0.00)	0.00 (0.00)	0.00 (0.00)	0.00 (0.00)	0.00 (0.00)	0.00 (0.00)	0.00 (0.00)
0.00 (0.00)	0.00 (0.00)	0.00 (0.00)	0.00 (0.00)	0.00 (0.00)	0.00 (0.00)	0.00 (0.00)
0.00 (0.00)	5.18 (0.00)	0.00 (0.00)	0.00 (0.00)	0.00 (0.00)	0.00 (0.00)	0.00 (0.00)
19.60 (28.27)	12.05 (28.27)	5.17 (0.00)	0.00 (0.00)	0.00 (0.00)	0.00 (0.00)	0.00 (0.00)
104.50 (113.08)	19.59 (28.27)	0.00 (0.00)	0.00 (0.00)	0.00 (0.00)	0.00 (0.00)	0.00 (0.00)

(v) A_{sx} at top (rr=12%) 6mm bars

0.00 (0.00)	0.00 (0.00)	0.00 (0.00)	0.00 (0.00)	0.00 (0.00)	0.00 (0.00)	0.00 (0.00)
0.00 (0.00)	0.00 (0.00)	0.00 (0.00)	0.00 (0.00)	0.00 (0.00)	0.00 (0.00)	0.00 (0.00)
0.00 (0.00)	0.00 (0.00)	0.00 (0.00)	0.00 (0.00)	0.00 (0.00)	0.00 (0.00)	0.00 (0.00)
0.00 (0.00)	0.00 (0.00)	0.00 (0.00)	0.00 (0.00)	0.00 (0.00)	0.00 (0.00)	0.00 (0.00)
0.00 (0.00)	0.68 (0.00)	0.00 (0.00)	0.00 (0.00)	0.00 (0.00)	0.00 (0.00)	0.00 (0.00)
3.67 (14.14)	0.94 (0.00)	0.68 (0.00)	0.00 (0.00)	0.00 (0.00)	0.00 (0.00)	0.00 (0.00)
11.81 (14.14)	3.67 (14.14)	0.00 (0.00)	0.00 (0.00)	0.00 (0.00)	0.00 (0.00)	0.00 (0.00)

(vi) A_{sy} at top (rr=12%) 6mm bars

fig.6.3.6(a) Slab SM6: Numerical & (Provided) Steel Areas in mm^2

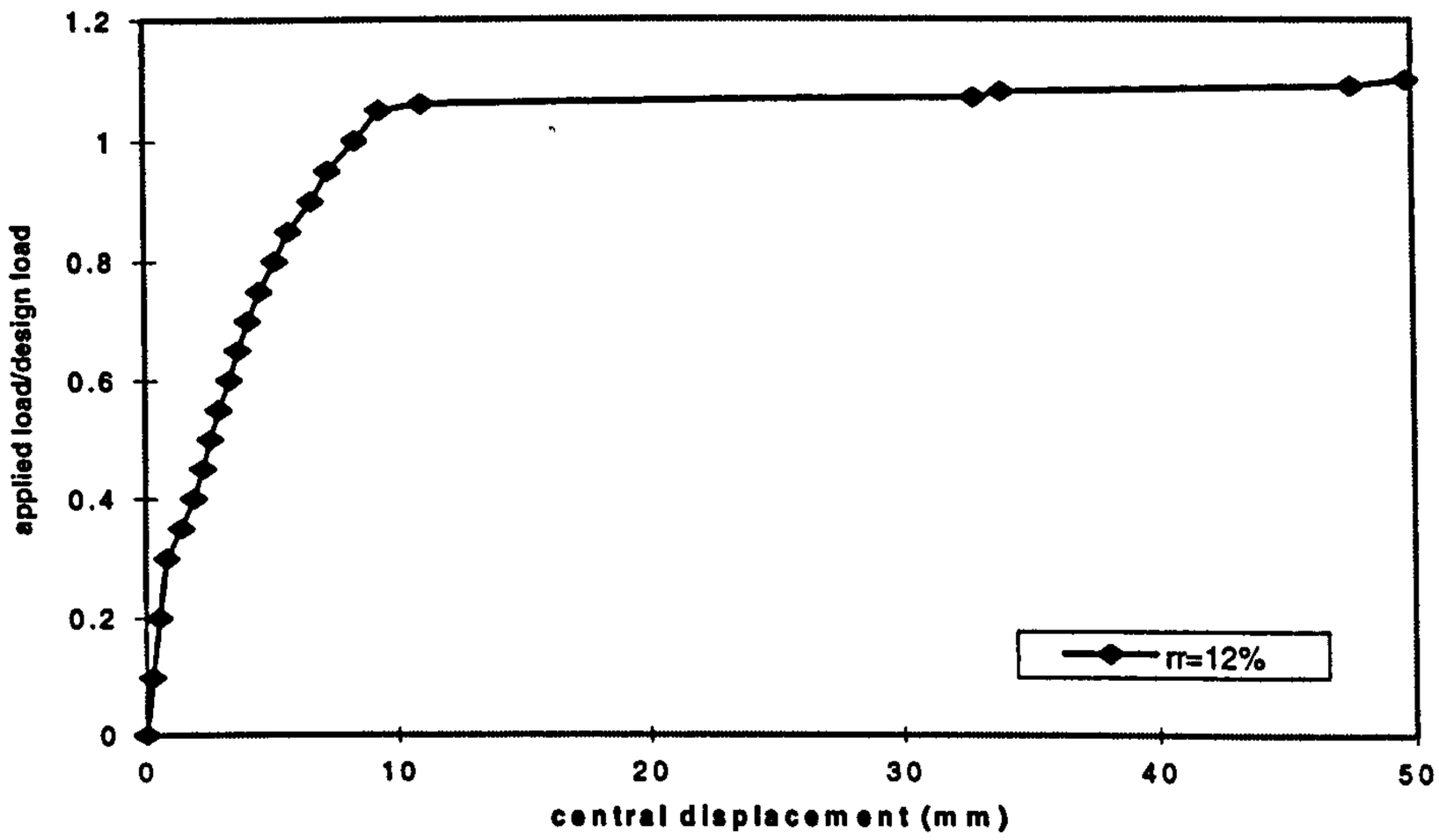

fig.6.3.6(b) Slab SM6: Load-displacement at centre

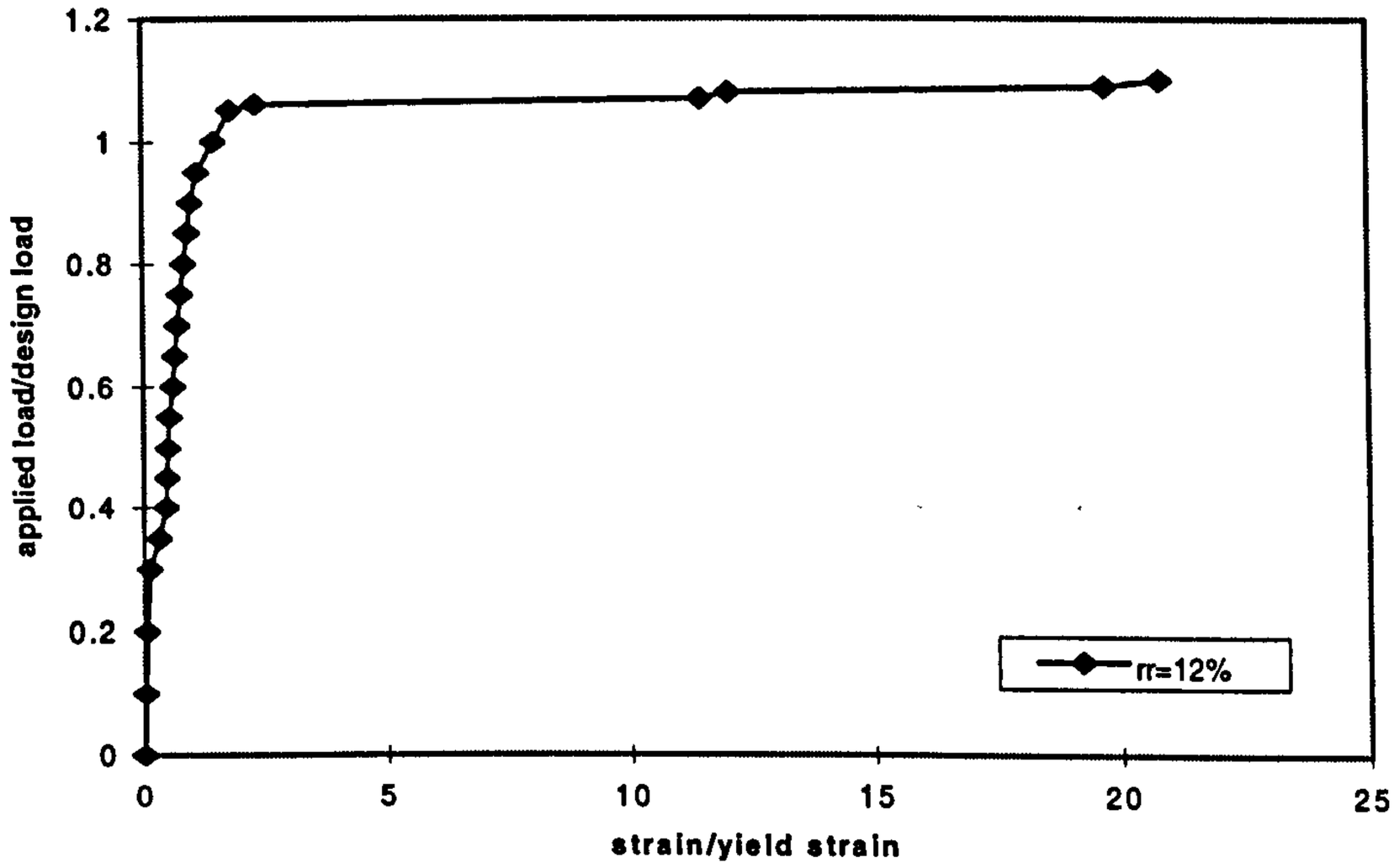

fig.6.3.6(c) Slab SM6 bottom steel strains at centre

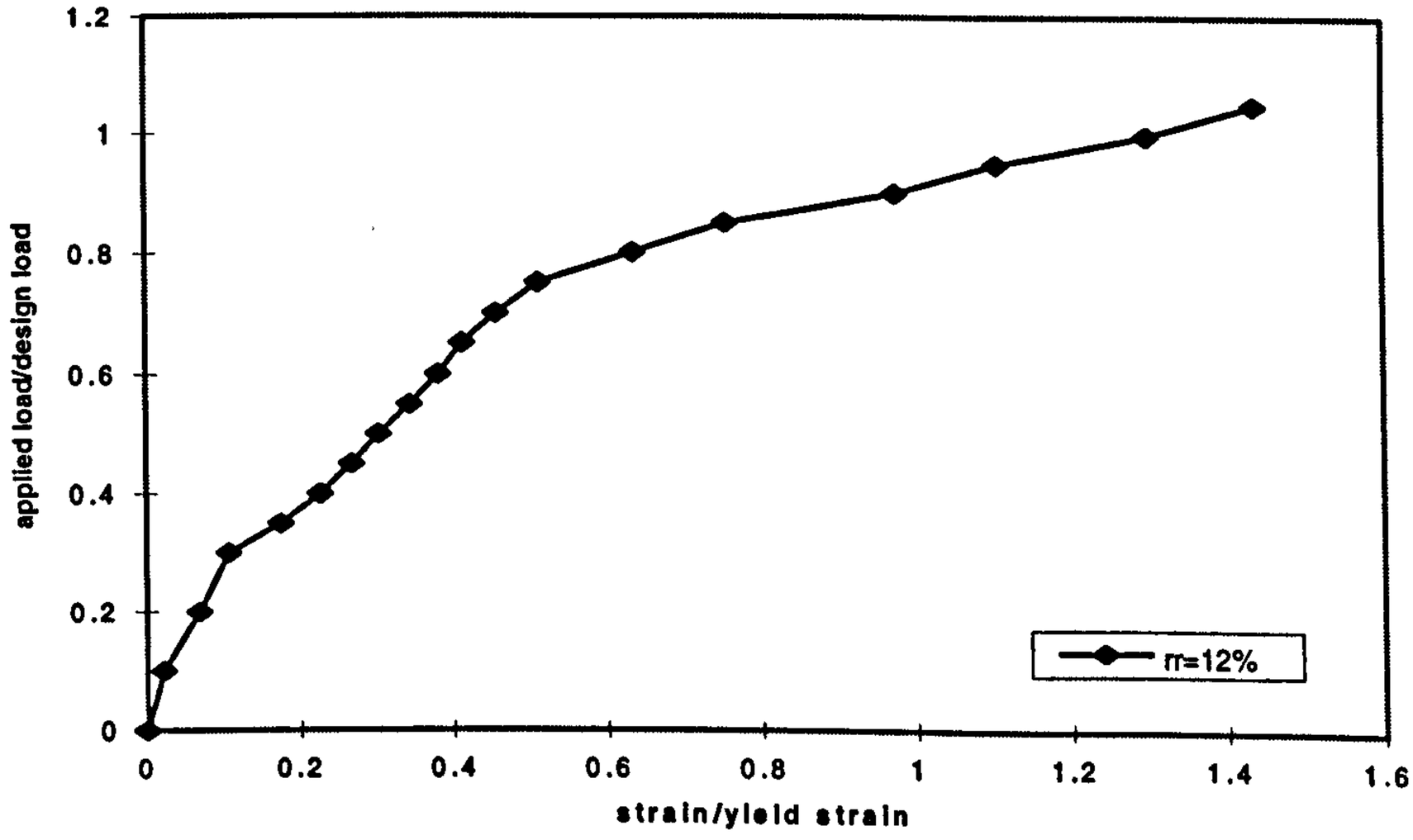

fig.6.3.6(d) Slab SM6: Top steel strains at corner support

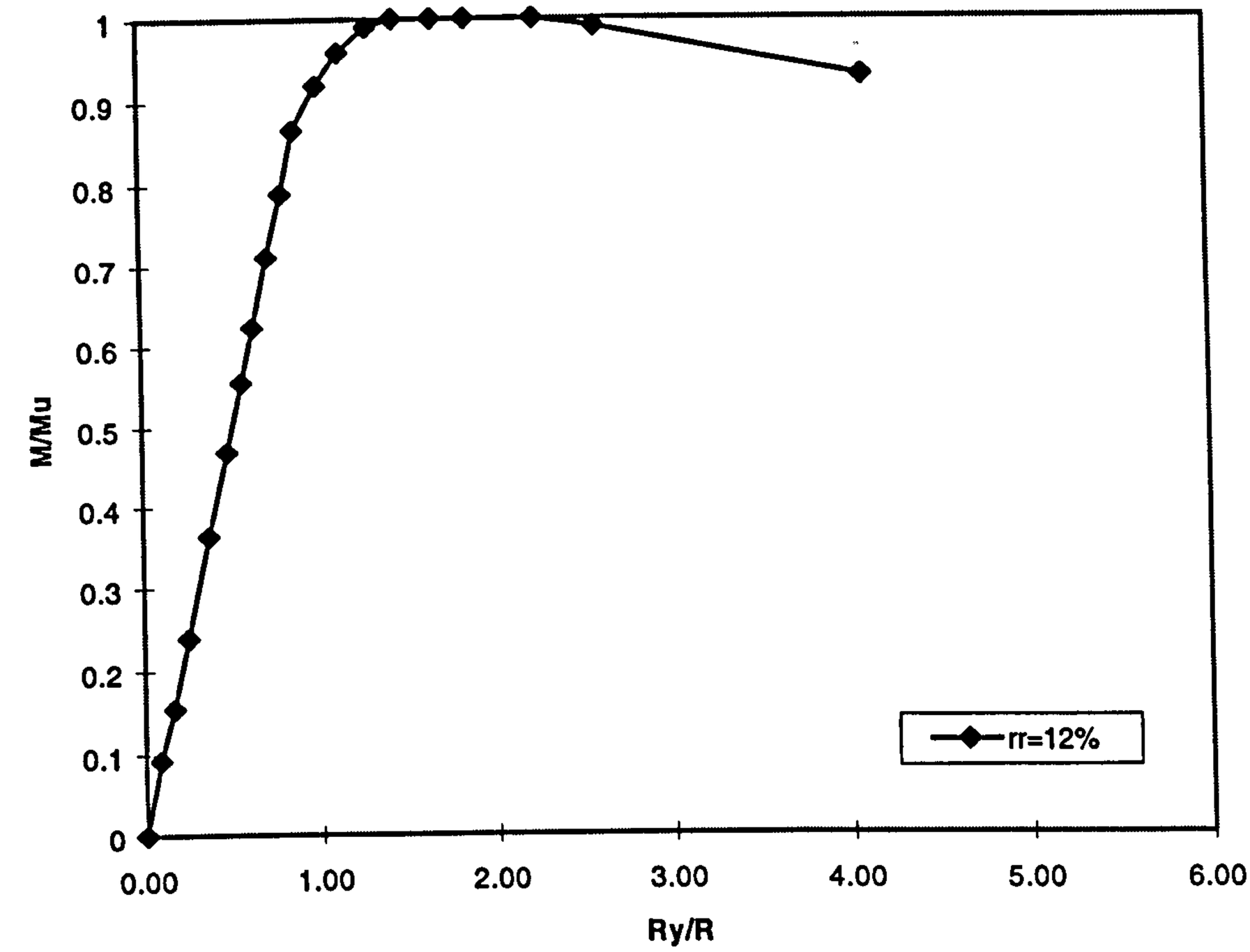

fig.6.3.6(e) Slab SM6: Principal moments near corner

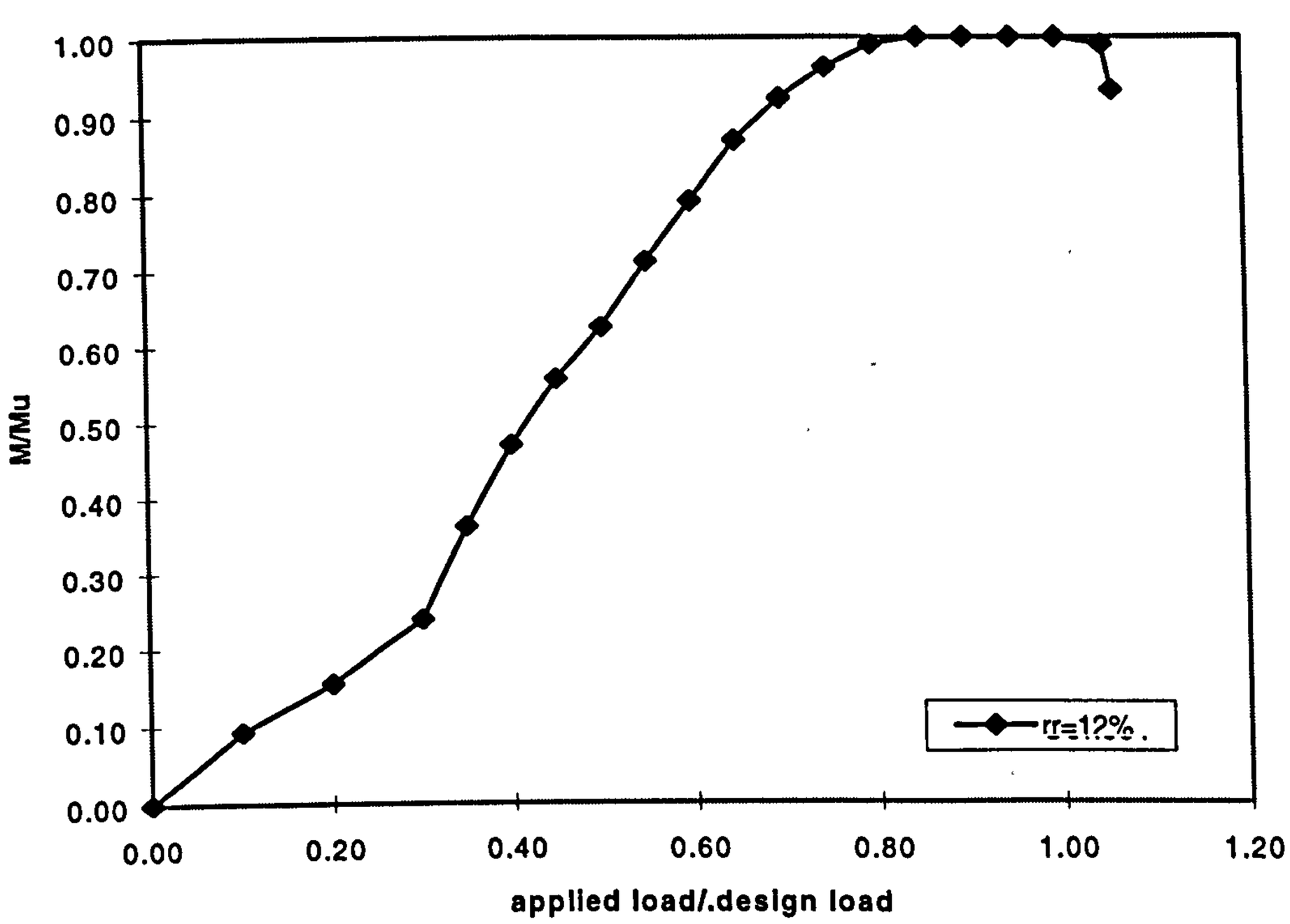

fig.6.3.6(f) Slab SM6: Principal moments at corner vs. Load

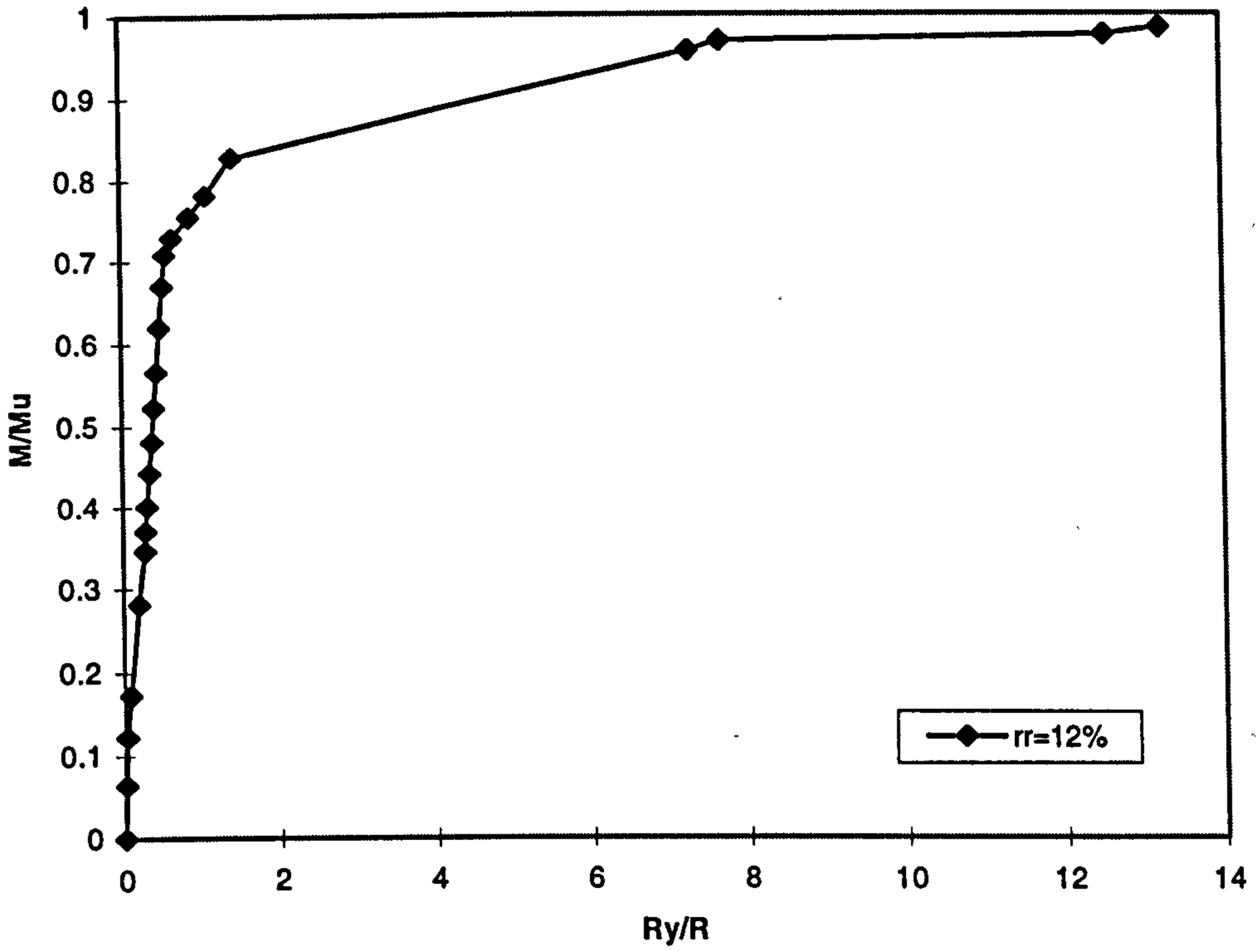

fig.6.3.6(g) Slab SM6: Principal Moments at centre

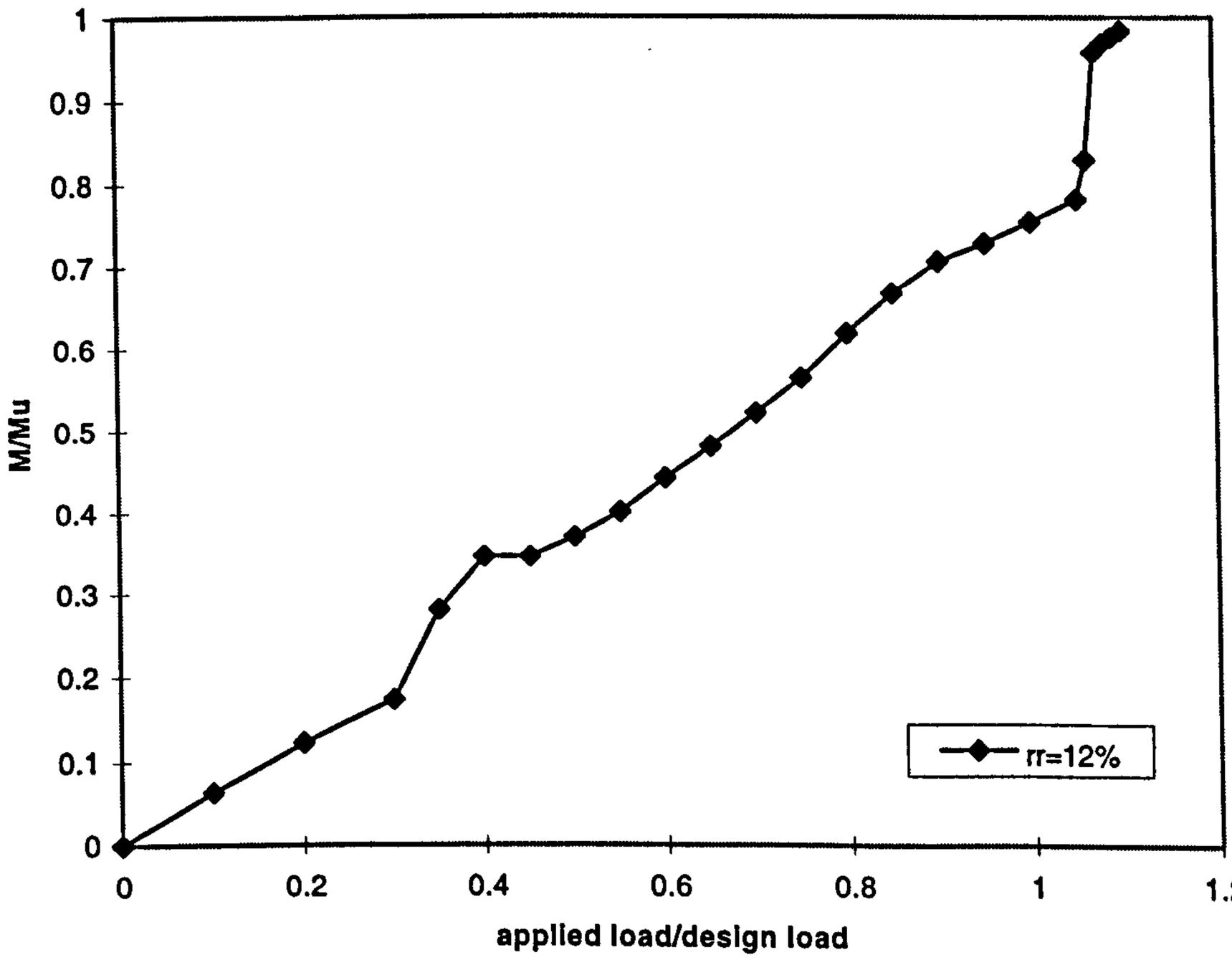

fig.6.3.6(h) Slab SM6: Principal moments at centre vs. Load

6.4 Adapting Load Path for Design

In some cases, the designer may wish to direct the main load paths in the slab in order to make a more practical layout. This is especially applicable in the case illustrated in Slab SM5 at rr=30%, where the nature of the evolved mesh led to a large increase in provided steel from numerical. Given a pre-determined load path, the designer can stipulate the elements not to be 'removed' from the mesh and hence generate the required steel from the customised load path. In the case of slab SM7, using a layout of steel which is orthogonal to the slab edges, a system of beams crossing the centre of the slab and spanning onto supporting beams around the edges was envisaged. The resulting principal moment plots for this are shown in figure (6.4.1a).

Steel Volumes (cm^3)	**(rr=0)**			**(rr=15%)**			**Total(15%) / Total(0)**
	A_s bottom	**A_s top**	**Total**	**A_s bottom**	**A_s top**	**Total**	
Numerical	48.2	5.4	53.6	46.3	15.9	62.2	1.1
Provided	69.1	8.4	77.5	66.7	17.2	83.9	1.1

Numerical areas for a quarter of the slab are shown in figure (6.4.1b). Comparisons of numerical and provided steel areas over the mesh are detailed in figures (6.4.1c). Observation of the total steel volumes shows that a similar amount of steel was required at rr=0 and at rr=15%.

The numerical analysis of this slab resulted in an ultimate load of around $1.1P_d$. The mid-span service deflection limit was reached at around $0.65P_d$, (fig6.4.1d). Yielding of the bottom steel occurred near the centre at a load of $0.8P_d$. No yielding was observed in the top steel. From inspection of the moment curvature relationship at the centre, it can be seen that the moment is being sustained beyond the design load, (fig.6.4.1f-g).

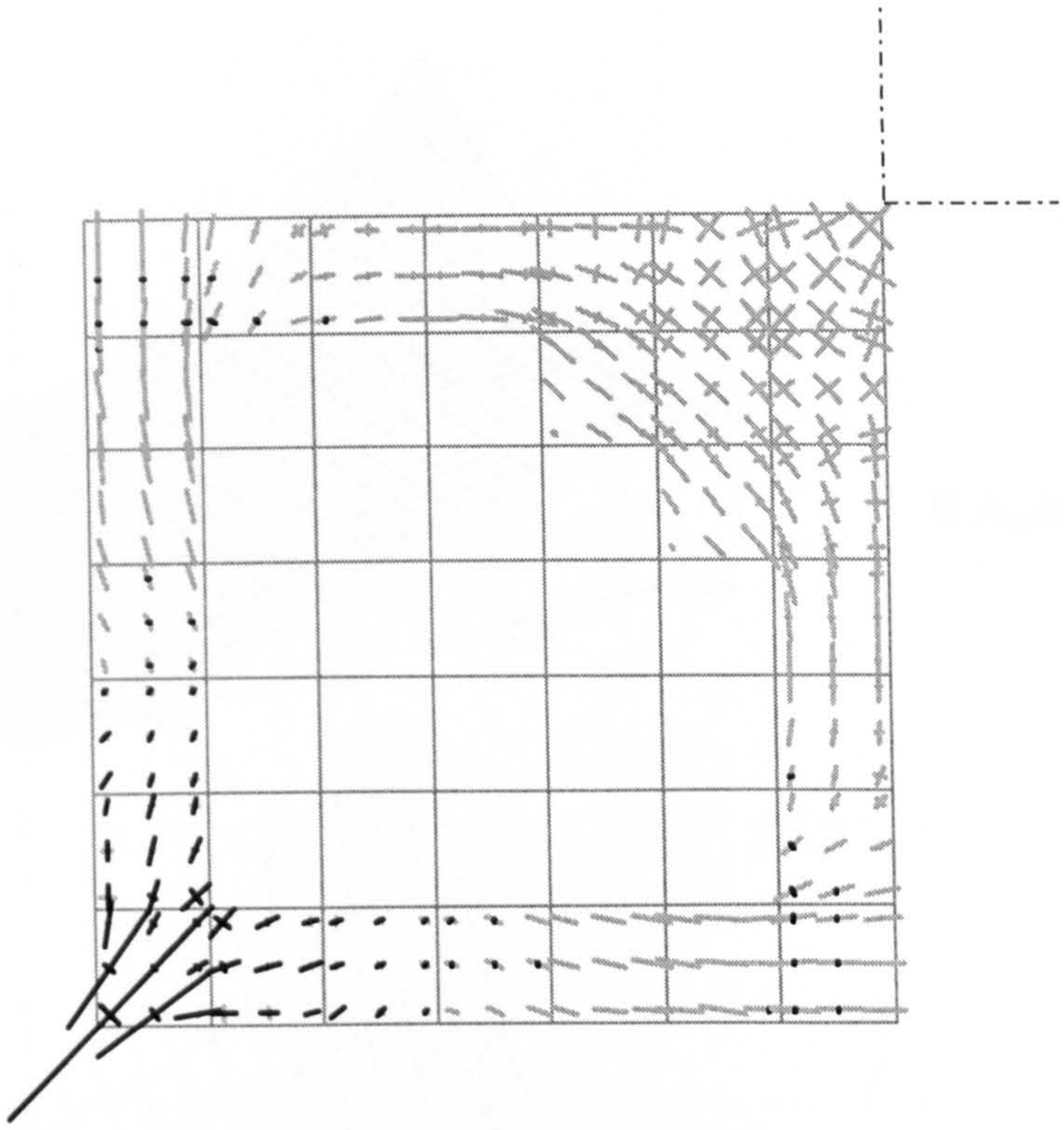

(i) rr=10%

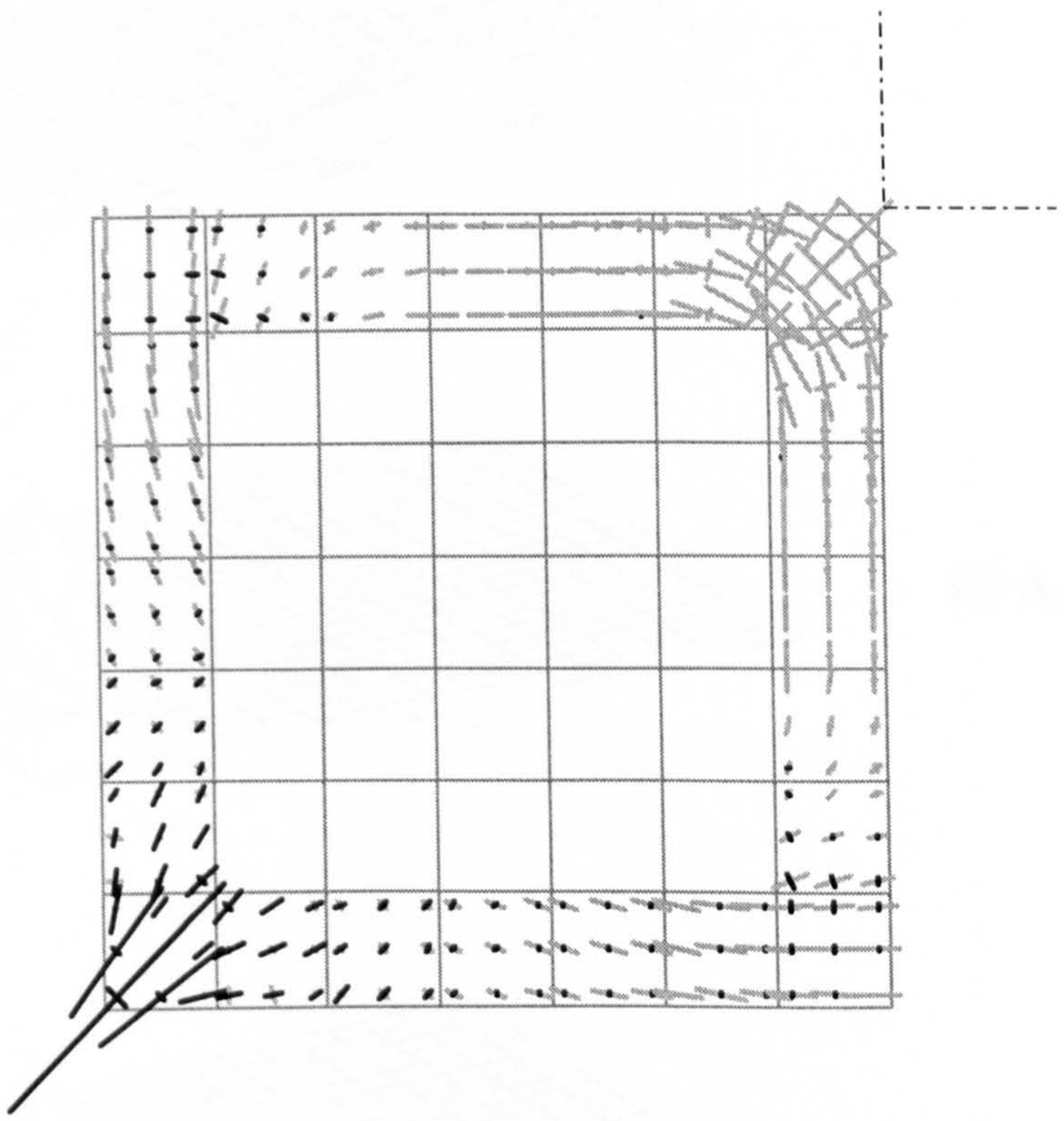

(ii) rr=15%

fig.6.4.1(a) Slab SM7, principal moments

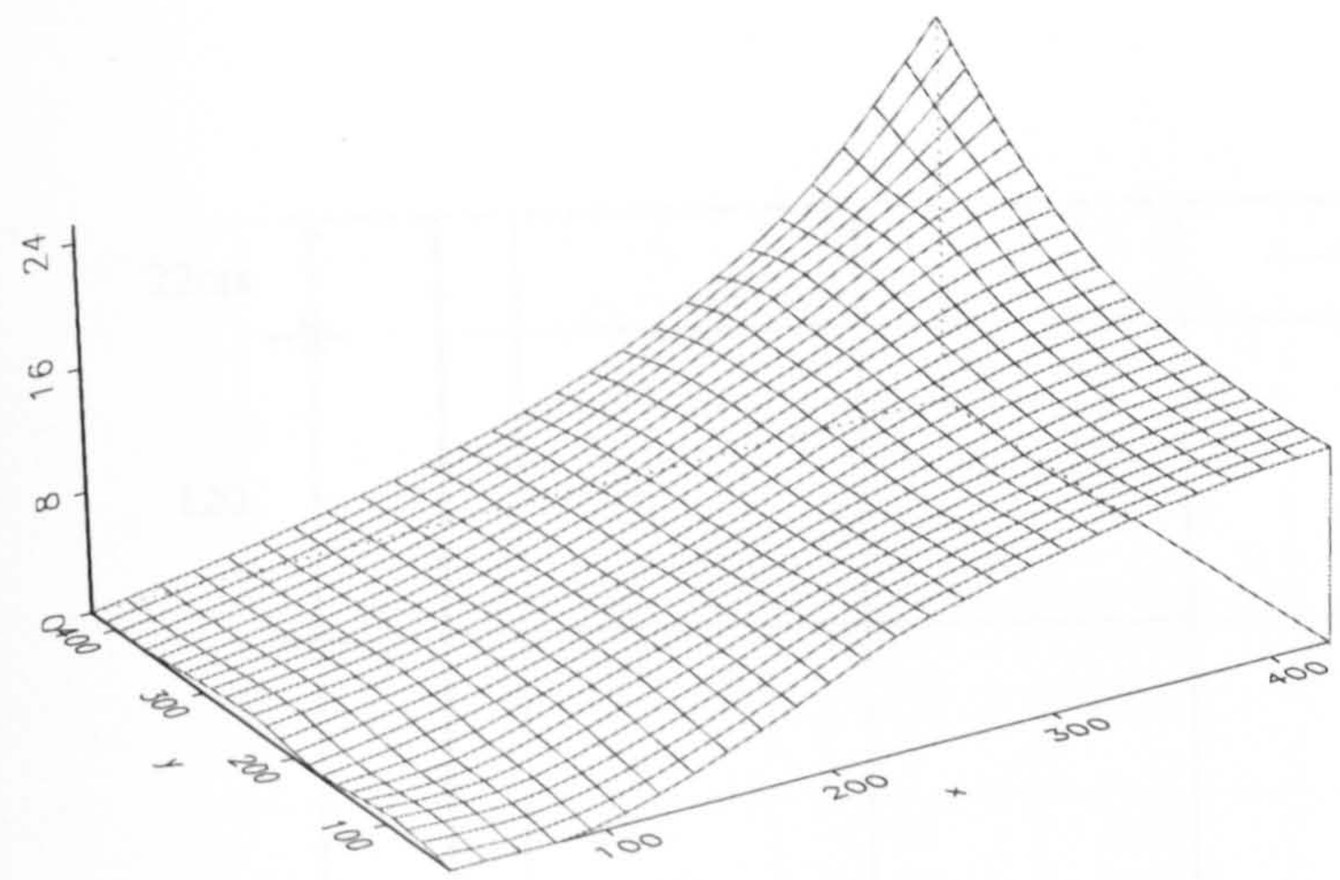

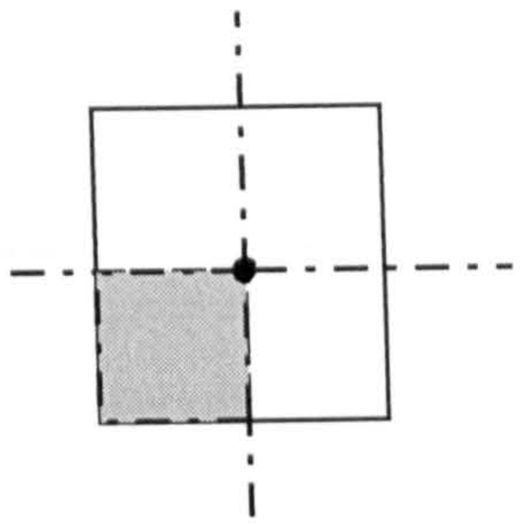

i) A_{sx}bottom (rr=0)

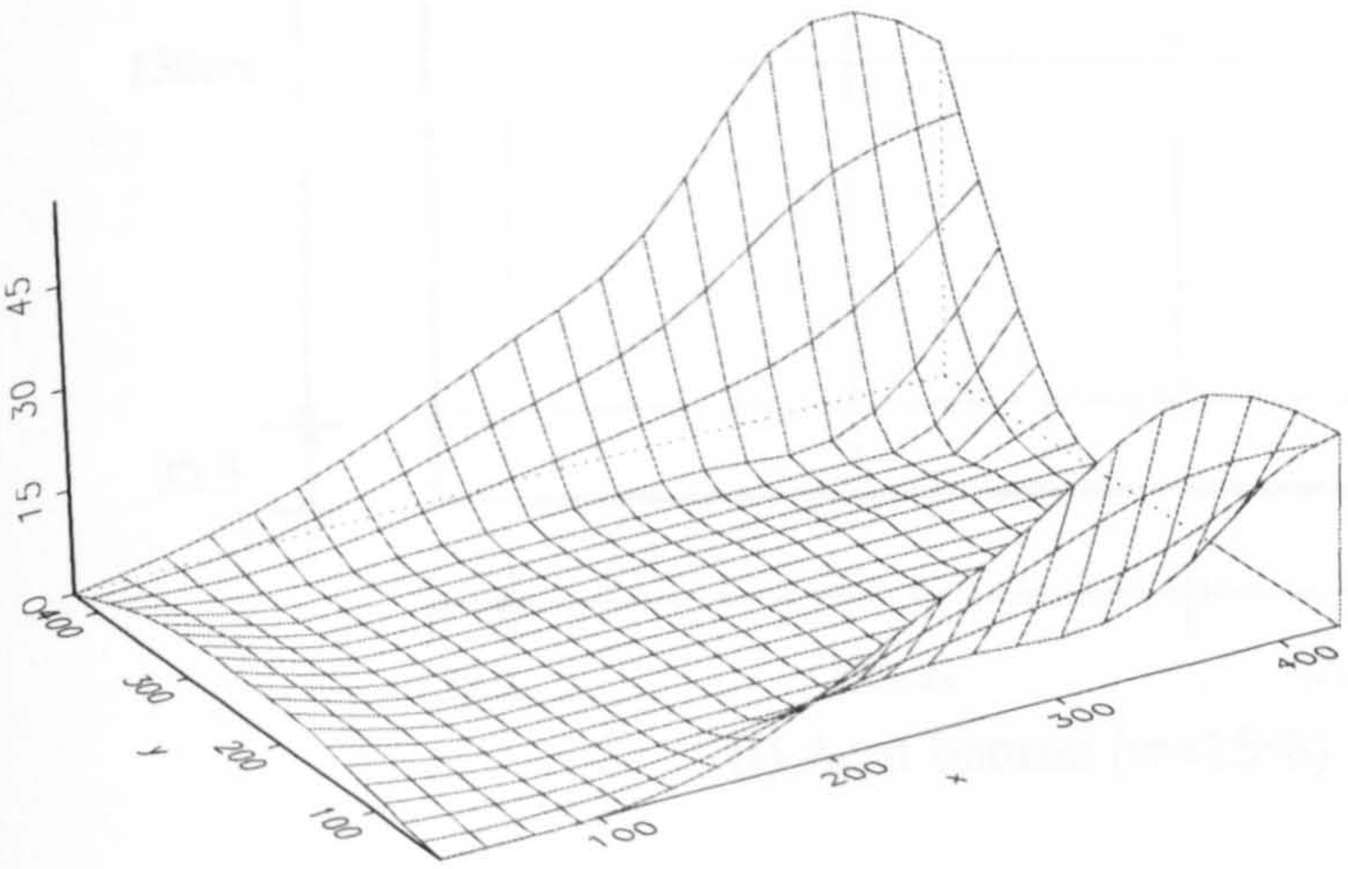

ii) A_{sx}bottom (rr=15%)

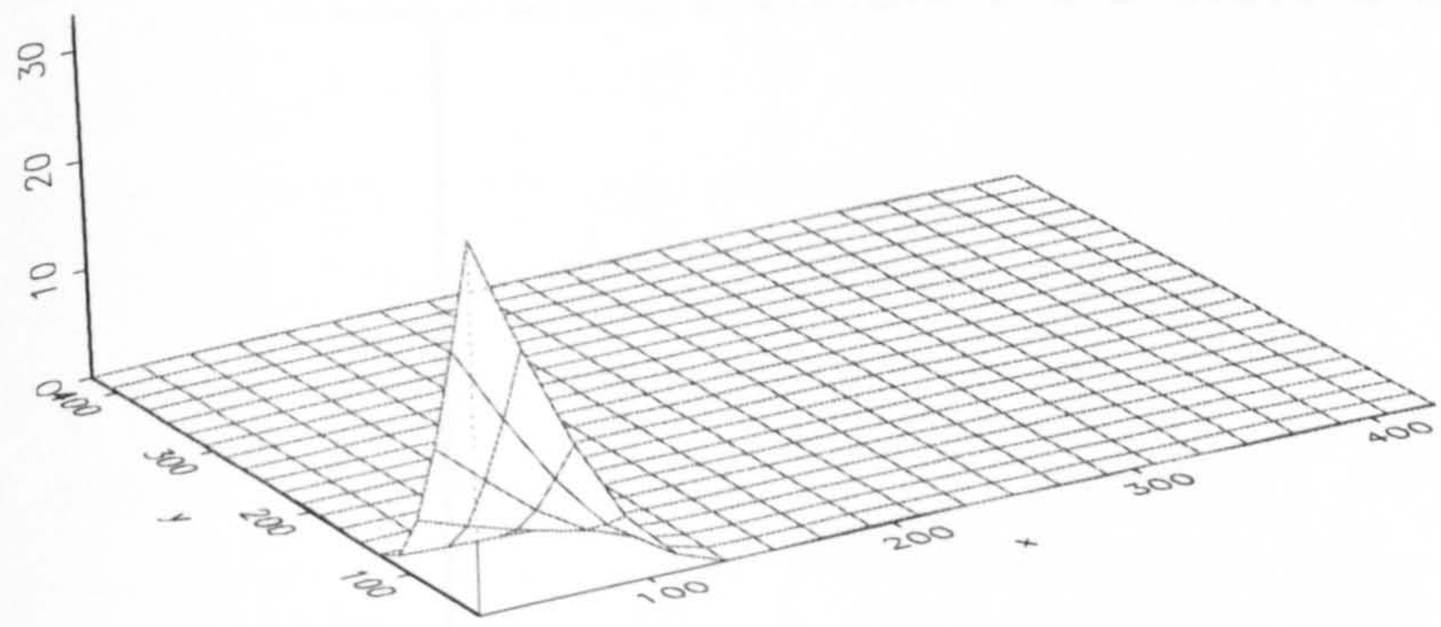

iii) A_{sx}top (rr=0)

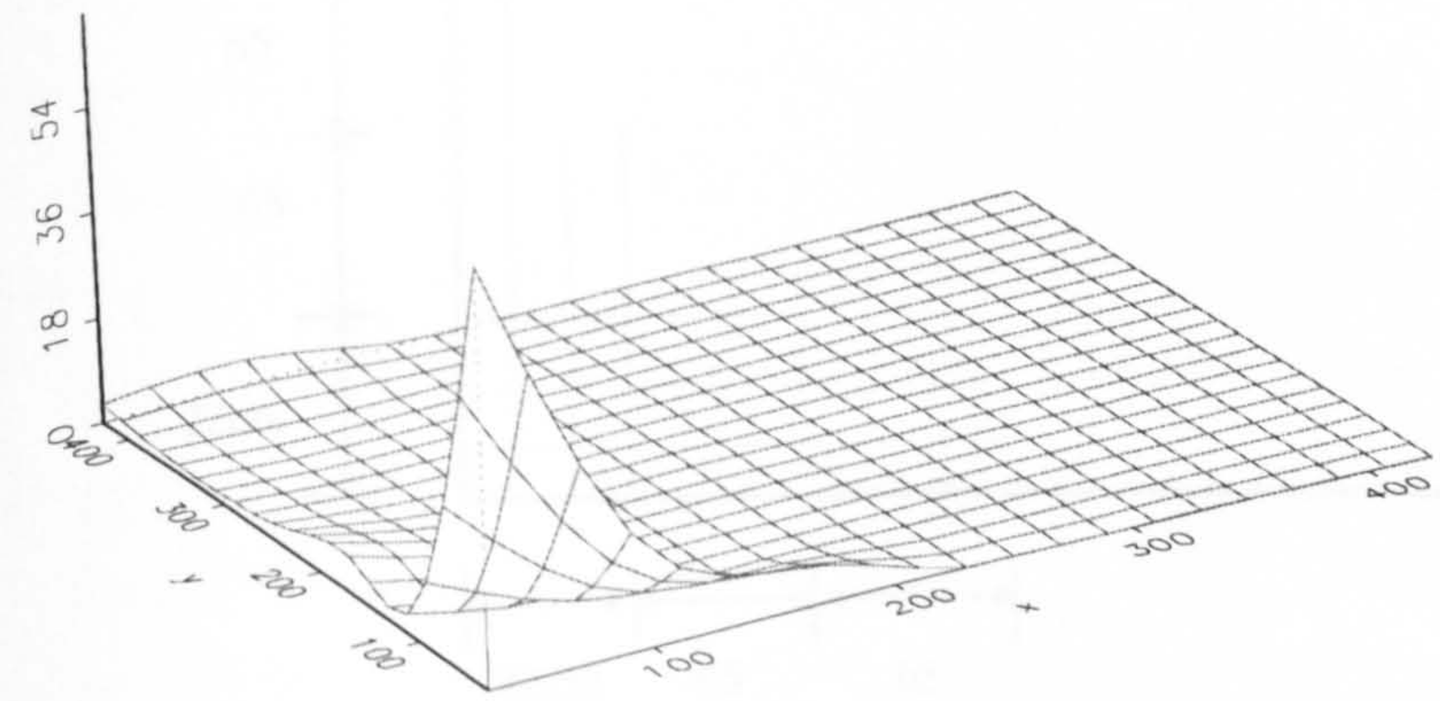

iv) A_{sx}top (rr=15%)

fig.6.4.1(b) Slab SM7, Symmetrical Quarter, Numerical Steel Areas (mm^2)

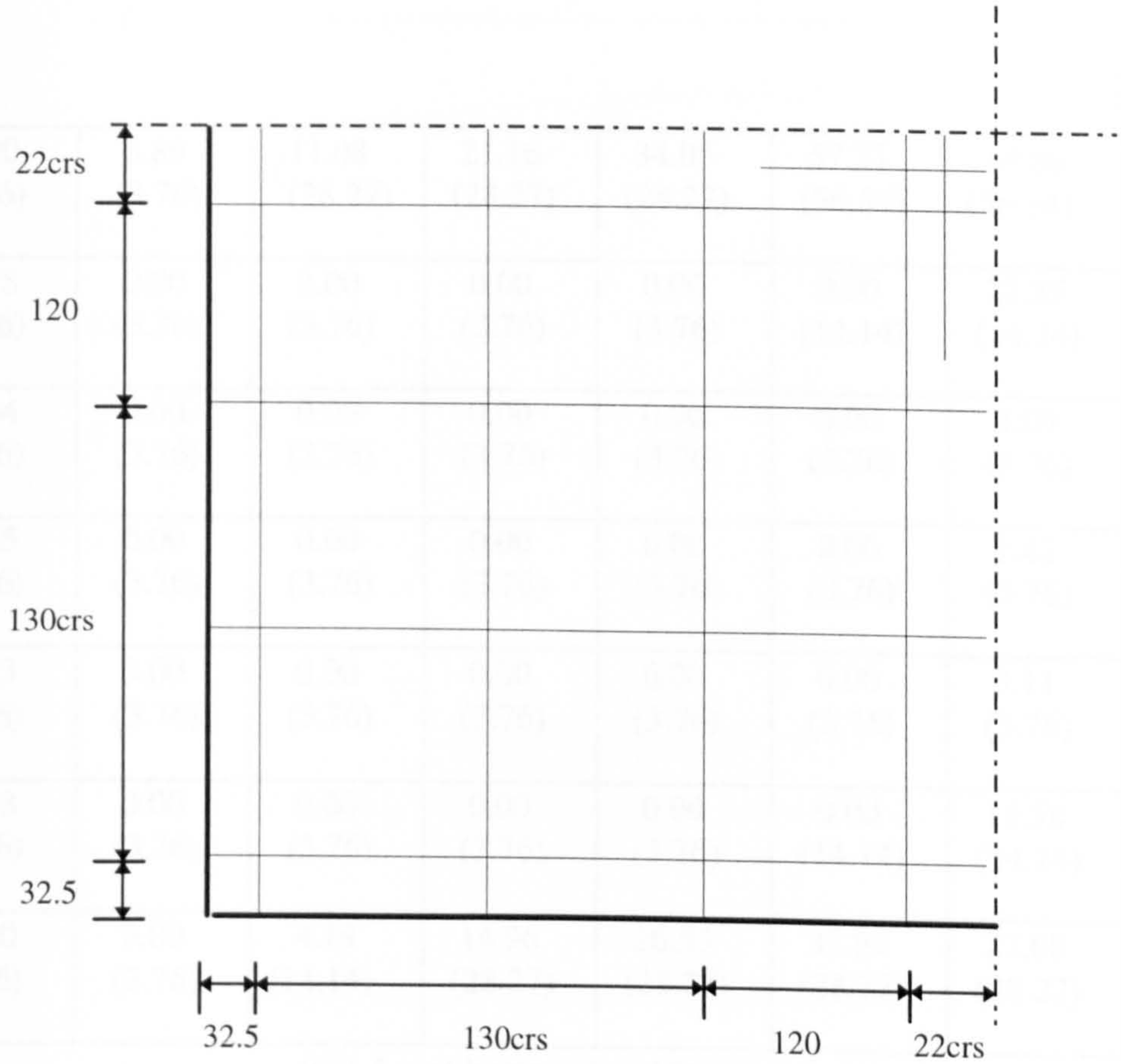

(i) A_s at bottom (rr=15%)

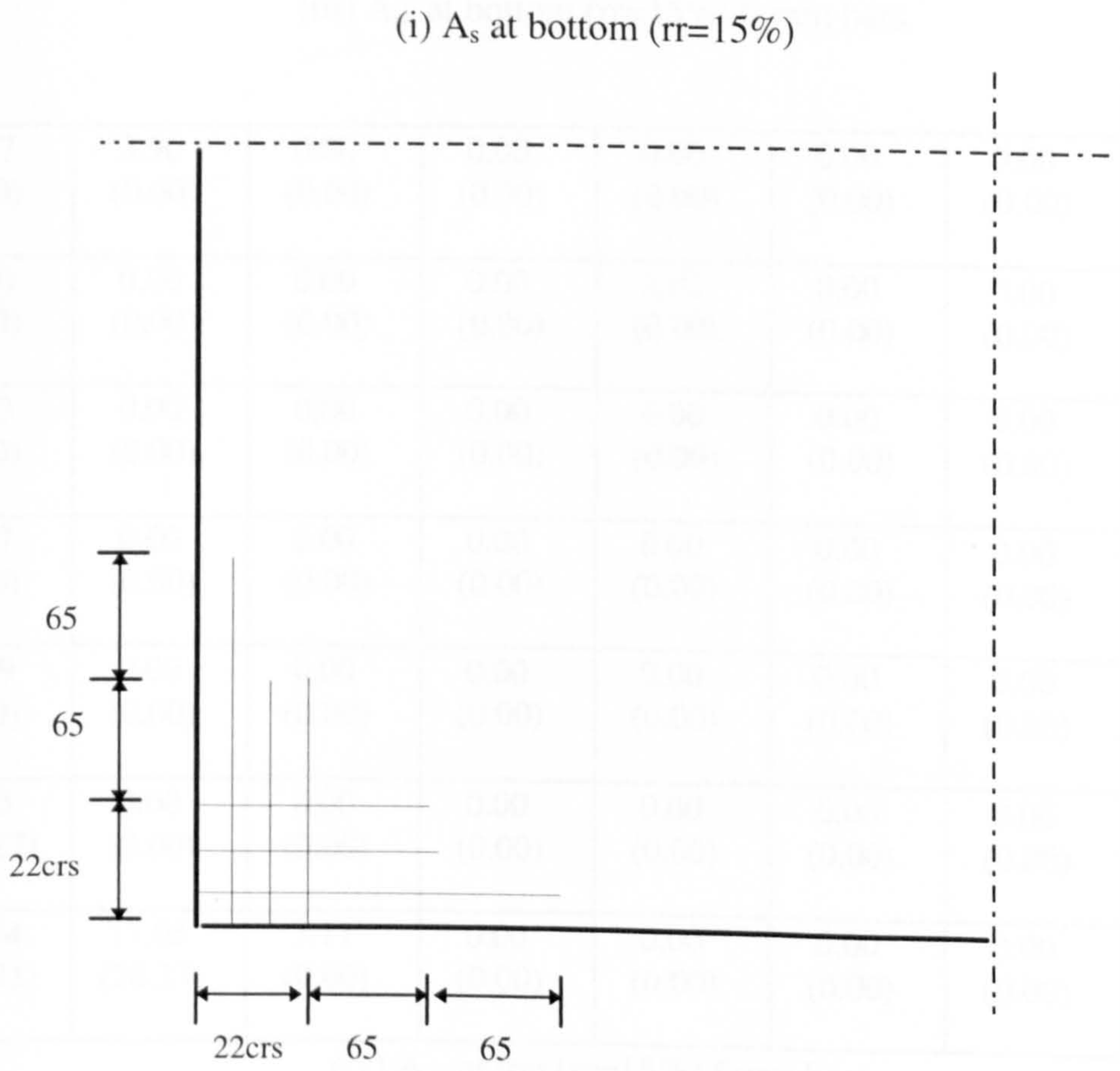

(ii) A_s at top (rr=15%)

fig.6.4.1(c) Slab SM7, Steel layout, All sizes in mm, all bars 6mm diameter

0.00 (3.76)	3.89 (3.76)	11.08 (28.27)	21.16 (28.27)	34.05 (28.27)	57.21 (56.54)	49.88 (56.54)
3.78 (3.76)	0.00 (3.76)	0.00 (3.76)	0.00 (3.76)	0.00 (3.76)	0.00 (14.14)	22.25 (14.14)
5.64 (3.76)	0.00 (3.76)	0.00 (3.76)	0.00 (3.76)	0.00 (3.76)	0.00 (3.76)	3.09 (3.76)
5.55 (3.76)	0.00 (3.76)	0.00 (3.76)	0.00 (3.76)	0.00 (3.76)	0.00 (3.76)	1.42 (3.76)
4.93 (3.76)	0.00 (3.76)	0.00 (3.76)	0.00 (3.76)	0.00 (3.76)	0.00 (3.76)	3.11 (3.76)
2.13 (3.76)	0.00 (3.76)	0.00 (3.76)	0.00 (3.76)	0.00 (3.76)	0.00 (14.14)	15.58 (14.14)
0.00 (3.76)	0.00 (3.76)	4.19 (14.14)	14.96 (28.27)	26.53 (28.27)	37.91 (28.27)	27.68 (28.27)

(iii) A_{sx} at bottom (rr=15%) 6 mm bars

3.17 (0.00)	3.96 (0.00)	0.00 (0.00)	0.00 (0.00)	0.00 (0.00)	0.00 (0.00)	0.00 (0.00)
1.50 (0.00)	0.00 (0.00)	0.00 (0.00)	0.00 (0.00)	0.00 (0.00)	0.00 (0.00)	0.00 (0.00)
1.53 (0.00)	0.00 (0.00)	0.00 (0.00)	0.00 (0.00)	0.00 (0.00)	0.00 (0.00)	0.00 (0.00)
3.77 (0.00)	0.00 (0.00)	0.00 (0.00)	0.00 (0.00)	0.00 (0.00)	0.00 (0.00)	0.00 (0.00)
5.79 (0.00)	0.00 (0.00)	0.00 (0.00)	0.00 (0.00)	0.00 (0.00)	0.00 (0.00)	0.00 (0.00)
7.55 (28.27)	0.00 (0.00)	0.00 (0.00)	0.00 (0.00)	0.00 (0.00)	0.00 (0.00)	0.00 (0.00)
70.54 (84.81)	17.05 (28.27)	7.11 (0.00)	0.00 (0.00)	0.00 (0.00)	0.00 (0.00)	0.00 (0.00)

(iv) A_{sx} at top (rr=15%) 6mm bars

fig.6.4.1(c) Slab SM7: Numerical & (Provided) Steel Areas in mm^2

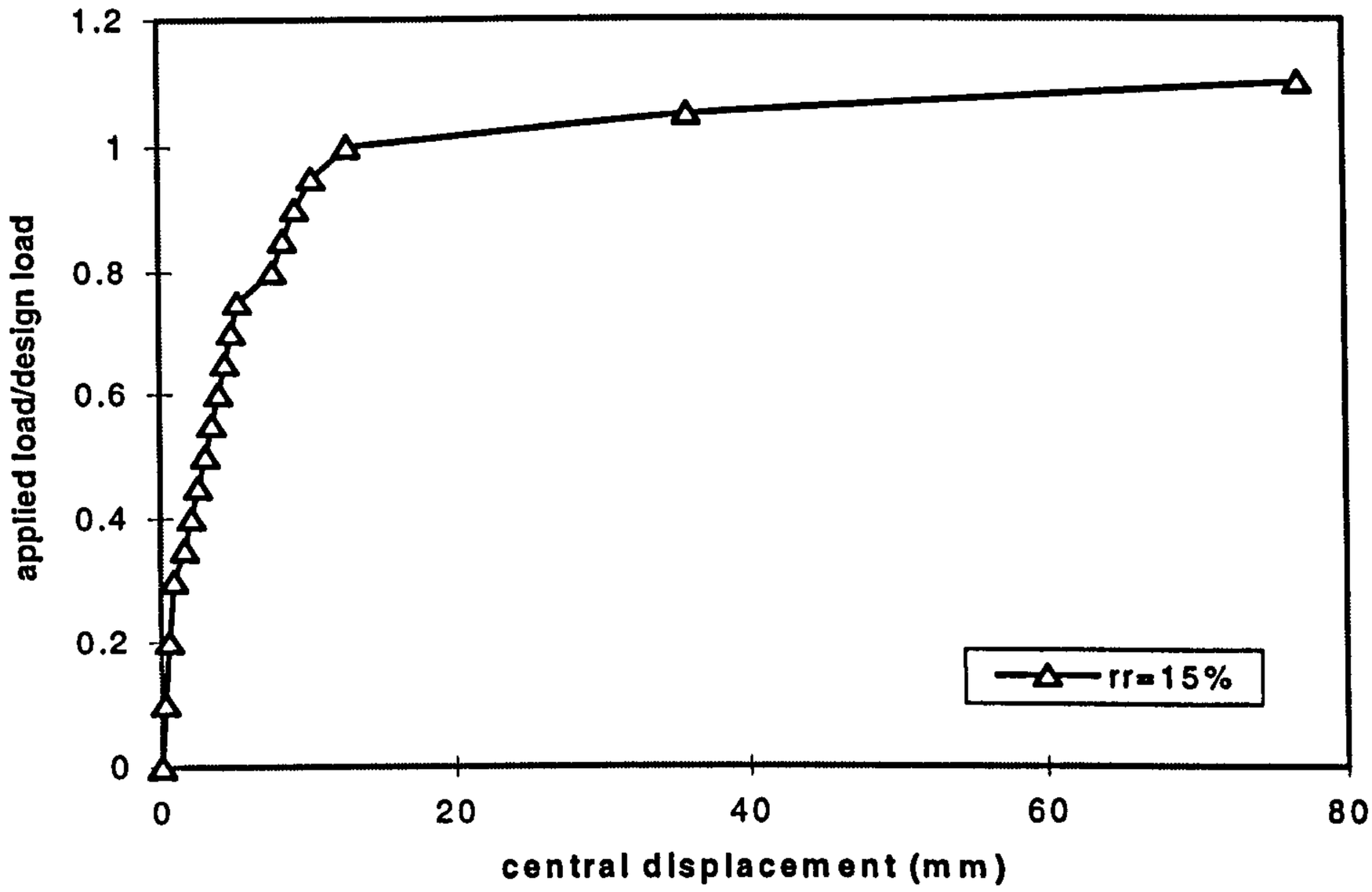

fig.6.4.1(d) Slab SM7: Load-displacement relationship

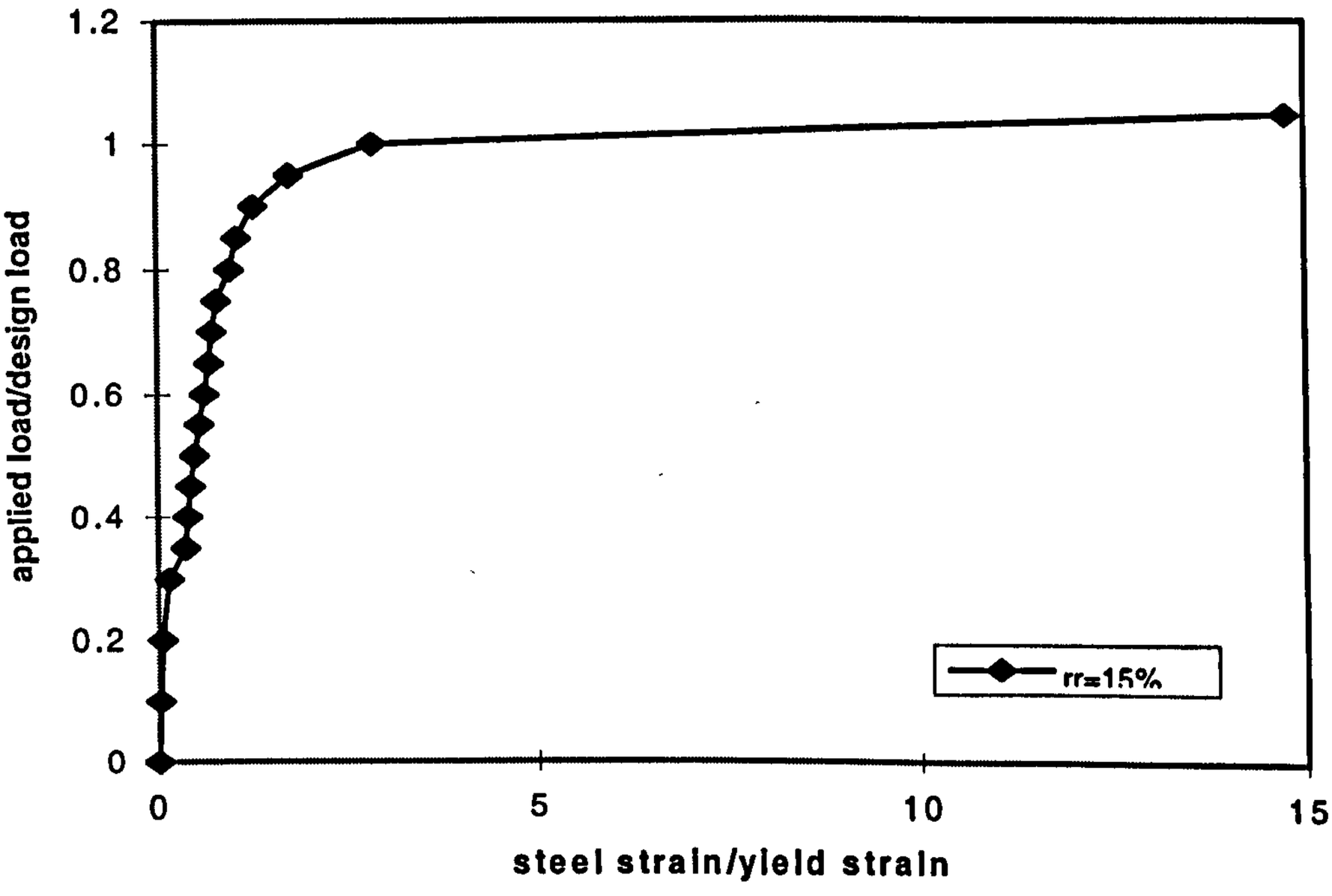

fig.6.4.1(e) Slab SM7: bottom steel strains at centre

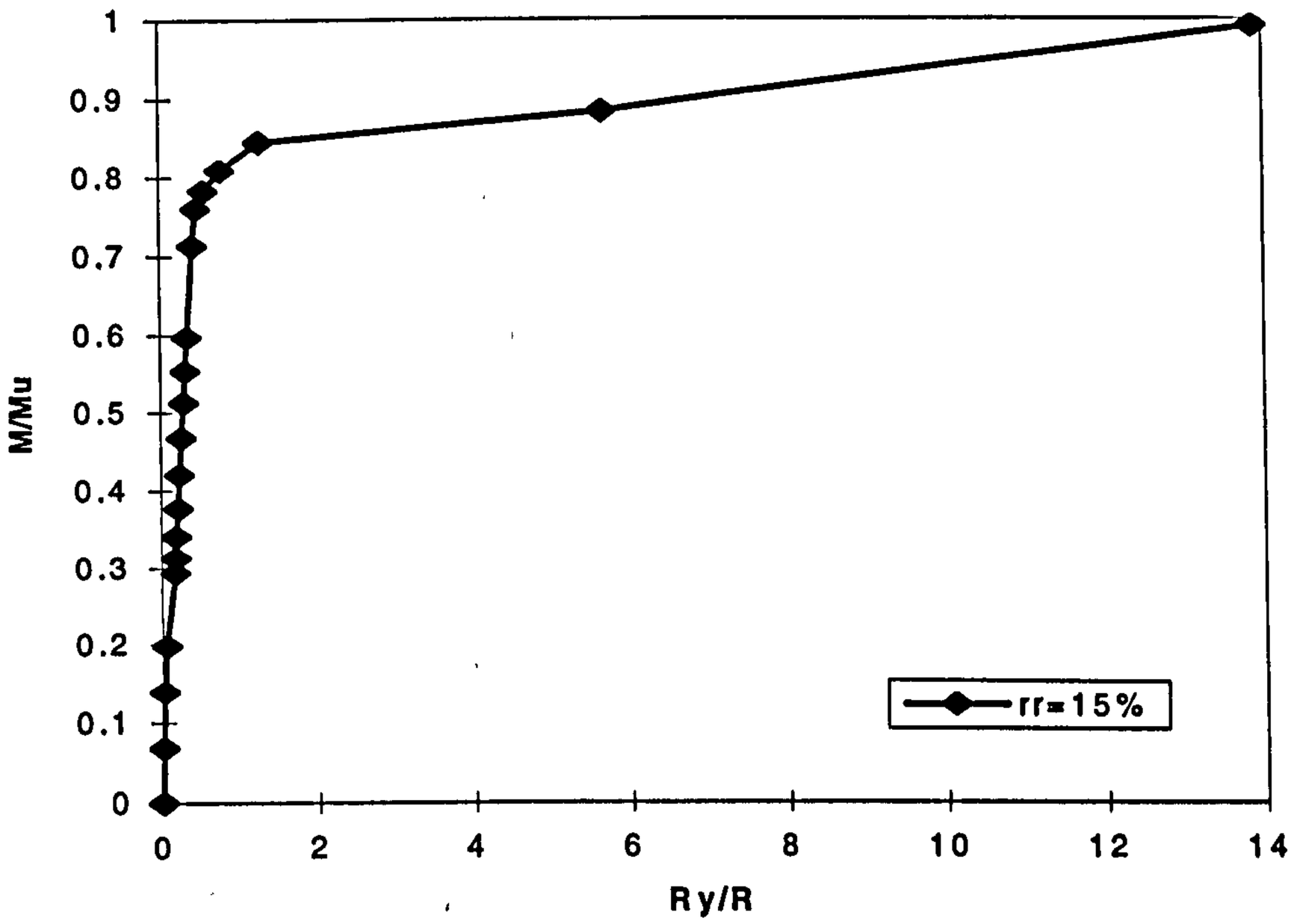

fig.6.4.1(f) Slab SM7: Principal Moment-curvature relationship at centre

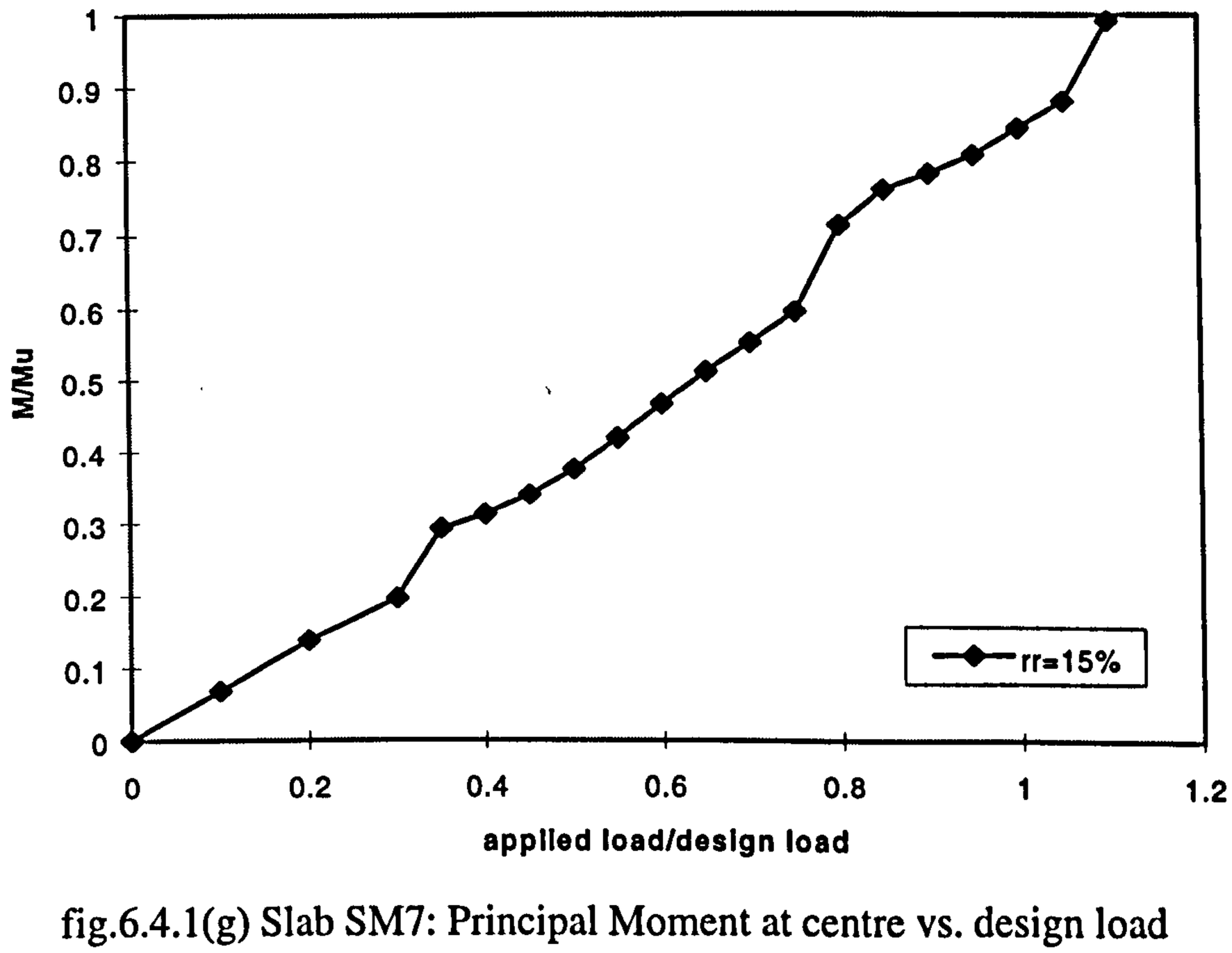

fig.6.4.1(g) Slab SM7: Principal Moment at centre vs. design load

6.5 Conclusions

Through the visualisation process, a deviation from the original elastic pattern of stresses is created in the slab, i.e., a redistribution of stresses occurs. It is important that this redistribution is not accompanied by a loss of ductility in the resulting slab design. The results from all the slabs tested in the series are presented in table 6.5.1. All slab designs were able to attain the design load readily. In most cases, an overall increase in the area of steel resulting from the evolved mesh over that resulting from the mesh at rr=0 was observed. An increase in the provided steel areas from the numerical steel areas was often necessary in order to generate a practical steel layout and to fulfil minimum steel requirements. This increase was particularly pronounced in slabs where the visualisation process resulted in a large % area 'removal' such as slabs SM3 and SM5. Orientation of the steel to coincide with the main direction of principal moments results in a more efficient volume of steel as in the case of SM6. Increasing provided steel areas leads to in most cases, a greater ultimate load from the designs at rr=0.

All the designs resulting from the evolved mesh maintain ductility. In all cases the slabs failed in a ductile manner. However, as observed in some cases, increases in steel areas may cause a loss of ductility in localised areas. The occurrence of compression softening in the concrete was evident in some cases but this was at loads in excess of $1.1P_d$ and as a result of yielding of steel in that region.

When considering the serviceability of the slabs resulting from the evolved meshes, an adequate performance was achieved. However, in some slabs, such as SM3 and SM4, the steel layouts derived from the evolved mesh were often more complicated and could lead to congestion of steel in localised areas. For this reason, it may concluded that it is not desirable to use the visualisation process in every case.

The greatest potential advantage of this design process comes from being able to control the visualisation process according to a pre-determined path. This allows the designer to take account of experience and practical considerations, in order to generate practical steel layouts.

As shown in slab SM7, this creates an efficient reinforcement pattern and is able to accommodate re-distribution of stresses while maintaining ductility.

Property	**SM1**		**SM2**		**SM3**	
(rr)	0	40%	0	30%	0	30%
% area 'removed'	-	24%	-	24%	-	53%
Σ Numerical steel volume (cm^3)	754	807	1588.9	1638.5	425	481
Σ Provided steel volume (cm^3)	980.9	990.7	1815.8	2061.7	564.8	740.5
P_u/P_d	1.2	1.2	1.0	1.05	1.1	1.3
Service deflection limit (span/250)	$0.65P_d$	$0.65\ P_d$	$0.7\ P_d$	$0.7\ P_d$	$0.7\ P_d$	$0.85\ P_d$
a)First yielding of bottom steel	$1.0\ P_d$	$1.0\ P_d$	$0.7\ P_d$	$0.7\ P_d$	$0.6\ P_d$	$0.7\ P_d$
Location of a)	centre	centre	centre	centre	load point	load point
b)First yielding of top steel	$1.2\ P_d$	$1.2\ P_d$	-	-	$0.6\ P_d$	$0.8\ P_d$
Location of b)	corner of support	corner of support	-	-	corner of support	corner of support

table 6.5.1: Summary of results from test program

Property	**SM4**		**SM5**		**SM6**	**SM7**
(rr)	0	12%	0	12%	12%	15%
% area 'removed'	-	38%	-	57%	57%	51%
Σ Numerical steel volume (cm3)	2730	4719	53.5	62.8	53.6	62.1
Σ Provided steel volume (cm3)	4587.4	6562.4	77.4	102.3	79.7	83.9
P_u/P_d	1.2	1.3	1.1	1.35	1.1	1.1
Service deflection limit (span/250)	$0.75\ P_d$	$0.7\ P_d$	$0.65\ P_d$	$0.7\ P_d$	$0.7\ P_d$	$0.65\ P_d$
a)First yielding of bottom steel	$1.2\ P_d$	$1.2\ P_d$	$0.8\ P_d$	$1.2\ P_d$	$0.9\ P_d$	$0.8\ P_d$
Location of a)	centre	centre	centre	centre	centre	centre
b)First yielding of top steel	$1.1\ P_d$	$1.0\ P_d$	$0.8\ P_d$	$0.8\ P_d$	$0.9\ P_d$	-
Location of b)	column support	column support	corner support	corner support	corner support	-

table 6.5.1 (contd): Summary of results from test program

Chapter 7

Experimental Program

7.1 Introduction

Five structures designed using the strut-tie method were tested physically in the laboratory. Two double sided corbels, one single sided corbel and two corner joints were tested, see table 7.1. The design of these structures and results from numerical and physical tests are detailed in the next chapter. This chapter describes the materials and instrumentation used in the physical models as well as the method of testing.

7.2 Preparation of Models

7.2.1 Formwork

The same formwork was used for each of the three corbels made. For each design, the formwork was easily adapted in order to accommodate changes in geometry. Since the two corner joints were of identical geometry, only one mould was needed here. The main body of the formwork comprised of 20mm thick plywood panels. For stability and strength, 50x50mm thick timber battens were fixed at regular intervals along the length of the mould. Prior to casting of the model, the walls of the mould were coated with oil in order to prevent the concrete from sticking

7.2.2 Concrete

For all the specimens tested, Rapid Hardening Portland Cement was used to give the required 7-day cube strength f_{cu}. A maximum aggregate size of 10mm was used. The casting of each model took place in a number of batches and was properly compacted through vibration.

Model	Schematic
Corbel C2A	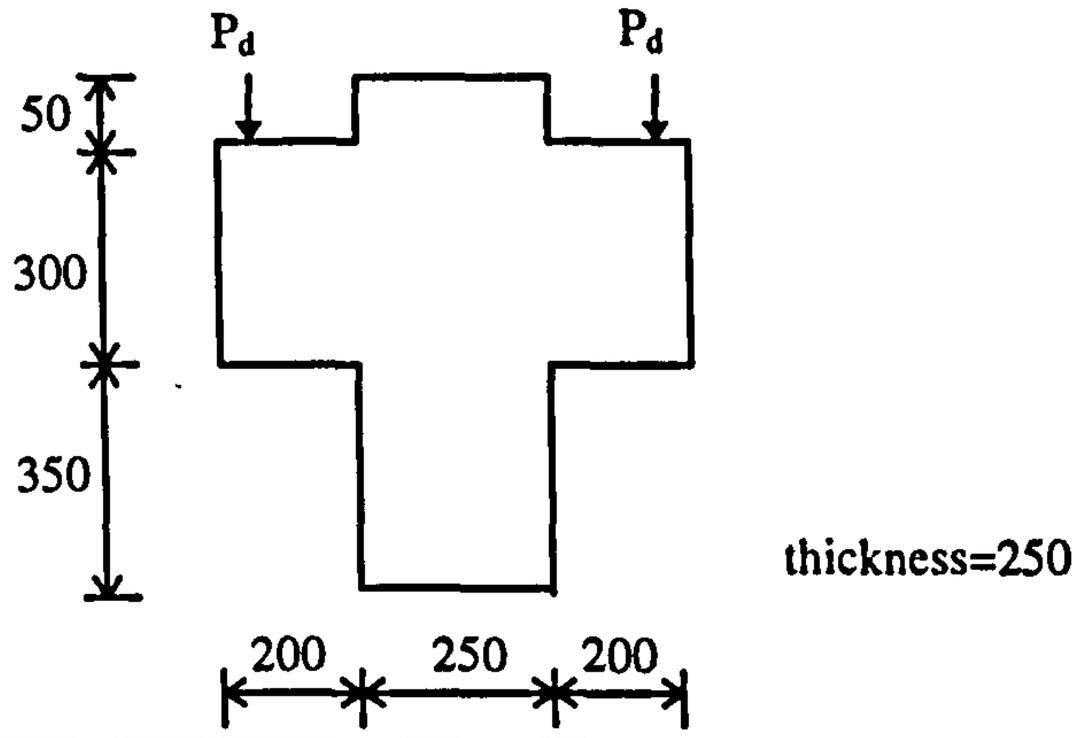
Corbel C3A	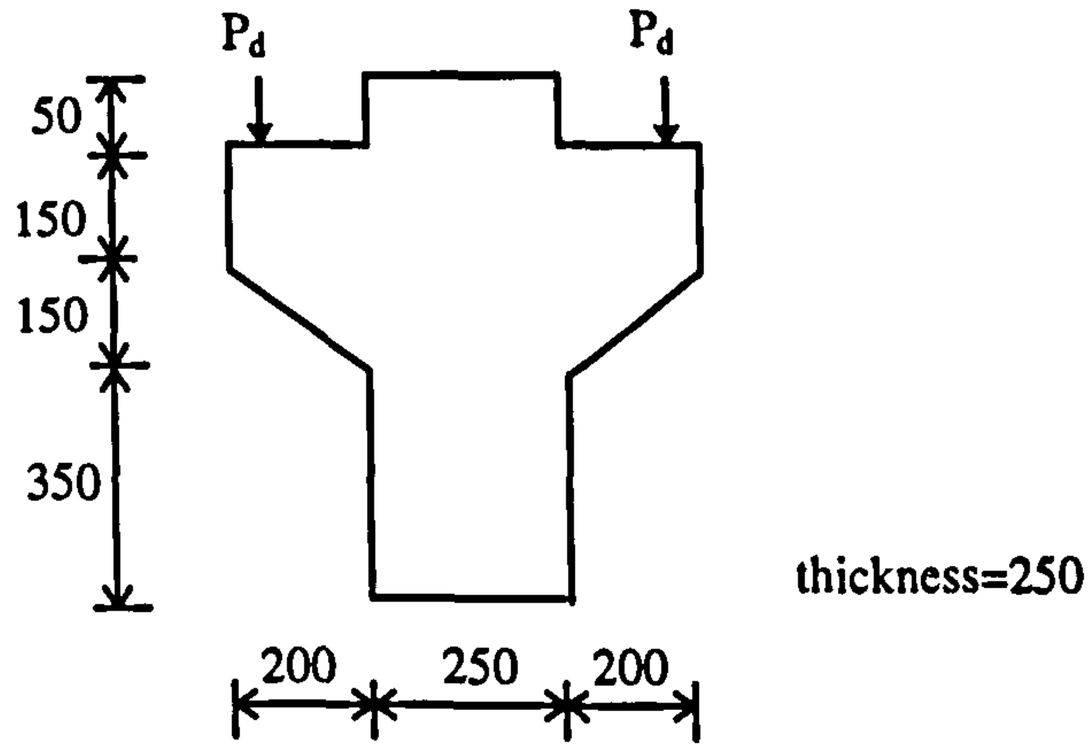
Corbel C4A	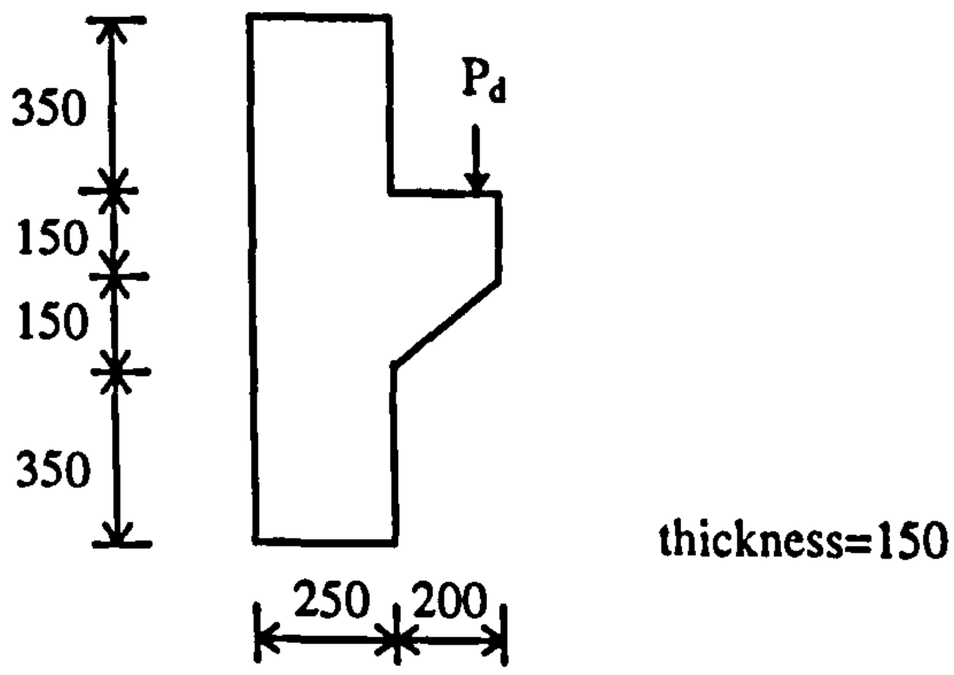
Corner Joints FJ1A & FJ2B	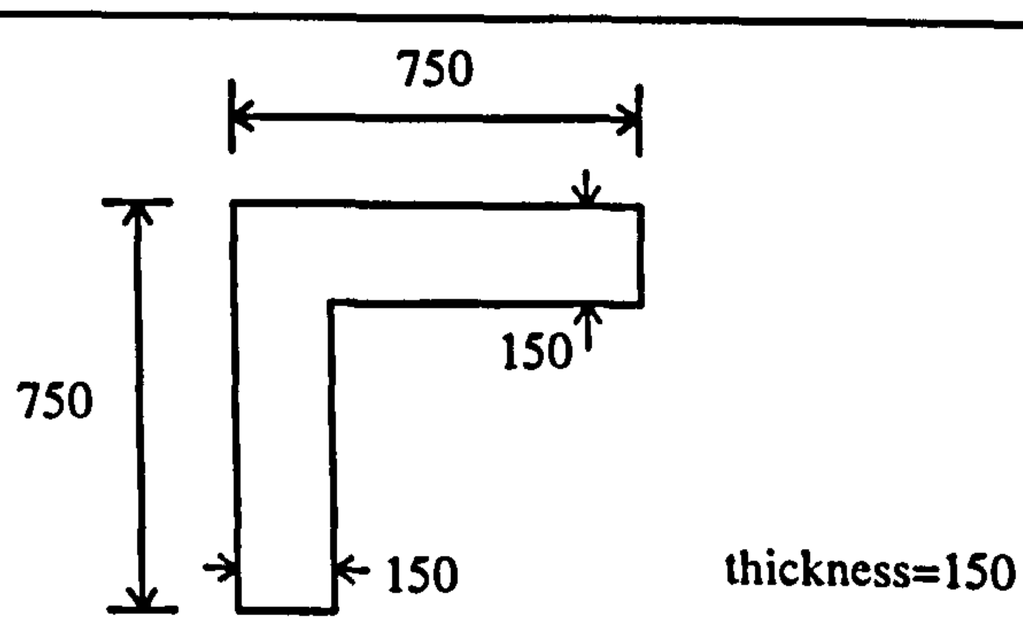

Table 7.1: Details of Experimental Program, all sizes in mm.

In addition to the main specimen, four 100x100x100mm cubes and four 150x300mm cylinders were cast. These control specimens were cured with the main specimen under polythene for 24 hours. After this period, half the control specimens were placed under water in the curing tank, while the rest remained with the main specimen under hessian. The cubes were used to determine the cube strength and the cylinders were used to determine the tensile strength and modulus of elasticity. The concrete tensile strength f_t was calculated using the cylinder splitting test from the following:

$$f_t = \frac{2P}{\pi DL}$$

where L=cylinder length (300mm), D=cylinder diameter (150mm), and P is the ultimate load. The results from each control specimen were averaged to give the experimental values presented in the next chapter.

7.2.3 Reinforcing Steel

Throughout the test series, high yield deformed bars were used from the same batches of ϕ8mm, ϕ10 and ϕ12 bars. The yield stress of the bars from each batch was measured using the Tinius Olsen Universal Testing Machine fitted with an S-type electronic extensiometer. The yield stress of the bars was taken as the stress at which a line starting from 0.2% strain, parallel to the initial slope of the curve, intersects the stress-strain curve, see figure 7.2.3.

7.2.4 Strain Gauges

During the experiments, strains in the bars were measured using 6mm electrical resistance strain gauges. The gauges were fixed to the steel bars at predetermined points in order to record the strain history. Before fixing the gauges, the surface of the bars at the appropriate area was prepared first by filing and then smoothing with sand paper. Care was taken during this process to avoid removing a significant area of the bar which could cause weakening. The smoothed surface was then treated with M-prep conditioner and M-prep neutralizer in order to remove any dirt and grease in order to achieve a perfect bond with the steel. The gauge was then fixed to the bar

using adhesive and checked for operational readiness using a voltmeter In order to provide protection from moisture and damage during fabrication and casting, an epoxy resin coating was applied to the gauge and terminal areas. At each required position, two gauges, each diametrically opposite one another, were fixed. The measured strain at each position was taken as the average between the gauge pairing.

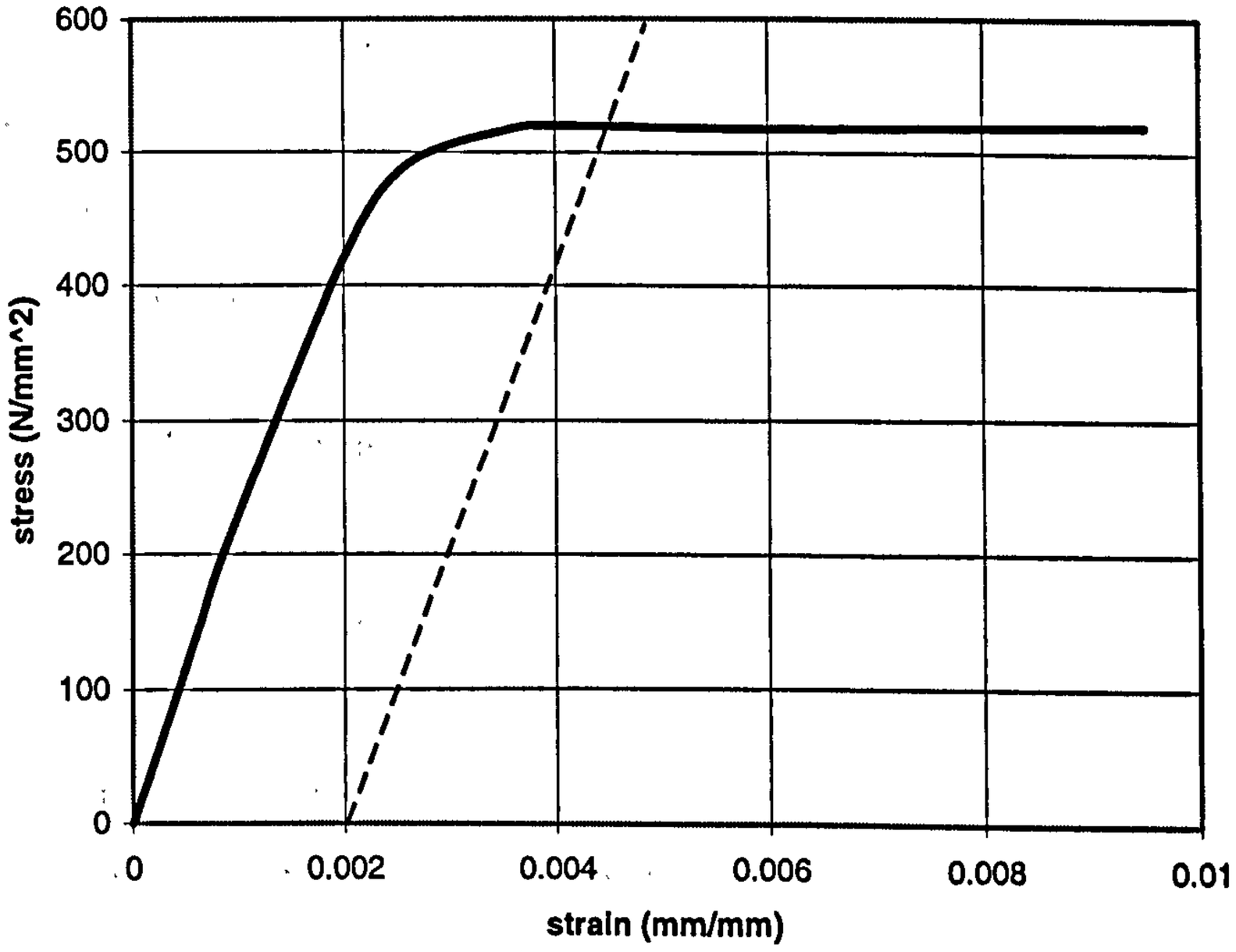

fig.7.2.3 Stress-Strain Relationship for ϕ12mm bar

7.3 Experimental Procedure

When the specimen was fully cured, it was painted white to assist in identification of cracks during testing. Each specimen was manoeuvred into it's respective testing rig by crane. All the strain gauges and load cells were connected to a 3530 Orion data logger for automatic recording. Each connection was checked prior to testing. Strain gauges were checked and defective ones disconnected. At each load increment, the results were stored to disc for later processing. The specimen was illuminated using a powerful light source in order to ease identification of cracks. The crack widths were measured at each load increment using a micro-crack reader. The crack development was traced with an ink marker at each load increment. This procedure was repeated at each increment until the ultimate load was achieved. Details of the test rig for each model are now described.

7.3.1 Double Sided Corbels

Experimental tests have been conducted in the past on double sided corbels, see Kriz & Raths (1965), Somerville (1974), Mattock et al. (1976). In these tests, the corbels were orientated upside-down, supported at the corbel ends, and the load was applied to the column end. This was the method of testing used in this work, see figures 7.3.1(a-b). The loading was applied using a 10000kN Losenhausen Universal Testing Machine. In order to ensure even distribution of the load, each side of the corbel was supported by steel bearing plates on rollers. At the supports, 500 kN load cells were placed to measure the reactions. Details of the steel layouts and strain gauge positions are given in the next chapter.

7.3.2 Single Sided Corbel

Testing of a single sided corbel presents more difficulties than double sided corbels because the ends of the corbel have to be prevented from rotating due to the eccentricity of the load. In this program, corbel C4A was tested in the Tinius Olsen Universal Testing Machine. The test set-up is shown in figure 7.3.2(a). The testing method was such as to prevent the ends of the column from rotation by providing a steel tie at the top and a steel block at the bottom. The model was tested using 10kN increments. The loading head of the Tinius Olsen Machine was fixed and a hydraulic jack and 500kN load cell were placed between the head and the corbel.

7.3.3 Corner Joints

Corner joint FJ1A was designed for a closing moment and FJ2B was designed for an opening moment. Both joints were of identical geometry. Details of the test set-up for each joint are given in figures 7.3.3(a-d). The vertical leg of each corner was fixed to the lab floor via a 30mm diameter steel rod as shown in the figure. For FJ1A, the closing moment was generated in the corner via the hydraulic jack at the end of the horizontal. The moment was then calculated as the product of the load and the lever arm distance to the centre of the vertical. For FJ2B, the opening moment was generated in the corbel by jacking upwards against the horizontal as shown in figure 7.3.3(c). In order to monitor rotation at the base of the corners, displacement transducers were used. In both cases, negligible rotations were observed during testing.

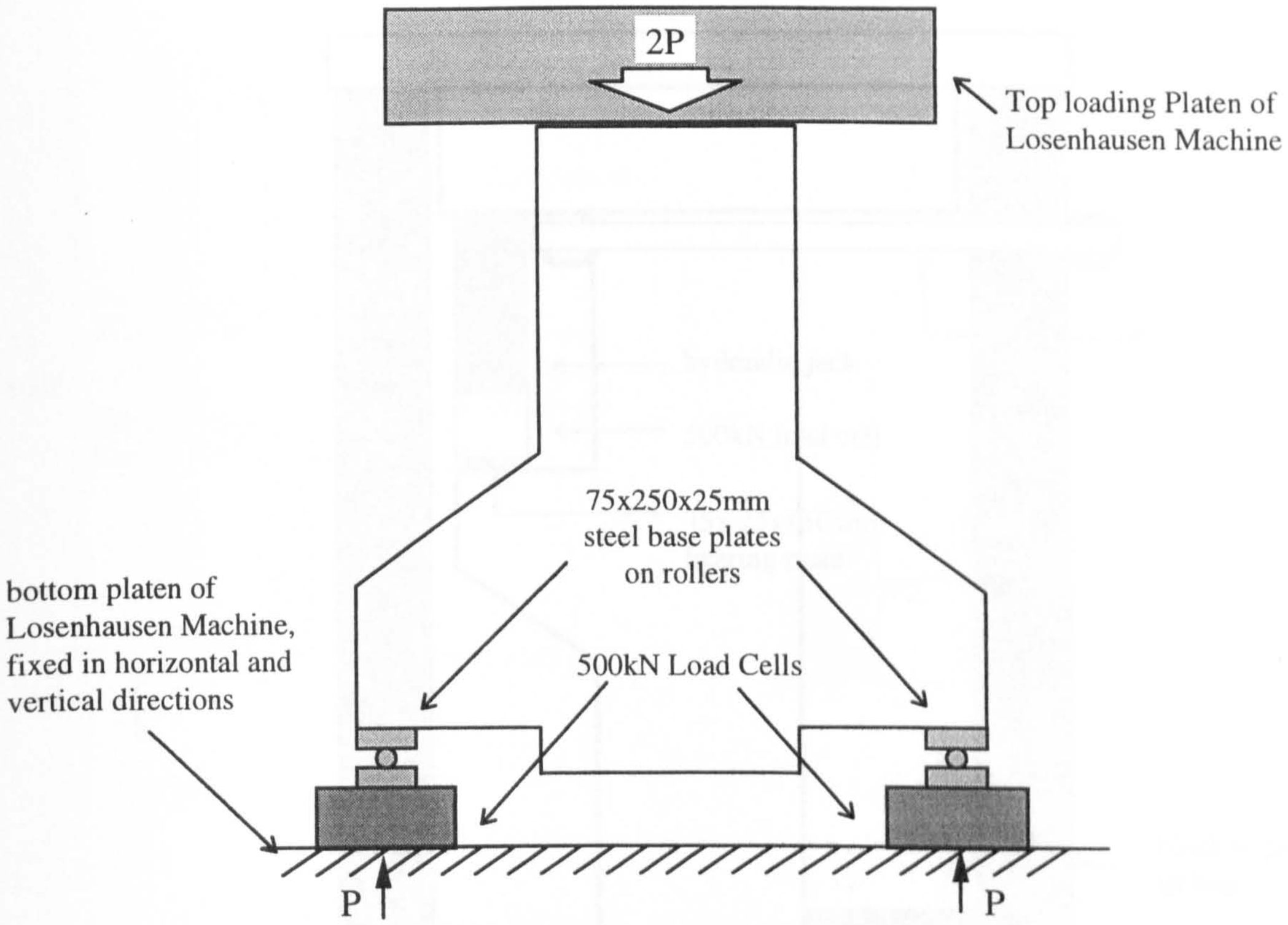

fig.7.3.1(a) Testing Method for Corbels C2A and C3A

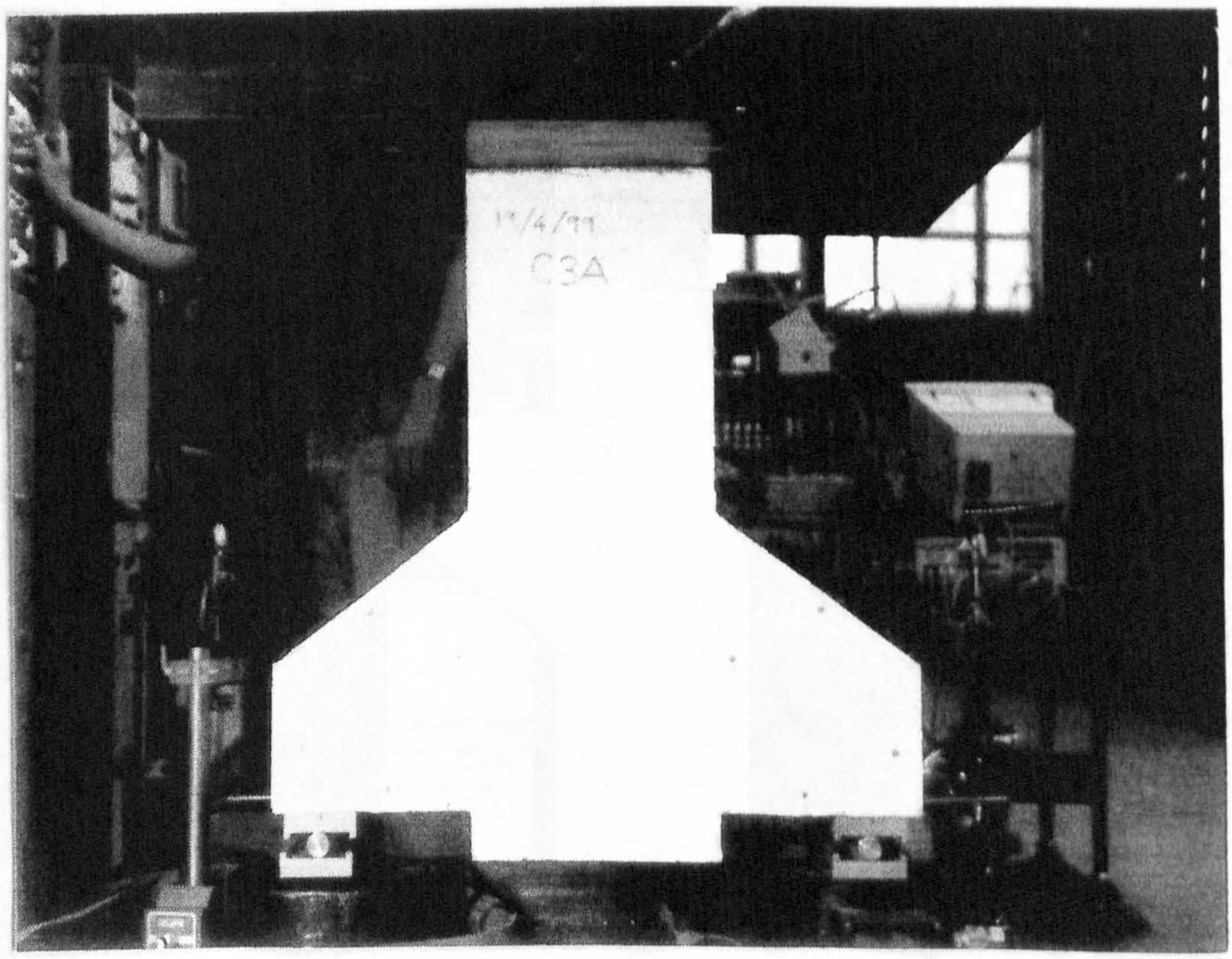

fig.7.3.1(b) Corbel C3A: Experimental Set-up

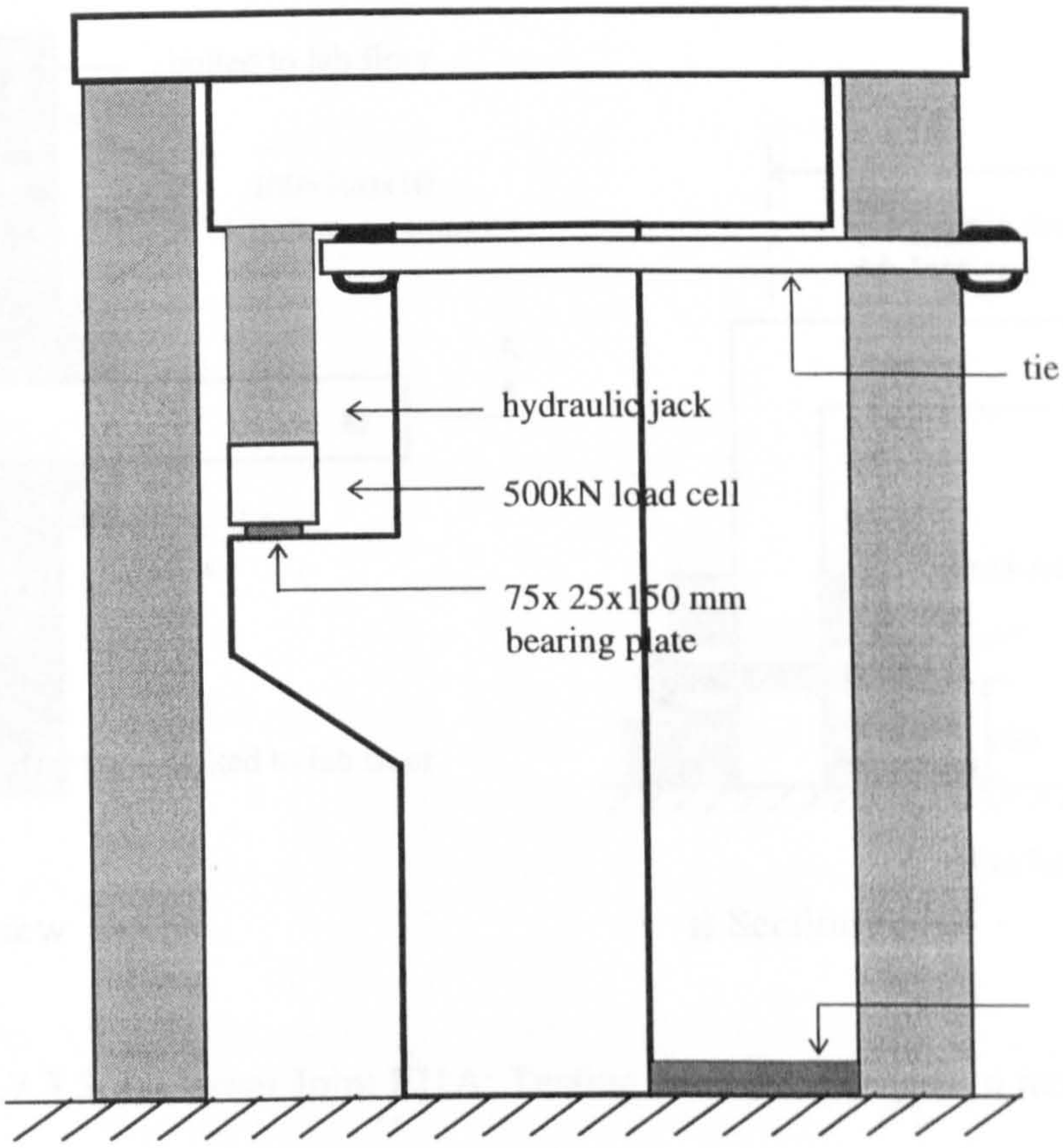

fig.7.3.2(a) Corbel C4A: Testing Method

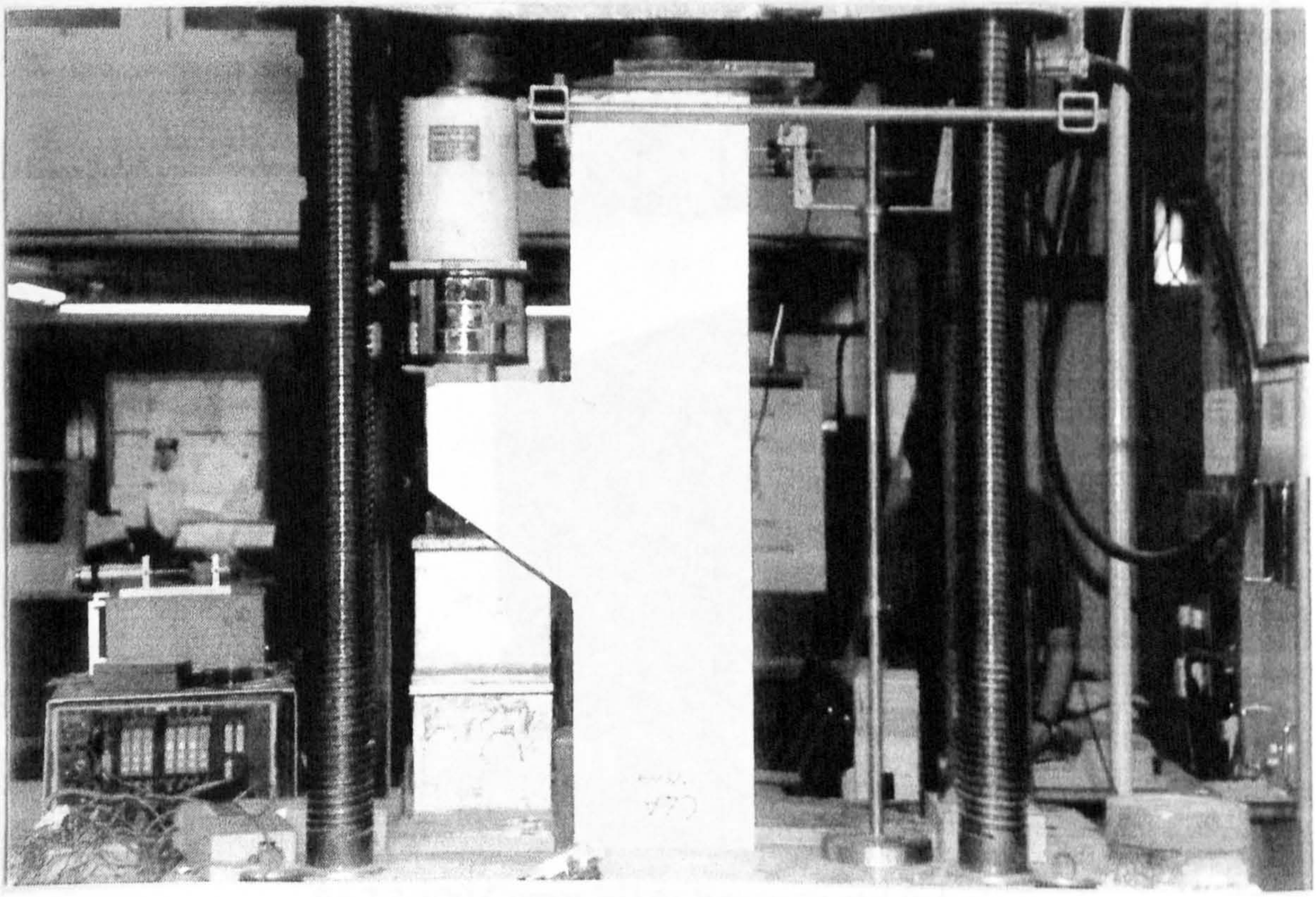

fig.7.3.2(b) Corbel C4A: Experimental Set-up

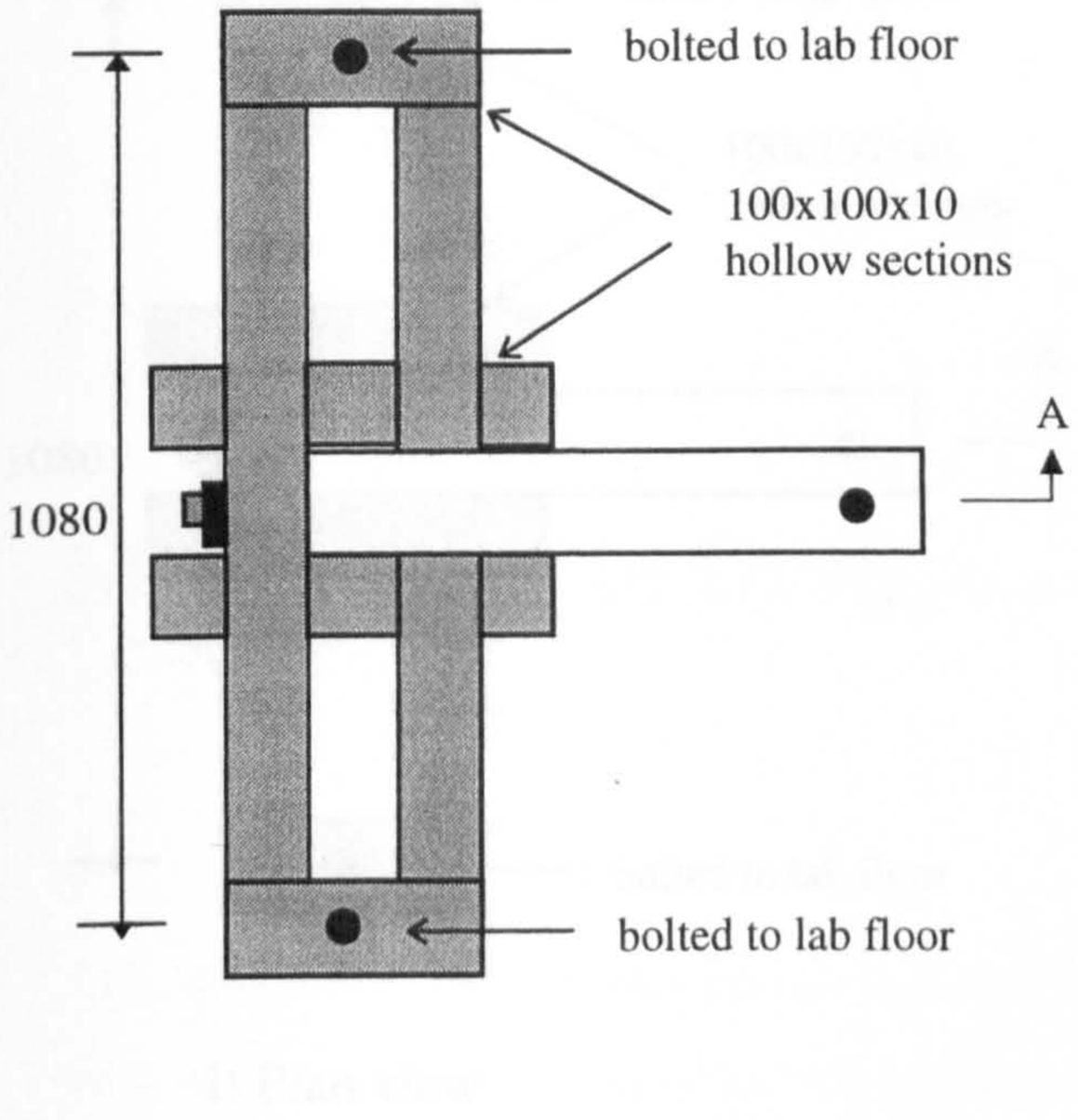

i) Plan view i) Section A-A

fig.7.3.3(a) Corner Joint FJ1A: Testing Method, all sizes in mm

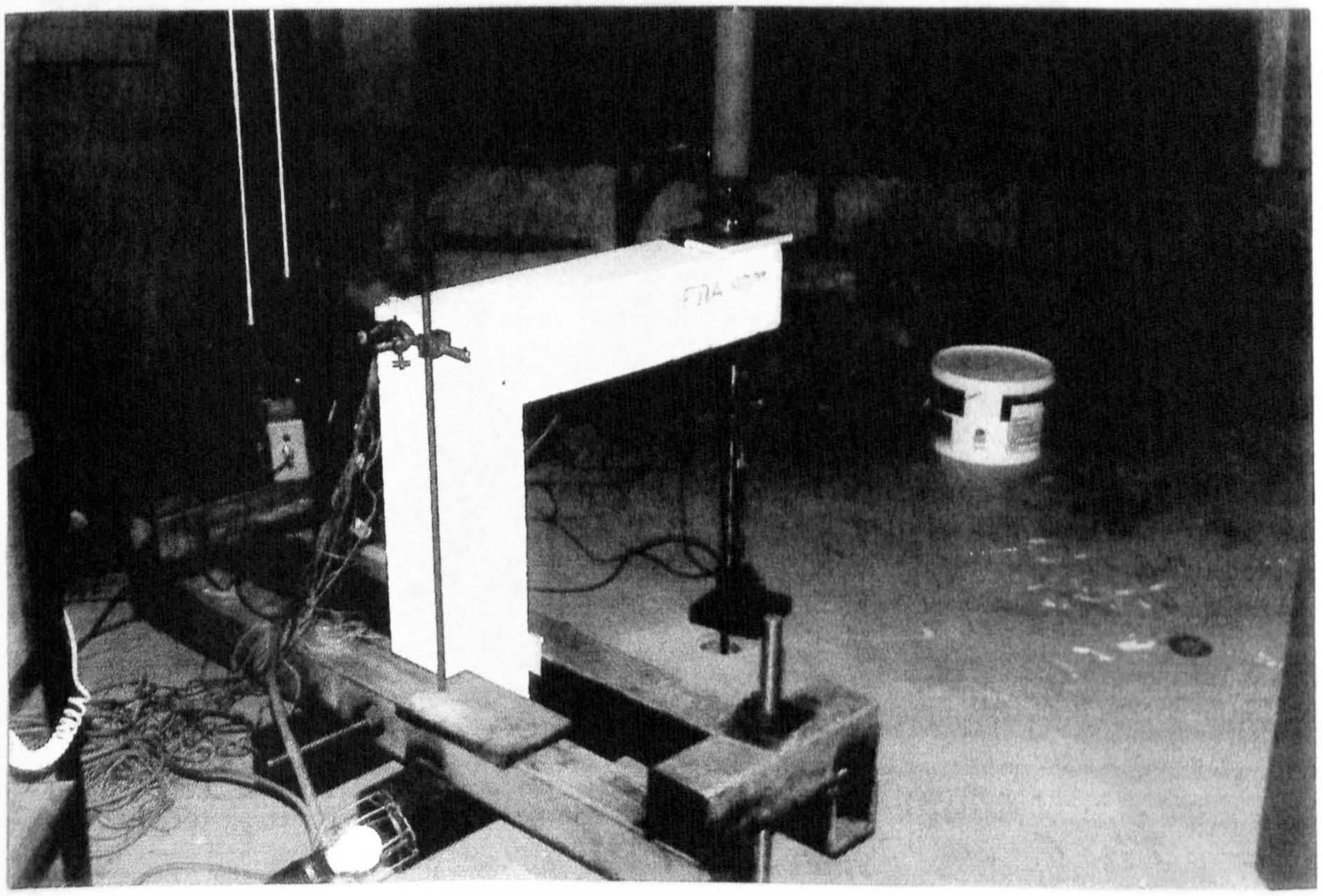

fig.7.3.3(b) Corner FJ1A: Experimental Set-up

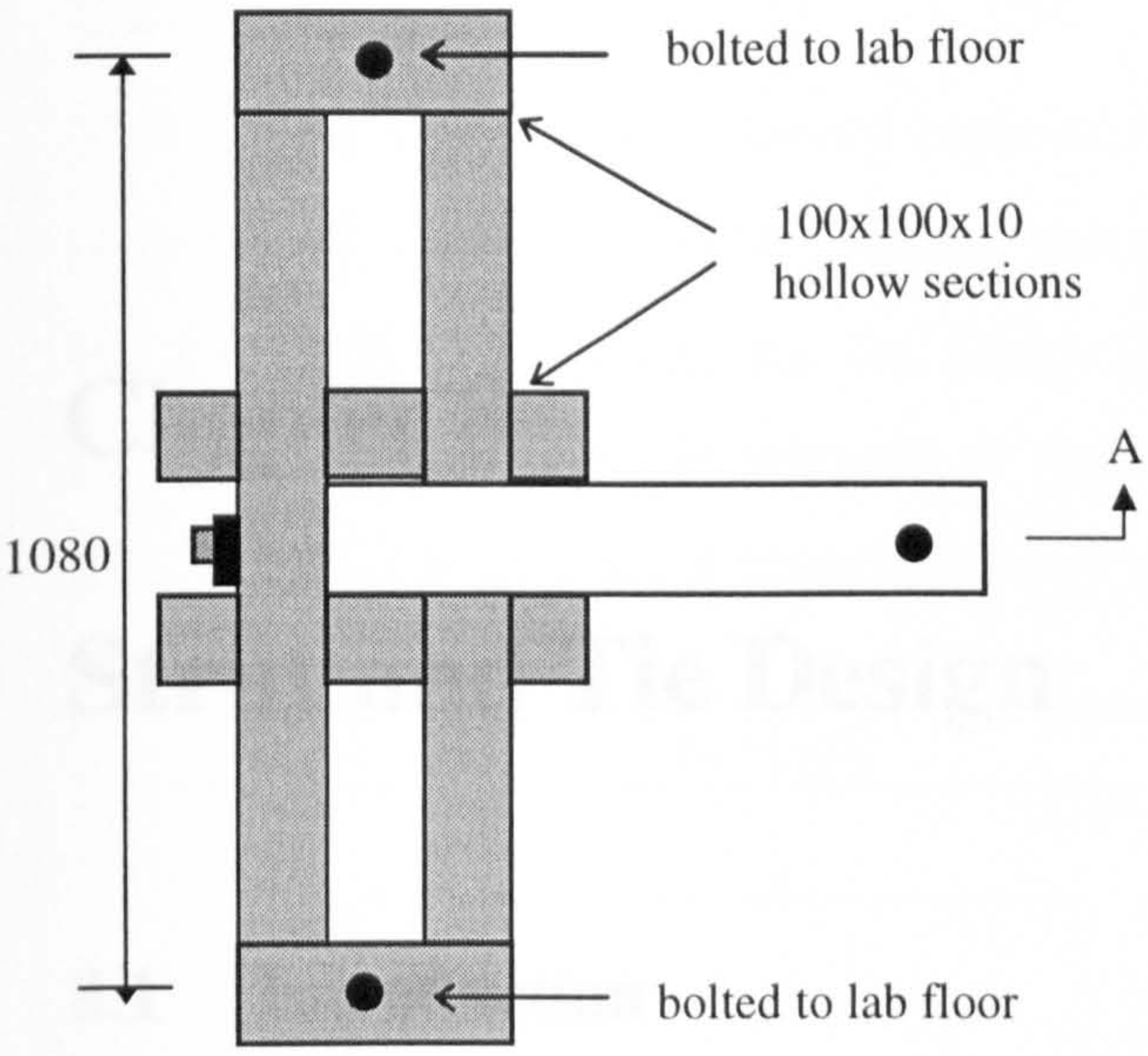

i) Plan view

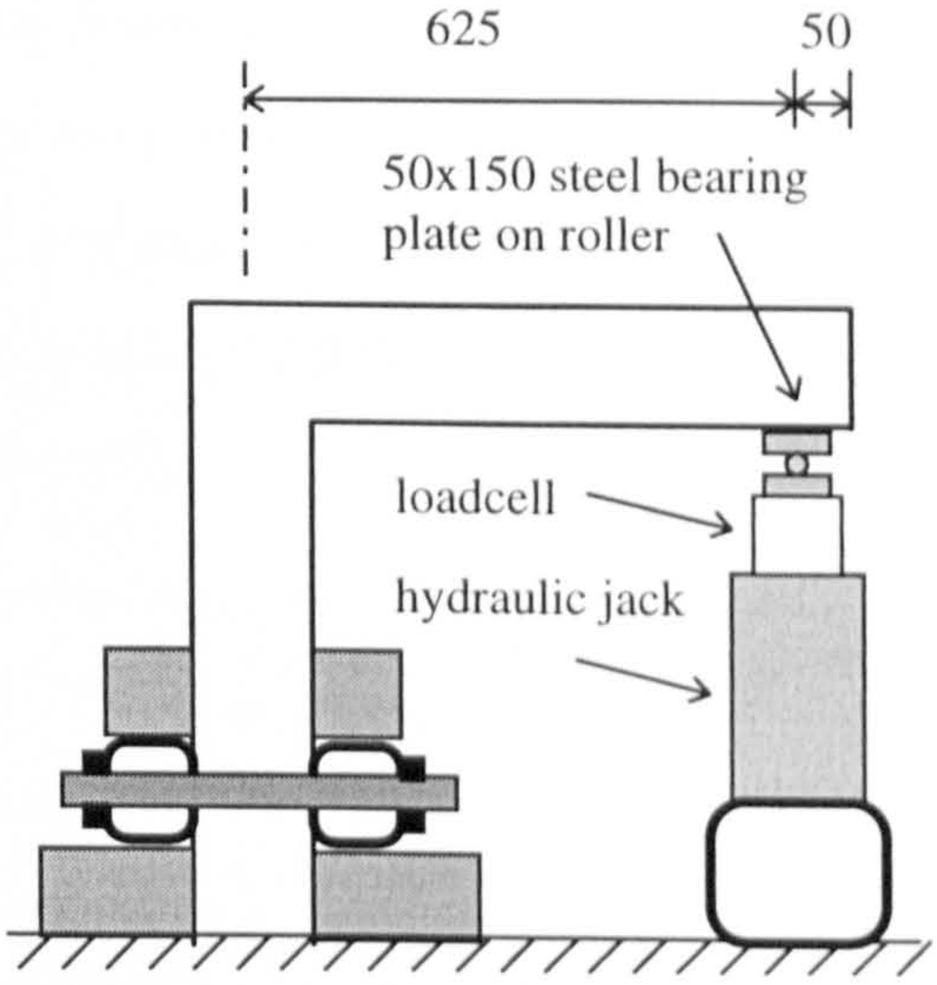

i) Section A-A

fig. 7.3.3(c) Corner FJ2B: Testing Method, all sizes in mm.

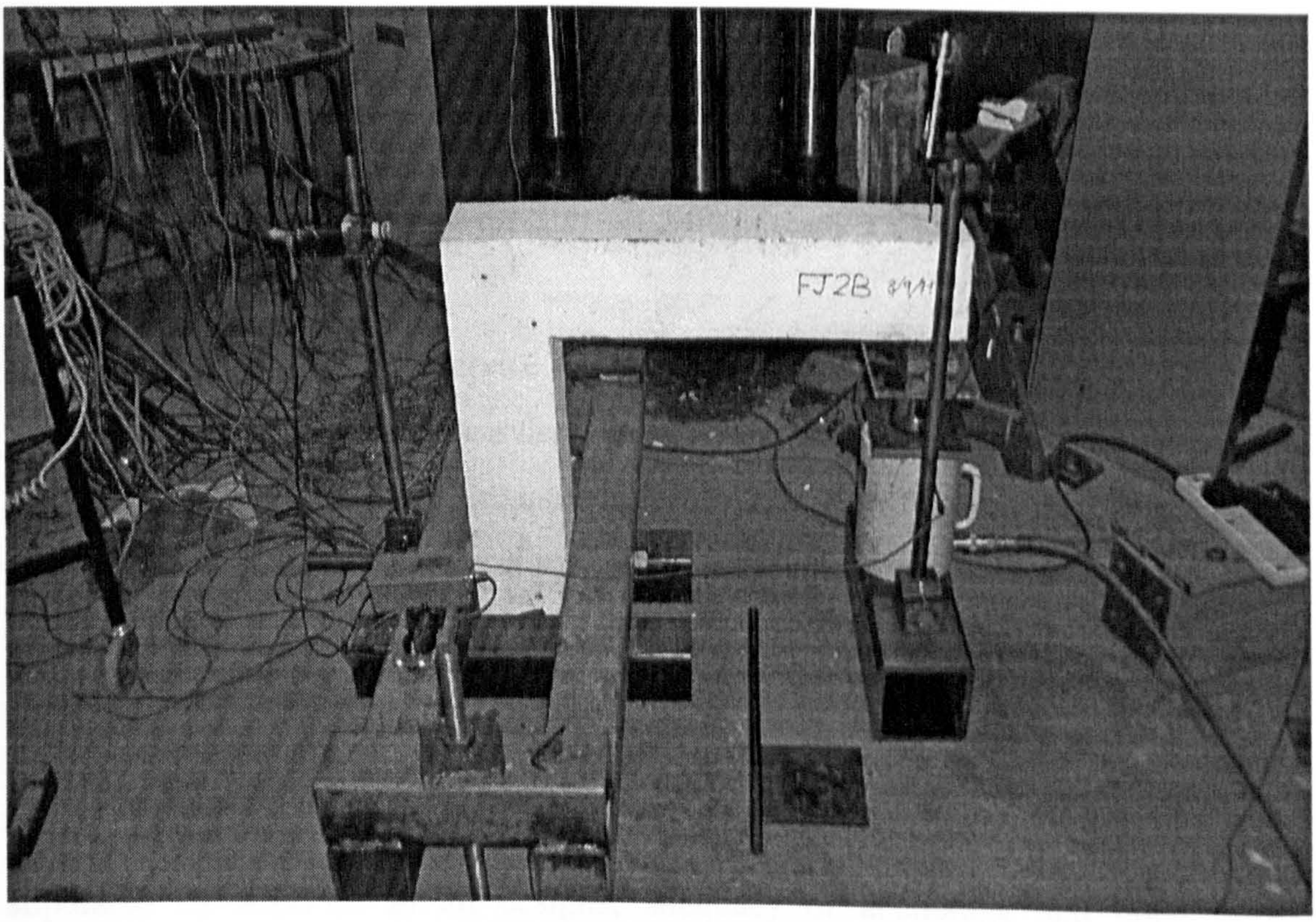

fig. 7.3.3(d) Corner FJ2B: Experimental Set-up

Chapter 8

Strut and Tie Design

8.1 Introduction

This chapter details the design by strut and tie models of a number of typical D-region type structures. The main objective of this work is to assess the suitability of the strut-tie method in achieving the required performance from a designed structure.

The visualisation process described previously is used to generate the outline of the strut-tie models. The test series comprises of six designs, 1 deep beam, 3 corbels and 2 frame corner joints. All of these designs were assessed through non-linear analysis. In addition to this, the corbels and corner joints were physically tested in the laboratory. Details of the experimental set-up were given in chapter 7.

As in the case of slabs, the service and ultimate load characteristics of the structures were investigated. It is important that the structures resulting from the strut-tie design possess a ductile response at ultimate load. This is achieved by ensuring that crushing of the concrete prior to yielding of the main steel is avoided at the design loads. In the case of deep beams and corbels, serviceability displacements are not a serious issue since the very low span-depth ratios of these structures results in very small deflections. However during the experimental test series, the major crack widths were monitored and compared with the maximum service crack width limit of 0.3mm stipulated by BS8110. In all designs, adequacy of anchorage and bond of the reinforcement was checked according to BS8110.

8.2 Deep Beam B1

This model was a typical simply supported deep beam with an effective span-depth ratio of 1.7. Dimensions and material properties are given in the table below, where P_d, f_{cu}, f_t, E_c, E_s and f_y are the design load, uni-axial cube crushing strength of concrete, uni-axial tensile strength of concrete, elastic modulus of concrete, elastic modulus of steel and yield strength of steel respectively.

Schematic	Design Material Properties
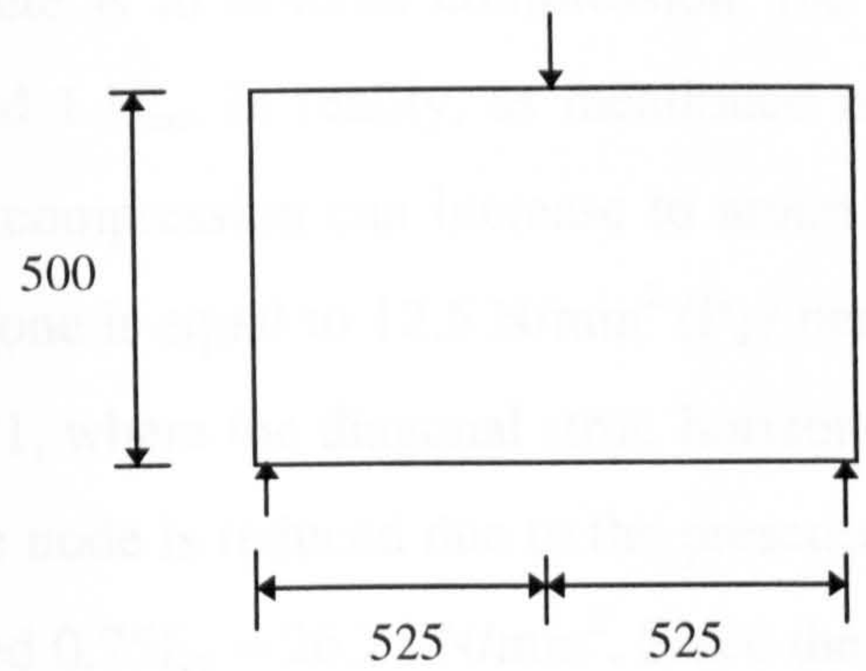	P_d=250kN **concrete:** f_{cu}=35N/mm^2 f_t=3.0N/mm^2 E_c=21.5kN/mm^2 **steel:** f_y=460N/mm^2 E_s=200kN/mm^2 thickness=100mm

The initial elastic principal stresses and resulting strut-tie model are given in figure 8.2(a). From figure 8.2a(ii), the main load paths in the structure can be clearly seen as the diagonal compression strut running from the load point to the support, and the horizontal tension tie at the bottom. The presence of transverse tensile stress along the length of the strut can also be observed. These transverse tensile stresses have a detrimental effect on the strength of the strut and are accounted for in the resulting strut-tie model (fig8.2a(iii)) by introducing ties along the strut at the third points. Using this model, the member stresses were evaluated and the resulting reinforcement was calculated. A summary of the analysis is given in table below. For dimensioning of struts and nodal zones, the cube crushing strength f_{cu} was used as the design strength f_{cd}. In practice, material factors would be applied to f_{cu}. Similarly, no material factors were applied to the yield strength of the steel. The tensile strength of the concrete was ignored.

Member	Force (kN)	A_s required (mm^2)	A_s provided (mm^2)	No. of Bars	$\frac{A_s \text{ provided}}{A_s \text{ required}}$
1	125	271.74	314.16	4(ϕ10)	1.15
4	53.52	133.73	157.08	2(ϕ10)	1.17
7	53.07	133.73	157.08	2 (ϕ10)	1.17

Nodal zones are the critical areas of the model and stresses must be checked to ensure that capacity under the given state of stress is not exceeded. Figure 8.2(b) gives details of the nodal zone dimensions. At node 6, (see fig 8.2a), where the load is applied, concrete is in bi-axial compression, the capacity of concrete in this zone must not exceed $1.1f_{cu}$. In reality, as mentioned in chapter 5, the concrete strength under bi-axial compression can increase to around $1.16\ f_{cu}$, Kupfer et al.(1969). The stress at this zone is equal to $12.5\ N/mm^2$ (P_d / bearing plate dimensions) and is hence safe. At node 1, where the diagonal strut, horizontal tie and vertical reaction meet the strength of the node is reduced due to the presence of the tie, in this case the stresses must not exceed $0.75f_{cu} = 26.25\ N/mm^2$. Since the stress in this node is the same as node 6, the node is safe. A schematic representation of nodes 1 and 6 is given in figure 8.2(g). The designed reinforcement layout is given in figure 8.2(c).

The results of the non-linear analysis are shown in figures 8.2(d-h). From the numerical load-displacement relationship figure 8.2(d), it can be seen that the structure attains an ultimate load of $1.32P_d$. In addition to this, a certain amount of ductility is observed before eventual collapse. If yielding of the steel is assumed to govern failure, then the strut and tie model would predict an ultimate load of $1.15P_d$, since 15% extra steel was used for the main tie.

As shown in figure 8.2(c), yielding of the main steel occurred at the mid-span at $1.25P_d$, which is close to the load predicted by the strut-tie model for the onset of yielding. Once yielding of the main steel began, crushing of the concrete at node 1 was initiated at $1.3P_d$. The concrete in this zone is in a state of bi-axial tension-compression, hence an ultimate stress of $0.8f_{cu}$ is reached. The strut-tie idealisation of this node suggested that at $1.0P_d$, a stress of $12.5N/mm^2$, $0.4P_d$, would be reached, see fig 8.2(g). From the finite element analysis, it was observed that a higher stress was reached due to the stress concentrations which occur around the edge of the bearing

plates. However, as can be seen from the stress plots in figures 8.2(i-j), the stresses along the diagonal were much more similar to those predicted by the strut-tie model. Details of the Gauss point positions at which the numerical stresses were obtained are given in figure 8.2(h)

In this example, a more detailed analysis of nodal zone 1 was carried out. Using the displacements from the original analysis, a displacement controlled analysis using a refined mesh was implemented. Details of the principal stresses and stress states are given in figures 8.2(i-j). It can be seen form the principal stress plot that the largest compressive stresses are concentrated along the outer edge of the bearing plate.

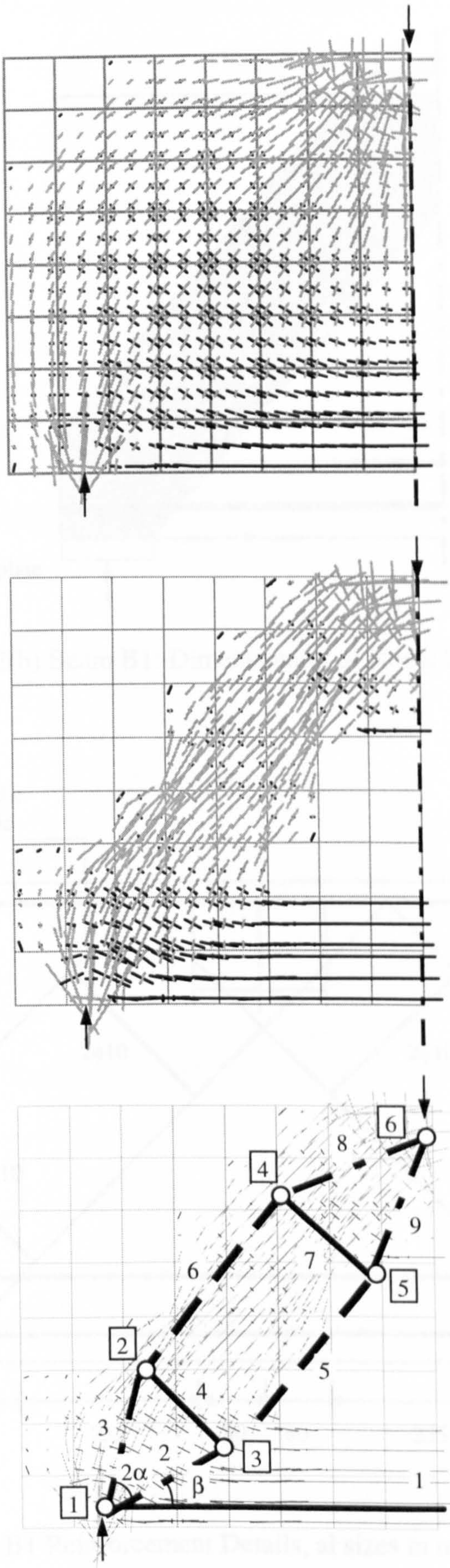

i) (rr=0)

compression
tension

ii) (rr=35%)

iii) Strut & Tie Model

α=26.56°
β=18.44°

strut
tie

fig.8.2(a) Beam B1: Elastic Stress Patterns and Strut Tie model

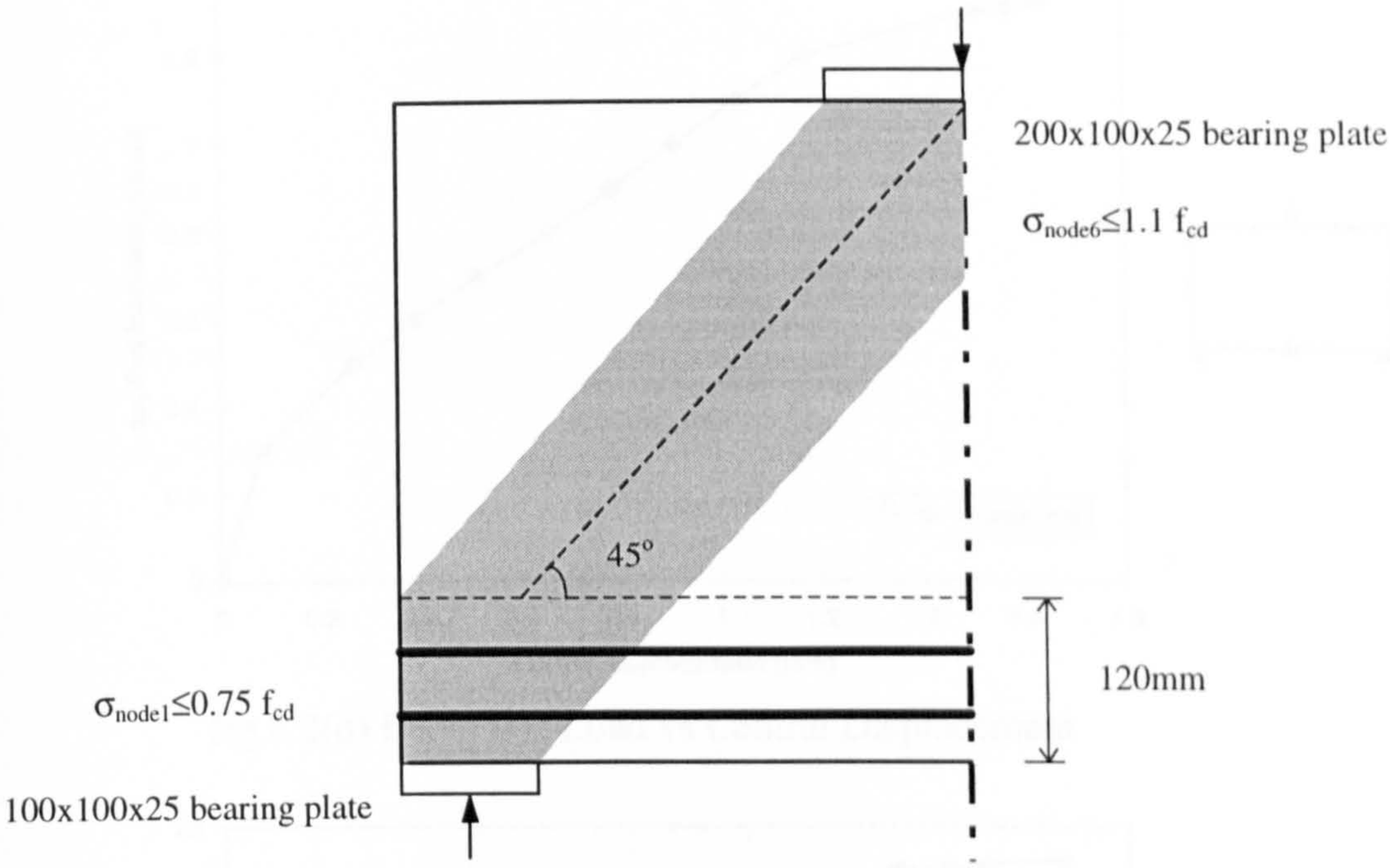

fig.8.2(b) Beam B1: Dimensioning of Nodal Zones

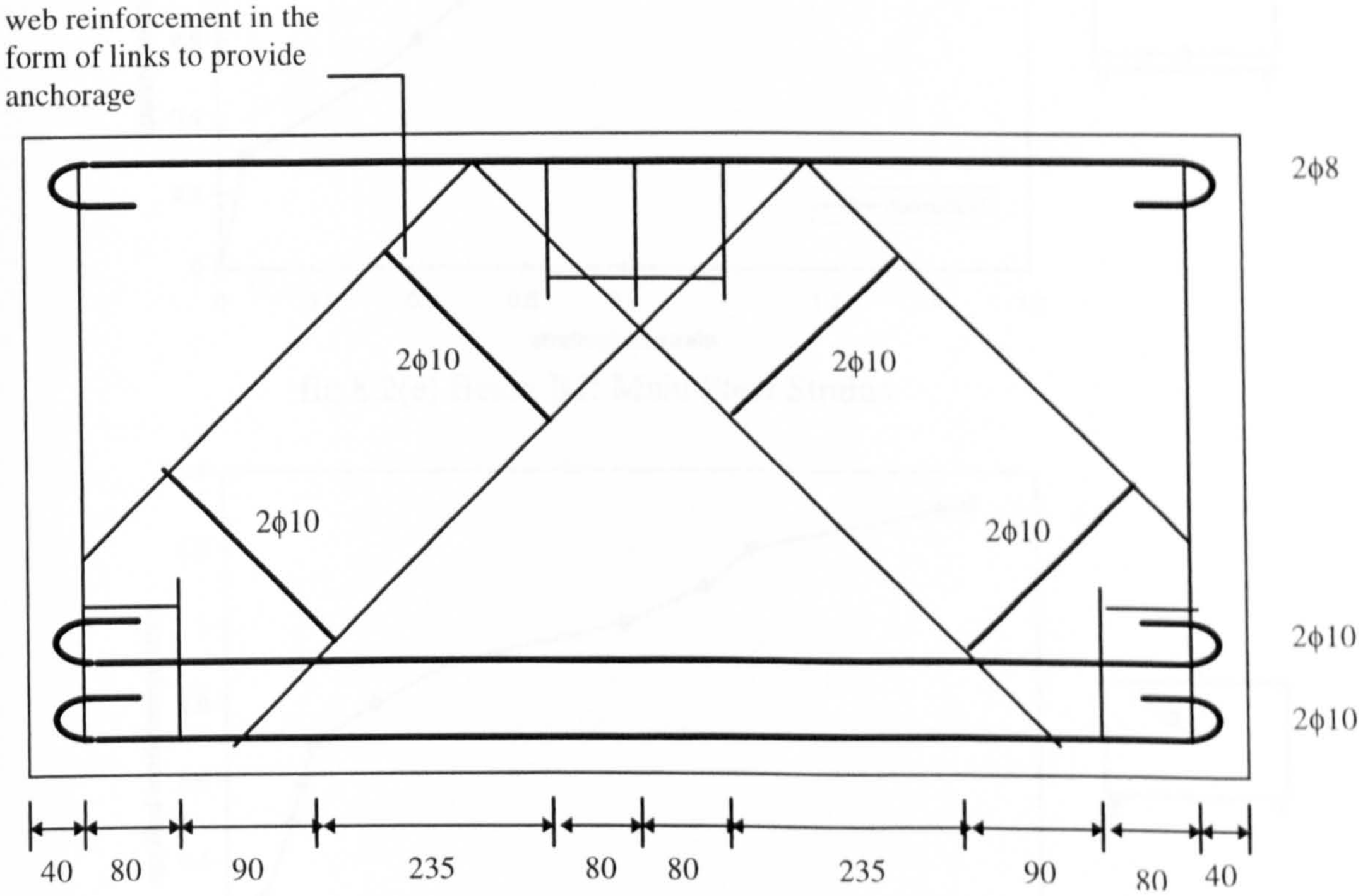

fig.8.2(c) Beam B1 Reinforcement Details, al sizes in mm, all stirrups ϕ6

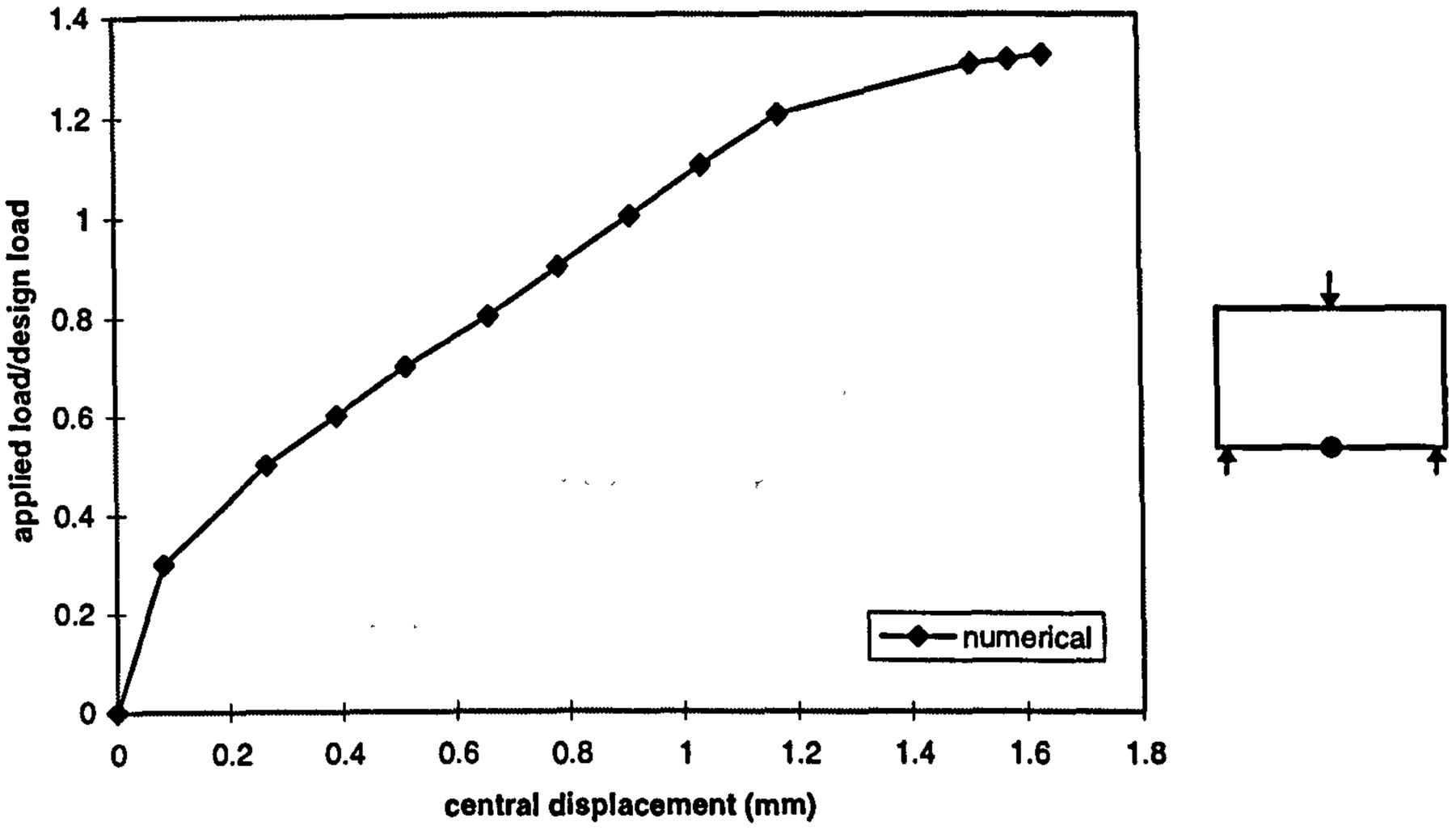

fig.8.2(d) Beam B1: Load vs Central Displacement

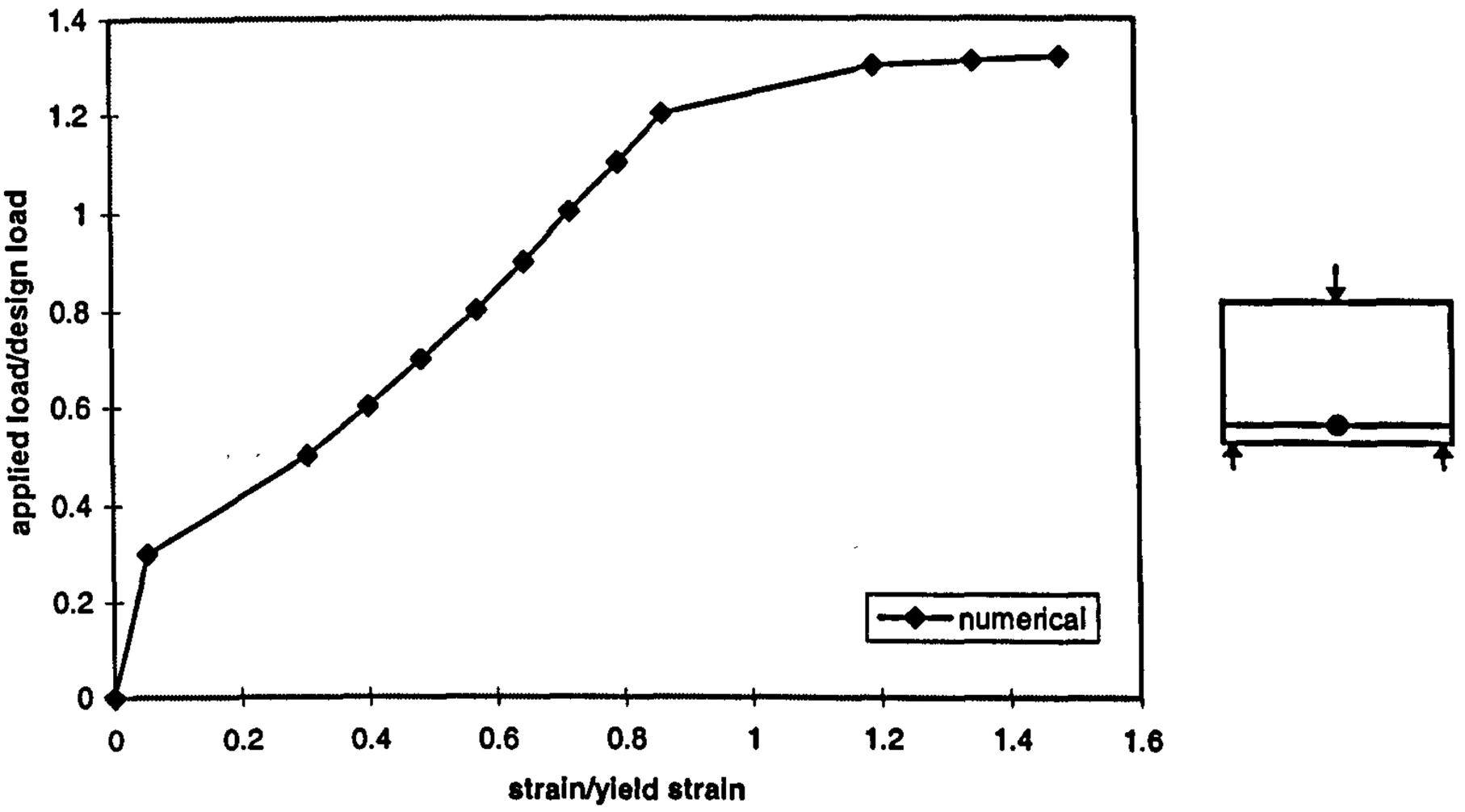

fig.8.2(e) Beam B1: Main Steel Strains

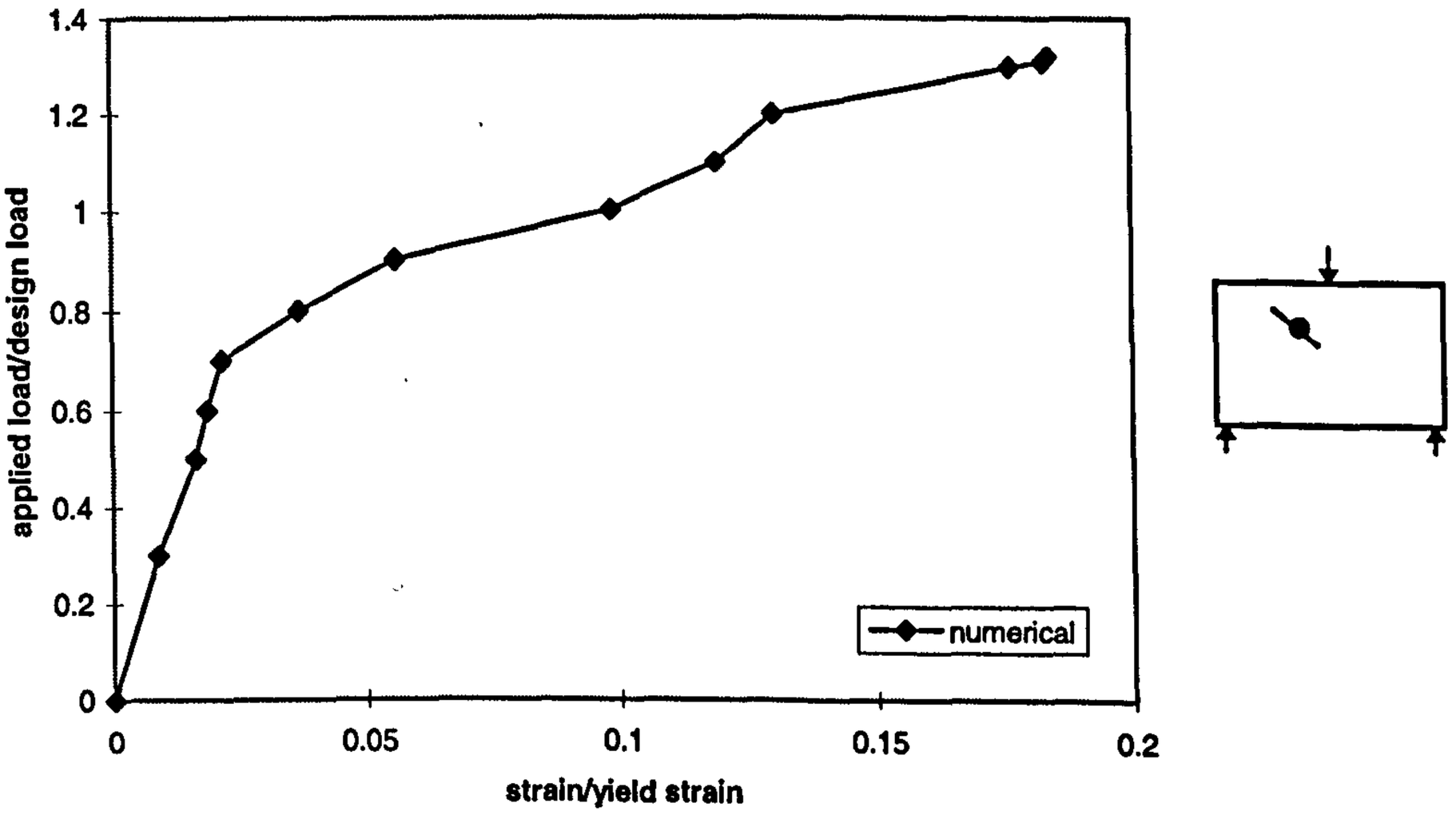

fig.8.2(f) Beam B1: Web Steel Strains

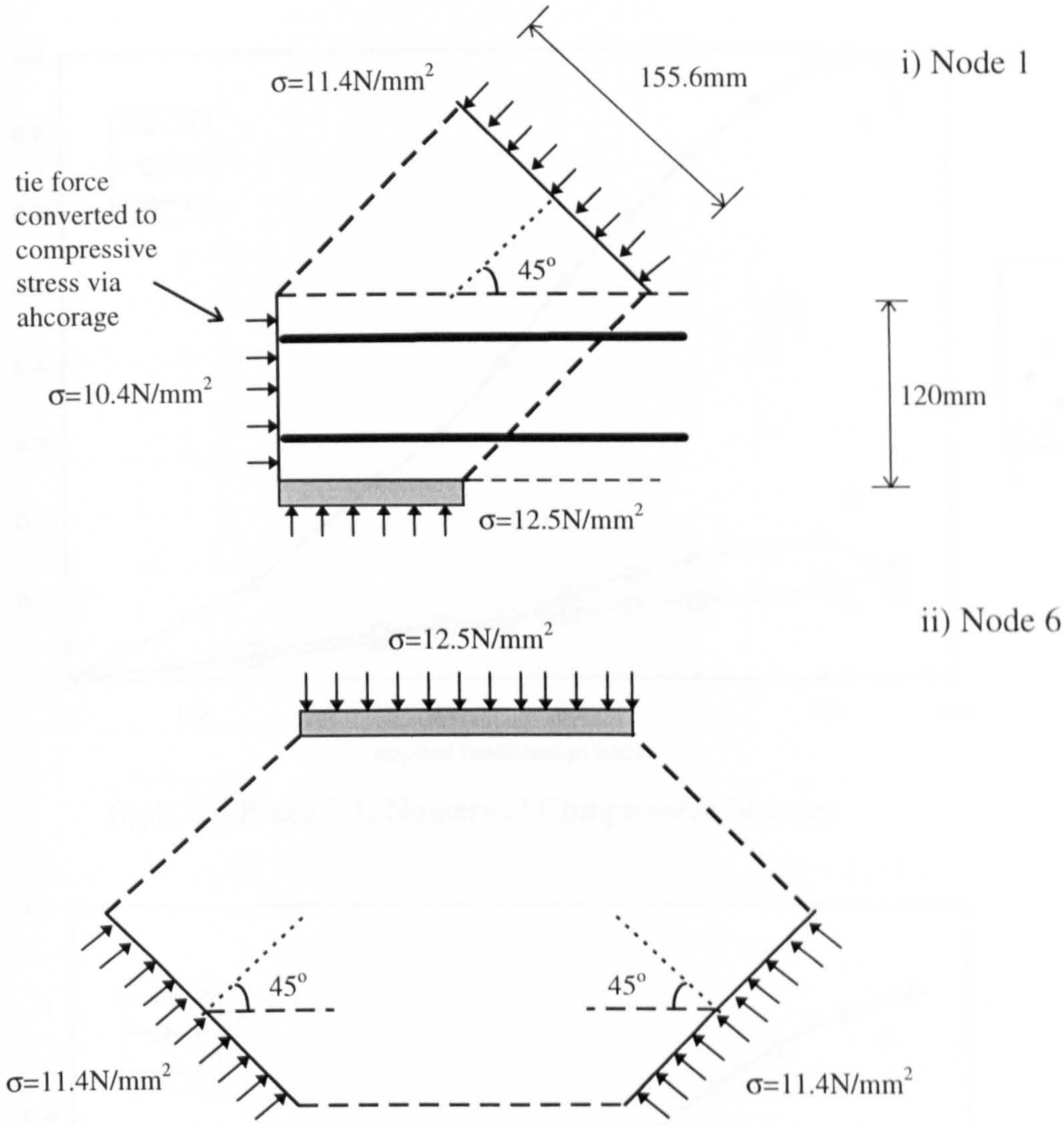

fig.8.2(g) Beam B1: Stresses in Nodes 1 and 6

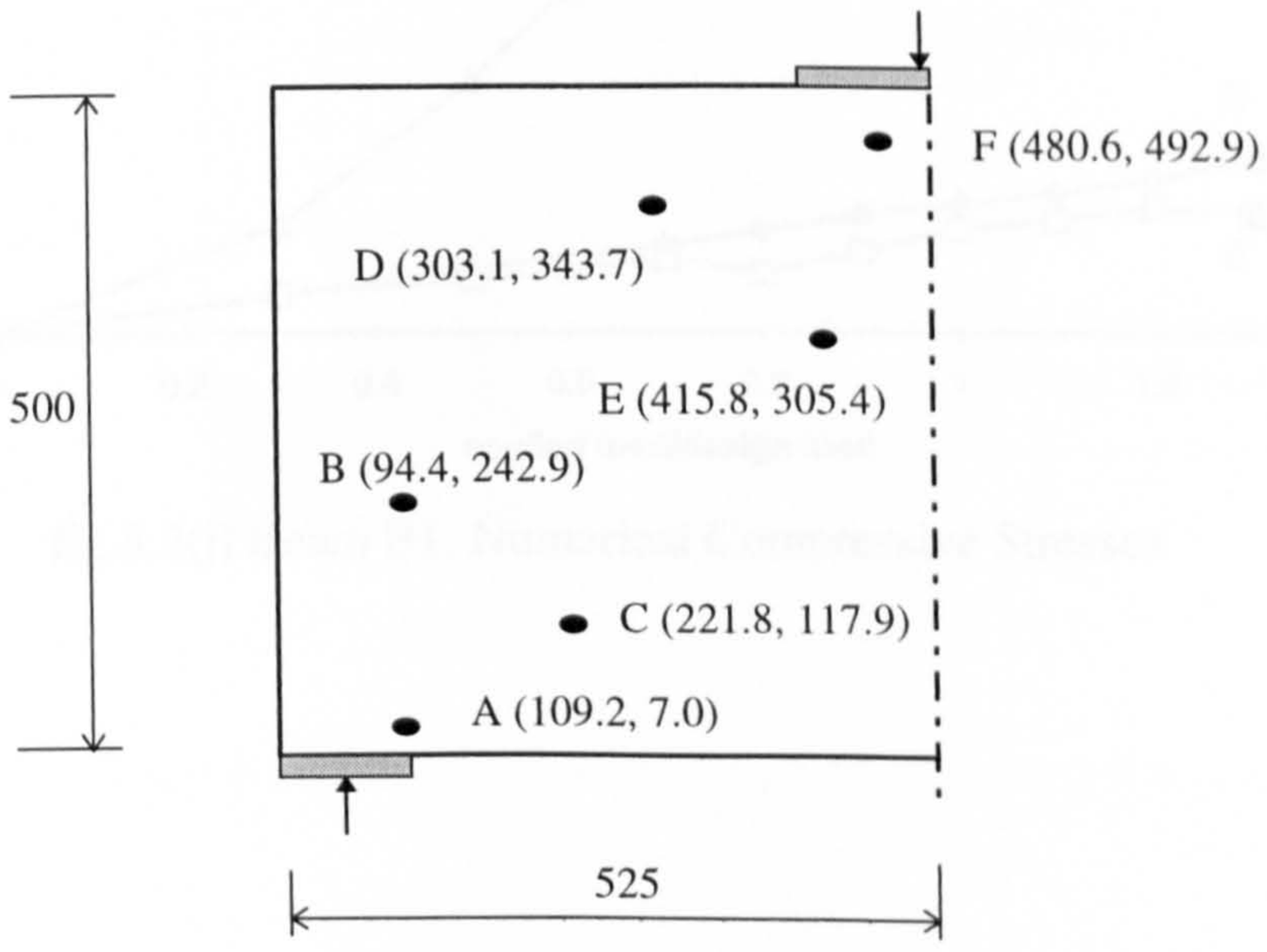

fig.8.2(h) Beam B1: Gauss Point Positions for Numerical Stresses

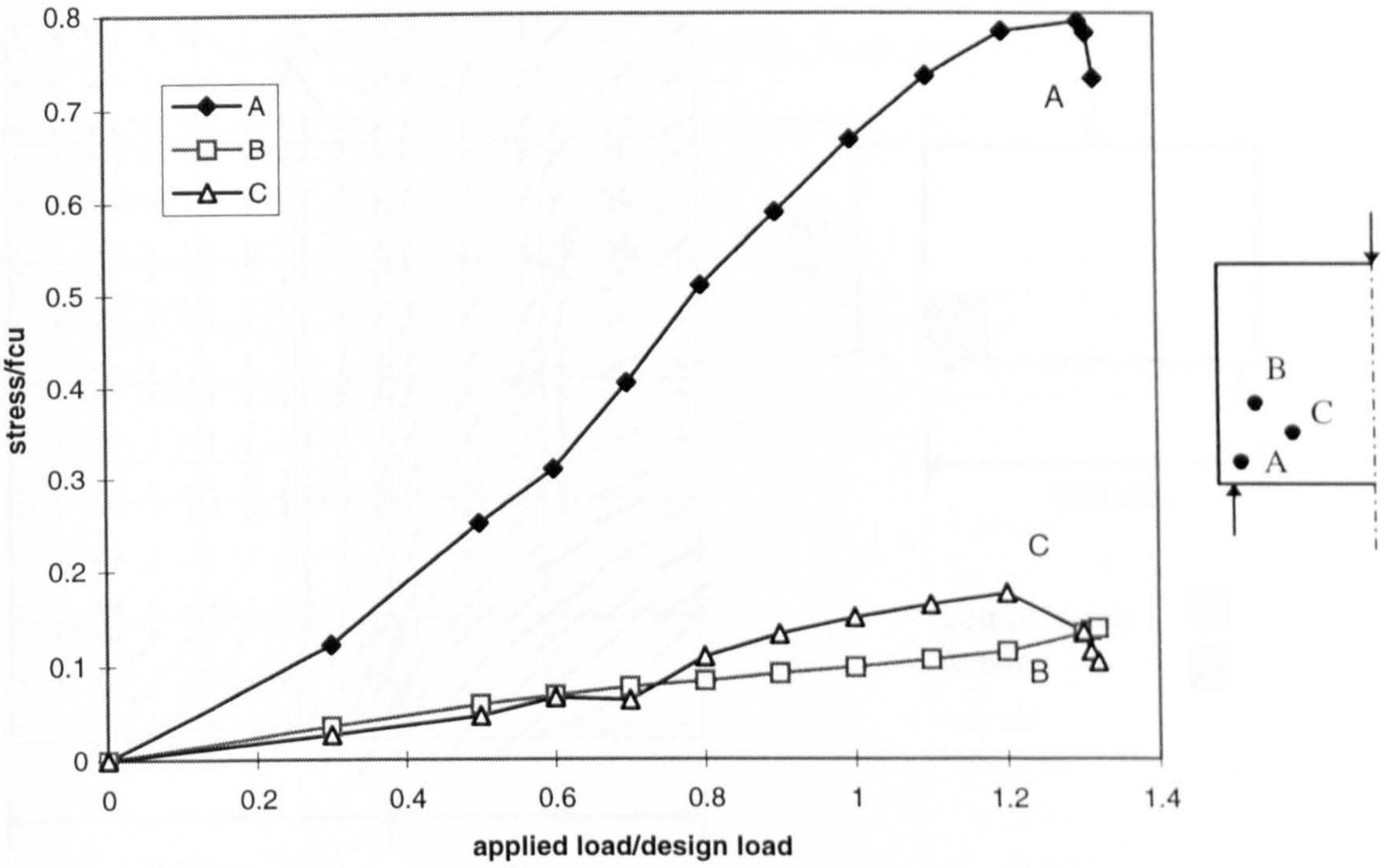

fig.8.2(i) Beam B1: Numerical Compressive Stresses

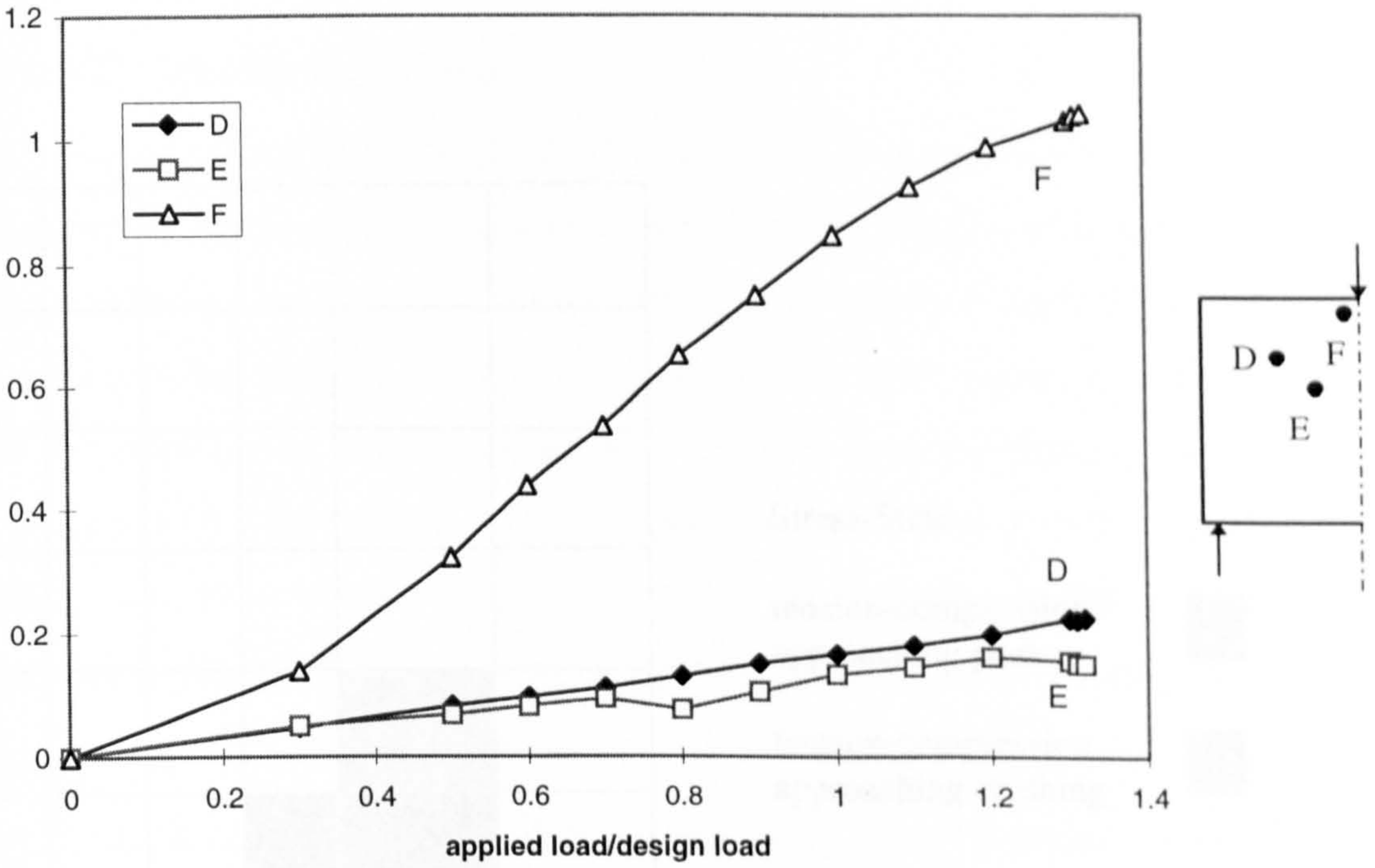

fig.8.2(j) Beam B1: Numerical Compressive Stresses

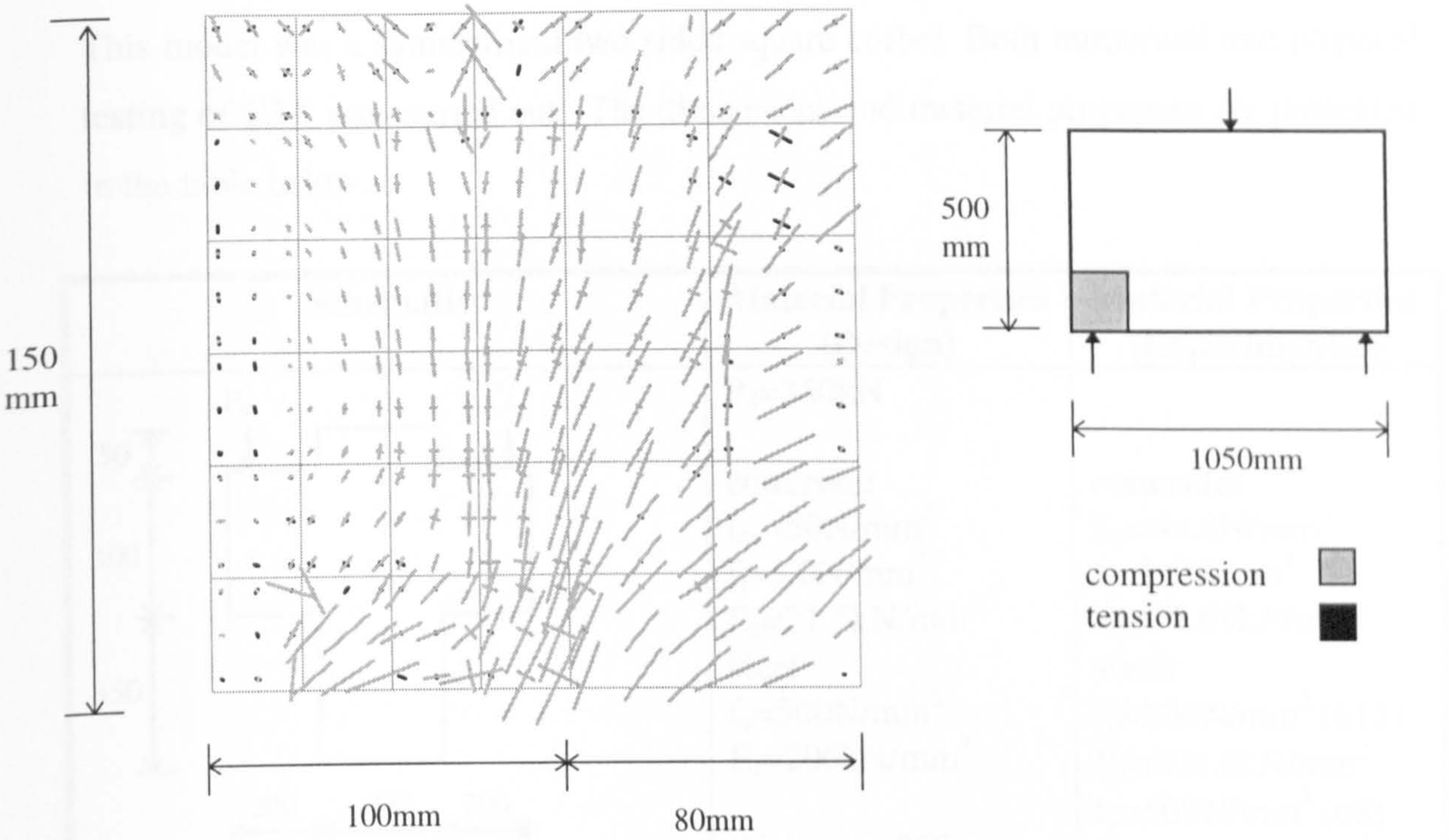

fig.8.2(k) Beam B1 Nodal Zone 1, Principal Stresses at ultimate load

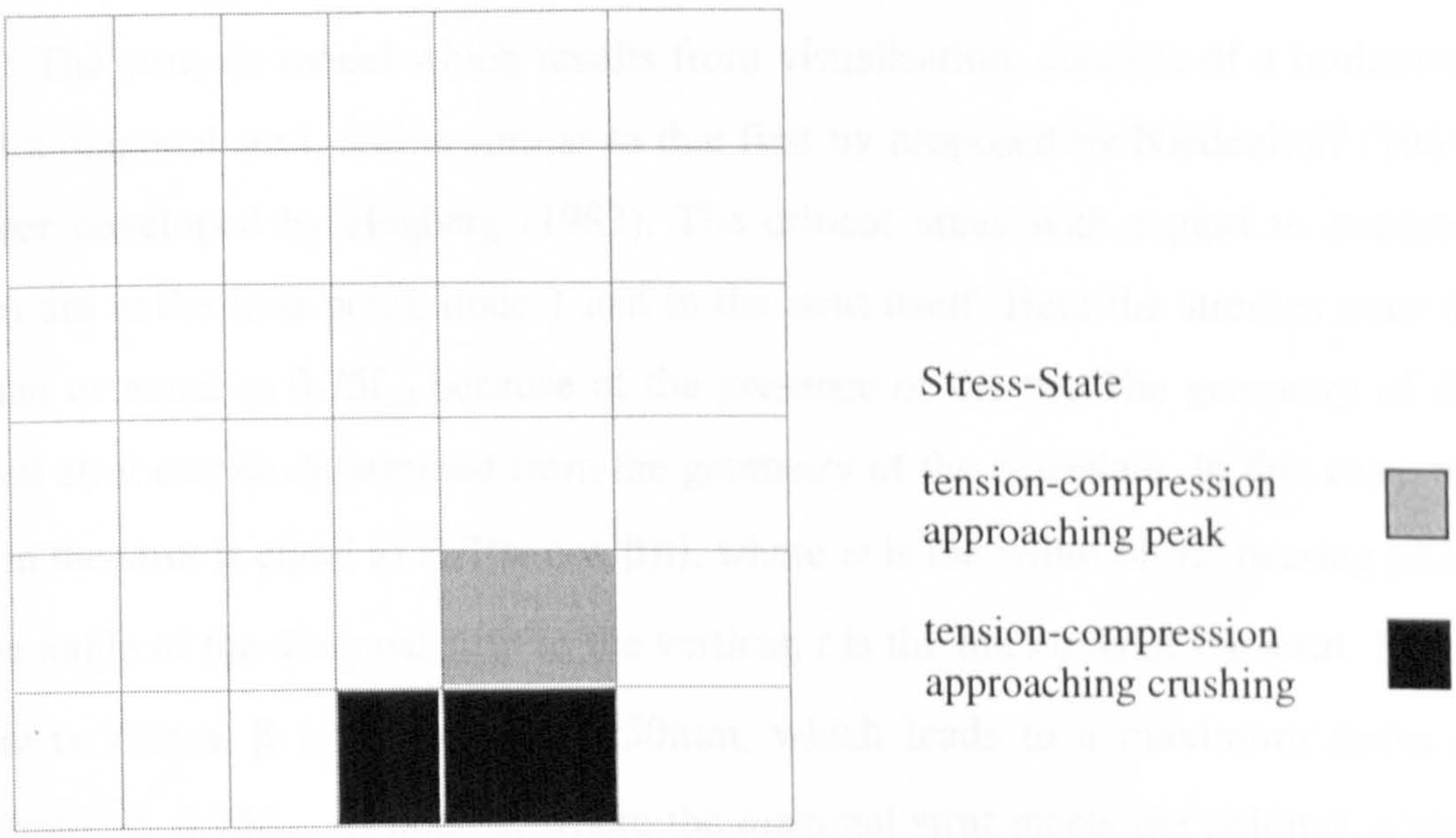

fig.8.2(l) Beam B1 Nodal Zone 1, Principal Stresses at ultimate load

8.3 Corbel C2A

This model was a symmetrical two sided square corbel. Both numerical and physical testing of C2A was carried out. The dimensions and material properties are presented in the table below.

Schematic	Material Properties (Design)	Material Properties (Experimental)
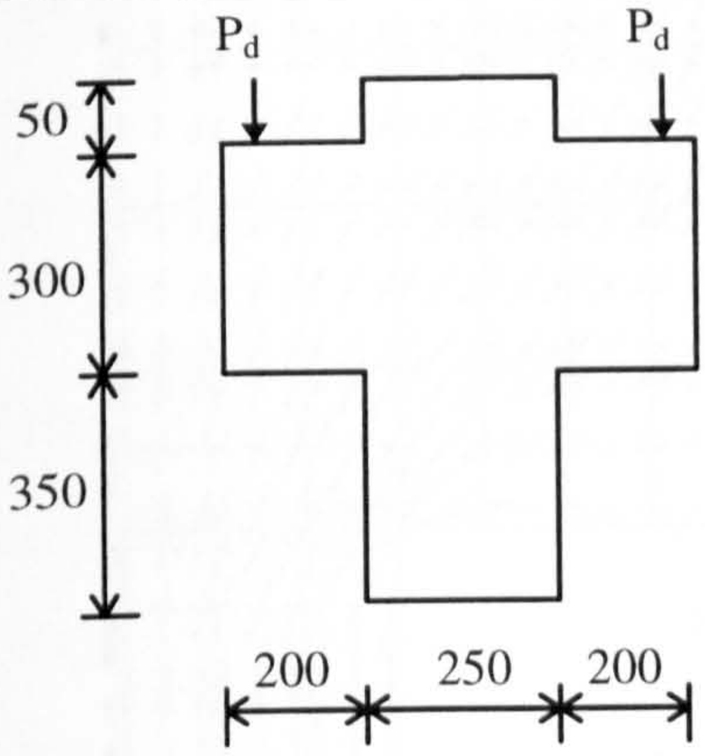	P_d=350kN **concrete:** f_{cu}=50N/mm^2 f_t=3.0N/mm^2 E_c=21.5kN/mm^2 **steel:** f_y=500N/mm^2 E_s=200kN/mm^2 thickness=250mm	**concrete:** f_{cu}=49.8N/mm^2 f_t=3.1N/mm^2 E_c=21.69kN/mm^2 **steel:** f_y=504N/mm^2 (ϕ12) E_s=201.6kN/mm^2 f_y=509N/mm^2 (ϕ8) E_s=214.5kN/mm^2

8.3.1 Strut-Tie Model and Design

The elastic principal stress fields and resulting strut-tie model are presented in figure 8.3(a). The strut-tie model which results from visualisation, consists of a horizontal tie and a diagonal strut, and is similar to that first by proposed by Niedenhoff (1961) and later developed by Hagberg (1983). The critical areas with regard to concrete stresses are at the load point, node 1 and in the strut itself. Here the stresses must be less than or equal to $0.75f_{cd}$ because of the presence of the tie. The geometry of the diagonal strut can be determined from the geometry of the baseplate. In this case, the stress in the strut is equal to $P_d/[(w.\cos^2\beta)t]$, where *w* is the width of the bearing plate, β is the angle of the diagonal strut to the vertical, *t* is the thickness of the strut. In this case, *w* is 75mm, β is 30° and *t* is 250mm, which leads to a maximum stress of 24.9N/mm^2 < $0.75f_{cd}$. At node 2, where the diagonal strut meets the column, a state of bi-axial compression is created and hence the stresses in this node must not exceed $1.1f_{cd}$. The column is designed to carry load in excess of 5 times the corbel loading. Hence it is not necessary to check concrete capacity in nodal zone 2 due to the level of reinforcement provided.

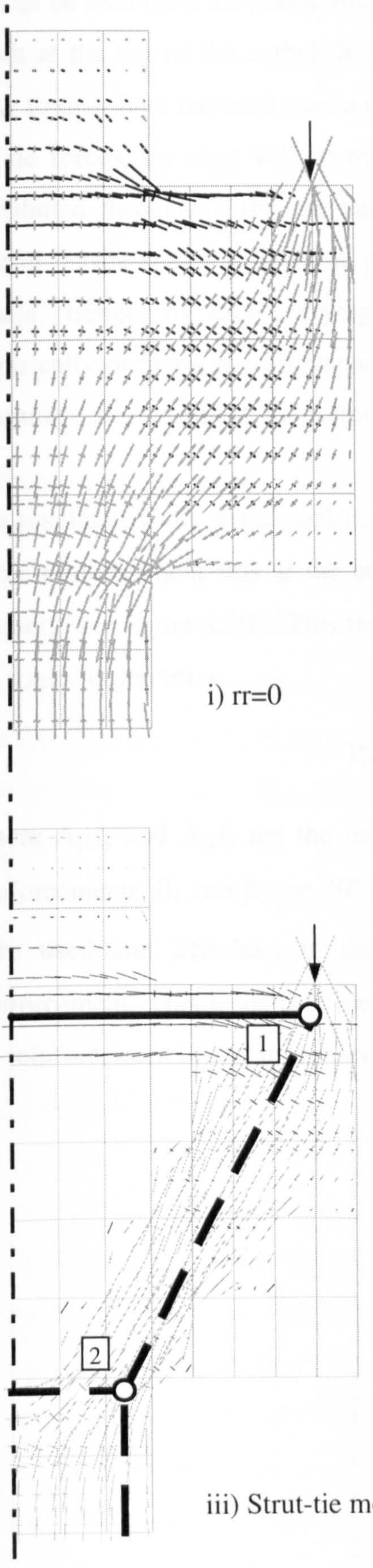

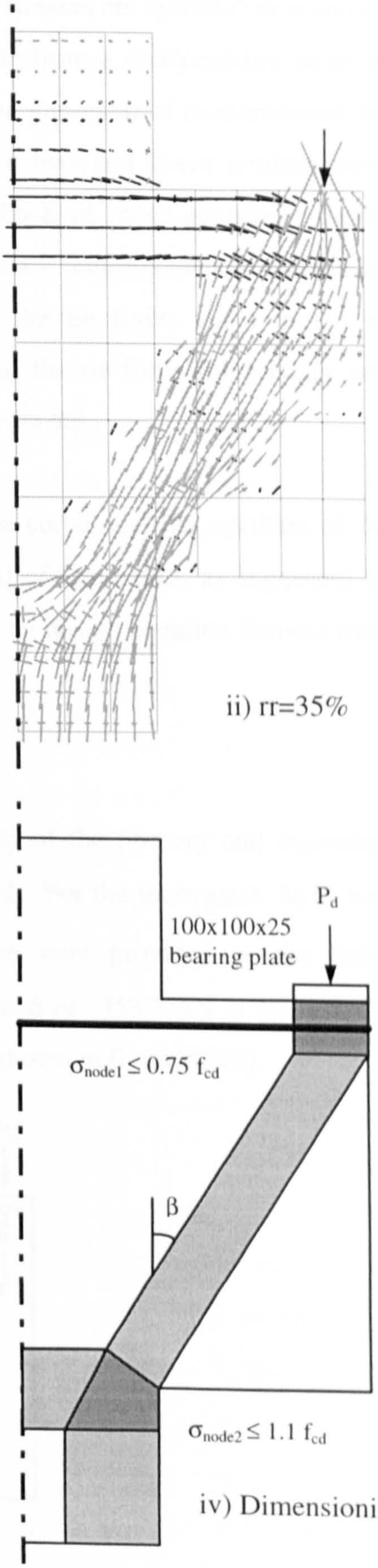

fig.8.3(a) Corbel C2A: Elastic Stress Paths and Strut-tie model

As can be seen from the elastic stress plot, the tensile stresses are spread over a certain depth at the top of the corbel. It is therefore sensible from a serviceability point of view to distribute the steel over a certain depth. In the provision of reinforcement for the tie forces, the steel will be made up of the main bars and lower reinforcement distributed throughout the top half of the corbel. Each of these contribute to the overall tensile strength. Both the primary and secondary reinforcement contribute to tensile strength by each carrying a proportion of the tie force. As a means of empirically deriving the corresponding proportion of the tie force for primary and secondary reinforcement, the following procedure is adopted.

The resultant of the main steel acts at the top of the corbel and the resultant of the lower reinforcement acts at the end of the top third of the corbel, as suggested by Hagberg, see figure 8.3(b). This results in the following design equation derived from the statics of the truss:

$$P_d = \frac{A_{s1} f_y}{\tan\beta_1} + \frac{A_{s2} f_y}{\tan\beta_2}$$

Where $A_{s1}f_y$ and $A_{s2}f_y$ are the tensile force capacity of the primary and secondary reinforcements, β_1 and β_2 are 30° and 40° respectively. For the main steel, 3ϕ12 bars were used and 2ϕ8 bars in the form of stirrups were provided as the lower reinforcement. This leads to a theoretical ultimate load of 353.73kN > 350 kN, P_d. the reinforcement layout in the designed structure is shown in figure 8.3(d).

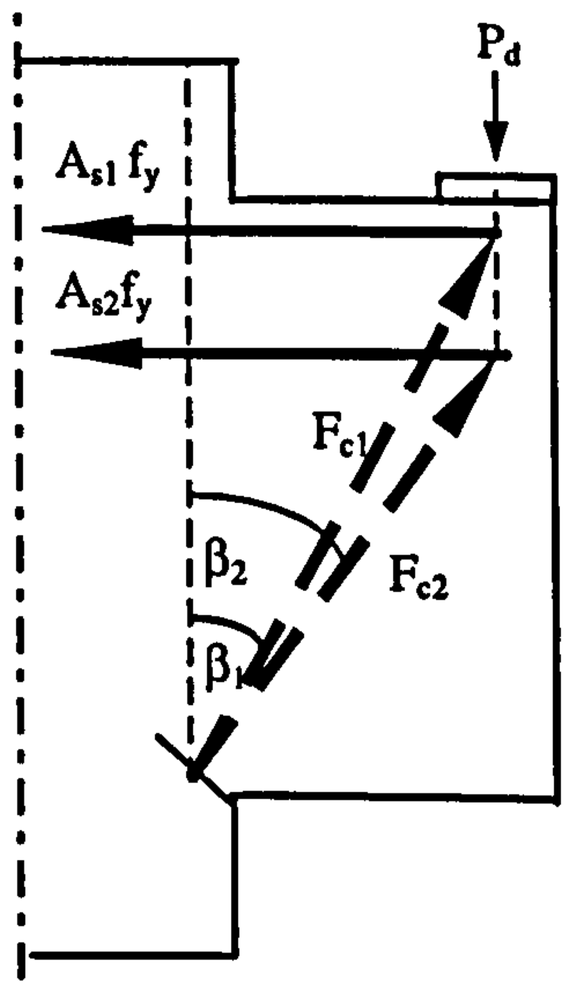

fig.8.3(b) Dimensioning of Ties

8.3.2 Numerical and Physical Testing

During testing, the load was applied in 25kN increments. The experimental ultimate total load of the corbel was recorded as 827kN, ($1.18P_d$) which compared well with the numerical ultimate total load of 805kN, ($1.15P_d$). As with all subsequent numerical analysis, the experimental material strengths were used. The first cracks occurred at 125kN, ($0.18P_d$) in the upper corbel, at the tie-column junction, see fig.8.3(e). The largest of these initial cracks was 0.05mm wide. These cracks gradually propagated up towards the column. At a load of 375kN, ($0.53\ P_d$), new cracks formed around the bearing plate, running upwards diagonally toward the centre of the column. The largest of these cracks was 0.15mm wide. The service crack limit width of 0.3mm was first reached in the cracks around the tie-column junction at a load of 550kN, ($0.78\ P_d$).

The steel strains obtained from the gauges are plotted together with the corresponding numerical values see fig.8.3(g-i). Failure in the corbel was initiated by yielding of the main steel at 770kN, ($1.1P_d$). The lower reinforcement in the tension zone also began to yield at this point, fig.8.3(i). A good agreement was achieved with the numerical and experimental steel strains. Subsequent straining of the main tension steel led to widening of the diagonal cracks, as can be seen from the Demec readings in figure 8.3(f). Figures 8.3(j-k) show the crack patterns at ultimate load.

The idealised stress distribution in nodal zone 1 is represented in figure 8.3(n) and the numerical compressive stresses are shown for the areas of highest compression in figure 8.3(o-p). As in the strut-tie model, the effective strength of the concrete is nowhere exceeded. The greatest compressive stress, $0.95f_{cu}$, occurred at the diagonal strut-column junction at ultimate load. This was due to the stress concentration brought about by the sharp change in geometry, i.e. right angle corner. In practice, it is common for the lower corbel edge to approach the column at an angle. This has the effect of reducing the stress concentration at the column corbel junction and was utilised in subsequent corbel designs C3A and C4A. Along the diagonal strut, the numerical compressive stresses are no greater than $0.55f_{cu}$, which is similar to the strut tie model prediction of $0.5f_{cu}$, $24.9N/mm^2$.

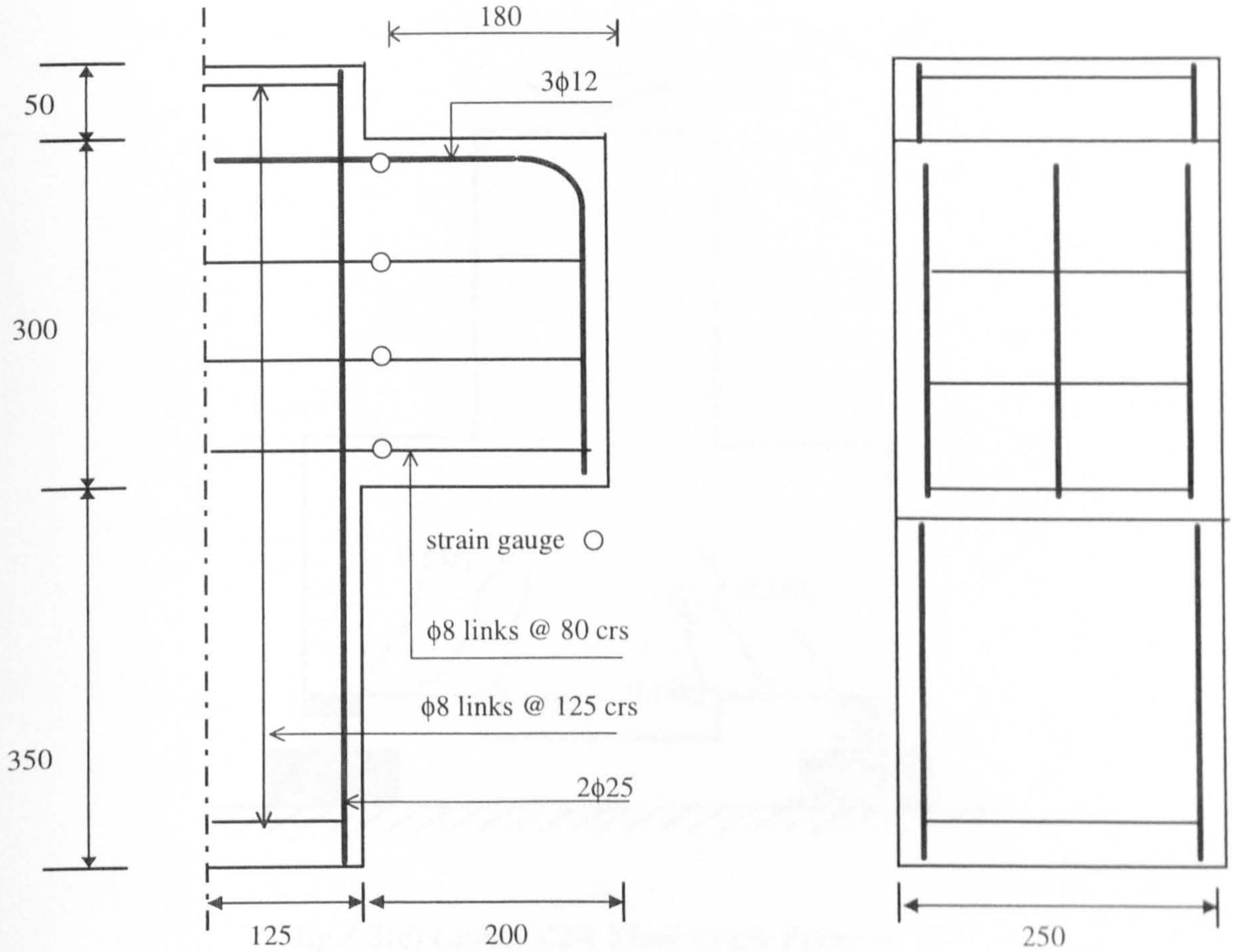

i) elevation ii) side elevation

fig.8.3(c) Corbel C2A, all sizes in mm, cover 20mm

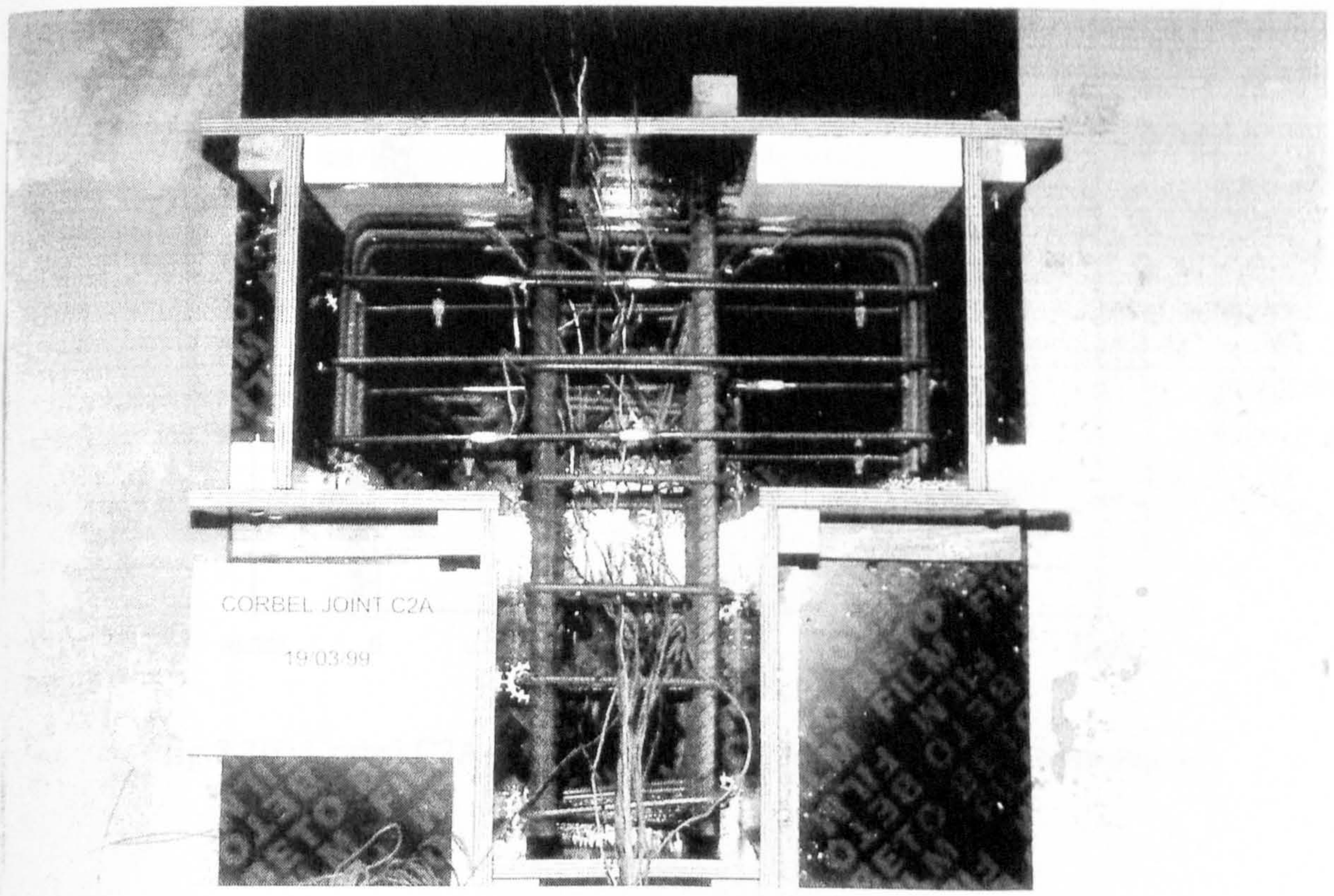

fig.8.3(d) Corbel C2A: Reinforcement & Formwork

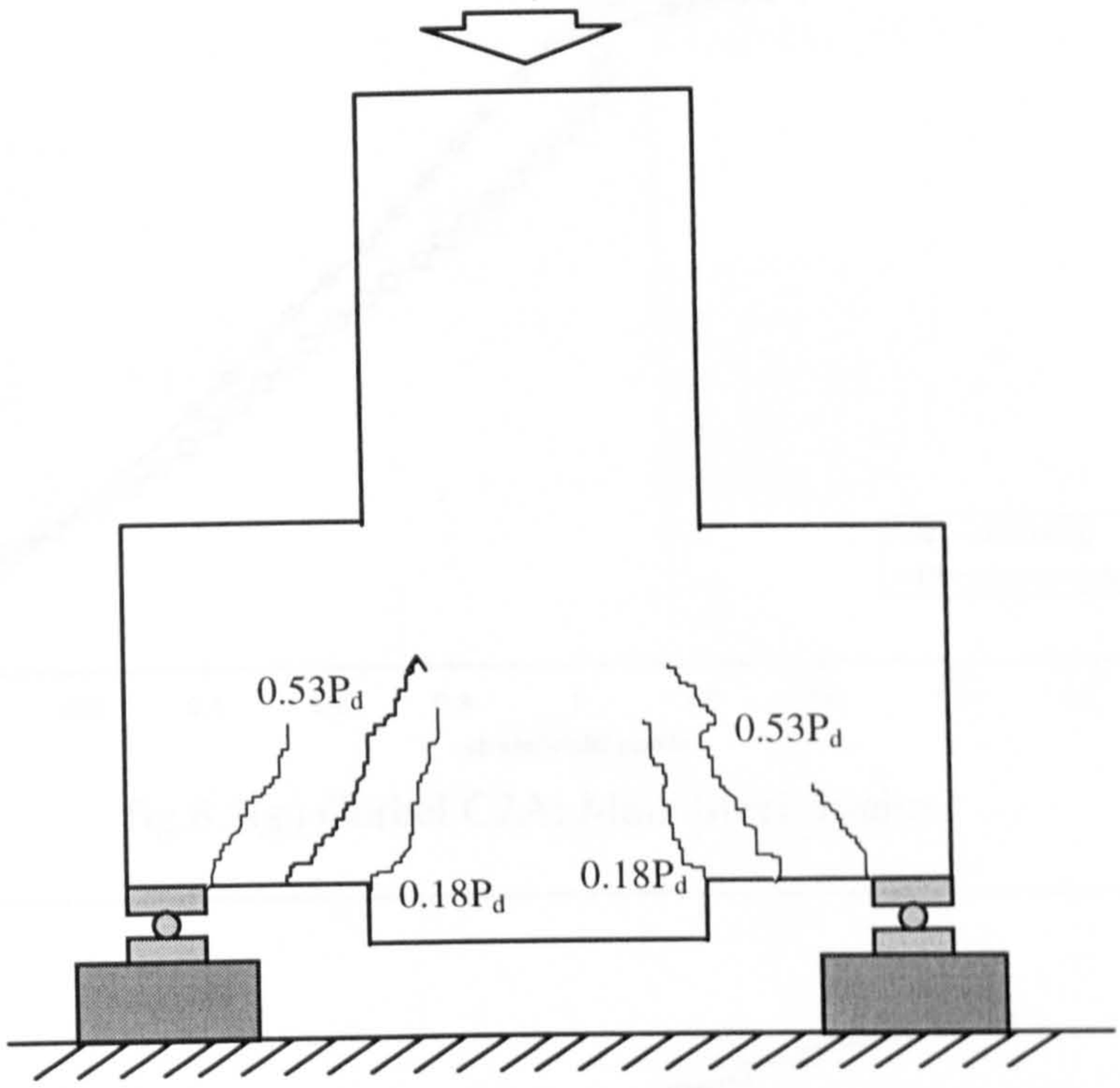

fig.8.3(e) Corbel C2A Main Crack Patterns

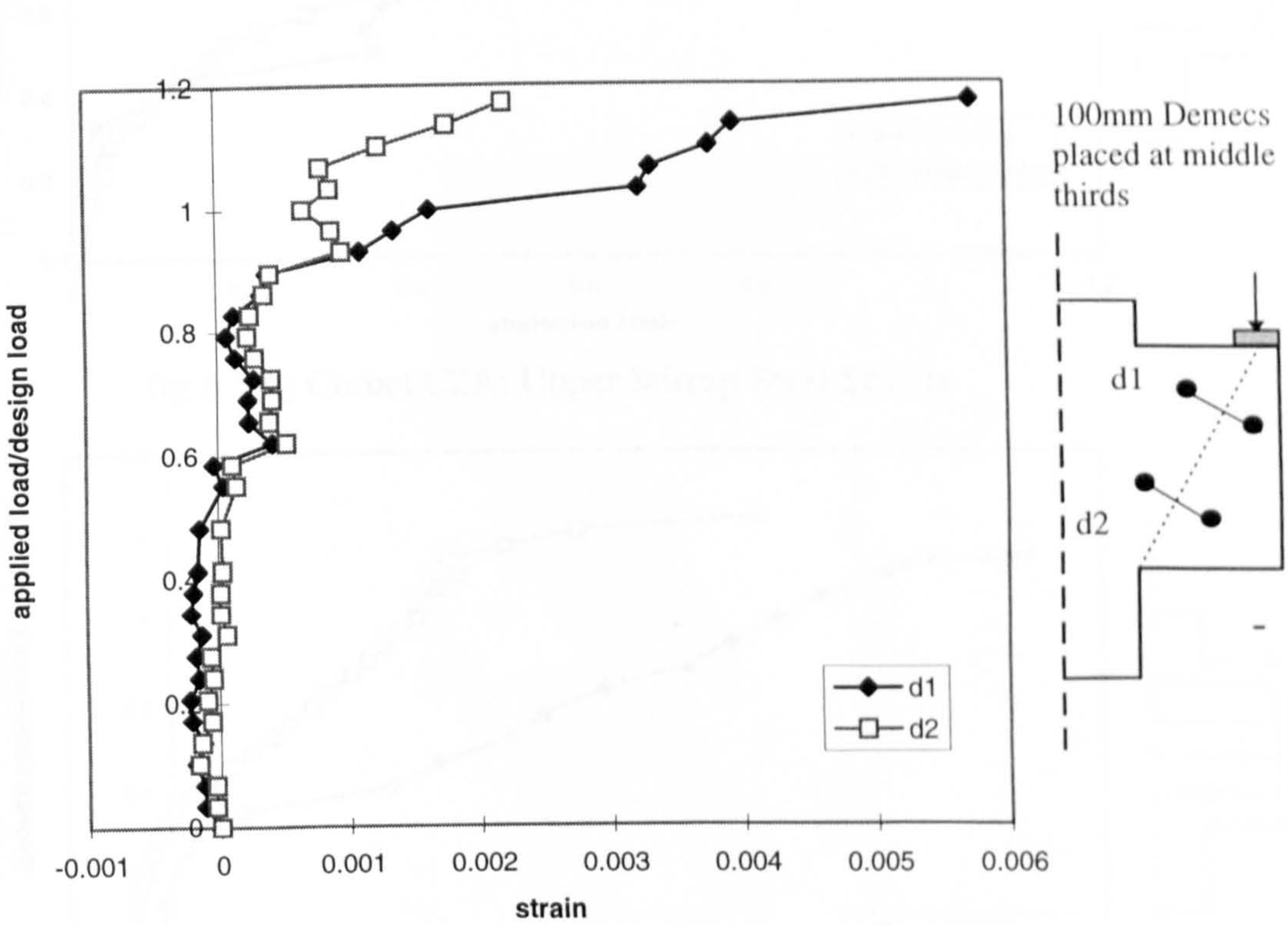

fig.8.3(f) Corbel C2A Demec Readings, +ve. tensile, -ve. compressive

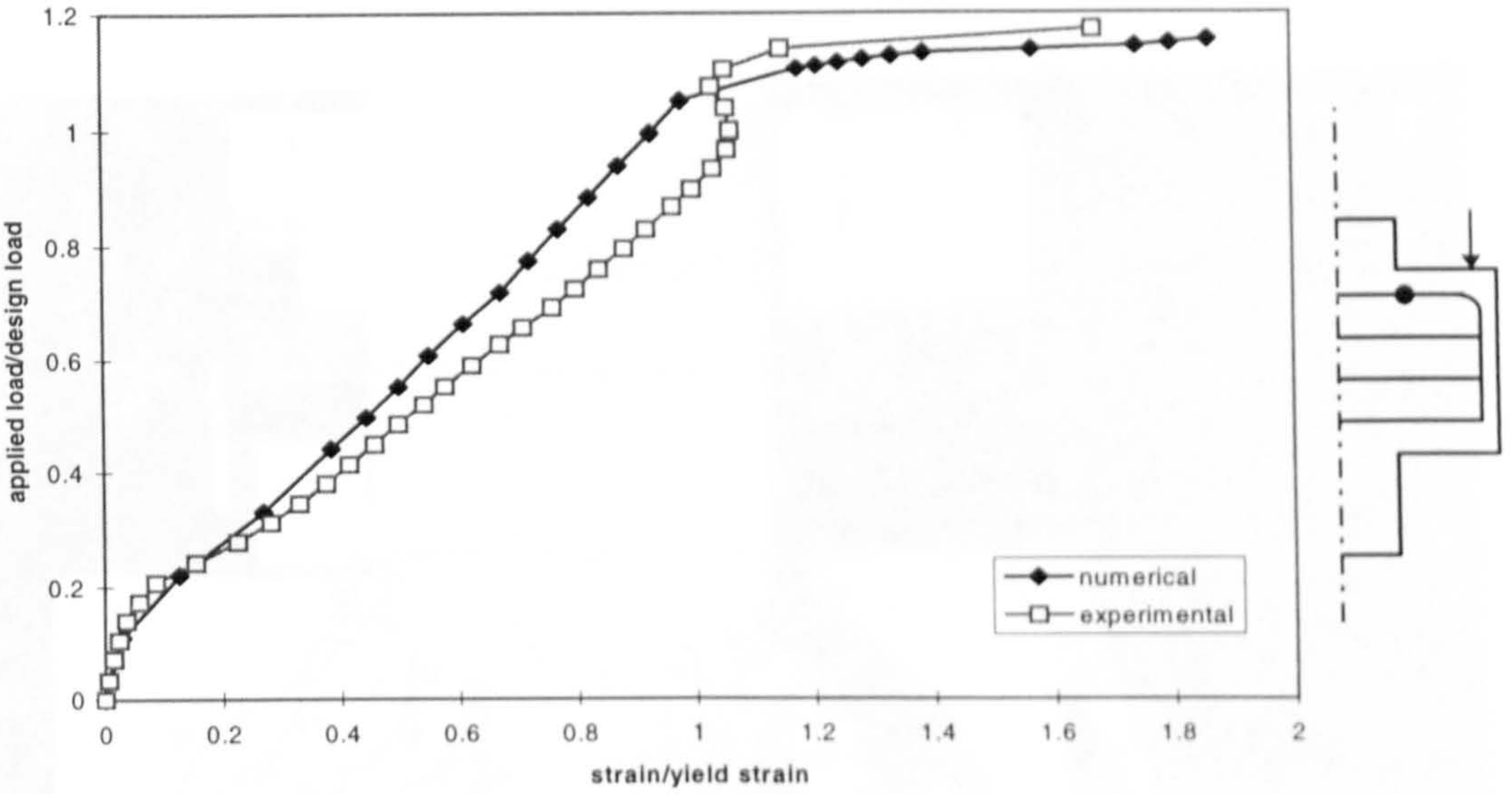

fig.8.3(g) Corbel C2A: Main Steel Strains

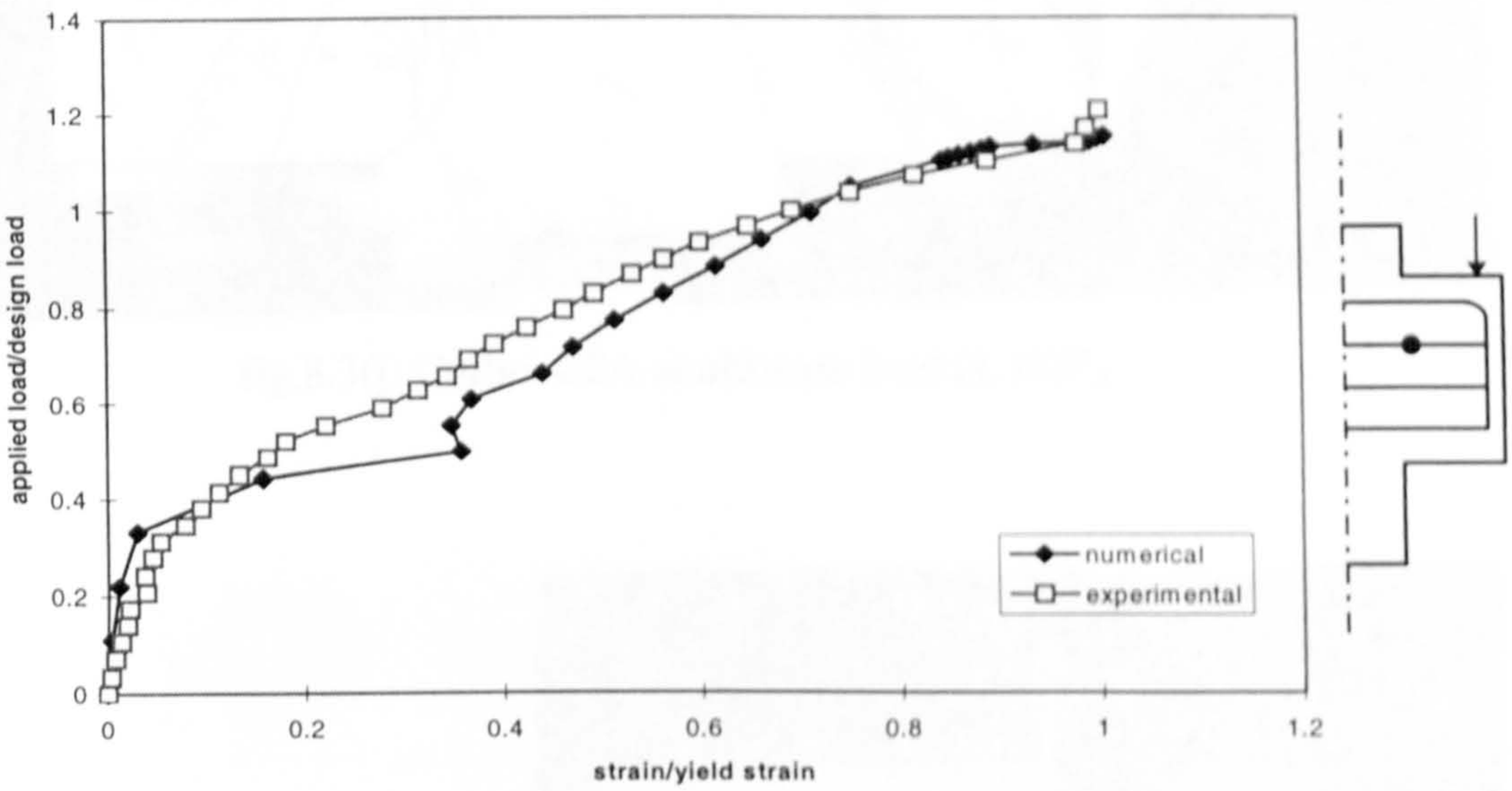

fig.8.3(h) Corbel C2A: Upper Stirrup Steel Strains

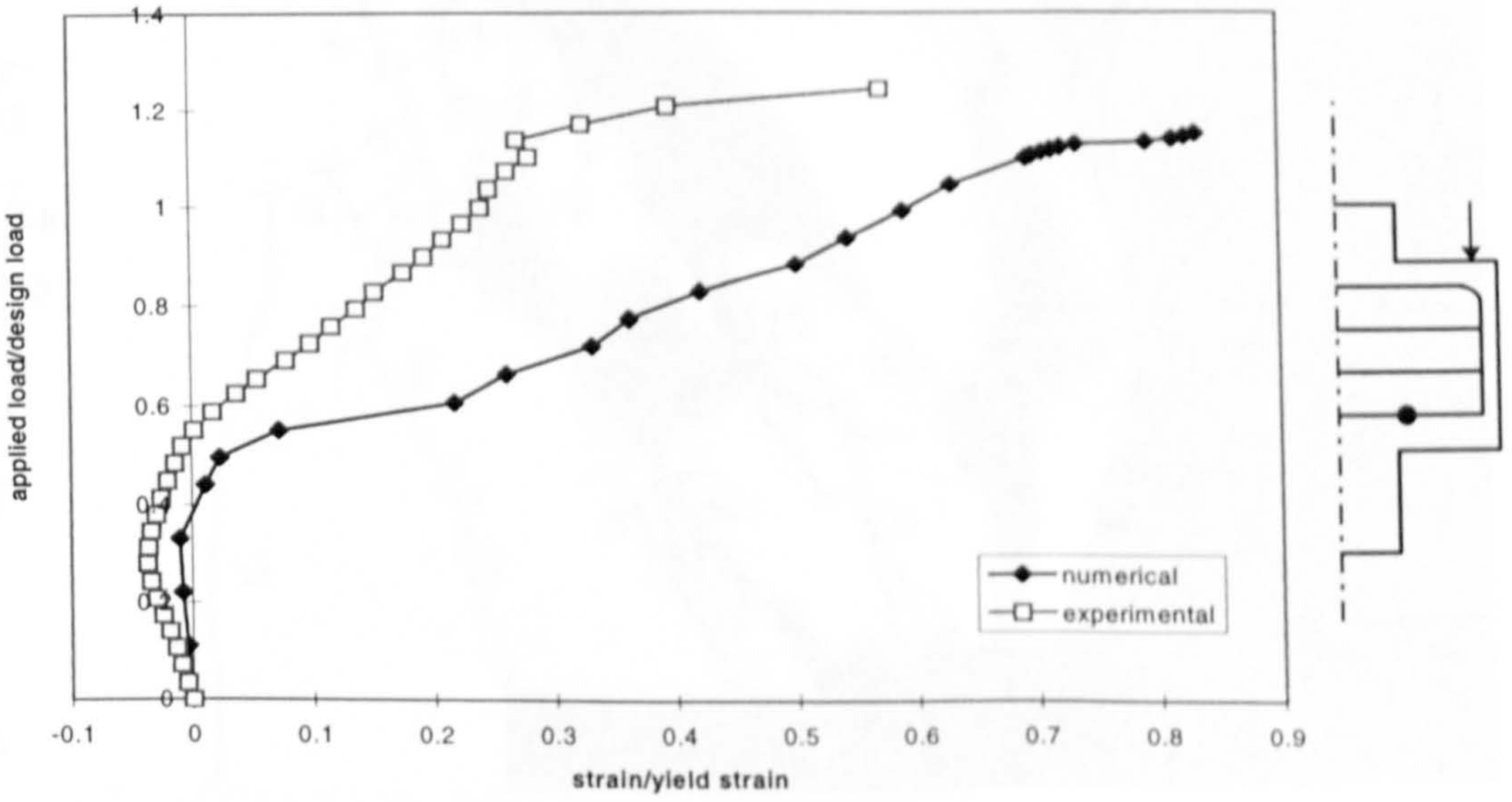

fig.8.3(i) Corbel C2A: Lower Stirrup Steel Strains

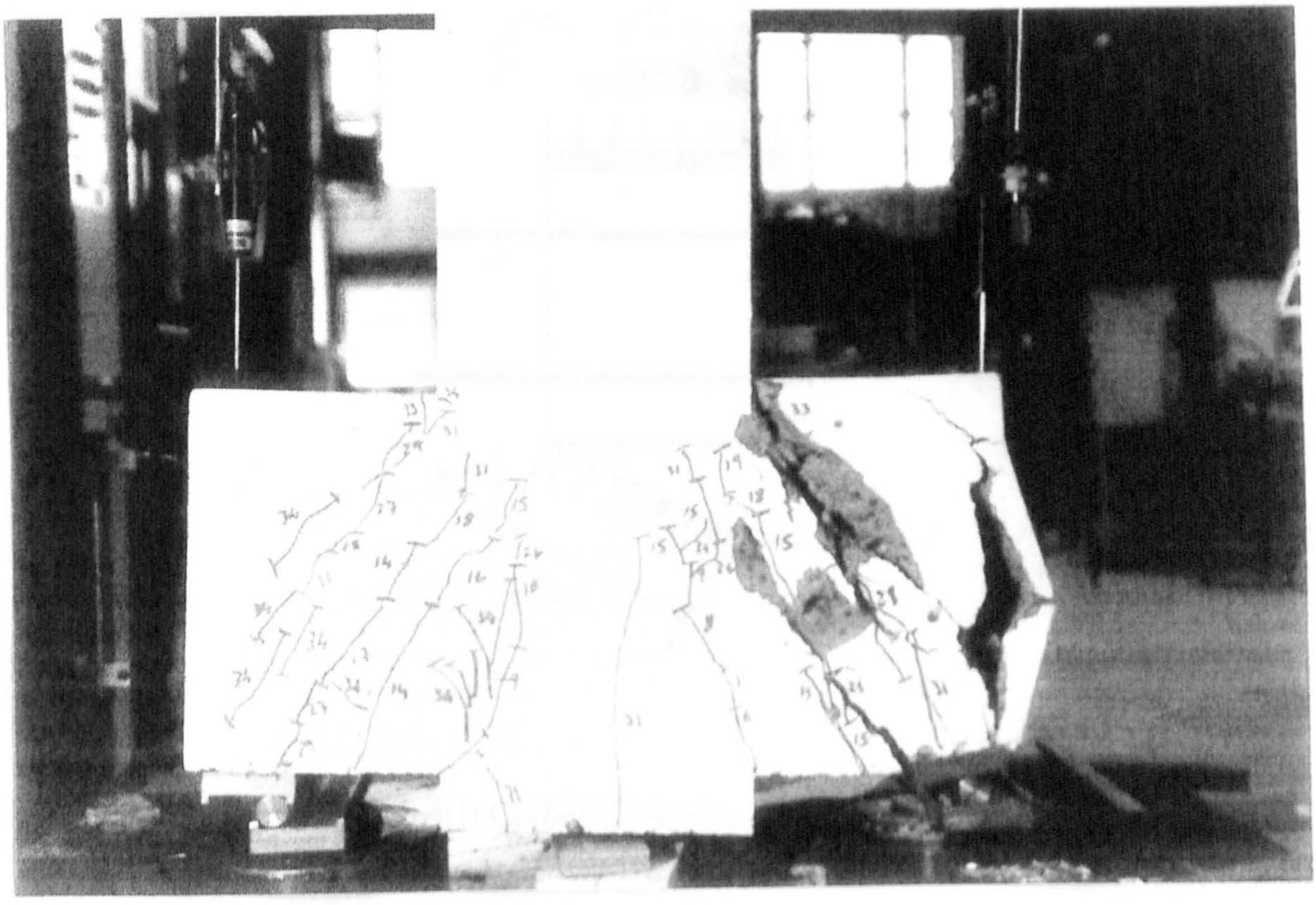

fig.8.3(j) Corbel C2A at ultimate load $(1.18)P_d$

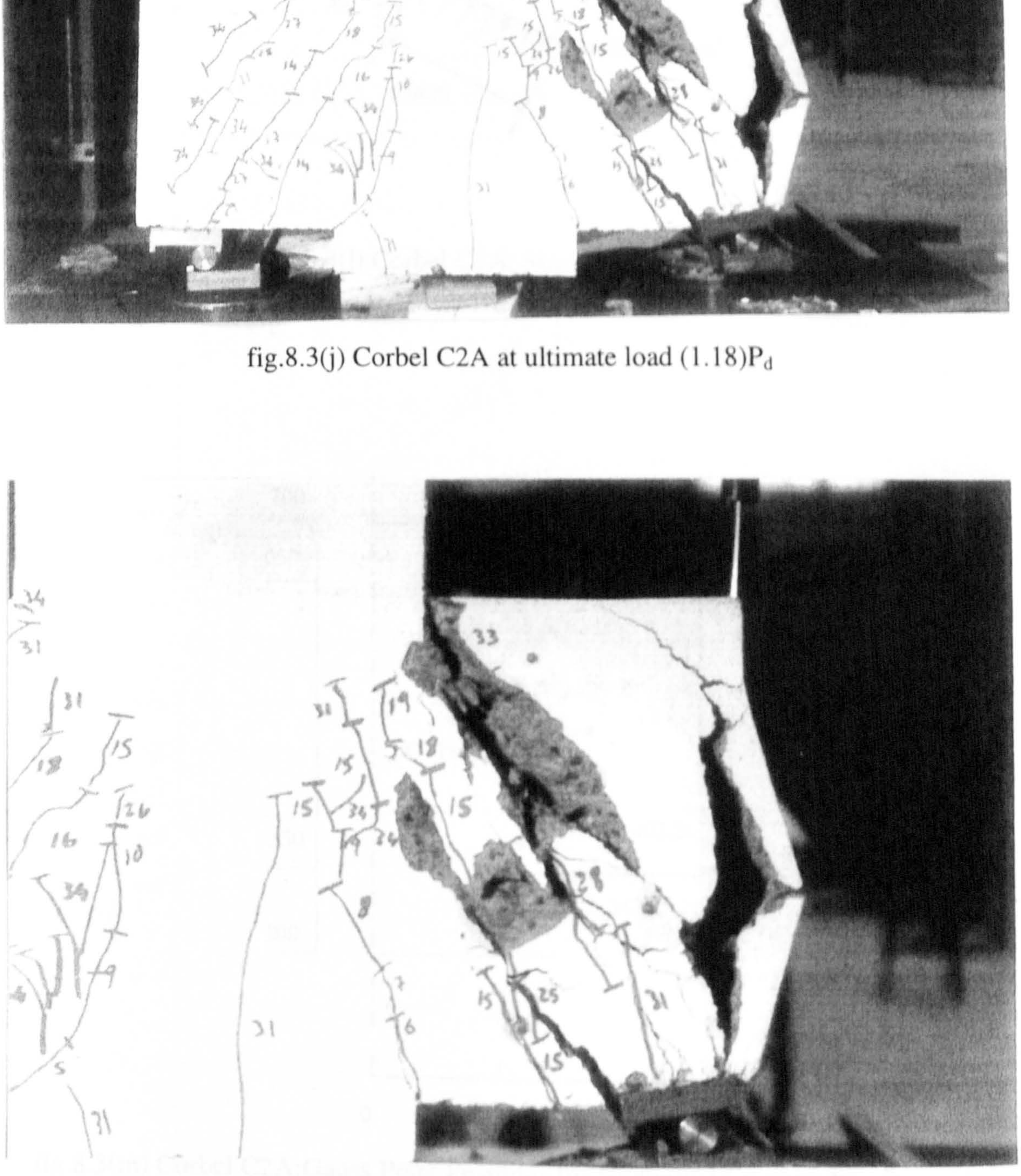

fig.8.3(k) Corbel C2A at ultimate load $(1.18)P_d$

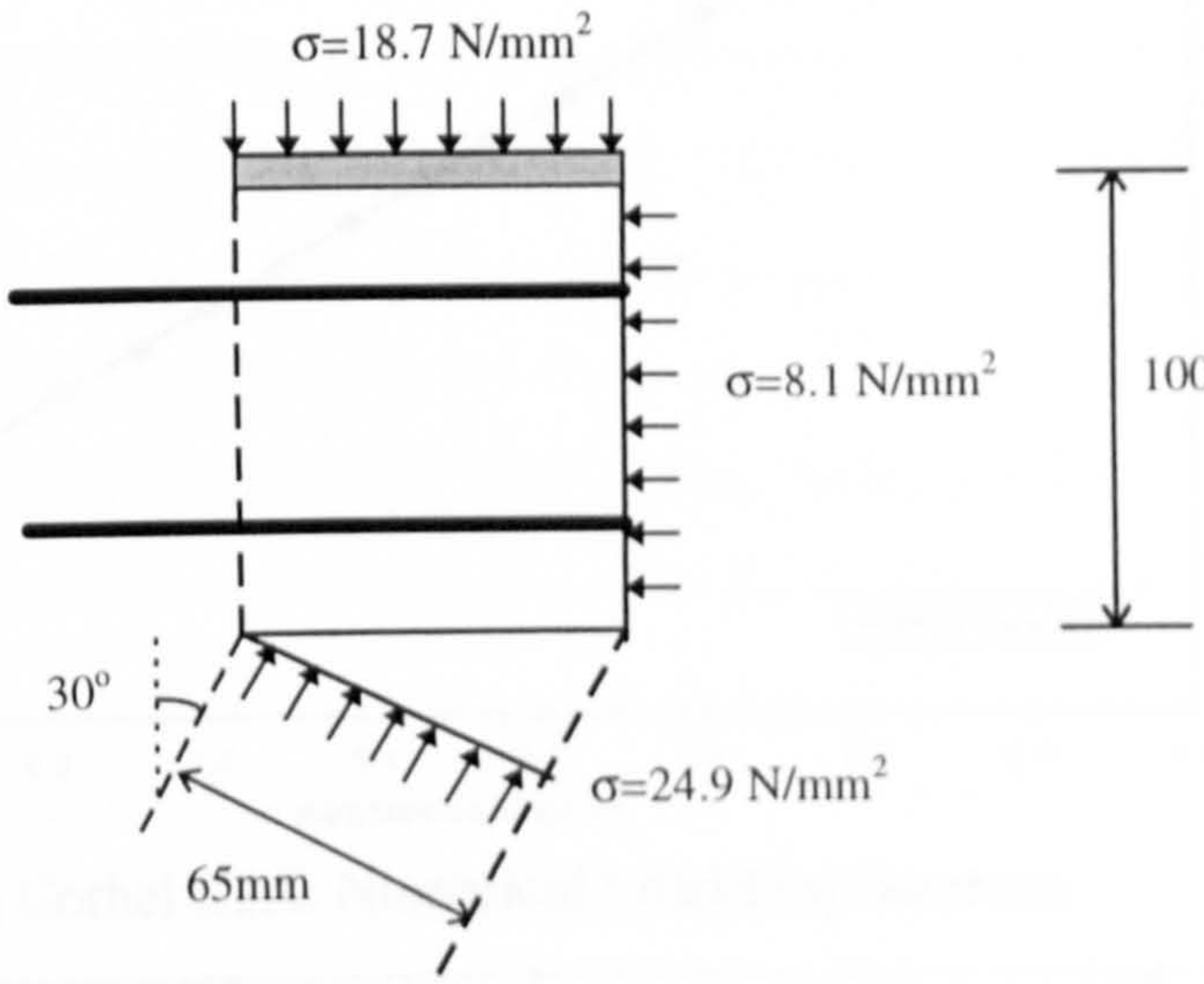

fig8.3(l) Corbel C2A: Stresses in Node 1

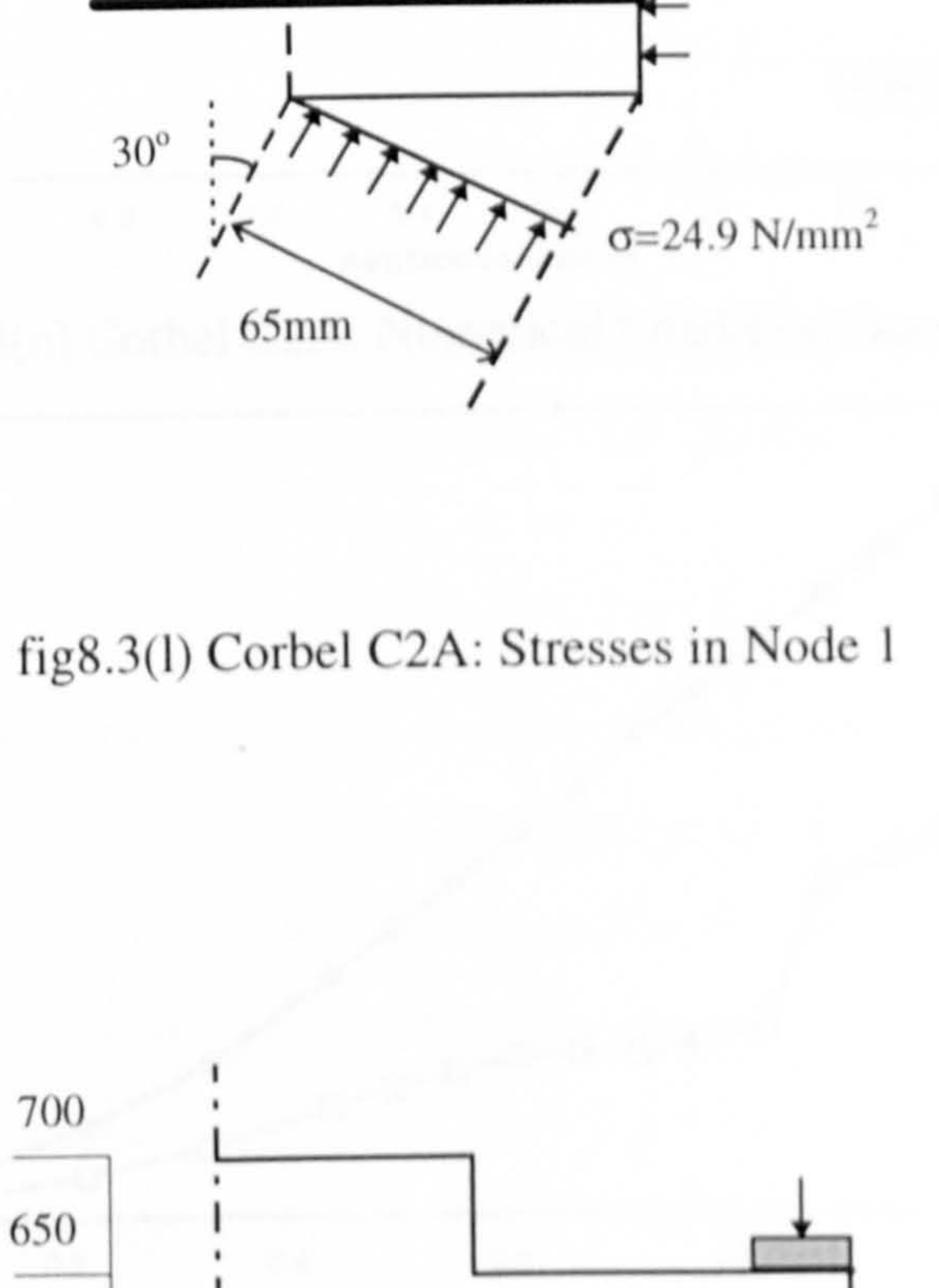

fig.8.3(m) Corbel C2A:Gauss Point Positions for Numerical Compressive Stresses

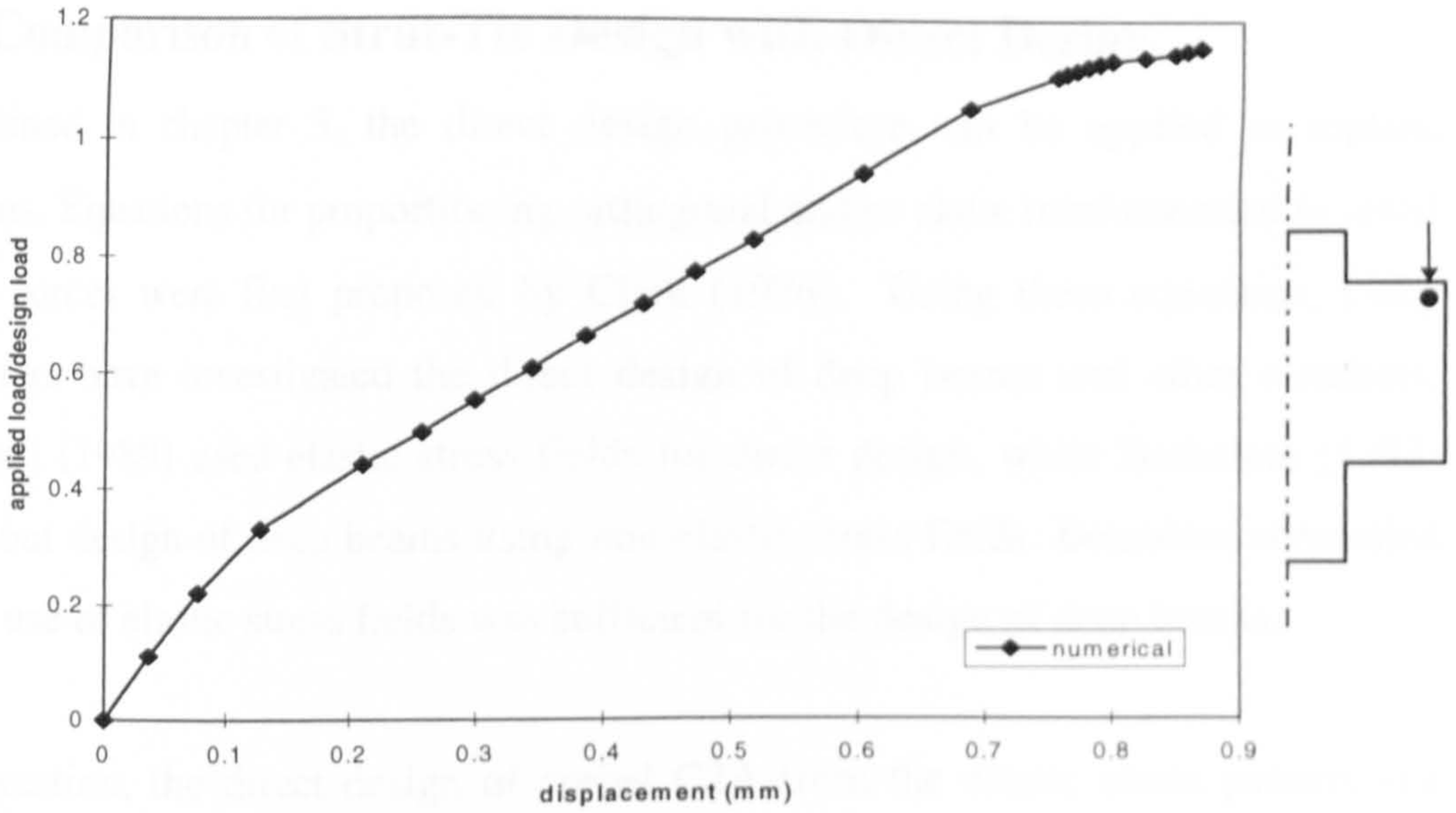

fig.8.3(n) Corbel C2A: Numerical Load-Displacement

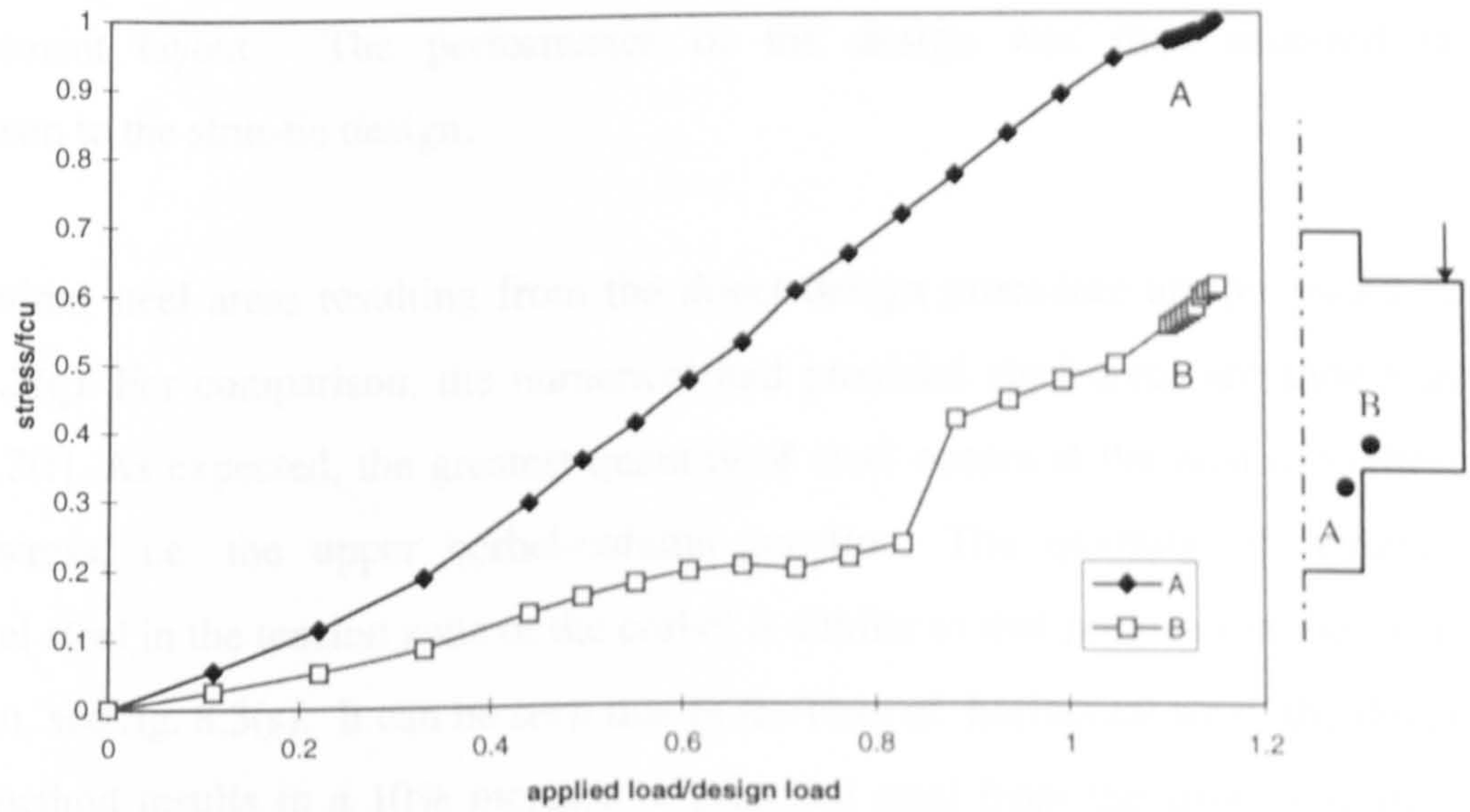

fig.8.3(o) Corbel C2A: Numerical Compressive stresses

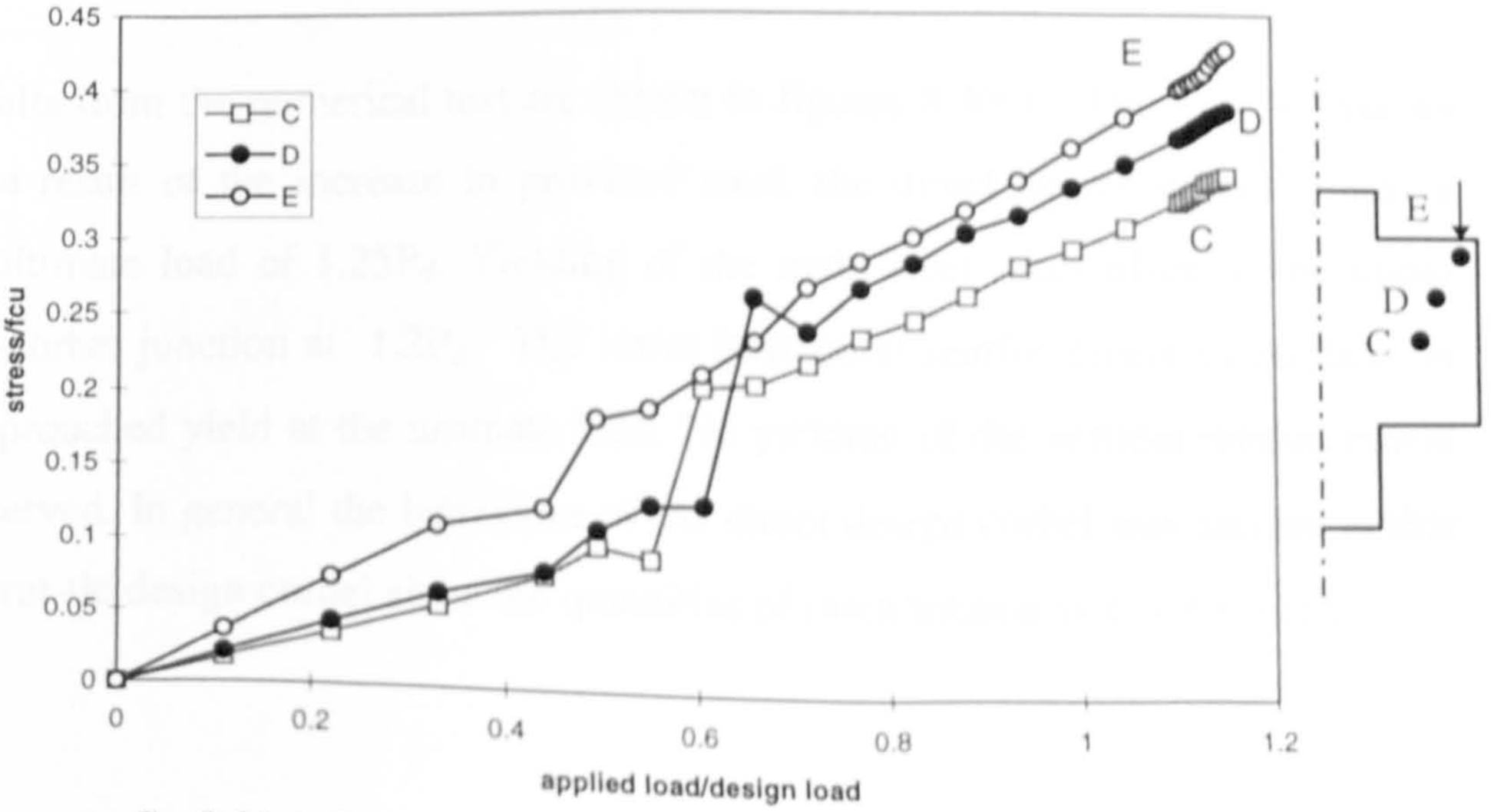

fig.8.3(p) Corbel C2A Numerical Compressive Stresses

8.3.3 Comparison of Strut-Tie Design with Direct Design

As outlined in chapter 3, the direct design procedure can be applied to inplane situations. Equations for proportioning orthogonal and/or skew reinforcement to resist inplane forces were first proposed by Clark (1976). Using these equations, many researchers have investigated the direct design of deep beams and other members. Khaskheli (1989) used elastic stress fields for direct design, while Bensalem (1993) carried out design of deep beams using non-elastic stress fields. Bensalem concluded that the use of elastic stress fields was sufficient for the design of deep beams.

In this section, the direct design of corbel C2A from the elastic stress pattern, (i.e rr=0) is carried out. The procedure described in chapter 3 was used to derive the reinforcement layout. The performance of the design was then assessed in comparison to the strut-tie design.

The required steel areas resulting from the direct design procedure are presented in figure 8.3(q). For comparison, the numerical and provided steel areas are shown in figure 8.3(r). As expected, the greatest quantity of steel occurs at the area of highest tensile stress, i.e. the upper corbel-column junction. The quantity of required horizontal steel in the tension zone of the corbel is similar to that provided in the strut-tie design, see fig. 8.3(s). It can be seen that in the case of horizontal steel, the direct design method results in a 10% increase in provided steel from the strut-tie design. Secondly, direct design also results in the provision of some vertical steel.

The results from the numerical test are shown in figures 8.3(t-v). Figure 8.3(t) shows that as a result of the increase in provided steel, the direct design corbel attains a higher ultimate load of $1.25P_d$. Yielding of the main steel takes place at the upper column-corbel junction at $1.2P_d$. The lower horizontal reinforcement in the tension zone approached yield at the ultimate load. No yielding of the vertical reinforcement was observed. In general the behaviour of the direct design corbel was similar to that of the strut-tie design corbel since the quantities of main tension steel were similar.

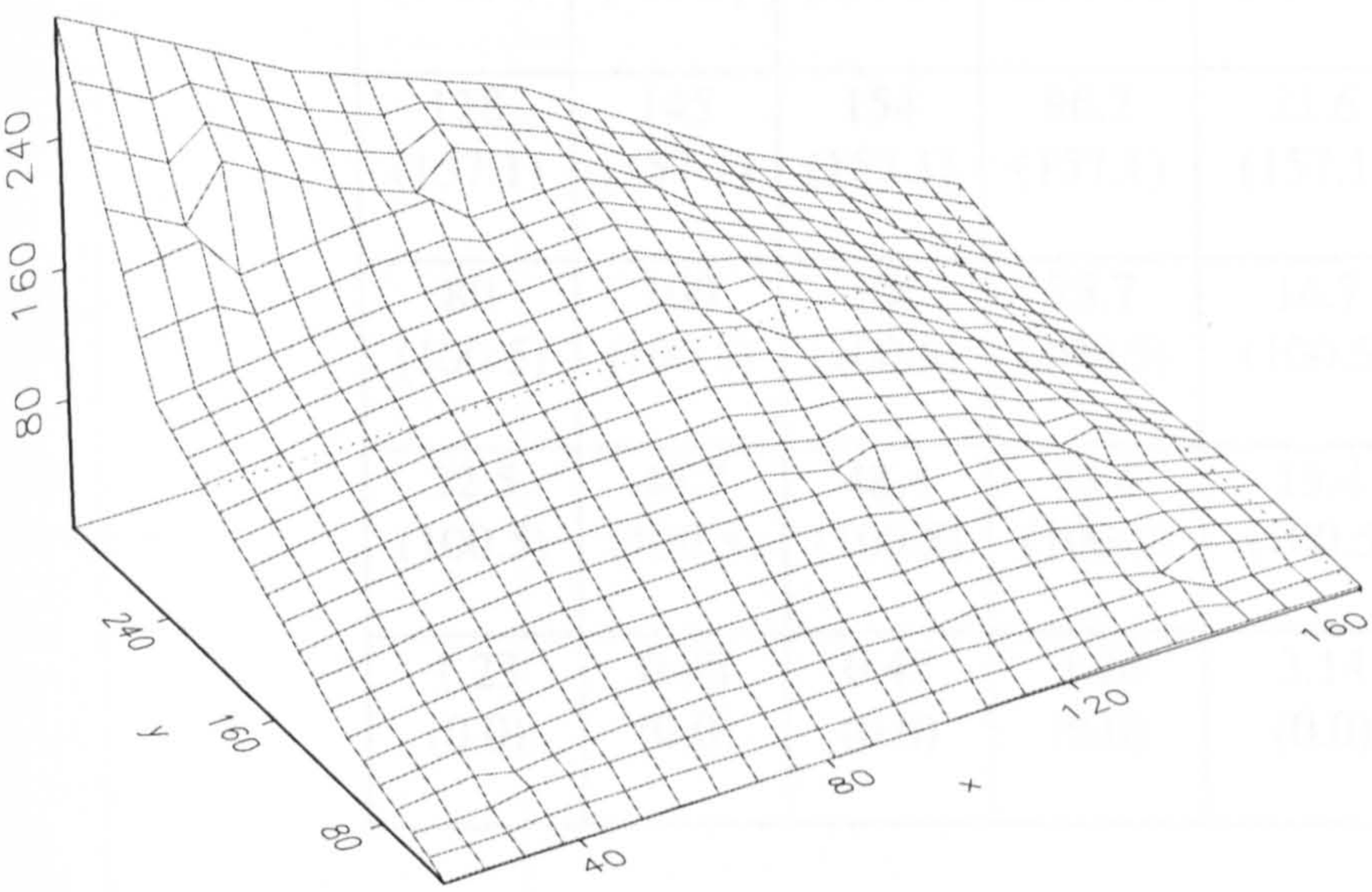

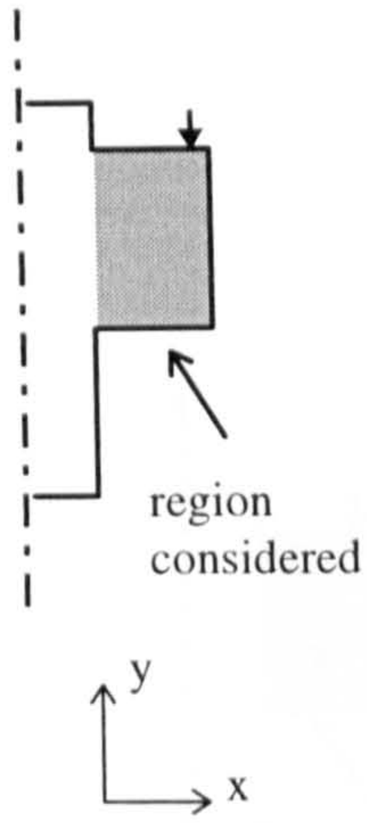

i) A_{sx} (rr=0)

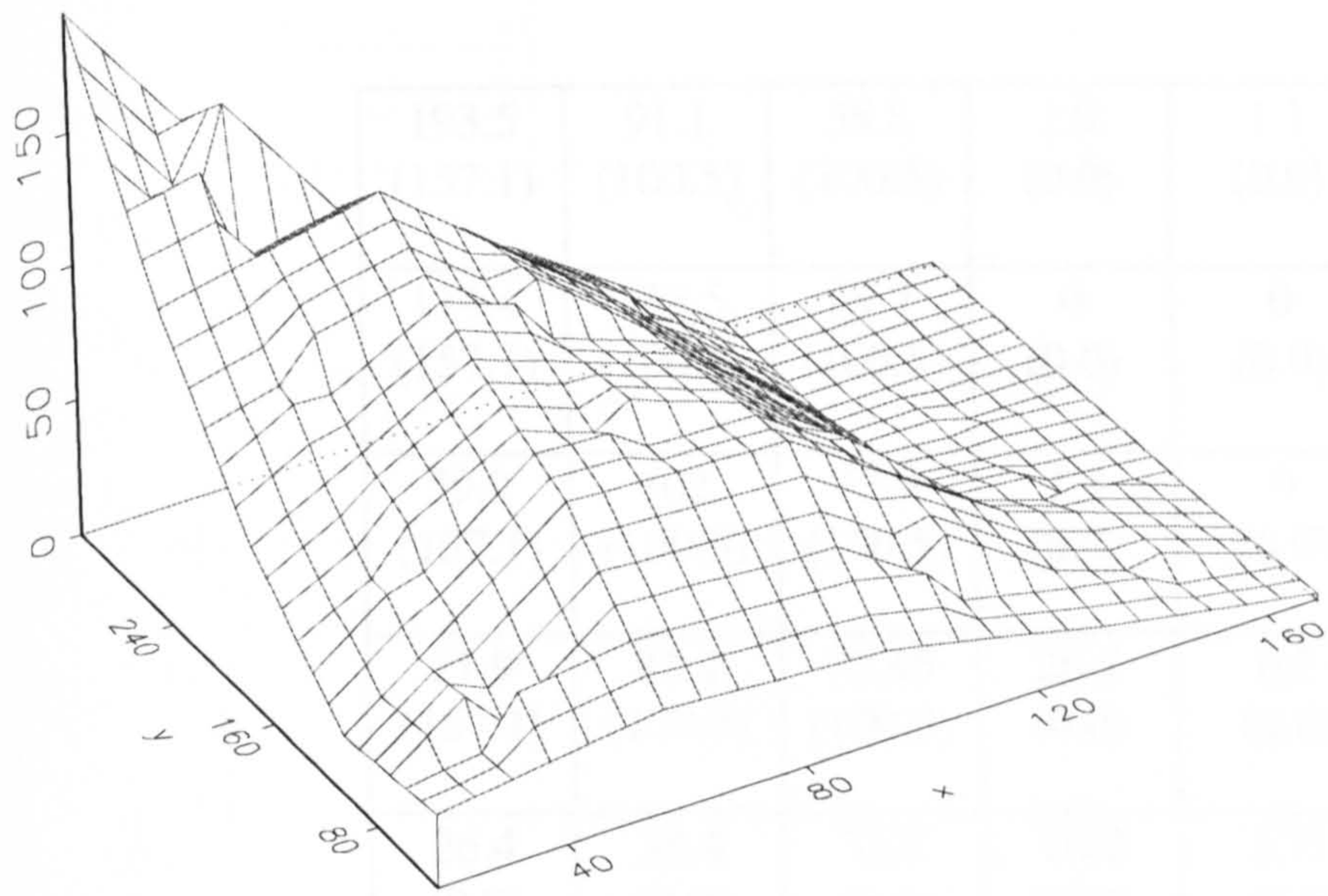

ii) A_{sy} (rr=0)

fig.8.3(q) Corbel C2A: Numerical Steel Areas Resulting from Direct Design, (mm^2)

313 (339.3)	240 (339.3)	191 (339.3)	110 (339.3)	50.2 (339.3)
128 (157.1)	145 (157.1)	154 (157.1)	96.2 (157.1)	21.6 (157.1)
80 (100.5)	100 (100.5)	106 (100.5)	75.7 (100.5)	14.7 (100.5)
32.5 (100.5)	46.7 (100.5)	48.4 (100.5)	43.6 (100.5)	13.4 (100.5)
1.23 (0.0)	0.98 (0.0)	0.47 (0.0)	3.36 (0.0)	3.14 (0.0)

(i) A_{sx} (rr=0)

193.5 (157.1)	91.1 (100.5)	58.8 (100.5)	1.9 (0.0)	1.1 (0.0)
114.4 (157.1)	133.5 (100.5)	69.7 (100.5)	0 (0.0)	0 (0.0)
59.9 (157.1)	102 (100.5)	73.9 (100.5)	7.9 (0.0)	0 (0.0)
21.9 (157.1)	82.2 (100.5)	78.45 (100.5)	26.5 (0.0)	0.2 (0.0)
26.4 (0.0)	38.4 (0.0)	33.8 (0.0)	16.2 (0.0)	2.71 (0.0)

(ii) A_{sy} (rr=0)

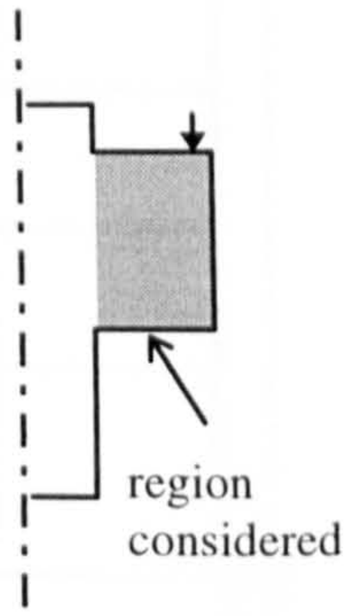

fig.8.3(r) Corbel C2A Numerical and (Provided) Steel Areas (mm^2)

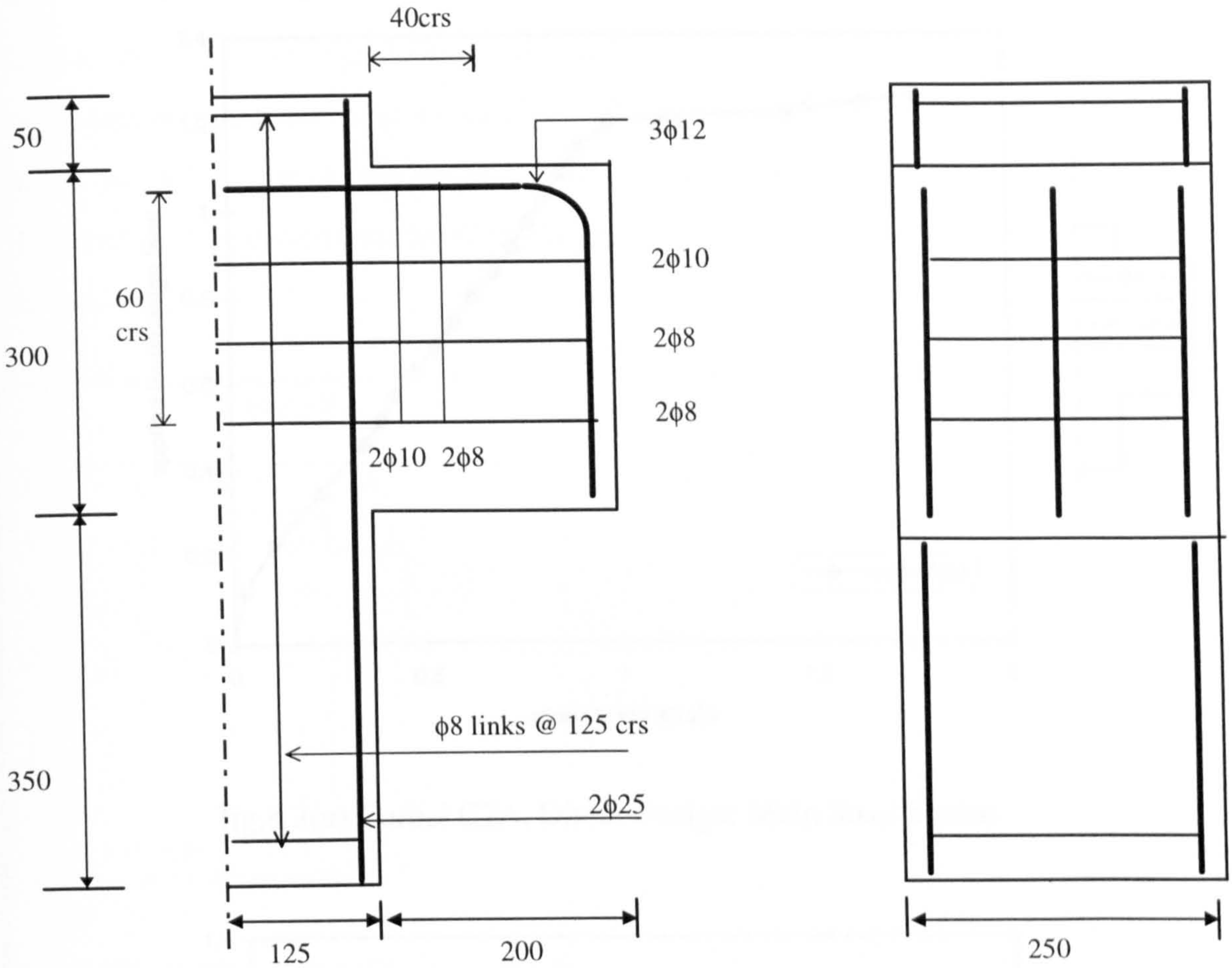

i) elevation ii) side elevation

fig.8.3(s) Corbel C2A, Direct Design: Steel Layout

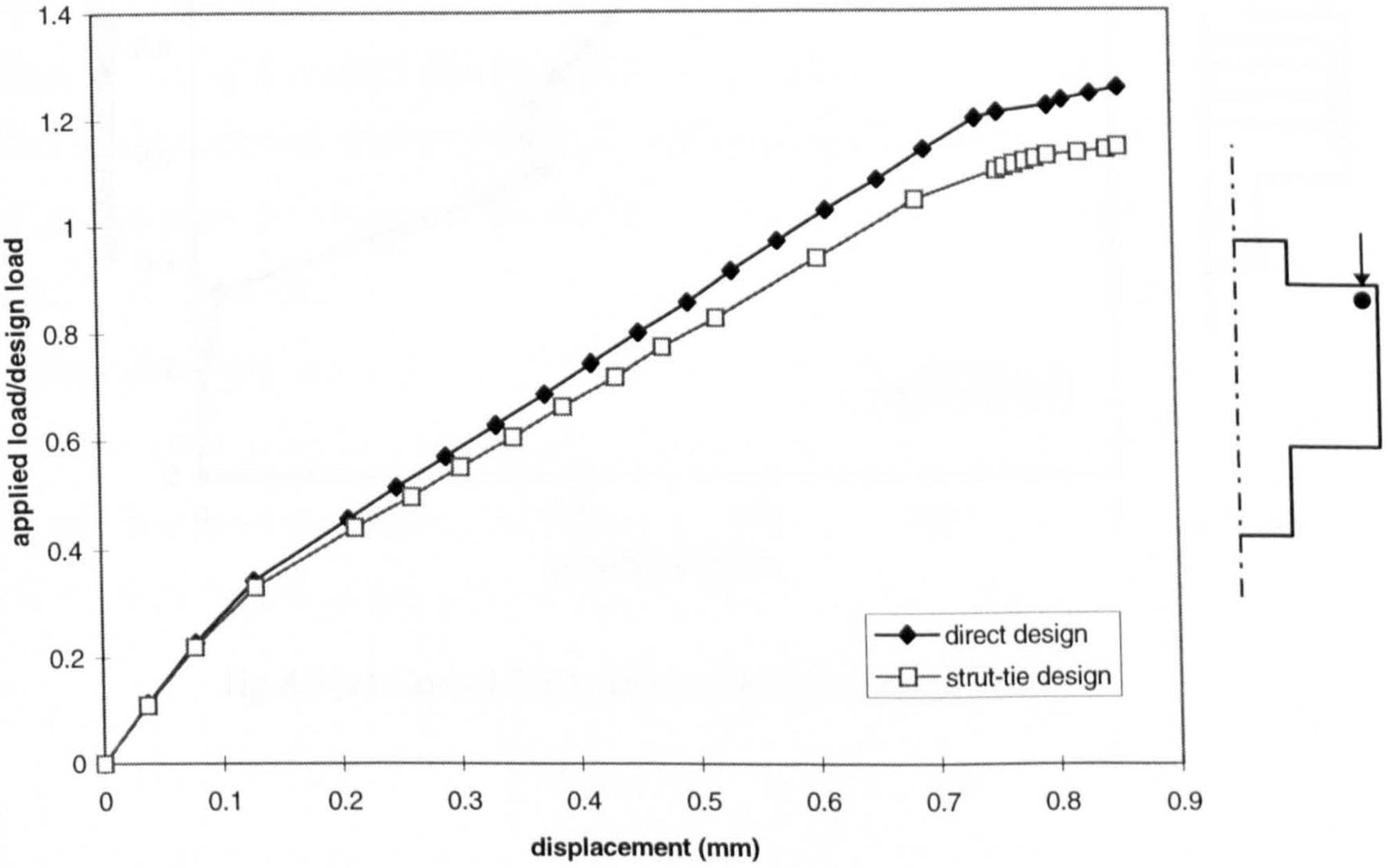

fig.8.3(t) Corbel C2A: Comparison of Direct Design and Strut-Tie Design

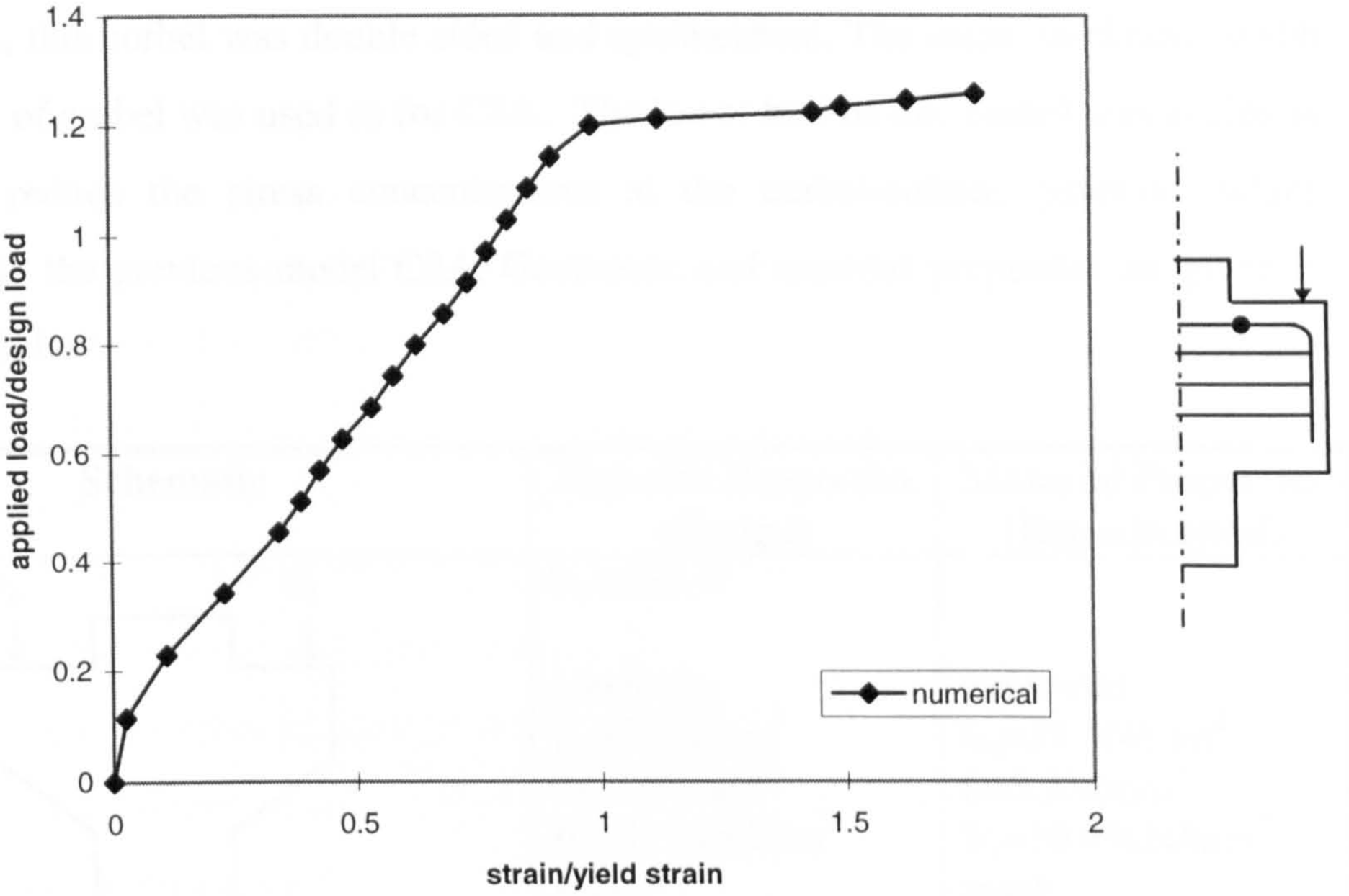

fig.8.3(u) Corbel C2A, Direct Design: Main Steel Strains

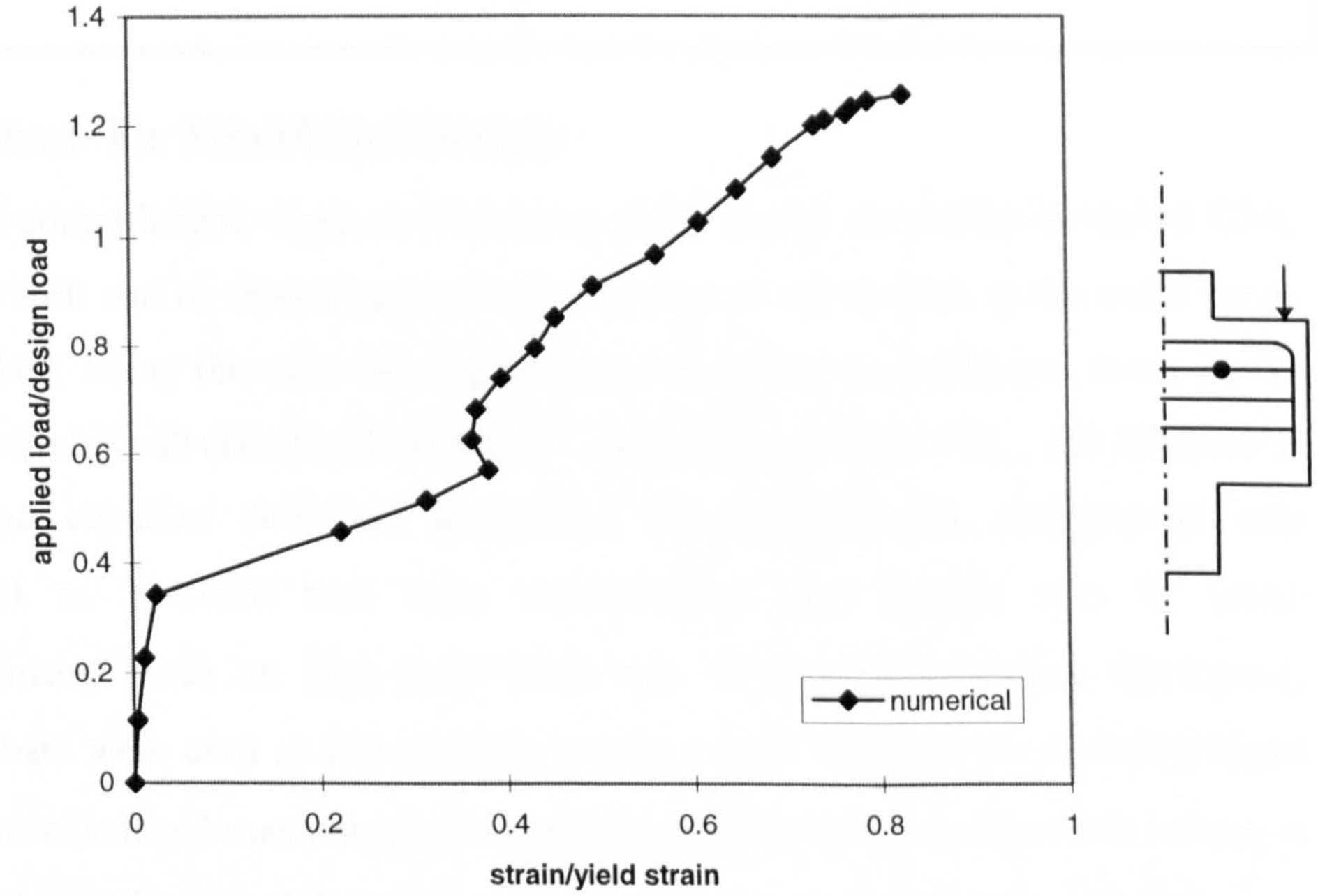

fig.8.3(v) Corbel C2A, Direct Design: Lower Steel

8.4 Corbel C3A

Like C2A, this corbel was double sided and symmetrical. The same, thickness, width and depth of corbel was used as for C2A. The lower half of this corbel was angled in order to reduce the stress concentrations at the corbel-column junction, which occurred in the previous model C2A. Geometric and material properties are given in the table below.

Schematic	Material Properties (Design)	Material Properties (Experimental)
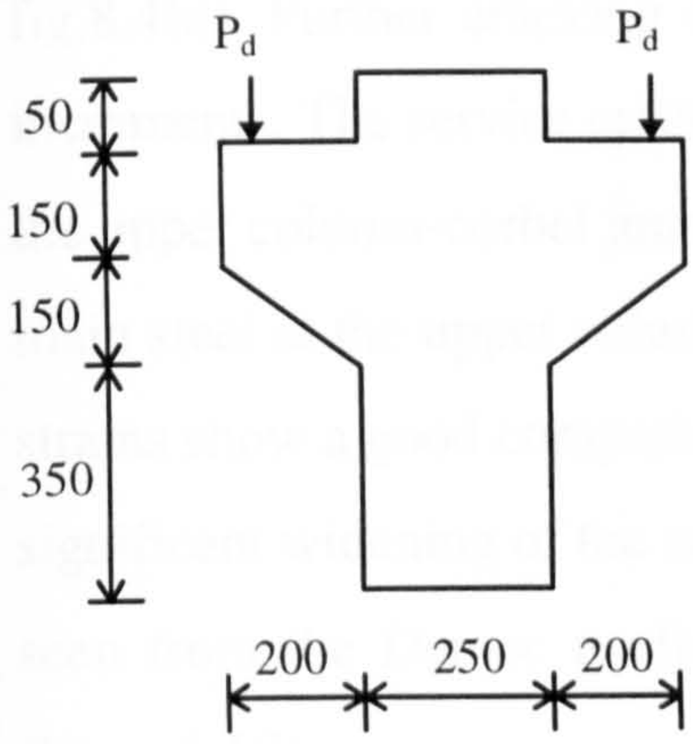	P_d=250kN **concrete:** f_{cu}=35N/mm^2 f_t=3.0N/mm^2 E_c=21.5kN/mm^2 **steel:** f_y=500N/mm^2 E_s=200kN/mm^2 thickness=250mm	 **concrete:** f_{cu}=37.0N/mm^2 f_t=3.3N/mm^2 E_c=19.95kN/mm^2 **steel:** f_y=508N/mm^2 (ϕ10) E_s=210.35kN/mm^2 f_y=509N/mm^2 (ϕ8) E_s=214.5kN/mm^2

8.4.1 Strut-Tie Model and Design

Since the corbel height, depth and thickness of the model are similar to that of C2A, the same strut and tie model can be used. Once again, the stresses in the nodal zones are checked. Using the same bearing plates as for C2A, the maximum stress in the diagonal strut is calculated as 17.8 N/mm^2 , which is less than $0.75f_{cu}$, (26.25N/mm^2). Using the equation described previously, the reinforcement arrangement was calculated as 3ϕ10mm bars main reinforcement and 4ϕ6mm bars as lower reinforcement. Since no high yield 6mm bars were available during fabrication, 4ϕ8mm bars were used as the auxiliary reinforcement. With the new reinforcement layout, the calculated maximum load, assuming yielding of the steel governs failure, is 325kN, ($1.3P_d$). Details of the reinforcement layout are given in figures 8.4(a-b).

8.4.2 Numerical and Physical Testing

The corbel was tested in the same manner as C2A, with the load being applied in 25kN increments. The experimental ultimate total load was recorded as 710kN, ($1.42P_d$) and the numerical ultimate load was 650kN, ($1.3P_d$). The first cracks occurred at $0.2P_d$, around the upper corbel-column junction. The largest of these cracks was measured as 0.05mm. On subsequent loading, these cracks continued to propagate downwards into the column, see fig.8.4(c). Cracking in the diagonal strut region did not occur until $0.7P_d$. The largest of these cracks was 0.1mm wide, see fig.8.4(d). Further cracking in the diagonal strut region was observed on successive increments. The service crack limit width of 0.3mm was reached at $1.0P_d$, in cracks at the upper column-corbel junction. Failure of the corbel was initiated by yielding of the main steel at the upper column-corbel junction. The numerical and experimental steel strains show a good comparison and are shown in figures 8.4(e-g). This yielding led to significant widening of the cracks both at this point and in the diagonal strut, as can be seen from the Demec readings, fig.8.4(h). The corbel at ultimate load is shown in figure 8.4(i).

The idealised stresses in node 1 are shown in figure 8.4(j). It can be seen that the applied stresses in this zone are all less than 0.55 f_{cu}. The numerical concrete stresses are displayed in figures 8.4(m-n) and show that at ultimate load, crushing of the concrete was initiated at the lower diagonal strut. This crushing was present in the experiment but did not happen until the steel had yielded and ultimate load was attained. It can be seen that closer to the column, the stresses in the diagonal are greater than those envisaged by the strut-tie model. This is due to the fact that as the strut approaches the column, a bottle neck effect occurs. However, it can also be observed that the level of stress concentration around the column-corbel junction is reduced to about $0.8f_{cu}$, in comparison to $1.1f_{cu}$ reached in C2A. The compressive stresses along the upper part of the diagonal strut are of a similar magnitude to those predicted by the strut-tie model, fig.8.4(n). As in beam B1, a more detailed finite element analysis of this nodal region was carried out using a displacement control analysis. The results of this are displayed in figures 8.4(o-p). The funnelling of the compressive stresses can clearly be seen from the principal stress plot.

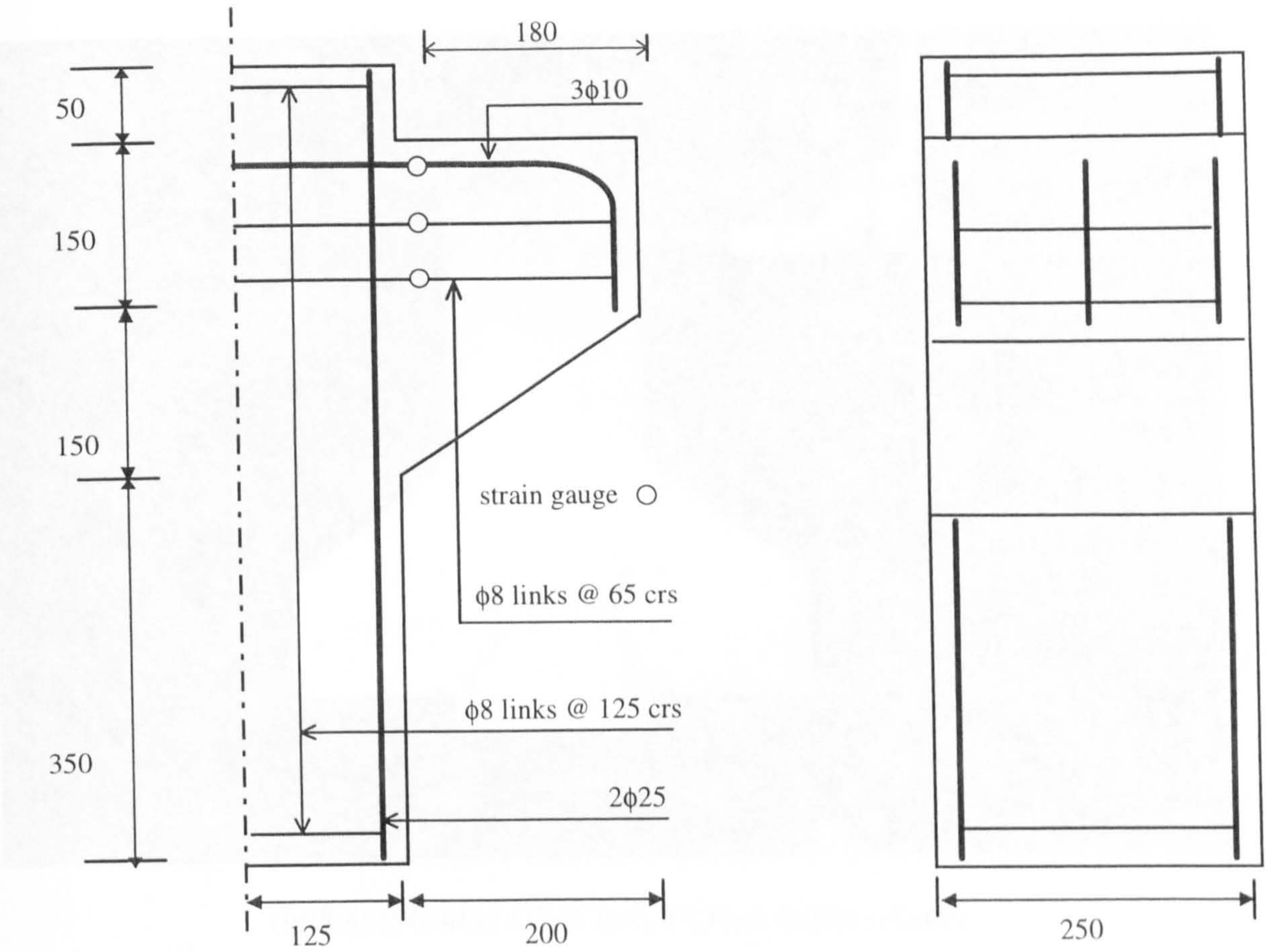

i) elevation ii) side elevation

fig.8.4(a) Corbel C3A, all sizes in mm, cover 20mm

fig.8.4(b) Corbel C3A Reinforcement & Formwork

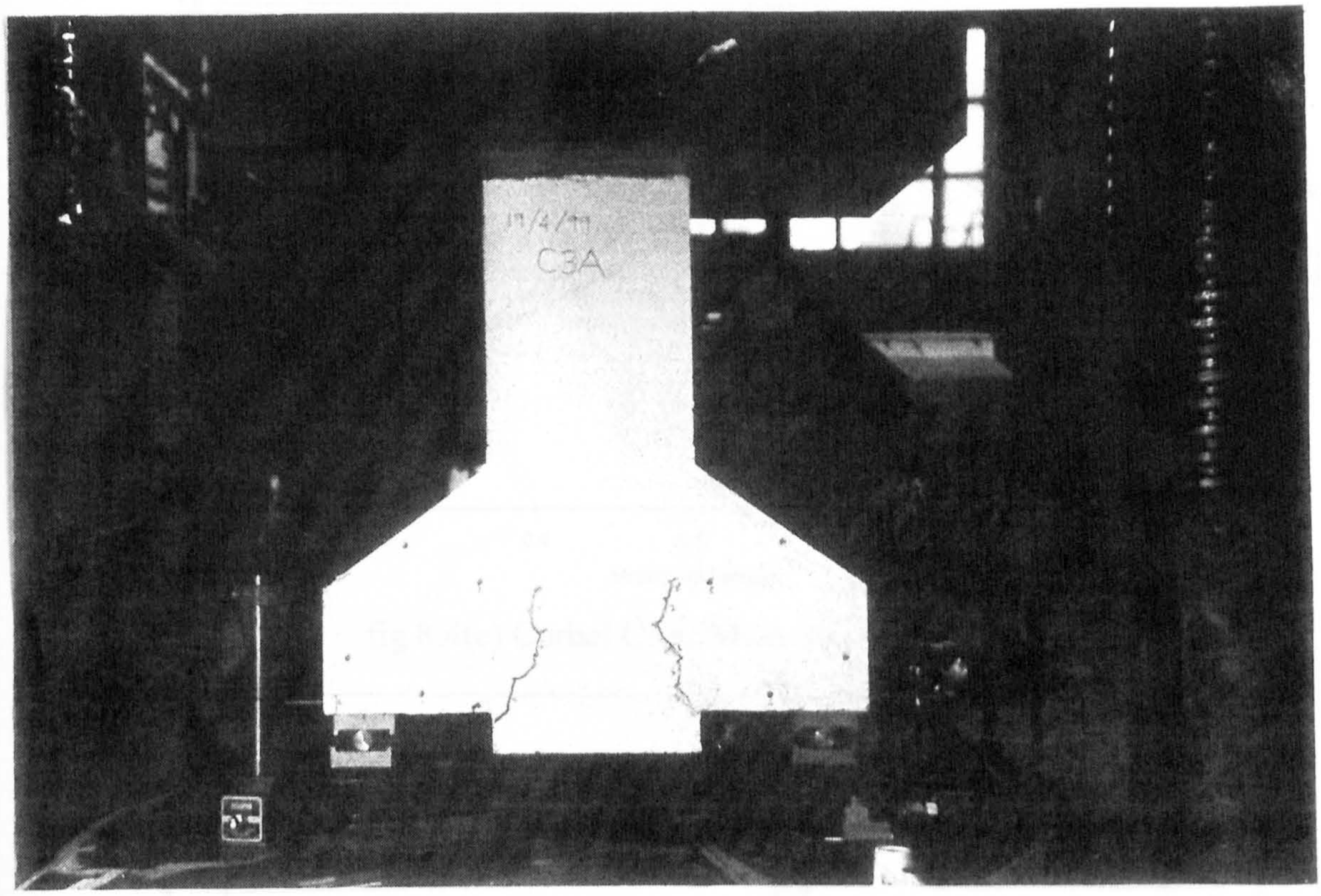

fig.8.4(c) Corbel C3A: Initial Crack Pattern ($0.4P_d$)

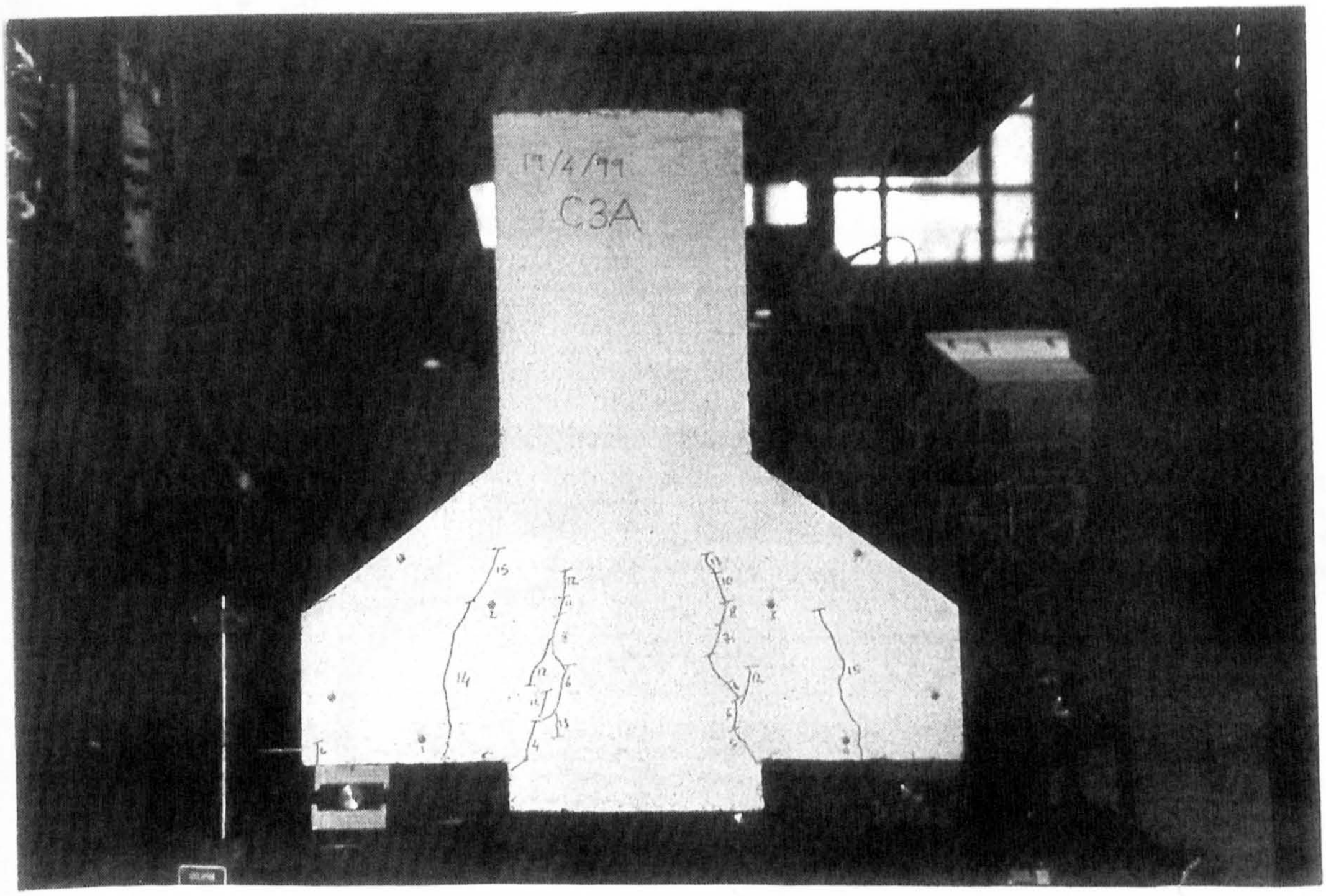

fig.8.4(d) Corbel C3A: Crack Pattern ($0.7P_d$)

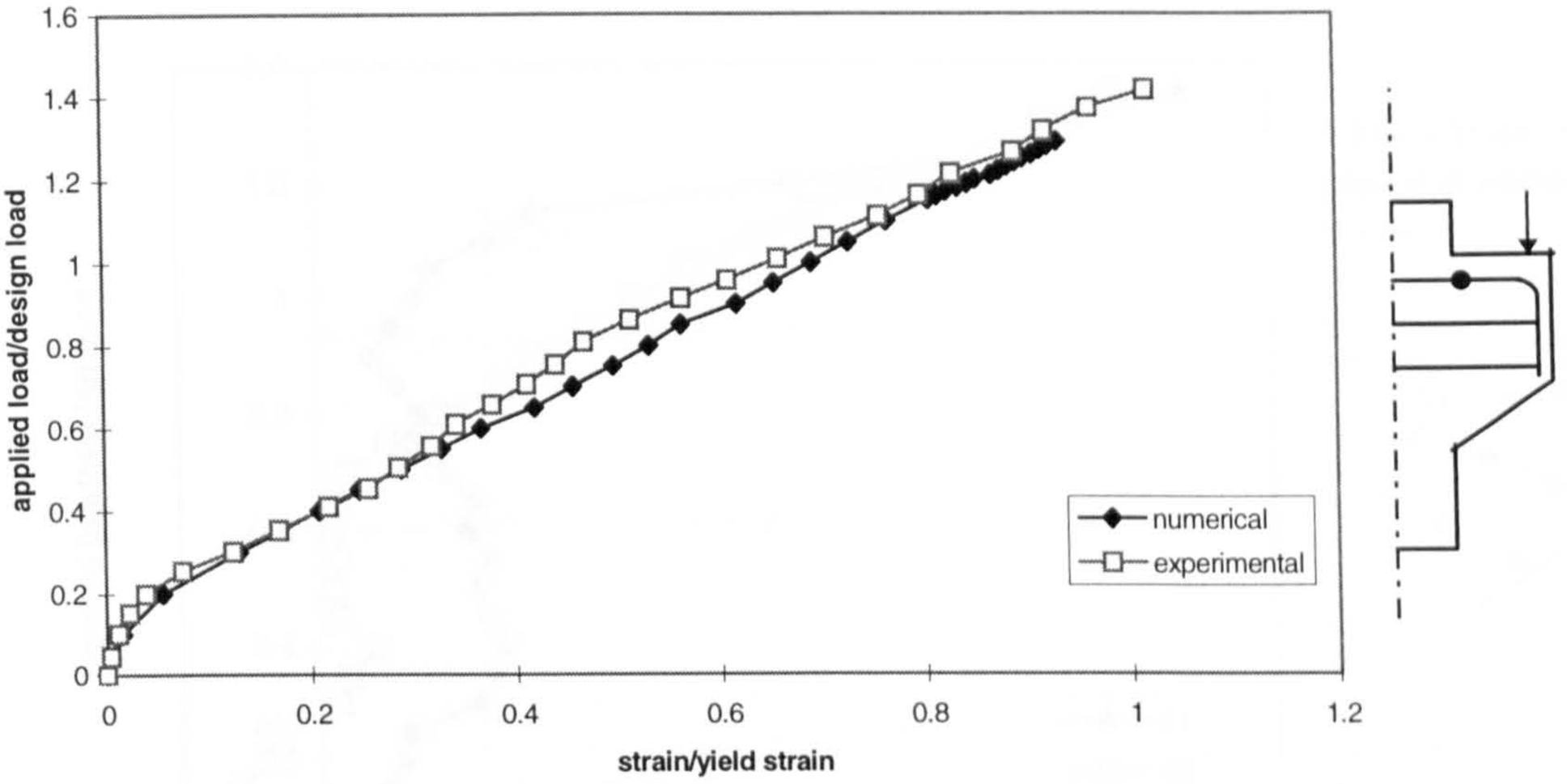

fig.8.4(e) Corbel C3A: Main Steel Strains

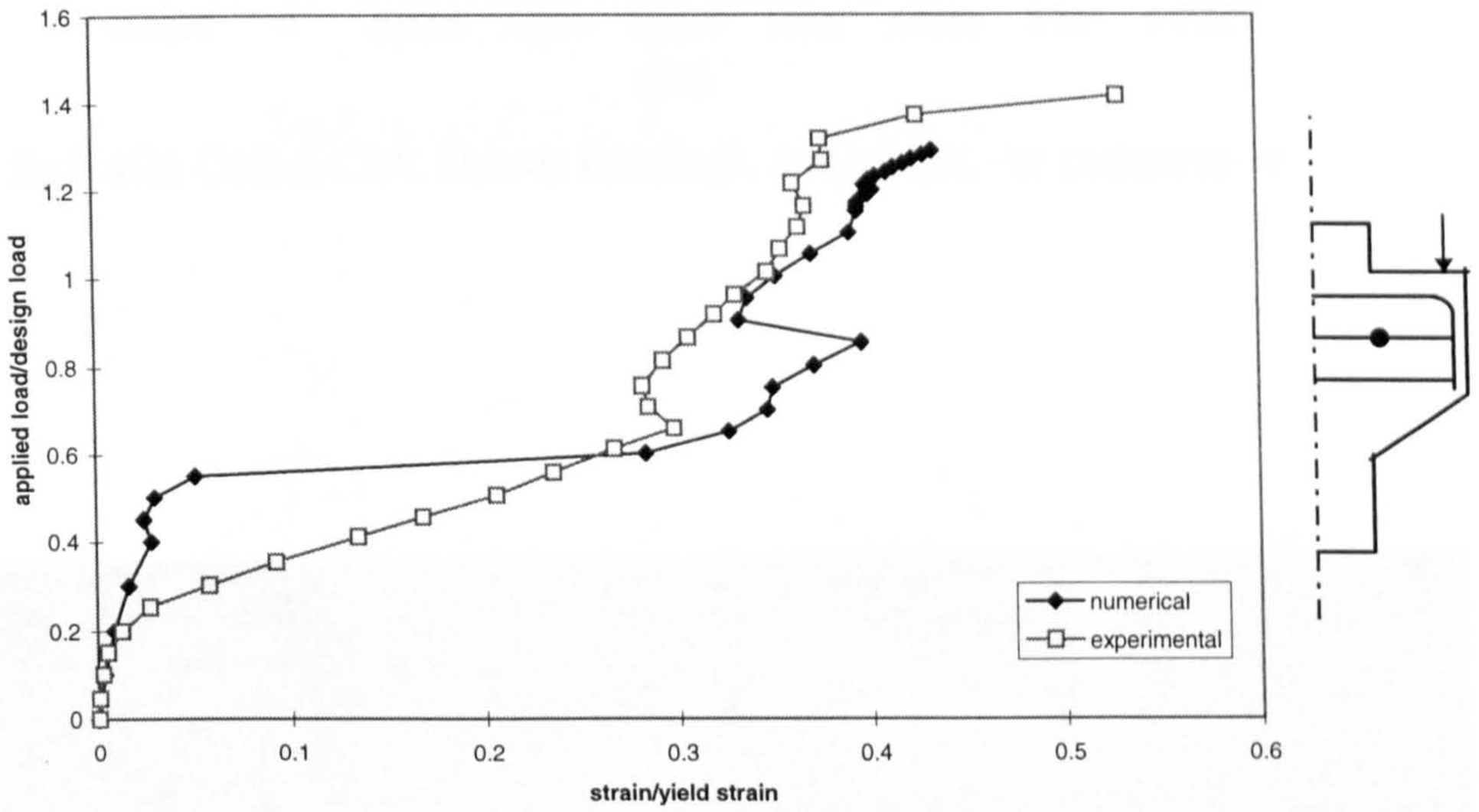

fig.8.4(f) Corbel C3A: Upper Stirrup Steel Strains

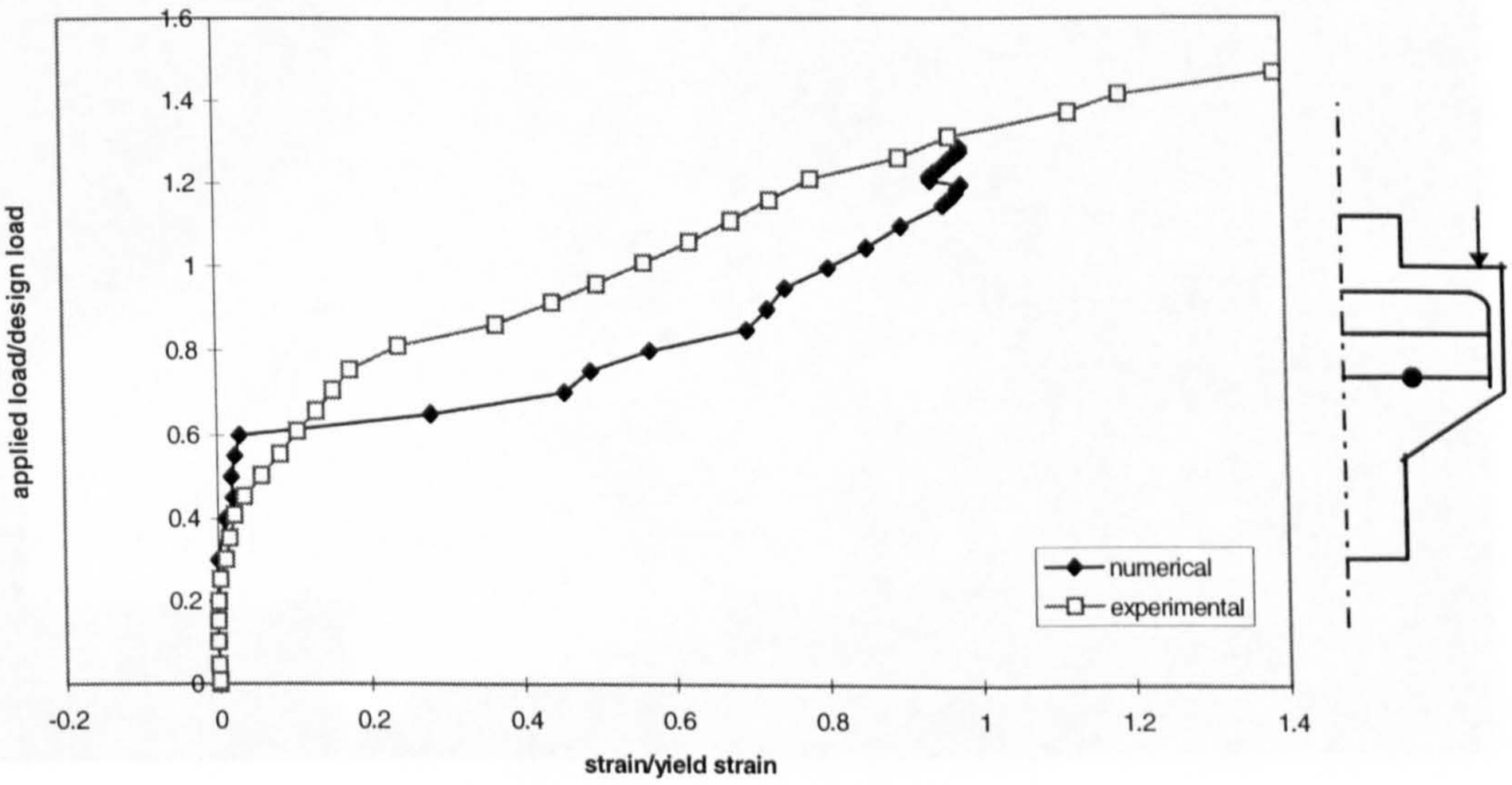

fig.8.4(g) Corbel C3A: Lower Stirrup Reinforcement

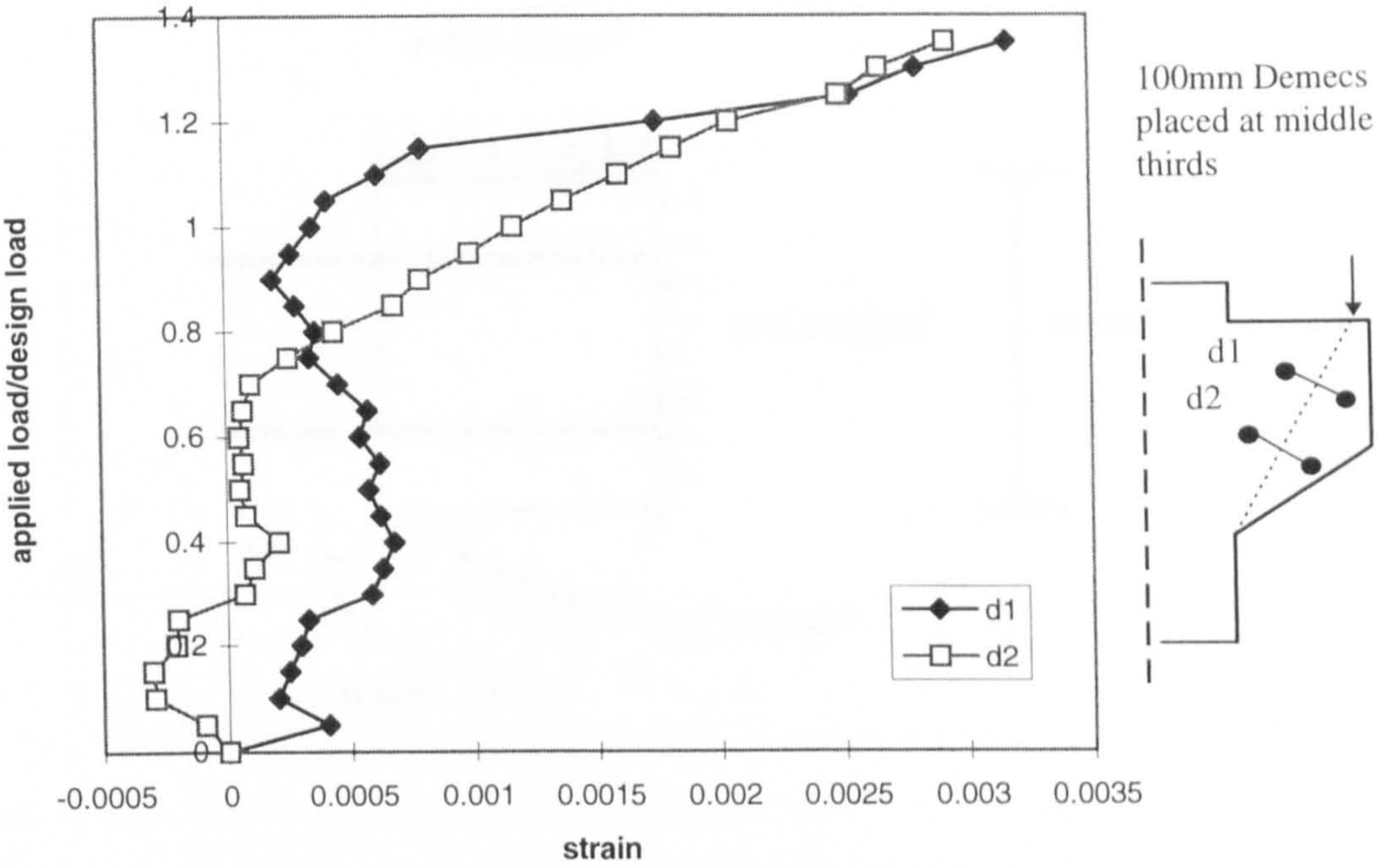

fig.8.4(h) Corbel C3A: Demec Readings, +ve tensile, -ve compressive

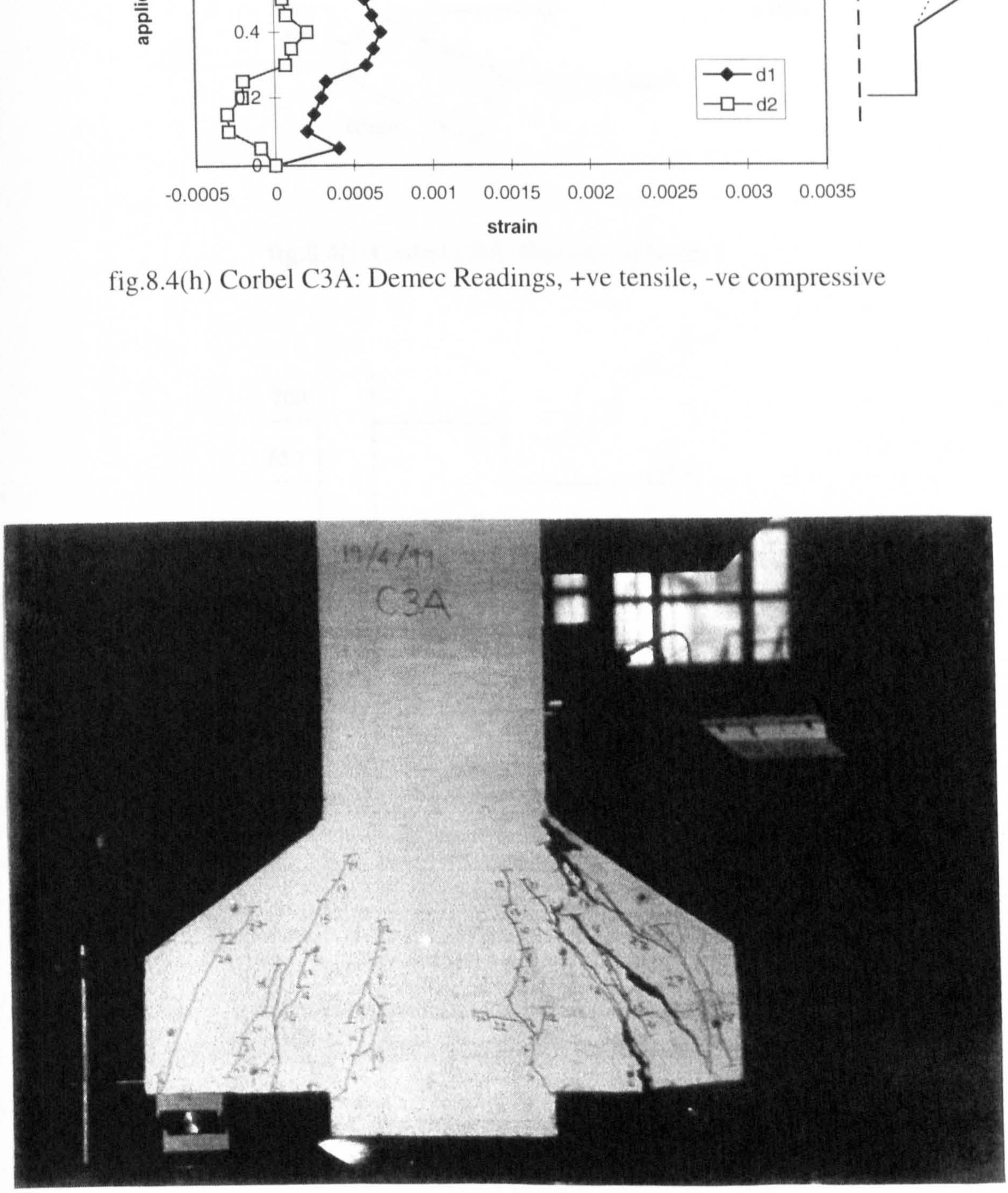

fig.8.4(i) Corbel C3A at ultimate load ($1.42P_d$)

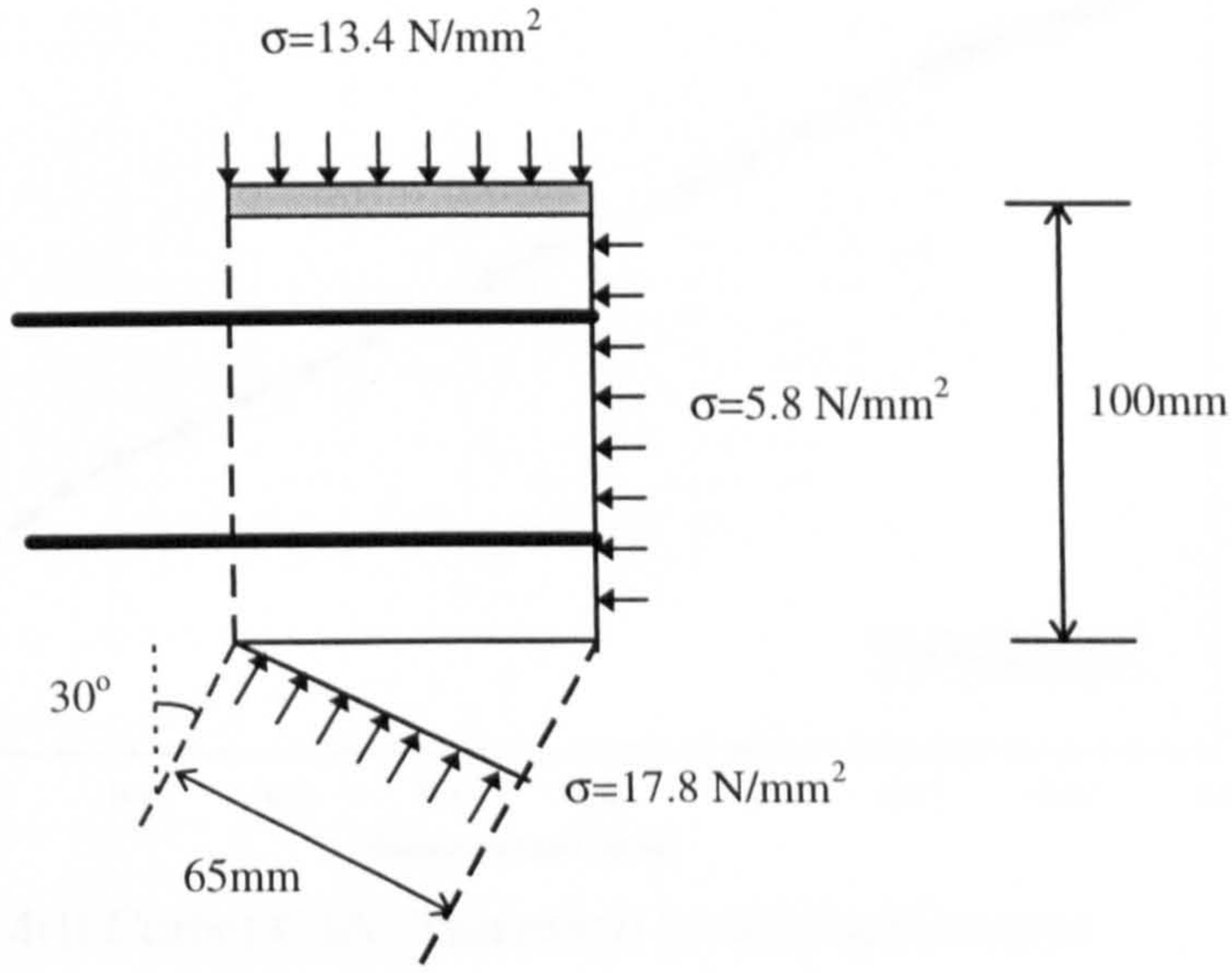

fig.8.4(j) Corbel C3A: Stresses in Node 1

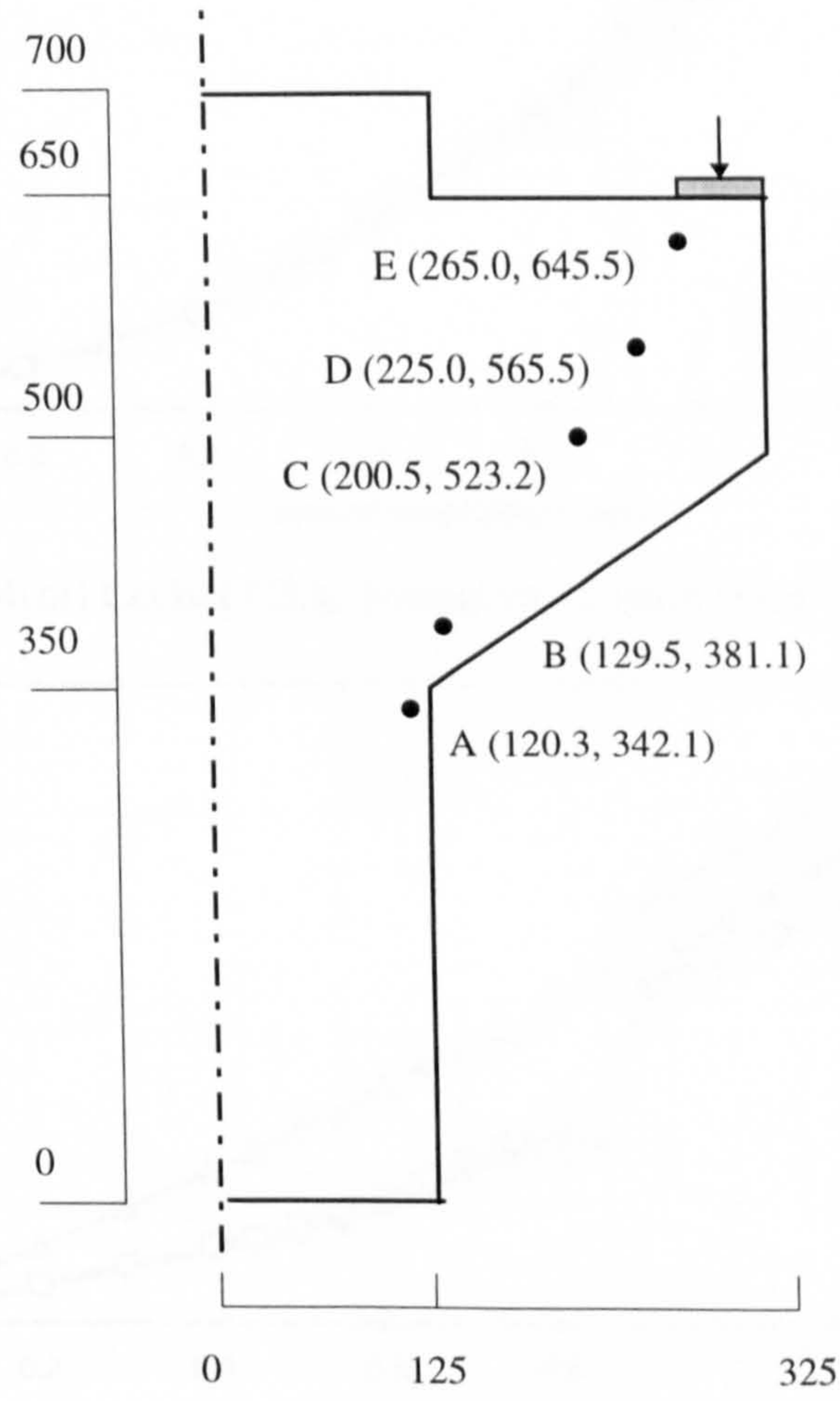

fig.8.4(k) Corbel C3A: Guass Point Positions for Numerical Stresses

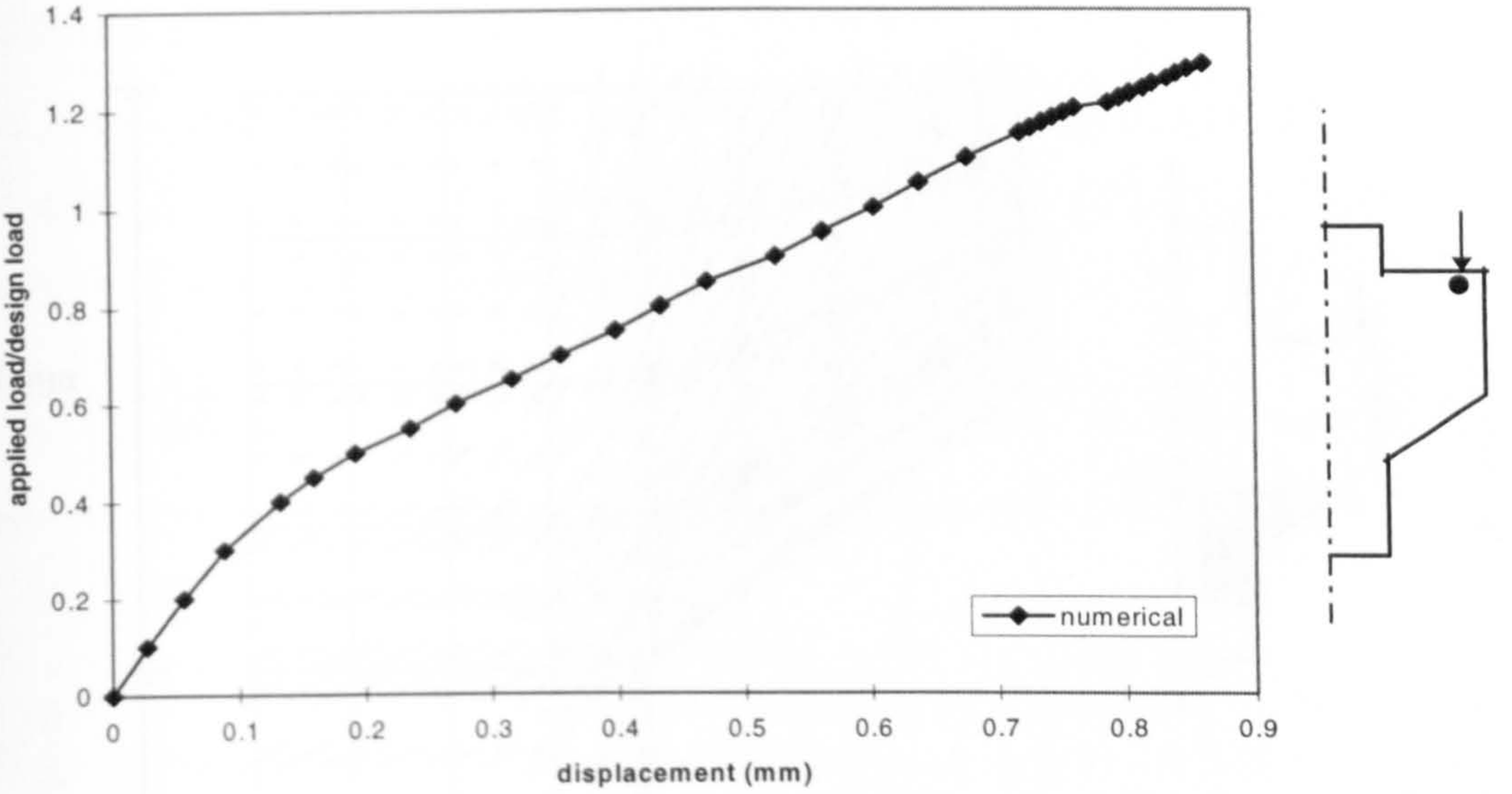

fig.8.4(l) Corbel C3A: Numerical Load-displacement

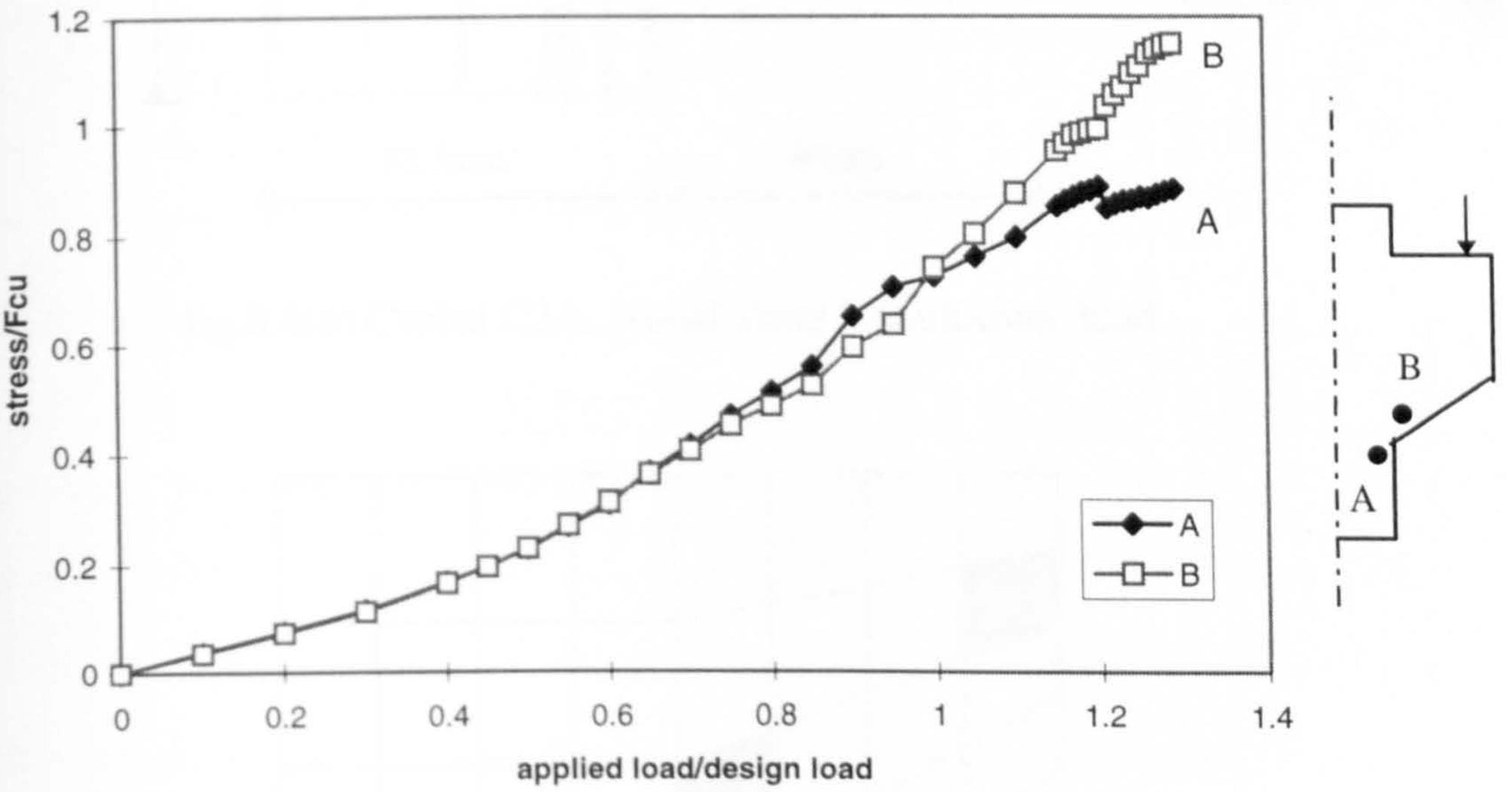

fig.8.4(m) Corbel C3A: Numerical compressive stresses

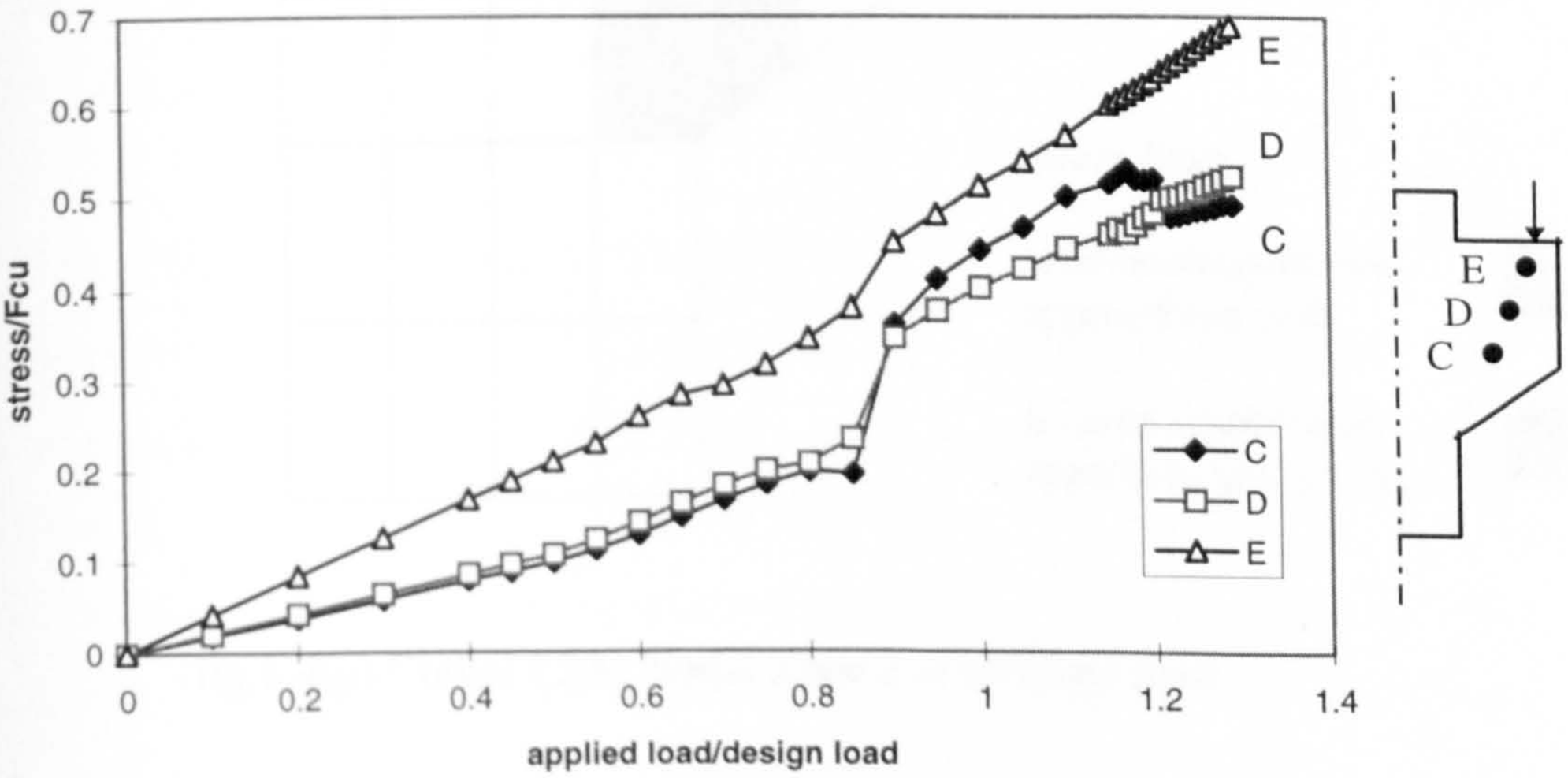

fig.8.4(n) Corbel C3A: Numerical Compressive stresses

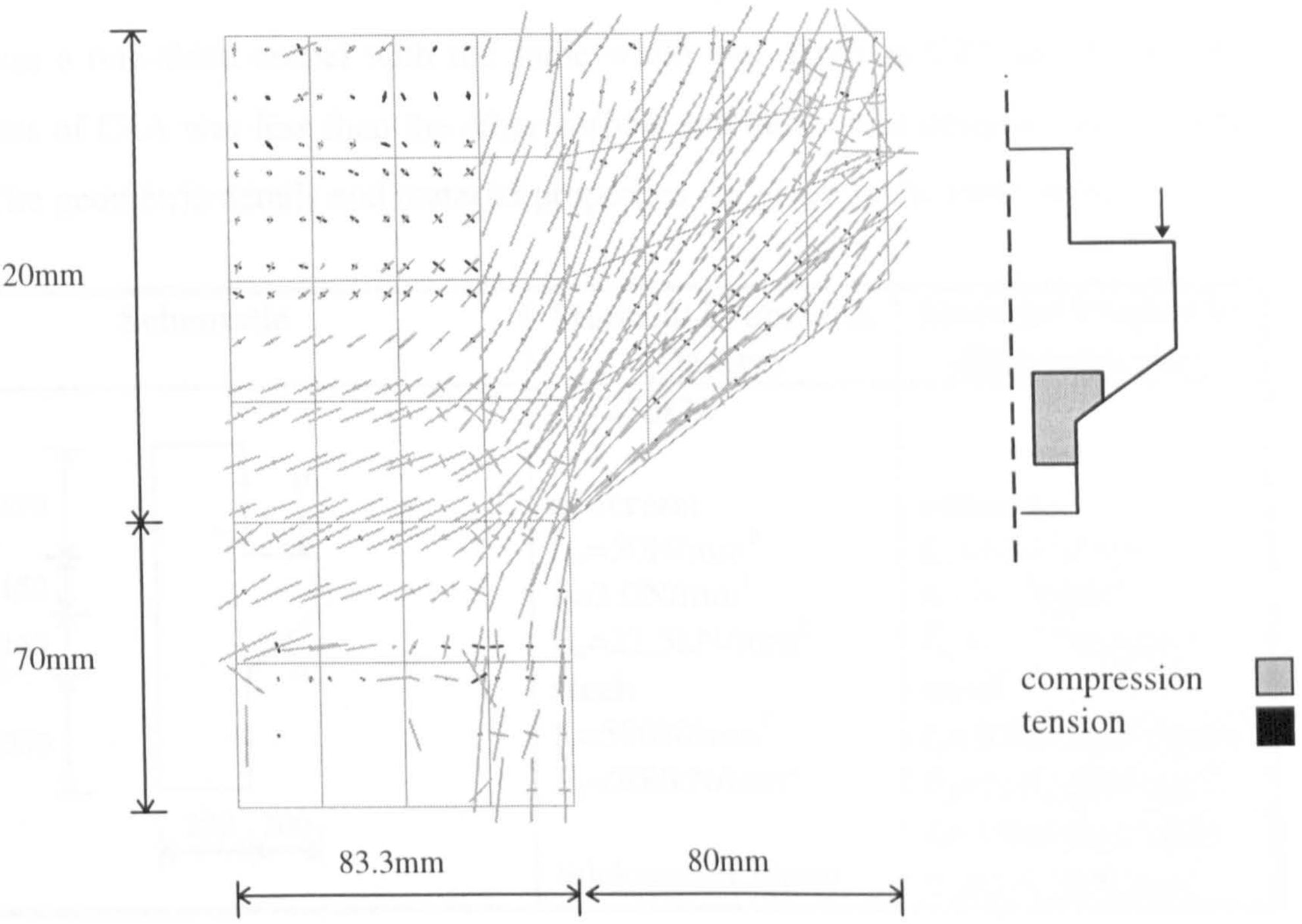

fig.8.4(o) Corbel C3A: Nodal Zone 2 at ultimate load

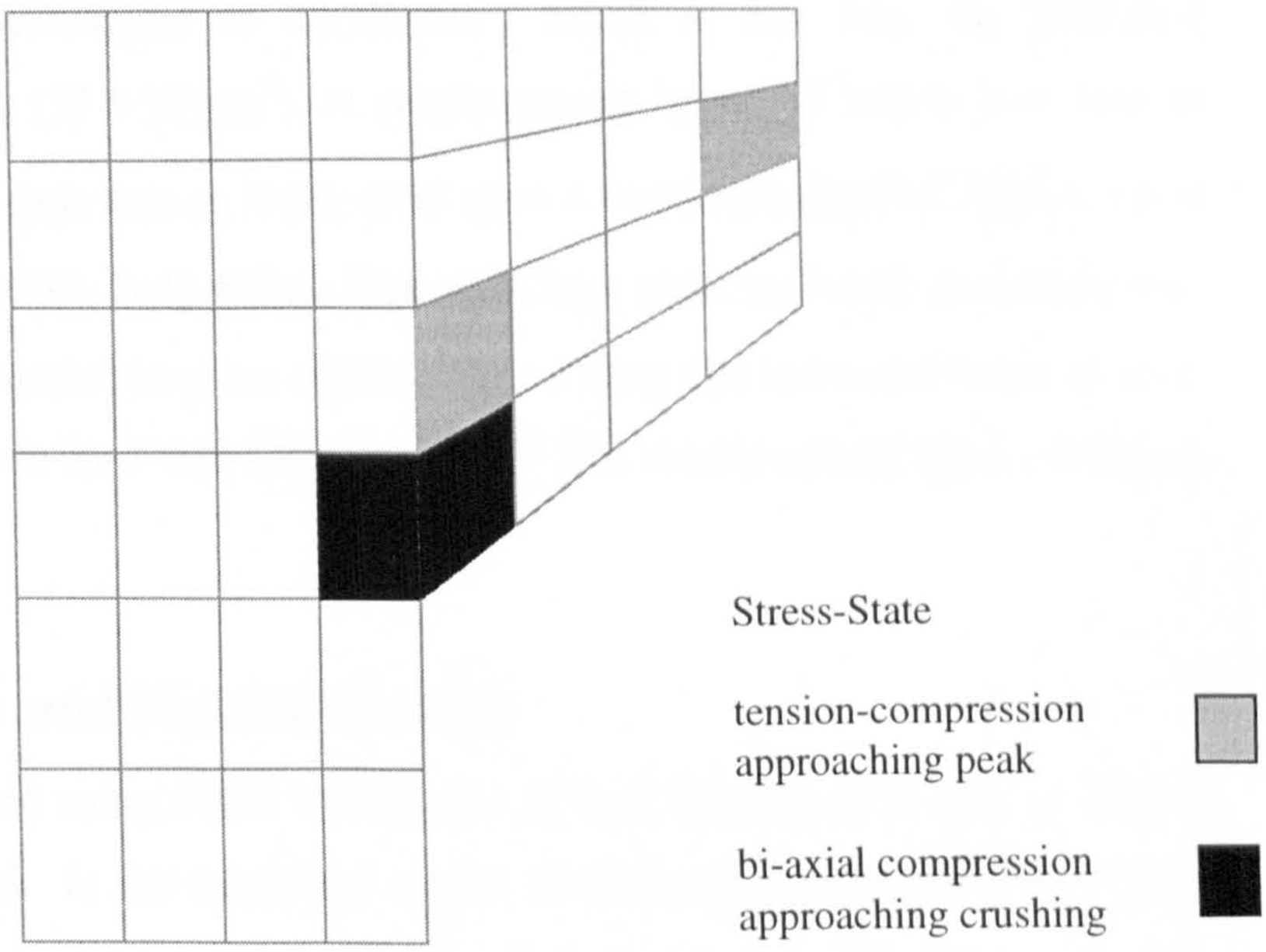

fig.8.4(p) Corbel C3A: Nodal Zone 2 at ultimate load

8.5 Corbel C4A

C4A was a one-sided corbel with the same width and depth as C2A and C3A. The thickness of C4A was less than the other corbels and hence was designed for a lower load. The geometric details and material properties are given in the table below.

Schematic	Material Properties (Design)	Material Properties (Experimental)
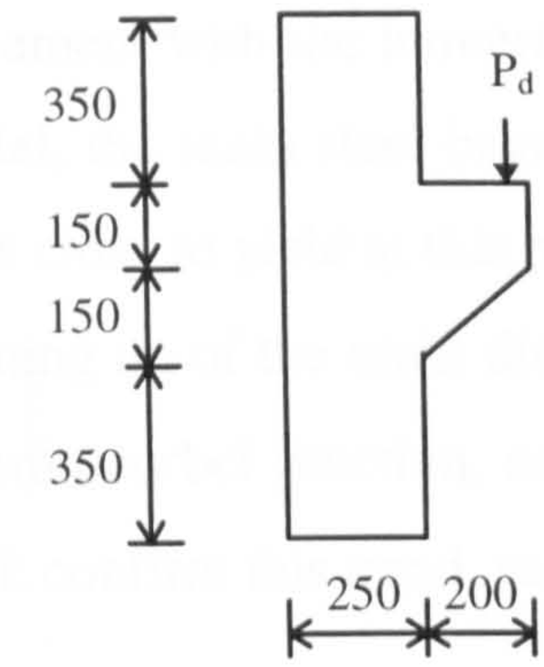	P_d=200kN **concrete:** f_{cu}=50N/mm^2 f_t=3.0N/mm^2 E_c=21.5kN/mm^2 **steel:** f_y=500N/mm^2 E_s=200kN/mm^2 thickness=150mm	 **concrete:** f_{cu}=49.6N/mm^2 f_t=3.3N/mm^2 E_c=21.77kN/mm^2 **steel:** f_y=508N/mm^2 (ϕ10) E_s=210.35kN/mm^2 f_y=509N/mm^2 (ϕ8) E_s=214.5kN/mm^2

8.5.1 Design

Using the same strut-tie model as for C2A and C3A, the maximum stress in the diagonal strut was calculated as 23.7N/mm^2, which is less than the permitted maximum of $0.75f_{cd}$, (37.5 N/mm^2). A reinforcement layout of 2xϕ10 mm bars as main steel and 4xϕ6 mm bars as lower steel gave a maximum load of 203kN. As in the case with corbel C3A, only ϕ8mm high yield bars were available, and these were used in the actual structure in place of 6mm bars. Using this increased value of steel, the theoretical ultimate load was 255kN, ($1.3P_d$). The reinforcement layout is shown in figures 8.5(a-b)

8.5.2 Numerical and Physical Testing

The model was tested using 10kN increments. A total experimental load of 240kN, ($1.2P_d$) was achieved. In the numerical model, an ultimate load of 250kN, ($1.25P_d$), was achieved. During the experiment, the first cracks, as with C2A and C3A, appeared at the upper column-corbel junction at the point of highest tension, at $0.2P_d$, see fig.8.5(c). The largest of these cracks was measured as 0.05mm. On further loading, these cracks propagated downwards towards the column. At $0.7P_d$, a diagonal

crack appeared in the compressive zone inside the column, see figure 8.5(d). A crack along the main diagonal strut, running from the baseplate along the line of the diagonal strut occurred at $0.8P_d$, see fig.8.5(e). This crack was 0.1mm wide. Subsequent loading led to further propagation and widening of the main diagonal crack and the service limit width of 0.3mm was reached at a load of $1.15P_d$.

The experimental steel strains are shown in figures 8.5(g-i). A relatively good agreement with the numerical strains is observed. In both the numerical and physical model, the main steel began to yield just prior to the ultimate load. Both lower bars were close to yield at this point, reaching around 85% yield strain. This yielding led to *opening up of the main diagonal crack* and led to crushing of the concrete around the column-corbel junction, *see figure 8.5(f). The Demec readings across the diagonal* track confirm this trend, see figures 8.5(l).

No crushing of the concrete was observed numerically, or during the experiment. The numerical compressive stresses are shown in figures 8.5(m-n). It can be observed that the largest stress occurred in the same area as C3A, as was of the order of $0.7f_{cu}$. Elsewhere, the stresses along the diagonal did not exceed the theoretical maximum of $0.5f_{cu}$, see figure 8.5(m). Figure 8.5(n) shows that the stress along the diagonal at point C suddenly increases from $0.15f_{cu}$ to $0.3f_{cu}$ at around $0.8P_d$. This sudden increase is due to cracking taking place in this region at the same load level.

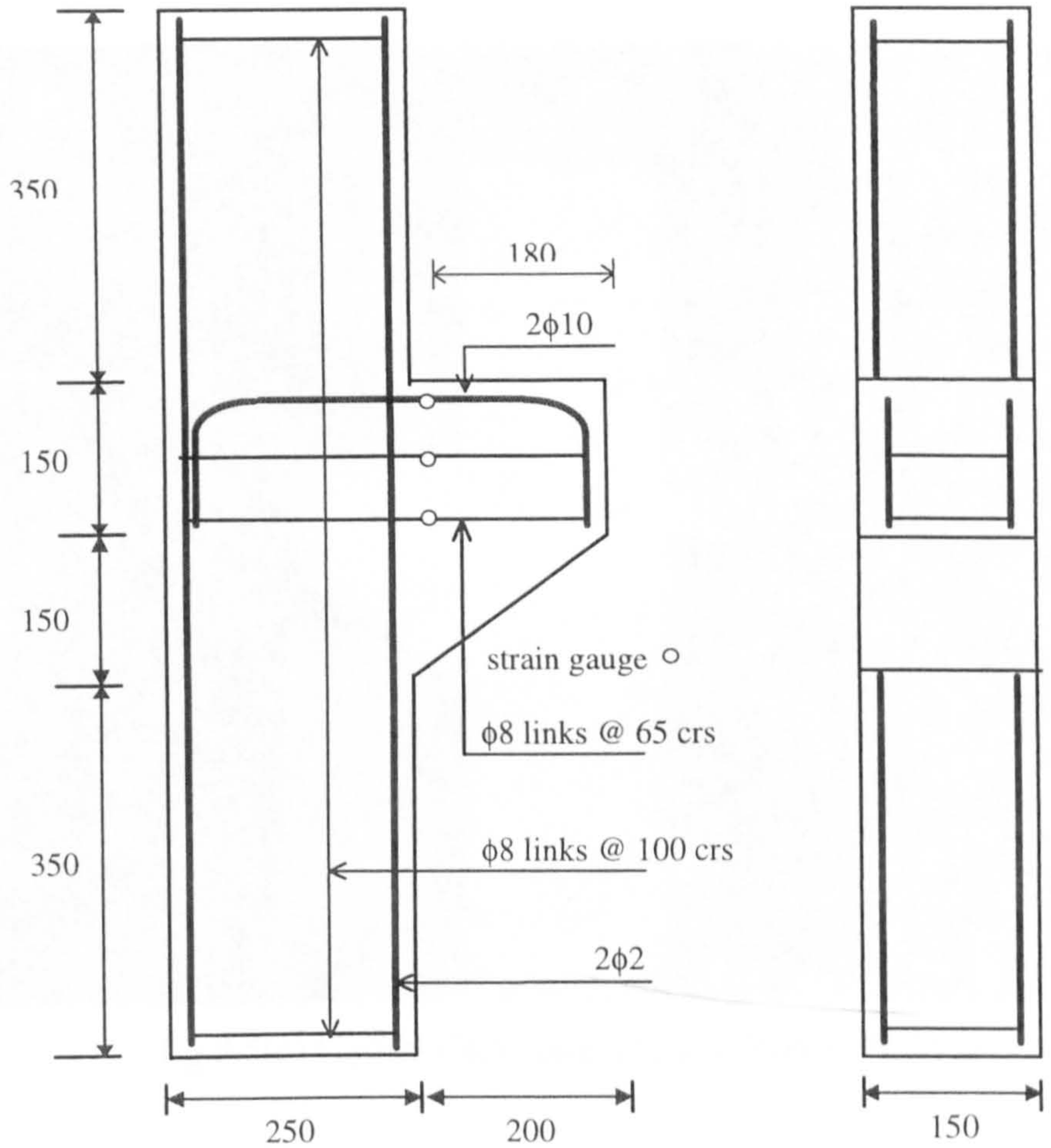

i) elevation ii) side elevation

fig.8.5(a) Corbel C4A, all sizes in mm, cover 20mm

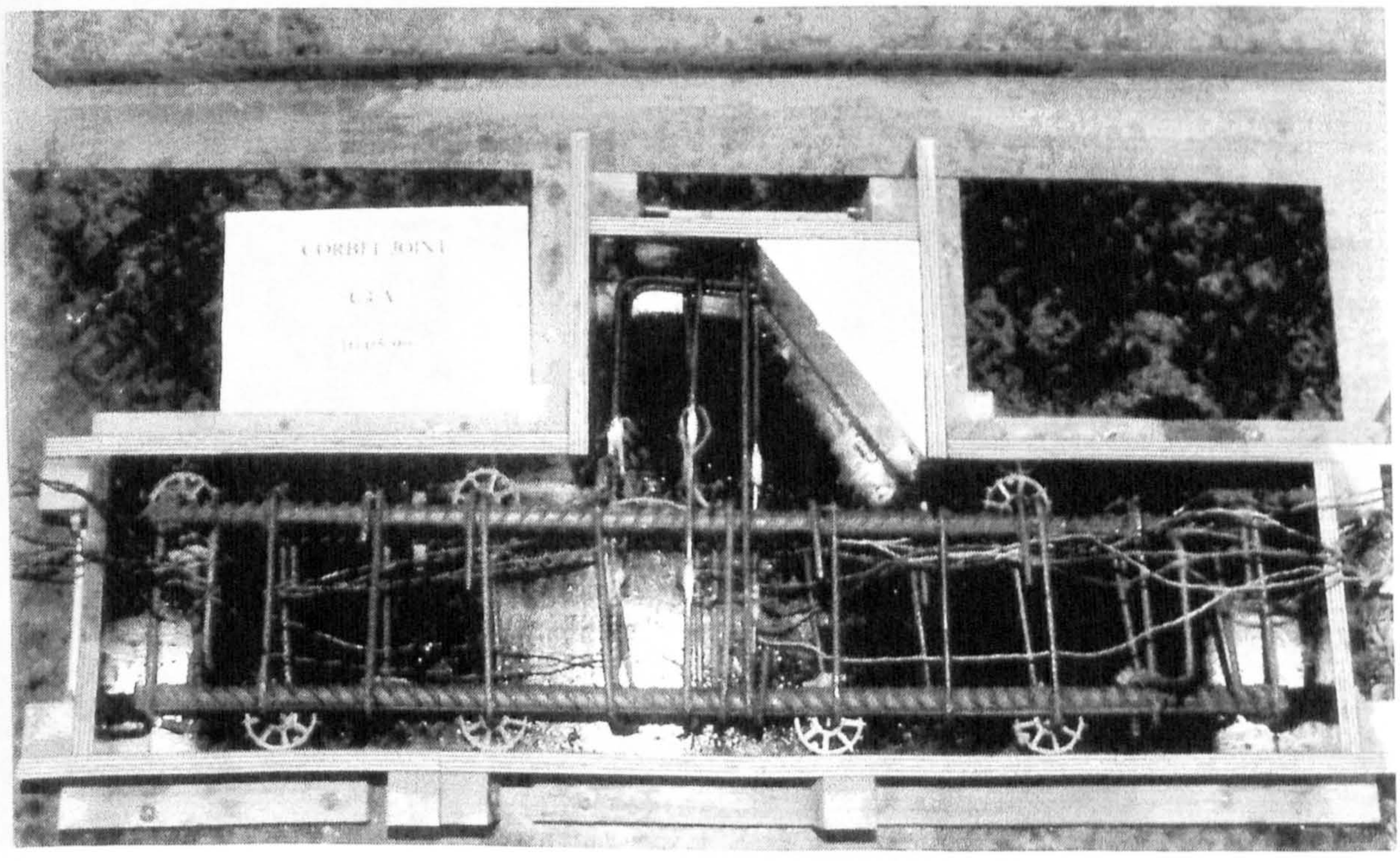

fig.8.5(b) Corbel C4A: Reinforcement Layout & Formwork

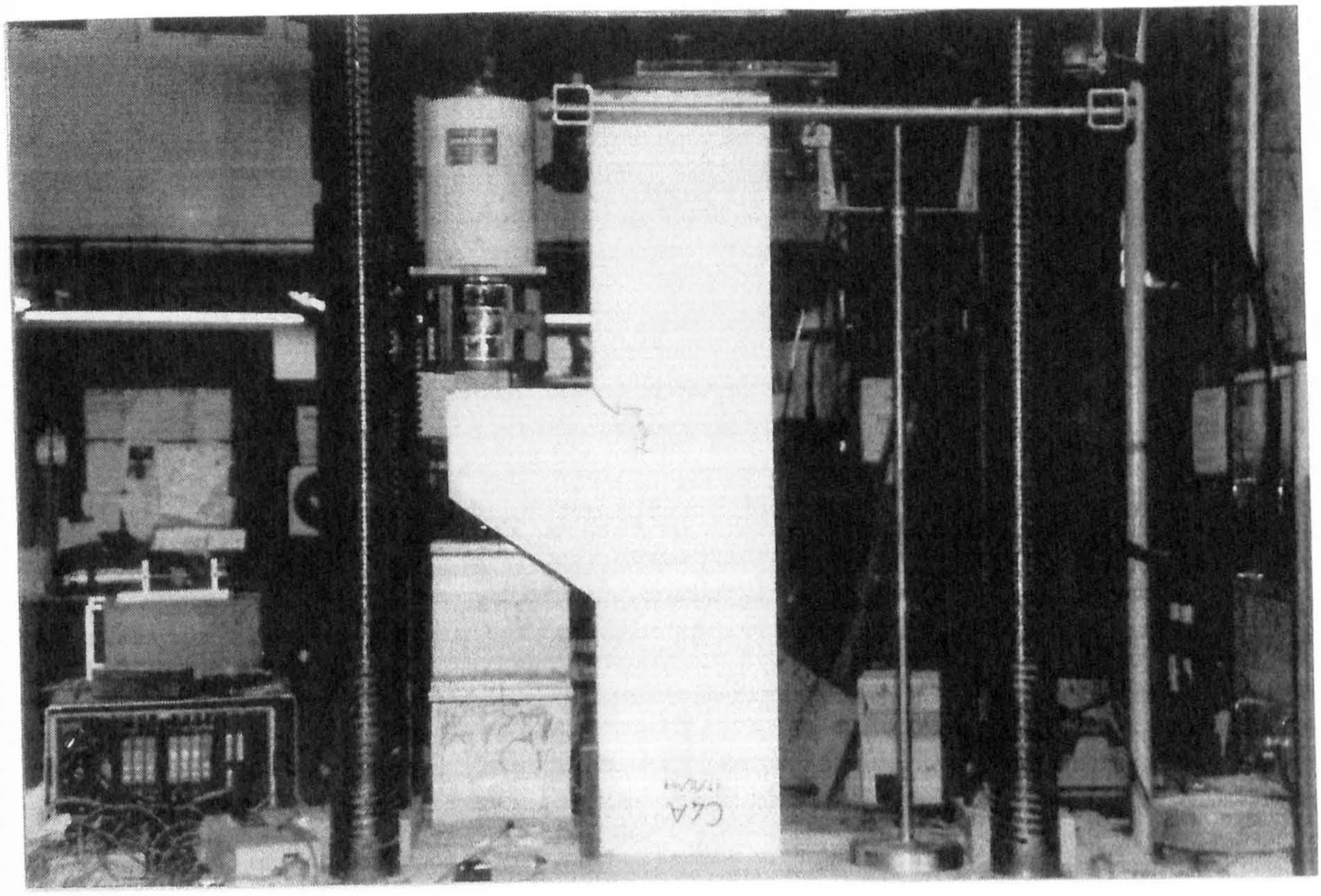

fig.8.5(c) Corbel C4A: Initial Crack Pattern ($0.2P_d$)

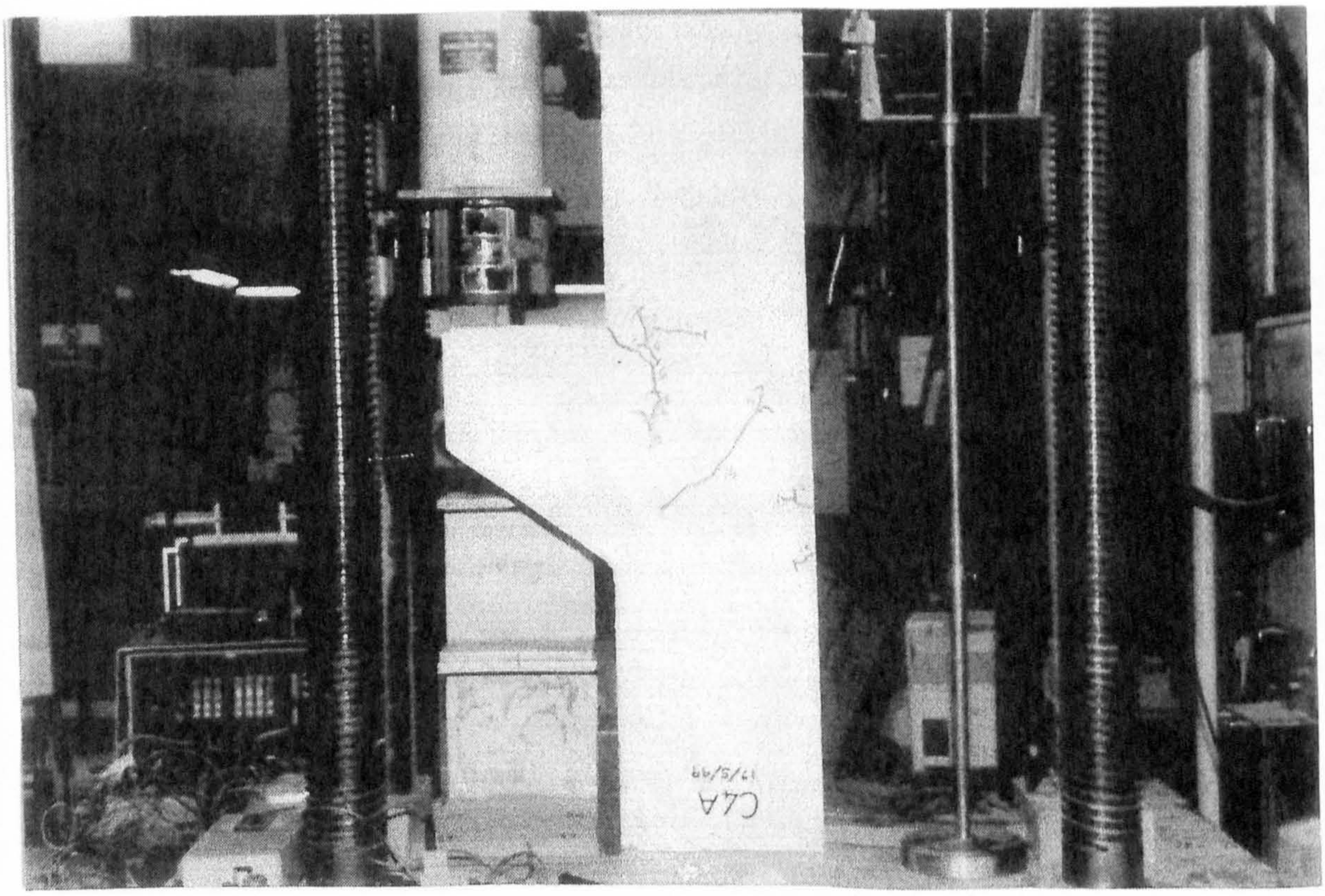

fig.8.5(d) Corbel C4A ($0.7P_d$)

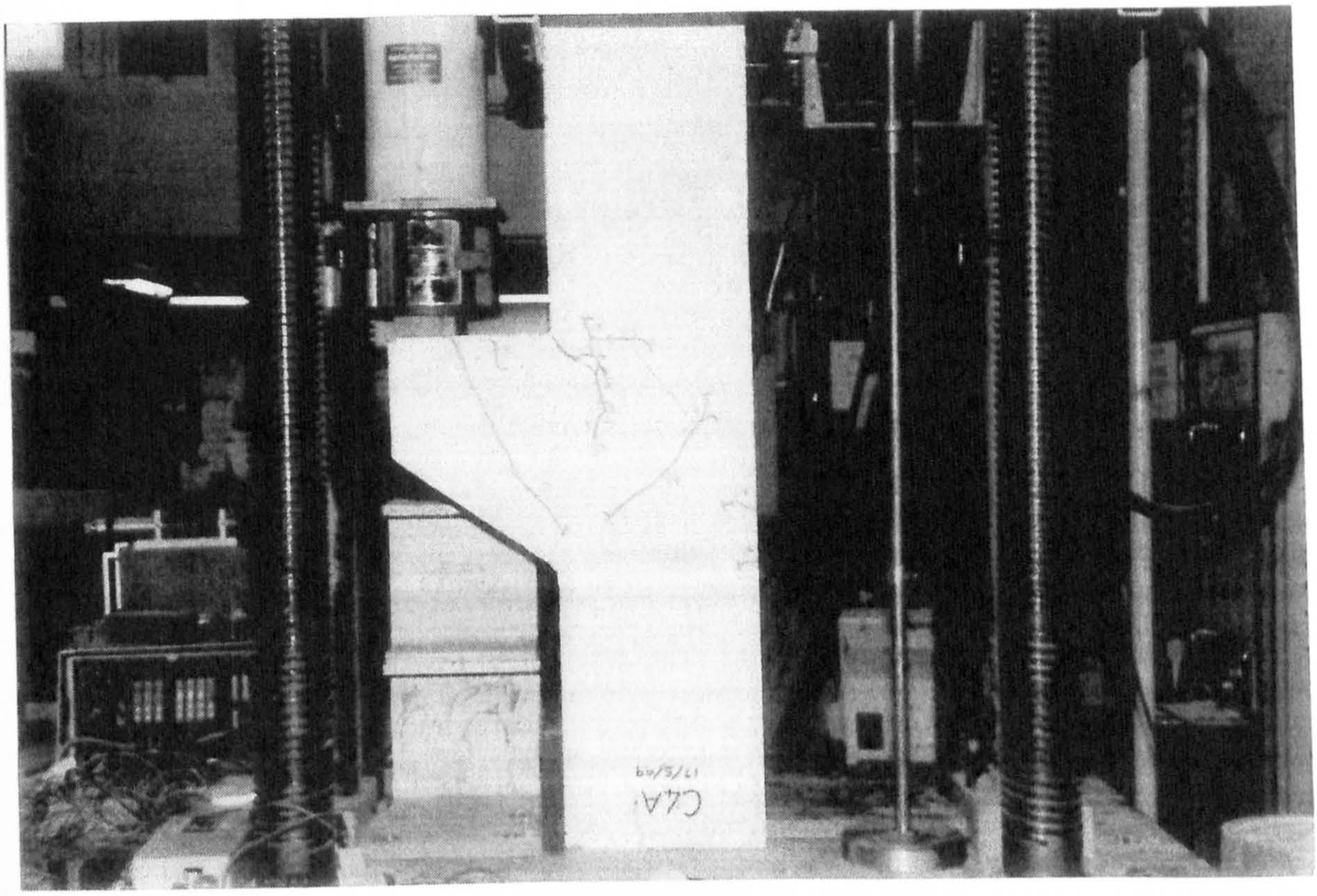

fig.8.5(e) Corbel C4A ($1.0P_d$)

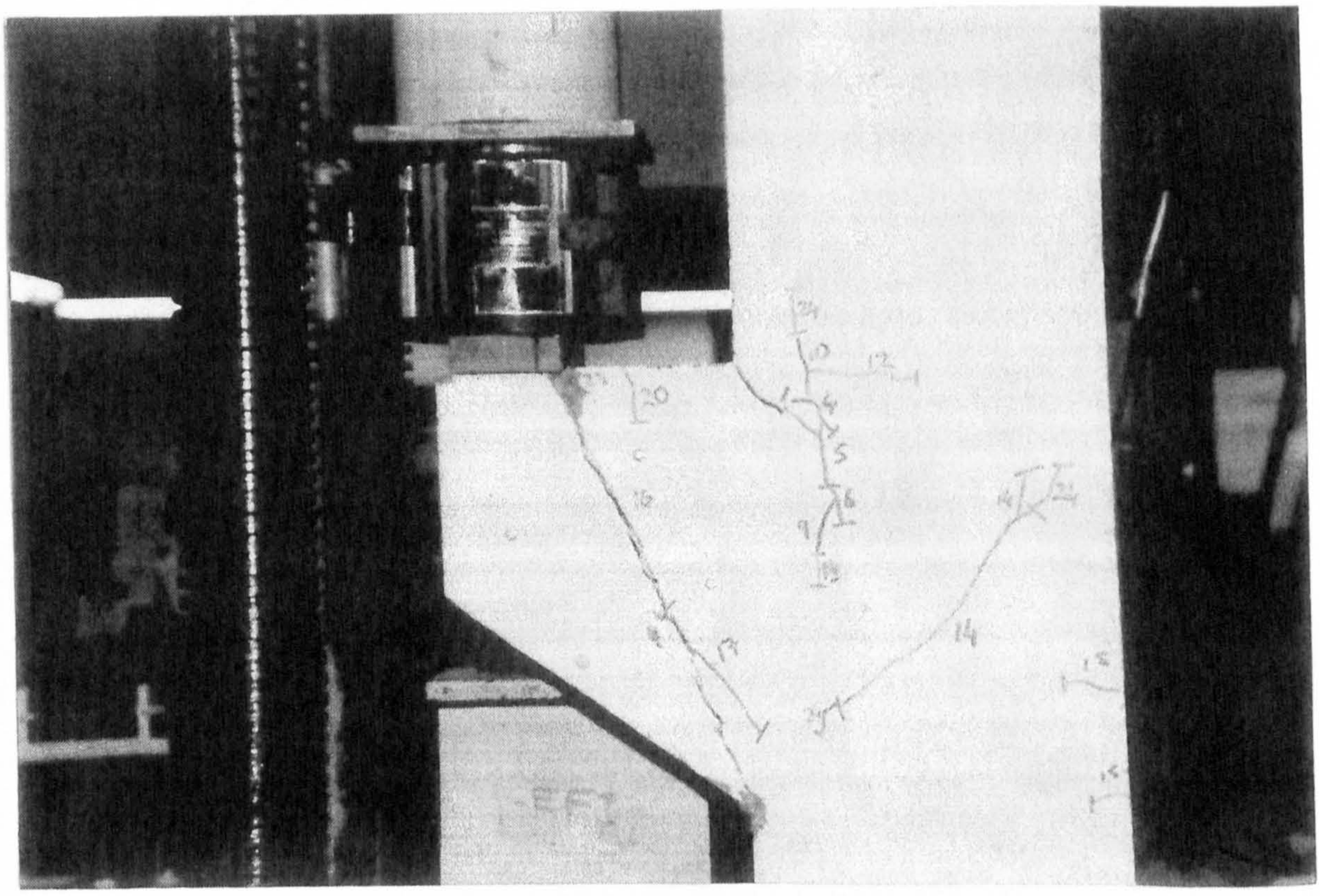

fig.8.5(f) Corbel C4A at ultimate load ($1.2P_d$)

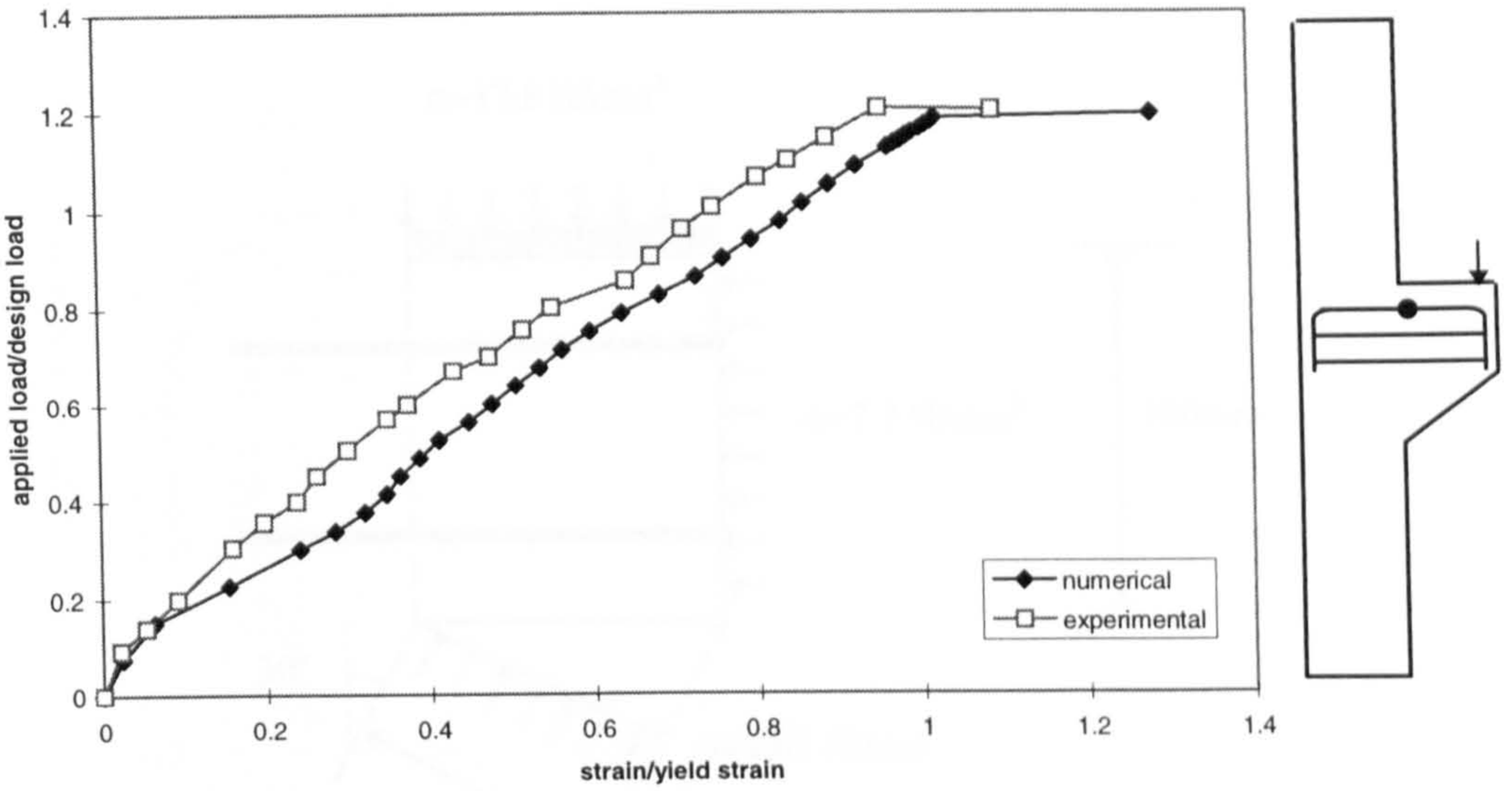

fig.8.5(g) Corbel C4A: Main Reinforcement

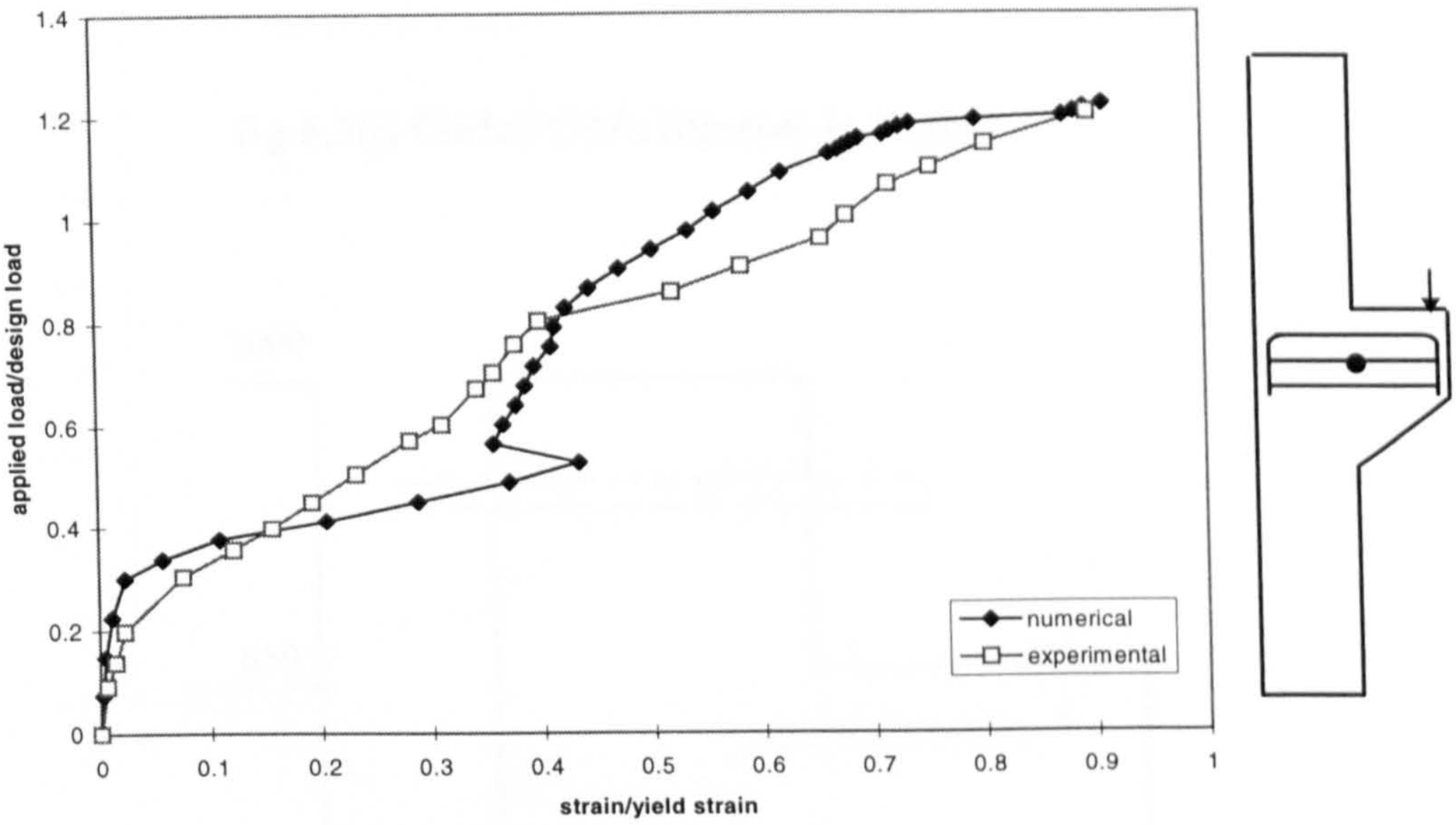

fig.8.5(h) Corbel C4A: Upper stirrup reinforcement

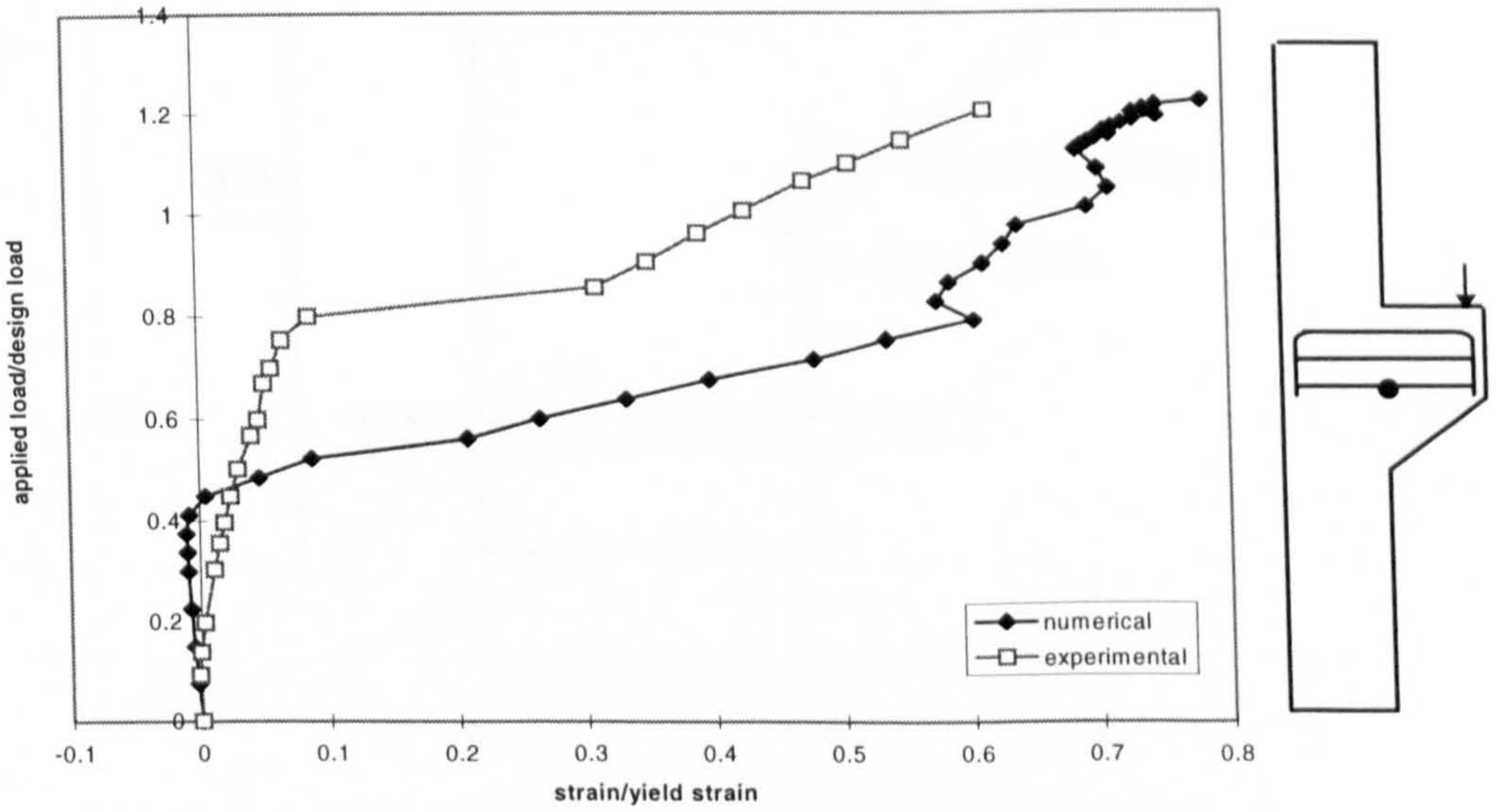

fig.8.5(i) Corbel C4A: Lower Stirrup reinforcement

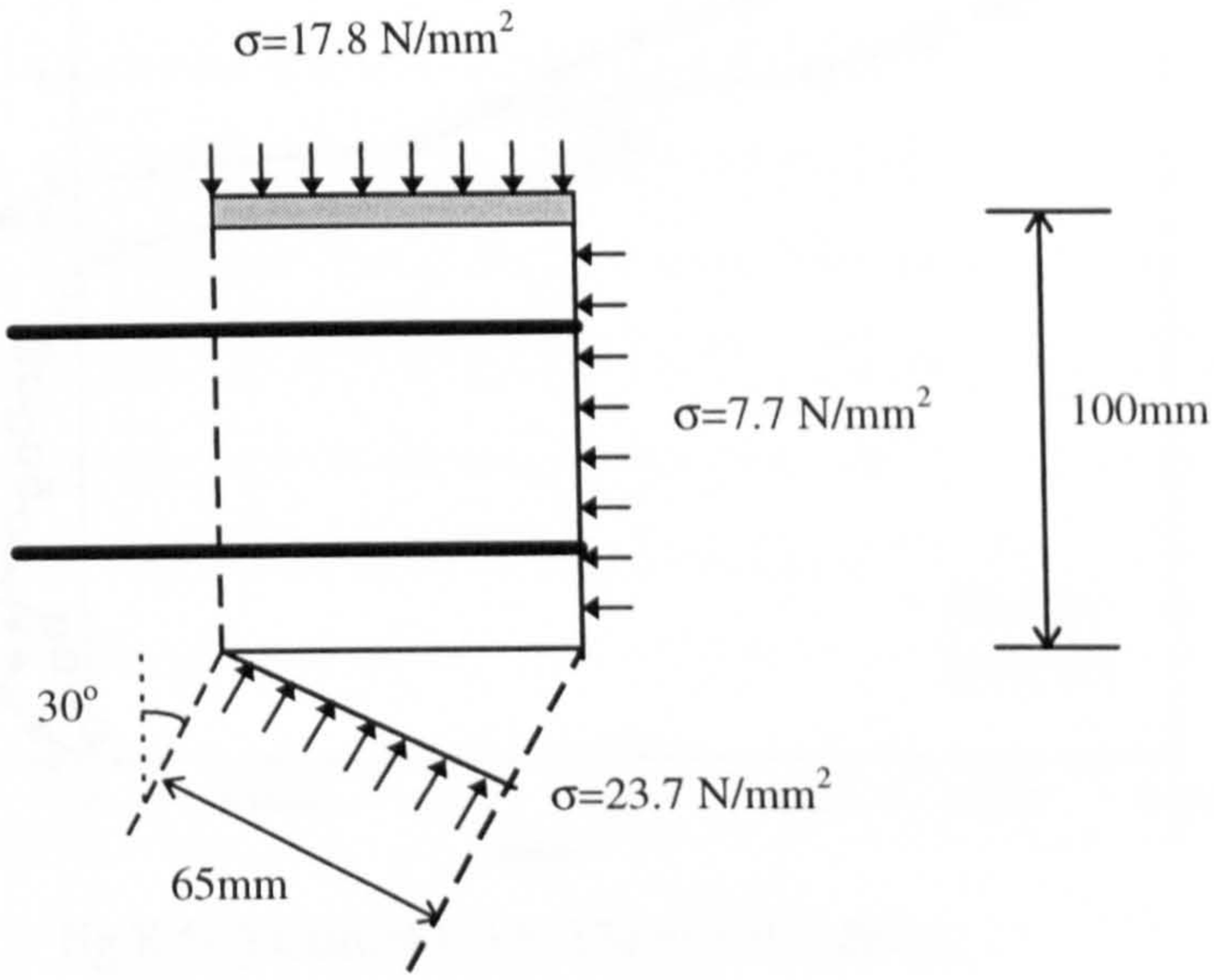

fig.8.5(j) Corbel C4A: Stresses in Node 1

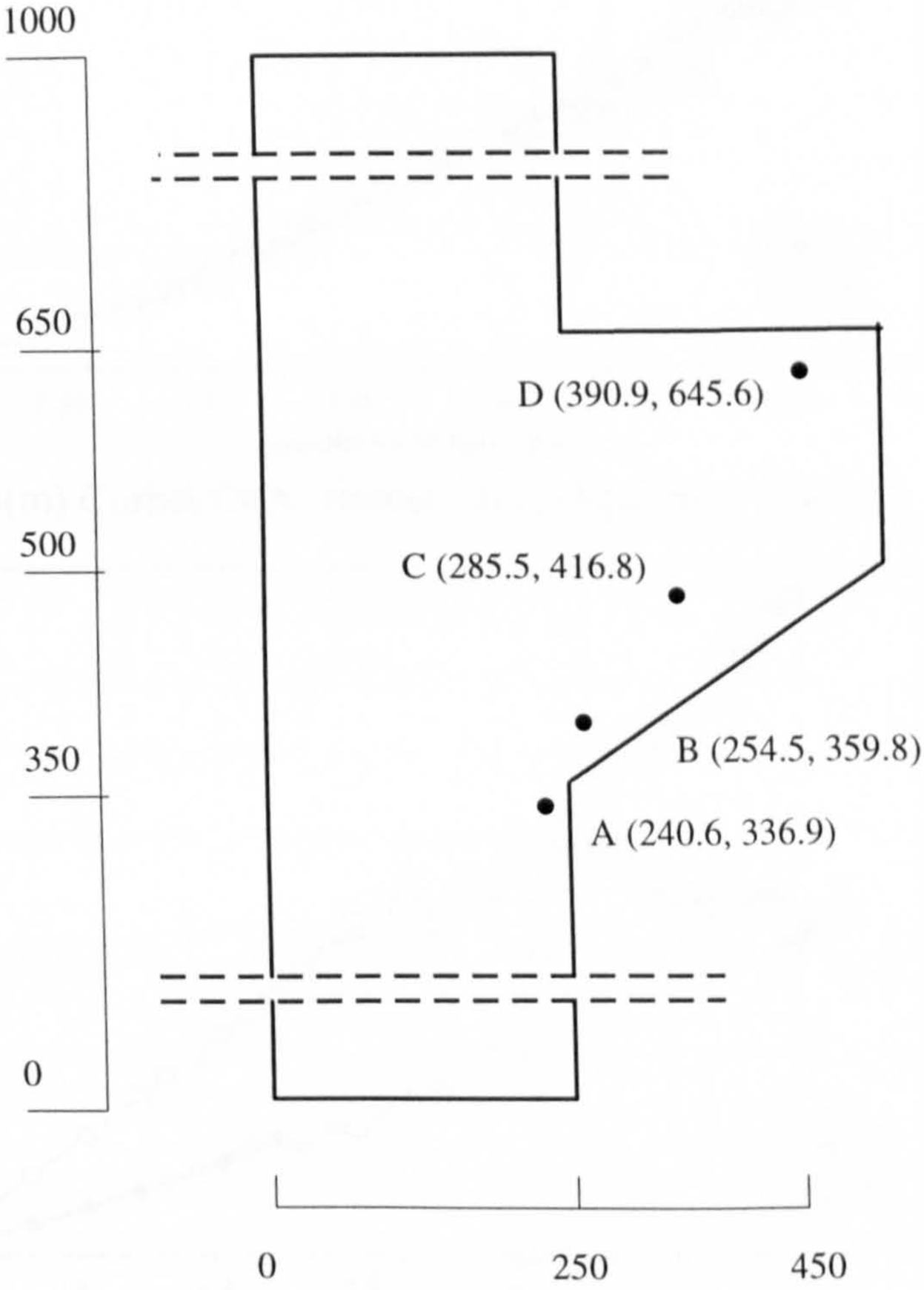

fig.8.5(k) Corbel C4A: Gauss point Positions for Numerical Stresses

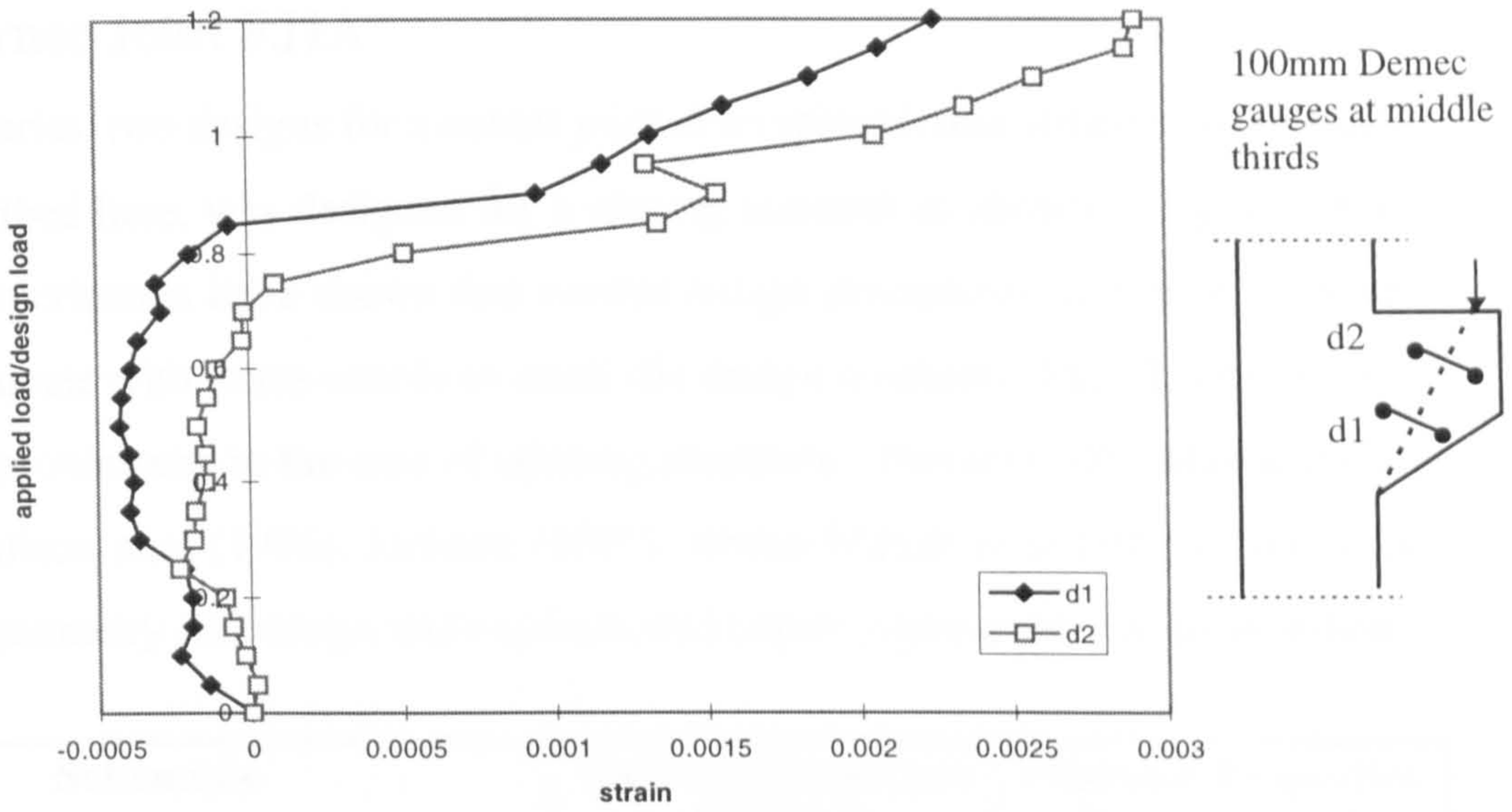

fig.8.5(l) Corbel C4A: Demec Readings

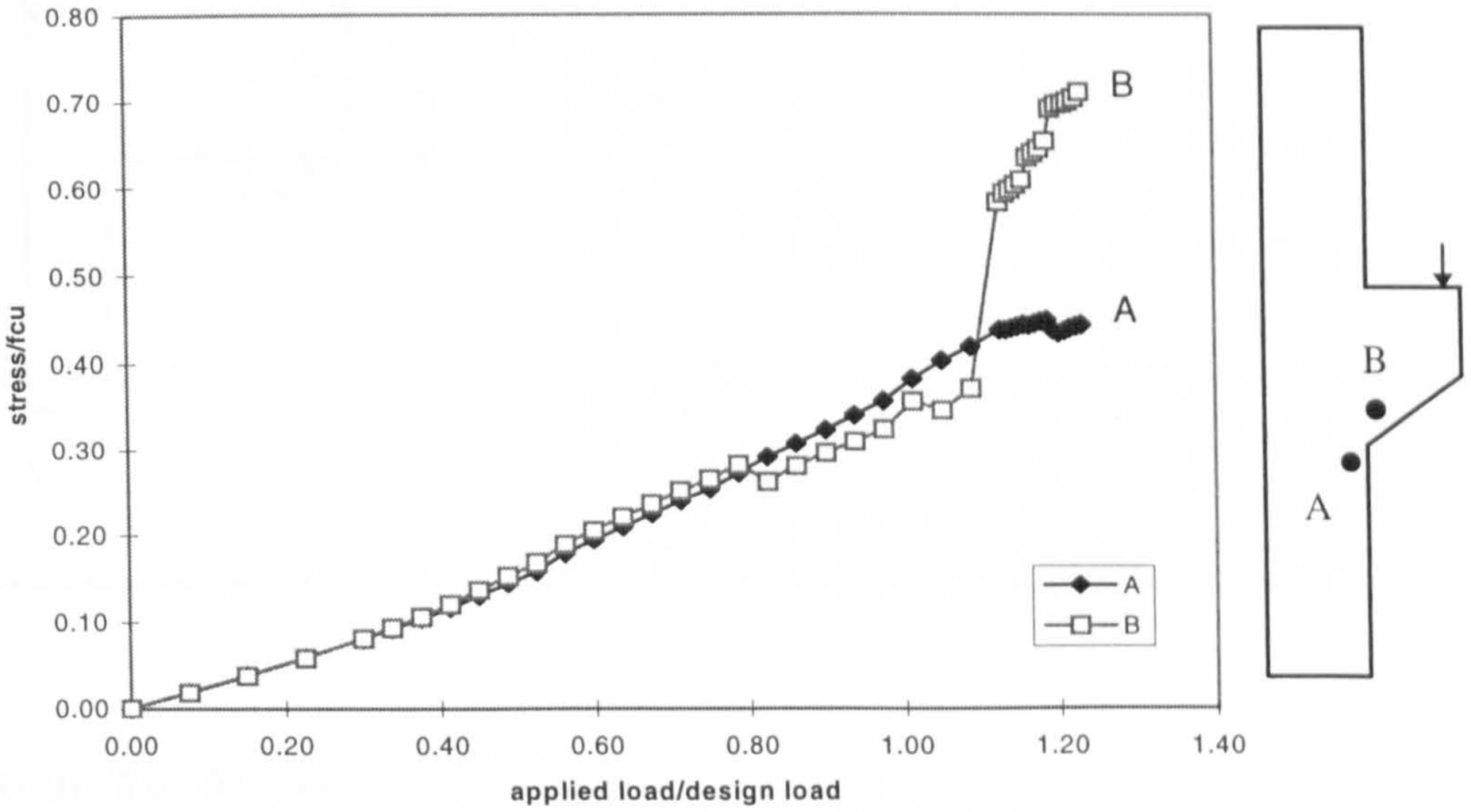

fig.8.5(m) Corbel C4A: Numerical Compressive Stresses

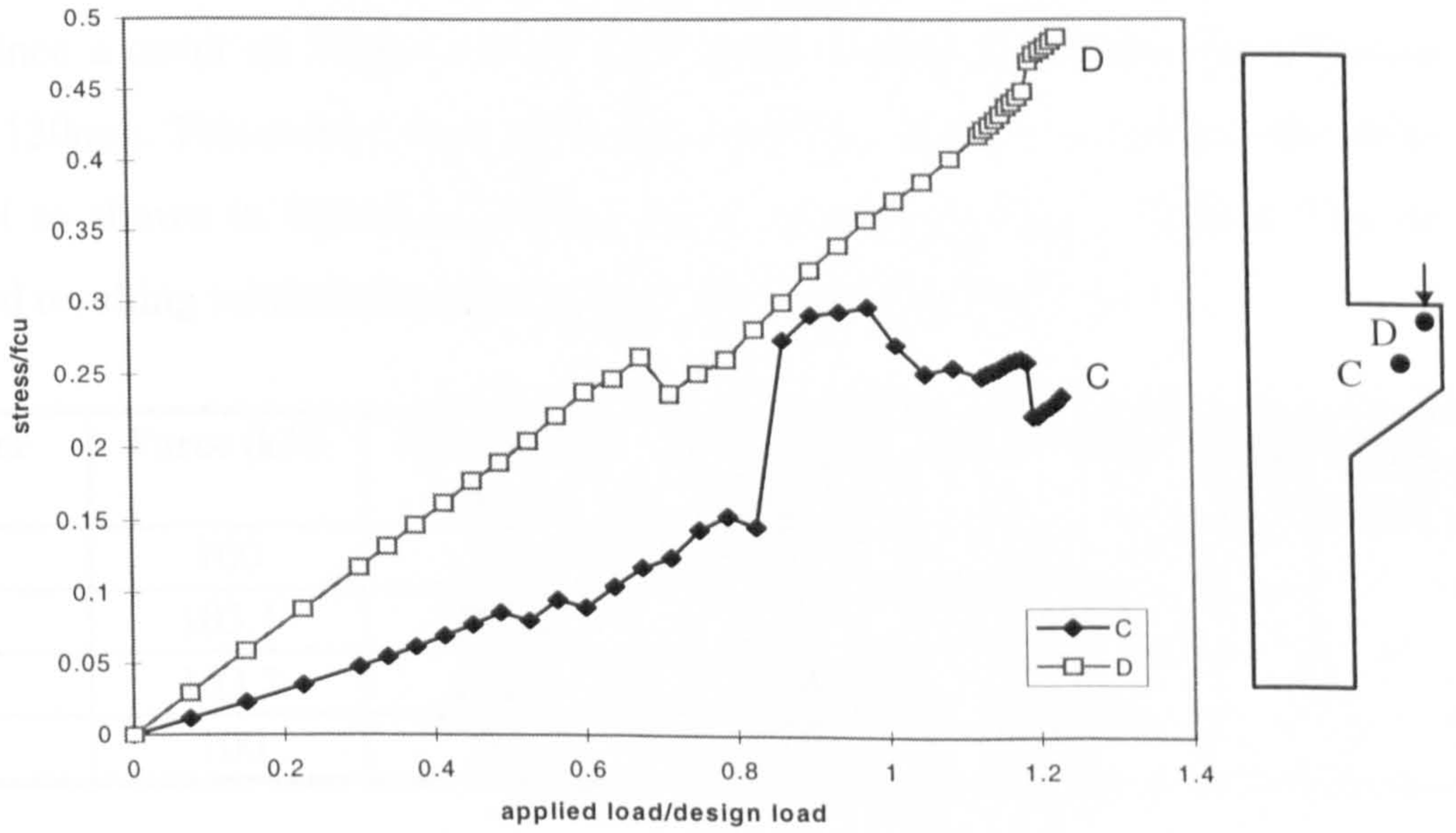

fig.8.5(n) Corbel C4A: Numerical Compressive

8.6 Corner Joint FJ1A

In the test series, two designs for a corner joint of a typical frame structure were made. FJ1A described here, was designed for a closing moment as shown in figure 8.6(a). Previous experiments have shown that current design procedures in corner joints are often inadequate with joints unable to attain the design moments, M_d. This problem is even more pronounced in the case of opening moments; Swann(1969), Mayfield et.al (1971), Nillson et.al (1976), Jackson (1995), Abdul-Wahab et al (1999). Details of the corner geometry and design and experimental material properties are given below.

Schematic	Material Properties (Design)	Material Properties (Experimental)
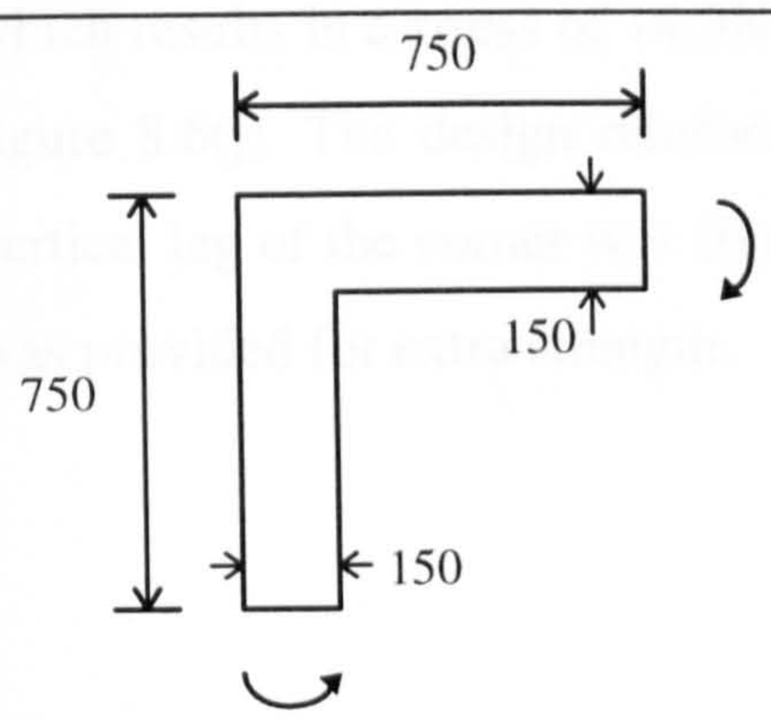	M_d=12kNm **concrete:** f_{cu}=40N/mm^2 f_t=3.0N/mm^2 E_c=21.5N/mm^2 **steel:** f_y=500N/mm^2 E_s=200kN/mm^2 thickness=150mm	 **concrete:** f_{cu}=38.9N/mm^2 f_t=3.2N/mm^2 E_c=21.76kN/mm^2 **steel:** f_y=504N/mm^2 (ϕ12) E_s=201.6kN/mm^2 f_y=509N/mm^2 (ϕ8) E_s=214.5kN/mm^2

8.6.1 Strut-Tie Model and Design

The results of the elastic analysis and corresponding strut-tie model are given in fig 8.6(a). Since a cover of 15mm will be used in the designed structure, the effective depth is 120mm. This results in an application of 100kN horizontal loads to the strut-tie model as shown in fig8.6a(iii) to create the design moment of 12kNm. The tie forces and resulting reinforcement provisions are given in the table below.

Member	Force (kN)	A_s required (mm^2)	A_s provided (mm^2)	No. of Bars	$\frac{A_s \text{ provided}}{A_s \text{ required}}$
1	100	200	226	2ϕ12	1.1
5	103.1	206.2	226	2ϕ12	1.1
6	103.2	206.2	226	2ϕ12	1.1
9	100	200	226	2ϕ12	1.1

At the inner corner of the structure, i.e. node 2, the concrete is in a state of bi-axial compression and hence the stress is limited to $1.1f_{cu}$. The depth of struts 2 and 8 is equivalent to the depth of the compressive stress block of reinforced member in bending, in this case 30mm. This value was calculated from simple bending theory. The critical area in this model is the TCT node 3. Here the tie forces cause compression along the inner circumference of the reinforcement.

From the geometry of the bar, the effective width of the strut at this point is equal to 50mm. Due to the presence of the two ties, the concrete stress in this zone must be less than $0.6f_{cu}$. From the strut-tie model, the force in this strut is equal to 107kN, which results in a stress of $14.3N/mm^2 < 0.6f_{cu}$. A schematic of this node is shown in figure 8.6(j). The design reinforcement layout is given in figure 8.6(b). Where the vertical leg of the corner was fixed to the floor, reinforcement in the form of a spiral was provided for extra strength.

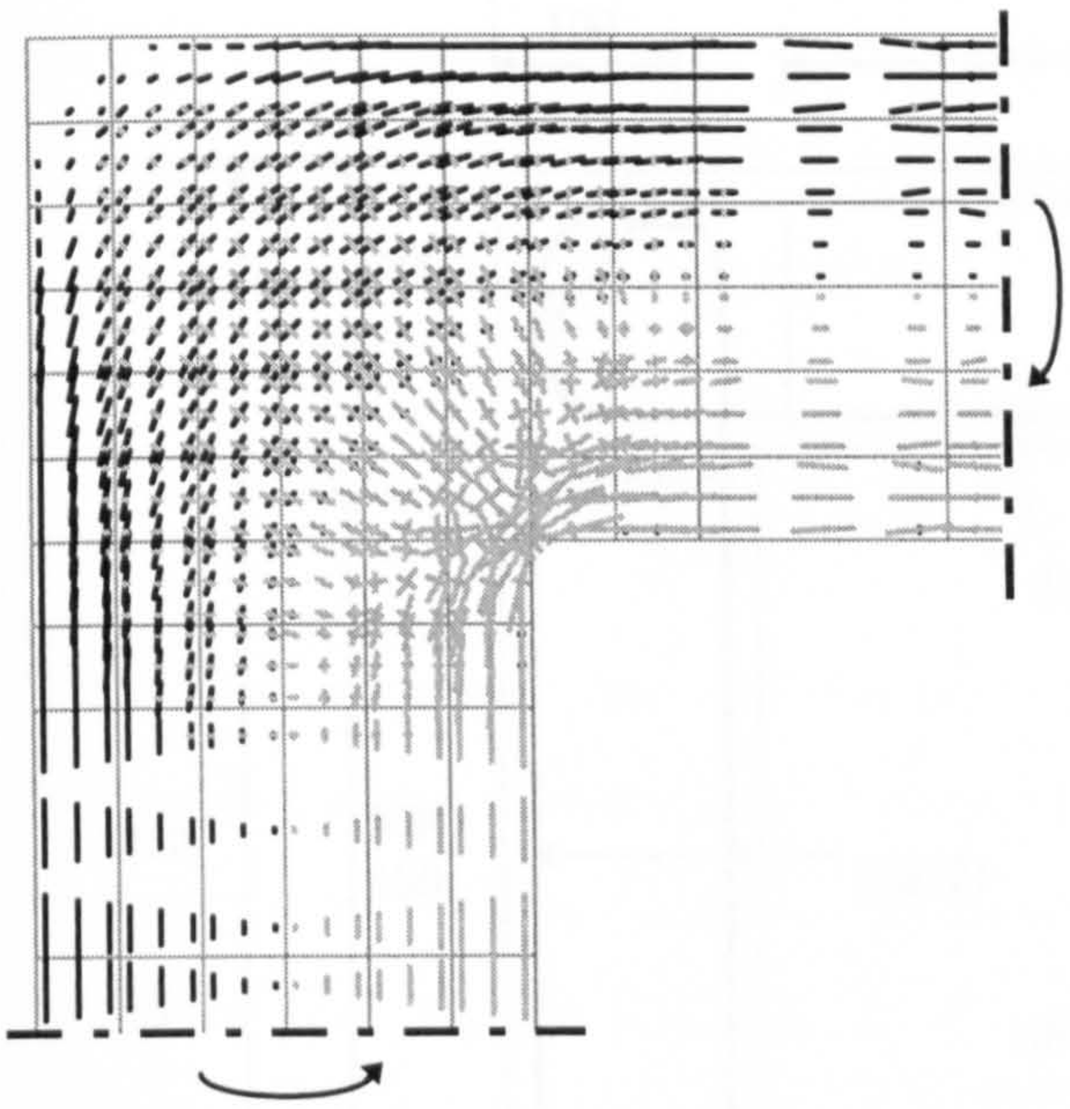

i) (rr=0)

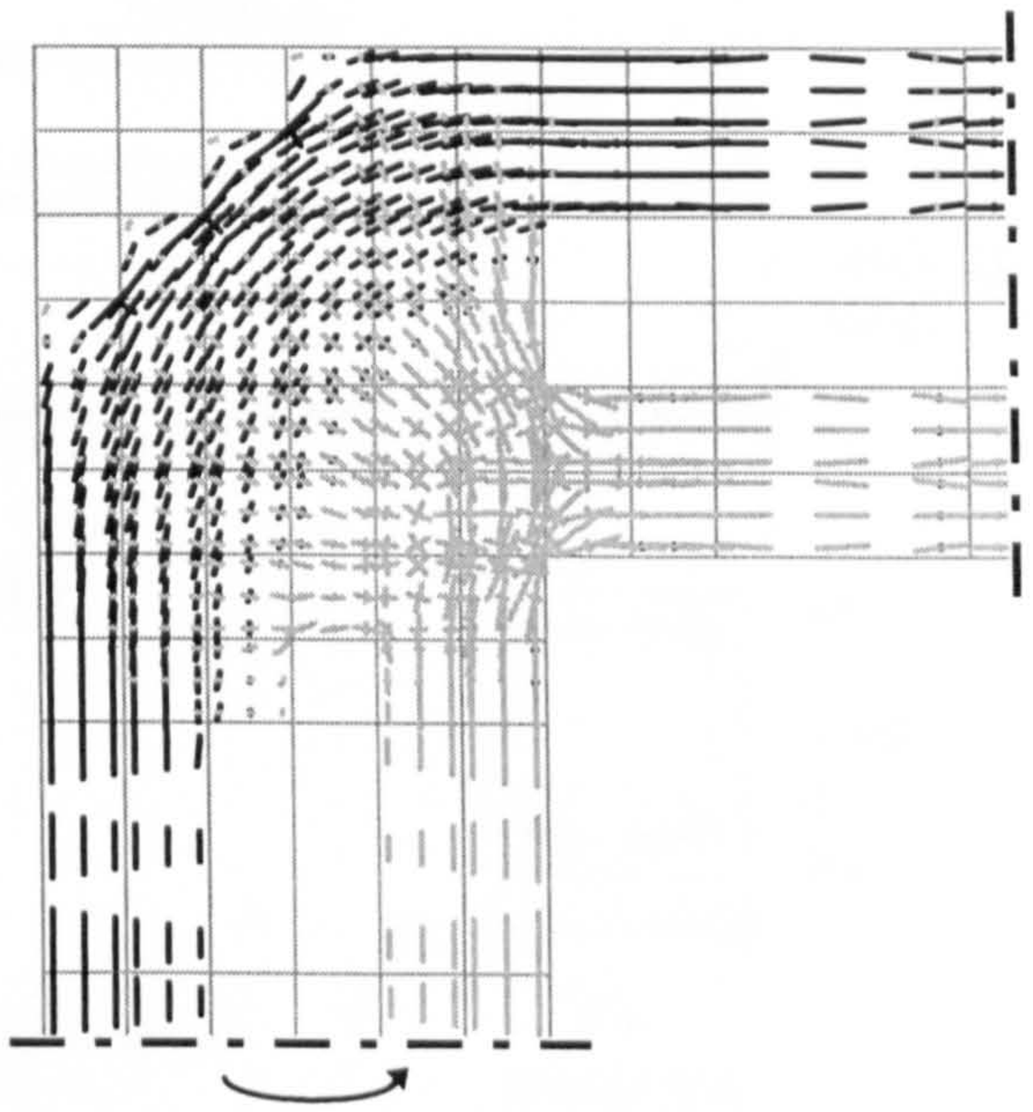

ii) (rr=30%)

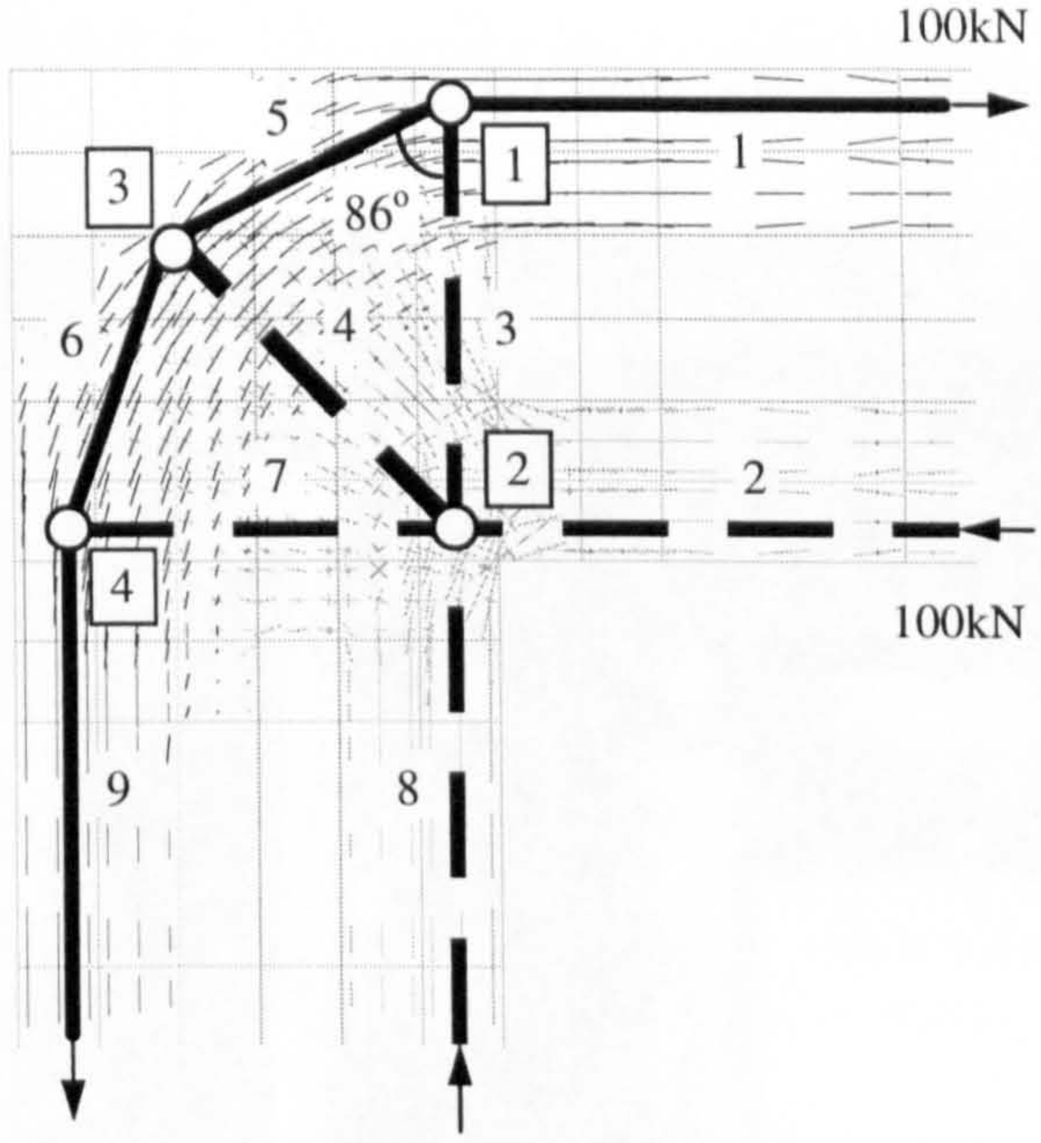

iii) Strut-tie Model

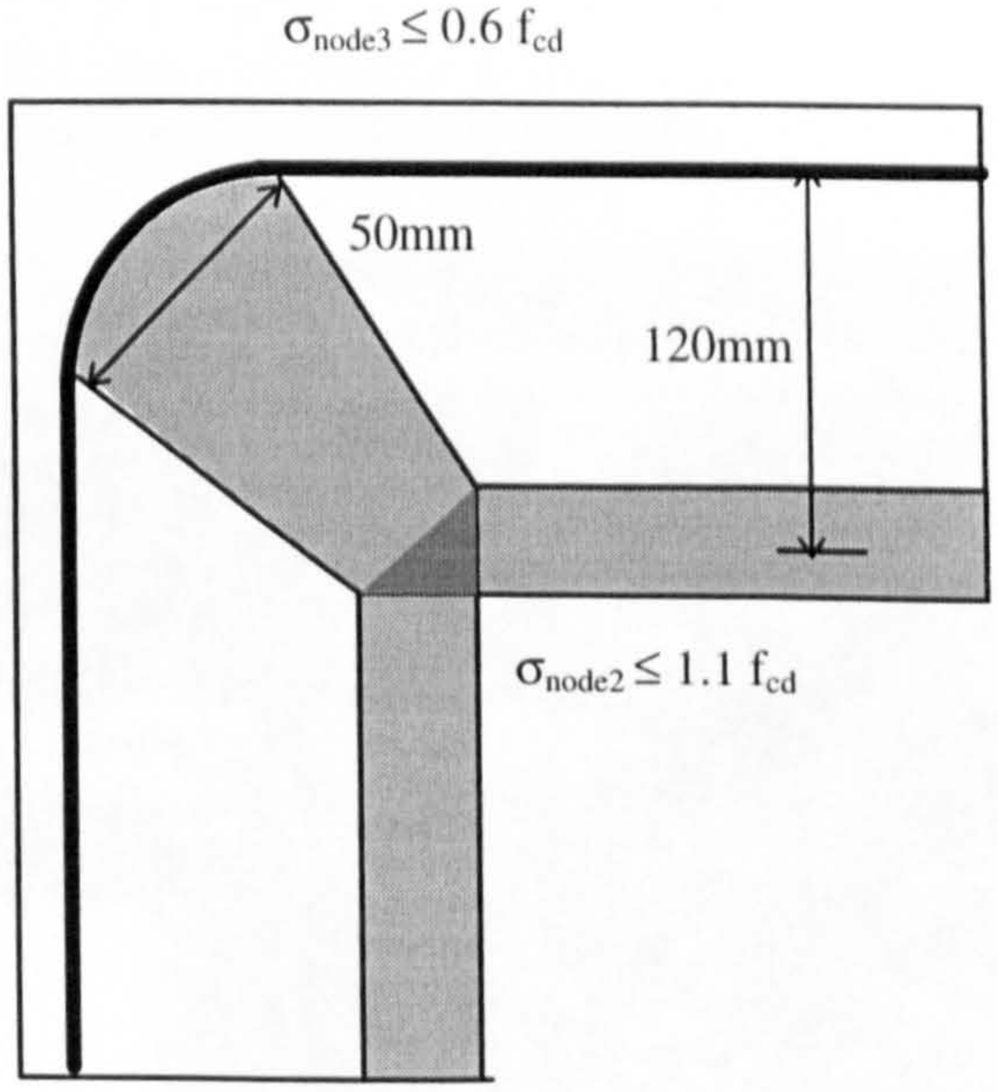

iv) Dimensioning

fig.8.6(a) Corner Joint FJ1A, Elastic stresses and Strut-tie mode

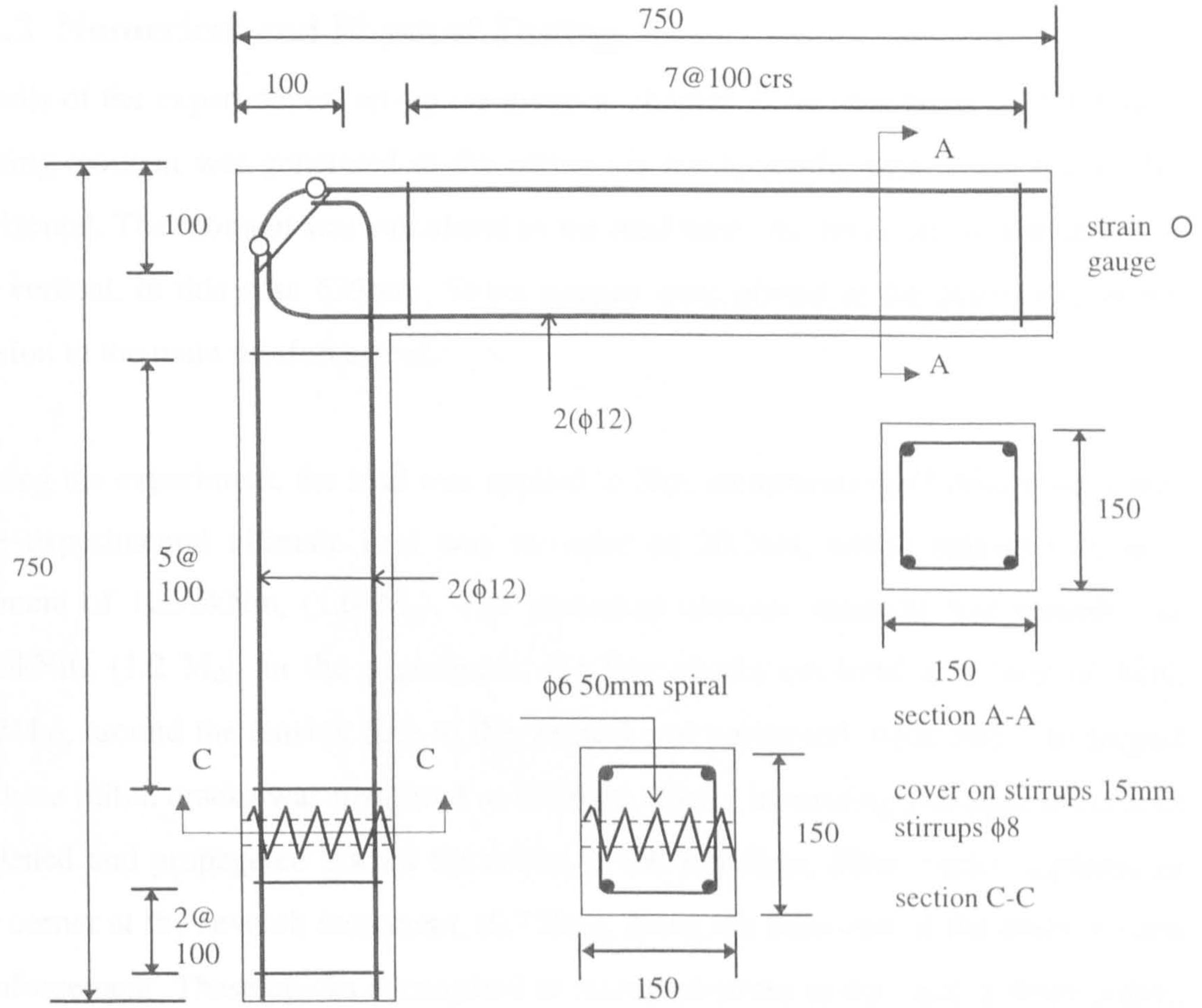

fig.8.6b(i) Corner FJ1A Reinforcement Layout, all sizes in mm

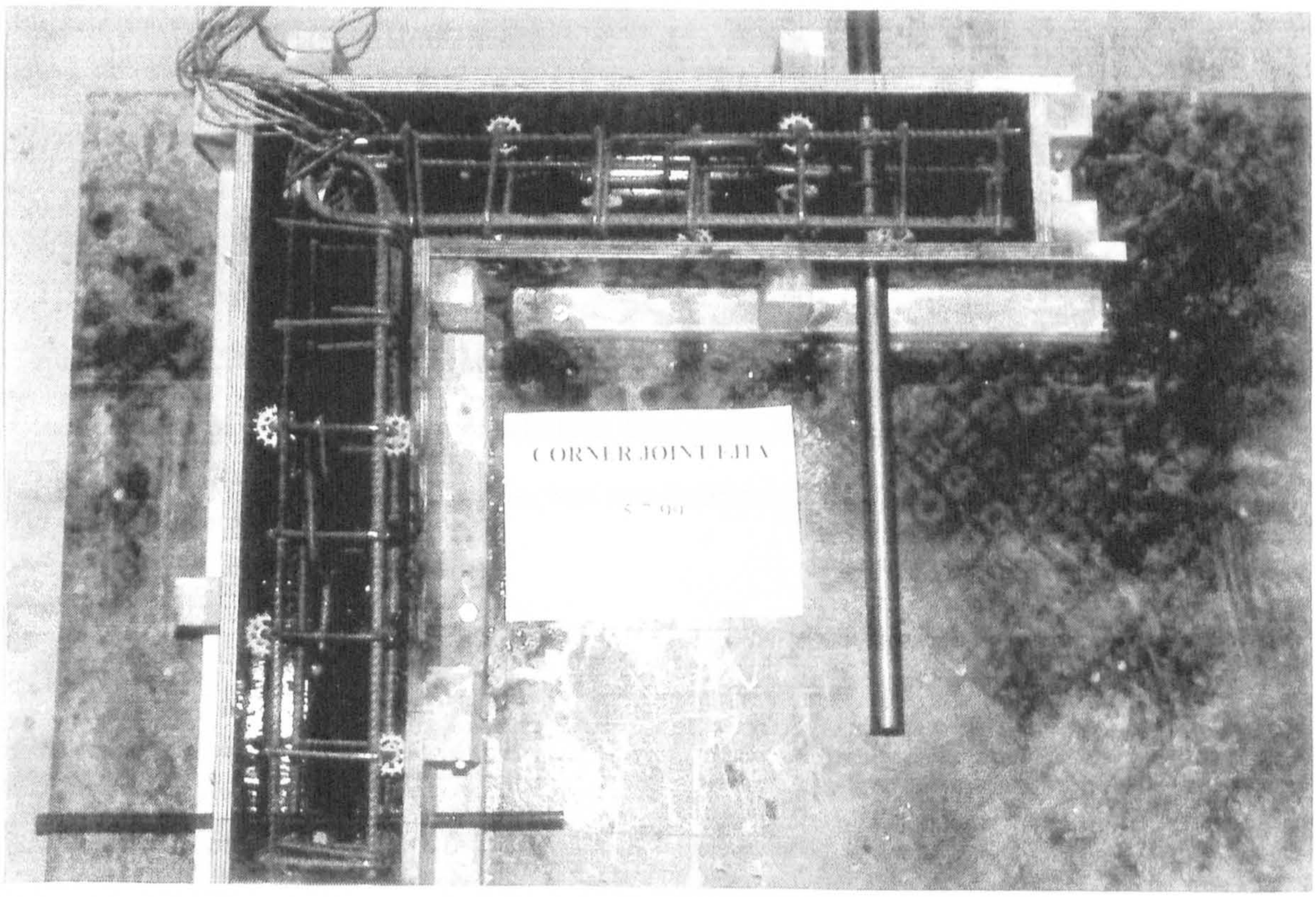

fig.8.6b(ii) Corner FJ1A Reinforcement & Formwork

8.6.2 Numerical and Physical Testing

Details of the experimental set-up are given in chapter 7. As seen from fig.7.3.3(a), a closing moment was generated in the corner via the hydraulic jack at the end of the horizontal. The moment was calculated as the load times the lever arm to the centre of the vertical, in this case 625mm. Strain gauges were placed at the points maximum tension in the main reinforcement.

During the experiment, the load was applied in 2kN increments until failure occurred. The experimental ultimate load was recorded as 20.7kN, which corresponds to a moment of 12.96kNm, ($1.08M_d$). The numerical ultimate moment was recorded as 14.5kNm, ($1.2\ M_d$). In the experiment, the first cracks occurred at a load of 4kN, ($0.2M_d$), around the tension face of the vertical and horizontal, fig.8.6(c). The largest of these initial cracks was measured as 0.02mm. Under increasing moment, the cracks widened and propagated toward the centre of the members. New cracks appeared in the corner at the seventh increment, ($0.73M_d$), along the direction of the main tension reinforcement. These cracks correspond to increased strain in the steel at these points, fig.8.6(d). The largest crack, at the beam column junction, reached the service crack limit width of 0.3mm at a load of 16kN, ($0.8\ M_d$). At the ultimate moment, the main horizontal and vertical steel yielded, and this was accompanied by widening of the cracks around the tension zone, fig.8.6(e-f). The numerical and experimental steel strains presented in figs.8.6(g-h) show a reasonable correlation.

The numerical compressive stresses show that stress concentrations occurred in the inner corner, which as previously stated is under bi-axial compression, fig.8.6(k). The limit stress of $1.1f_{cu}$ was not reached at this point. Similarly, as predicted in the strut-tie model, the limit stress of $0.6f_{cd}$ was not reached in the diagonal strut, fig.8.6(l)

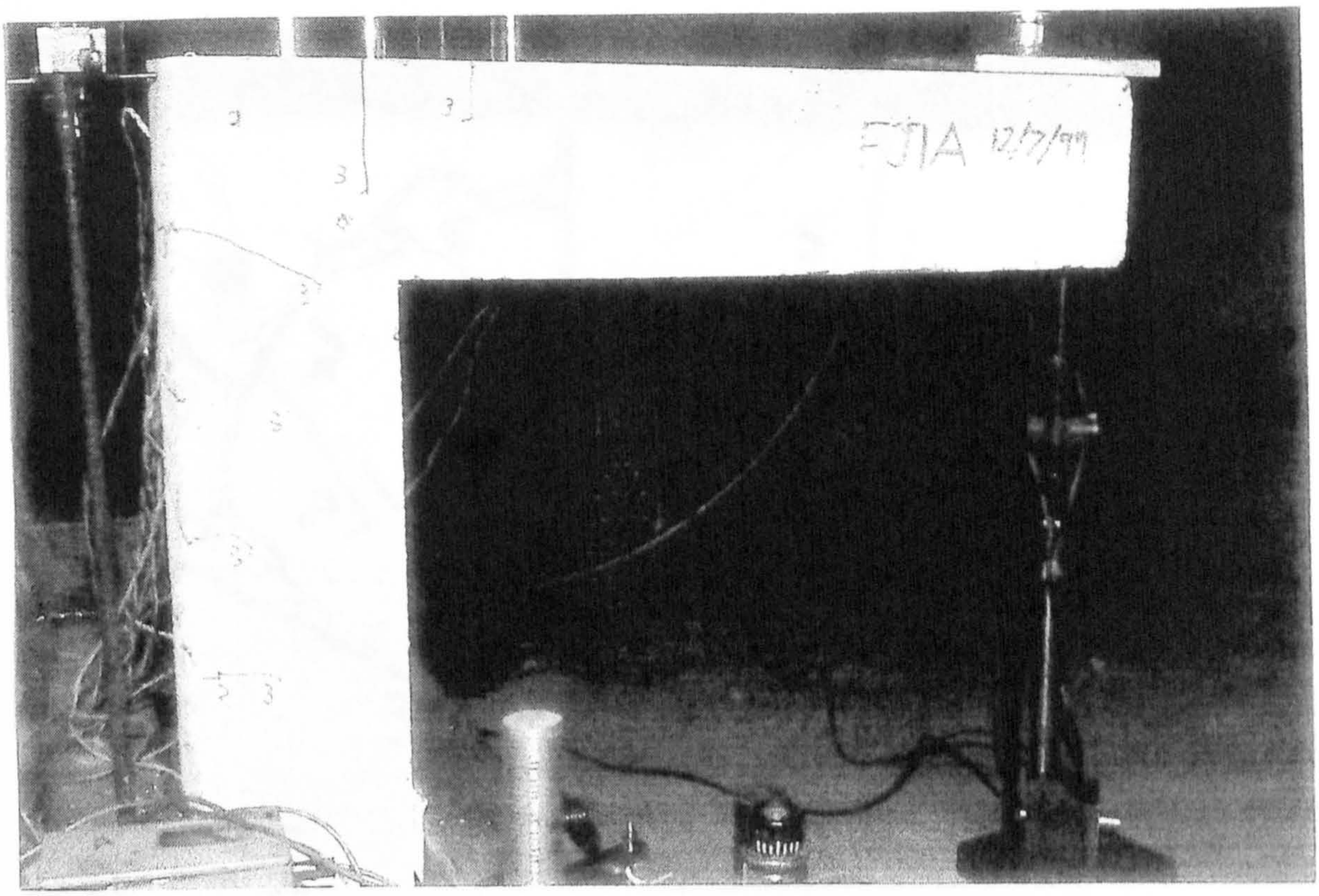

fig.8.6(c) Corner FJ1A ($0.3M_d$)

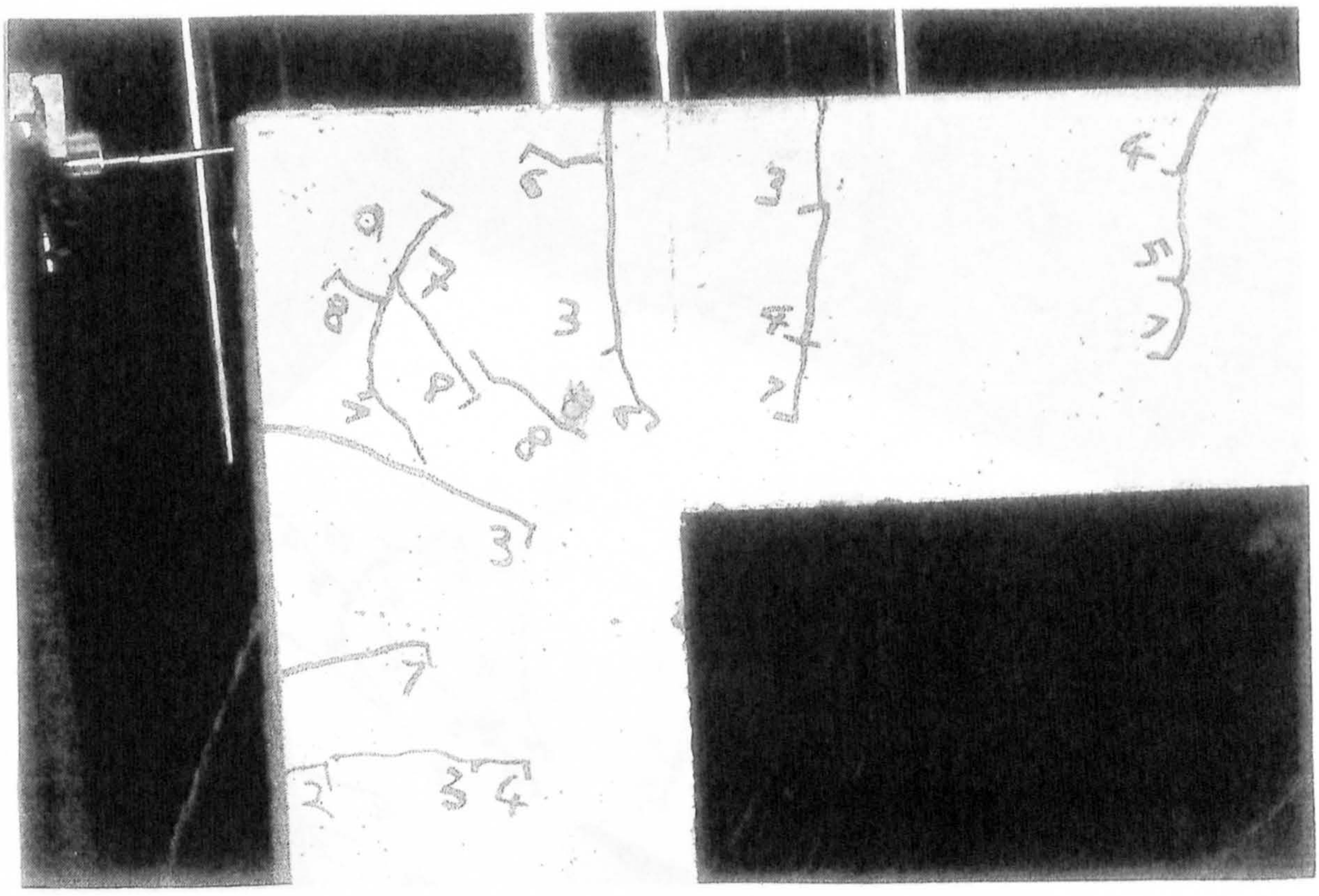

fig.8.6(d) Corner FJ1A ($0.73M_d$)

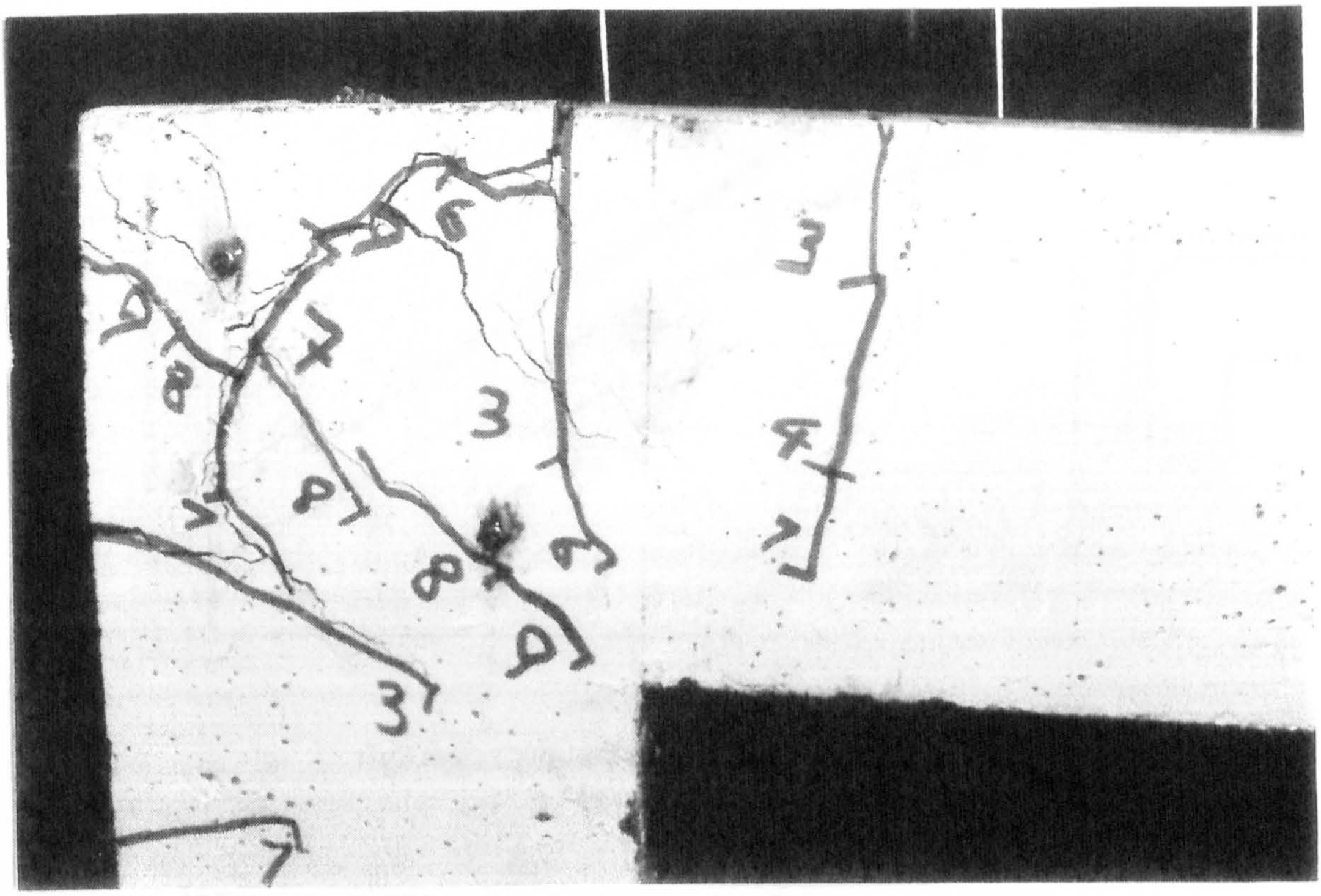

fig.8.6(e) Corner FJ1A at ultimate ($1.08M_d$)

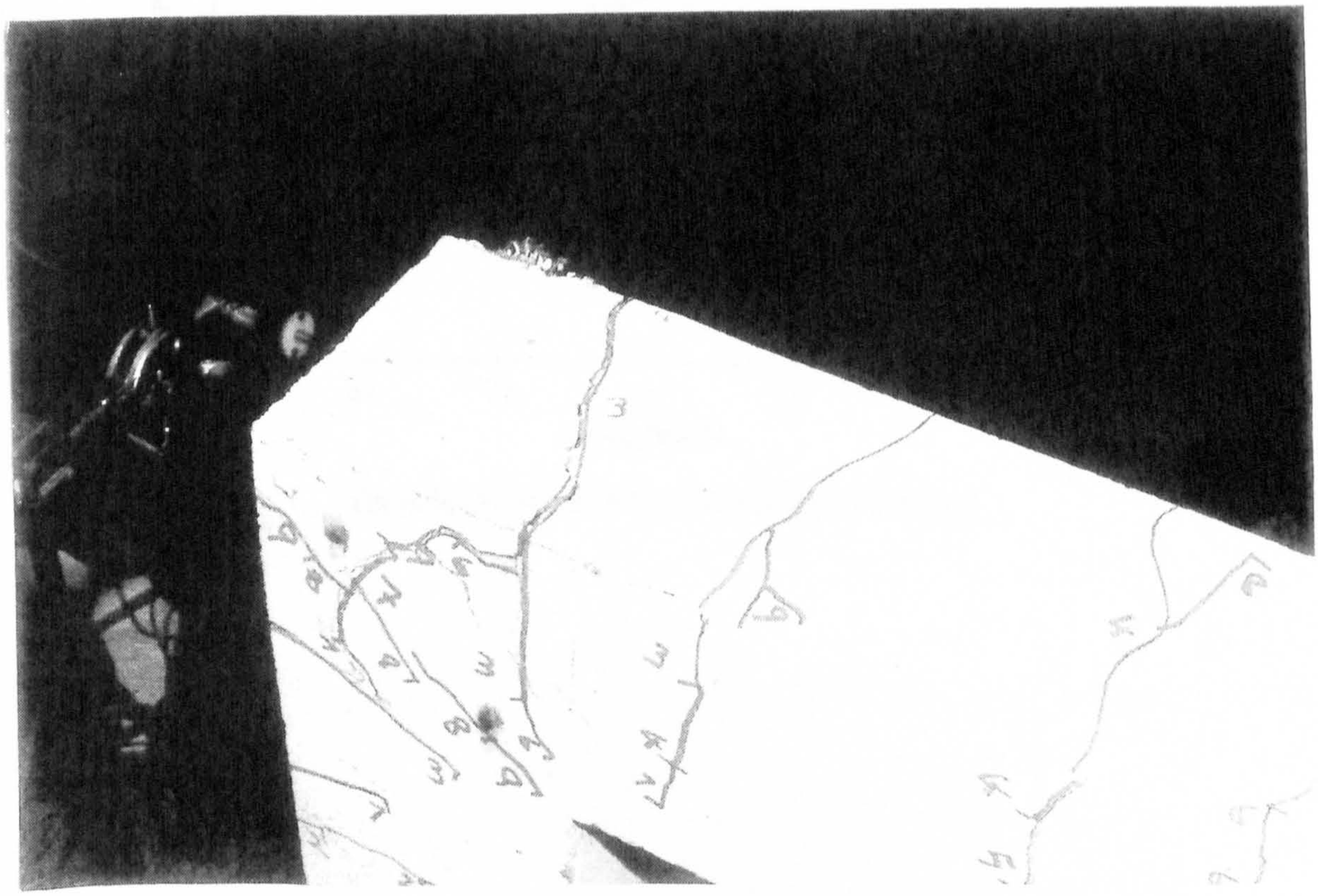

fig.8.6(f) Corner FJ1A at ultimate ($1.08M_d$)

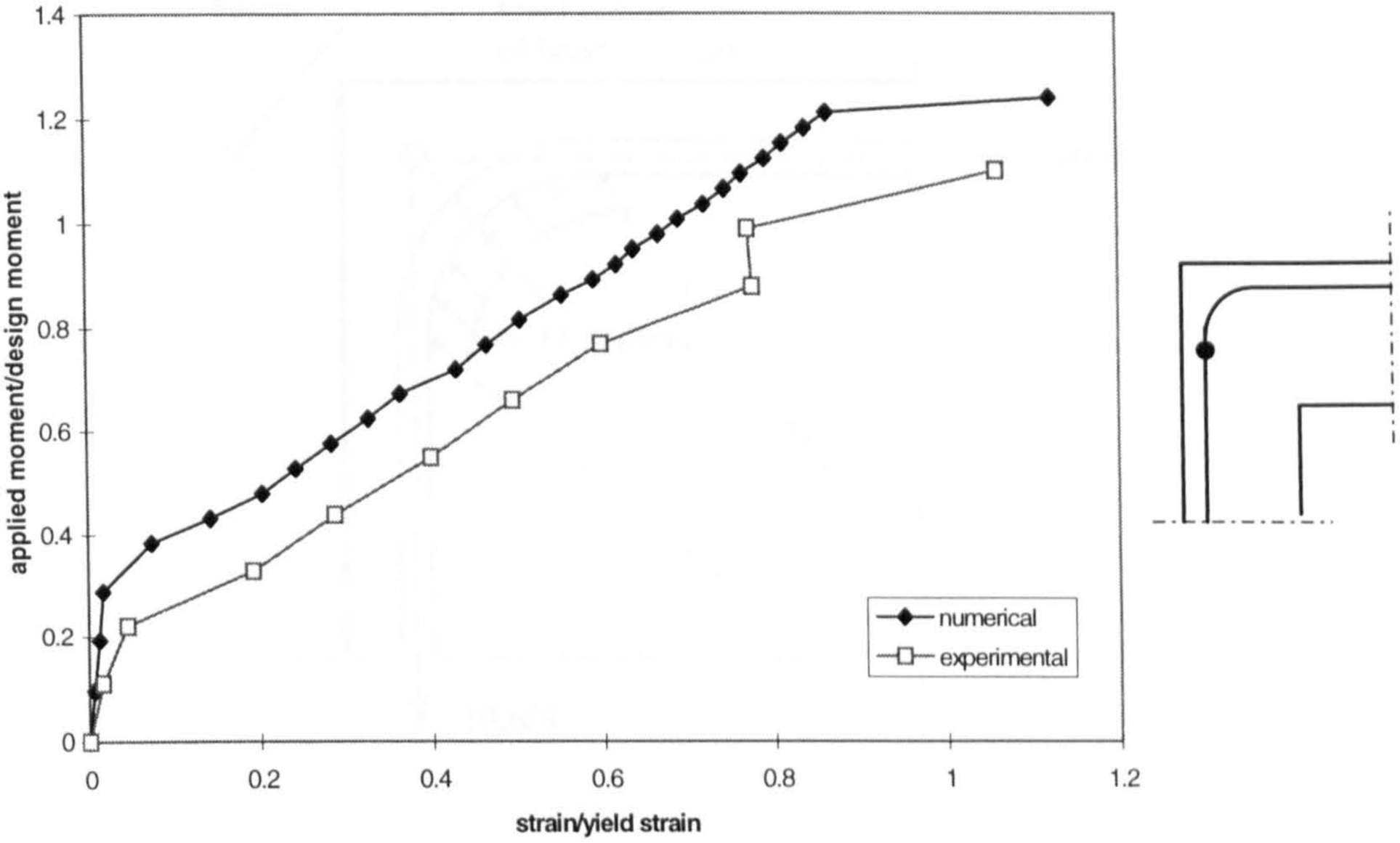

fig8.6(g) Corner FJ1A: Main Steel Strains

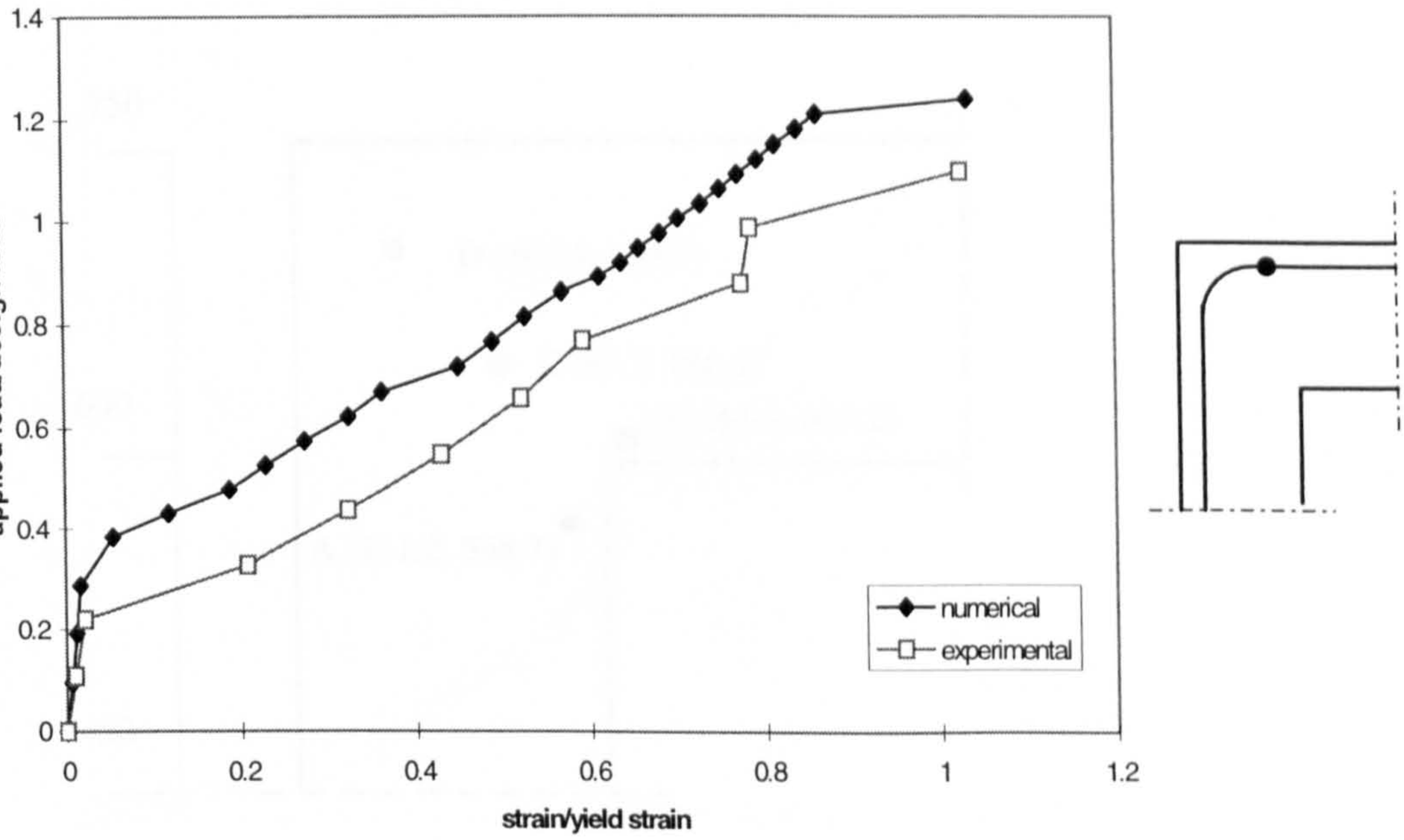

fig.8.6(h) Corner FJ1A: Main Steel Strains

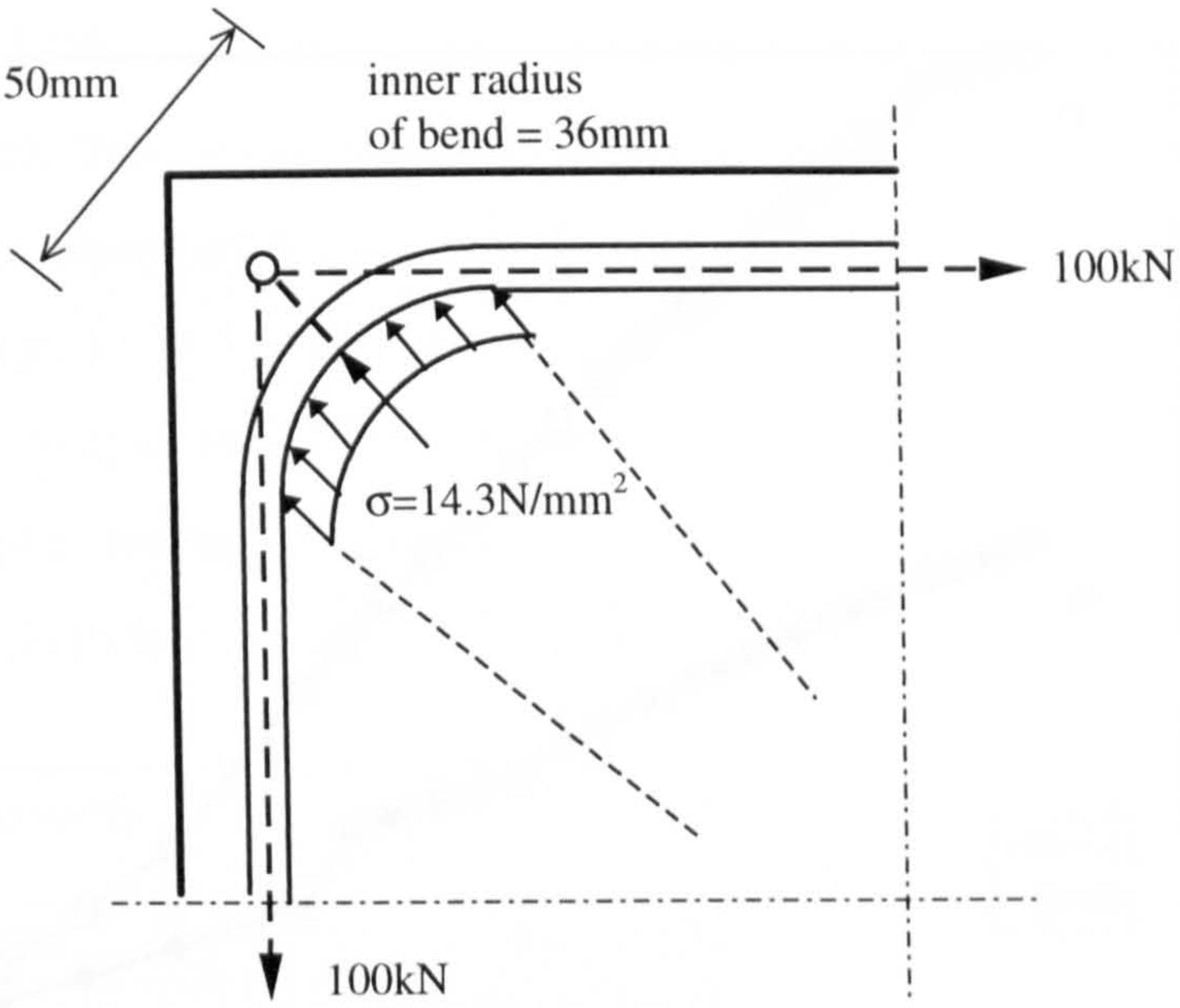

fig.8.6(i) Corner FJ1A: Node 3 Stresses

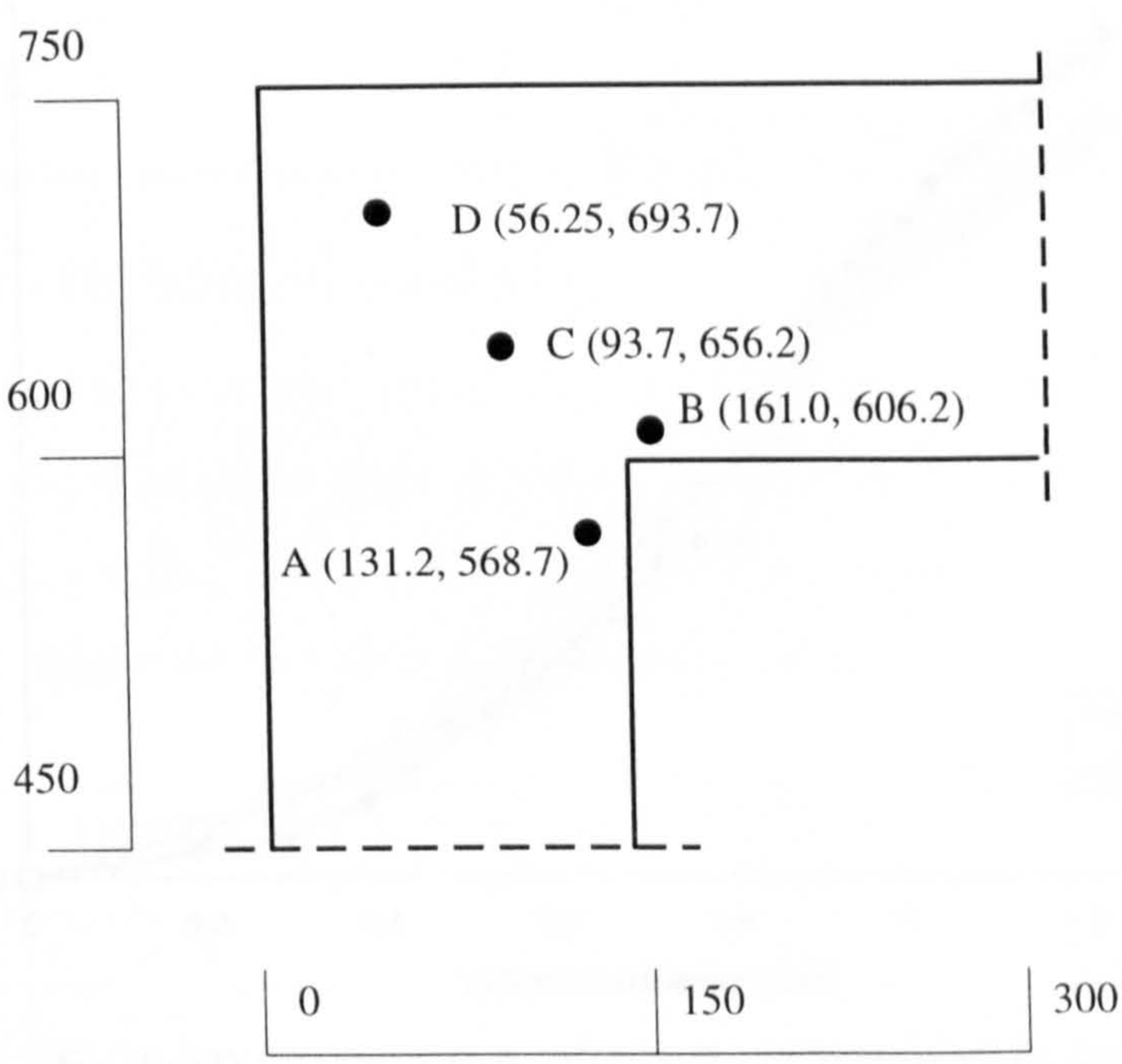

fig.8.6(j) Corner Joint FJ1A: Gauss Point Positions for Numerical Stresses

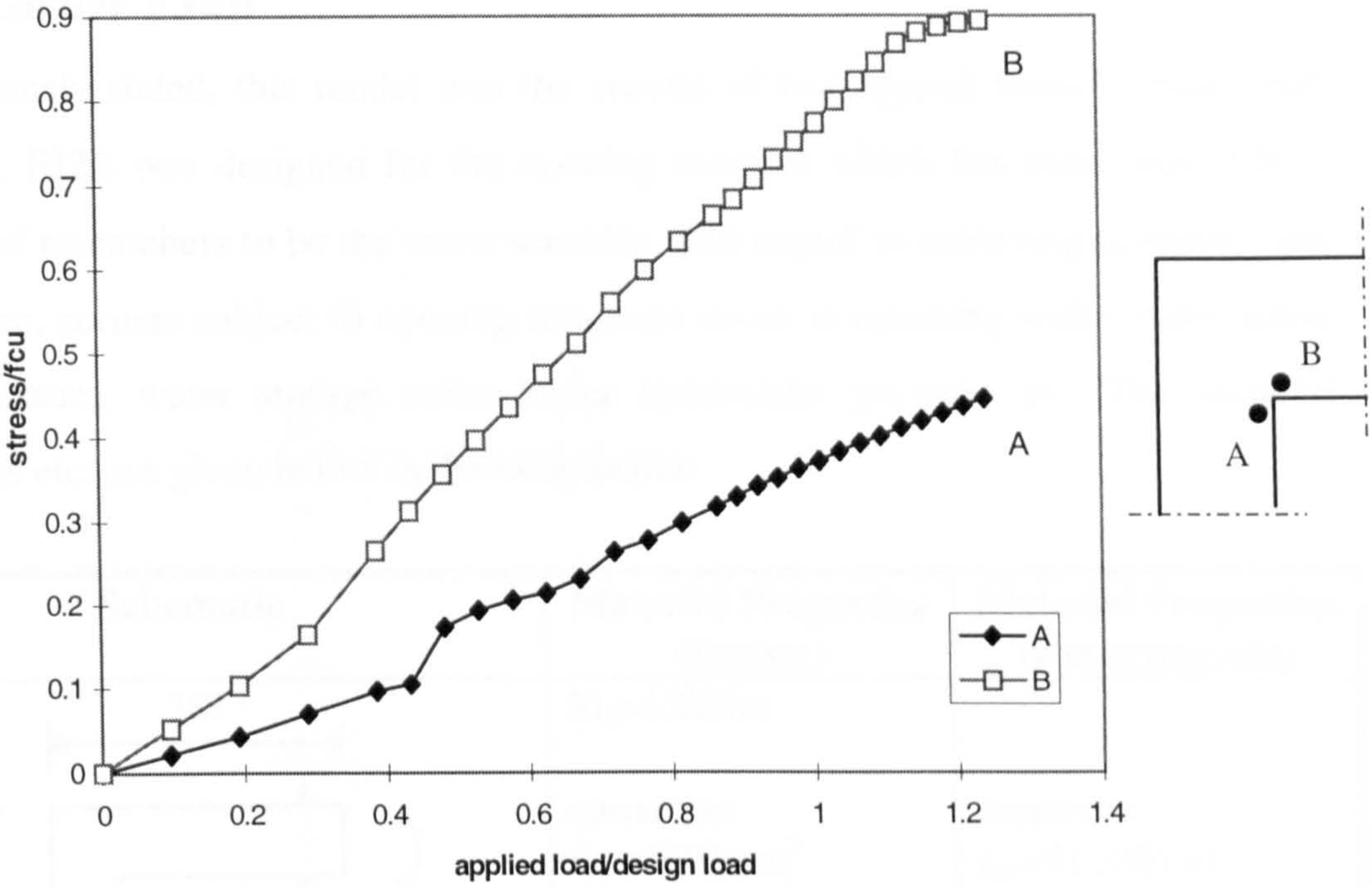

fig.8.6(k) Corner FJ1A: Numerical Compressive Stresses

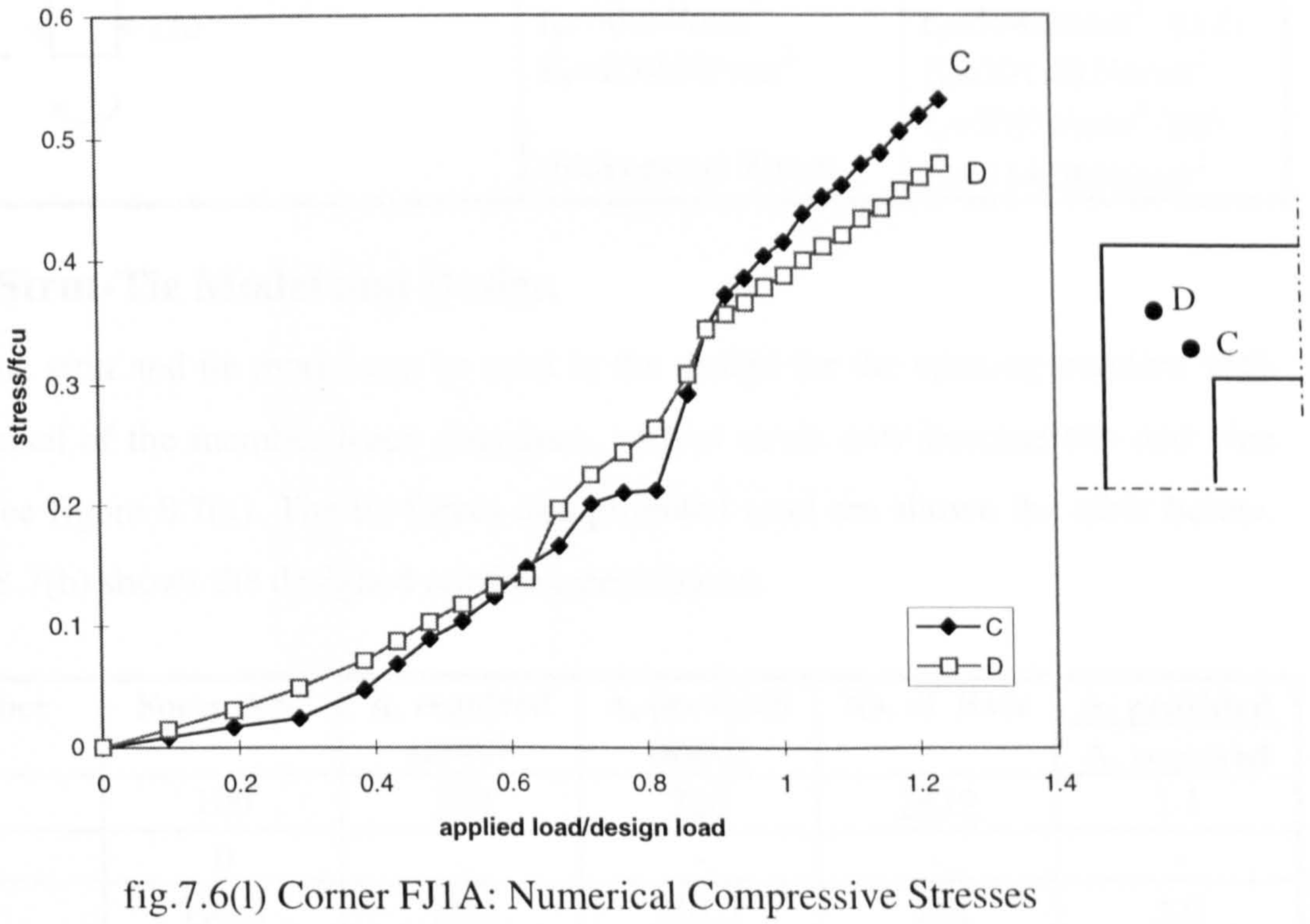

fig.7.6(l) Corner FJ1A: Numerical Compressive Stresses

8.7 Corner FJ2B

As previously stated, this model was the second of two typical frame corner joints designed. FJ2B was designed for the opening moment which has been proved by a number of researchers to be the worst scenario with regard to achieving ultimate load. In practice, corners subject to opening moments occur in retaining walls under active earth pressure, water storage tanks under hydrostatic pressure etc. The material properties etc. are given below in the table below

Schematic	Material Properties (Design)	Material Properties (Experimental)
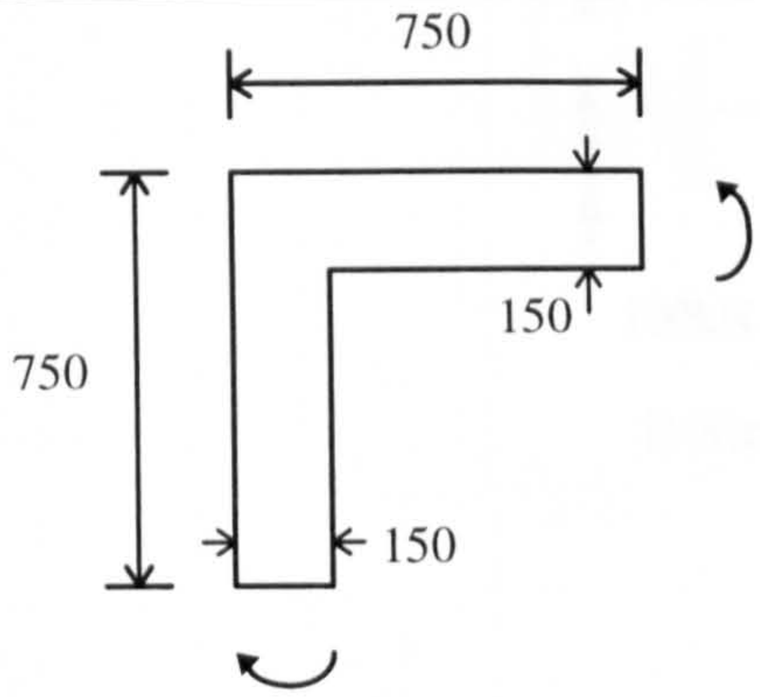	M_d=12kNm **concrete:** f_{cu}=40N/mm^2 f_t=3.0N/mm^2 E_s=21.5kN/mm^2 **steel:** f_y=500N/mm^2 E_s=200kN/mm^2 thickness=150mm	 **concrete:** f_{cu}=41.3N/mm^2 f_t=3.5N/mm^2 E_s=23.73kN/mm^2 **steel:** f_y=504N/mm^2 (ϕ12) E_s=201.6kN/mm^2 f_y=509N/mm^2 (ϕ8) E_s=214.5kN/mm^2

8.7.1 Strut-Tie Model and Design

The same strut and tie model can be used in the design for the opening moment with the reversal of the member force directions, so that struts now become ties and vice versa, see figure 8.7(a). The tie forces and provided steel are shown the table below. Figure 8.7(b) shows the designed reinforcement layout.

Member	Force (kN)	A_s required (mm^2)	A_s provided (mm^2)	No. of Bars	$\frac{A_s \text{ provided}}{A_s \text{ required}}$
2	100	200	226	2ϕ12	1.1
3	0	-	-	-	-
4	106.4	200	201.1	4ϕ8	1.0
7	0	-	-	-	-
8	100	200	226	2ϕ12	1.1

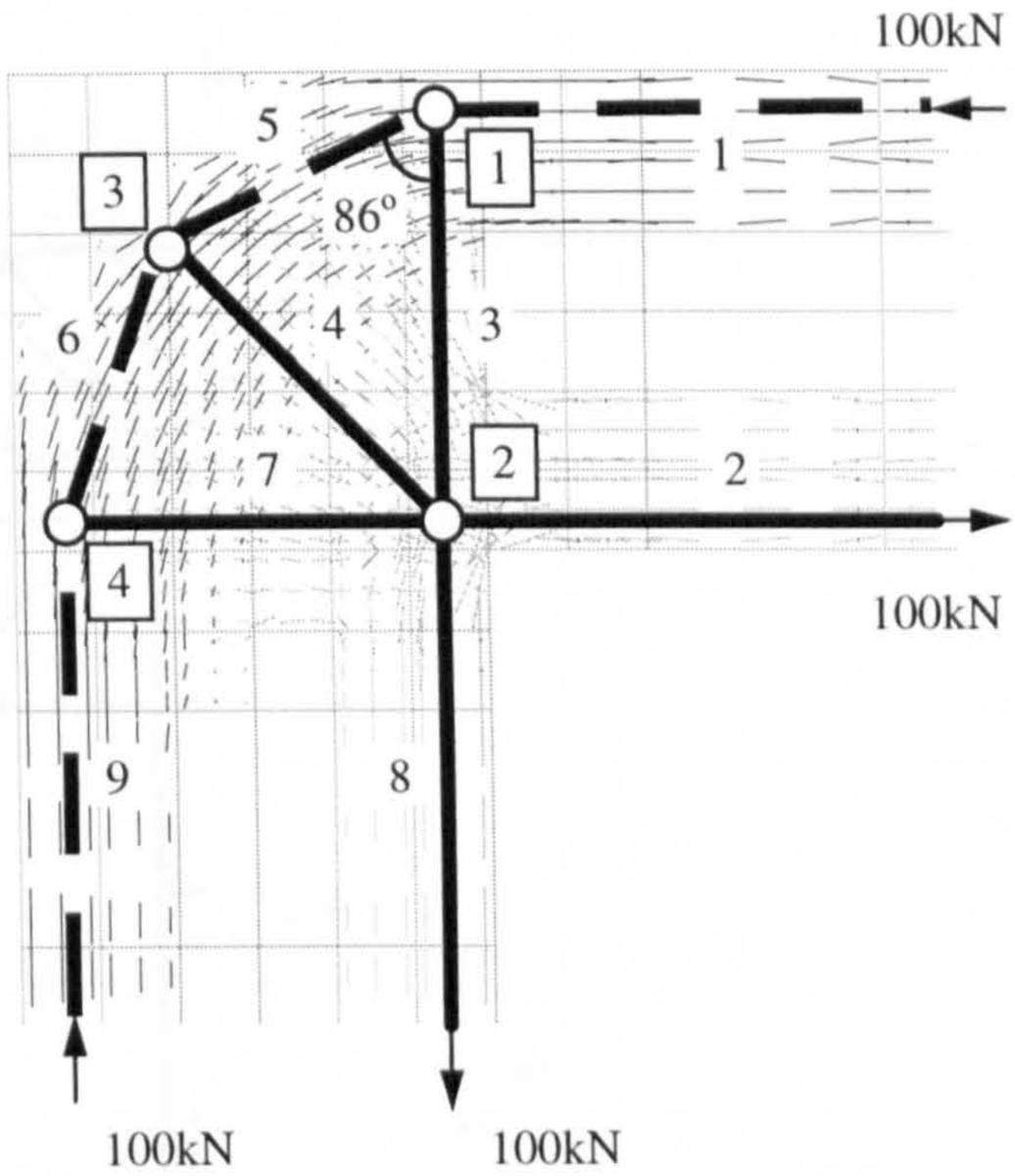

i) Strut-tie Model

$\sigma_{node3} \leq 0.75\ f_{cd}$

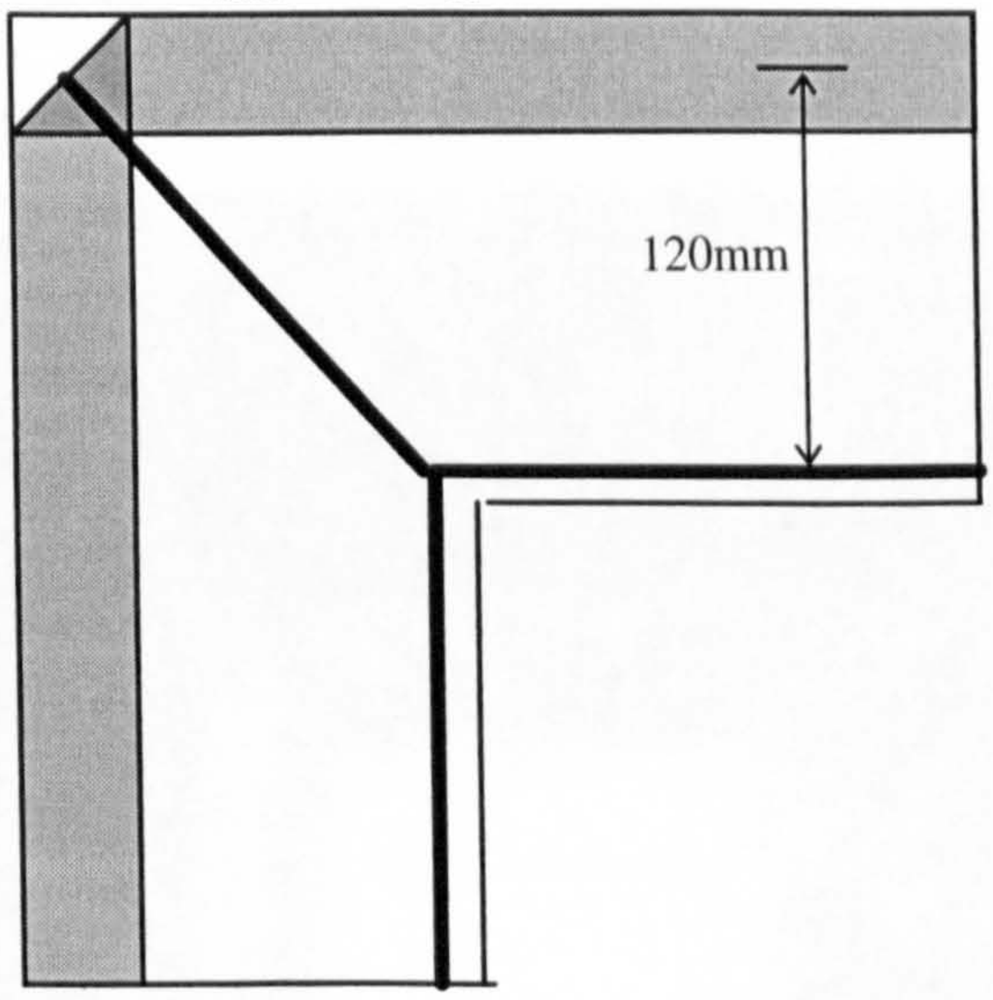

ii) Dimensioning

fig.8.7(a) Corner FJ2B Strut-Tie Model

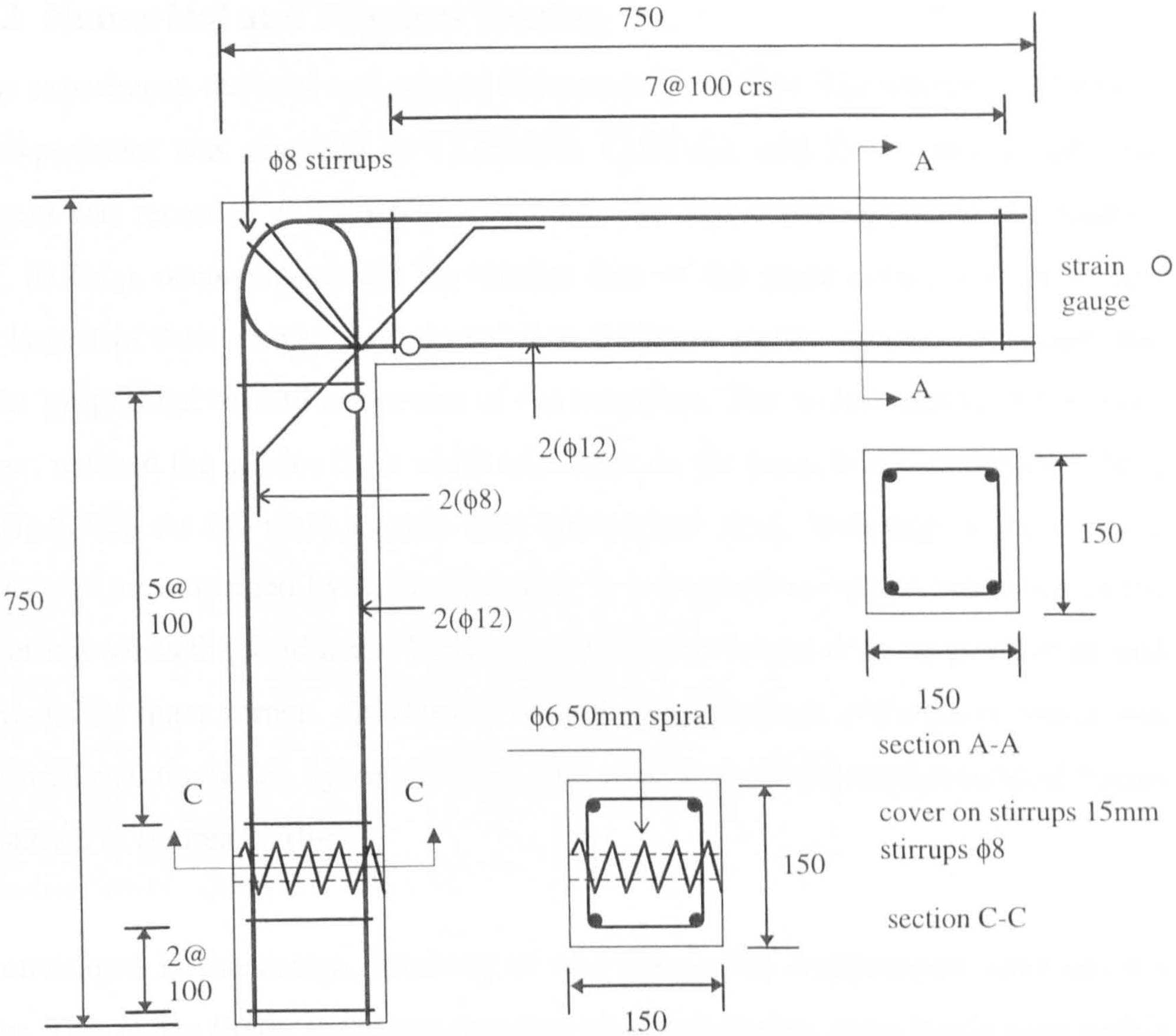

fig8.7b(i) Corner FJ2B Reinforcement Details

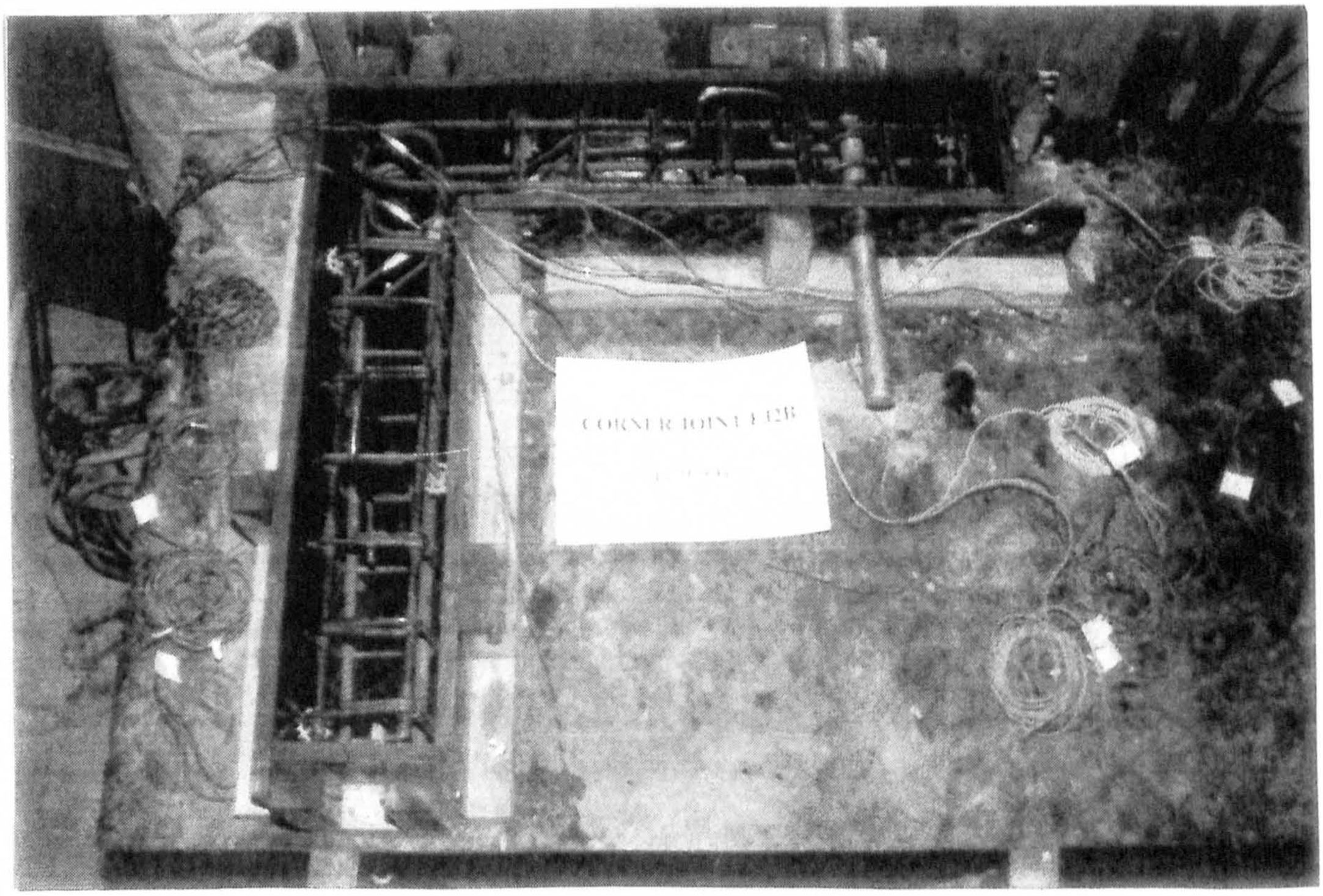

fig.8.7b(ii) Corner FJ2B: Reinforcement Layout & Formwork

8.7.2 Numerical and Physical Testing

In the experiment, the load was applied in increments of 2kN. The ultimate moment in the experiment was recorded as 12.48kNm, ($1.04M_d$), and the numerical ultimate moment was recorded as 12.6kNm, ($1.05M_d$). The first cracks appeared at a load of 4kN, ($0.2M_d$), occurring around the tension face of the inner corner, see fig.8.7(d). The largest of these cracks was measured as 0.05mm. As the moment increased, the cracks propagated toward the centre of the members. The widest crack, at the inner corner, reached the service limit width of 0.3mm on the seventh increment, ($0.73M_d$), see fig.8.7(e). As the main tension steel approached yield, widening of the existing cracks was accompanied by further cracking in a diagonal along the outer face of the corner known as the dead zone. Yielding of the main vertical steel occurred at around $0.9M_d$ in the inner corner. At ultimate load, the largest crack at the inner corner was measured as 0.6mm, see figures 8.7(f-g). The experimental and numerical steel strains are shown in figures 8.7(h-j).

As envisaged in the design, crushing of concrete in the compression zone did not occur. This is due firstly to the fact that the calculated design stress levels were within those permitted, and secondly due to the additional contribution to strength from the additional steel in the compressive zone. The numerical compressive stresses in the corner are shown in figures 8.7(l-m). It can be seen that the largest compressive stress in the concrete is around $0.32f_{cu}$. The sudden increases in stress observed at points C, F and E correspond to the formation of cracks on the tension side of the beam and column, close to the inner corner.

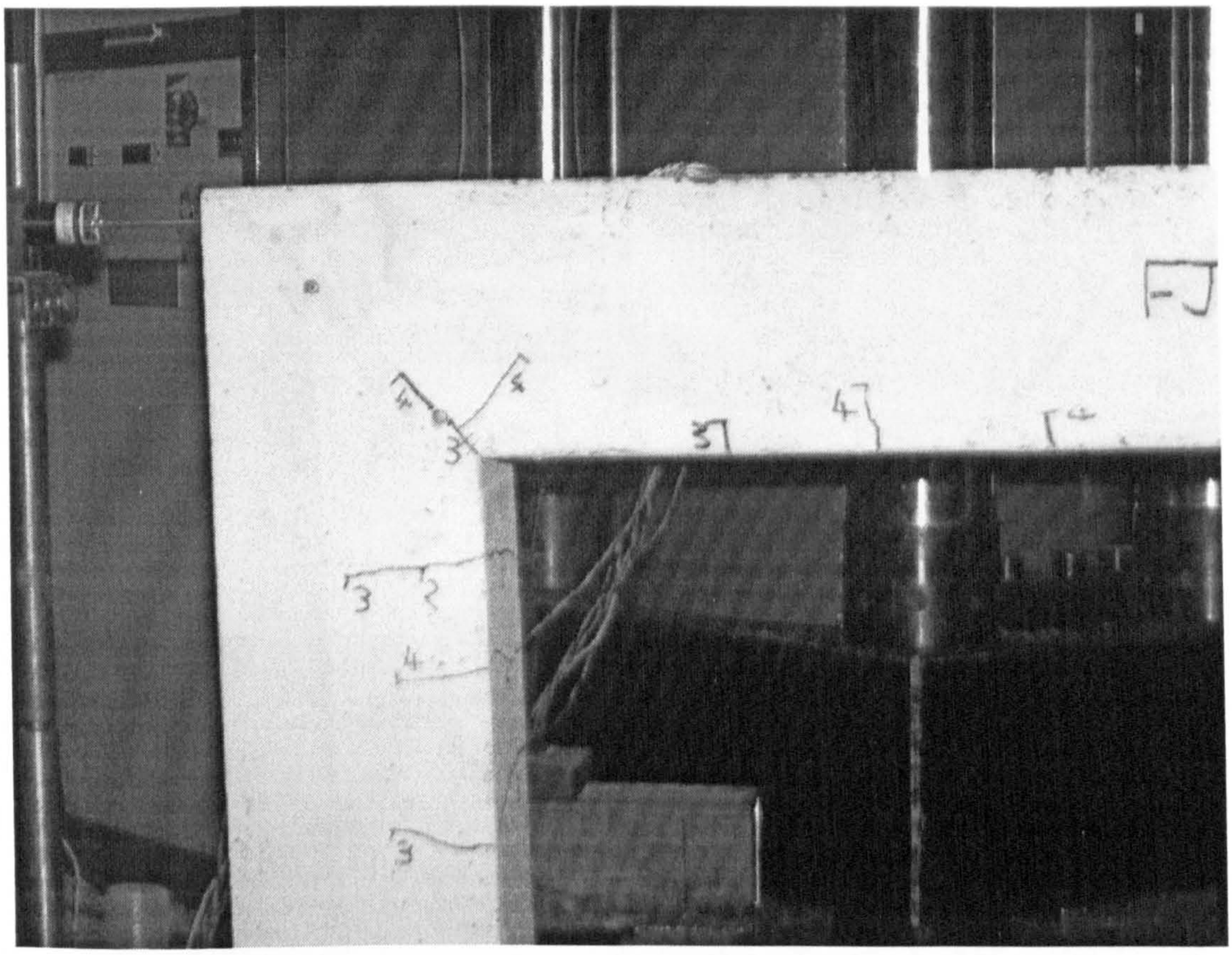

fig.8.7(d) Corner FJ2B ($0.42M_d$)

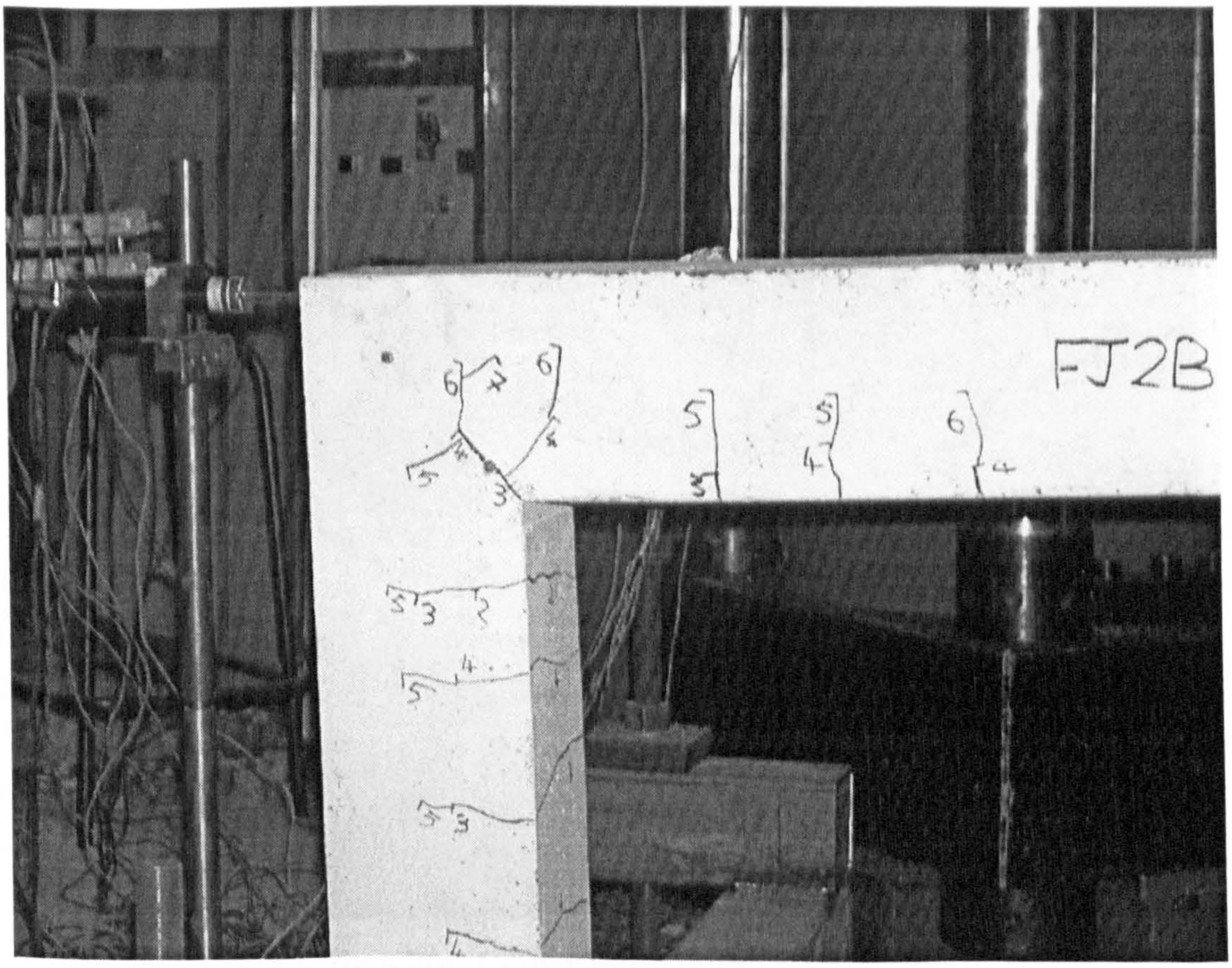

fig.8.7(e) Corner FJ2B ($0.73M_d$)

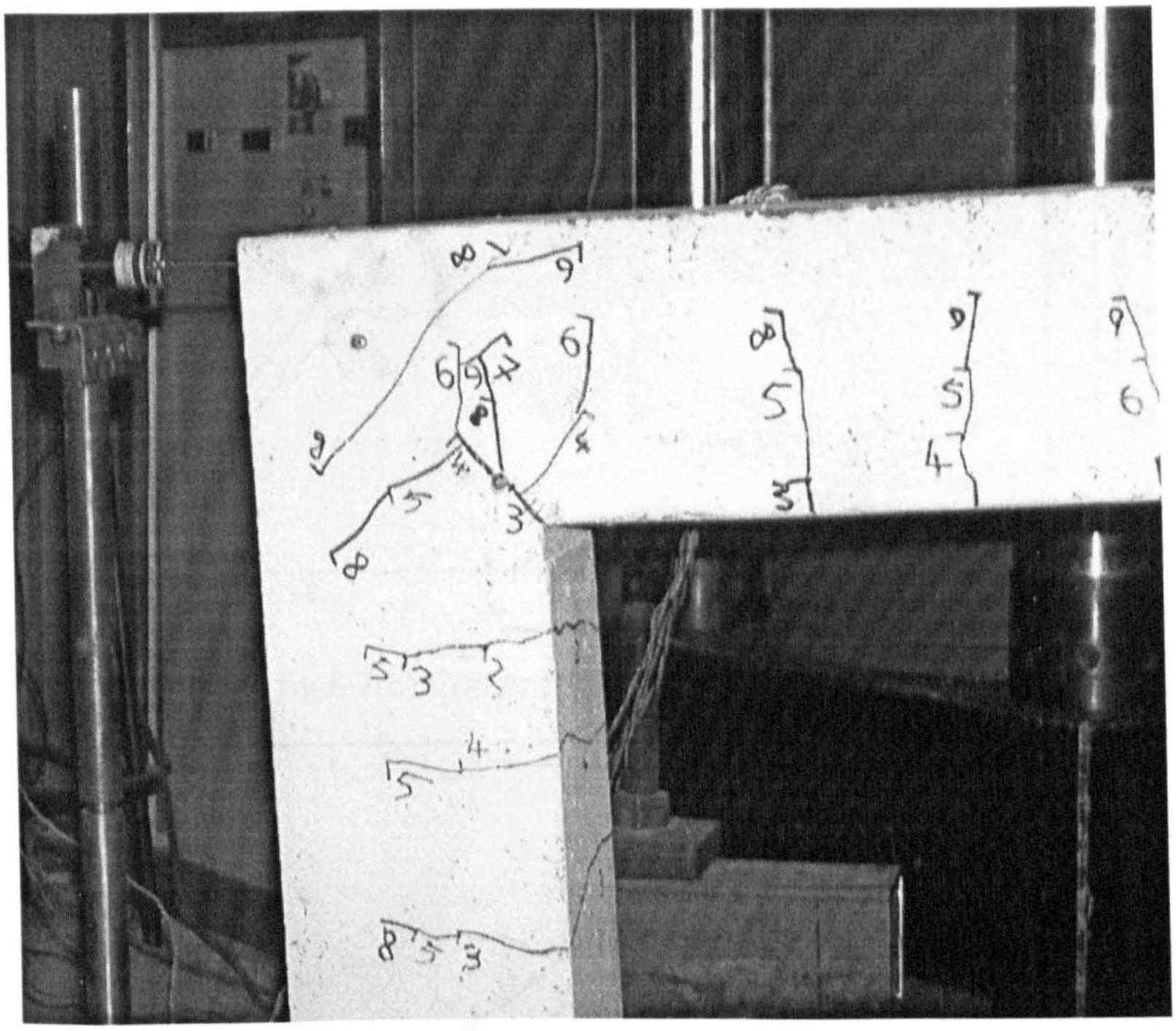

fig.8.7(f) Corner FJ2B at ultimate ($1.04M_d$)

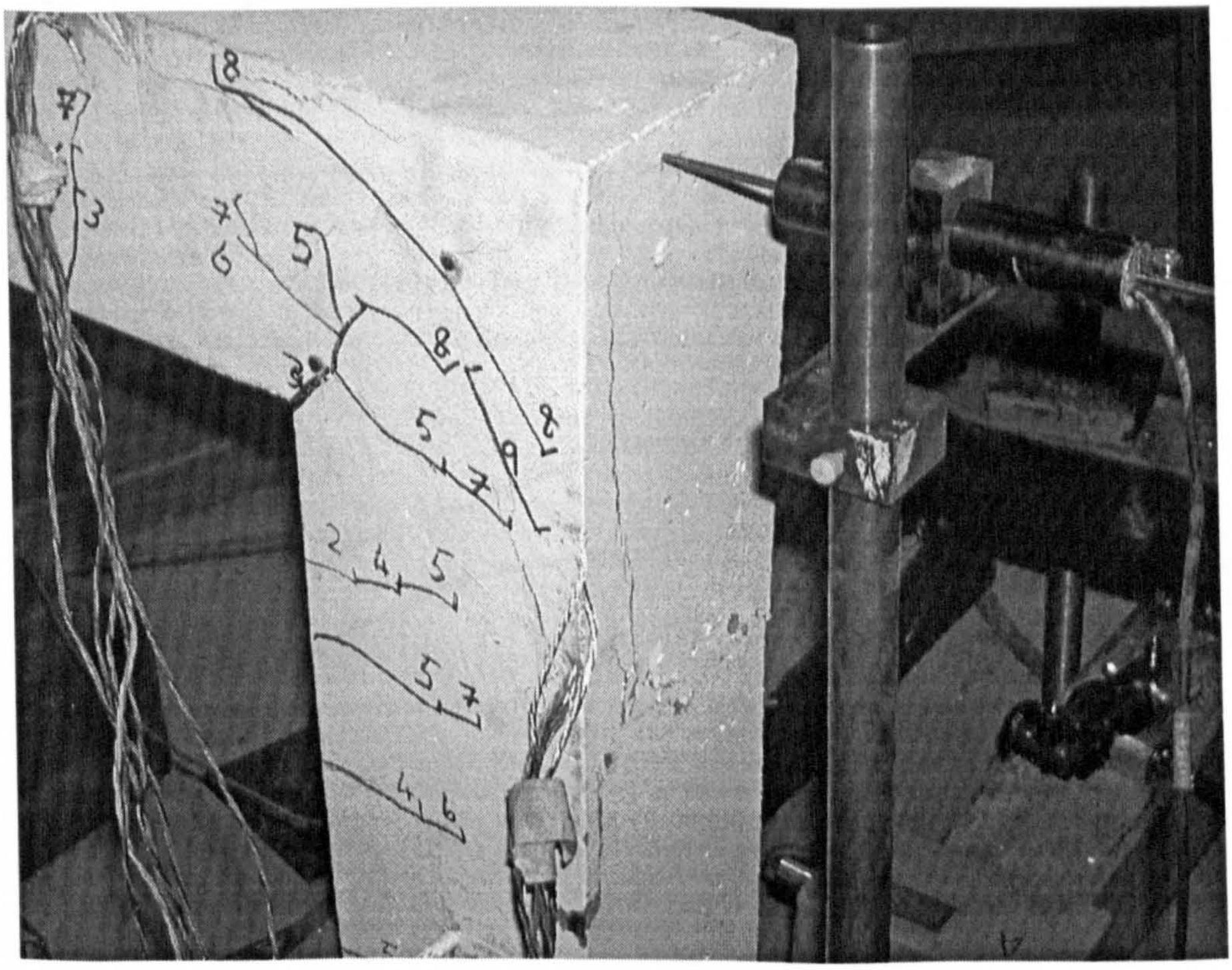

fig.8.7(g) Corner FJ2B at ultimate ($1.04M_d$)

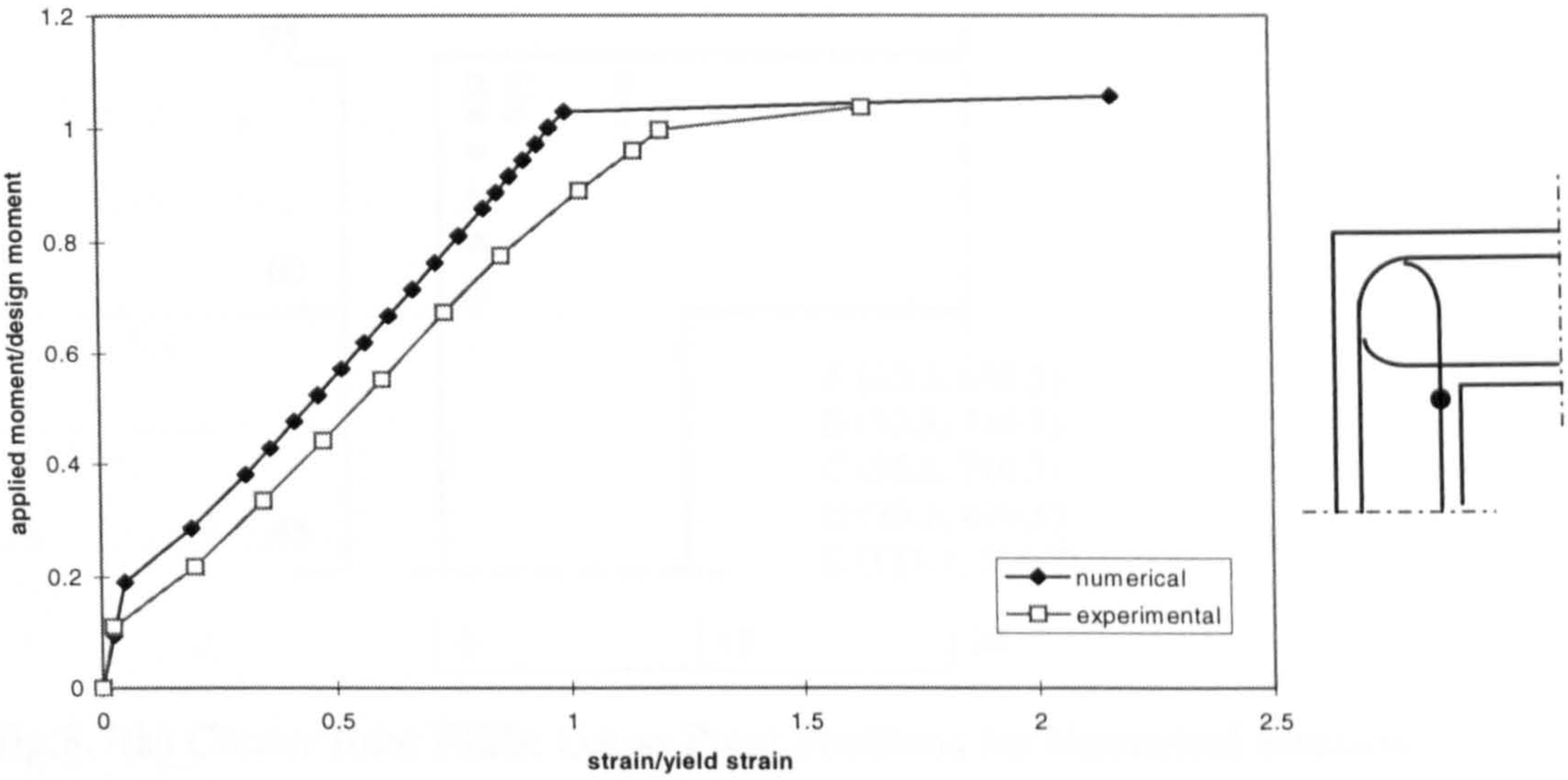

fig.8.7(h) Corner FJ2B Main Steel Strains

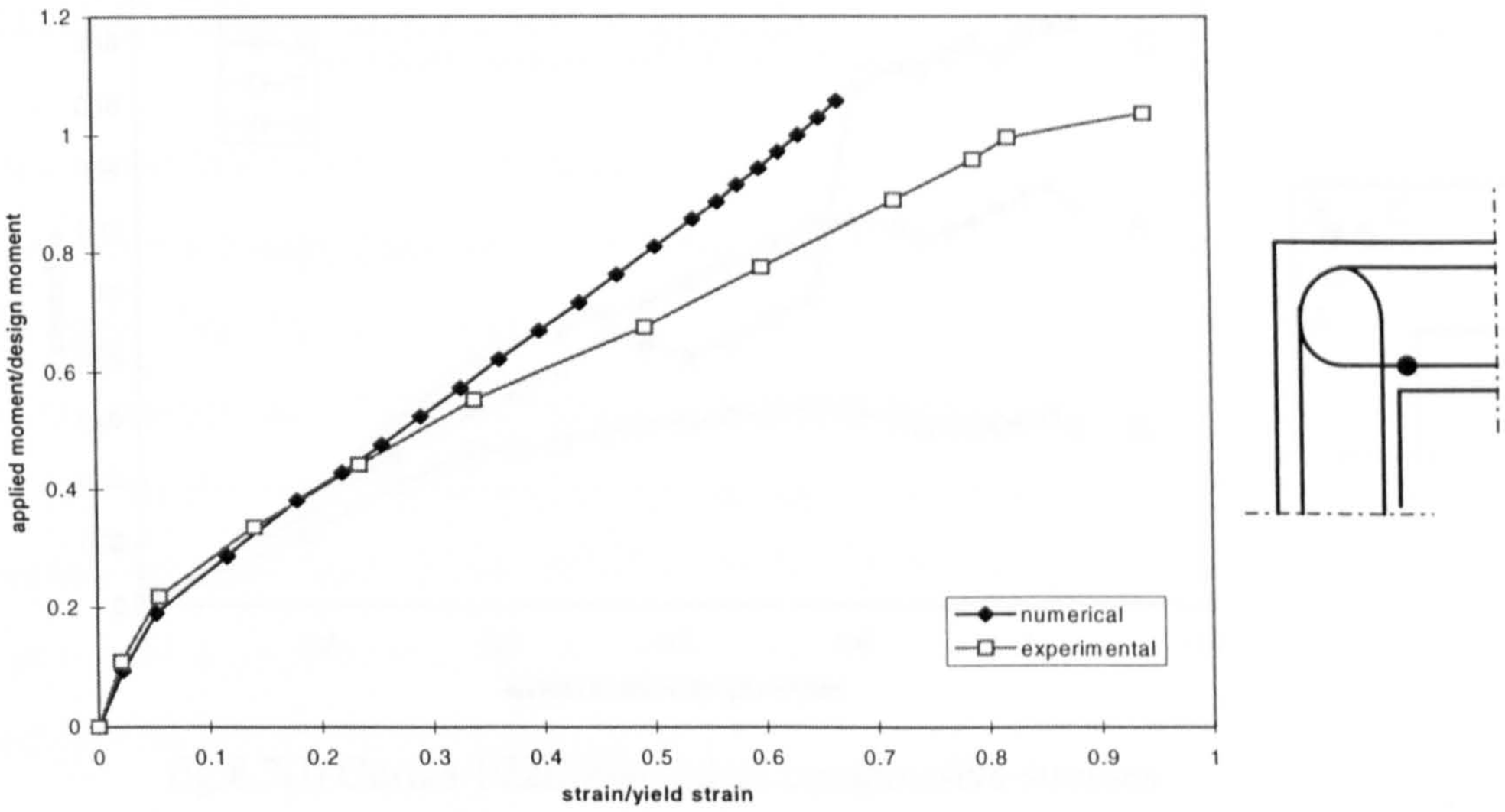

fig8.7(i) Corner FJ2B Main Steel Strains

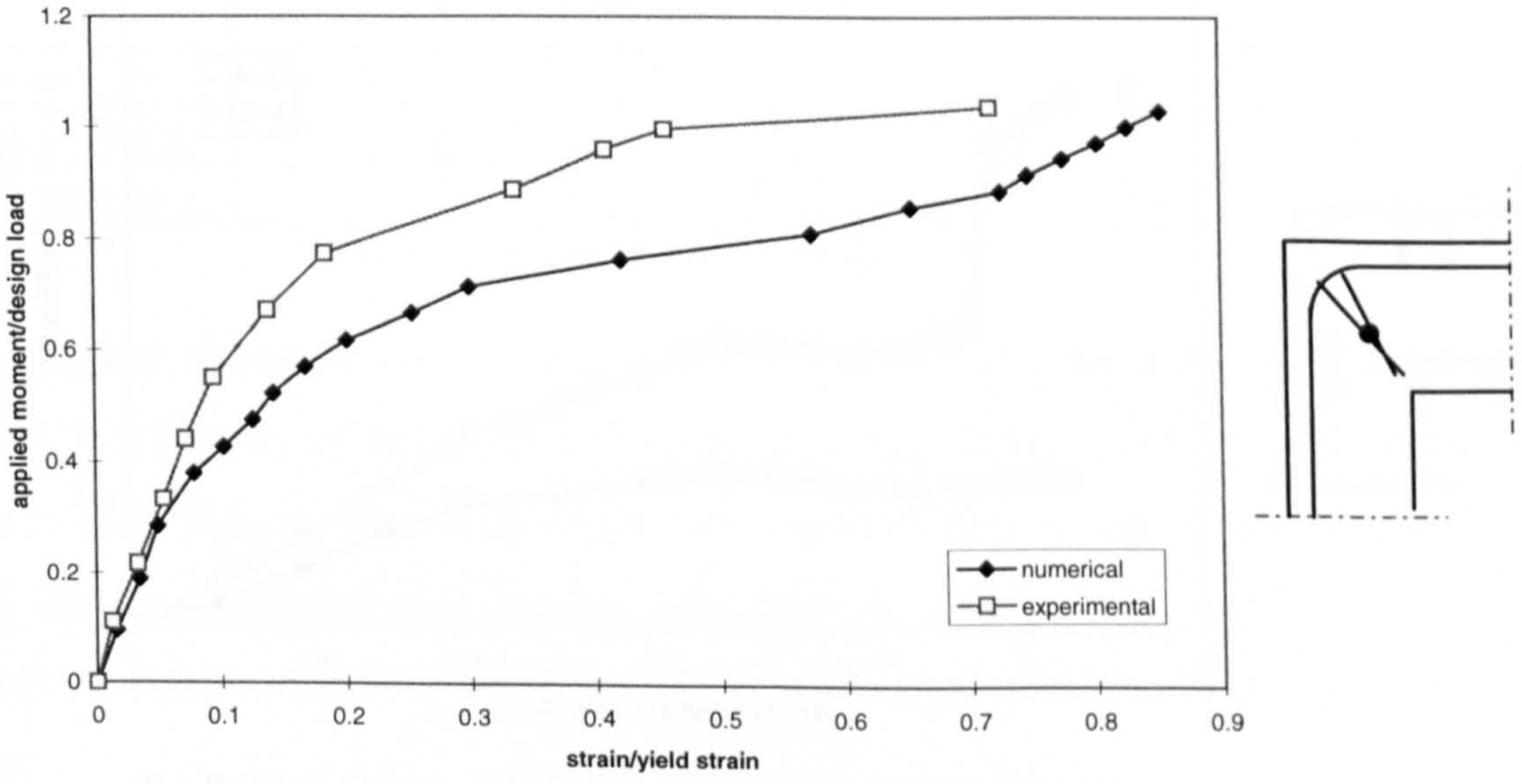

fig8.7(j) Corner FJ2B Diagonal Steel Strains

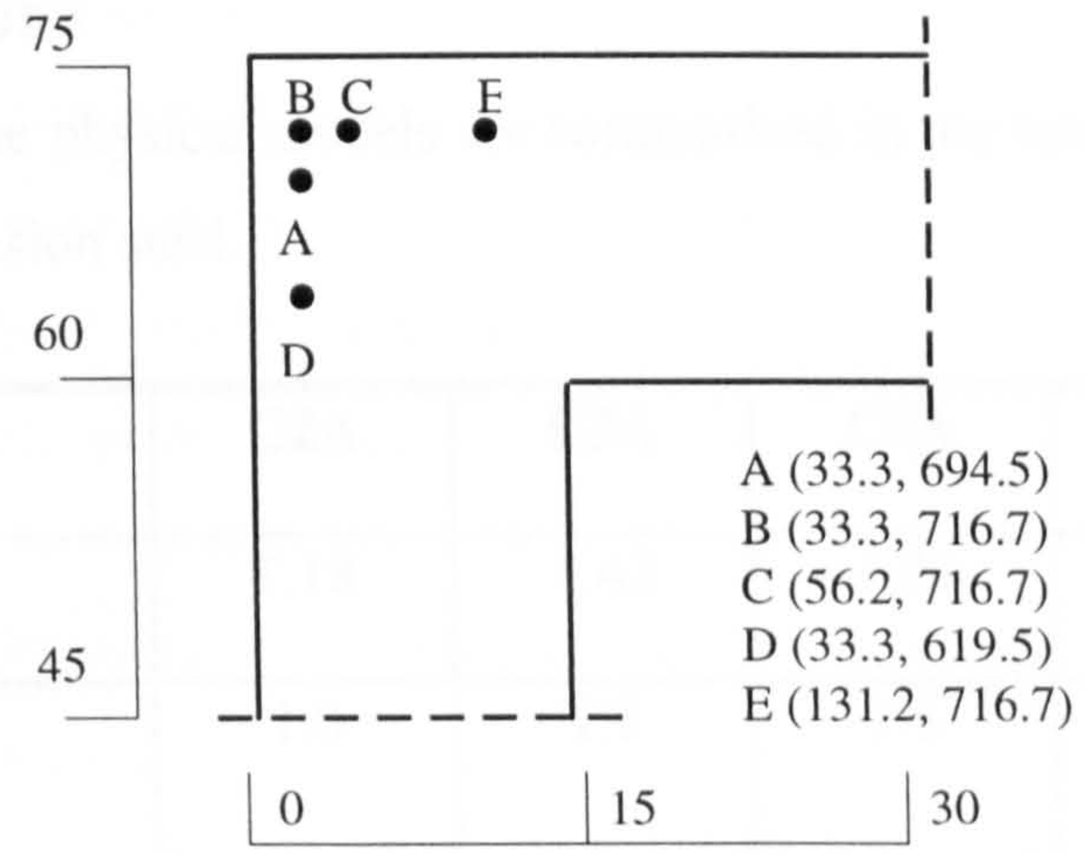

fig.8.7(k) Corner Joint FJ2B: Gauss Point Positions for Numerical Stresses

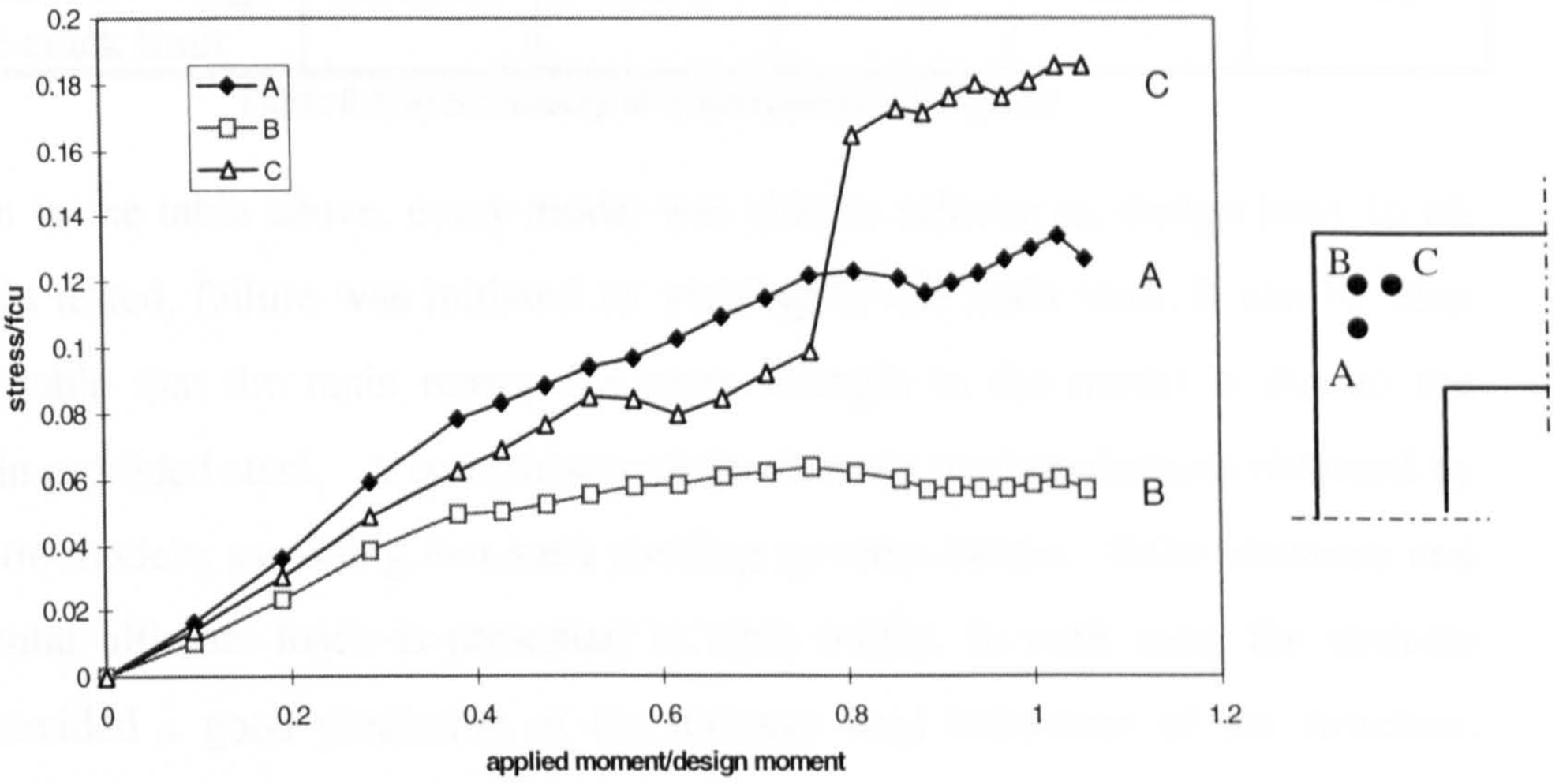

fig.8.7(l) Corner FJ2B Numerical compressive stresses

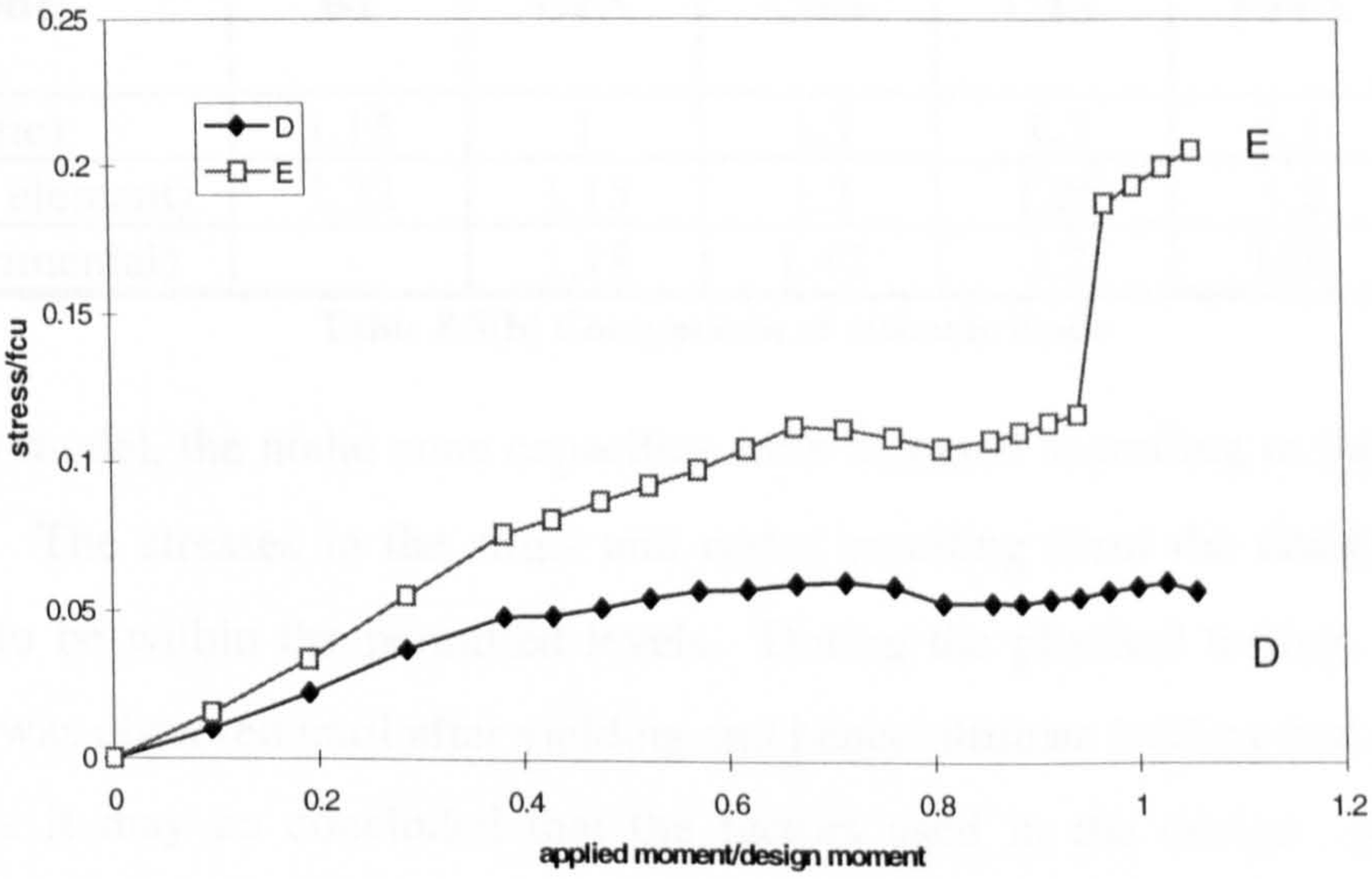

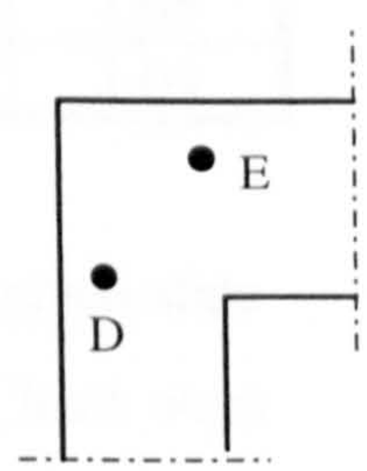

fig.8.7(m) Corner FJ2B Numerical compressive stresses

8.8 Conclusions

The results from the physical models are summarised in the table below, where A_{st} is the total area of tension steel.

Model	C2A	C3A	C4A	FJ1A	FJ2B
P/P_d	1.18	1.42	1.20	1.08	1.04
$\frac{A_{st}\,provided}{A_{st}\,required}$	1.0	1.3	1.3	1.1	1.1
Load at first fielding of main steel	$1.1P_d$	$1.3P_d$	$1.2P_d$	$1.1P_d$	$0.9P_d$
Load at first reaching service crack limit	$0.78P_d$	$1.0P_d$	$1.15P_d$	$0.8P_d$	$0.7P_d$

Table 8.8(a) Summary of Experimental Program

As shown in the table above, every model was able to achieve its design load. In all the models tested, failure was initiated by yielding of the main steel. It can be seen from the table that the main reason for extra strength in the model is due to the increase in provided steel. A comparison of the ultimate load predictions obtained by the strut-tie models, assuming that steel yielding governs failure, finite elements and experimental ultimate loads is presented in table 8.8(b). In each case, the strut-tie model provided a good prediction of the ultimate load behaviour of the structure, comparable with that of the finite element model.

Model	B1	C2A	C3A	C4A	FJ1A	FJ2B
P_u (strut-tie)	1.15	1	1.3	1.3	1.1	1.1
P_u (finite element)	1.32	1.15	1.3	1.25	1.2	1.05
P_u (experimental)	-	1.18	1.42	1.2	1.08	1.04

Table 8.8(b) Comparison of ultimate loads

For every model, the nodal zone capacities were assessed according to the given state of stress. The stresses in the struts and nodes resulting form the design load were checked to be within the permitted levels. During the physical testing, no concrete crushing was observed until after yielding and hence ultimate loading had occurred. From this it may be concluded that the factors used in the design process were adequate.

It was also shown that the strut and tie method as a design tool, can produce designs with comparable performance to the direct design procedure. The advantage that the strut-tie method has over the direct design method is that it allows the designer to gain an insight into the load carrying behaviour of the structure. It would be possible to use the direct design procedure in combination with the visualisation process for plane stress applications as was done for slabs in chapter 6. However, some difficulties in this application may arise due to the fact that the steel must be orientated to the principal stress directions in each element.

Chapter 9

Conclusions

9.1 Summary

The main stress paths in a structure were isolated using an evolutionary procedure, termed as visualisation. Using these stress paths, strut and tie models were developed and reinforcement layouts designed accordingly. These stress fields, were also used for the direct design of reinforced concrete slabs. All the designed structures were tested numerically using non-linear finite elements, and a number of structures were tested physically in the laboratory.

9.2 Slab Design

- Design using the visualisation process results in satisfactory behaviour both at service and ultimate loads
- The method does not always result in a practical reinforcement layout and it is often found that a greater quantity of steel than the numerical amount is required for practical considerations. This increase in provided steel often leads to higher ultimate loads being achieved.
- The visualisation process is not always applicable in slabs where the stresses are evenly distributed, such as in a 2-way simply supported slab subject to a uniformly distributed load. It is necessary for there to be a good spread of initial elastic stresses before visualisation can be effective.
- The degree of mesh refinement does not have on effect upon the direction of the evolved stress paths. However, it is necessary to use a mesh fine enough to model the stress variation adequately.

- In areas where a reinforcement layout is anticipated by the designer, e.g. in situations dictated by practical considerations, the visualisation process can be very useful.

9.3 Strut and Tie Design

- The visualisation process is useful in developing strut-tie models. The re-distribution of stress caused by the evolutionary process is similar to the re-distribution taking place in the actual reinforced concrete structure.
- Design from strut and tie models can produce satisfactory behaviour both at ultimate and service loads.
- As a design tool, the strut and tie method can produce designs comparable to the direct design method. In addition, the strut and tie method helps the designer to understand the load carrying mechanism of the structure whereas the direct design method may often be treated as a 'black box' type system.
- As an analytical tool, strut and tie models can lead to ultimate load predictions with comparable accuracy to non-linear finite elements.
- Nodal areas are the critical areas in the structure and the strut strength used for design must take into account the stress state of the node. Sometimes, compressive stresses in the nodal areas are not evenly spread over the width of the node, but concentrated at a localised point. This may lead to compressive stresses in excess of the design strength.

9.4 Suggestions for Further Work

- All the structures designed in this work were subjected to a single load case. The method can be extended to multiple load cases. In this scenario, it may be necessary to use more refined meshes in anticipation of more complicated stress paths. Similarly more complex structures could be examined.
- The use of designer intervention in the stress path evolution should be further developed both in slab design and in strut-tie model development.
- Further investigation in nodal zone behaviour is necessary. In particular the nature of compressive stress concentrations such as the funnelling effect observed in the corbels.

References

1. Abdel-Hafez, L.M., 'Direct Design of Reinforced Concrete Skew Slabs', Ph.D. Thesis, University of Glasgow, Civil Engineering Dept., (1986)

2. Abdel-Kader, M., 'Prediction of Shear Strength of Reinforced and Prestressed Concrete Beams by Finite Element Analysis', Ph.D. Thesis, University of Glasgow, Civil Engineering Dept., (1993)

3. Abdul-Wahab, H.M.S. & Salman, S.A.R., 'Effect of Corner Angle on Efficiency of Concrete Joints under Opening Bending Moment' *ACI Structural Journal*, Vol.96, No. 1, pp. 115-121, (Jan/Feb 1999)

4. Adebar, P., Kuchma, D., & Collins, M.P., 'Strut and Tie Models for the Design of Pile Caps: An Experimental Study' *ACI Structural Journal*, Vol. 87, No.1, (Jan/Feb 1990)

5. Adebar, P., & Zhou, L.Z., 'Bearing Strength of Compressive Struts Confined by Plain Concrete' *ACI Structural Journal*, Vol. 90, No.5, (Sep/Oct 1993)

6. Adebar, P. & Zhou L.Z., 'Design of Deep Pile caps by Strut and Tie Models' *ACI Structural Journal*, Vol. 93, No.4, (Jul/Aug 1996)

7. Ahmad, S.H., & Mallare M.P., 'A Comparative Study of Models for Confinement of Concrete by Spirals' *Magazine of Concrete Research*, Vol 46, No.166, pp.49-56, (Mar 1994)

8. Al-Mahaidi, R.S.H., 'Non-linear Finite Element Analysis of Concrete Deep Members' Report No. 79-1, Cornell University, (Jan 1979)

9. Almusallam, T.H.,& Alsayed S.H., 'Stress-Strain Relationship of Normal, High Strength and Lightweight Concrete' *Magazine of Concrete Research*, Vol 47, No.170, pp.39-44, (May 1995)

10. Alshegeir, A., & Remirez, J.A., 'Strut-tie Approach in Pretensioned Deep Beams' *ACI Structural Journal*, Vol. 89, pp.296-304 (1992)

11. Alshegeir, A., & Remirez, J.A., 'Computer graphics in Detailing Strut-tie models' *ASCE Journal of Computing in Civil Engineering*, No.6, pp.220-232 (1992)

12. Armer, G.S.T., Discussion of Ref. 129. *Concrete*, Vol. 2, pp.319-320, (Aug. 1968)

13. Bazant, Z.P., & Cedolin , L., 'Fracture Mechanics of Reinforced Concrete', *ASCE Journal of Mechanical Division*, Vol. 106, pp.1287-1306, (1980)

14. Bell, J.C., & Elms, D.G., 'Finite Element Approach to Post-elastic Slab Behaviour'
ACI Special Publications, SP30-15, pp.325-344, (Mar 1971)

15. Bensalem, A., 'Direct Design of RC Structures using Non-elastic Stress Fields'
Ph.D. Thesis, University of Glasgow, Civil Engineering Dept. (1993)

16. Bergmeister, K., Breen, J.E., & Jirsa, J.O., 'Dimensioning of the Nodes in and Development of Reinforcement'
IABSE Colloqium, Stuttgart, Germany, pp.551-556, (1991)

17. BS8110 Part 1 & 2, 'Structural Use of Concrete'
British Standards Inst., (1985)

18. Buyukozturk, O., Nilson, A.H., Slate, F.O., 'Stress-Strain Response and Fracture of a Concrete Model in Biaxial Loading'
ACI Journal, Vol.68, pp. 590-599, (Aug 1971)

19. Cedolin, L. & Deipoli, S., 'Finite Element Studies of Shear Critical Reinforced Concrete Beams'
ASCE Journal of Mech. Div., Vol.103, No.EM3, pp.359-410, (Jun 1972)

20. Cervenka, V., Gerstle, K., 'Inelastic Analysis of Reinforced Concrete Panels Part 1: Theory'
IABSE Publications, Vol. 31-II, (1971)

21. Cervenka, V., Gerstle, K., 'Inelastic Analysis of Reinforced Concrete Panels Part 2: Experimental Verification and Application'
IABSE Publications, Vol. 31-II, (1971)

22. Chen, W.F., 'Plasticity in Reinforced Concrete',
McGraw Hill, New York, ISBN 0-07-010687-8, (1982)

23. Clark, L.A., 'The Provision of Tension and Compression Reinforcement to Resist In-plane Forces'
Magazine of Concrete Research, Vol 28, No. 94, (Mar 1976)

24. Clark, L.A., & Speirs, D.M., 'Tension Stiffening in RC Beams and Slabs under Short Term Load'
Cement & Concrete Association, Technical Report 42.521, (1978)

25. Collins, M.P., Vecchio, F.J. & Mehlhorn, G., 'An International Competition to Predict the Response of Reinforced Concrete Panels'
Canadian Journal of Civil Engineering, Vol.12, pp.624-644, (1985)

26. Collins, M.P., & Mitchell, D., 'A Rational Approach to Shear Design - The 1984 Canadian Code Provisions'
ACI Journal, (Nov/Dec 1986)

27. Collins, M.P., Mitchell, D., Adebar, P., & Vecchio, F.J., 'A General Shear Design Method'
ACI Structural Journal, Vol. 93, No.1, (Jan/Feb 1996)

28. Cook, W.D., & Mitchell, D., 'Studies of Disturbed Regions near Discontinuities in Reinforced Concrete Members'
ACI Structural Journal, (Mar/Apr 1988)

29. Cope, R.J., & Vasudeva Rao P., 'Non-linear Finite Element Analysis of Concrete Slab Structures'
Proceedings of ICE, Vol 63, Part 2, pp. 159-179, (Mar 1977)

30. Crisfield, M.A., 'Non-Linear Finite Element Analysis of Solids and Structures, vol. 1: Essentials'
John Wiley & Sons, (1991)

31. Desayi, P., & Krishnan, S., 'Equation for the Stress-Strain Curve of Concrete'
Journal of the American Concrete Institute, (Mar 1964)

32. Eibl, J., Akkermann, J., Idda, K., Lucero-Cimas H, 'Rotational Behaviour of Reinforced Concrete Corners and bond under Lateral Tension'
CEB Bulletin d'Information, No. 242, 'Ductility of Reinforced Concrete Structures', (May 1998)

33. El-Mezaini, N., & Citipitioglu, E., 'Finite Element Analysis of Prestressed and Reinforced Concrete Structures'
ASCE Journal of Structural Engineering, Vol. 117, No.10, (Oct. 1991)

34. Elwi, A.E., & Hrudey, M.T., 'Finite Element Model for Curved Embedded Reinforcement'
ASCE Journal of Mech. Div., Vol. 115, No.4, pp.740-754 (Apr 1989)

35. Foster, S.J., & Gilbert, R.I., 'Experimental Studies on High-Strength Concrete Deep Beams'
ACI Structural Journal, Vol. 95, No.4, (Jul/Aug 1998)

36. Gerstle, K,H, 'Simple Formulation of Biaxial Concrete Behaviour'
ACI Journal, (Jan/Feb 1991)

37. Gopalaratnam, V.S., & Shah, S.P., 'Softening Response of Plain Concrete in Direct Tension',
ACI Journal, Vol.82, pp. 310-322, (1985)

38. Gupta, A.K., Akbar, H., 'Cracking in Reinforced Concrete Analysis'
ASCE Journal of Structural Eng., Vol.110, No.8, pp.1735-1747, (Aug. 1984)

39. Hagberg, T., 'Design of Concrete Brackets: On the Application of the Truss Analogy'
ACI Journal, Vol.80, pp. 3-12, (Jan/Feb 1983)

40. Hago, W.A., 'Direct Design of Reinforced Concrete Slabs'
PhD Thesis, University of Glasgow, Civil Engineering Dept., (1982)

41. Hago, W.A., & Bhatt, P., 'Tests on Reinforced Concrete Slabs Designed by Direct Design Procedure'
ACI Journal, (Nov/Dec 1986)

42. Hermansen, B.J. & Cowan, J., 'Modified Shear-friction Theory for Bracket Design'
ACI Journal, Vol. 71, No.2, pp.3-12, (Feb 1974)

43. Hillerborg, A., 'Reinforcement of Slabs and Shells Designed According to the Theory of Elasticity'
Betong, 38(2), pp.101-109, (1953)

44. Hong, S.G., 'Truss Model for Tension Bars in Reinforced Concrete Beams: Tension-Tension-Compression Regions'
ACI Structural Journal, Vol. 93, No.6, (Nov/Dec 1996)

45. Huang, F.C., Lee, I.S.,& Mo, Y.L., 'Designing Pier Caps with Strut and Tie Models'
Concrete International, 43-47, (Jan 1998)

46. Issa, M.A., & Tobaa, H., 'Strength and Ductility Enhancement in High Strength Confined Concrete'
Magazine of Concrete Research,Vol 46, No.168, pp.177-189, (Sep 1994)

47. Jackson, N., 'Design of Reinforced Concrete Opening Corners'
The Structural Engineer, Vol. 73, No.13, (Jul.1995)

48. Jain, S.C., & Kennedy, J.B., 'Yield Criterion for Reinforced Concrete Slabs'
Proceedings of ASCE, Journal of the Structural Division, Vol. 100, (Mar 1974)

49. Jofriet, J.C., & McNeice, G.M., 'Finite Element Analysis of Reinforced Concrete Slabs'
Proceedings of ASCE, Journal of the Structural Division, (Mar 1971)

50. Johnarry, T., 'Elasto-plastic Analysis of Concrete Structures using Finite Elements',
Ph.D. Thesis, University of Strathclyde, Dept. of Civil Eng., (May 1979)

51. Kemp, K.O., 'Optimum Reinforcement in a Concrete Slab Subjected to Multiple Loading'
IABSE Publication, Vol. 31, pp. 93-105, (1971)

52. Kent, D.C., & Park, R, 'Flexural Members With Confined Concrete',
Proceedings of ASCE, Journal of the Structural Division, Vol. 61, (Jul 1971)

53. Khaskheli, G.B., 'Direct Design of Reinforced Concrete Transfer Girders'.
Ph.D. Thesis, University of Glasgow, Civil Engineering Dept., (1989)

54. Kong, F.K., Robins, P.J., & Cole, D.F., 'Web Reinforcement Effects on Deep Beams'
ACI Journal, (Dec 1970)

55. Kong, F.K., Robins, P.J., Kirby, D.P. & Short, D.R., 'Deep Beams with Inclined Web Reinforcement'
ACI Journal, Vol.69, pp. 172-176, (Mar. 1972)

56. Kong, F.K., Robins, P.J., Singh, A., & Sharp, G.R., 'Shear Analysis and Design of Reinforced Concrete Deep Beams'
The Structural Engineer, Vol. 50, No.10, (Oct. 1972)

57. Kong, F.K., & Sharp, G.R., 'Structural Idealization for Deep Beams with Web Openings'
Magazine of Concrete Research, Vol. 29, No. 99, pp.81-91, (Jun. 1977)

58. Kong, F.K., Sharp, G.R., Appleton, S.C., Beaumont, C.J, & Kubik, L.A., 'Structural idealization for Deep Beams with Web Openings: Further Evidence'
Magazine of Concrete Research, Vol. 30, No. 103, (Jun. 1978)

59. Kong, F.K., 'Reinforced Concrete Deep Beams',
Blackie and Son Ltd, Glasgow, ISBN 0-216-92695-5, (1990)

60. Kotsovos, M.D., & Pavlovic, M.N., 'Structural Concrete Finite Element Analysis for Limit State Design'
Thomas Telford Publications, London, ISBN 0-7277-2027-9, (1995)

61. Kriz, L.B. & Raths C.H., 'Connections in Precast Concrete Structures: Strength of Corbels'
Journal of The Prestressed Concrete Inst., Vol. 10, No.1, pp.16-61, (Feb 1965)

62. Kupfer, H., Hilsdorf, H.K. & Rusch, H., 'Behaviour of Concrete Under Bi-axial Stresses'
ACI Journal, Vol.66, pp. 656-667, (Aug 1969)

63. Leonhardt, F., 'Reducing the Shear reinforcement in RC beams and Slabs'
Magazine of Concrete Research 17, No.53 (1965)

64. Liu, T.C.Y., Nilson, A.H., & Slate, F.O., 'Stress-Strain Response and Fracture of Concrete in Uniaxial and Biaxial Compression'
ACI Journal, Vol.69, pp. 291-295, (May. 1972)

65. MacGregor, J.G., 'Reinforced Concrete Mechanics and Design'
Prentice-Hall, Englewood Cliffs, N.J., (1988)

66. Manickarajah, D., Xie, Y.M., & Steven, G.P., 'An Evolutionary Method for Optimization of Plate Buckling Resistance'
Finite Elements in Analysis & Design, Vol.29, pp.205-230, (1998)

67. Mansur, A., Wee, T.H., Chin, M.S., 'Derivation of the Complete Stress-Strain Curves for Concrete in Compression'
Magazine of Concrete Research,Vol 47, No.173, pp.285-290, (May 1994)

68. Marti, P., 'Basic Tools of RC Beam Design'
Journal of the American Concrete Inst. 82, pp.46-56, (1985)

69. Marti, P., 'Truss Models in Detailing'
Concrete International, (Dec 1985)

70. Marti, P., 'Dimensioning and Detailing'
IABSE Colloqium, Structural Concrete, Stuttgart, (1991)

71. Mast, R.F., 'Auxiliary Reinforcement in Concrete Connections'
Proceedings of ASCE, Journal of the Structural Division, (Jun 1968)

72. Mattock, A.H., Chen, K.C., Soongswang, K., 'The Behaviour of Reinforced Concrete Corbels'
Journal of The Prestressed Concrete Inst, Vol.21, No.2, pp.52-77, (Mar/Apr 1976)

73. Mayfield, B., Kong, F.K., Bennison, A., & Davies, J.C.D.T, 'Corner Joint Details in Structural Lightweight Concrete'
ACI Journal, Vol.68, pp. 366-372, (May 1971)

74. Mayfield, B., Kong, F, & Bennison, A., 'Strength and Stiffness of Lightweight Concrete Corners'
ACI Journal, Vol.69, pp. 420-427, (Jul. 1972)

75. Meyer, C. & Bathe, K.J.,'Non-linear Analysis of R.C Structures in Practice',
Proceedings of ASCE, Journal of the Structural Division, Vol. 108, No.7, pp.1605-1622, (Jul 1982)

76. McNeice, A.M., 'Elastic-Plastic Bending of Plates and Slabs by the Finite Element Method'
PhD. Thesis, London University, (1967)

77. Millar, S.G. & Jonson, R.P., 'Shear Transfer in Cracked Reinforced Concrete'
Magazine of Concrete Research, Vol.37, No.130, pp.3-15, (1985)

78. Morsch, E., 'Concrete-steel Construction',
English Translation by E.P. Goodrich, MacGraw-Hill, New York, (1909)

79. Muller, P., 'Failure Mechanisms for RC Beams in Torsion & Bending'
International Association for Bridge & Structural Engineering
Publications 36-II, 147-163 (1976)

80. Ngo, D. & Scordelis, A.C., 'Finite Element Analysis of R.C. Beams',
ACI Journal, Vol.64, No.3, pp. 152-163, (1967)

81. Nielsen, M.P., 'Yield Condition for Reinforced Concrete Shells in the Membrane State, Non Classical Shell Problems'
IASS Symposium, Warsaw 1963, Ed. W.Olsak, Amsterdam, North Holland Publishing Co., pp.1030-1038, (1964)

82. Nielsen, M.P., Braestrup, M.W., Jensen, B.C., Bach. F., 'Concrete Plasticity, Beam Shear-Shear in Joints-Punching Shear'
Spec. Publ., Danish Soc. for Stuct. Sci. & Engrg., Tech. University of Denmark, Lyngby, (1978)

83. Nielsen, M.P., 'Limit Analysis and Concrete Plasticity',
Prentice Hall, New Jersey, (1984)

84. Nilsson, I.H., & Losberg, A.,Discussion of ACI Paper 'Opportunities in Bond Research'
ACI Journal, Vol.67, pp. 393-396, (May 1971)

85. Nilsson, I.H., & Losberg A., 'Reinforced Concrete Corners and Joints Subjected to Bending Moments'
Proceedings of ASCE, Journal of the Structural Division, Vol. 102, pp.1229-1254, (Jun 1976)

86. Noor, F.A., 'Ultimate Strength and Cracking of Wall Corners'
Concrete, Vol. 11, pp. 31-35, (Jul. 1977)

87. Park, R., & Paulay, T., 'Reinforced Concrete Structures'
John Wiley and Sons Inc., London, ISBN 0-471-65917-7, (1975)

88. Phillips, D.V., & Zienkiewicz, O.C., 'Finite Element Non-linear Analysis of Concrete Structures'
Proc. of the Inst. of Civil Engineers, Part 2, No.61, pp.59-88, (Mar.1976)

89. Phillips, D.V, & Wu, Z.P., 'An Orientated Embedded Bar Formulation with Bond-slip'
Numerical Methods in Engineering; Theory and Application, Ed. Pande and Middleton, J., Vol. 1, pp.320-328, (1990)

90. Popovics, S., 'A Review of Stress-Strain Relationships for Concrete'
ACI Journal, (Mar 1970)

91. Prakhya, G.K.V., & Morely, C.T., 'Tension-Stiffening and Moment-Curvature Relations of Reinforced Concrete Elements'
ACI Structural Journal, Vol. 87, No.5, (Sep/Oct 1990)

92. Ramirez, J.A., & Breen, J.E., 'Evaluation of a Modified Truss-Model Approach for Beams in Shear'
ACI Structural Journal, Vol. 88, No.5, (Sep/Oct 1991)

93. Ranjbaran, A., 'Embedding of Reinforced Concrete Elements Implemented in DENA'
Computers & Structures, Vol. 40, No.4, pp.925-930, (1991)

94. Rashid, Y.R., 'Ultimate Strength Analysis of Reinforced Concrete Pressure Vessels'
Nuclear Engineering and Design, Vol.7, No.4, pp.334-344, (Apr 1968)

95. Reinhardt, H.W., 'Crack Softening Zone in Plain Concrete Under Static Loading',
Cement & Concrete Research, Vol.15, pp.42-52, (1985)

96. Reinke, H.G., 'Assessment of Concrete Tensile Strength in the Design of Structural Concrete'
Thesis, Institut fur Massivbau, Stuttgart, (1986)

97. Renuka Prasad, H.N, Channakeshava, C., Raghu Prasad, B.K., & Sundara Raja Iyengar, K.T., 'Non-linear Finite Element Analysis of Reinforced Concrete Corbel'
Computers & Structures, Vol. 46, No.2, pp 343-354, (1993)

98. Ritter, W., 'Die Bauweise Hennebique', (Hennebique's Construction Method),
Schweizerische Bauzeitung, Zurich, v.17, pp.41-43, 49-52, 59-61, (1899)

99. Rogowsky, D.M., MacGregor J.G., & See, Y.O., 'Tests of Reinforced Concrete Deep Beams'
ACI Journal, (Jul/Aug 1986)

100. Rogowsky, D.M., & MacGregor J.G., 'Design of Reinforced Concrete Deep Beams'
Concrete International, (Aug 1986)

101. Saatcioglu, M., & Razvi, S.R., 'Strength and Ductility of Confined Concrete'
ASCE Journal of Structural Engineering, Vol. 118, No.6, (Jun. 1992)

102. Saint Venant, B de., as quoted in 'Theory of Elasticity', by Timoshenko, S., & Goodier, J.N., "ed., p.33, (1951)

103. Scanlon, A., & Murray, D.W., 'Time Dependent Reinforced Concrete Slab Deflections'
Proceedings of ASCE, Journal of the Structural Division, Vol. 100, No.ST9 pp.1911-1924, (1974)

104. Schlaich, J., Schaefer, K., & Jennewein, M., 'Towards a Consistent Design of Structural Concrete'
Journal of the Prestressed Concrete Inst. 32, pp.74-150, (1987)

105. Schlaich, J., & Schafer, K., 'Design and Detailing of Structural Concrete using Strut and Tie Models'
The Structural Engineer, Vol. 69, No.16, (Mar 1991)

106. Schlaich, M., & Anagnostou, G., 'Stress Fields for Nodes of Strut and Tie Models'
ASCE Journal of Structural Engineering, (Jan. 1990)

107. Siao, W.B., 'Strut and Tie Model for Shear Behaviour in Deep Beams and Pile Caps Failing in Diagonal Splitting'
ACI Structural Journal, Vol. 90, No.6, (Jul/Aug 1993)

108. Somerville, G., & Taylor, H.P.J., 'The Influence of Reinforcement Detailing on the Strength of Concrete Structures'
The Structural Engineer, Vol. 50, No.1, (Jan.1972)

109. Somerville, G., & Taylor, H.P.J., Discussion of reference above
The Structural Engineer, Vol. 50, No.8, (Aug.1972)

110. Somerville, G., 'The Behaviour and Design of Reinforced Concrete Corbels'
Shear in Reinforced Concrete, SP-42, ACI, Vol.2, Detroit, pp.477-502, (1974)

111. Stroband, J. & Kolpa, J.J., 'The Behaviour of Reinforced Concrete Column-Beam Joints, Part 1: Corner Joints Subjected to Negative Moments'
Research Report 5-83-9, Delft University of Technology, Dept. of Civil Engineering, (1983)

112. Suidan, M., Schnobrich, W.C., 'Finite Element Analysis of Reinforced Concrete'
ASCE Journal of Structural Division, Vol.99, No. ST10, pp 2109-2122, (Oct.1973)

113. Sundermann, W., & Schaefer, K., 'Tragfahigkeit von Druckstreben und Knoten in D-Bereichen'
Deutscher Ausschuss fur Stahlbeton, Heft 478 Berlin (1997)

114. Swann, R.A., 'Flexural Strength of Corners of Reinforced Concrete Portal Frames'
Technical Report TRA/434, Cement and Concrete Assoc., London, pp.1-14, (Nov 1969)

115. Tan, K.H., & Mansur, 'Partial Prestressing in Concrete Corbels and Deep Beams'
ACI Structural Journal, Vol. 89, No.3, (May/Jun 1992)

116. Tan, K.H., & Naaman, A.E., 'Strut and Tie Model for Externally Prestressed Concrete Beams'
ACI Structural Journal, Vol. 90, No.6, (Nov/Dec 1993)

117. Tan, K.H., Weng, L.W., & Teng, S., 'A Strut and Tie model for Deep Beams Subjected to Combined Top and Bottom Loading'
The Structural Engineer, Vol 75, No. 13, (Jul. 1997)

118. Tan, K.H., Kong, F.K., & Li, W.W., 'High Strength Reinforced Concrete Deep and Short Beams: Shear Design Equations in North American and UK Practice'
ACI Structural Journal, Vol. 95, No.3, (May/Jun 1998)

119. Tasuji, M.E., Nilson, A.H., & Slate, F.O., 'Biaxial Stess-Strain Relationships for Concrete'
Magazine of Concrete Research, Vol 31, No. 109, (Dec 1979)

120. Taylor, C.P., Cote, P.A., & Wallace, J.W., 'Design of Slender Reinforced Concrete Walls with Openings'
ACI Structural Journal, Vol. 95, No.4, (Jul/Aug 1998)

121. Taylor, R., Maher, D.R.H, & Hayes, B., 'Effect of the Arrangement of Reinforcement on the Behaviour of Reinforced Concrete Slabs'
Magazine of Concrete Research, Vol. 18, No.55, pp.85-94, (Jun 1966)

122. Thurliman, B.,Grob, J., & Luchinger, P., 'Torsion, Biegung und Schub in Stahlbetontragern (torsion, flexure & shear in RC girders)'
Inst. of Structural Engineering, ETH Zurich, (1975)

123. Van Mier, J.G.M.,'Strain-softening of Concrete Under Multi-axial Loading'
Dissertation, Eindhoven University of Technology, Holland, (1984)

124. Van Mier, J.G.M., 'Examples of Non-linear Analysis of Reinforced Concrete Structures with DIANA'
HERON, Vol. 32, No.3, (1987)

125. Vecchio, F.J., & Collins, M.P., 'The Response of Reinforced Concrete to Inplane Shear and Normal Stress'
Publ. No. 82-03, Dep. of Civil Eng., Toronto University, (1982)

126. Vecchio, F.J., & Collins, M.P., 'The Modified Compression-Field Theory for Reinforced Concrete Elements Subjected to Shear'
ACI Journal, (Mar/Apr 1986)

127. Vonk, R.A., 'Softening of Concrete Loaded in Compression'
Dissertation, Eindhoven University of Technology, Holland, (1992)

128. Wegmuller, A.W.,'Elasto-plastic Finite Element Analysis of Concrete Slab Structures'
Proceedings of ICE, Technical Note TN99, Vol.57, pp.535-543, (Sep 1974)

129. Wood, R.H., 'The Reinforcement of Slabs in Accordance with a Predetermined Field of Moments'
Concrete, Vol. 2, pp.69-75, (Feb. 1968)

130. Xie, Y.M., & Steven, G.P., 'A Simple Evolutionary Procedure for Structural Optimization'
Computers & Structures, Vol 49, No.5, pp.885-896, (1993)

131. Xie, Y.M., & Steven, G.P., 'Optimal Design of Multiple Load Case Structures using an Evolutionary Procedure'
Engineering Computations, Vol 11 , pp.295-302, (1994)

132. Yun, Y.M., Alshegeir, A., & Remirez, J.A., 'Strut-Tie Model Design of Disturbed Regions in Concrete Structures'
Proceedings, ASCE Structural Congress XII, Vol. 1, pp.233-238, (1994)

133. Yun, Y.M., & Ramirez, J.A., 'Strength of Struts and Nodes in Strut-Tie Model'
ASCE Journal of Structural Engineering, (Jan. 1996)

134. Yun, Y.M., 'Non-linear strut-tie Model Approach and its Application Tool for Analysis and Practical Design of Structural Concrete'
Kyungpook National University, Korea (1997)

135. Yun, Y.M., 'A Refined Strut-tie model Approach and its Application Tool'
ICE Proc., Structures & Buildings Journal, No.140, pp.13-24, (Feb. 2000)

136. Zienkiewicz, O.C, 'The Finite Element Method'
McGraw Hill Book Company, 3rd Edition, (1977)